CR 137492 16

[redacted]

(NASA-CR-137492) SYSTEM DESIGN OF THE PIONEER VENUS SPACECRAFT. VOLUME 5: PROBE VEHICLE STUDIES Final Report (Hughes Aircraft Co.) 623 p HC $34.25 CSCL 22B G3/31
N74-27373
Unclas
[illegible]

FINAL REPORT
SYSTEM DESIGN OF THE PIONEER VENUS SPACECRAFT

VOLUME 5
PROBE VEHICLE STUDIES

By
L. J. NOLTE
D. S. STEPHENSON
ET AL.

July 1973

JUL 1974
RECEIVED
NASA STI FACILITY
ACQ. BRANCH

Prepared Under
Contract No. [redacted] NAS 2-7250
By
HUGHES AIRCRAFT COMPANY
EL SEGUNDO, CALIFORNIA
For
AMES RESEARCH CENTER
NATIONAL AERONAUTICS AND
SPACE ADMINISTRATION

JUL 1974
RECEIVED
NASA STI FACILITY
INPUT BRANCH

[redacted]

CR-137492

[redacted]

FINAL REPORT
SYSTEM DESIGN OF THE PIONEER VENUS SPACECRAFT

VOLUME 5
PROBE VEHICLE STUDIES

■

By
L. J. NOLTE
D. S. STEPHENSON
ET AL.

■

July 1973

Prepared Under
Contract No. [redacted] NAS 2-7250
By
HUGHES AIRCRAFT COMPANY
EL SEGUNDO, CALIFORNIA
For
AMES RESEARCH CENTER
NATIONAL AERONAUTICS AND
SPACE ADMINISTRATION

PREFACE

The Hughes Aircraft Company Pioneer Venus final report is based on udy task reports prepared during performance of the "System Design Study f the Pioneer Spacecraft." These task reports were forwarded to Ames esearch Center as they were completed during the nine months study phase. he significant results from these task reports, along with study results eveloped after task report publication dates, are reviewed in this final eport to provide complete study documentation. Wherever appropriate, the sk reports are cited by referencing a task number and Hughes report reference number. The task reports can be made available to the reader specifically interested in the details omitted in the final report for the sake of brevity.

This Pioneer Venus Study final report describes the following baseline onfigurations:

- "Thor/Delta Spacecraft Baseline" is the baseline presented at the midterm review on 26 February 1973.
- "Atlas/Centaur Spacecraft Baseline" is the baseline resulting from studies conducted since the midterm, but prior to receipt of the NASA execution phase RFP, and subsequent to decisions to launch both the multiprobe and orbiter missions in 1978 and use the Atlas/Centaur launch vehicle.
- "Atlas/Centaur Spacecraft Midterm Baseline" is the baseline presented at the 26 February 1973 review and is only used in the launch vehicle utilization trade study.

The use of the International System of Units (SI) followed by other nits in parentheses implies that the principal measurements or calculations ere made in units other than SI. The use of SI units alone implies that the rincipal measurements or calculations were made in SI units. All conversion factors were obtained or derived from NASA SP-7012 (1969).

The Hughes Aircraft Company final report consists of the following ocuments:

Volume 1 - Executive Summary - provides a summary of the major issues and decisions reached during the course of the study. A brief description of the Pioneer Venus Atlas/Centaur baseline spacecraft and probes is also presented.

PRECEDING PAGE BLANK NOT FILMED

ORIGINAL PAGE IS POOR

Volume 2 - Science - reviews science requirements, documents the science-peculiar trade studies and describes the Hughes approach for science implementation.

Volume 3 - Systems Analysis - documents the mission, systems, operations, ground systems, and reliability analysis conducted on the Thor/Delta baseline design.

Volume-4 - Probe Bus and Orbiter Spacecraft Vehicle Studies - presents the configuration, structure, thermal control and cabling studies for the probe bus and orbiter. Thor/Delta and Atlas/Centaur baseline descriptions are also presented.

Volume 5 - Probe Vehicle Studies - presents configuration, aerodynamic and structure studies for the large and small probes pressure vessel modules and deceleration modules. Pressure vessel module thermal control and science integration are discussed. Deceleration module heat shield, parachute and separation/despin are presented. Thor/Delta and Atlas/Centaur baseline descriptions are provided.

Volume 6 - Power Subsystem Studies

Volume 7 - Communication Subsystem Studies

Volume 8 - Command/Data Handling Subsystems Studies

Volume 9 - Altitude Control/Mechanisms Subsystem Studies

Volume 10 - Propulsion/Orbit Insertion Subsystem Studies

Volumes 6 through 10 - discuss the respective subsystems for the probe bus, probes, and orbiter. Each volume presents the subsystem requirements, trade and design studies, Thor/Delta baseline descriptions, and Atlas/Centaur baseline descriptions.

Volume 11 - Launch Vehicle Utilization - provides the comparison between the Pioneer Venus spacecraft system for the two launch vehicles, Thor/Delta and Atlas/Centaur. Cost analysis data is presented also.

Volume 12 - International Cooperation - documents Hughes suggested alternatives to implement a cooperative effort with ESRO for the orbiter mission. Recommendations were formulated prior to the deletion of international cooperation.

Volume 13 - Preliminary Development Plans - provides the development and program management plans.

Volume 14 - Test Planning Trades - documents studies conducted to determine the desirable testing approach for the Thor/Delta spacecraft system. Final Atlas/Centaur test plans are presented in Volume 13.

Volume 15 - Hughes IR&D Documentation - provides Hughes internal documents generated on independent research and development money which relates to some aspects of the Pioneer Venus program. These documents are referenced within the final report and are provided for ready access by the reader.

Data Book - presents the latest Atlas/Centaur Baseline design in an informal tabular and sketch format. The informal approach is used to provide the customer with the most current design with the final report.

The General Electric Company as a major subconstractor to Hughes Aircraft Company provided the analysis and test data for the deceleration module subsection in Volume 5, Probe Vehicle Studies.

CONTENTS

Page

1. SUMMARY 1-1
   1.1 Probes Major Issues 1-1
   1.2 Probe Design For Thor/Delta Mission 1-3
      Large Probe 1-3
      Small Probe 1-13
   1.3 Probe Design For Atlas/Centaur Mission 1-15
      Large Probe 1-15
      Small Probe 1-23

2. INTRODUCTION 2-1

3. REQUIREMENTS 3-1

4. PRESSURE VESSEL MODULE 4-1
   4.1 Configuration 4-6
      Requirements 4-7
      Trade Studies 4-9
      Pressure Vessel Module Configurations 4-37
      Atlas/Centaur Baseline Configuration 4-40
      References 4-46
   4.2 Aerodynamics/Flight Dynamics 4-47
      Requirements 4-47
      Tests, Analyses, and Trades 4-47
      Thor/Delta Baseline Configuration 4-81
      Atlas/Centaur Baseline Configuration 4-83
      References 4-90
   4.3 Structure 4-91
      Function and Requirements 4-95
      Tests, Analysis and Trade Studies 4-95
      Selection of Buckling Coefficient 4-97
      Large Probe 4-113
      Description of Thor/Delta Pressure Vessel Structure 4-129
      Description of Atlas/Centaur Pressure Vessel Structure 4-134
      References 4-137
   4.4 Thermal Control 4-139
      Thermal Control Design Summary 4-139
      Pressure Vessel Module Thermal Control Requirements During Descent 4-143

PRECEDING PAGE BLANK NOT FILMED

	Thermal Control Trade and Test Results	4-149
	Thor/Delta Pressure Vessel Module Thermal Design and Performance for the Descent Phase	4-180
	Atlas/Centaur Pressure Vessel Module Thermal Design and Performance for the Descent Phase	4-185
	References	4-197
4.5	Science and Housekeeping Structural Penetrations	4-198
	Penetration Requirements	4-198
	Trade Studies	4-203
	Thor/Delta Baseline Configuration Description	4-253
	Atlas/Centaur Baseline Configuration Description	4-285
4.6	Unit Packaging and Integration	4-295
	Summary	4-295
	Requirements	4-297
	Studies and Tests	4-297
	Conformal Packaging	4-305
5.	DECELERATION MODULE	5-1
5.1	Configuration	5-1
	Requirements	5-6
	Thor/Delta Configuration Trades	5-6
	Thor/Delta Configuration	5-17
	Atlas/Centaur Configuration	5-17
5.2	Aerodynamics/Flight Dynamics	5-19
	Summary	5-19
	Requirements	5-19
	Analysis	5-20
	Effect of Atmospheric Horizontal Wind on Communication Angle Deviation	5-43
	Aerodynamic Test Summary	5-48
	Thor/Delta Summary	5-49
	Atlas/Centaur Summary	5-49
5.3	Structure	5-70
	Requirements	5-71
	Tests/Trades	5-71
	Thor/Delta Baselines	5-78
	Atlas/Centaur Trades	5-82
	Atlas/Centaur Baselines	5-86
5.4	Heat Shield	5-91
	Requirements	5-93
	Trade Studies	5-93
	Heat Shield Baseline - Thor/Delta	5-161
	Heat Shield Baseline - Atlas/Centaur	5-163
	References	5-164
5.5	Parachute	5-166
	Requirements	5-16
	Trades/Studies	5-167
	Thor/Delta Baseline Description	5-190
	Atlas/Centaur Baseline Description	5-190

5.6 Separation and Despin 5-193
Summary 5-193
Requirements 5-193
Tests and Trade Studies 5-193
Thor/Delta Description 5-209
Atlas/Centaur Description 5-215

APPENDICES

A. Deceleration Module Aerodynamic Characteristics A-1
B. Small Probe Langley Spin Tunnel Tests B-1
C. Small Probe Test Analysis Techniques C-1
D. Small Probe Ames Water Tunnel Tests D-1
E. Auxiliary Stabilization - Small Probe E-1

1. SUMMARY

This volume addresses the probes' vehicular subsystems in a three-part presentation: 1) this summary of key issues/studies and the resultant probe designs; 2) a section devoted to the pressure vessel module and the subsystems it comprises; and 3) a section describing the deceleration module, its subsystems, trades, and studies.

1.1 PROBES MAJOR ISSUES

The major issues encountered in the probes studies are summarized in Table 1-1. The selections listed where trades are involved refer to the Atlas/Centaur mission; Thor/Delta choices are described in the body of the volume.

The key deceleration module issues are aerodynamic configuration and heat shield material selection. The aerodynamic configuration is important because of vehicle stability, overall system weight, motion predictability, and development cost. A series of wind tunnel tests led to the choice of a 45 deg half angle conical forebody for both large and small probes.

The heat shield material selection has two important implications: weight and the predictability of probe mass at any point during the entry. The latter is of concern in the atmosphere reconstruction experiment. The material chosen was carbon phenolic since it satisfies both criteria and has a sizable body of flight experience behind it. Tests were performed during the study that support this choice.

The pressure vessel module issues are more numerous because of the relative complexity of this portion of the vehicle and the more severe environment in which it must operate. Large probe aerodynamic configuration heads the list because of the necessity to provide a stable platform for the instrument payload. Again, wind tunnel tests were run and it was determined that several acceptable configurations exist, all of a basically spherical shape. The shape chosen, a ring-stabilized sphere, was selected because it is structurally the most efficient for withstanding high external pressures and is the easiest to integrate mechanically into the deceleration module.

The pressure vessel module must be thermally protected during its final descent, and the choice between an internal and an external insulation system influences instrument access, development cost, environmental test requirements, and system weight. An internal fiberglass insulation is

TABLE 1-1. MAJOR PROBE ISSUES

Issue	Baseline Configuration	Alternatives	Rationale for Selection
Deceleration module			
Aerodynamic configuration	45 deg half-angle cone, both probes	55 deg cone angle	45 deg allows same small probe stability margin for smaller base diameter; large probe same as small for lower wind tunnel costs
Heat shield material	Carbon phenolic	Phenolic nylon	Less susceptible to uncertainties in atmosphere, modeling; more predictable probe mass loss
Pressure vessel module			
Aerodynamic configuration	Ring-stabilized stepped sphere with integral spin vanes	Steps, fins, rings, flares for stabilization	Easiest of stable configurations to integrate into deceleration module
Thermal protection	Internal fiberglass insulation, heat sinks	External Min-K insulation	Lower development cost, easier equipment access, lower risk
Structural configuration	Spherical monocoque steel shell	Waffle, sandwich; titanium, beryllium	Monocoque lightest, lowest cost structure; steel most compatible with environment
Equipment integration	Two horizontal equipment shelves; top shelf supported from bottom shelf; bottom attached to shell flange	Vertical shelves; both mounted on shell flanges	Easiest equipment access, best thermal isolation
Instrument integration	All instruments shelf-mounted; all windows heated; outer windows jettisoned at 40 km	Shell mounting; window wipers	Instrument access, alignment, and protection are key considerations

REPRODUCIBILITY OF THE ORIGINAL PAGE IS POOR.

superior in cost, reliability, accessibility and acceptable in weight and hence was selected for Atlas/Centaur.

The pressure vessel module structure configuration and material selection was also the subject of experimental investigation, where it was found that a spherical monocoque structure was the most efficient design. Steel was chosen as the material because it affords the fewest number of environmental incompatibilities. The pressure vessel structure together with the thermal control systems are of prime importance because together they account for 40 percent of the total probe weight.

An almost equally important factor in probe design is the integration of instruments and subsystems into the pressure vessel module, because of the need for equipment accessibility on the one hand and the desire to keep package volume as low as possible on the other (structural weight is directly proportional to enclosed volume). Consequently a great deal of effort was devoted to subsystem packaging concepts as well as to equipment arrangement within the pressure vessel.

Each of the science instruments poses its own integration problem, and most require some penetration of the pressure vessel shell. Instrument integration was considered a major issue, because of the number and variety of instruments and their accommodation in a volume-limited, spherical vehicle. The design effort expended in this area was considerable, as may be seen later in this volume.

This summary has only highlighted a few items of a rather detailed study program. The list of issues outlined above highlights key facets of the study effort; however, it represents a small number of the total 28 studies in the pressure vessel module design alone.

1.2 PROBE DESIGN FOR THOR/DELTA MISSION

Large Probe

The external configuration of the large probe for the Thor/Delta mission is shown in Figure 1-1. The probe is 116.8 cm (46.0 in.) in diameter, 73.2 cm (28.8 in.) long, and weighs 114.5 kg (252.6 lbs.) mounted on the multiprobe bus. It has a 55-deg half angle, conical forebody with nose radius half the base radius. This is the PAET forebody configuration, so that a considerable body of aerodynamic data exists for it, and it is also the minimum weight configuration. The base diameter was selected to provide sufficient volume for packaging the parachute subsystem in the annulus around the pressure vessel module and to ensure that the probe c.g. is forward of the base plane. The latter in turn assures adequate dynamic stability.

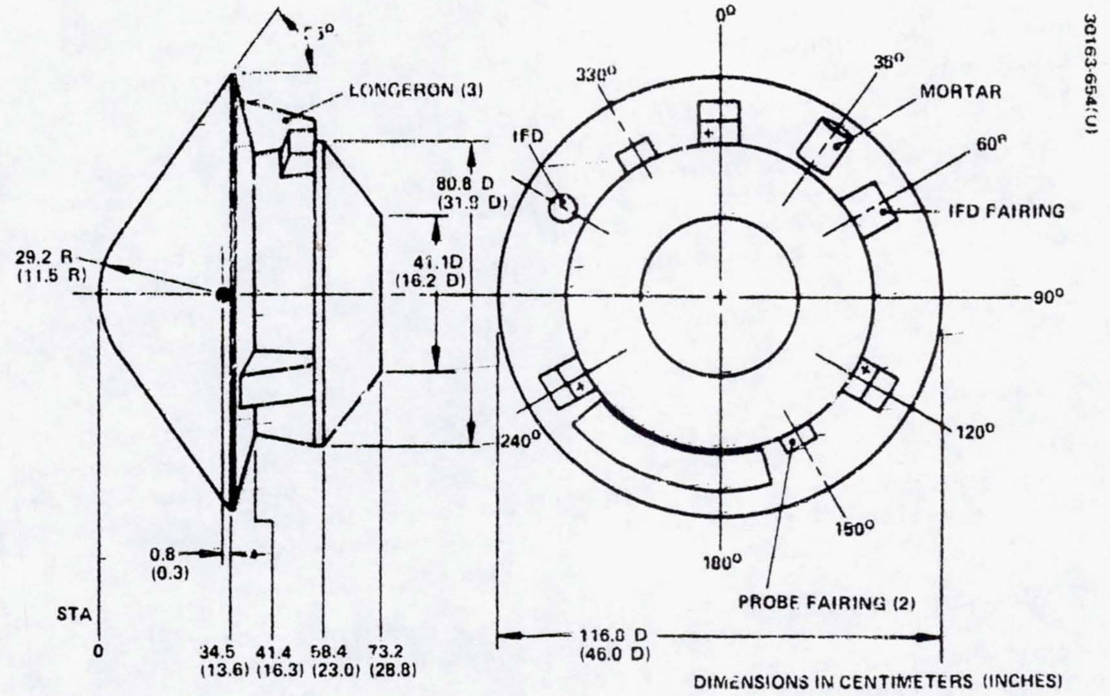

FIGURE 1-1. THOR/DELTA LARGE PROBE CONFIGURATION

The other obvious external features found in Figure 1-1 are the three longerons which support the probe on the multiprobe bus and the afterbody structure which protects the pressure vessel module from the entry aerodynamic heating pulse. The portion of the afterbody aft of station [illegible] is removed in flight by the parachute subsystem to allow extraction of the pressure vessel module. The flat disc at the aft end of the afterbody is rf transparent, which permits communication with the antenna mounted on the pressure vessel prior to entry.

The probe is attached to the multiprobe bus with three bolts and explosive nuts. Three springs provide the separation force between vehicles. A 61-pin, hot-wire-activated in-flight disconnect (IFD) is mounted on the aft face of the aeroshell structure and provides electrical separation.

Heat Shield

The forebody heat shield material selected for the Thor/Delta mission is phenolic nylon, primarily because it is the lightest weight of all materials that satisfy the low cost criterion. Phenolic nylon is a moderately high density, low conductivity material which decomposes into a char layer as it is heated. In the aerodynamic environment expected in this mission, most of the char layer will be scrubbed from the vehicle as it is formed, and the material acts primarily as an ablative heat shield. Average shield thickness along the conical frustum is 0.7 cm, of which 90 percent is removed in the ablation process.

The forebody heat shield is bonded to the aeroshell structure using PD-200 bond system designed to permit cold soak to -73°C (-100°F).

All external surfaces of the afterbody are protected by a low density chemically foamed silicone elastomer (ESM) approximately 0.3 cm thick. The material remains rf transparent as it is heated.

Aeroshell Structure

The primary aeroshell structure is a ring-stiffened monocoque shell, made of beryllium. Both construction and material were chosen solely on the basis of minimum weight. The internal structure is also beryllium and may be seen in Figure 1-2 and in the inboard profiles shown in Section 5.

The afterbody structure is beryllium except for the aft disc, which is made of phenolic fiberglass. It is attached to the forebody structure by a system of mechanically actuated, i.e. nonpyrotechnic, latches. The pilot chute operates these latches and removes the aft cover just before main parachute deployment.

Parachute/Separation

The pressure vessel module is extracted from the aeroshell and slowed during the initial phases of its descent by a parachute subsystem.

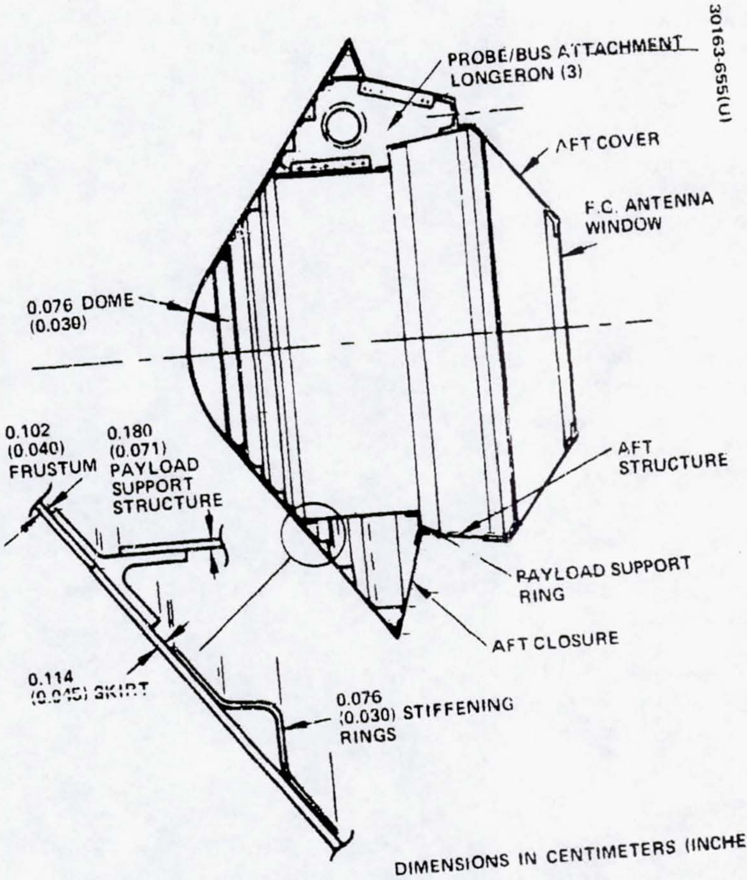

FIGURE 1-2. THOR/DELTA LARGE PROBE STRUCTURE

The subsystem comprises a 3.5 m (11.5 ft) diameter main parachute and a mortar-deployed, 0.84 m (2.75 ft) pilot chute. The pilot chute has a conical ribbon configuration and the main chute configuration is a disc gap band. Both are made of nylon. The mortar is initiated at about Mach 0.8 based on a pre-set time from a deceleration event, and fires the pilot chute into the airstream normal to the probe flight path. The pilot chute in turn removes the aft cover and extracts the main chute from its housing at about Mach 0.7. Two seconds after mortar initiation the wire harness connecting the pressure vessel module to the deceleration module is severed by a cable cutter. Three seconds after mortar initiation, the three explosive nuts that attach the pressure vessel module to the aeroshell mounting bolts are actuated. By this time the main parachute has deployed and stabilized, so that it is now free to extract the pressure vessel module. The parachute diameter is chosen so that it will provide 2 g relative acceleration between pressure vessel and deceleration modules.

The pressure vessel module/parachute subsystem is stabilized and at terminal velocity at an altitude of approximately 68.5 km. It remains in this configuration to an altitude of 55 km, at which time the three explosive nuts attaching the parachute to the pressure vessel module are initiated and the pressure vessel falls free. The 55 km jettison altitude results from a weight minimization study involving transmitter power, battery size, and insulation thickness, described in Volume 3.

Pressure Vessel Configuration

The large probe pressure vessel module is a sphere of 60 cm (23.6 in.) external diameter, which provides an internal volume 54.6 cm (21.5 in.) in diameter. It houses all science instruments (except the shock layer radiometer) and the complete power, radio, and data/command subsystems. It is illustrated in ~~an~~ exploded view in Figure 1-3, while a cross-section showing subsystem locations appears in Figure 1-4.

The pressure vessel is stabilized in free fall by a ring 6 cm (2.4 in.) aft of the equator. The ring stabilizes by causing flow separation to occur at a fixed point on the body regardless of angle of attack. It also contains three open areas which in turn contain small, canted vanes to provide pressure vessel rotation. This stabilization technique was selected as the result of a series of wind tunnel tests in which several candidate configurations were found to have adequate stability. In this configuration the ring also serves as the structural adapter between pressure vessel and aeroshell and does so while minimizing heat leaks to the pressure vessel structure, thereby minimizing system weight.

The basically spherical shape is also dictated by weight considerations. Because of the inherent structural efficiency of a spherical shell, this configuration was found to be lighter than alternate configurations which housed the same payload with less "waste" volume.

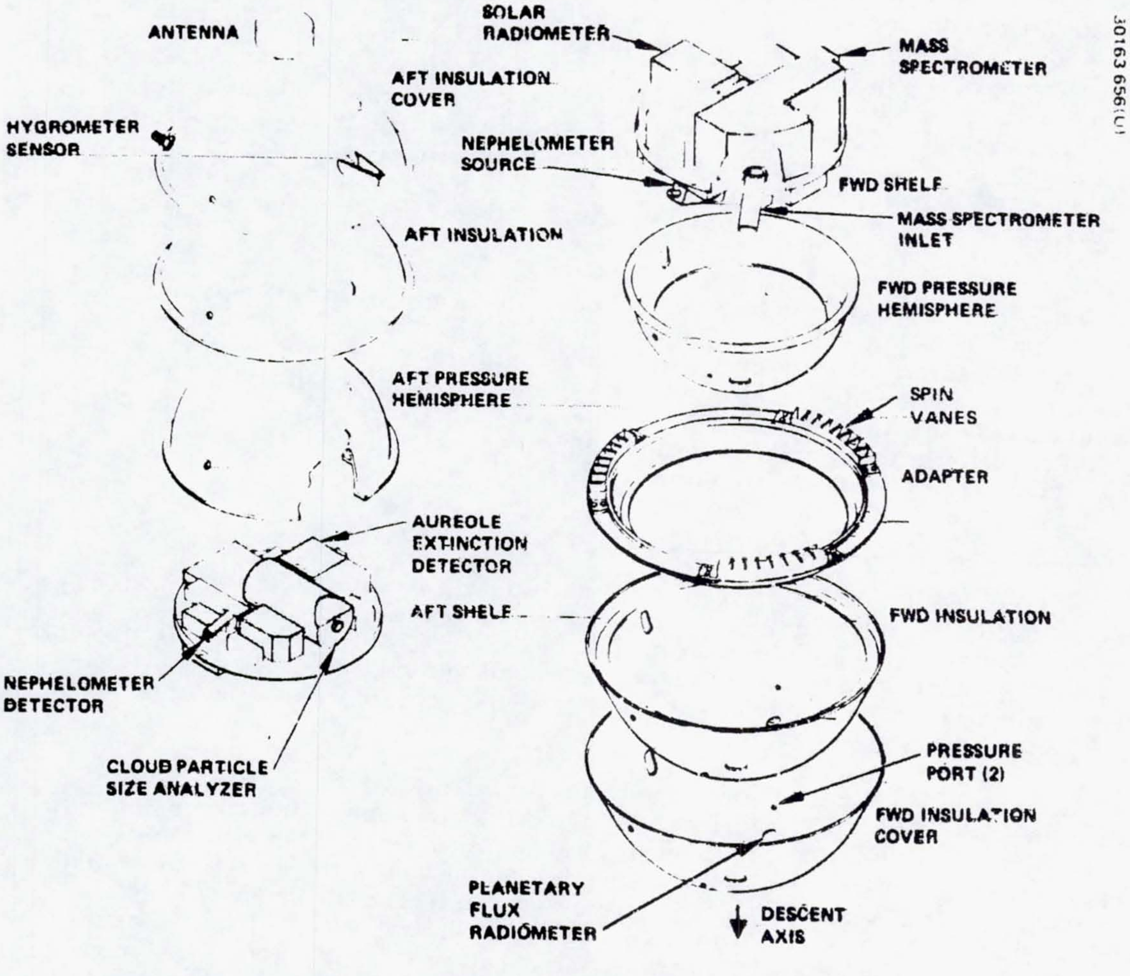

FIGURE 1-3. THOR/DELTA LARGE PROBE PRESSURE VESSEL MODULE

REPRODUCIBILITY OF THE ORIGINAL PAGE IS POOR.

...OF THE ORIGINAL PAGE IS POOR.

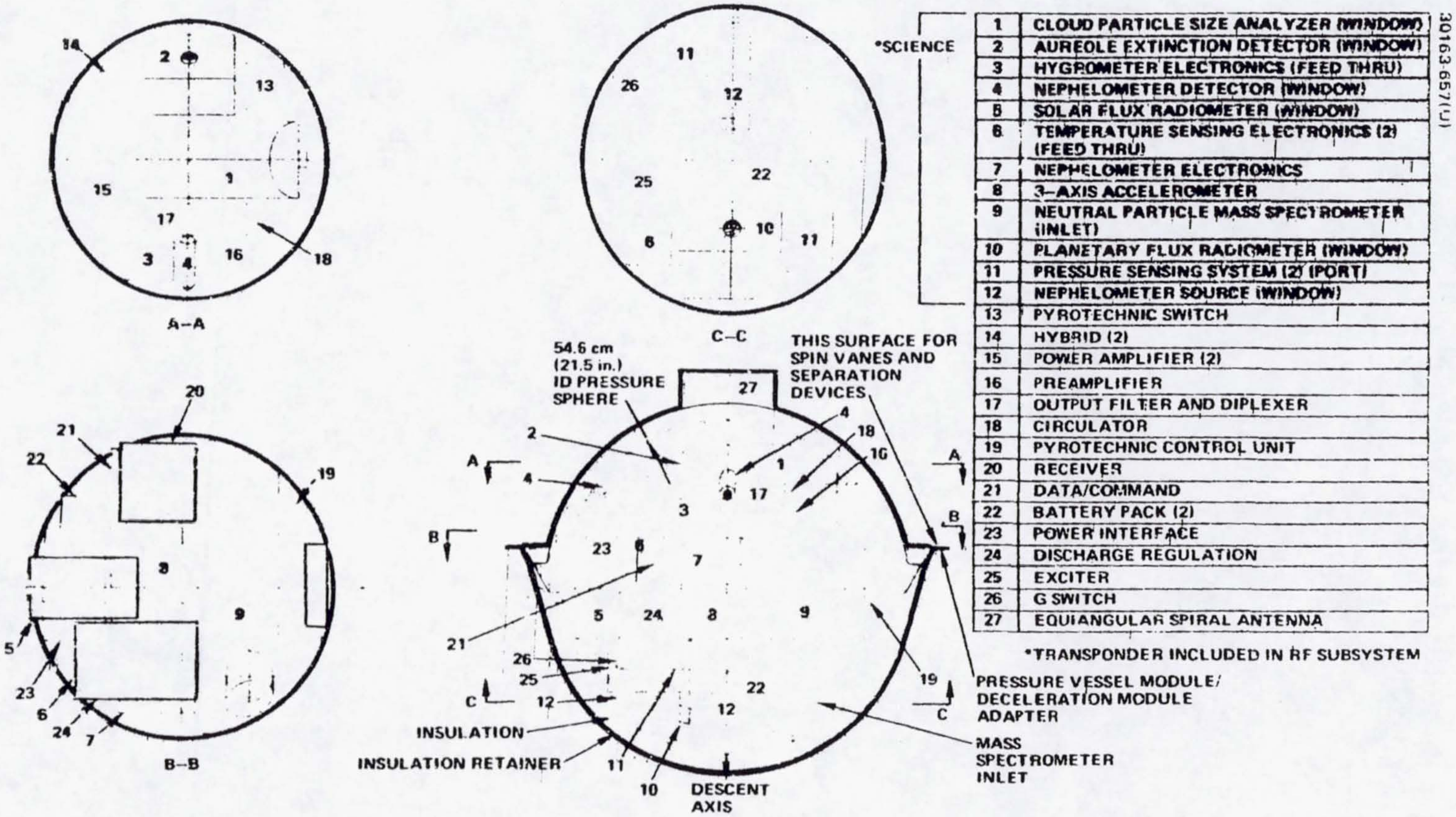

*SCIENCE	1	CLOUD PARTICLE SIZE ANALYZER (WINDOW)
	2	AUREOLE EXTINCTION DETECTOR (WINDOW)
	3	HYGROMETER ELECTRONICS (FEED THRU)
	4	NEPHELOMETER DETECTOR (WINDOW)
	5	SOLAR FLUX RADIOMETER (WINDOW)
	6	TEMPERATURE SENSING ELECTRONICS (2) (FEED THRU)
	7	NEPHELOMETER ELECTRONICS
	8	3–AXIS ACCELEROMETER
	9	NEUTRAL PARTICLE MASS SPECTROMETER (INLET)
	10	PLANETARY FLUX RADIOMETER (WINDOW)
	11	PRESSURE SENSING SYSTEM (2) (PORT)
	12	NEPHELOMETER SOURCE (WINDOW)
	13	PYROTECHNIC SWITCH
	14	HYBRID (2)
	15	POWER AMPLIFIER (2)
	16	PREAMPLIFIER
	17	OUTPUT FILTER AND DIPLEXER
	18	CIRCULATOR
	19	PYROTECHNIC CONTROL UNIT
	20	RECEIVER
	21	DATA/COMMAND
	22	BATTERY PACK (2)
	23	POWER INTERFACE
	24	DISCHARGE REGULATION
	25	EXCITER
	26	G SWITCH
	27	EQUIANGULAR SPIRAL ANTENNA

*TRANSPONDER INCLUDED IN RF SUBSYSTEM

FIGURE 1-4. THOR/DELTA LARGE PROBE PRESSURE VESSEL MODULE CONFIGURATION

TABLE 1-2. LARGE PROBE WEIGHT SUMMARY – THOR/DELTA MISSION

Deceleration module		39.5 kg (87.0 lb)
Heat shield	12.0 (26.5)	
Structure	15.5 (34.1)	
Aft cover	3.9 (8.6)	
Parachute	3.7 (8.2)	
Cabling	1.0 (2.3)	
Pressure vessel separation	1.3 (2.8)	
Instrumentation	0.2 (0.4)	
Ballast	0.7 (1.6)	
Science instruments	1.1 (2.5)	
Pressure vessel module		73.1 kg (161.1 lb)
Structure	25.0 (55.1)	
Thermal control	7.5 (16.5)	
Radio	3.6 (8.0)	
Command/data handling	2.1 (4.7)	
Power	11.2 (24.7)	
Antenna	0.7 (1.5)	
Cabling	0.9 (1.9)	
Equipment	0.7 (1.6)	
Science instruments	21.4 (47.1)	
Entry weight		112.5 kg (248.1 lb)
Bus separation	2.0 (4.5)	
Weight on bus		114.5 kg (252.6 lb)

Pressure Vessel Construction

Referring to Figure 1-3, the pressure vessel module is seen to contain two shelves on which all science instruments and housekeeping subsystems are mounted. The shelves are attached to flanges machined into each half of the basic structural shell. The shelves are of aluminum honeycomb sandwich construction, while the shell is a 0.3 cm (0.12 in.) thick titanium monocoque structure. Titanium was tentatively chosen early in the study as the result of an analytical and experimental program which demonstrated that it afforded the minimum weight solution. The hemispheres are joined by flanges which contain the main pressure seal and to which the aeroshell adapter is mounted. Each hemisphere is protected by a layer of Min-K insulation 2.3 cm (0.9 in.) thick held in place by a 0.03 cm (0.01 in.) titanium retainer.

The pressure vessel shell, insulation, and retainer have 19 penetrations: six for instrument windows, six for other instrument access ports, and seven for harness and housekeeping access panels. Each of these penetrations must be pressure sealed, each represents a potential structural failure point, and only four are similar in construction.

The instrument windows are of two types: those that must function in visible wavelengths, and those that must function in infrared wavelengths. Sapphire has been chosen as the material for the former on the basis of maximum transmittance and hardness and minimum weight, while chemically vapor deposited zinc selenide is chosen for the latter on the same basis plus minimum in-band emittance. All windows have heaters. All windows that must function below 40 km altitude have jettisonable outer elements (see Section 3.1). Sections 4.5 and 4.6 provide detailed descriptions of these penetrations.

Pressure Vessel Insulation

The pressure vessel is externally insulated with a 2.3 cm (0.9 in.) layer of Min-K, a rigid, low-density, porous material whose conductivity is about equal to the conductivity of the gas in which it is immersed. This selection was made after considering other insulating materials applied on both the inside and the outside of the pressure vessel. It provides the minimum combined weight of structure plus insulation. Average shelf mounting surface temperatures are held below 52°C (125°F) with no local peak temperature above 60°C (140°F).

Probe Weight

The large probe weighs 114.8 kg (252.6 lbs.) mounted on the multiprobe bus. 73.1 kg of that total are in the pressure vessel module, of which 21.4 kg are science instruments. The probe has a ballistic coefficient (W/C_DA) at entry of 78 kg/m^2 (16 lb/ft^2). A weight breakdown by subsystem is given in Table 1-2.

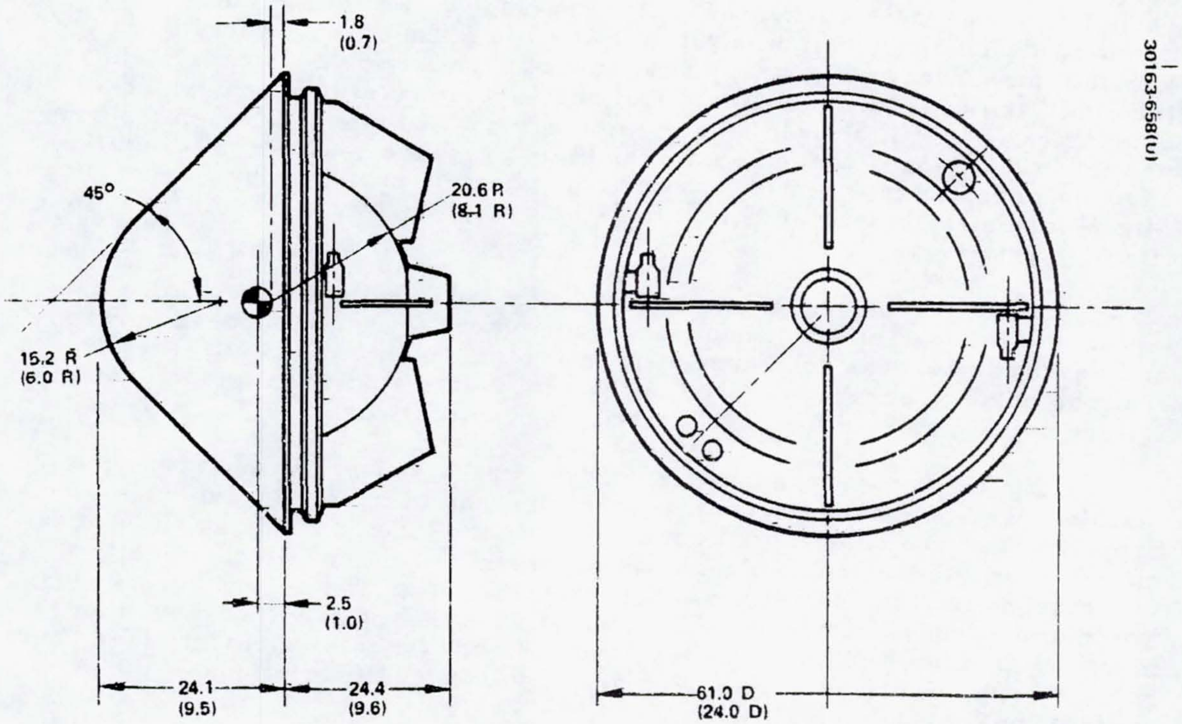

DIMENSIONS IN CENTIMETERS (INCHES)

FIGURE 1-5. THOR/DELTA SMALL PROBE CONFIGURATION

Small Probe

Configuration

The small probe external configuration is illustrated in Figure 1-5. It is 61.0 cm (24.0 in.) in diameter, 48.5 cm (19.1 in.) long, and weighs 34.0 kg (74.9 lb.) mounted on the bus. It has a 45 deg half angle and conical forebody with nose radius/base radius = 0.5. Four fins mounted on the aft face of the probe provide roll damping. This configuration was chosen as the result of a series of wind tunnel tests of both 45 and 55 deg cones which revealed low speed, roll induced dynamic instability. The problem became severe for both cone angles as the c. g. was moved close to the probe base and a c. g. position about 4 percent of a base diameter ahead of the base was indicated, requiring a much larger base diameter for the 55 deg cone angle and hence a heavier probe. Consequently 45 deg was chosen. The fins, also proven in the wind tunnel tests, are to damp roll caused by ablation or other asymmetries. The aft heat shield is applied directly to the pressure vessel and a small, jettisonable cover protects the instrument window.

Separation/Despin

The three small probes are each mounted on the multiprobe bus using a clamp which attachs to the ring visible just aft of the base in Figure 1-5. The outward half of the clamp is pivoted at one end and held in place by an explosive nut/bolt at the other end. As the nut is broken, the clamp rotates 160 deg and locks in place. Centrifugal force caused by the spinning bus moves the probes away from the bus and each other. Electrical separation is provided by the same model in-flight di connect used on the large probe.

The small probes are initially spinning at a high rate because of the targeting procedure. Since the targeting also precludes orienting the probes for zero angle of attack at entry, it is necessary to limit spin rate so that angle of attack convergence will not be impeded. This is done by firing two small despin solid propellant rocket motors located at the base of the vehicle.

Heat Shield/Aeroshell Structure

Heat shield and structural materials are the same for the small probe as for the large probe, i.e., phenolic nylon, ESM, and beryllium. The reasons for the choices are also similar. The structure differs only in that it is a monocoque shell, and is illustrated in Figure 1-6.

The structure mounts portions of two science instruments: the temperature and pressure sensors. The temperature sensor is on a swing-out arm which is stowed on the base of the vehicle and deployed after entry. The pressure sensor port is located at the stagnation point of the aeroshell and is protected by a teflon plug which is removed after entry. Electronics for both instruments are located inside the pressure vessel.

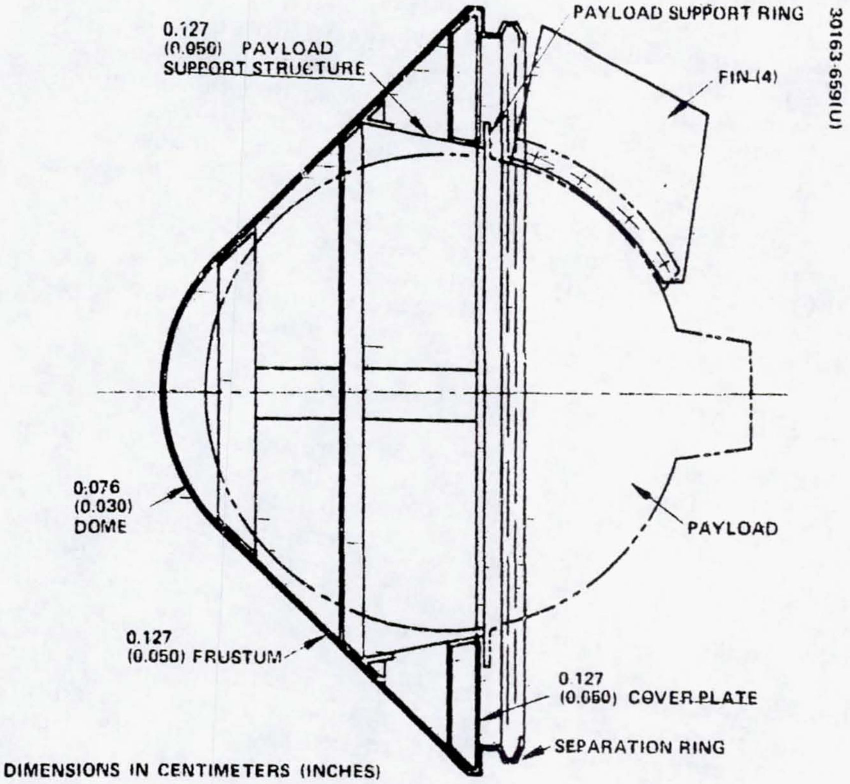

FIGURE 1-6. THOR/DELTA SMALL PROBE STRUCTURE

Pressure Vessel Configuration/Construction

The small probe pressure vessel module (Figure 1-7) is also a sphere and has an internal diameter of 32.5 cm (12.8 in.). Like the large probe, it contains most of the instruments and all of the housekeeping subsystem. The structure is a titanium monocoque shell. It houses two equipment mounting shelves and is mounted to the aeroshell structure by an adapter which is quite similar to the one used for the large probe.

The upper hemisphere is protected by a 4.1 cm (1.6 in.) layer of Min-K insulation and the lower hemisphere by 3.0 cm (1.2 in.), each held in place by titanium retainers. The pressure vessel has far fewer penetrations than the large probe. Again, these penetrations are covered in Sections 4.5 and 4.6 and will not be described here. The only window (for the nephelometer) is protected during entry by a heat resistant cover.

Probe Weight

The small probe weighs 34.0 kg (74.9 lb) mounted on the multiprobe bus. It carries 2.2 kg (4.9 lb) of instruments in a 23.6 kg pressure vessel module and has a ballistic coefficient of 107 kg/m^2 (21.9 lb/ft^2). A weight breakdown by subsystem is given in Table 1-3.

1.3 PROBE DESIGN FOR ATLAS/CENTAUR MISSION

Large Probe

The external configuration of the large probe for the Atlas/Centaur mission is shown in Figure 1-8. The probe is 139.7 cm (55.0 in.) in diameter, 90.3 cm (35.5 in.) long, and weighs 243.9 kg (541.7 lb) mounted on the multiprobe bus. It has a 45 deg half angle, conical forebody with nose radius half the base radius. To minimize aero-dynamic testing and hence developmental cost, the forebody configuration is the same as the small probe. The base diameter provides sufficient volume for packaging the parachute subsystem in the annulus around the pressure vessel module. The resultant c.g. is well forward of the base plane, and adequate dynamic stability is assured.

As in the Thor/Delta configuration, three longerons support the probe on the multiprobe bus and an afterbody structure is used to protect the pressure vessel module from the aerodynamic heating pulse. The conical aft portion of the afterbody is removed by the parachute to allow separation of the pressure vessel module after entry. The aft face of this cover is transparent to allow use of the pressure vessel antenna for pre-entry communication.

Attachment to and separation from the multiprobe bus is effected as in the Thor/Delta configuration: three bolts, explosive nuts, and separation springs supply the mechanical interface, while an in-flight disconnect is used for the electrical separation.

REPRODUCIBILITY OF THE ORIGINAL PAGE IS POOR.

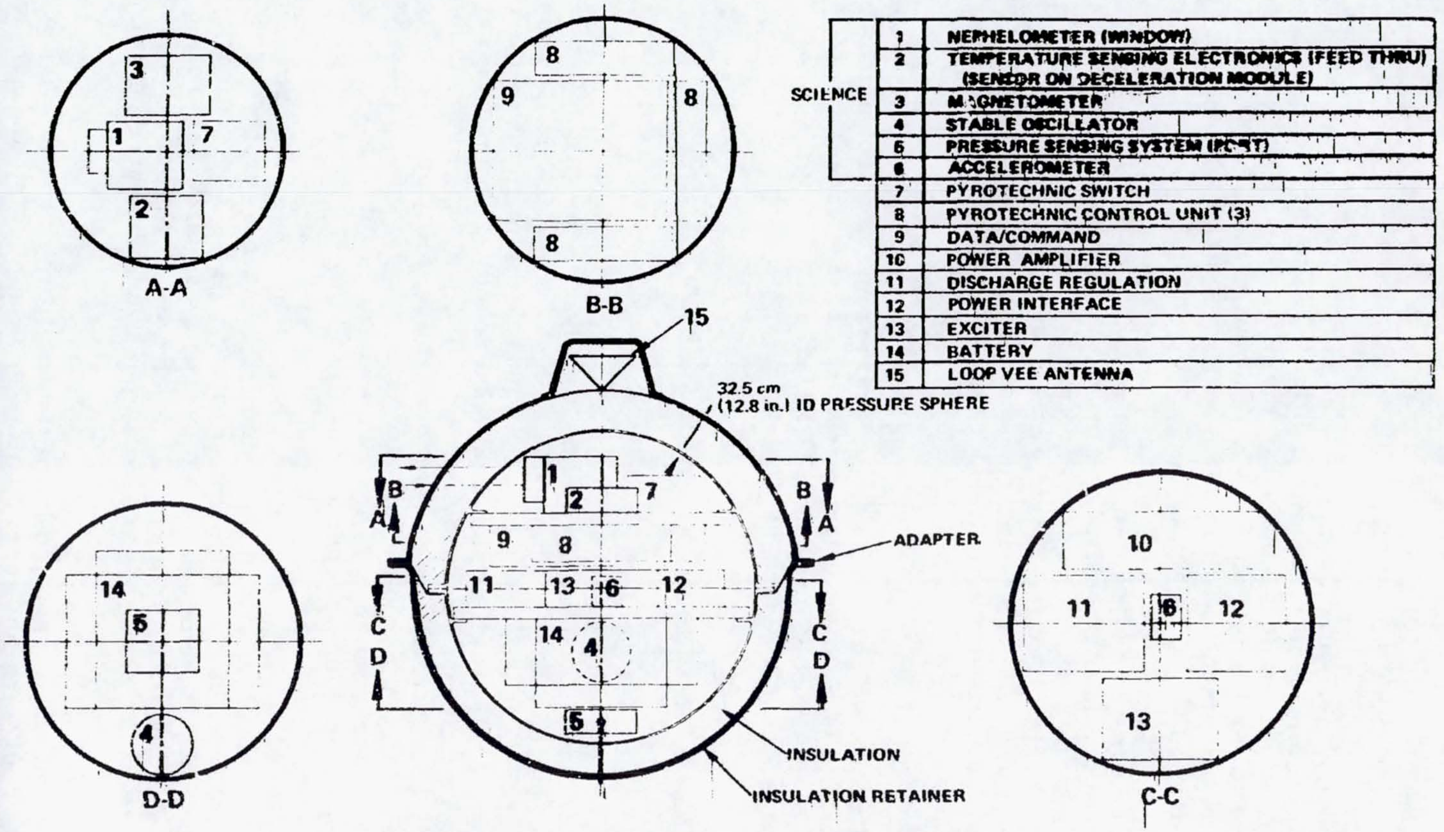

SCIENCE	1	NEPHELOMETER (WINDOW)
	2	TEMPERATURE SENSING ELECTRONICS (FEED THRU) (SENSOR ON DECELERATION MODULE)
	3	MAGNETOMETER
	4	STABLE OSCILLATOR
	5	PRESSURE SENSING SYSTEM (PORT)
	6	ACCELEROMETER
	7	PYROTECHNIC SWITCH
	8	PYROTECHNIC CONTROL UNIT (3)
	9	DATA/COMMAND
	10	POWER AMPLIFIER
	11	DISCHARGE REGULATION
	12	POWER INTERFACE
	13	EXCITER
	14	BATTERY
	15	LOOP VEE ANTENNA

FIGURE 1-7. THOR/DELTA SMALL PROBE PRESSURE VESSEL MODULE

TABLE 1-3. SMALL PROBE WEIGHT SUMMARY -- THOR/DELTA MISSION

Deceleration module		9.1 kg (20.1 lb)
Heat shield	4.6 (10.2)	
Structure	3.9 (8.5)	
Cabling	0.1 (0.3)	
Science instruments	0.5 (1.1)	
Pressure vessel module		23.6 kg (52.0 lb)
Structure	6.8 (14.9)	
Thermal control	4.9 (10.8)	
Radio	1.1 (2.5)	
Command data handling	1.2 (2.7)	
Power	7.1 (15.6)	
Antenna	0.2 (0.5)	
Cabling	0.3 (0.6)	
Equipment	0.2 (0.5)	
Science instruments	1.8 (3.9)	
Entry weight		32.7 kg (72.1 lb)
Separation/despin	1.3 (2.8)	
Weight on bus		34.0 kg (74.9 lb)

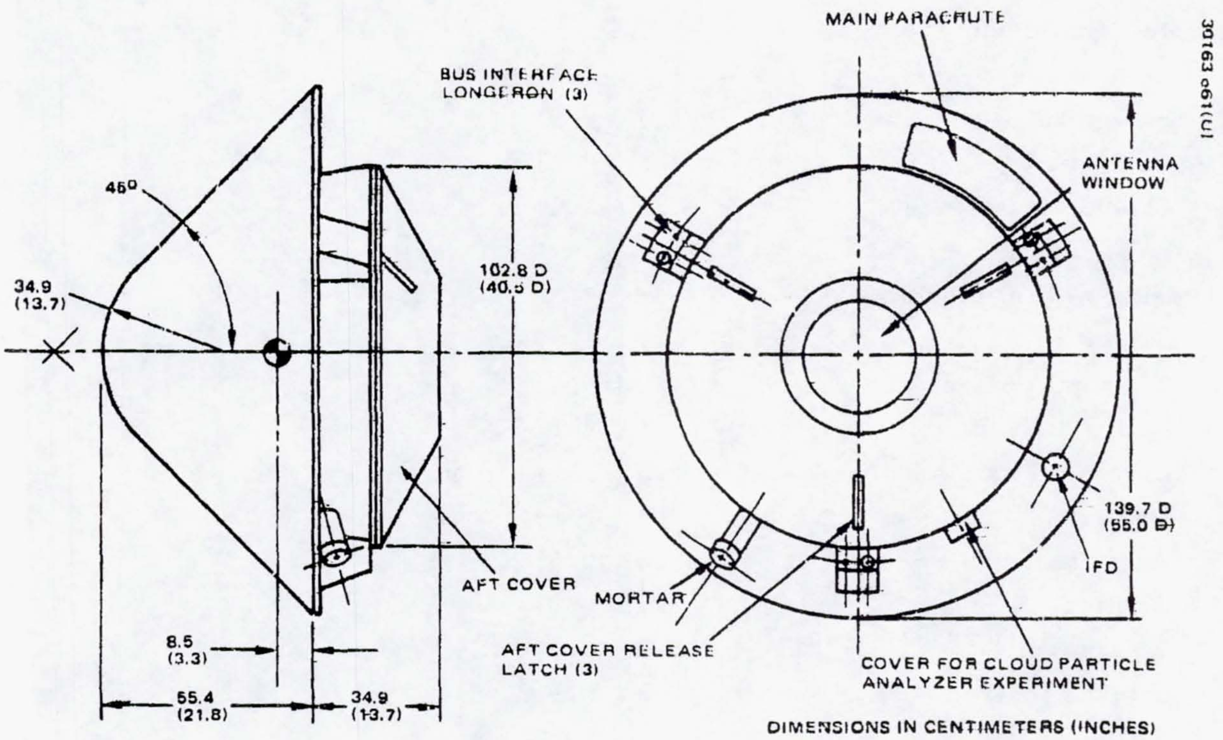

FIGURE 1-8. ATLAS/CENTAUR LARGE PROBE CONFIGURATION

Heat Shield

The forebody heat shield material selected for the Atlas/Centaur mission is carbon phenolic. This is a high density material which forms a very stable, refractory char as it is heated. Next to phenolic nylon, it is the lightest of the materials compatible with a low cost mission; furthermore, it has the least mass loss (by a large margin) of any of the materials considered. Carbon phenolic was chosen because it permitted a much more predictable probe mass history during entry, assuring significantly greater accuracy in the atmosphere reconstruction experiment.

Heat shield thickness averages 0.94 cm (0.37 in.) along the conical frustum. This thickness includes a 50 percent margin, chosen to provide a very safe design, thereby reducing the requirement for developmental testing and hence the program cost. The heat shield is bonded to the aeroshell structure using an RTV-630 bonding system similar to that described in the Thor/Delta design. The large probe afterbody is protected by a 0.3 cm thick layer of silicone elastomer (ESM).

Aeroshell Structure

The primary aeroshell structure is a ring-stiffened aluminum monocoque shell, which has skin thickness ranging from 0.16 cm (0.063 in.) at the stagnation point to 0.28 cm (0.12 in.) at the end of the skirt. The conical portion of the shell is machined as a single unit including rings, a technique that has proven cost competitive with other fabrication methods. The shell and the rest of the structure are aluminum because the deceleration module does not have to survive below parachute deployment altitude, about 67 km. As with the heat shield, a 50 percent safety margin is used in structural design, virtually eliminating developmental testing.

The afterbody/aft cover structural concept is identical with the Thor/Delta design: an aluminum structure with fiberglass rf window attached and a system of latches to attach and remove the aft cover at parachuted deployment.

Parachute/Separation

The Atlas/Centaur parachute subsystem uses a 4.6 m (15 ft) diameter main parachute and an 0.84 m (2.75 ft) pilot chute. The configurations are: disc-gap-band for the main chute and conical ribbon for the pilot chute. Both are nylon. The parachute system is subsonicly deployed, resulting in a much lower cost flight demonstration than if deployment were supersonic. The sequence is exactly as in the Thor/Delta design; the mortar is initiated by a firing current from the pressure vessel module. It ejects the pilot chute which in turn removes the aft cover and the main chute. After chute stabilization, the pressure vessel is released and the aeroshell falls free.

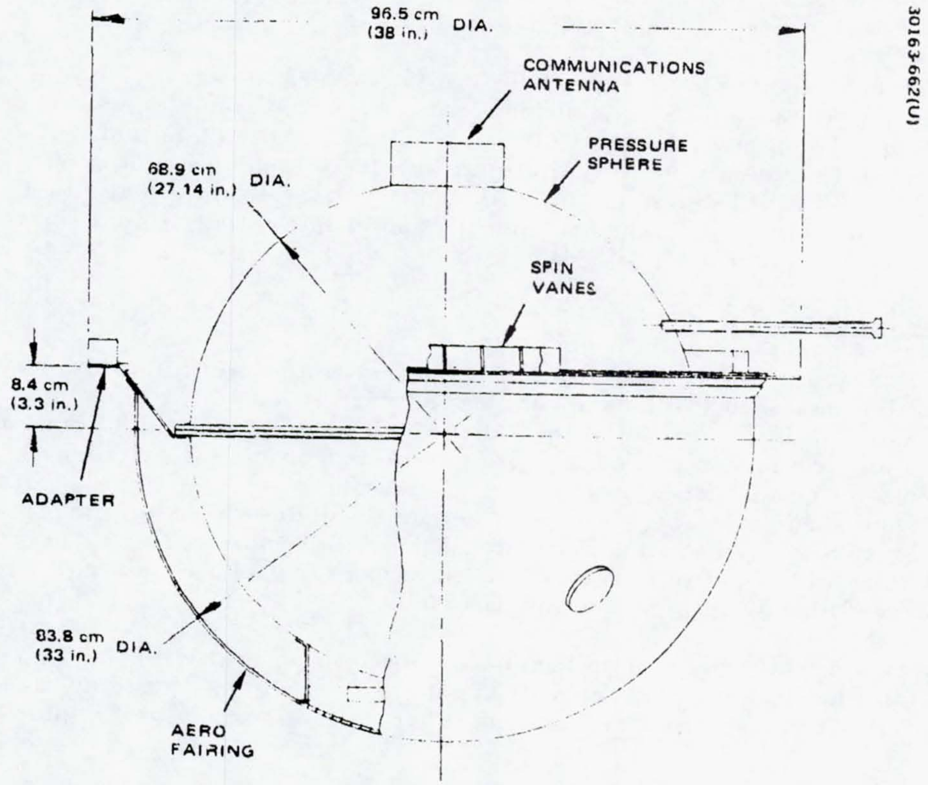

FIGURE 1-9. ATLAS/CENTAUR LARGE PROBE PRESSURE VESSEL MODULE CONFIGURATION

Parachute release from the pressure vessel module takes place at 40 km altitude. The jettison altitude is chosen to allow maximum probe exposure in the altitude regime between 40 and 50 km where several atmospheric anomalies appear to exist and are therefore of scientific interest.

Pressure Vessel Configuration

The external configuration of the large probe pressure vessel module is illustrated in Figure 1-9. It is a ring-stabilized, stepped sphere whose larger diameter is 81.3 cm (32.0 in.) and whose smaller diameter is 68.6 cm (27.0 in.). It houses all of the scientific instruments and the housekeeping subsystem in a spherical volume 68.1 cm (26.8 in.) in diameter. The smaller, aft hemisphere is the pressure vessel shell itself. The larger diameter hemisphere is an aerodynamic fairing totally encompassing the wind/altitude radar antenna. Like the Thor/Delta, the pressure vessel module is aerodynamically stabilized by a porous ring located 8.6 cm (3.4 in.) aft of the equator. This ring contains spin vanes for module rotation and also acts as the structural adapter to the aeroshell. Geometric similarity with the Thor/Delta design has been maintained for the ring radius, ring distance aft of the equator, and c.g. distance forward of the equator, all referenced to the radius of the forward hemisphere. This geometry has been substantiated by wind tunnel, tests.

The pressure vessel shell itself is also spherical, the most structurally efficient configuration. Its diameter is determined as the result of a detailed packaging design exercise which assumed experiment volumes 15 percent greater than the nominal values.

Pressure Vessel Construction

The pressure vessel module construction is illustrated in Figure 1-10. It is significantly different in the Atlas/Centaur design than in Thor/Delta, representing as much a design evolution as a response to different design requirements. The fundamental difference between the two is in the location of the insulation: the Atlas/Centaur design is internally insulated, so that the pressure vessel structural shell is exposed to the environment. Internally, a blanket of fiberglass insulation is held in place against the shell by a retainer structure which is in turn mounted on the shelf structure. Trade studies indicate a slight weight advantage to the external insulation scheme; hence, it was adopted in the Thor/Delta design. The internal insulation, however, functions in a relatively benign environment. Its performance is already well characterized, and the developmental testing required should be relatively minimal. Furthermore, its application appears to be far less complex than the Min-K insulation externally applied, leading to better internal accessibility. Both factors indicate a lower cost system, which is the principle criteria for selecting the internal insulation for the Atlas/Centaur design.

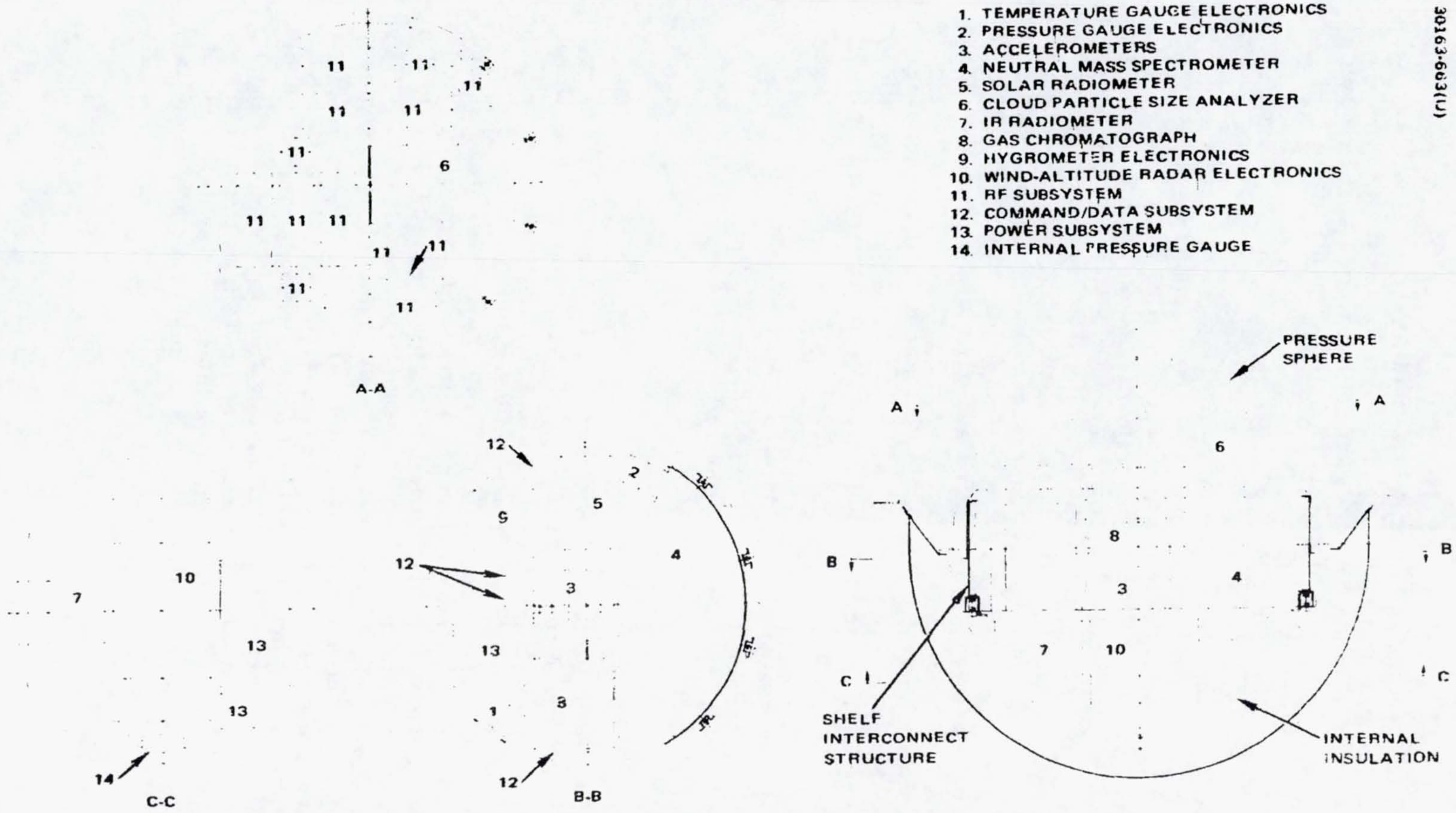

FIGURE 1-10. ATLAS/CENTAUR LARGE PROBE PRESSURE VESSEL MODULE CONFIGURATION

The pressure vessel shell uses a high temperature, high strength maraging steel which is fabricated relatively easily. Considering only the pressure and temperature environment, titanium would provide a minimum weight structure. On the other hand, a body of experimental evidence exists which implies that oxide-free titanium could spontaneously ignite and burn in the Venus lower atmosphere. None of the high temperature steels appear to have this problem, and Hughes has taken a conservative position in recommending one of them for the Atlas/Centaur design. Maraging steel was chosen because it promises to have a lower potential for distortion during insert welding than any of the other candidate steels.

The equipment is mounted on two shelves, both solid aluminum to augment the heat capacity of the units. The top shelf is structurally attached to the bottom shelf rather than to the pressure vessel shell for two reasons: this reduces heat flow to the top shelf, and it also permits more rapid disassembly of the pressure vessel module.

Design concepts for windows and penetrations are similar to the Thor/Delta design (Sections 4.5 and 4.6). All windows have heaters and jettisonable outer elements. With the internal insulation design, however, window heater power is somewhat reduced.

Pressure Vessel/Insulation

The pressure vessel is internally insulated with a blanket of FA fiberglass, 1.3 cm (0.5 in.) thick. The blanket is mounted on a rigid support structure which is attached to the shelf structure and holds the blanket against the outer shell. The bottom shelf is thermally isolated from the outer shell by multiple washer stacks at each mounting bolt. The system maintains temperatures of all units below 52°C (125°F) at impact with the exception of the rf output power amplifiers, which are allowed to reach 60°C (140°F).

Probe Weight

The large probe weighs 245.7 kg (541.7 lb) mounted on the multiprobe bus. It carries science instruments weighing 31.6 kg (69.6 lb) in a 152.9 kg (337.1 lb) pressure vessel module. It has a ballistic coefficient of 149 kg/m^2 (31 lb/ft^2) at entry. A weight breakdown by subsystem is given in Table 1-4.

Small Probe

Configuration

The small probe external configuration is illustrated in Figure 1-11. It is 67.3 cm (26.5 in.) in diameter, 52.5 cm (20.7 in.) long and weighs 63.3 kg (139.6 lb) mounted on the multiprobe bus. It has a 45 deg half-angle, conical forebody with nose radius/base radius = 0.5. Four fins mounted on the aft face of the probe provide roll damping. The configuration rationale has been described earlier, and this Atlas/Centaur version differs only in that it has a c.g. about 6-1/2 percent of a base diameter ahead of the base instead of the 4 percent used in the Thor/Delta design. The base diameter was chos

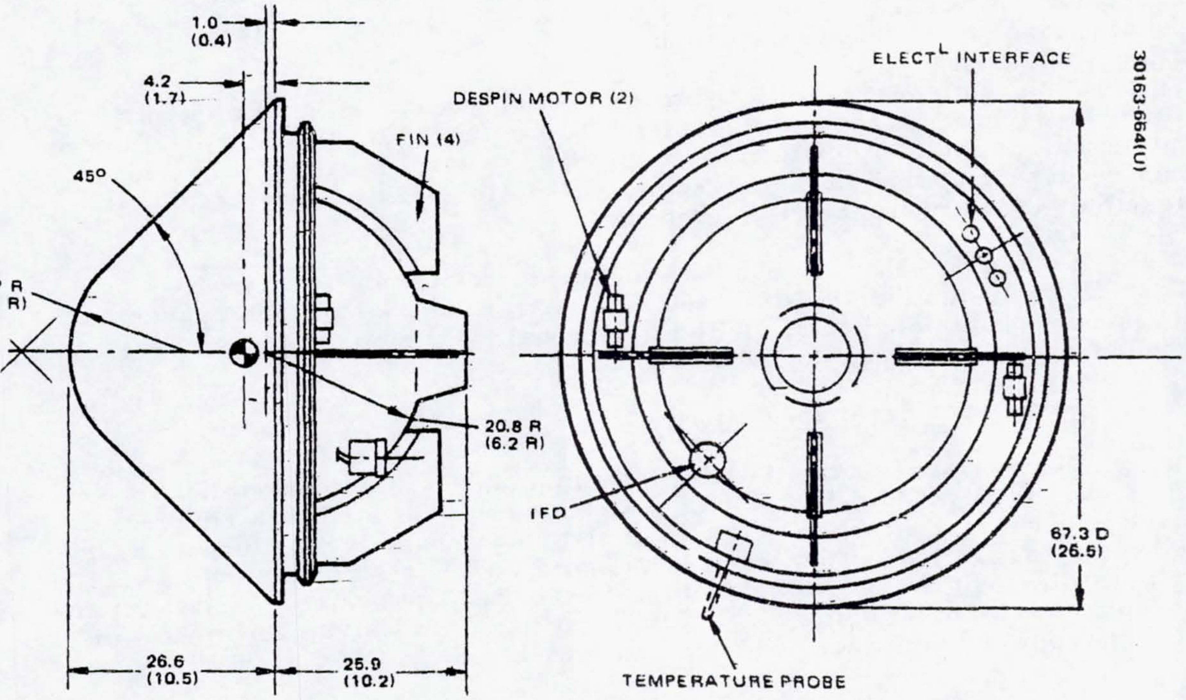

DIMENSIONS IN CENTIMETERS (INCHES)

FIGURE 1-11. ATLAS/CENTAUR SMALL PROBE CONFIGURATION

TABLE 1-4. LARGE PROBE WEIGHT SUMMARY
– ATLAS/CENTAUR MISSION

Deceleration module		90.8 kg (200.2 lb)
Heat shield	35.5 (78.3)	
Structure	39.1 (86.3)	
Aft cover	7.5 (16.5)	
Parachute	4.7 (10.4)	
Harness	1.7 (3.8)	
Pressure vessel separation	0.7 (1.5)	
Instrumentation	0.2 (0.4)	
Ballast	1.4 (3.0)	
Pressure vessel module		152.5 kg (336.2 lb)
Structure	69.7 (153.6)	
Thermal control	27.2 (60.0)	
Radio	5.8 (12.7)	
Command/data handling	3.5 (7.8)	
Power	12.9 (28.5)	
Antenna	0.2 (0.5)	
Harness	1.0 (2.3)	
Instrumentation	0.5 (1.1)	
Science instruments	31.6 (69.7)	
Entry weight		243.3 kg (536.4 lb)
Bus separation	1.8 (4.0)	
Weight on bus		245.1 kg (540.4 lb)

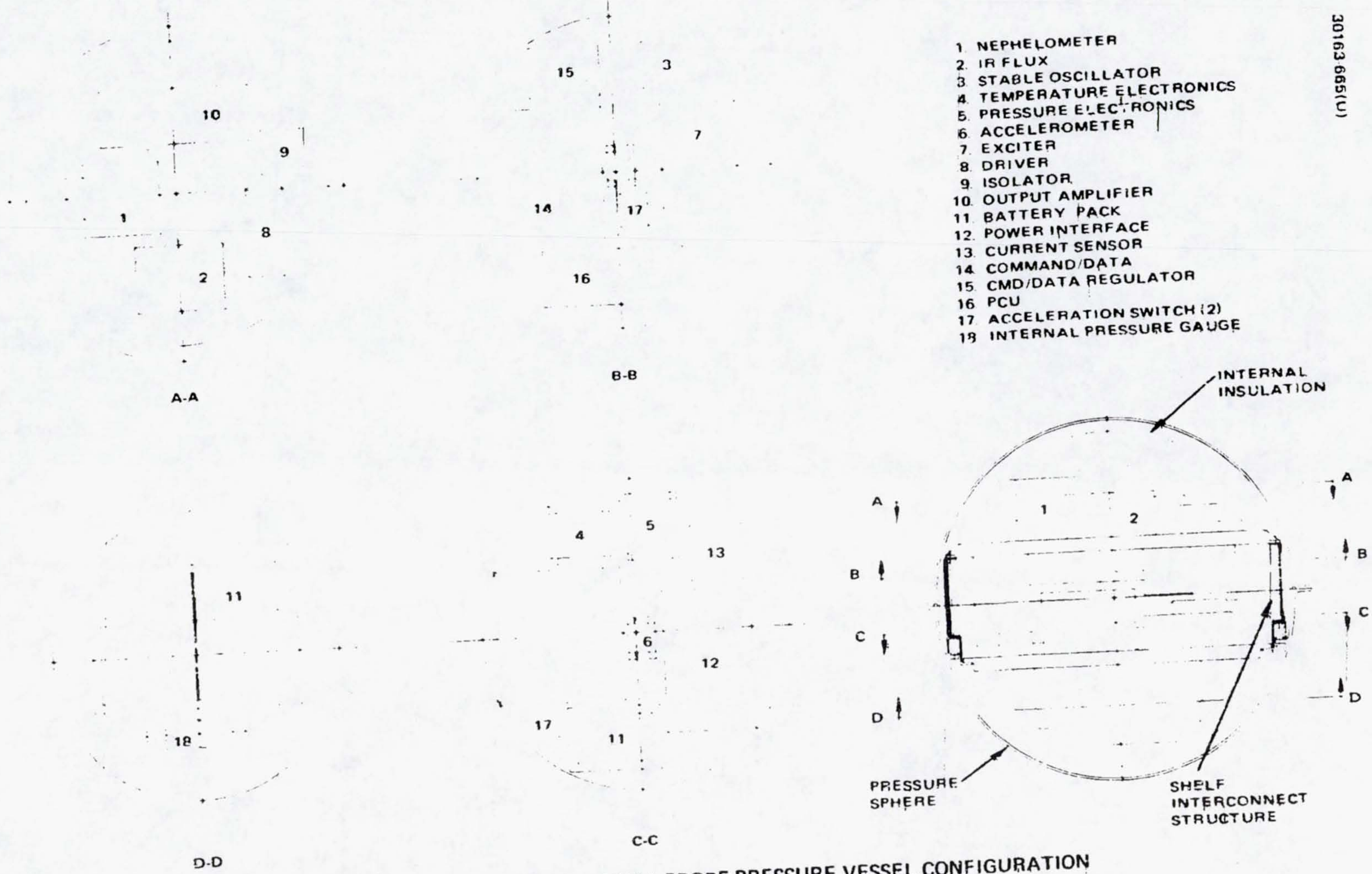

FIGURE 1-12. ATLAS/CENTAUR SMALL PROBE PRESSURE VESSEL CONFIGURATION

large enough to give a 50 percent greater static stability margin than Thor/Delta to allow more pressure vessel design flexibility.

The Atlas/Centaur small probe, like Thor/Delta, does not have an aft cover, but instead provides insulation directly on the pressure vessel and separate covers.

Separation/Despin

The Atlas/Centaur separation and despin subsystems are identical in concept with those used in the Thor/Delta design, and differ only in size.

Heat Shield/Aeroshell Structure

The small probe heat shield material is the same as for the large probe, carbon phenolic, for identical reasons.

The aeroshell structure is of stainless steel and monocoque in construction. Steel was chosen rather than titanium because of the uncertainty about the chemical compatibility of titanium with the lower atmosphere.

Pressure Vessel Configuration/Construction

The small probe pressure vessel module (Figure 1-12) is a sphere of outer diameter 41.4 cm (16.3 in.). It contains all of the instrument electronics and the housekeeping subsystems. The basic shell structure is a monocoque constructed of maraging steel and is internally insulated. The pressure vessel contains two equipment mounting shelves, with the upper shelf mounted from the lower shelf rather than to the shell, as in the large probe.

The internal insulation/heat sink thermal control scheme is the same as in the large probe: a fiberglass blanket held in place against the shell by an internal retainer and solid aluminum shelves which are also heat sinks. The stacked washer concept is also used for shelf thermal isolation.

Because it is feasible with the internal insulation design and also greatly simplifies the pressure vessel/aeroshell interface, several items of equipment are mounted on the pressure vessel rather than the aeroshell. Specifically, the four roll-damping fins, the IFD, and the two swing-out arms which house temperature sensor and radiometer mirror are all pressure vessel mounted.

Probe Weight

The small probe weighs 63.3 kg (139.6 lb) mounted on the multiprobe bus. It carries 2.6 kg (5.7 lb) of instruments in a 38.4 kg (84.7 lb) pressure vessel module, and has a ballistic coefficient of 169 kg/m^2 (34.6 lb/ft^2). A weight breakdown by subsystem is given in Table 1-5.

TABLE 1-5. SMALL PROBE WEIGHT SUMMARY
– ATLAS/CENTAUR MISSION

Deceleration module		23.8 kg (52.5 lb)
Heat shield	10.0 (22.1)	
Structure	13.2 (29.2)	
Harness	0.2 (0.4)	
Ballast	0.4 (0.8)	
Pressure vessel module		38.4 kg (84.7 lb)
Structure	15.9 (35.0)	
Thermal control	9.8 (21.5)	
Radio	1.6 (3.6)	
Command/data handling	2.7 (5.9)	
Power	5.2 (11.4)	
Antenna	0.2 (0.5)	
Harness	0.3 (0.6)	
Instrumentation	0.2 (0.5)	
Science instruments	2.6 (5.7)	
Entry weight		62.2 kg (137.2 lb)
Separation/despin	1.4 (3.0)	
Weight on bus		63.6 kg (140.2 lb)

2. INTRODUCTION

The probe bus transports four smaller vehicles to the vicinity of Venus, a large probe and three small probes. Each of these has two major components: a deceleration module to provide atmospheric braking and thermal protection from aerodynamic heating, and a pressure vessel module which contains and protects a science instrument payload and the power, data command, and radio subsystem necessary to support it. The nstruments and housekeeping subsystems are covered in separate volumes of this report. The present volume is concerned with the design of the probe vehicles, i.e., the nonelectronic probe subsystems. Designs for both Thor/Delta and Atlas/Centaur missions and the studies, trades, and ests which led to these designs are described in the following pages.

The volume is organized into three principal sections: a summary description of the probes, and sections devoted to the pressure vessel module and the deceleration module. In each of the latter two sections, the vehicular subsystems and technology disciplines are considered ndividually. Each of these subsections contains, typically, a statement of requirements; a summary of studies, trades, and tests; and a description of the Thor/Delta and Atlas/Centaur subsystem baseline design. The studies/tests subsections are necessarily heavily Thor/Delta oriented. Where the conclusions differ for Atlas/Centaur because of, or instance, different evaluation criteria, the differences are so noted.

REPRODUCIBILITY OF THE ORIGINAL PAGE IS POOR.

3. REQUIREMENTS

The probes have a single primary requirement: to deliver a set of science instruments into the atmosphere of Venus while simultaneously protecting them and giving them access to the atmosphere. Tables 3-1 and 3-2 summarize the representative science payloads used in large and small probe design for Thor/Delta mission; Tables 3-3 and 3-4 are similar summaries for the Atlas/Centaur mission. The Atlas/Centaur instrument descriptions include 15 percent weight and volume contingencies and 20 percent power contingencies, while the Thor/Delta lists do not.

Each of these instruments has its own subset of requirements for physical integration into the probe vehicles; since all are covered in some detail in Section 4.5, they will not be repeated here. The general requirement, however, is that all instruments be deployed and operating substantially above the top of the opaque clouds, and Hughes has assumed that a minimum initial operational altitude of 66 km will satisfy this requirement. Furthermore, the probes are required to remain operational until impact.

Other probe requirements imposed by the science payload are:

1) The large probe pressure vessel module must spin. This is required for wind/altitude radar scanning in the Atlas/Centaur mission and aureole scanning in the Thor/Delta mission.

2) The small probe must spin in the Thor/Delta mission to provide magnetometer resolution.

3) Both large and small probes must be aerodynamically well behaved in order to permit interpretation of accelerometer, temperature, and pressure data in the atmosphere reconstruction experiment.

Probe atmosphere entry conditions are determined by launch date (and trajectory type) and by targeting of the impact locations on the planet. Targeting is in turn a function of science and communication requirements, all of which are described in Volumes 2 and 3. The net result of these considerations is a set of probe design conditions which are summarized in Table 3-5. The maximum (most nearly vertical) entry angle trajectories lead to structural design conditions, the minimum entry angles lead to heat shield design conditions, and both structural and heating loads increase with entry velocity.

The atmosphere model used in the probes design is Model No. 1 of NASA SP8011 (1972). It is considered the most probable of the several models proposed in that document and results in a planet surface pressure of 94.9 earth atmospheres and a surface temperature of 768 deg K.

An important environmental consideration is the effect of cloud constituents, aerosols, and dust on the probes, particularly on instrument windows. Elements which have either been identified or inferred from earth-based measurements range from mercury compounds to hydrochloric and sulfuric acids. It is difficult to place a quantitative design requirement in this area and instead a design philosophy has been adapted to heat all windows to temperatures slightly higher than the local ambient, thereby preventing condensation. Furthermore, it is required that all windows be designed as double windows: an inner pressure/temperature resistant element and an outer element which is jettisoned at 35 to 40 km altitude and therefore does not carry pressure loads. This concept provides a one-time removal of contaminants just below the altitude range where aerosols are most likely to occur.

The Thor/Delta launch vehicle has marginal payload capability for the constraints of this mission. Consequently, the driving Thor/Delta design criterion is to minimize weight. Low cost is also very important, but the weight problem is so severe that it dominates the design.

The Atlas/Centaur mission, on the other hand, provides more than adequate weight margin, so that low cost can indeed be the primary design criterion.

TABLE 3-1. SCIENCE INSTRUMENT PAYLOAD - LARGE PROBE (THOR/DELTA MISSION)

Instrument	Weight, kg	(lb)	Volume, cm^3	(in^3)	Power W
Temperature sensing	0.59	(1.3)	197	(12)	1.0
Pressure sensing	0.82	(1.8)	229	(14)	1.0
Accelerometers	1.13	(2.5)	655	(40)	2.3
Mass spectrometer	7.71	(17.0)	10,651	(650)	12.0
Solar flux radiometer	1.81	(4.0)	1,966	(120)	4.0
Planetary flux radiometer	2.27	(5.0)	1,966	(120)	4.0
Cloud particle analyzer	3.63	(8.0)	3,277	(200)	20.0
Nephelometer	1.13	(2.5)	1,311	(80)	2.0
Aureole extinction detector	1.81	(4.0)	1,966	(120)	2.0
Hygrometer	0.45	(1.0)	197	(12)	0.3
Shock layer radiometer	1.13	(2.5)	442	(27)	1.0
Total	22.48	(49.6)	22,857	(1,395)	49.6

NOTE: No weight, volume or power contingency.

TABLE 3-2. SCIENCE INSTRUMENT PAYLOAD - SMALL PROBE
(THOR/DELTA MISSION)

Instrument	Weight, kg	(lb)	Volume, cm^3	(in^3)	Power W
Temperature sensing	0.34	(0.75)	98	(6)	0.5
Pressure sensing	0.41	(0.9)	115	(7)	0.5
Nephelometer	0.45	(1.0)	377	(23)	1.0
Accelerometer	0.18	(0.4)	33	(2)	1.0
Magnetometer	0.50	(1.1)	213	(13)	1.0
Stable oscillator	0.34	(0.75)	131	(8)	0.25
Total	2.22	(4.9)	967	(59)	4.25

NOTE: No weight, volume or power contingency.

TABLE 3-3. SCIENCE INSTRUMENT PAYLOAD - LARGE PROBE (ATLAS/CENTAUR MISSION)

Instrument	Weight*, kg	(lb)	Volume*, cm^3	(in^3)	Power**, W
Temperature sensing	0.34	(0.75)	115	(7)	0.6
Pressure sensing	0.47	(1.04)	131	(8)	0.6
Accelerometers	1.32	(2.90)	754	(46)	2.8
Mass spectrometer	10.43	(23.0)	11,307	(690)	14.4
Solar flux radiometer	2.61	(5.75)	1,885	(115)	4.8
Cloud particle analyzer	4.17	(9.2)	3,769	(230)	24.0
Planetary flux radiometer	2.61	(5.75)	1,885	(115)	3.6
Gas chromatograph	4.44	(9.8)	4,719	(288)	7.2
Hygrometer	0.59	(1.3)	377	(23)	0.3
Wind altitude radar	4.59	(10.12)	9,423	(575)	48.0
Total	31.57	(69.61)	34,365	(2,097)	106.3

* Contain 15 percent weight and volume contingencies

** Contain 20 percent power contingencies.

TABLE 3-4. SCIENCE INSTRUMENT PAYLOAD - SMALL PROBE (ATLAS/CENTAUR MISSION)

Instrument	Weight*, kg	(lb)	Volume*, cm^3	(in^3)	Power** W
Temperature sensing	0.34	(0.75)	115	(7)	0.6
Pressure sensing	0.47	(1.04)	131	(8)	0.6
Accelerometer	0.23	(0.50)	33	(2)	1.2
IR flux detector	0.63	(1.40)	377	(23)	1.2
Stable oscillator	0.41	(0.90)	147	(9)	0.3
Nephelometer	0.52	(1.15)	606	(37)	1.2
Total	2.60	(5.74)	1,409	(86)	5.1

* Contain 15 percent weight and volume contingencies.

** Contain 20 percent power contingency.

TABLE 3-5. PROBE ENTRY CONDITIONS

	Velocity, km/sec	(ft/sec)	Flight Path Angle, deg down from horizontal	Angle of Attack deg
Thor/Delta mission				
Large probe	11.14	(36,550)	35 to 60	0
Small probes	11.14	(36,550)	20 to 90	< 35
Atlas/Centaur mission				
Large probe	11.60	(38,060)	25 to 60	0
Small probes	11.60	(38,060)	20 to 90	< 30

4. PRESSURE VESSEL MODULE

The pressure vessel modules play a key role in the Pioneer Venus probes mission. Their prime functions are to house and protect the scientific instruments, communications, and housekeeping equipment from the hostile Venusian environment and to provide a stable and predictable descent that will allow the instruments to perform as intended. Because of the modules' importance to the mission, the severe environment to be encountered, and the necessity to minimize weight and cost, it is essential that the design be thoroughly optimized.

To this end a series of trades and tests were conducted during the study which were used to support the pressure vessel module design process. The roles which these trades and tests play in the design process are illustrated in Figure 4-1. These trades were performed with much interchange and feedback during the study; this assured a coherence in the overall module design.

The following sections discuss each of the several trades and tests performed in support of the pressure vessel module design. The results are summarized in Table 4-1.

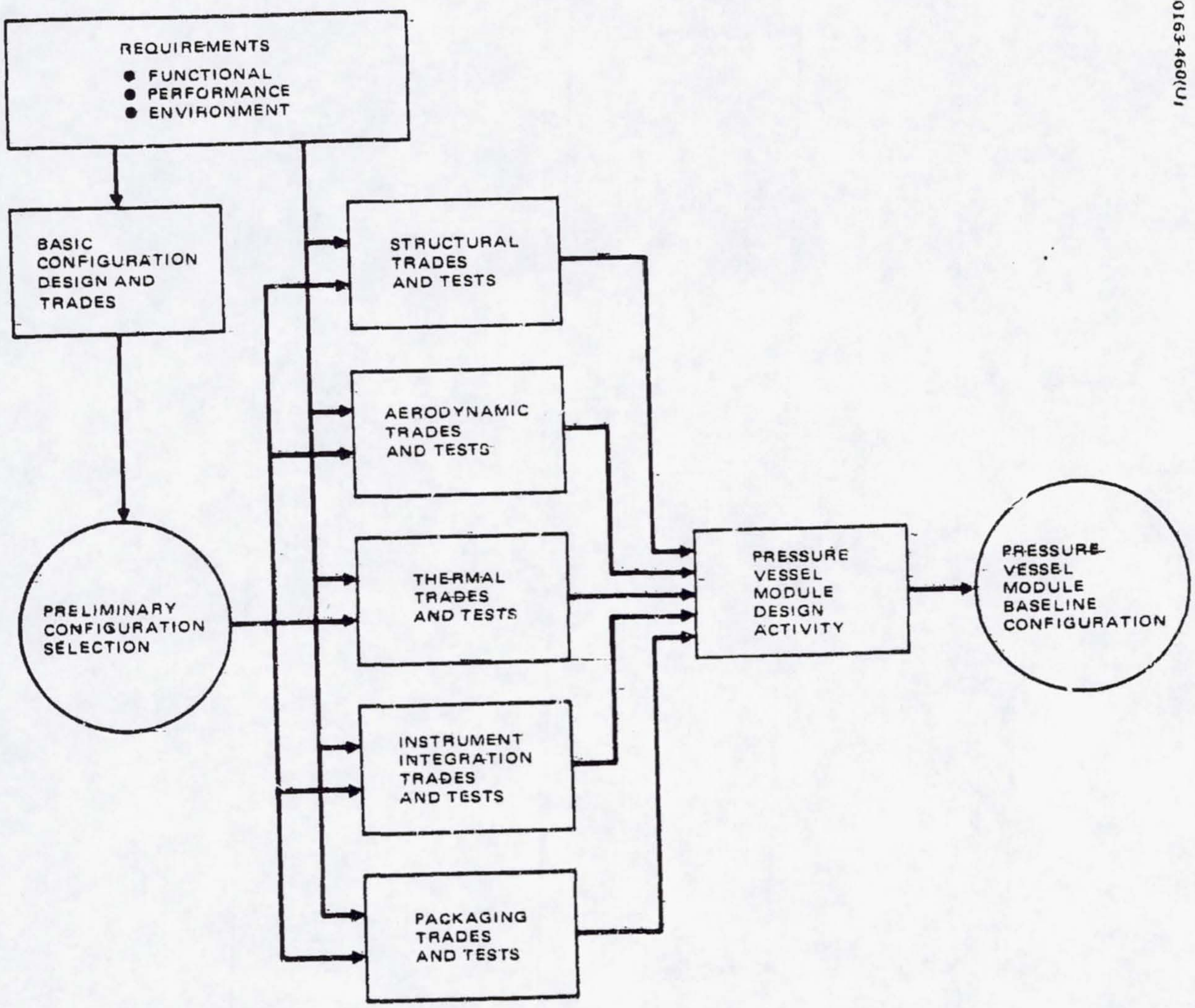

FIGURE 4-1. PRESSURE VESSEL MODULE DESIGN PROCESS

TABLE 4-1. PRESSURE VESSEL TRADE STUDIES

Trades, Tests, Studies	Alternatives	Selection and Reasons	Reason for Trade
Configuration			
Container shape	Spherical versus nonspherical	Spherical — structurally most efficient weight wise, cost wise	Basis for selection of lightest weight, lowest cost configuration. Affects most subsequent module design activity
Equipment shelf arrangement	Horizontal versus vertical	Horizontal — most efficient weight wise; good packaging accessability and producibility	To minimize overall module cost and weight
Pressure protection	Complete encapsulation: vessel stands full pressure. Various alternatives of partial pressure vessels	Complete encapsulation — lowest cost, minimum weight	Minimize overall module cost and weight
Pressure vessel construction	Hemispherical versus multisegmented spherical construction	Hemispherical — more reliable, lower cost	Minimize cost, maximize reliability
Packaging	Conformal versus parallelopiped packaging of units	Conformal packaging for power subsystems, parallelopiped for others — maximum overall packaging density, with negligible cost increase	Maximize packaging density which minimizes module size, weight, and overall cost
Aerodynamic Configuration			
Water tank tests	Five spherical configurations modified to include basic sphere plus stems, flares, discs, and fins	All but one configuration (5) acceptable for further tests — acceptable stability	Preliminary screening to select configurations for more extensive (and expensive) wind tunnel tests
Spin tunnel tests (LRC)	Eleven basically spherical configurations including those selected in above water tunnel tests	Configuration 7, a ring with vanes stabilized sphere — good stability, simplest construction	Selection of baseline aerodynamic configuration for pressure vessel module
Dynamic behavior analysis			Aid in selection of baseline configuration and provide aerodynamic characteristics and flight dynamic performance during descent, including gust disturbances
Structure			
Selection of pressure vessel structural design	Structural design alternatives: Monocoque versus waffle stiffened material Material Alternatives: Titanium Aluminum Beryllium Steel	Steel monocoque — construction compatible with Venusian atmosphere, good for hot wall construction, low cost, acceptable weight	Optimize basic structural design for minimum weight and cost
Steel selection	Maraging steel 17-4PH steel D6AC steel	Maraging steel — best in welding and heat treat characteristics; equivalent in forming and machining. Raw material cost slightly higher but acceptable. Compatible with Venusian atmosphere.	Optimize basic structural design for minimum weight and cost
Internal versus external insulation	All insulation external to shell versus internal insulation with heat sink masses on shelves	Internal insulation heat sink — significantly lower in cost, more reliable, not appreciably heavier	Minimize overall cost
Thermal			
External insulation material selection	Min-K TE 1400 FA fiberglass Paralite	Min-K and FA fiberglass for further consideration. Min-K prime candidate because of low thermal conductivity	Obtain lightest weight, minimum size, lowest cost insulation design
External versus internal insulation	External application: Min-K TE 1400 Multilayer insulation (MLI) with vacuum around internal package	Internal insulation — lower cost, weight increase not significant for Atlas-Centaur	Minimize insulation cost
Phase change material	PCM attached to [illegible] internal components No PCM	PCM not recommended — high development cost, although lower in weight	Obtain minimum cost insulation installation with acceptable weight

TABLE 4-1. (continued)

Trade – Test – Study	Alternatives	Selection and Reasons	Need for Trade
Science, [illegible] structure - Integration			
Window material selection	Visible wavelengths: Sapphire, fused silica	Sapphire – overall superiority in nearly all physical and optical properties; readily available and acceptable in cost	Selection of material to best meet wide variety of requirements at acceptable cost
	Infrared wavelengths: Hot pressed zinc sulfide (Irtran II) Hot pressed zinc selenide (Irtran IV) Chemically vapor deposited zinc selenide (CVD Zn Se)	CVD Zn Se – meets all criteria for window. Other candidates inferior in one or more requirements	Selection of material to meet wide variety of requirements at acceptable cost
Window mechanical design	Seals Hollow metallic O-ring Rigid brazed seal	Brazing for windows remote from pressure vessel, O-rings for interface with pressure vessel wall – optimum use	Optimization of seal methods
	Fabrication methods for penetrations Integral machining of doubler into wall Axisymmetric plug welded into hole Bonding doubler around penetrations	Electron beam welding of axisymmetric plugs – cost low, no effect on pressure vessel structural integrity	Minimize overall cost, maximize reliability
Window configuration	Nephelometer source windows Prism configuration Remote window configuration	Remote window configuration – less heater power, easier integration with insulation	Minimize power, simplify integration
	Solar radiometer window Pressure vessel mounted External scanning mirror Remote mounted window, external scanning element	Remote mounted window, external scan – minimum weight, eliminates hot spot	Minimize weight, increase reliability
	Planetary flux radiometer window Brazed window, CVD Zn Se O-ring sealed	Brazed window – lightest weight, equal or lower power	Minimize weight and power
	Cloud particle size spectrometer window Dual window, separate source and sensor lenses Remote mounted window, single lens Integral mirror mount	Integral mirror mount – best alignment	Increase ability to maintain precise alignment at acceptable cost
Window heater design	Film heaters Thin wires – sandwich Edge heating	Film heaters or edge heater, depending on application	Minimize power
Contaminant removal systems	Frangible, squib-actuated tempered glass cover Transparent, jettisonable protective cover Transparent rotary shutter Mechanical shutter Mechanical wiper Gas jet	Jettisonable, protective covers – lowest weight, lowest power, low development risk	Minimize weight, power and risk
Large probe pressure sensor inlet system	Shelf mounted Wall mounted	Shelf mounted – minimizes pressure sensor temperature	Obtain accurate pressure measurement with acceptable weight and complexity
Stagnation point pressure sensor, small probe	Refractory tube survivable probe Jettisonable plug protected during entry Moveable piston cutter, pyrotechnic activated	Jettisonable plug – integration most straightforward, most confidence in functioning	Obtain most reliable method with acceptable weight and cost
Cloud particle size spectrometer mirror	Mirror mounted to pressure vessel wall Mirror mount integral with instrument	Integrally mounted mirror – most reliable alignment	Obtain accurate alignment with acceptable weight and cost
Large probe pressure vessel module aeroshell in-flight disconnect	Cable cutter disconnect Electrically released	Pyrotechnic cable cutter best for high g, superior electrical isolation, lowest weight	Obtain most reliable, lightest weight in-flight disconnect

TABLE 4-1 (continued)

Trades, Tests, Studies	Alternatives	Selection and Reasons	Need for Trade
Small probe nephelometer window protective cover	Mechanically latched door Pyrotechnically activated jettisonable cover	Pyro-activated, jettisonable cover – highest reliability under high g	Obtain most reliable protective cover with acceptable weight and cost
Communications antenna rf feedthrough configuration	Remotely located feed-through Axial feedthrough	Axial mounted feedthrough lower rf losses, approximately equal otherwise	Obtain minimum rf loss with acceptable reliability, weight, and cost
Unit Packaging and Integration			
High g study	Component assembly techniques (MICAM) micro connection and assembly method (countdown chain) Cordwood (preregulator) Point-to-point (cross strap converter) Printed circuit (quartz oscillator-Hewlett Packard)	All methods acceptable for Venusian atmospheric entry – survived 500 to 800 g in centrifuge test	Verify acceptability of Hughes methods of construction and assembly for this application
Connectors and small gage wire	28 AWG wires and micro-miniature connectors 24-22 AWG wires and sub-miniature connectors	28 AWG wire and micro-miniature connectors – large weight and volume advantage	Determine lowest weight, volume combination with acceptable reliability and cost
Conformal packaging	Conventional nonconformal packaging Conformal packaging of power subsystem Conformal packaging of digital subsystem Conformal packaging of rf subsystems	Conformal packaging of power systems only is recommended – for digital units. It is too expensive for rf systems. it is not required.	Minimize packaging volume hence overall vessel weight with acceptable cost

4.1 CONFIGURATION

In selecting the configuration for the large- and small probe pressure vessel module, the key design goals were:

1) Compatibility with mission and functional requirements

2) Structural efficiency

3) Efficient packaging arrangement

4) Ready producibility

5) Minimum cost

The most significant aspect of the configuration finally chosen is its spherical geometry. While numerous evolutionary changes in other aspects of the configuration have taken place during the course of the Phase B program, particularly after the decision to use the Atlas/Centaur as the launch vehicle, the sphere has been retained due to its pressure load carrying efficiency. Modifications of the Thor/Delta baseline configuration after the change to Atlas/Centaur stemmed primarily from increases in the required volume of science equipment, from the addition of a wind/altitude radar antenna, and from a decision to convert from an externally insulated design to an internally insulated one. An external fairing was necessary once the wind/altitude radar antenna was added so that the same tested external shape as the Thor/Delta design could be retained. Similarity in shape was required to assure that the aerodynamic performance of the Atlas/Centaur design will be equivalent to the test proven aerodynamic performance of the Thor/Delta configuration.

The significant trade studies that justify the selection of the final baseline configuration were all performed during the Thor/Delta-oriented design period. However, the results of these studies are equally valid for the Atlas/Centaur based design. The following is a summary list of these trade studies together with a brief statement of the essential results. These trade studies are described in greater detail in the following subsection.

Trade Study	Principal Result
1) Spherical versus nonspherical pressure vessel geometry	Spherical superior because most weight efficient pressure load structure
2) Separate horizontal shelves versus vertical shelf assembly	Separate horizontal shelves superior because of best packaging efficiency

3) Single container protecting all contents from external pressure versus vented container with discrete unit protection as required	Single vessel protection superior. It is less costly and lower weight.
4) Hemispherical construction versus multisegmented spherical construction	Hemispherical construction more reliable and lower cost.
5) Conformally packaged units versus parallelopiped packaged units	Conformal packaging advantageous for some subsystems.

The final Thor/Delta configuration selected is described in detail in a later subsection. Briefly however, this configuration may be described as a thin shelled spherical metallic vessel constructed of two hemispheres joined together by a sealed main assembly flange. The vessel is covered with a thick insulation which is in turn surrounded by a thin, nonstructural metalic retainer. The pressure-vessel shell includes numerous reinforced and sealed pentrations which extend thru the insulation and retainer. Internal to this vessel, the contained units are attached to and supported by two horizontal circular shelves which are readily removable. One of these shelves is attached to the upper hemisphere, the other to the lower. A multipinned connector provides electrical continuity between the hemispheres. These connections are automatically broken upon separation of the hemispheres. The pressure vessel module is attached to the aeroshell by means of a thin metallic conical adapter. This adapter which stays with the pressure vessel module after aeroshell seperation, also provides a thin annular horizontal ring which is used for aerodynamic stabilization during free fall.

The Atlas/Centaur pressure vessel module baseline configuration, while identical in concept to the previously described Thor/Delta design, does not have external insulation or its retainer. To provide external aerodynamic characteristics identical to the Thor/Delta design, a thin metallic fairing encapsulates the bottom hemisphere and provides the proper external contour to the annular aero-stabilization ring. Penetrations for science requirements are provided for in this fairing.

The Atlas/Centaur baseline design is described in greater detail in a subsection which follows.

Requirements

The design requirements and criteria that formed the basis for the final selection of the configuration are summarized as follows:

1) An efficient structural shape for carrying high external pressure and high deceleration loads.

2) Must be compatible with science requirements

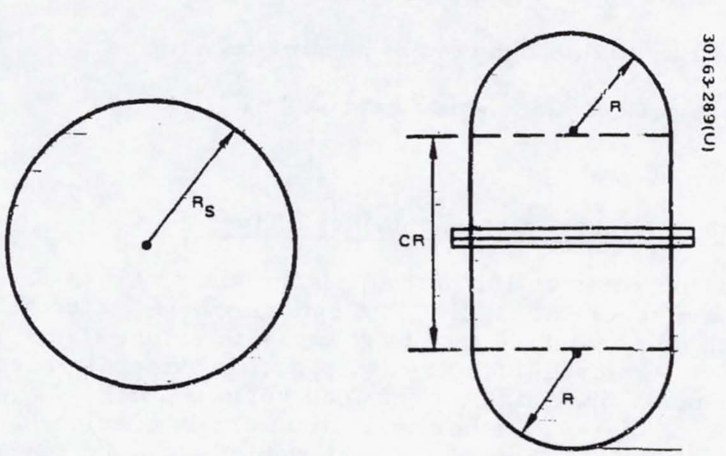

FIGURE 4.1-1. PRESSURE VESSEL CONFIGURATIONS

3) High packaging density

4) Good producibility at minimum cost.

5) Easy mounting and ready interconnecting for all on-board equipment as well as simple and ready access to all on-board equipment for servicing.

6) Aerodynamic stability

7) Convenient mating with the deceleration module.

8) Adaptable to reliable convenient sealing techniques.

9) Convenient reliable insulation approaches.

Trade Studies

Spherical versus Nonspherical Container Shape

The configuration selected for both the large and small probe pressure vessels is that of a thin spherical shell. The sphere was selected as a result of a trade study which demonstrated that it would be the most structurally efficient (and therefore lightest) geometry for reacting external pressure loads while simultaneously providing a contained volume which was just as adaptable to efficient packaging as other less structurally efficient designs. In the trade study an analytical comparison was made between a spherical shell and a sphere/cylinder combination, with both providing the identical internal volume.

With the geometrical shape parameters as shown in Figure 4. 1-1, the trade study analyses first derived an expression for the ratio of the surface area of the sphere, A_s, to the surface area of the sphere/cylinder A_c. The ratio described was found to be

$$\frac{A_s}{A_c} = \frac{\left(1 + \frac{3C}{4}\right)^{2/3}}{\left(1 + \frac{C}{2}\right)}$$

From this result it can be seen that for any value of $C > 0$, $A_s/A_c < 1$ which means that the surface area of the sphere will always be less than that for the sphere/cylinder of equal volume. As a result, if the same shell thickness were selected for both configurations, the sphere would weight less.

Next, in the trade study, a comparison was made of the shell thickness that would be required for each configuration to produce the same maximum stress in each as a result of both being exposed to the same external design pressure. These are the thicknesses that would be selected for each design when fabricated from the same material and when the mode of failure for each is a material yielding. For each configuration, the weight of the resulting shell in the calculated thickness was computed. In the case of the sphere, the weight, W_s was found to be

$$W_s = \frac{2\pi P R^3 \left(1 + \frac{3C}{4}\right) w}{F_c}$$

where

P = The design pressure

F_c = Material yield strength allowable

w = Material density

In the case of the sphere/cylinder configuration it was found that the cylindrical portion would require a thickness twice as great as required for the spherical ends. Assuming that each portion is fabricated to its required thickness, the weight of the sphere/cylinder configuration, $W_{s/c}$, was found to be:

$$W_{s/c} = \frac{2 \; PR^3 (1 + C)w}{F_c}$$

with the symbol definitions as previously specified. The ratio of these weights becomes

$$\frac{W_s}{W_{s/c}} = \frac{1 + \frac{3c}{4}}{1 + C}$$

from which it can be seen that, again, the spherical configuration would produce the lighter design.

$$\left(\frac{W_s}{W_{s/c}} = < 1 \text{ for all } C > 0\right)$$

Finally, the trade study made a comparison of the weights of these configurations assuming that local buckling rather than material yield might be the governing mode of failure. The ratio of the weights of the resulting designs was found to be:

$$\frac{W_s}{W_{s/c}} = \frac{1 + \frac{3C}{4}}{1 + (.584)\, C^{1.4} \left(\frac{E}{P}\right)^{0.1}}$$

where

E = The modulus of elasticity of the selected shall material and all other symbols are as previously defined.

The weight of the sphere will thus be less than the weight of the sphere/cylinder if and only if

$$\frac{3C}{4} < 0.584C^{1.4} \left(\frac{E}{P}\right)^{0.1}$$

To evaluate this inequality for a typical selection of shell material and design pressure, the value of E for 6Al-4V titanium, (the Thor/Delta baseline material) and the ultimate design pressure corresponding to the Venus surface were chosen.

These values are

$E = 11.3 \times 10^6\ N/cm^2\ (16.4 \times 10^6\ psi)$

$P = 1200\ N/cm^2\ (1740\ psi)$

Using these values, the inequality becomes $0.75 < 1.45C^{1.4}$. It can be seen that this inequality will be true for any value of C greater than zero, thus proving that when using titanium, the sphere would be the lighter configuration should buckling prove to be the governing failure mode. This inequality can also be evaluated for the selected material in the Atlas/Centaur baseline design which is steel. In that case,

$E = 20.7 \times 10^6\ N/cm^2\ (30 \times 10^6\ psi)$

and the inequality reduces to:

$0.75C < 1.55C^{1.4}$

Since this will be satisfied by any value of C greater than zero, the sphere will be lighter than the sphere/cylinder if both are fabricated from steel. Thus the trade study clearly demonstrates that the sphere is the more structurally efficient design from a weight standpoint, regardless of the mode of failure.

TABLE 4.1-1. PROBE SHELF DESIGN COMPARISON

	Horizontal Shelf	Vertical Shelf
Number of independent shelves or subassemblies	(Parallel shelves) Two	(Orthogonal assembly) One
Shelf area (cm^2)	8120 (1260 in.^{2})	8300 (1284 in.^{2})
Degree of stacking units	None	Very high
Freedom to locate units to obtain desired center of gravity	Fair	Very limited
Shelf attaching bolt pattern	Full circle (360 deg)	Semicircle (180 deg)
Bolt loading mode	Tension	Shear and bending (close tolerance holes required)
Subsystem unit loading mode	Compression and tension	Shear and bending
Harness service loops between shelves	One required	None
Unit accessibility before shelf and pressure vessel mating	Good	Poor (accelerometer inaccessible)
Accessibility when pressure vessel is opened	Midsection: Good Upper third, lower third: Inaccessible	Lower half: Poor Upper half: Fair
Pressure vessel shell loading	Upper hemisphere: compression Lower hemisphere: tension	Entire internal mass reacted in lower hemisphere
Unit interconnection and cabling	Easy	Difficult

Several less efficient (and this heavier) configurations per unit volume such as the cylinder with hemispherical ends which was just discussed, and a rectangular box as well were considered and quickly abandoned as it became apparent that packaging efficiency was not improved to compensate for the excessive structural weight. Furthermore, no advantages in producibility or improvements in science instrument compatibility could be found in these other designs.

Horizontal versus Vertical Equipment Shelf Arrangement

The existing baseline design for both equipment shelves for the large probe and small probe consists of two parallel shelves which are orthogonal to the axis of symmetry (spin axis).

Each of these two shelves is attached to one of two mating hemispheres of the pressure vessel (Figure 4. 1-2 and 4. 1-3). This selection of shelf arrangement was confirmed by a study of a large and small probe vertical shelf concept. The large probe had two vertical shelves intersecting each other orthogonally along the axis of symmetry of the pressure vessel sphere (Figure 4. 1-4).

The small probe vertical shelf was a version of the same approach with one-fourth of the shelf deleted to provide for bulky units, i. e., command and data unit and discharge regulator (Figure 4. 1-5). All packages were identical to those on the horizontal shelf to make a fair comparison between two designs, and the conclusions are valid for either the Thor/Delta or the Atlas/Centaur.

The vertical shelf design divides the available volume into four equal segments and limits the lengths in two directions to that of the pressure vessel inside radius while the baseline design doubles the lengths in the same direction. This geometric restruction is reflected in "degree of stacking units" in Table 4. 1-1. In the vertical shelf arrangement, the capability for obtaining a desired center of gravity location by unit arrangement is severely hampered by this geometric restriction. Also, the unit attaching fasteners are primarily loaded in shear and consequently necessitate close tolerance matching holes in the units. Accessibility is rather difficult in either case but the vertical shelf seems to be inferior.

In Table 4. 1-2, these units which are desired to be located on the shelf or be close to the shelf because of dynamic loads, thermal dissipation, physical location requirement or configuration are listed. The totals of this table indicate that a minimum total shelf area of (3, 384 cm^2) is necessary to accommodate them. But the actual required shelf area is nearly twice this area due to geometric restrictions or nonconformity of shapes. Consequently, the units listed in Table 4. 1-2 which amount to 67 percent of the total mass to be packaged will require about 6500 cm^2 of shelf area, which is approximately 80 percent of that available. Obviously, to package the remaining components which amount to 33 percent by weight in only 20 percent of the available shelf area is difficult, if not impossible. Consequently,

REPRODUCIBILITY OF THE ORIGINAL PAGE IS POOR.

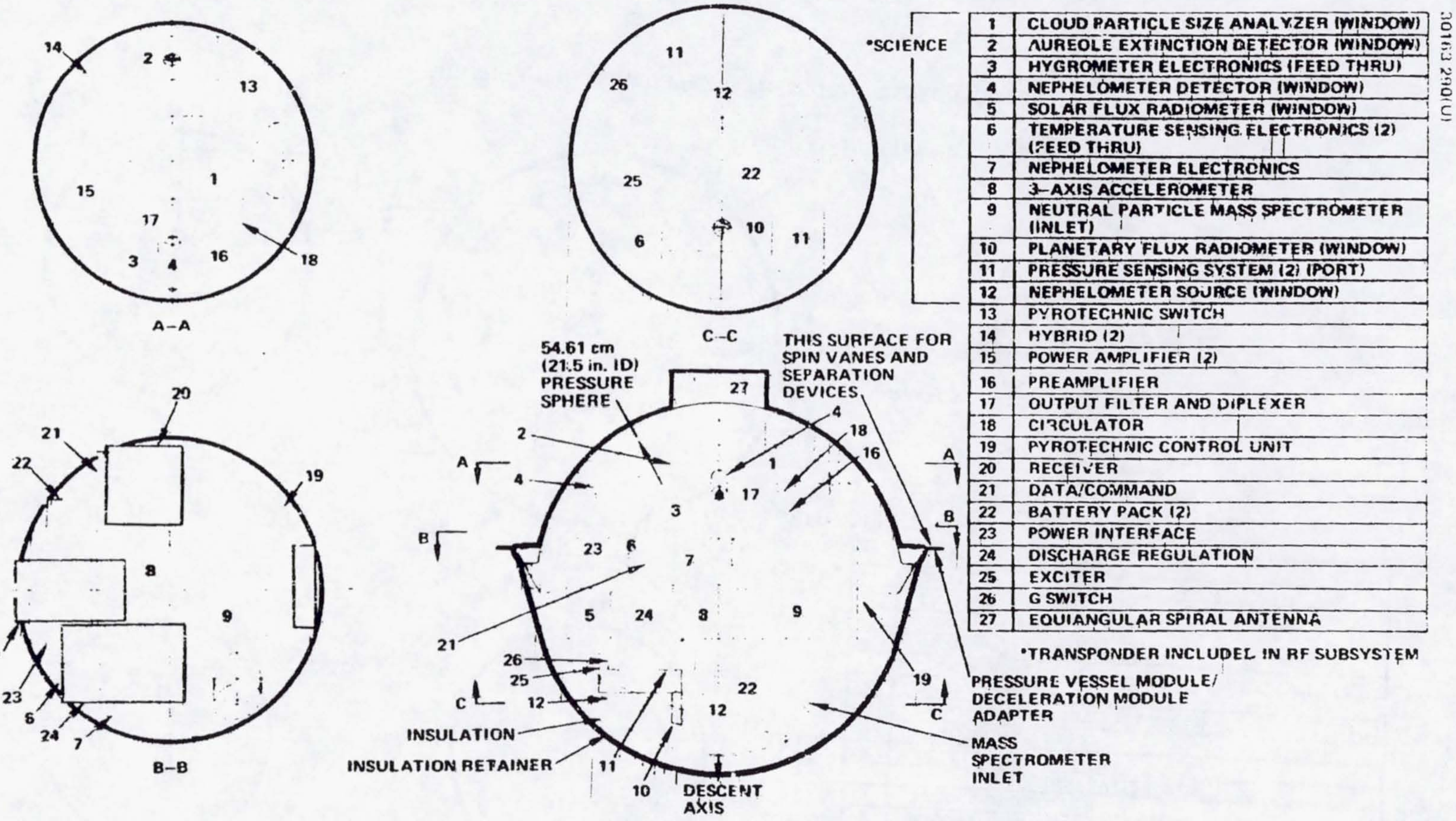

*SCIENCE	1	CLOUD PARTICLE SIZE ANALYZER (WINDOW)
	2	AUREOLE EXTINCTION DETECTOR (WINDOW)
	3	HYGROMETER ELECTRONICS (FEED THRU)
	4	NEPHELOMETER DETECTOR (WINDOW)
	5	SOLAR FLUX RADIOMETER (WINDOW)
	6	TEMPERATURE SENSING ELECTRONICS (2) (FEED THRU)
	7	NEPHELOMETER ELECTRONICS
	8	3-AXIS ACCELEROMETER
	9	NEUTRAL PARTICLE MASS SPECTROMETER (INLET)
	10	PLANETARY FLUX RADIOMETER (WINDOW)
	11	PRESSURE SENSING SYSTEM (2) (PORT)
	12	NEPHELOMETER SOURCE (WINDOW)
	13	PYROTECHNIC SWITCH
	14	HYBRID (2)
	15	POWER AMPLIFIER (2)
	16	PREAMPLIFIER
	17	OUTPUT FILTER AND DIPLEXER
	18	CIRCULATOR
	19	PYROTECHNIC CONTROL UNIT
	20	RECEIVER
	21	DATA/COMMAND
	22	BATTERY PACK (2)
	23	POWER INTERFACE
	24	DISCHARGE REGULATION
	25	EXCITER
	26	G SWITCH
	27	EQUIANGULAR SPIRAL ANTENNA

*TRANSPONDER INCLUDED IN RF SUBSYSTEM

FIGURE 4.1-2. LARGE PROBE PRESSURE VESSEL MODULE

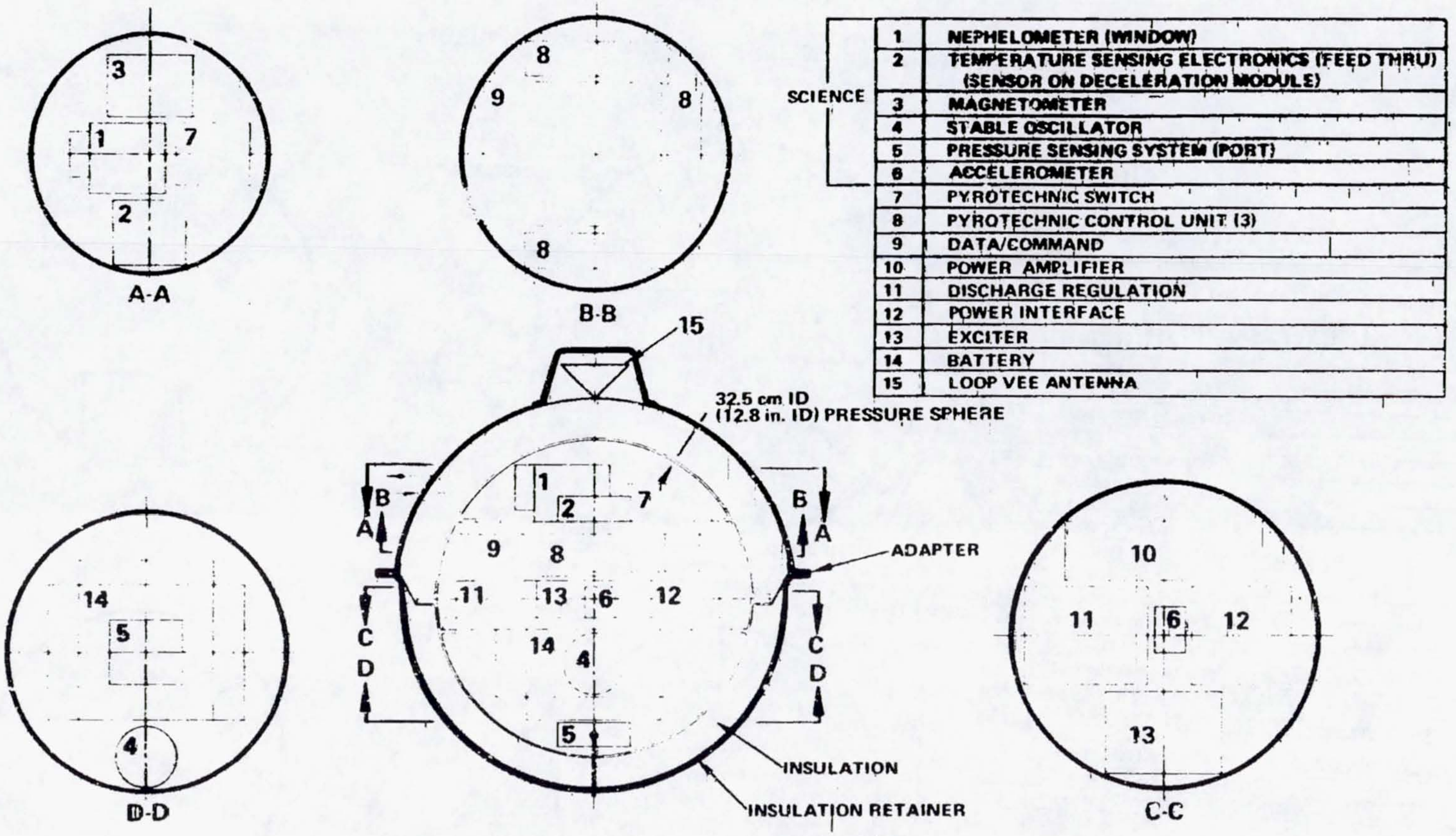

SCIENCE	1	NEPHELOMETER (WINDOW)
	2	TEMPERATURE SENSING ELECTRONICS (FEED THRU) (SENSOR ON DECELERATION MODULE)
	3	MAGNETOMETER
	4	STABLE OSCILLATOR
	5	PRESSURE SENSING SYSTEM (PORT)
	6	ACCELEROMETER
	7	PYROTECHNIC SWITCH
	8	PYROTECHNIC CONTROL UNIT (3)
	9	DATA/COMMAND
	10	POWER AMPLIFIER
	11	DISCHARGE REGULATION
	12	POWER INTERFACE
	13	EXCITER
	14	BATTERY
	15	LOOP VEE ANTENNA

FIGURE 4.1-3. SMALL PROBE PRESSURE VESSEL MODULE

REPRODUCIBILITY OF THE ORIGINAL PAGE IS POOR.

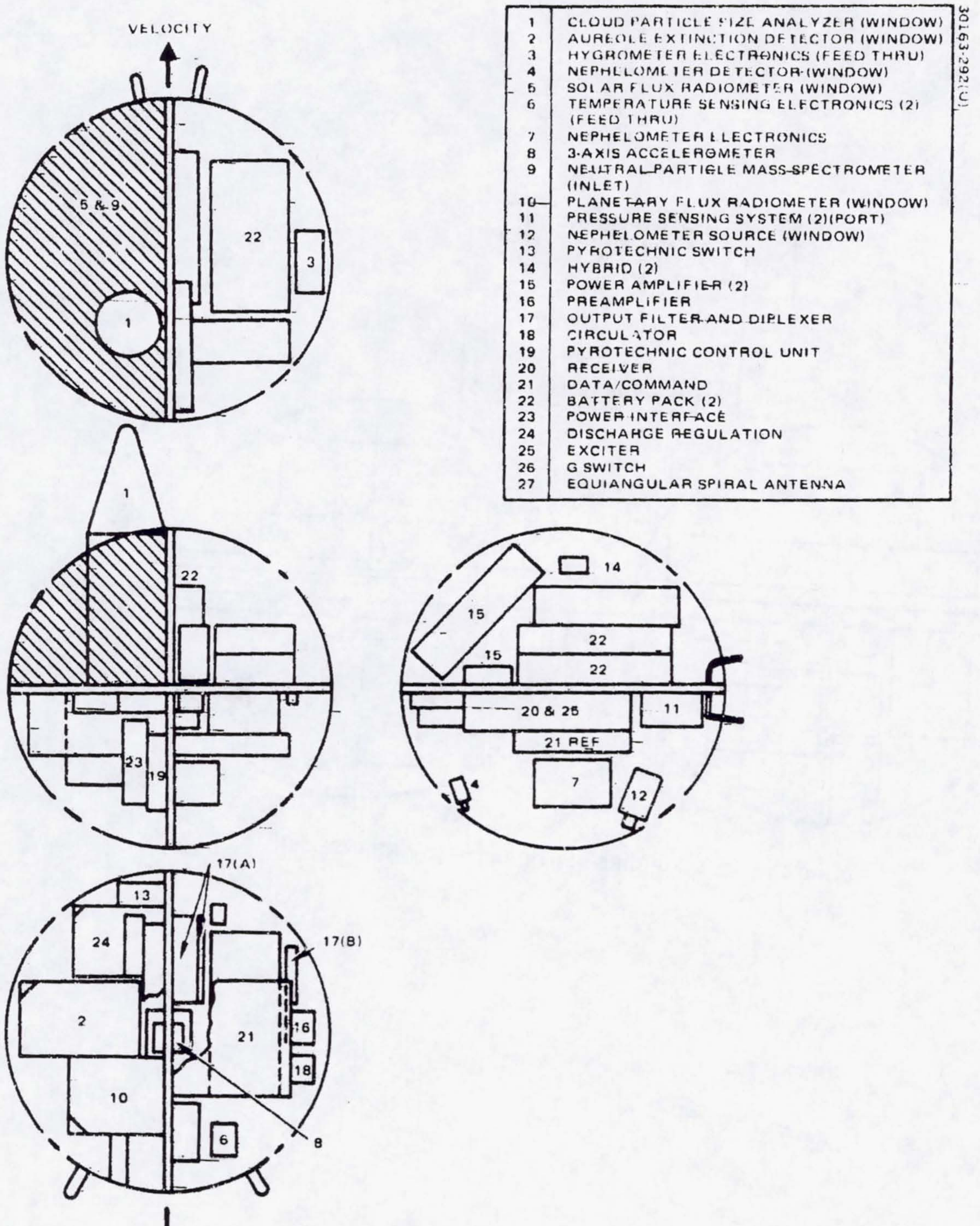

1	CLOUD PARTICLE SIZE ANALYZER (WINDOW)
2	AUREOLE EXTINCTION DETECTOR (WINDOW)
3	HYGROMETER ELECTRONICS (FEED THRU)
4	NEPHELOMETER DETECTOR (WINDOW)
5	SOLAR FLUX RADIOMETER (WINDOW)
6	TEMPERATURE SENSING ELECTRONICS (2) (FEED THRU)
7	NEPHELOMETER ELECTRONICS
8	3-AXIS ACCELEROMETER
9	NEUTRAL PARTICLE MASS SPECTROMETER (INLET)
10	PLANETARY FLUX RADIOMETER (WINDOW)
11	PRESSURE SENSING SYSTEM (2)(PORT)
12	NEPHELOMETER SOURCE (WINDOW)
13	PYROTECHNIC SWITCH
14	HYBRID (2)
15	POWER AMPLIFIER (2)
16	PREAMPLIFIER
17	OUTPUT FILTER AND DIPLEXER
18	CIRCULATOR
19	PYROTECHNIC CONTROL UNIT
20	RECEIVER
21	DATA/COMMAND
22	BATTERY PACK (2)
23	POWER INTERFACE
24	DISCHARGE REGULATION
25	EXCITER
26	G SWITCH
27	EQUIANGULAR SPIRAL ANTENNA

FIGURE 4.1-4. LARGE PROBE VERTICAL SHELF ARRANGEMENT

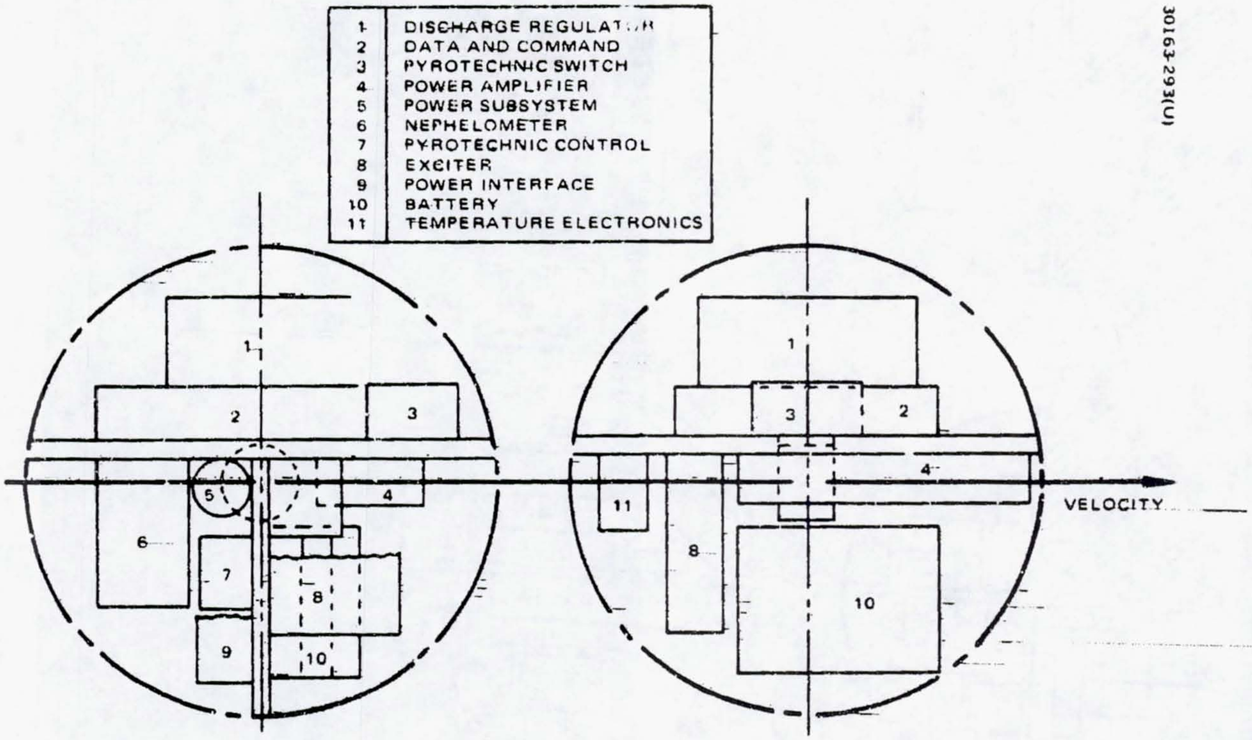

FIGURE 4.1-5. SMALL PROBE VERTICAL SHELF ARRANGEMENT

TABLE 4.1-2. UNITS REQUIRING EITHER FOOT-PRINTS ON SHELF OR ALLOTTED AREAS CLOSE TO SHELF

Unit	Size cm (in.)	Number Required	Total Mass kg (lb)	Unit, (W)	Foot Print Area, cm^2	Reason for Area Requirement
Power amplifier	20.3 x 7.6 x 3.2 (8.0 x 3.0 x 1.25)	2	0.91 (2.0)	45.4	310	Thermal
Exciter/receiver	27.3 x 12.7 x 6.4 (10.75 x 5.0 x 2.5)	1	1.82 (9.0)	7.0	346	Thermal
Discharge regulator	20.3 x 12.7 x 7.6 (8.0 x 5.0 x 3.0)	1	2.72 (6.0)	0.4	258	Thermal
Battery	27.3 x 12.7 x 6.6 (10.75 x 5.0 x 2.5)	3	6.67 (14.7)	-	1038	Mass and configuration
Accelerometer	10.2 x 7.6 x 7.6 (4.0 x 3.0 x 3.0)	1	1.13 (2.5)	-	78	Location
Cloud particle analyzer	12.7 dia x 25.4 (50.0 dia. x 10.0)	1	4.54	-	323	Location
Planetary flux radiometer	15.2 x 15.2 x 12.7 (6.0 x 6.0 x 5.0)	1	2.27 (5.0)	-	232	Configuration
Neutral mass spectrometer:						
Electronics	25.4 x 15.2 x 12.7 (10.0 x 6.0 x 5.0)	1	4.54	-	387	Configuration
Sensor	40.6 x 10.2 x 10.2 16.0 x 4.0 x 4.0	1	4.45	-	412	Configuration
Sum:			29.14 (60.2)		3384	
Ratio to total area or mass, percent			67		41	

stacking of units would be required if the same diameter shell is to be considered. This creates attendent problems in accessability, physical support, and thermal control which could seriously affect the design.

Pressure Protection Tradeoff

Probe science and subsystem equipment must be capable of operating during descent into the Venusian atmospheric high temperature and pressure environment. The basic purpose of this pressure protection trade is to obtain the lowest cost and weight pressure protection equipment for the program.

The design concept chosen to achieve this goal on both the Thor/Delta and Atlas/Centaur versions is one in which all descent module equipment is encapsulated and pressure protected by a single vessel. The choice was made on the basis of an early trade study that compared several alternative designs. This section is a summary description of that trade study. Although the study was performed during the Thor/Delta phase of the program, the conclusions are equally applicable to the Atlas/Centaur based design.

The study assumed the basic thermal control to be Min-K insulation around the outside of the equipment vessel as required to maintain equipment temperature below 60°C during the descent into the Venus atmosphere. Lower weight and cost design alternatives to external Min-K are available for thermal control, but changes in thermal control do not significantly affect this pressure protection alternative trade.

Candidate Approaches: Postulated candidate approaches for survival in a high pressure environment are:

1) Equipment vessel with structural capability to withstand the high pressure and encapsulate all descent module equipment.

2) Equipment vessel vented to the atmosphere, with the incoming gas cooled by a phase change material (PCM). Several small pressure vessels within the equipment vessel encapsulate the equipment that cannot survive the high pressure environment.

3) Closed equipment vessel with stored high pressure gas vented to the inside of the vessel equalizing inside and outside pressure during descent. Small pressure vessels encapsulate the pressure sensitive equipment.

4) Closed equipment vessel with bellows to transmit the pressure to a fluid surrounding the equipment. Small pressure vessels encapsulate the pressure sensitive equipment.

5) Equipment vessel internally pressurized at a compromise level between vacuum and maximum expected pressure. Small pressure vessels encapsulate the pressure sensitive equipment.

The postulated advantage for reduced or nonpressure-vessel designs (candidates 2 through 5) are weight reduction, because the structural weight of the shell can be reduced if the vessel does not carry high pressure loads. The primary structure comparison occurs between candidate 1, one large pressure vessel, and candidate 2, small pressure vessels within a larger equipment vessel. Any differences between candidates 2, 3, and 4 are associated with differences in thermal control and/or special equipment for pressure control.

Payload Pressure Capability. The pressure protection trade philosophy adopted was to make optimistic assumptions concerning the capability of components and devices to operate within a high pressure environment. Such assumptions simplify the analysis and favor the low or nonpressure approches. If the analysis shows the single pressure vessel encapsulating all equipment (candidate 1) is the lowest weight and cost then a definite trend is indicated using simplified analysis. If one of the other candidate approaches is favored more detailed analysis is required.

Following the above philosophy, this study assumes all science instrument and housekeeping electronic components except crystal devices can operate in a high pressure environment. Realistically, additional weight will be required to increase the structural integrity of the larger hermetically sealed electronic components, which is ignored during this study.

Each of the following large probe experiments has separate and unique requirements for windows or access to the Venus atmosphere:

1) Neutral mass spectrometer
2) Cloud particle size spectrometer
3) Solar flux radiometer
4) Planetary flux radiometer
5) Nephelometer (source and detector)

It is assumed that all of the above experiment sensors or inlet chambers require protection from high pressure. A detailed integration study could possibly show feasible methods to combine one or two of the sensors in the same pressure vessel. However, it is obvious that several pressure vessels will be needed to meet all of the field of view and access requirements. Consequently, it is assumed that five separate small spherical pressure vessels are required to protect the science instruments and to meet the field of view and access requirements. Housekeeping equipment such as batteries, receivers and oscillators along with the science accelerometers are encapsulated within one of the small pressure vessels.

Weight Comparison. Weight comparison calculations are based on structural analysis for the pressure shells, equipment vessel, and high pressure gas container and thermal analysis to determine weight of phase change material required to maintain desired temperature. Titanium is assumed for the structure material in all of the alternative approaches. The weight of the spherical shells is:

$$W = \gamma\, 4 \pi R^2 t$$

where

W = shell weight

γ = density of titanium = t/. 53 x 10^{-3} k/cm^2 (0. 164 lb/in^3

R = radius of sphere

t = thickness of shell

and the shell thickness required to survive the outside high pressure is:

$$t = R \sqrt{\frac{P}{(K)\, 1.21\, E}}$$

where

R = sphere radius

P = pressure ≈ 100 atm

K = knockdown factor ≈ 0. 7 (titanium)

E = modules of elasticity = 11. 3 x 10^6 N/cm^2 (16. 4 x 10^6 psi)(titanium)

The sphere inside diameter for the single pressure vessel approach (candidate 1) is 57. 1 cm (22. 5 in.). The assumed diameter for the individual pressure vessels encapsulating the pressure sensitive science and housekeeping equipment are 35. 6 cm (14 in.), 23. 9 cm (9. 4 in.), 11. 2 cm (2. 2 in.), and two at 12. 7 cm (5 in.).

The mass of the equipment vessel structure to encapsulate the small pressure vessels and the nonpressure sensitive equipment is determined by calculating the structure thickness required to withstand the entry load. Assuming a conical shape between the probe ring and the shelf the classical buckling formula for a cone is used to calculate the necessary thickness to carry a 500 g load.

$$F = 0.606\, K\, 2 \pi E\, t^2 \cos^2 \alpha$$

where

F = deceleration load on shelves

K = buckling factor ≈ 0. [illegible]

E = modules of elasticity

t = thickness

α = cone half angle ≈ 0 deg

The mass of the equipment vessel structure to encapsulate the small pressure vessels and the nonpressure sensitive equipment is determined by calculating the structure thickness required to withstand the entry load. Assuming a conical shape between the probe-ring and the shelf the classical buckling formula for a cone is used to calculate the necessary thickness to carry a 500 g load.

$$F = 0.606\,K\,2\pi\,E t^2 \cos^2 \alpha$$

where

F = deceleration load on shelves

K = buckling factor ≈ 0.5

E = modules of elasticity

t = thickness

α = cone half angle ≈ 0 deg

The spherical shell above and below the shelves doe not need to support any loads but must be capable of withstanding the handling environment. A minimum thickness of 0.038 cm (0.015 in.) is selected for the handling environment.

The analysis assumed phase change material is used to cool the hot vented gas and to offset the heat capacity lost using a thinner wall vessel. A linear relationship between temperature/pressure and time is assumed to simplify the analysis. The simplified approximation to the heat exchanger quantity of heat to maintain the inside temperature at 60°C with hot vented gas is:

$$\frac{Q_H}{V_D} = \frac{P_{max}\,C_p}{R}\left[\frac{C_v}{C_p} - \left(\frac{T_{max}}{T_D} - 1\right)\right]$$

where

Q_H = quantity of heat from PCM

V_D = volume of empty space in vessel ≈ 82,000 cm^3 (5000 in^3)

P_{max} = maximum atmospheric pressure

C_p = heat capacity at constant pressure

C_V = heat capacity at constant volume

R = universal gas constant

T_{max} maximum temperature of atmosphere

T_D maximum temperature in descent module (maintained by PCM)

The assumed heat of fusion for the phase change material is 279 J/$_{kg}$ (120 Btu/lb).

The weight of the spherical storage container for the high gas is calculated assuming the gas is stored at 0.69 N/$_m 2$ (104 psi). Hydrogen is assumed to be the stored gas to provide the lowest weight even though it would not be practical.

Weight calculations for each of the alternative pressure protection candidates are summarized in Table 4.1-3. The lightest weight approach is encapsulating all equipment within a large pressure descent module, candidate 1. The conclusion is based on rather simplified tradeoff analysis but the trend is definitely indicated. Additional detailed tradeoffs would only show a greater advantage for the one pressure module approach because of the optimistic assumptions in all other approaches. Examples of optimistic assumptions are:

1) Capability of all electronics to withstand 100 atm of pressure

2) Omitting heat exchange weight estimate for candidate 2

3) Omitting weight estimates of valves and pressure rings for stored high pressure gas chamber

4) Omitting weight estimates for bellows

5) Assuming optimistic packaging density when small pressure vessels are packaged inside the larger equipment vessel

6) Optimistic form factor for all science instruments.

Candidate 4 weight could realistically be reduced if the void space within the pressure vessel were not completely filled with phase change material, which is assumed in the study, but partially filled with a less dense filler. However, it would still be much heavier than candidate 1. The weight for the phase change material in candidate 2 is overstated because pressure and temperature is assumed to increase linearly with time during descent. This high weight estimate is more than offset by the omission of the heat exchange weight.

A trend has been established indicating weight increases occur when solutions to the high pressure protection problem for planetary in site measurements deviate from the one pressure vessel encapsulates all equipment approach. This trend is established by the simplified analysis used to

TABLE 4.1-3. MASS COMPARISON SUMMARY

Item	Mass, kg (lb)				
	Candidate				
	1	2	3	4	
Pressure shells	15.4 (34)	6.8 (15)	6.8 (15)	6.8 (15)	5.4 (12)
Equipment vessel structure enclosing small pressure vessels	–	3.2 (7)	3.2* (7)	3.2 (7)	13.6 (30)
Phase-change material – cool hot gas	–	13.6 (30)	–	–	–
Phase change material – offset structure capacity	–	2.7 (6)	2.7 (6)	–	0
High pressure gas / container	–	–	6.8 (15)	–	–
Phase change material to fill void space	–	–	–	11.1* (244)	–
Mass of stored gas	–	–	1.4 (3)	–	3.2 (7)
Total	15.4 (34)	26.3 (58)	20.9 (46)	(266)	22.2 (49)

*Neglects increase in equipment vessel size and mass due to enclosed high pressure gas container

**Net of PCM liquid and removal of all Min-K insulation obtain the mass comparison results shown in Table 4.1-3 and probe studies conducted by Martin Marietta Corporation and AVCO during their Jupiter study contracts with JPL (References 4.1-1 and 4.1-2). The weight increase for low or nonpressure approaches occurs because:

1) Some science sensors and payload components require protection from the high pressure; consequently, a total nonpressure protection probe is not practical.

2) Equipment or material must be added to the probe to cool the vented hot air or store gas to equalize the inside probe pressure with the outside atmospheric pressure.

The Pioneer-Venus baseline approach using one pressure vessel to encapsulate all equipment is thus verified as the minimum weight approach.

All of the alternatives to the one pressure vessel encapsulating all equipment, contain separte small pressure vessels to protect science sensors and to meet field of view and access requirements. Several small pressure vessels will be more costly than a one large pressure vessel approach because the vessel design, fabrication and test cycle must be repeated for different vessels. Principal cost increase would be in the tests needed for qualification and acceptance of each small pressure vessel. In addition, manufacturing and access also become more complex. Since the weight trade study shows a weight increase and qualitative observations indicate a cost increase with a nonpressure vessel approach, a quantitative cost trade is not justified. The baseline design is also verified from the qualitative cost observation.

Hemisphere Versus Multisegmented Pressure Vessel Construction

The Thor/Delta and Atlas/Centaur baseline pressure vessels are both configured as spheres constructed by joining two hemispheres at a pressure sealed main (or meridianal) flange. Although the hemisphere concept provides satisfactory accessibility to all internal units, superior accessibility can be provided by a design in which the sphere is formed by multiple segments. In this section, a trade study which compared both configurations is described. The conclusion of this trade study is that the hemisphere concept is more desirable in spite of the improved accessibility afforded by the multisegmented concept.

Two ground rules were observed:

1) Attachment to the aeroshell was kept identical

2) Internal arrangement was identical - two horizontal shelves forming three equipment bays.

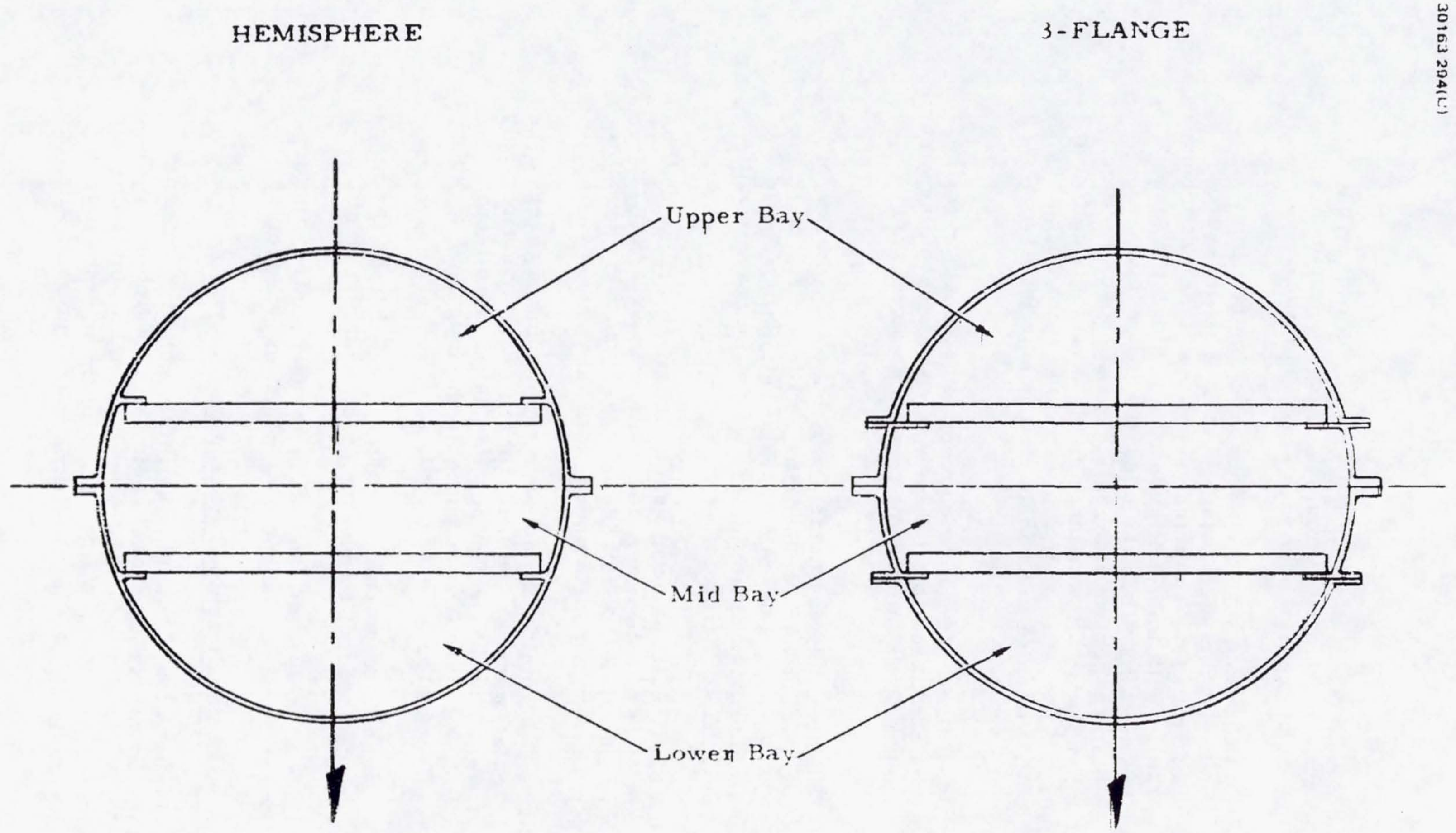

FIGURE 4.1-6. PRESSURE VESSEL HEMISPHERE CONSTRUCTION

In the hemipshere approach (see Figure 4.1-6) the midbay units are readily accessible when the single meridional flange is opened, but the upper and lower bays are exposed only with shelf removal.

Accessibility is maximized with the addition of another joint in each hemisphere, located at the shelf attach plane. The pressure vessel is then constructed from four spherical segments joined at three flanges (see Figure 4.1-6). With this configuration, besides the usual midbay accessibility, the units in either the upper or lower bay are exposed by separating their respective flanges. This approach further allows the shelves to be supported in a manner most advantageous to the direction of entry loads. However, for maximum subsystem efficiency, before reopening the ball, the units to be inspected and its location should be known.

Having established the three flange concept to be superior for accessibility, it was then compared to the hemisphere concept using other important criteria. The results of this comparison are summaried below:

1) Weight. With the multisegmented construction, addition of two flanges and accessories will increase total pressure vessel weight. For the large probe in titanium, for example, the weight increase would be 3.62 kg (8/lb).

2) Fabrication. Greater care in design and manufacture of the multisegments would be required to assure accuracy in sphericity. Such accuracy is necessary to obtain maximum strength under external pressure.

3) Reliability. The multisegmented design requires three large seals, whereas the hemisphere design requires only one. This has a serious impact on the mission reliability and is undoubtedly the most undesirable effect of the multisegments.

4) Cost. The multisegmented design is judged to be the more costly concept to develop, test, and manufacture.

Thus, considering the entire system, and all of the comparison factors in total, the less costly hemisphere concept was judged to be superior.

Conformal versus Parallelepiped Packaging

Summary. In the Atlas/Centaur baseline design, the external configurations of the nonscience or housekeeping units which are packaged within the pressure vessel were selected to produce maximum volume utilization at minimum cost. As a result, some of these units may be configured with an external shape that conforms to the interior surface

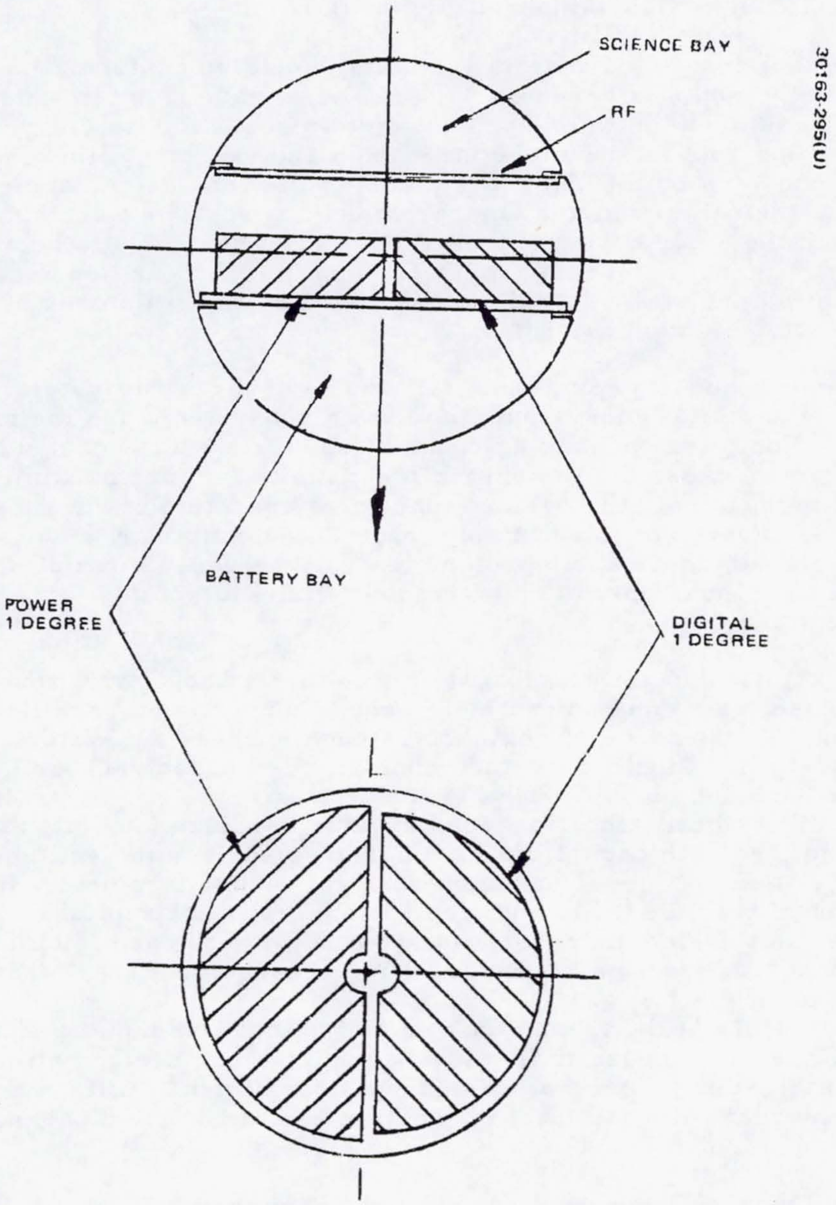

FIGURE 4.1-7. SMALL PROBE CONFORMAL PACKAGE

of the pressure vessel (conformal) while others will be configured in the more conventional box shape (parallelepiped).

The decision as to which of the units should be conformal and which parallelepiped was based on a Thor/Delta trade study in which a comparison was made between each relative to cost, accessibility, and the system impact on total volume utilization and weight. Although the study was conducted on the Thor/Delta design the conclusions are equally applicable to the Atlas/Centaur design. Science packages were not considered in the study because it was considered desirable to be able to accept the configuration of these units as supplied, and further because information was not available relative to the case with which any of these packages could be made conformable.

All of the housekeeping units fall in one of three subsystem categories: the digital subsystem, the power subsystem, and the rf subsystem. Conformal packaging of the rf subsystem was not included in the trade study because the lumping of the rf units in close proximity to each other might impair the desired functional operation of the subsystem. Further, this subsystem is relatively fragmented with many small already developed, units and therefore lends itself well to flexible packaging arrangements. Thus, only the power and digital subsystems were included in the trade study.

The digital and power subsystem were first packaged within the pressure vessel as a conglomerate of several conventional parallelopiped units. Then, for purposes of comparison each of these subsystems were repackaged within a single curvature conformally shaped package, one package for each subsystem. This exercise was repeated, first with each package configured utilizing 1 degree curvature surface (a section of a cylinder) and then with each utilizing a 2 degree surface (a section of a sphere). For each of these packaging configurations, a complete internal arrangement of both the large and small probes was accomplished. The pressure vessels inside diameter was selected in each case to be the minimum necessary to contain the resulting arrangement.

The results of the trade study indicated that conformal packaging, appropriately applied, results in a lower weight probe design with added arrangement flexibility and that this can be accomplished without a significant increase in cost. See subsection 4.6 for detailed packages and cost comparisons.

Small Probe Conformally Packaged (Figure 4.1-7)

In the small probe, a single curvature, power unit (except batteries) and digital unit (See Figures 4.1-8 and 4.1-9) were used in the midbay, resulting in a ball diameter decrease of 0.76 cm (0.3 in.) from the parallelopiped design. This translates to a 0.45 kg (1 lb) reduction per probe pressure vessel module. Although size and weight results were not dramatic, the ability to conformally unitize these subsystems

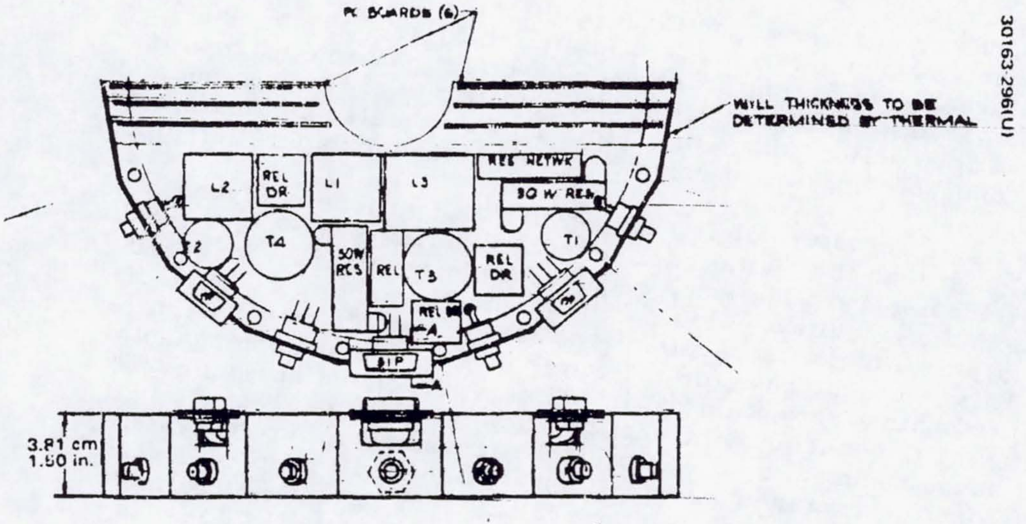

FIGURE 4.1-8. SMALL PROBE POWER ELECTRONICS

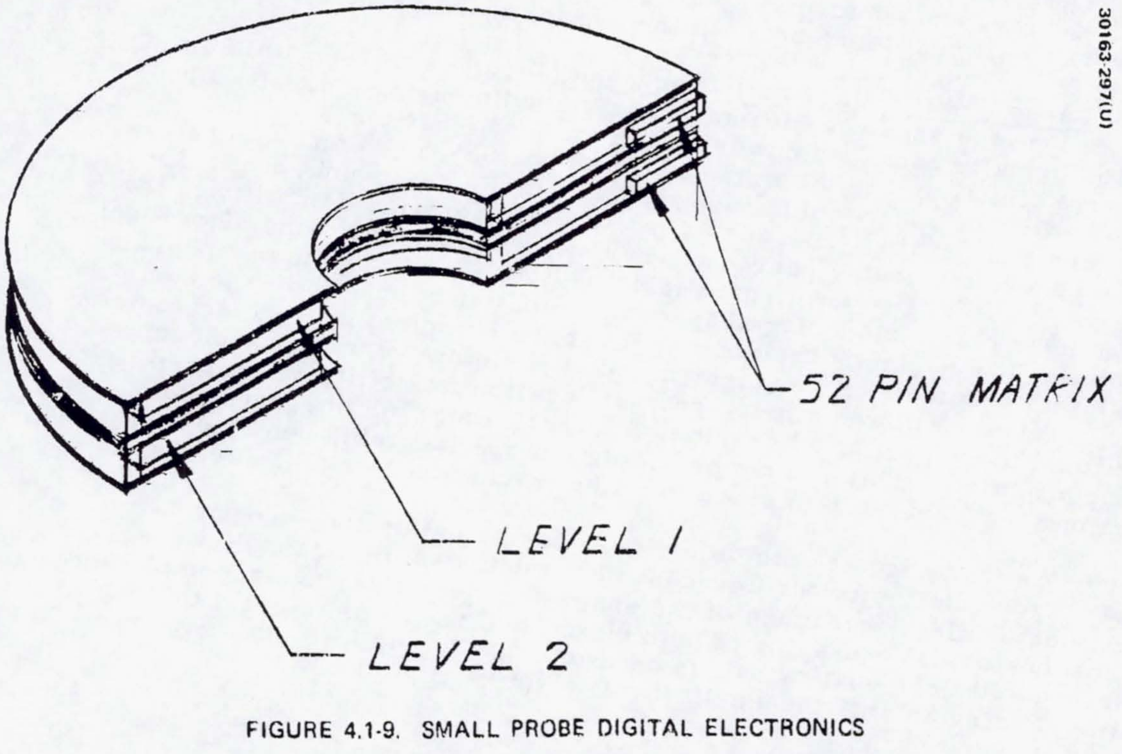

FIGURE 4.1-9. SMALL PROBE DIGITAL ELECTRONICS

REPRODUCIBILITY OF THE ORIGINAL PAGE IS POOR.

permitted a greater degree of functional positioning of other units such as rf components nearer the antenna to minimize losses. Thus, the single curvature conformal units were achieved for the same volume as the combined parallelopipeds but without the necessity of leaving space between boxes for cabling, mounting, etc. There was also no loss of pie-shaped, unusable pockets of volume as is the case with parallelepipeds.

The single curvature digital unit incurs a significantly higher incremental cost than the digital parallelopipeds because the shape factor and a need for restricting the size, required a departure from standard components in the circuitry. This cost plus development costs indicate that, at least in the digital subsystem, the small rewards do not warrant the cost. This is not the case for the power unit. Standard components were still used with a very minimal initial cost increment due primarily to restructuring the housing. Internal location flexibility at least is still enhanced (though reduced) by use of a single curvature power subsystem. The use of double curvature conformal units is the small probe was also investigated, but no advantage could be realized. Apparently, the small volume remaining after the bulky battery pack unit is installed does not permit sufficient arrangement flexibility to derive benefit from this type of conformal packaging.

A size and volume comparison is shown in Table 4. 1-4 between a parallelepiped and conformal small probe. The numbers indicate the relatively small difference between the two for these parameters.

Large Probe Conformally Packaged (Figure 4. 1-10). Unlike the small probe, the greatest advantage was gained by using a double curvature conformally packaged power unit in the lower bay and a single curvature digital unit in the mid-bay (See Figures 4. 1-11 and 4. 1-12). This resulted in a 2. 54 cm (1 in.) decrease in diameter and about a 3. 62 kg (8 lb) weight saving. Because of an inherent location flexibility in the larger sphere the double curved power unit, although enclosing 50 percent more volume than the power parallelepipeds, utilized volume peripherally and in depth that rectangular shapes could not use. This ability to use a previously low packing efficiency area for the complete power electronics subsystem vacated a rather large block of premium volume in the center bay. It further allowed a much greater location flexibility which permitted functional placement of other units with more room for integration and interconnection. This in turn providing a more favorable center of mass location (see Table 4. 1-6) since it did not require battery displacement.

As in the small probe the digital conformal unit was costly to repackage while the power unit cost increment was minimal. However, it was determined that much of the space and weight savings accomplished by full conformal packaging of both digital and power units could be obtained with less cost by using conformed packaging for only the power unit and using an "off-the-shelf" parallelepiped digital unit.

TABLE 4.1-4. CONFORMALLY PACKAGED SMALL PROBE VOLUME COMPARISON

	Parallelepiped	Conformal
Inside diameter, cm (in)	31.24 (12.3)	30.48 (12.0)
Available volume, cm^3 (in^3)	15,961 (974)	14,814 (904)
Equipment volume, cm^3 (in^3) (no supports)	6,538 (399)	*6,096 (372)
Equipment packing factor	2.44	2.42
Equipment packing density, percent	41.0	41.2
Total packaged volume, cm^3 (in^3) (includes supports)	7,948 (485)	7,423 (453)
Total packing factor	2.0	1.98
Total packing density, percent	49.8	50.1

*Volume smaller for 1 deg conformal units.

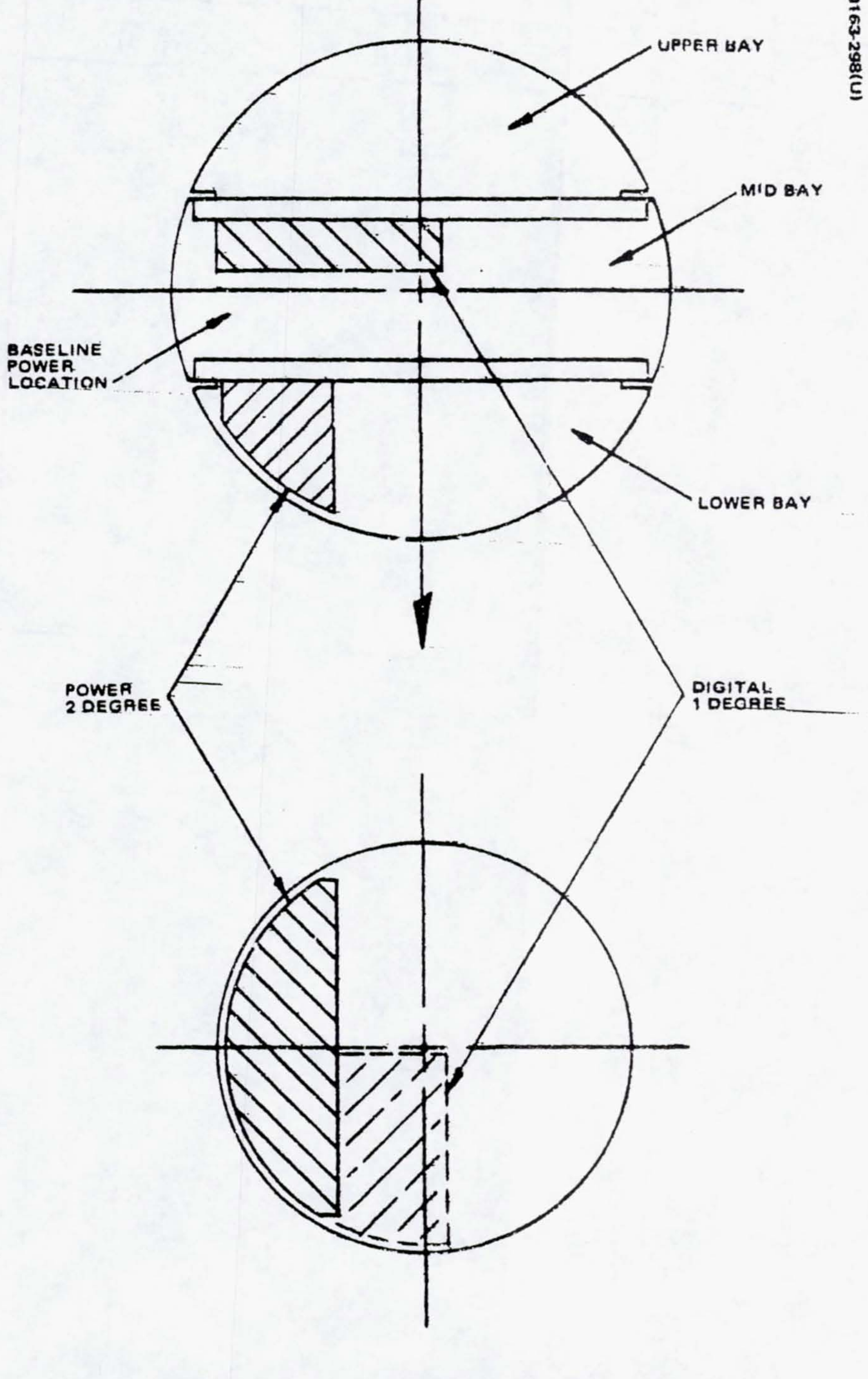

FIGURE 4.1-10. LARGE PROBE CONFORMAL PACKAGE

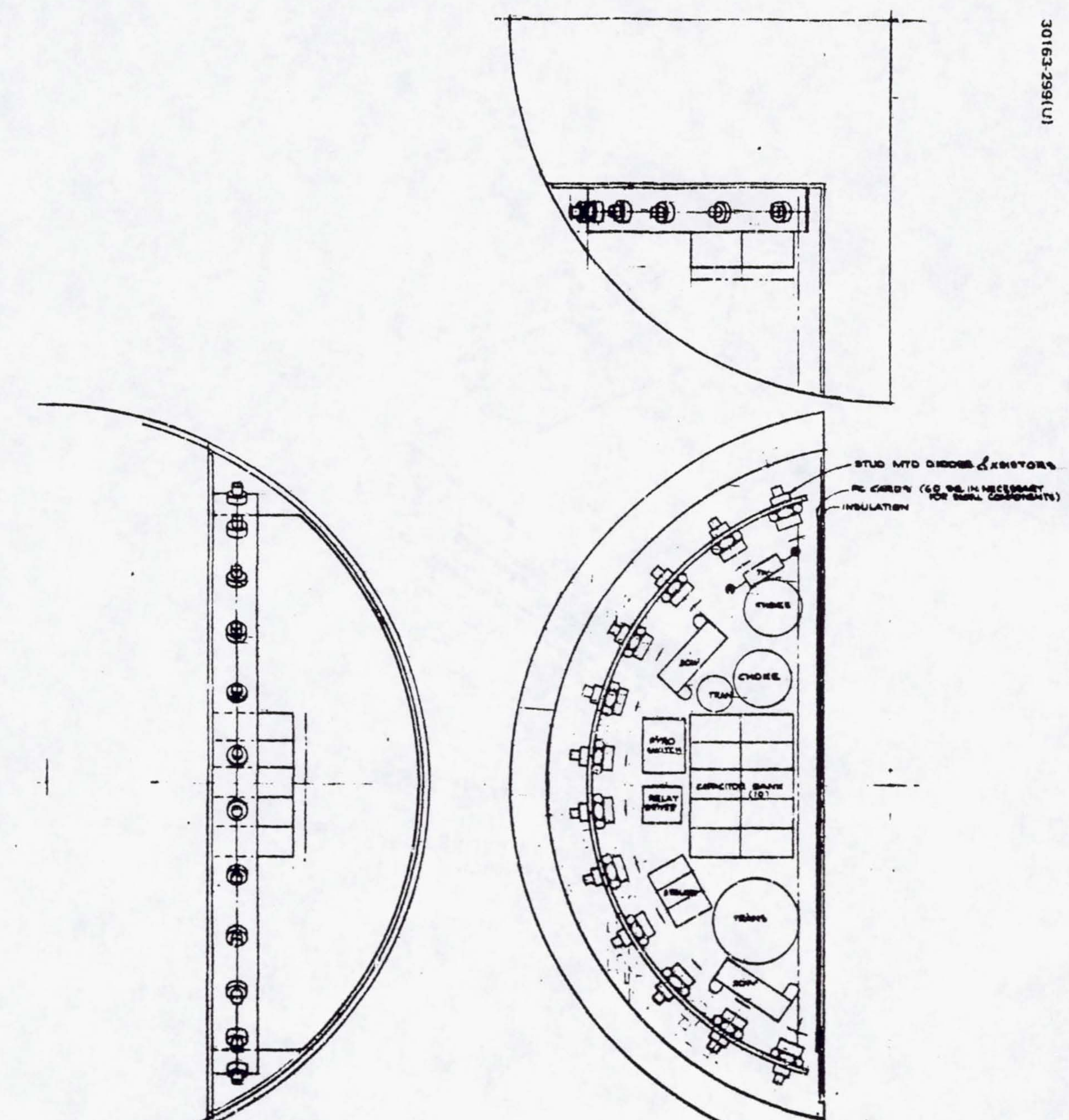

FIGURE 4.1-11. 2 DEGREE LARGE PROBE POWER ELECTRONICS

REPRODUCIBILITY OF THE ORIGINAL PAGE IS POOR.

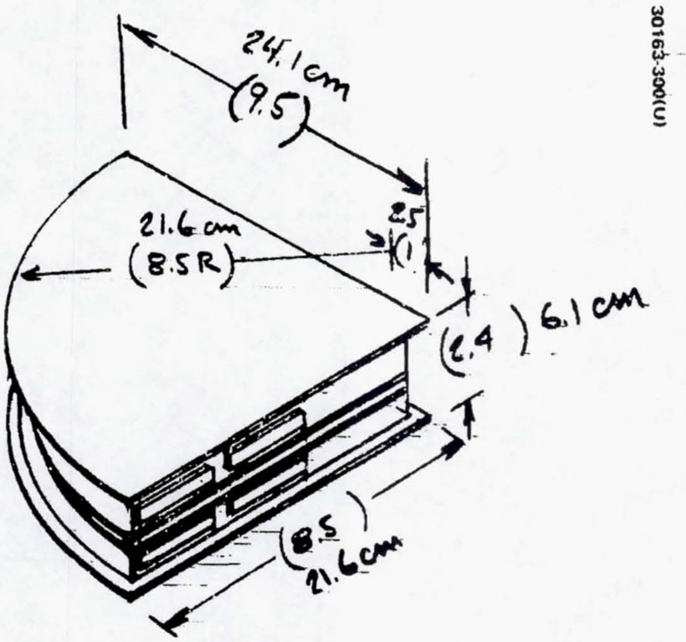

( ) DIMENSIONS IN INCHES

FIGURE 4.1-12. 1 DEGREE LARGE PROBE DIGITAL ELECTRONICS

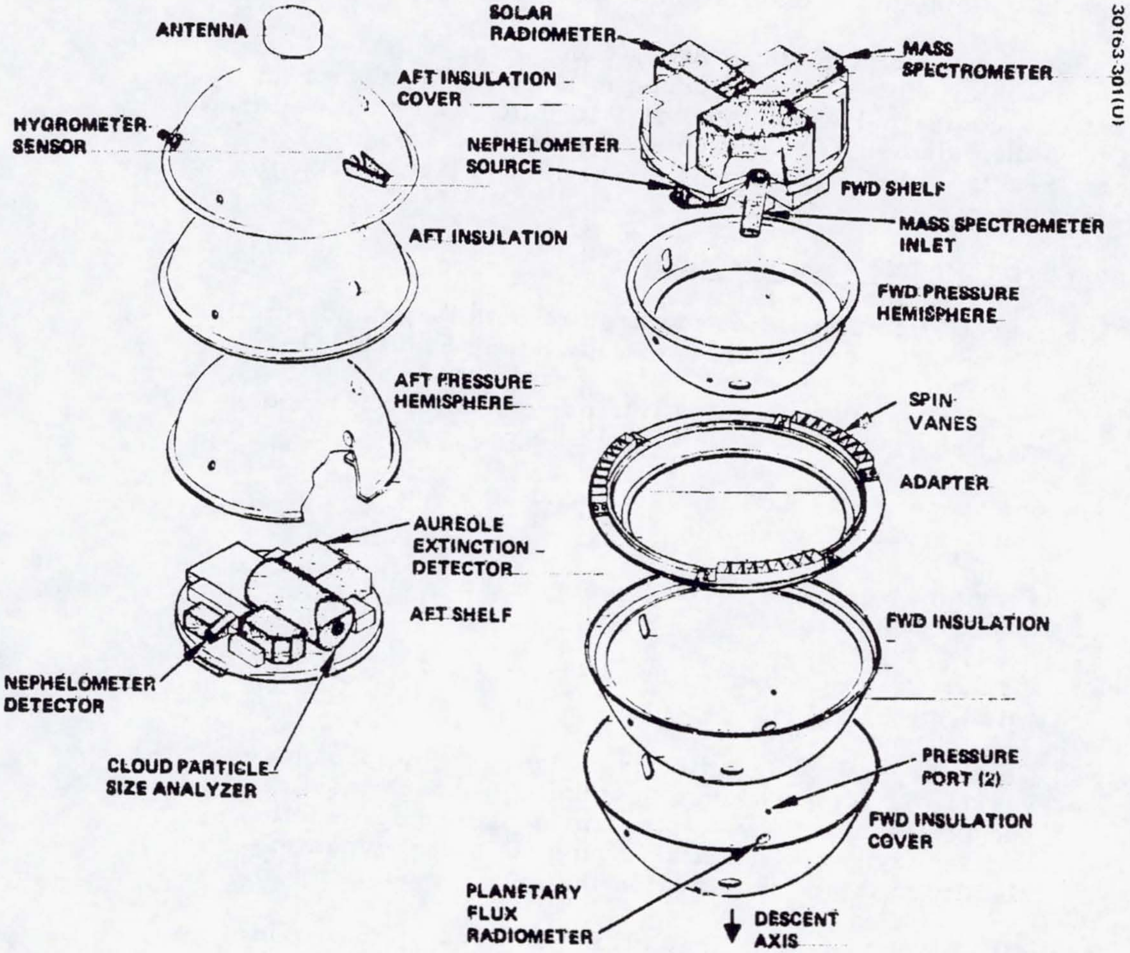

FIGURE 4.1-13. LARGE PROBE PRESSURE VESSEL CONFIGURATION

REPRODUCIBILITY OF THE ORIGINAL PAGE IS POOR.

A numerical comparison of parallelepiped versus conformally packaged large probes is given in Tables 4.1-5 and 4.1-6. Table 4.1-5 shows the overall size and volume-comparison while Table 4.1-6 gives relative volume and mass distributions by bay.

Conclusions (Applicable to Atlas/Centaur as well). The size and weight advantage for the small probe is not enough to warrant the added cost of a conformally packaged digital unit. The greater functional location flexibility demonstrated in this exercise, at a small cost increment, requires that a conformal power unit be seriously considered in future arrangements.

Pressure Vessel Module Configurations

The essential configuration features of both large and small probe pressure vessel modules are as follows (see Figure 4.1-13):

- Science and housekeeping (rf, power, data/command, etc.) resting on two horizontal shelves
- Shelves are attached to a surrounding spherical metal pressure vessel
- Pressure vessel is surrounded by spherically formed insulation
- Insulation is surrounded by thin metal spherical retainer
- Conical metal 'Z' adapter is attached to the pressure vessel meridional flange protruding through insulation and retainer to provide structural path to aeroshell and aerodynamic stabilizing ring (this aerodynamic stabilizer is not required on the small probe).
- All elements (shell, insulation, and retainer) provide egress for science and housekeeping penetrations.

The Thor/Delta large probe is shown in Figure 4.1-2. Science and housekeeping subsystems are pressure protected in a 54.61 cm (21.5 in.) inside diameter metallic spherical pressure vessel. The sphere is constructed of two hemispheres joined at a meridional flange which incorporates a metallic seal capable of withstanding space vacuum and Venus pressure. For entry loading the units are supported by two metal honeycomb shelves placed horizontal to the descent axis. The shelves are attached peripherally to machined flanges (one in each hemisphere) which react the shelf loads into the shell wall. Experiments are located so that optical, atmospheric, and electrical penetrations meet maximum mission requirements and do not compromise strucutral integrity.

TABLE 4.1-5. CONFORMALLY PACKAGED LARGE PROBE VOLUME COMPARISON

	Parallelepiped	Conformal
Inside diameter, cm (in.)	54.61 (21.5)	52.07 (20.5)
Available volume, cm^3 (in^3)	85,181 (5,198)	73,873 (4,508)
Equipment volume (no supports), cm^3 (in^3)	37,461 (2,286)	*38,836 (2,370)
Equipment packing factor	2.27	1.9
Equipment packing density, percent	44.0	52.6
Total packaged volume, cm^3 (in^3) (includes supports)	47,523 (2,900)	47,752 (2,914)
Total packing factor	1.79	1.55
Total packing density, percent	55.8	64.5

*50 percent greater volume for 2 deg power unit over parallelepiped.

TABLE 4. 1-6. LARGE PROBE VOLUME AND MASS DISTRIBUTION BY BAY

	Parallelepiped			Conformal		
	Mid	Lower	Upper	Mid	Lower	Upper
Available volume, cm^3 (in^3)	35, 232 (2, 150)	24, 974 (1, 524)	24, 974 (1, 524)	31, 955 (1, 950)	20, 959 (1, 279)	20, 959 (1, 279)
Equipment volume, cm^3 (in^3)	22, 434 (1, 369)	7, 882 481	7, 145 436	22, 188 (1, 354)	10, 619 (648)	6, 030 (368)
Equipment packing factor	1. 57	3. 17	3. 5	1. 44	1. 97	3. 48
Equipment packing density, percent	63. 5	31. 5	28. 6	69. 5	50. 6	28. 8
Mass distribution, kg (lb)	102. 76 (46. 71)	49. 92 (22. 69)	40. 26 (18. 3)	104. 19 (47. 36)	62. 57 (28. 44)	25. 96 (11. 8)
Center of mass (relative to center of geometry), cm (in)		+0. 76 (+0. 3)			+20. 32 (+0. 8)	

Approximately 2.3 cm (0.9 in.) of insulation is formed to match the external sphericity and fit snugly around the various penetrations. The insulation is enclosed and held in place by two thin hemispherical metal retainers. These retainers also provide egress for penetrations.

The sphericity of the forward retainer coupled to an adapter ring provide the external aerodynamic characteristics that were successfully tested at the Langley wind tunnel. The conical metal adapter ring attaches to the descent side of the pressure shell meridianal flange then flares out 30 deg and terminates at a horizontal flange 6.35 cm (2.5 in.) aft of the sphere center of geometry. The entire pressure vessel module entry load is transmitted through this adapter to the aeroshell by bearing circumferentially around the entire adapter horizontal flange. Lateral and boost loads (opposite to entry loads) are reacted by three separation bolts attaching Aeroshell and P.V.M. at the locally thickened adapter ring. This aft adapter ring is perforated at three equally spaced sections to allow the atmosphere to freely impinge on slightly canted spin vanes spanning the aft face of the perforations.

The communications antenna protrudes through the aft insulation retainer directly on the descent axis. The protrusion is sufficient to provide the required rf view angle.

The small probe is shown in Figure 4.1-3.

While similar in concept to the large probe, the small probe differs basically in the following areas:

- Since it does not separate from the aeroshell, it does not require separation bolts or spin vanes on the adapter
- It does have to support fixed stabilizing fins through the aft insulation retainer
- Base heating at entry and through descent requires thicker insulation
- Inside diameter is 32.5 cm (12.8 in.)

Atlas/Centaur Baseline Configuration

The following is a description of the Atlas/Centaur pressure vessel module (PVM) configuration, much of which is common to large and small probes. Unlike the Thor/Delta which featured external insulation, the Atlas/Centaur preserves the essential environmental protection and aerodynamic features while shifting thermal protection internal to the pressure vessel in what is assessed as an equally effective, lower cost technique.

External Features

Large Probe (Figure 4.1-14). A thin maraging steel pressure sphere, 68.1 cm (26.8 in.) inside diameter, is formed by hemispheres joined through thick meridional flanges that incorporate a metal V-seal to withstand both space vacuum and the reverse high external Venus pressure. Reinforced penetrations for science, housekeeping, test, cooling, etc., are placed through the sphere in locations that meet mission and functional requirements while maintaining spacings that do not degrade the structural integrity of the pressure vessel. No external insulation permits a much cleaner, simpler, interface for attachment of external protuberances such as the communications and wind altitude radar antennas. Such protuberances can be mounted by properly selected high temperature materials. No external insulation has another advantage in that internal accessibility to the pressure vessel is vastly simplified.

A conical 'Z' adapter constructed of steel is attached to the descent side of the meridional flange and flares aft to a horizontal flange that interfaces structurally with the deceleration module. This horizontal flange is also a key feature of the aerodynamic subsystem, aiding stability after aeroshell separation and providing spin vanes for roll control on its aft surface.

To complete the aerodynamic subsystem successfully tested in the Langley wind tunnel, a thin lightly stiffened metal hemispherical aero fairing encapsulates the forward pressure sphere. The fairing directs the flow into the adapter ring and through the spin vanes. The fairing attaches to a pressure shell mounted ring that holds the wind altitude radar antenna and an RF transparent heat shielding radome over the antenna. The radome is shaped to provide the spherical continuity from the aero fairing. The fairing attaches peripherally to the adapter slight inboard of the horizontal flange. This small offset is required to provide a prescribed angular clearance for separation from the deceleration module.

In summary, the basic elements of the external configuration are:

1) Spherical pressure shell

2) Conical structural/aerodynamic adapter

3) Hemispherical aero fairing over forward pressure hemisphere

Small Probe (Figure 4.1-15). The small probe spherical pressure vessel, 40.6 cm (16 in.) inside diameter, is common in concept and construction to the large probe. Since it does not separate from the deceleration module, no adapter or aero fairing is required. The pressure vessel module mounts directly to the deceleration module at the meridional flange. It does, however, incorporate four roll damping fins on its aft hemisphere, which protrudes aft of the deceleration module base plane. Although the bulk of the thermal protection is internal, as in the large probe, a thin coating of ESM is applied to the aft hemisphere and antenna protuberance for additional entry thermal protection.

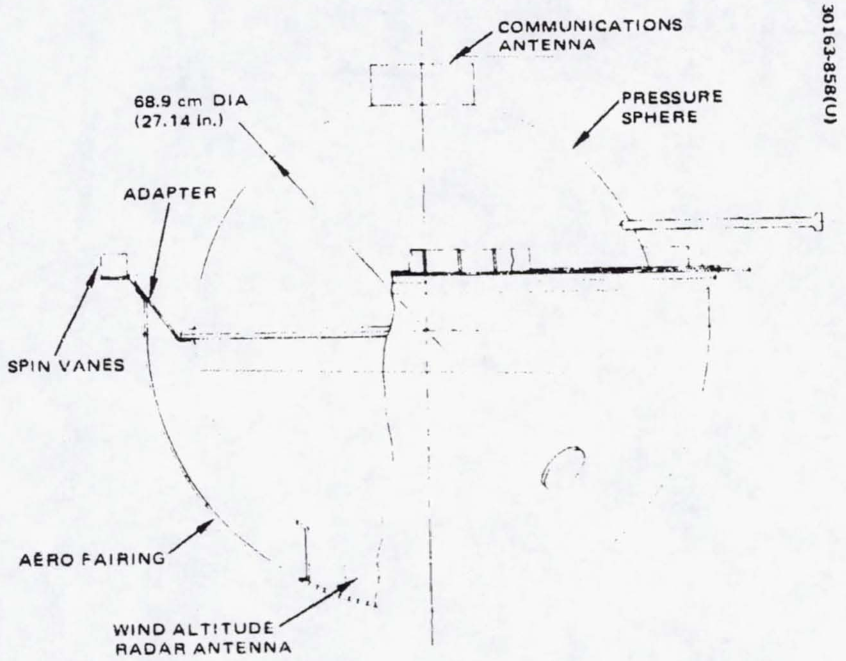

FIGURE 4.1-14. ATLAS/CENTAUR LARGE PROBE EXTERNAL CONFIGURATION

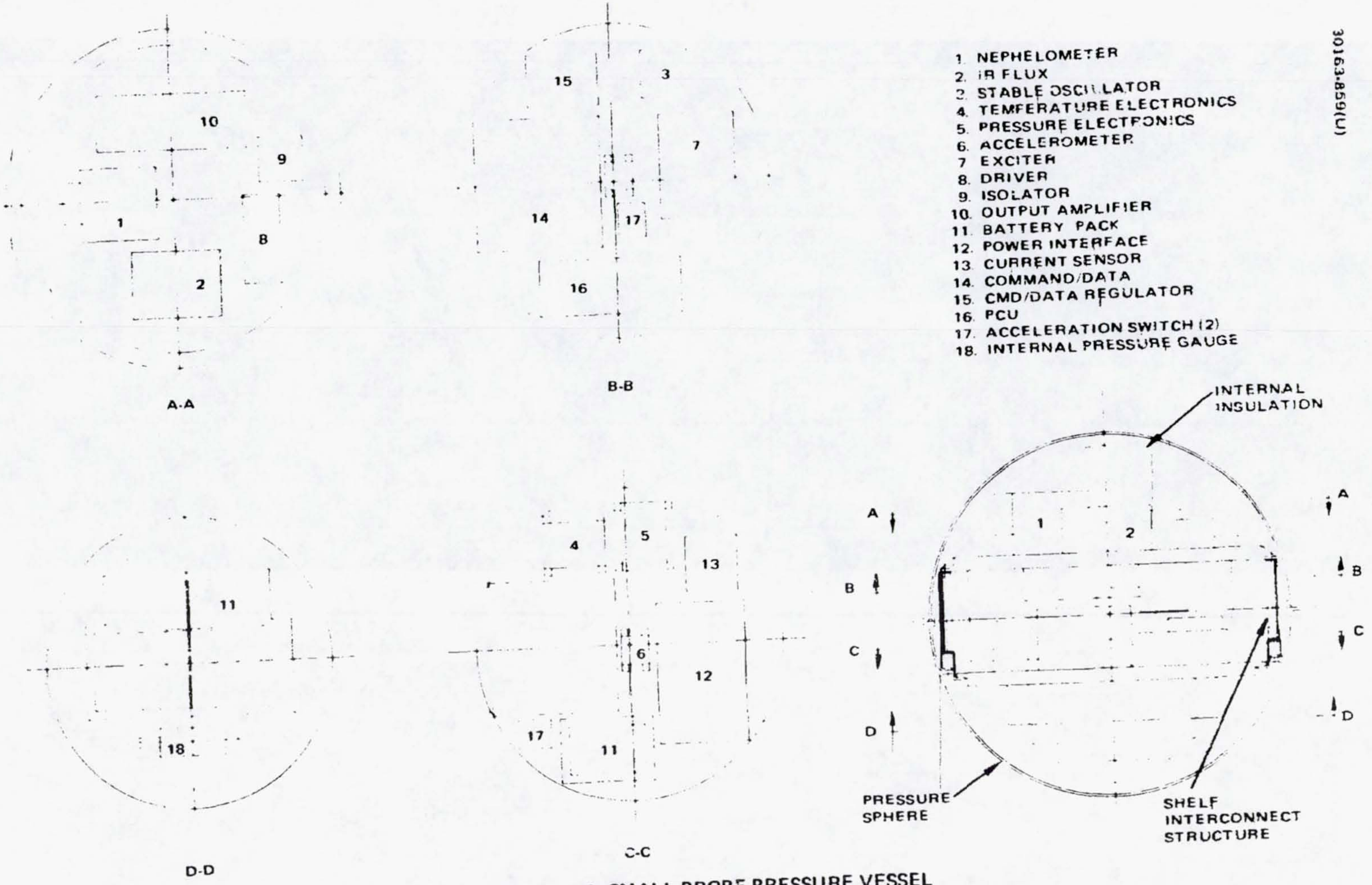

1. NEPHELOMETER
2. IR FLUX
3. STABLE OSCILLATOR
4. TEMPERATURE ELECTRONICS
5. PRESSURE ELECTRONICS
6. ACCELEROMETER
7. EXCITER
8. DRIVER
9. ISOLATOR
10. OUTPUT AMPLIFIER
11. BATTERY PACK
12. POWER INTERFACE
13. CURRENT SENSOR
14. COMMAND/DATA
15. CMD/DATA REGULATOR
16. PCU
17. ACCELERATION SWITCH (2)
18. INTERNAL PRESSURE GAUGE

FIGURE 4.1-15. SMALL PROBE PRESSURE VESSEL

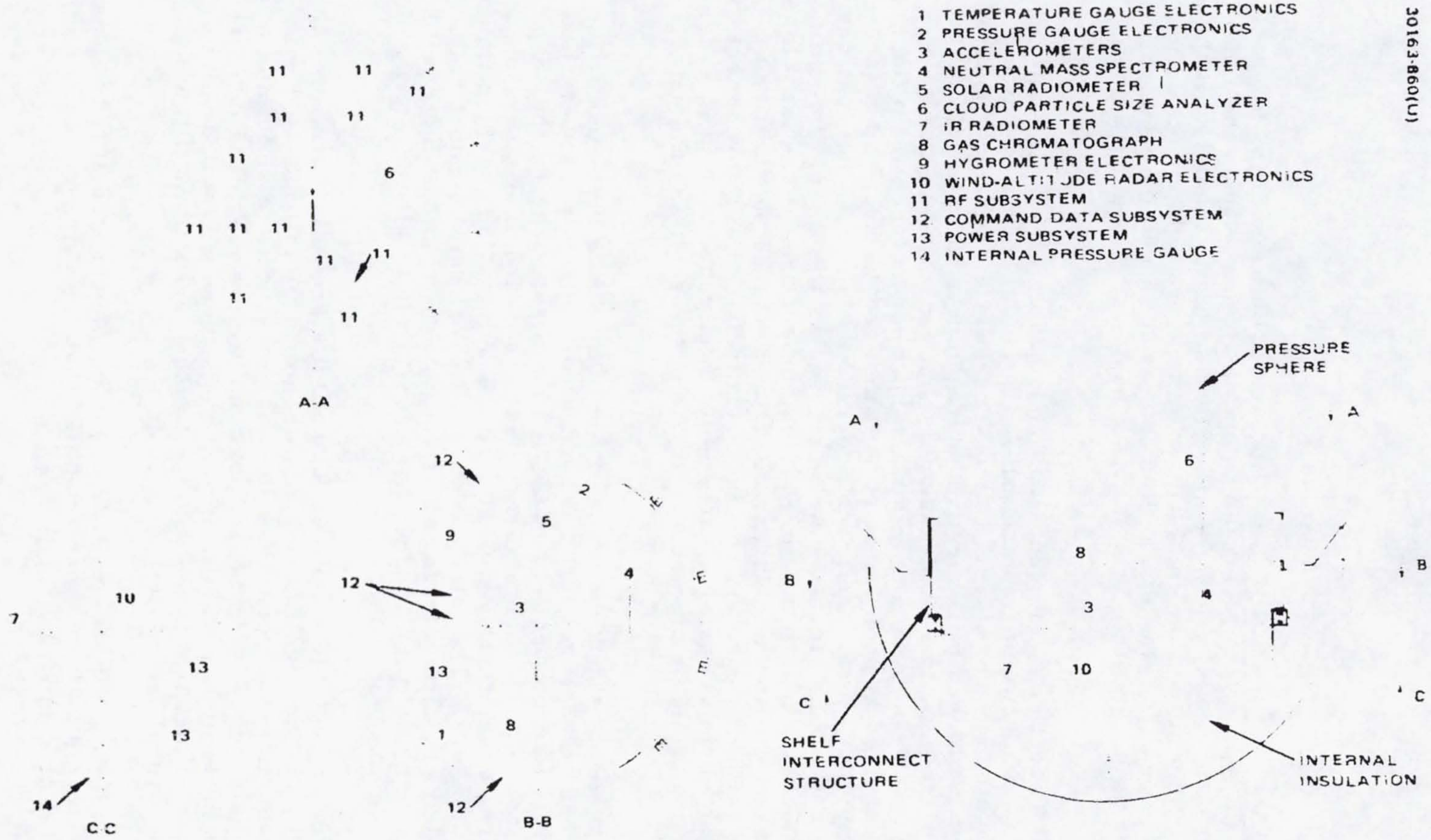

FIGURE 4.1-16. LARGE PROBE PRESSURE VESSEL

Internal Features

Large Probe (Figure 4.1-16). A fiberglass Batt insulation approximately 1.27 cm (0.5 in.) thick conforms to and bears directly on the inner surface of the pressure shell. It is retained by thin metal inner hemispheres that separate the insulation from the inner structure and equipment. The internal insulation and its retainer can be configured around the penetrations in such a manner as to facilitate assembly and removal of pressure hemispheres.

As in the Thor/Delta, the spherical packageable volume is segmented into three bays by using two horizontal solid aluminum shelves to which equipment is mounted on both sides. Unlike Thor/Delta where both shelves were independently attached to respective hemispheres, the Atlas/Centaur shelves are connected in a two shelf assembly and supported by the lower hemisphere only. This was done to minimize heat conductance from the hot shell wall. The shelves are interconnected at their edges by 12 open faced hat section columns. Lateral support is provided by thin webs between intermittent columns and a light closure ring on top and at mid-span. Intermittent webs permit visibility into the mid-bay equipment area. The mid-span ring allows passage of numerous wires, coax, and science penetrations between columns without providing special ports through the interconnect structure. It also permits easier disassembly of the top shelf and interconnect structure by minimizing disturbance to the lower shelf and the numerous protrusions.

The interconnect structure transfers only the loads imparted by the upper shelf, through a shelf support ring that also supports the lower shelf circumferentially. Interconnect structure and shelf support ring then are attached at the base of each column directly into 12 cylindrical stacks of washers for thermal isolation, and finally into an integrally machined flange in the lower hemisphere. The interconnect structure, shelf support ring, and stacked washers are titanium for relatively low thermal conductivity. The stacked washers minimize conductance from the hot wall while providing a structurally adequate load path.

Packaging concepts developed on Thor/Delta are fully utilized on the Atlas/Centaur decks. Science instruments are preferentially located with adequate space remaining for housekeeping equipment while maintaining a favorable mass balance. The increased size and weight capability of Atlas/Centaur permits units to be packaged in lower cost conventional parallelopipeds. It further allows increased spacing between units to facilitate mounting, cabling, and overall accessibility.

The assembly of two shelves with the interconnect structure all attached at a single plane forms an "equipment module" that can be assembled or disassembled in total or section by section.

In summary the basic features of the internal arrangement are:

1) A two shelf interconnected equipment module supported at 12 thermally isolated points on the lower hemisphere.

2) A fiberglass Batt insulation surrounding the equipment module, bearing on the pressure vessel wall and retained by thin metal hemispheres.

Small Probe. The internal arrangement of the small probe is identical to the large probe. It differs only in size and structural gauges. The insulation, however, is the same thickness, 1.27 cm (0.5 in.), as in the large probe.

REFERENCES

4.1-1 "Jupiter Atmospheric Entry Mission Study, Volume 2; Mission and System Evolution," NASA-CR-118022, Martin-Marietta Corporation, dated April 1971.

4.1-2 "A Study of Jupiter Atmospheric Entry Probe Mission, Volume 2; Technical Summary," NASA-CR-122986, Avco Corporation, dated 13 August 1971.

4.2 AERODYNAMICS/FLIGHT DYNAMICS

The large probe pressure vessel configuration is a sphere, modified to provide pitch and yaw stability and a predictable spin rate. The sphere modifications considered included: steps, flares, discs (hat brim) and fins. Models of a number of the configurations have been built and tested in the Ames Research Center water tank facility. The results indicate that a number of these configurations have the required stability and develop the predicted spin rate. These tests are considered to be primarily screening tests prior to building and testing larger scale models for test in the Langely Research Center spin tunnel. The Reynolds number of the water tank drop tests is 50,000. which is well below the critical Reynolds number for a sphere. However, the qualitative behavior of the stable configurations indicated that they will be stable at the full scale Reynolds number.

The best performing models from the water tank test, plus a new configuration, have been selected for spin tunnel tests. Models, fabricated of fiberglass and balsa, with adjustable weight and c.g., have been tested in the Langley spin tunnel. The dynamic behavior is recorded on film and the film record has been analyzed using a stop motion movie projector. From the time history of the pitchmotion, the aerodynamic characteristics of the configuration have been determined. All of the configurations tested are stable with the nominal c.g. location. One of these has been selected as the baseline and tested with various protuberances simulating the typical scientific instruments.

The effects of these protuberances on the aerodynamic characteristics of the pressure vessel are within the scatter of the data.

Using a 6 degree-of-freedom computer program, the dynamic behavior of the pressure vessel during subsonic descent in the Venusian atmosphere has been analyzed. The aerodynamic coefficients used in the analysis are those derived from the spin tunnel tests and reported in Reference 4.2-1. This analysis shows the motion due to the mass unbalance, sharp edged gusts, wind shears and initial disturbances, is within the acceptable limits.

Requirements

To meet the needs of the science payload, the aerodynamic design requirements for the large probe pressure vessel during the subsonic descent are:

1) The configuration must be dynamically stable

2) Spin axis deviation from vertical must be less than 10 deg

3) Spin rate must be less than 15 rpm

Tests, Analyses, and Trades

The process leading from the aerodynamic requirements to the establishment of an aerodynamic configuration baseline for the pressure vessel

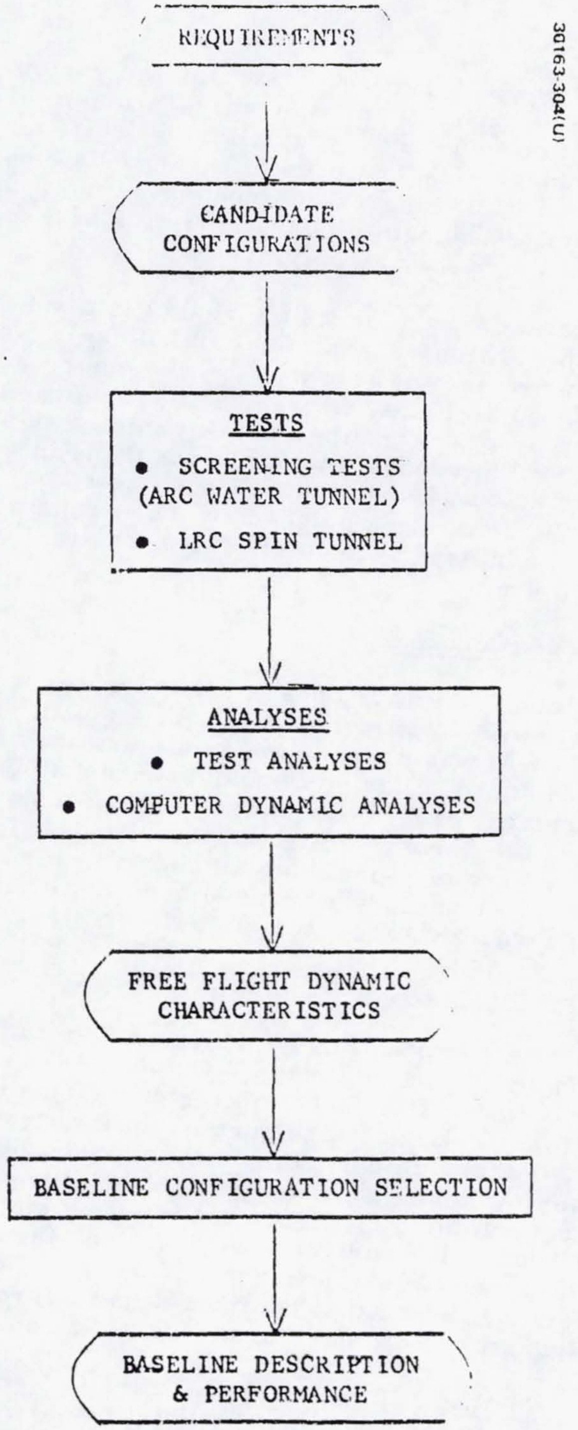

FIGURE 4.2-1. PROCESS FOR ESTABLISHING AERODYNAMIC BASELINE OF PRESSURE VESSEL MODULE

module is illustrated in Figure 4.2-1. In this section the various steps of the process will be discussed. The candidate configurations will be presented, and the water tunnel screening tests and the spin tunnel free flight tests to these models briefly described. The analyses of these tests and the use of a digital computer program for six-degree-of-freedom simulation of the entry trajectory provide the free flight dynamic characteristics of the configurations and a basis for selection of the baseline configuration.

The basic configuration for the pressure vessel is a sphere, primarily for structural reasons. In addition, it has the desirable aerodynamic characteristic that its center of pressure is the center of the sphere. Hence, if the center of gravity can be just slightly forward of the sphere center, it will be stable in pitch and yaw. In practice, the sphere exhibits an erratic flight behavior due to wandering of the separation point, resulting in varying lateral forces. To remedy this, various discontinuities such as steps, rings, and conical flares, which fix the separation point, have been considered. In addition, tails and vanes have been used to augment the pitch stability and provide roll.

Candidate Test Configurations

The aerodynamic configurations chosen for the water tank screening tests are shown in Figures 4.2-2 through 4.2-6. As a result of these tests, configuration 4 (Figure 4.2-5) was dropped and configurations 6 and 7 (Fig (Figures 4.2-7 and 4.2-8) added. Various protuberances which simulated the typical external instrument probes are added in some tests in order to determine their effects on the aerodynamic characteristics. In addition, other minor modifications have been included as shown in Figures 4.2-9 through 4.2-13. All of these configurations have been tested in the Langley spin tunnel and their aerodynamic characteristics determined.

Water Tank Screening Tests

Hughes, as part of a company funded program, conducted tests in the Ames Research Center's (ARC) water tank, 17 October 1972, to investigate the relative aerodynamic stability characteristics of the candidate atmospheric entry configurations. The primary purpose of this test is to determine which configurations have acceptable dynamic behavior and hence are candidates for test in the Langley Research Center's (LRC) 6.1 m (20 ft) spin tunnel facility. To be acceptable a configuration must be stable in pitch and yaw, must exhibit small lateral excursions when "flying" through the still water, and must provide a repeatable spin rate. Configurations 1 through 5 were tested and the results indicate that configurations 1 through 4 are satisfactory, and configuration 5 did not warrant further consideration.

Test Models and Method. The test models are 6.1 cm (2.4 in.) in diameter and were dropped in the 4.88 m (16 ft) high, 0.61 m (2 ft) square water tank at Ames Research Center. Two sets of orthogonal cameras photograph the model as it descends through the lower 3.05 m (10 ft) of the tank as shown in Figure 4.2-14. Model images are obtained on the film plates at known time increments by illuminating the tank with stroboscopic

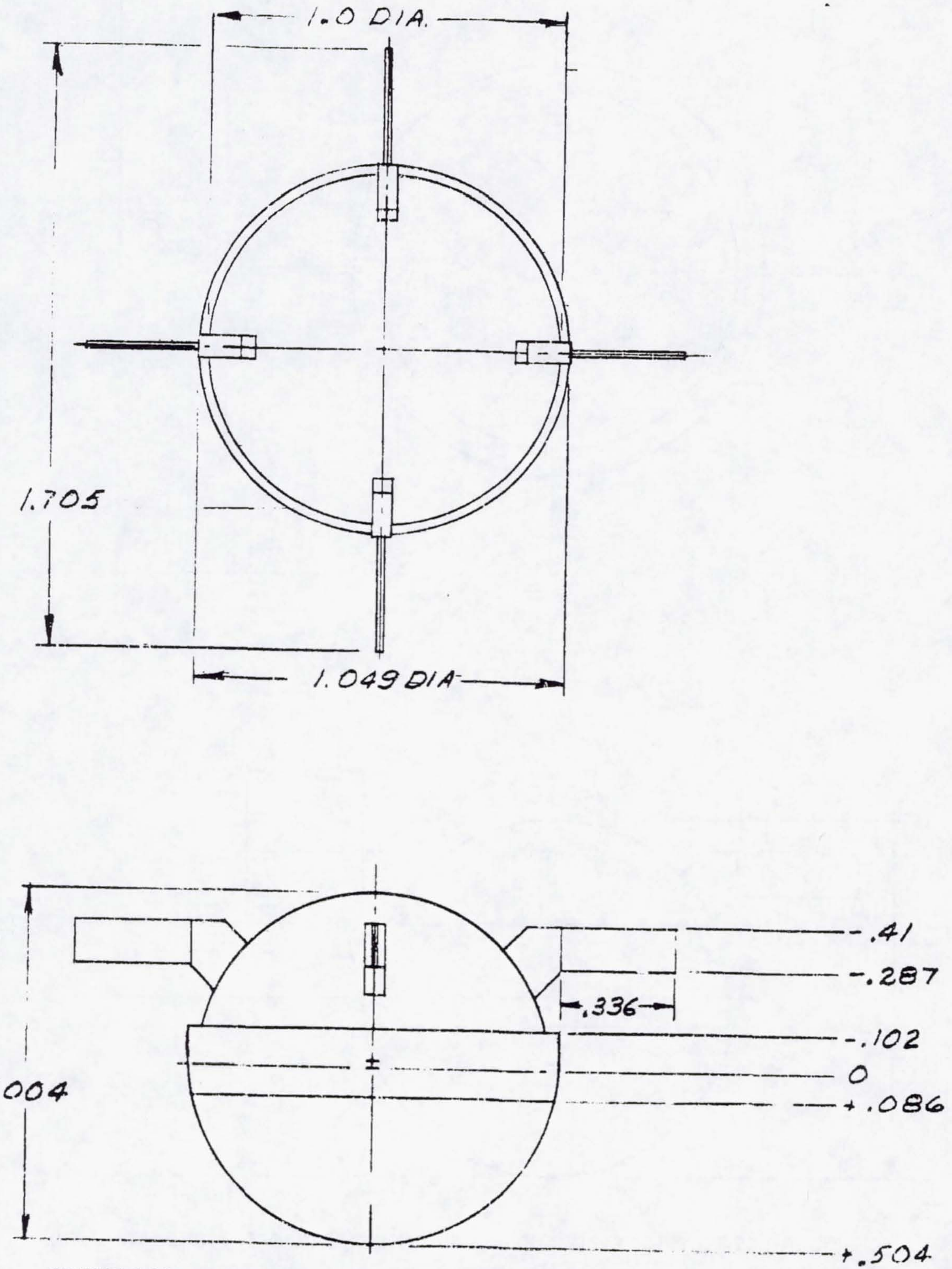

FIGURE 4.2-2. AERODYNAMIC CONFIGURATIONS I (TAIL OFF) AND 1A (TAIL ON)

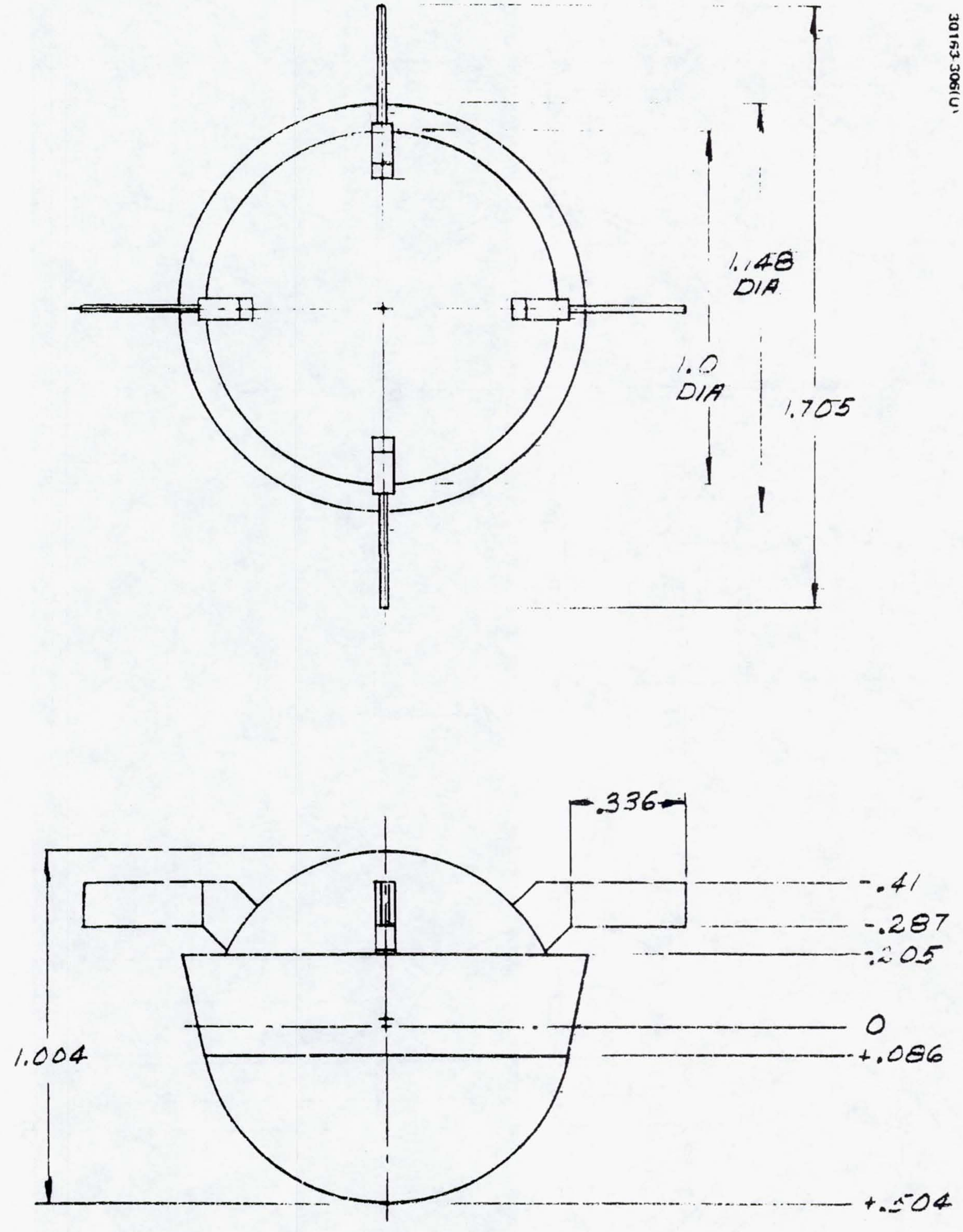

FIGURE 4.2-3. AERODYNAMIC CONFIGURATIONS 2 (TAIL OFF) AND 2A (TAIL ON)

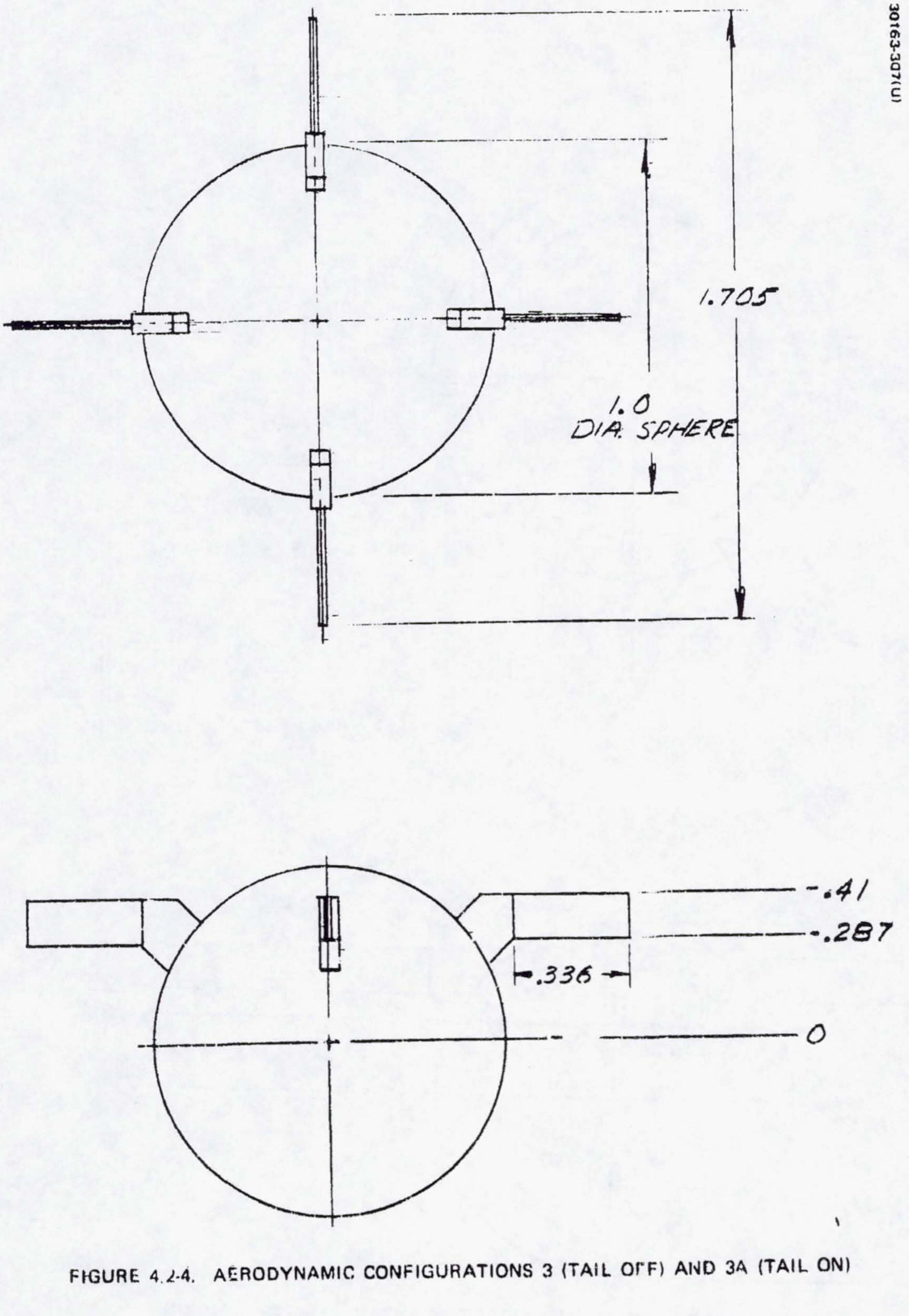

FIGURE 4.2-4. AERODYNAMIC CONFIGURATIONS 3 (TAIL OFF) AND 3A (TAIL ON)

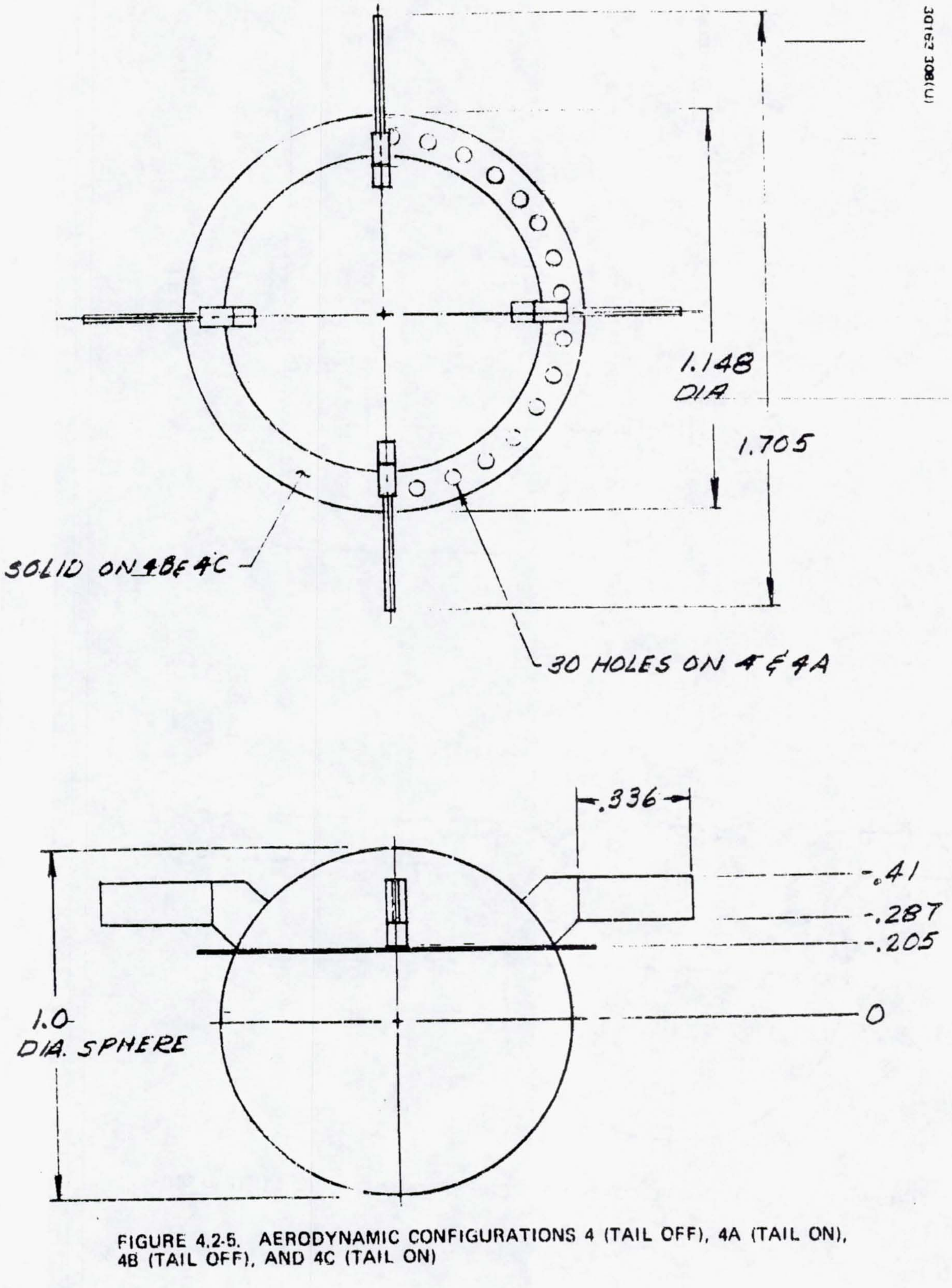

FIGURE 4.2-5. AERODYNAMIC CONFIGURATIONS 4 (TAIL OFF), 4A (TAIL ON), 4B (TAIL OFF), AND 4C (TAIL ON)

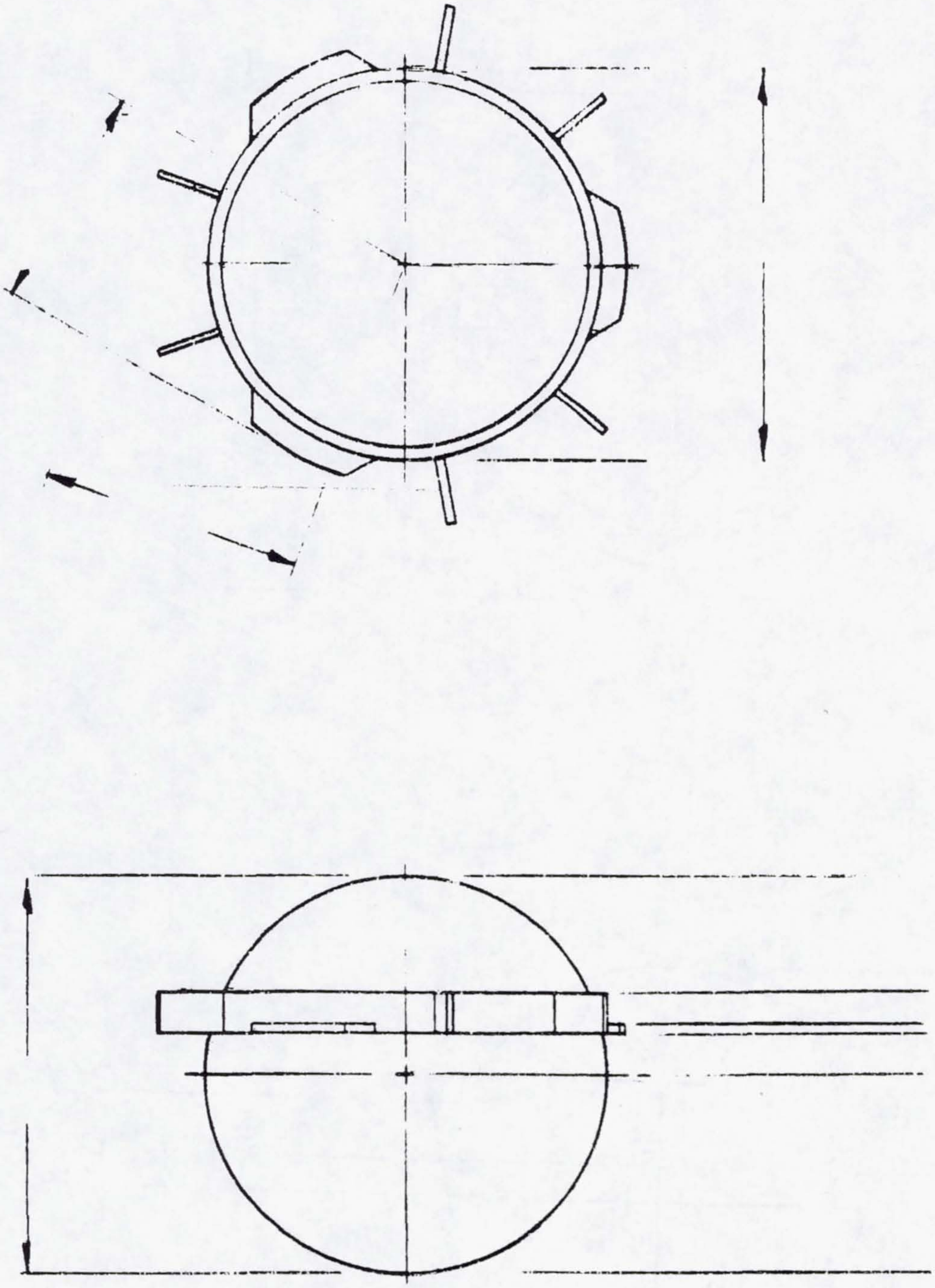

FIGURE 4.2-6. AERODYNAMIC CONFIGURATION 5

30163-310(U)

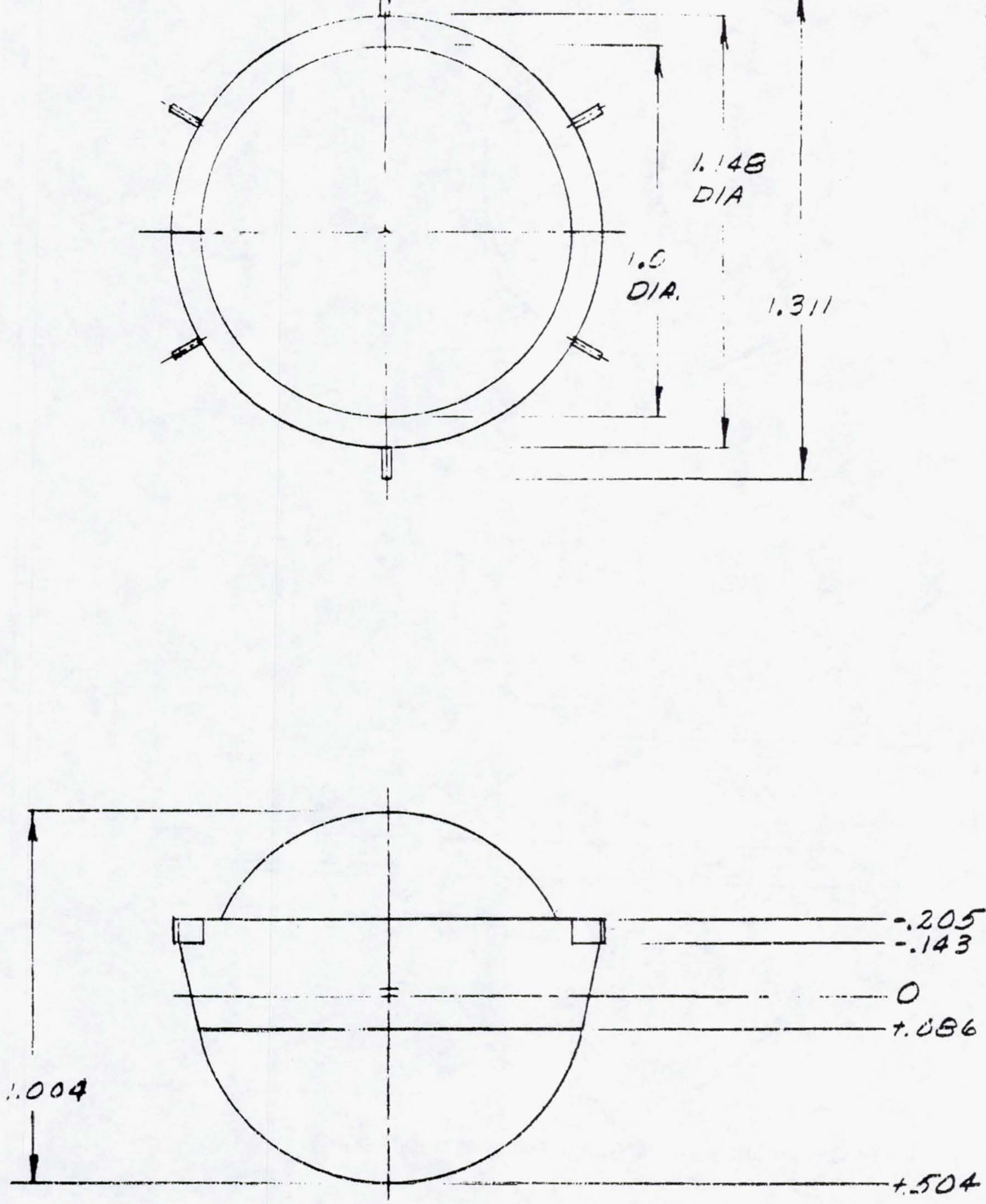

FIGURE 4.2-7. AERODYNAMIC CONFIGURATION 6

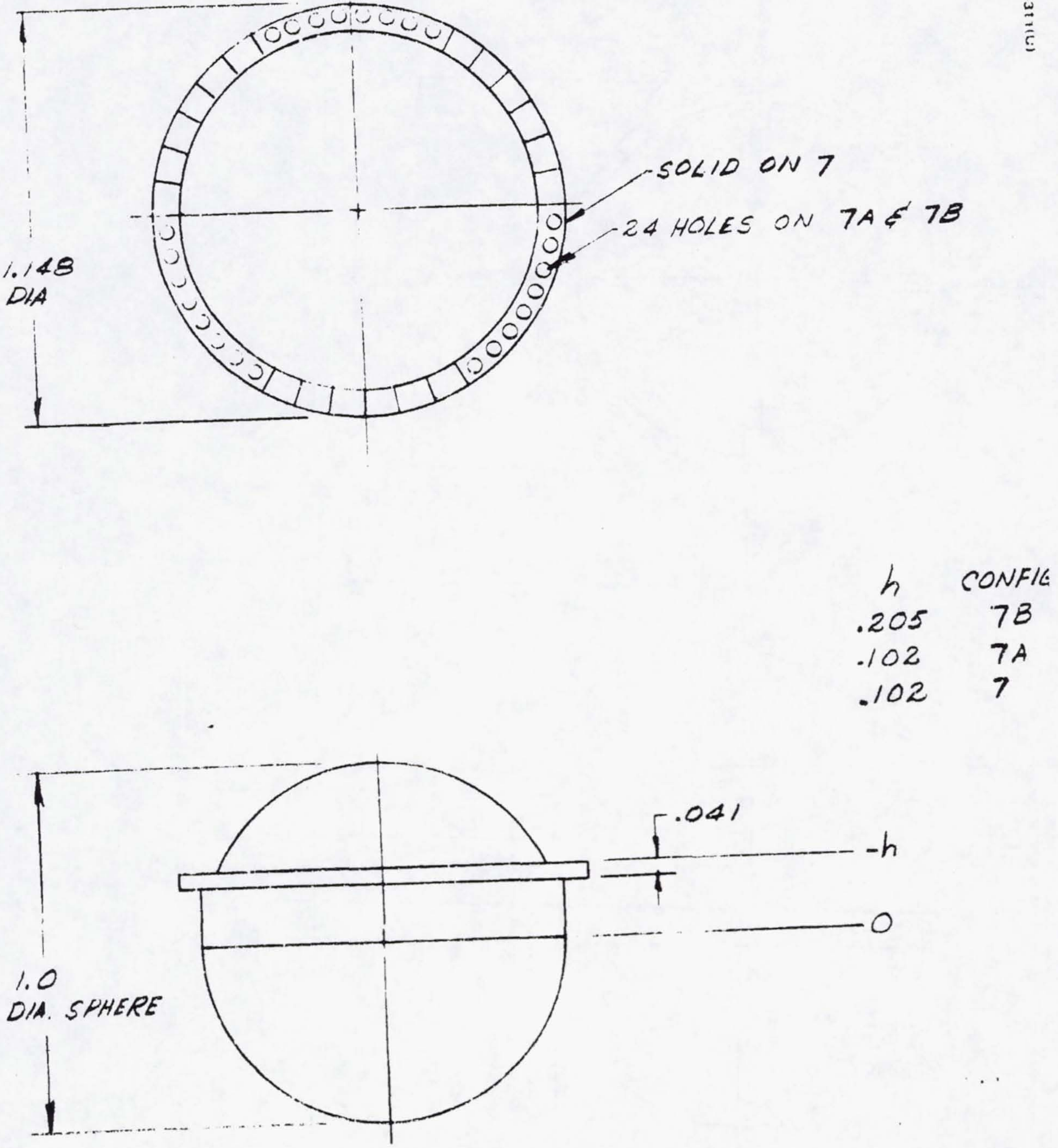

FIGURE 4.2-8. AERODYNAMIC CONFIGURATIONS 7, 7A, AND 7B

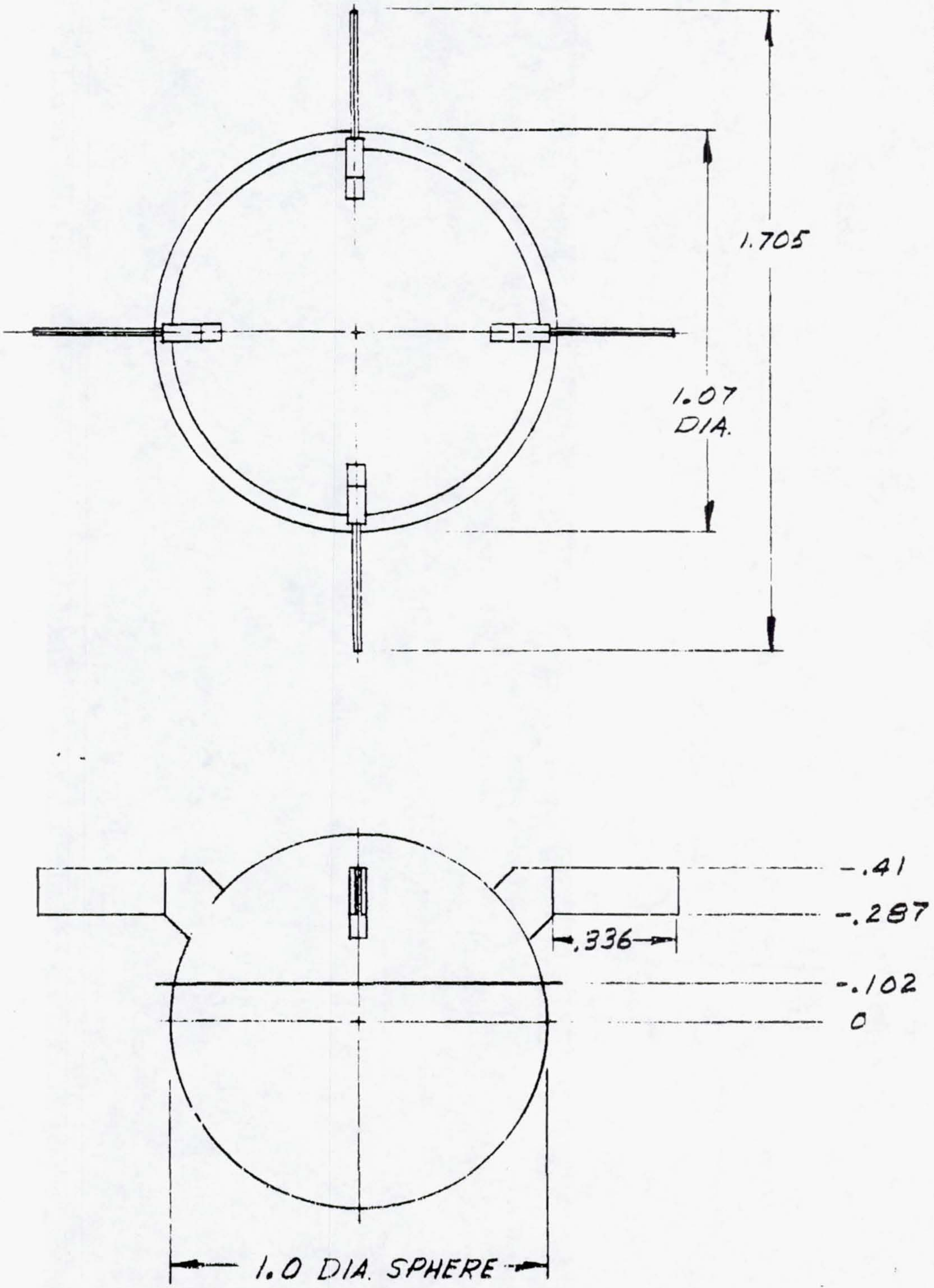

30163-312(U)

FIGURE 4.2-9. AERODYNAMIC CONFIGURATIONS 8 (TAILS OFF) AND 8A (TAILS ON)

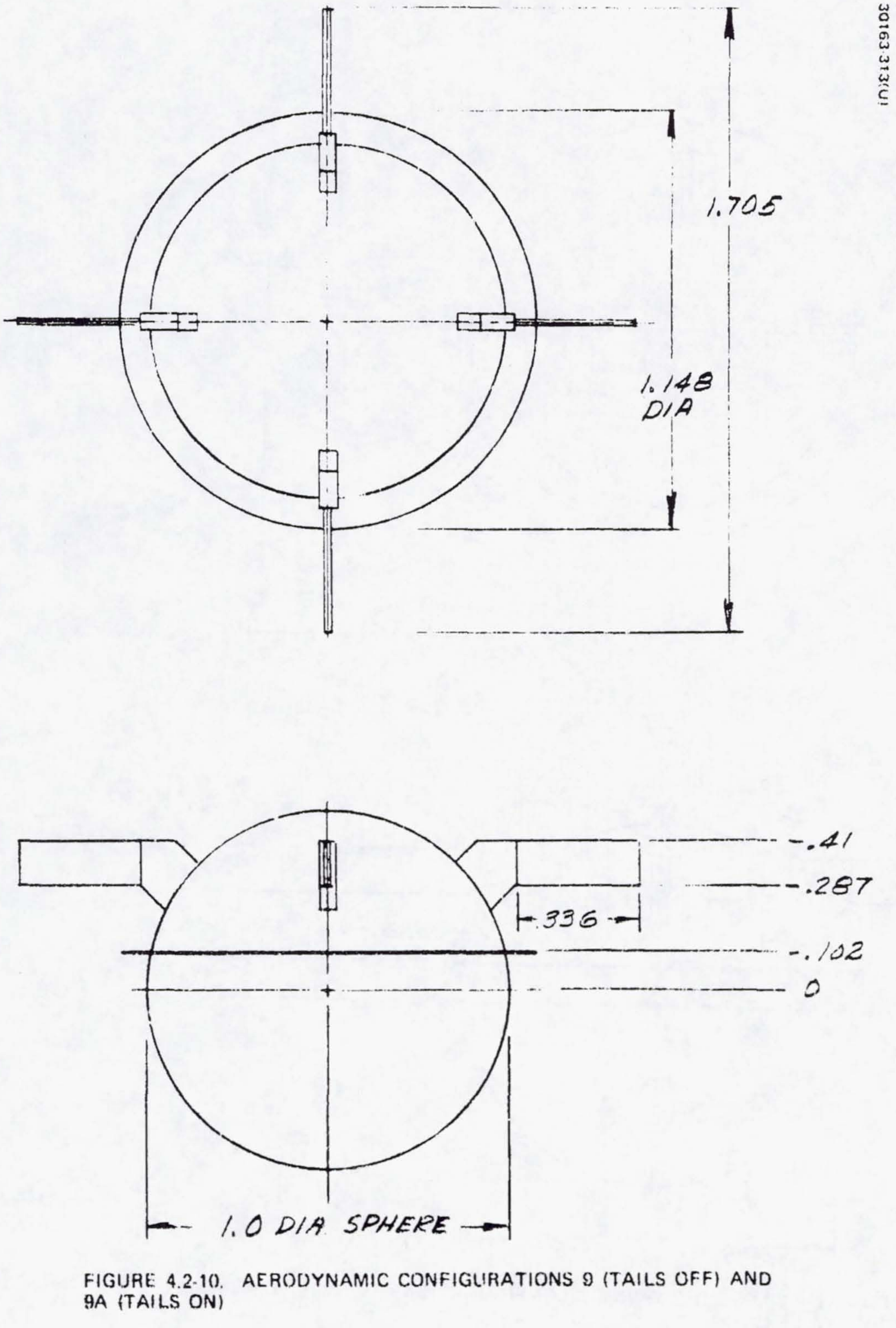

FIGURE 4.2-10. AERODYNAMIC CONFIGURATIONS 9 (TAILS OFF) AND 9A (TAILS ON)

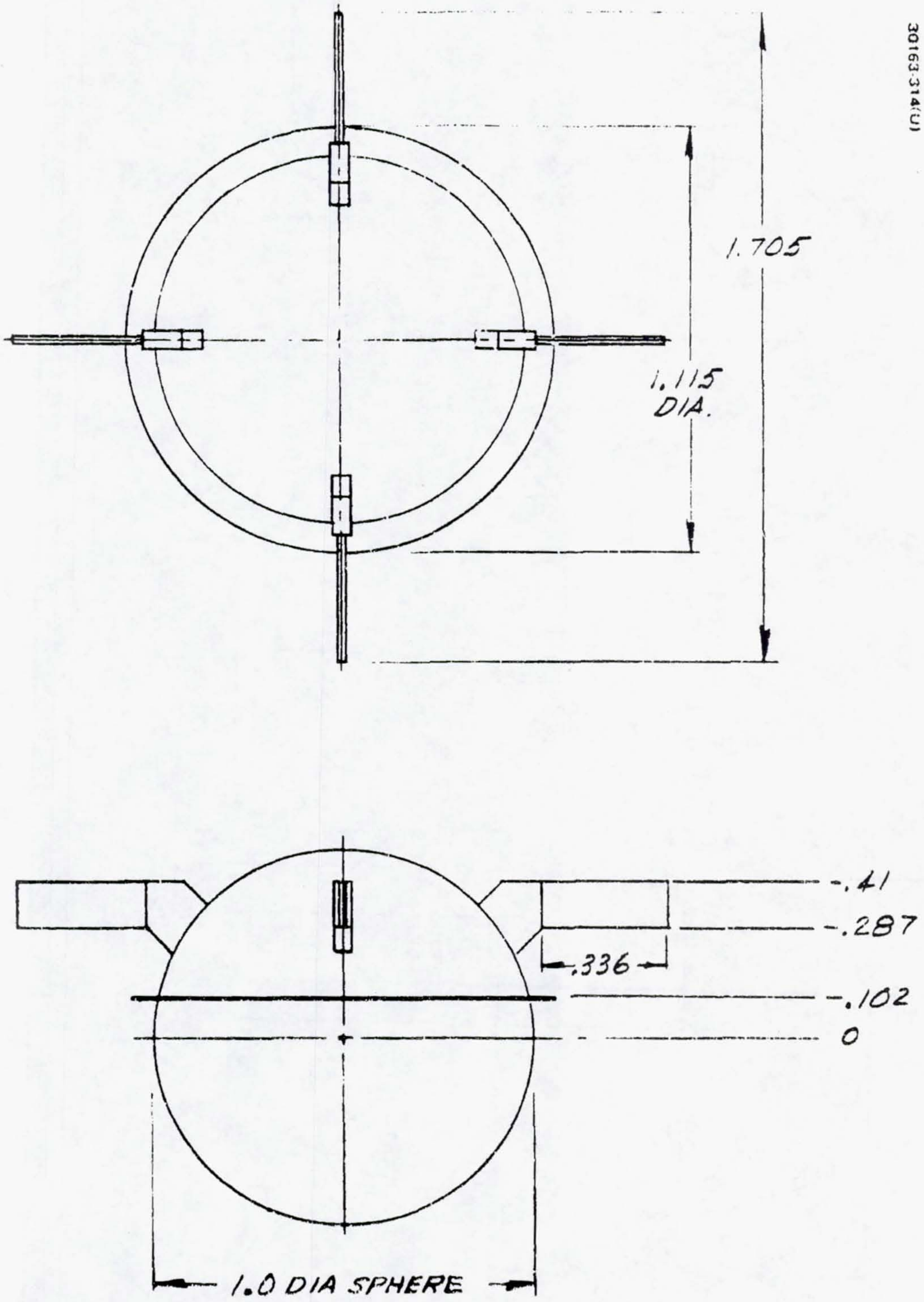

FIGURE 4.2-11. AERODYNAMIC CONFIGURATIONS 10 (TAILS OFF) AND 10A (TAILS ON)

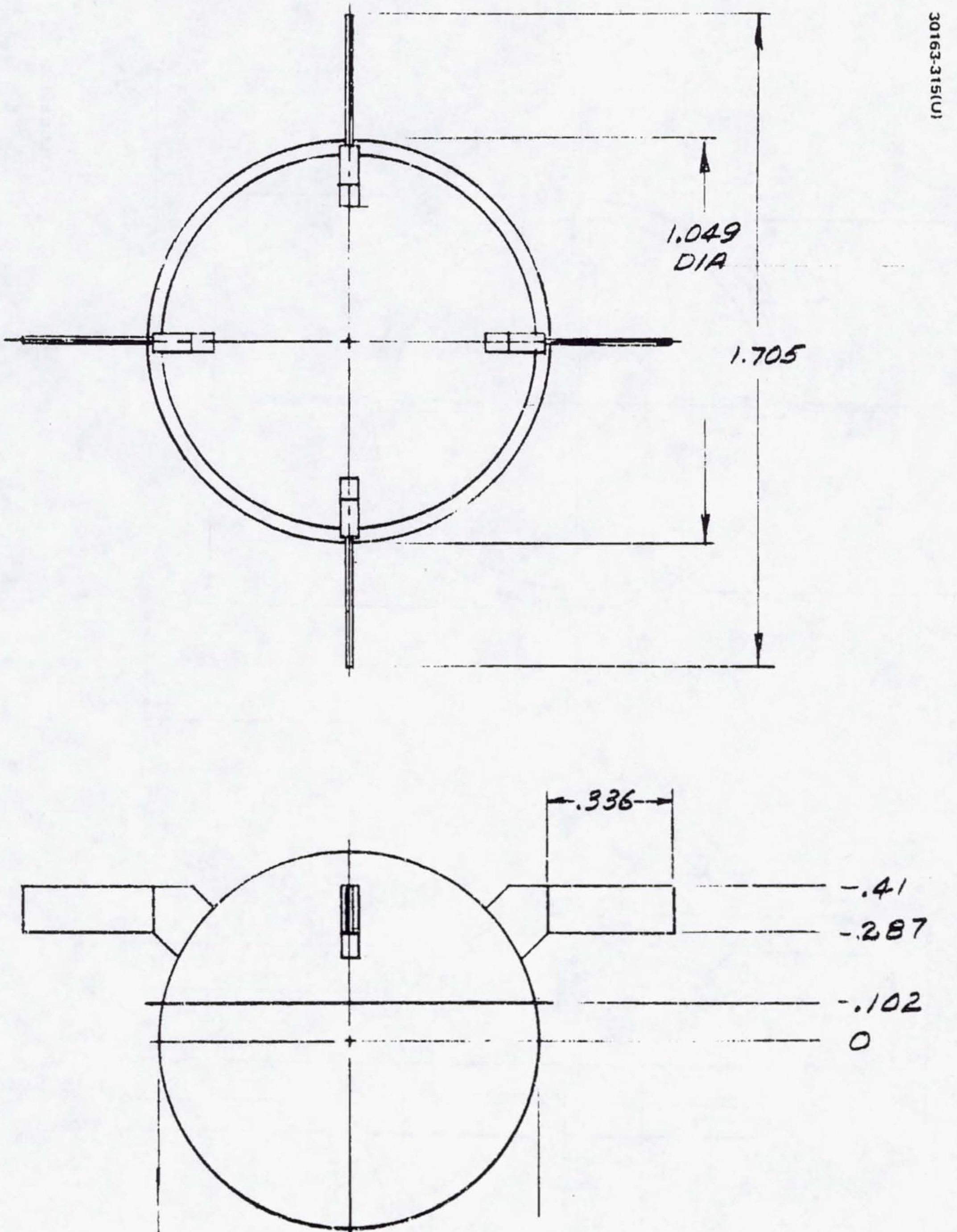

FIGURE 4.2-12. AERODYNAMIC CONFIGURATIONS 11 (TAILS OFF) AND 11A (TAIL ON)

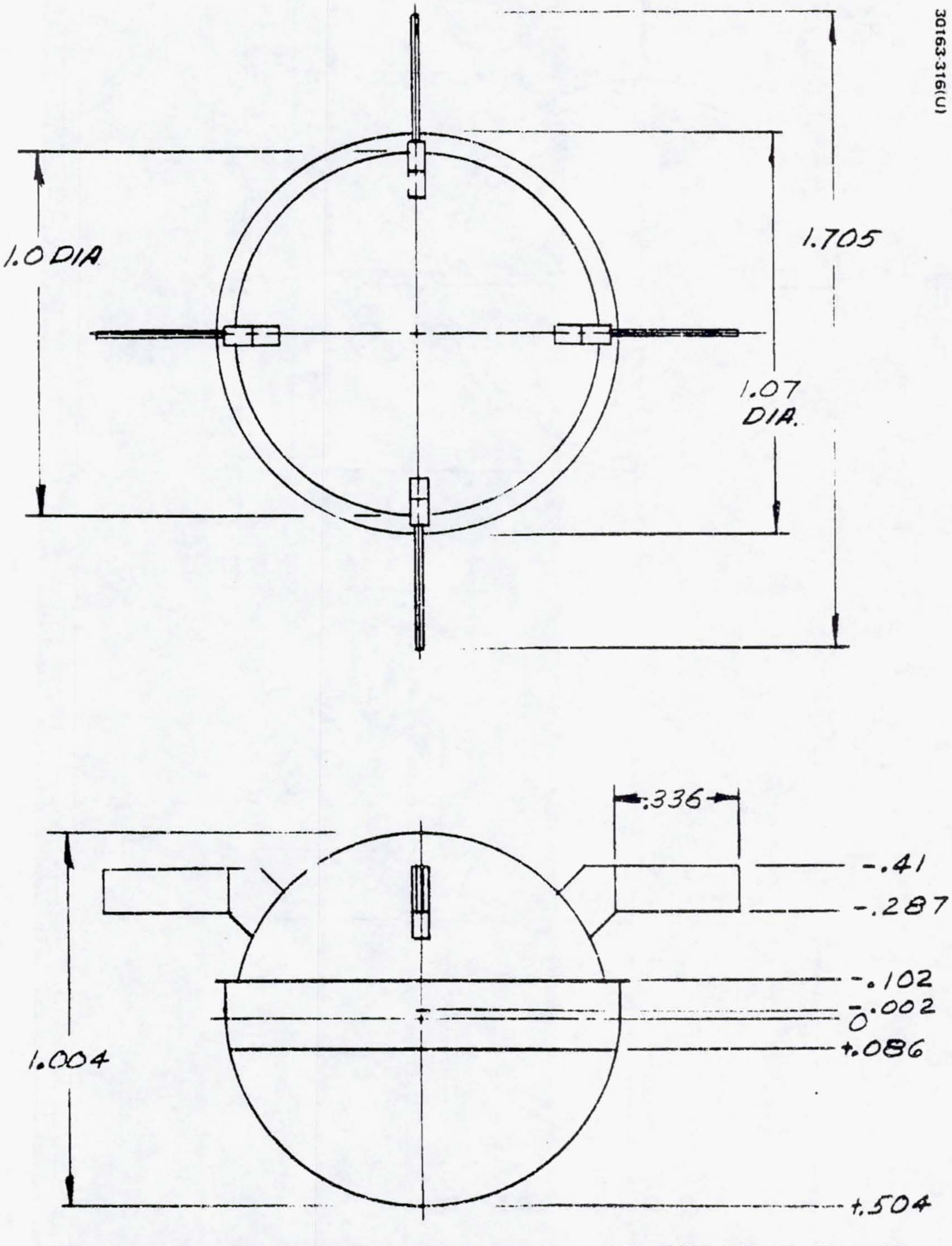

FIGURE 4.2-13. AERODYNAMIC CONFIGURATIONS 12 (TAIL OFF) AND 12A (TAIL ON)

30163-316(U)

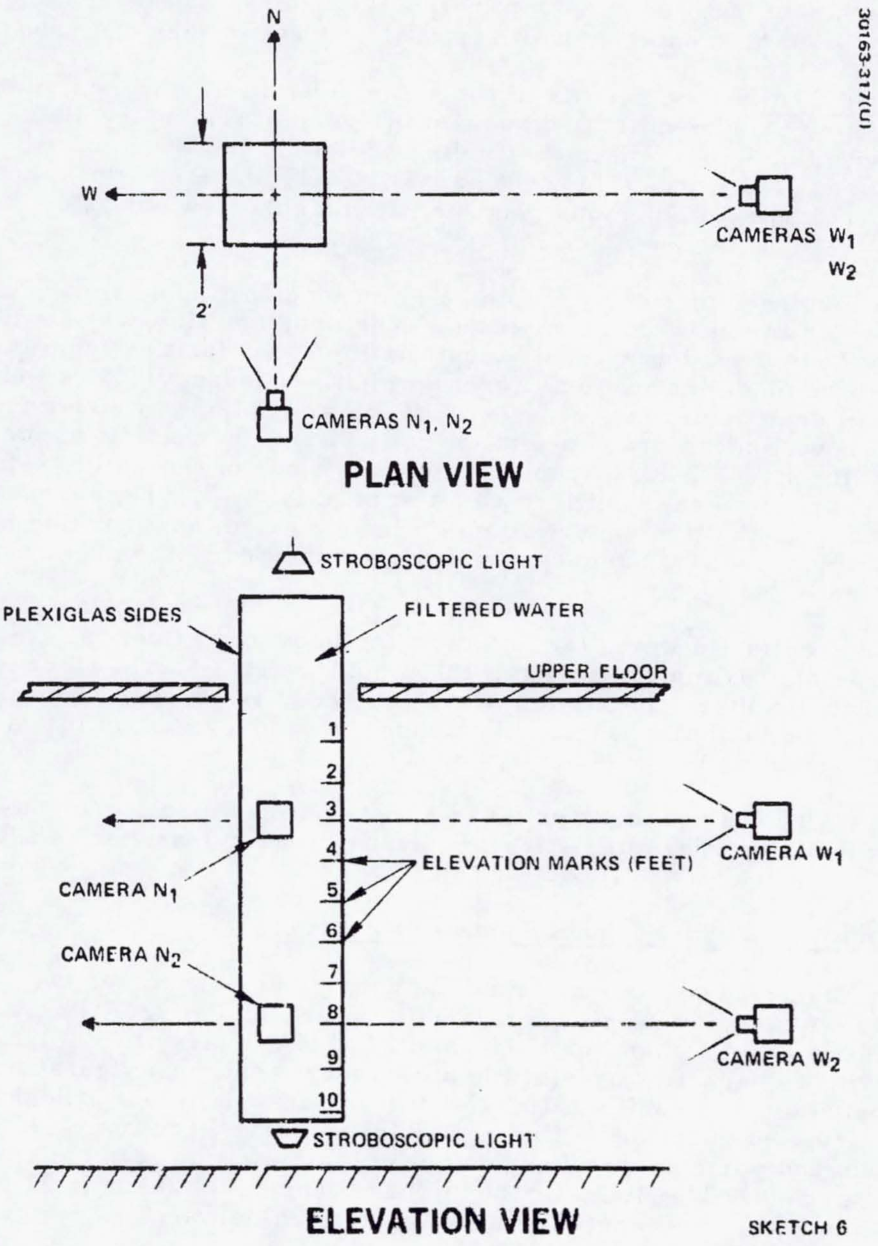

FIGURE 4.2-14. WATER TANK SCREENING TEST SETUP

lights at a frequency of 668 flashes per minute; the camera shutters being open. In Figure 4.2-15, montages of two typical test recordings are shown.

Results of Tests. The results of the water tunnel tests are summarized in Table 4.2-1. The results are grouped in order of trajectory dispersion, starting with the 50 percent porosity disk which presents comparatively the least disperions, the flare, 0 percent porosity disk, the step, the vaned step which has the highest disperions, and finally the sphere which is used as reference.

The tail incidence of 2 deg provides a helix length of approximately 7.9 m (26 ft), which is observed in the tests. The drag coefficients shown in the final column have been determined by estimating the velocities from the photographs and the model net weights (gross weight - buoyancy). For the sphere, values of drag coefficient of 0.74 and 0.85 are obtained which do not agree with the known sphere drag coefficient for either subcritical or supercritical flow (Reference 4.2-2). At the Reynolds number of the water test (50,000) the subcritical drag coefficient of a sphere is 0.47. The discrepancy may be due to the fact that the sphere is not "clean", since tape marking has been applied for photographic purposes, and slots provided in the aft hemisphere to hold the tails.

A factor peculiar to water tank tests is the buoyancy effect, since the buoyancy force is approximately one-half the model weight, and in all cases acts near the model center. In one test the model c.g. is aft of the buoyancy center and motion is unstable. In all other cases the model c.g. is forward of the center of buoyancy.

All models tested in the water tank except configuration 5 are considered to have suitable characteristics to warrant further tests in the LRC facility.

Pressure Vessel Spin Tunnel Tests and Analyses

Hughes, as part of a company funded program has conducted two series of aerodynamic tests at the Langley Research Center's 6.1 m (20 ft) spin tunnel facility on 11 - 13 December 1972, and 24 - 25 January 1973, to determine the free flight characteristics of the atmospheric entry configurations. The models tested are the configurations shown in Figures 4.2-2 through 4.2-13, excepting configuration 4 (Figure 4.2-6) and have been tested with and without tails and various protuberances which simulate the typical external instrument probes. The diameter of the basic spherical shape is 31 cm (12.2 in.) and the reference length for aerodynamic calculations is the external diameter of the disc, 35.6 cm (14.0 in.)

One of these, configuration 7, is selected as the baseline configuration. This is shown in Figure 4.2-16. Its aerodynamic characteristics are presented in Table 4.2-2.

Test Facility. The Langley Research Center's spin tunnel, a 12 sided vertical test section which is 6.1 m (20 ft) across the flats and 6.1 m (20 ft)

TABLE 4.2-1. TRAJECTORY CHARACTERISTICS

			Trajectory Description		[illegible]		
[illegible]	Stabilization Device	C.G.	Location	Motion Type	[illegible]	[illegible]	[illegible]
1	80 percent porosity disk	Center	Down tan. C_T	Slight divergence		[illegible]	
		Forward		Small dispersion	[illegible]	[illegible]	
[illegible]	With tail	Center				Yes	
		Forward				Yes	
		Aft	Unstable, hit wall		Unstable		
2	Flare	Center	Down tan. C_T	Slight divergence	[illegible]	[illegible]	2
		Forward		Damped		[illegible]	
2A	With tail	Center		Damped		Yes	
		Forward		Damped		Yes	—
[illegible]	40 percent porosity disk	Center	Down tan. near C_T	Slightly erratic		[illegible]	[illegible]
		Forward	Down tan. C_T	More erratic		Yes	[illegible]
[illegible]	With tail	Center		Slightly erratic	[illegible]	Yes	
		Forward		Slight oscillation		Yes	
	Stepped sphere	Center	Near wall, may be wall effects	Coning, erratic		[illegible]	[illegible]
		Forward		Coning, erratic	[illegible]	Yes	[illegible]
[illegible]	With tail	Center		Oscillation	[illegible]	Yes	—
		Forward		Oscillation	[illegible]	Yes	—
[illegible]	Stepped sphere with vanes	Center	Hit wall	—	[illegible]	Yes	
		Center	Near wall, may be wall effect	Oscillation	[illegible]	Yes	
		Forward	Down tan. C_T	Oscillation	[illegible]	Yes	
[illegible]	Sphere	Center		Erratic	[illegible]	Yes	[illegible]
		Forward	May be wall effect	Erratic	—	Yes	—
[illegible]	With tail	Center	Hit wall at [illegible] ft level	Large excursion	—	—	—
		Forward	Hit wall at 2 ft level	—	—	—	—

[illegible] refer to Figures 4.2-2 and 4.2-[illegible] respectively.

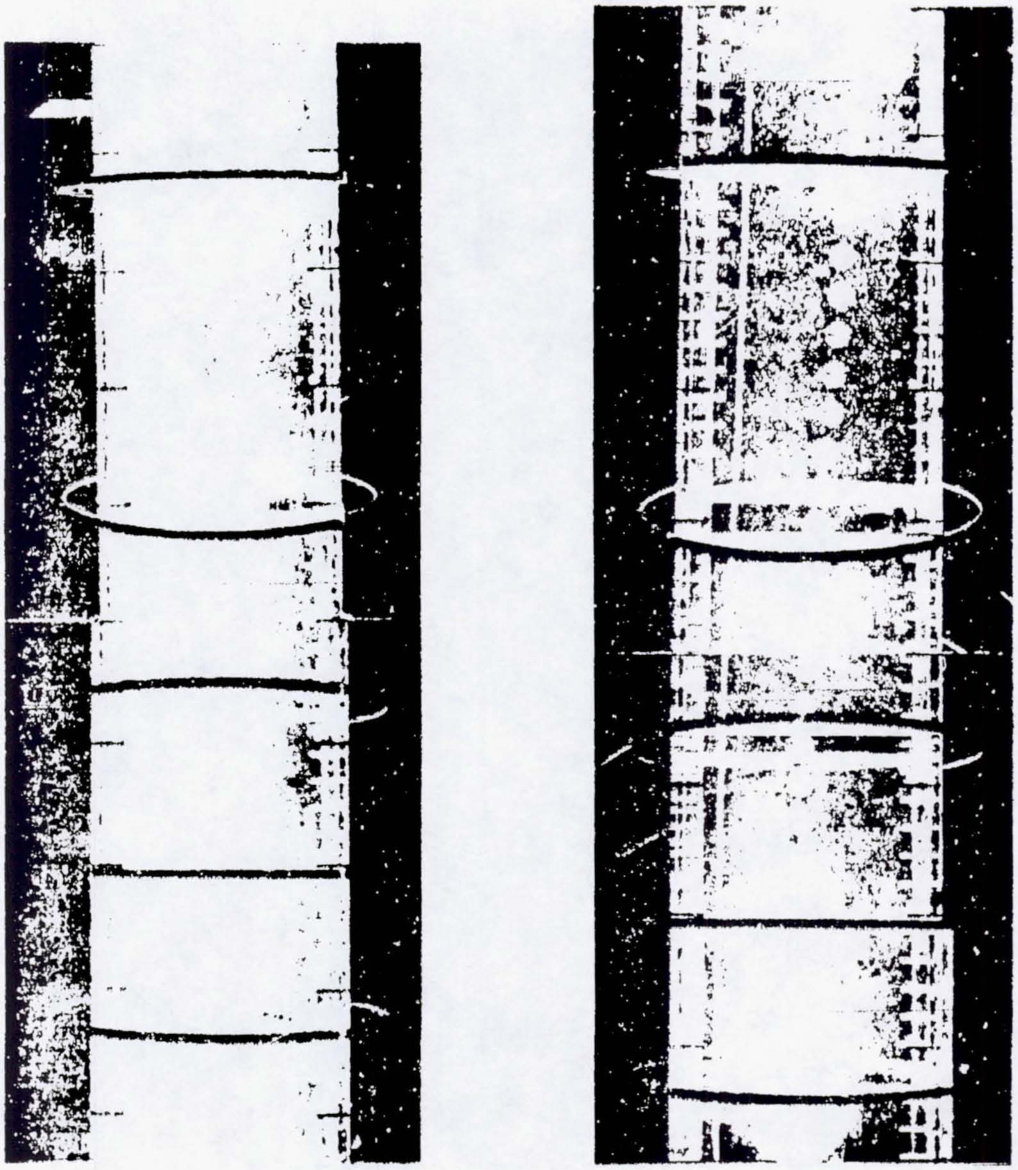

N

W

FIGURE 4.2-15. TYPICAL TEST RECORDINGS

REPRODUCIBILITY OF THE ORIGINAL PAGE IS POOR.

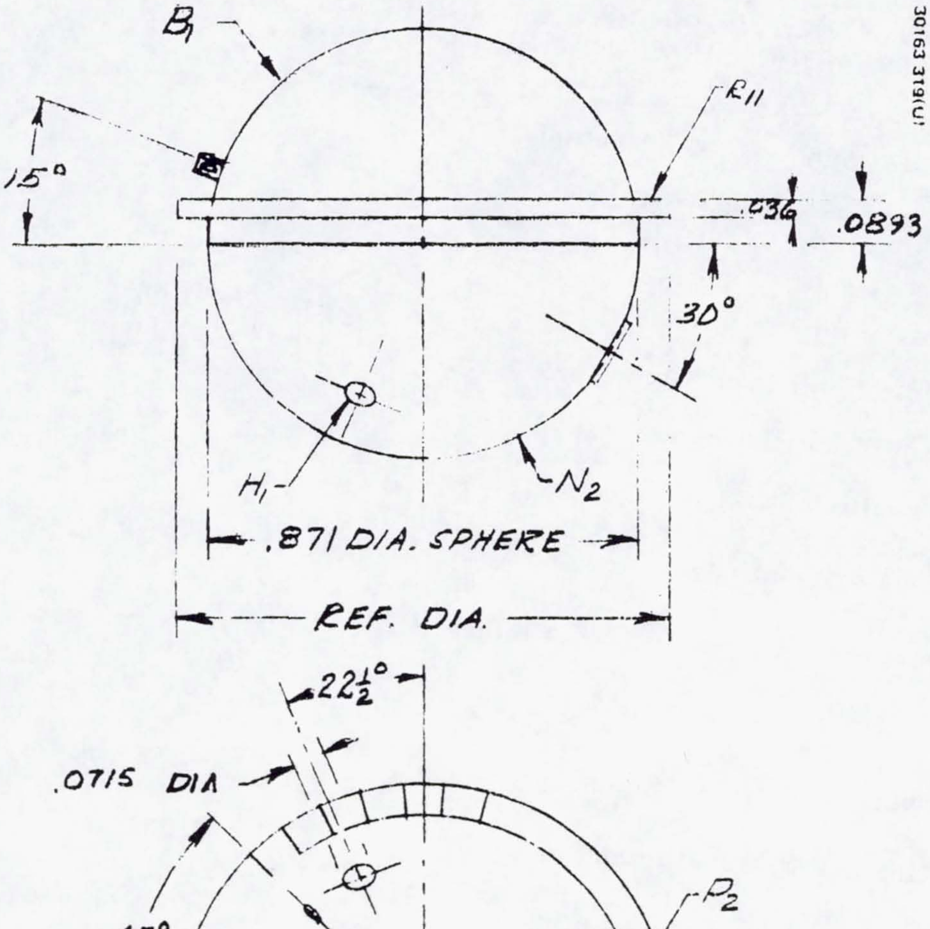

FIGURE 4.2.16. THOR/DELTA BASELINE CONFIGURATION

TABLE 4.2-2. LARGE PROBE BASELINE (THOR DELTA) DIMENSIONS, MASS PROPERTIES, AND AERODYNAMIC COEFFICIENTS

Reference length (ring diameter)	0.7366 m
Reference area (ring area)	0.4261 m^2
Mass	75.75 kg
Moment of inertia in roll, Ixx	2.97 kg-m^2
Moment of inertia in pitch, Iyy	2.69 kg-m^2
Moment of inertia in yaw, Izz	2.99 kg-m^2
Drag coefficient, C_{D_o}	0.55
Pitching moment curve slope coefficient, C_{m_α}	-0.0382/rad
Normal force curve slope coefficient, C_{N_α}	1.60/rad
Lift curve slope coefficient, C_{L_α}	1.05/rad
Damping in pitch coefficient $C_{m_q} + C_{M_\alpha}$	-0.052/rad/sec
Rolling moment coefficient, C_{o}	0.002/rad
Damping in roll coefficient, C_{p}	-0.10/rad/sec

high. Nets are stretched across the upper and lower ends of the test section, the upper net to prevent the model from entering the fan blades and the lower net to protect the model from the air straightening vanes and tunnel sides.

A platform surrounds the tunnel test section, and six of the tunnel sides have windows. An operator at one window controls the tunnel velocity to hold the model at viewing level. A gimbal mounted 16 mm cinecamera is provided at one window for manually tracking the model. Two of the other windows can be opened for launching and retrieving the model.

Model Construction. Because the nature of the spin tunnel testing requires the model to be supported solely by the upward stream of air, the wind tunnel models were constructed of lightweight fiberglas hemispheres with provisions for adjusting the c.g. location and the total weight of the model. All models used a basic spherical design of 31 cm(12.2 in.) diameter (approximately 1/2 scale) to which interchangeable parts could be attached thus providing maximum configuration variation from a minimum number of parts.

Because of the difficulty of matching parameters over the wide range of flight conditions, the models are not dynamically similar to a full scale pressure vessel descent in the Venusian atmosphere. Instead, the approach taken is to record the model response and analytically determine the basic aerodynamic characteristics. Using these characteristics and the full scale mass properties, the hynamic behavior to be expected in the Venusian atmosphere is computed.

Test Operation. The tunnel operator adjusts the tunnel upward velocity to that required for model hovering. The model is then hand launched into the tunnel from a window across from the camera and the launch dynamics filmed. The tunnel operator continually adjusts the velocity to sustain hovering flight. In general, the model wanders about the tunnel because of flow irregularities and tends to rise or fall, causing the operator to continually readjust the velocity. The model may be struck by a pole from a window so that the transient response to a disturbance can be observed. The model motion is recorded on film with the time and tunnel velocity recorded on each frame.

Data Taking Technique. The only data obtained is the filmed motion of the model. To determine the drag, the velocity is read from the film at those times when the model sustains a hovering flight. Roll position data are obtained by recording the times at which the vertical reference markings on the model are normal to the frame. Pitch angular motion is obtained by recording the model pitch angle relative to the horizontal reference lines painted on the tunnel wall as a function of time.

Flow Visualization Tests. To assure that the measured aerodynamic characteristics can be applied to the full scale atmospheric descent case, it is necessary that the test Reynolds number be supercritical. At Reynolds number higher than the critical value, the flow pattern does not change significantly, and the aerodynamic characteristics apply at any higher Reynolds number.

To verify that the flow was supercritical in these tests a series of tuft runs were made.

Wool tufts were attached forward and aft of the center of a sphere and the tuft motion was filmed at the following velocities and Reynolds number:

V, m/sec	(V, ft/sec)	Reynolds Number
4.3	(14)	90,000
6.4	(21)	135,000
8.2	(27)	173,000
10.4	(34)	220,000
12.8	(42)	270,000

At the lowest velocity and Reynolds number the tufts indicate flow separation forward of the center. For the Reynolds numbers 135,000 and above, the tufts indicated attached flow well aft of the center of the sphere, thus verifying that supercritical flow exists.

A further verification of supercritical flow was obtained from smoke flow tests. For visualization of the flow, the model (configuration 7) is constrained by three lines in the tunnel. A smoke sources traverses from one side to the other, upstream of (below) the model. In repeated tests with the tunnel speed varied from 12.5 m/sec (41 ft/sec) to 15.5 m/sec (51 ft/sec) there is no indication of flow dissimilarity. The separation point is aft of the center of the sphere indicating supercritical flow.

Further smoke tests provide a time history of the base flow exchange to assess the lag associated with measurements made in that area. Although the filmed data does not extend long enough to show the complete clearing of the smoke, it indicates that the base flow is exchanged in approximately 1 sec.

Drag Analysis. The drag coefficient is computed from the model weight and the velocity recorded on the film. Since the model is in vertical flight, the drag equals the weight when the vertical model motion is zero and the tunnel velocity is constant. In some of the runs, this stead state condition is not achieved, and an estimated velocity is obtained by bounding the upper and lower velocities as the model motion changes from upward to downward flight. The drag coefficient is computed from

$$C_D = \frac{mg}{\rho/_2 \, S \, V^2}$$

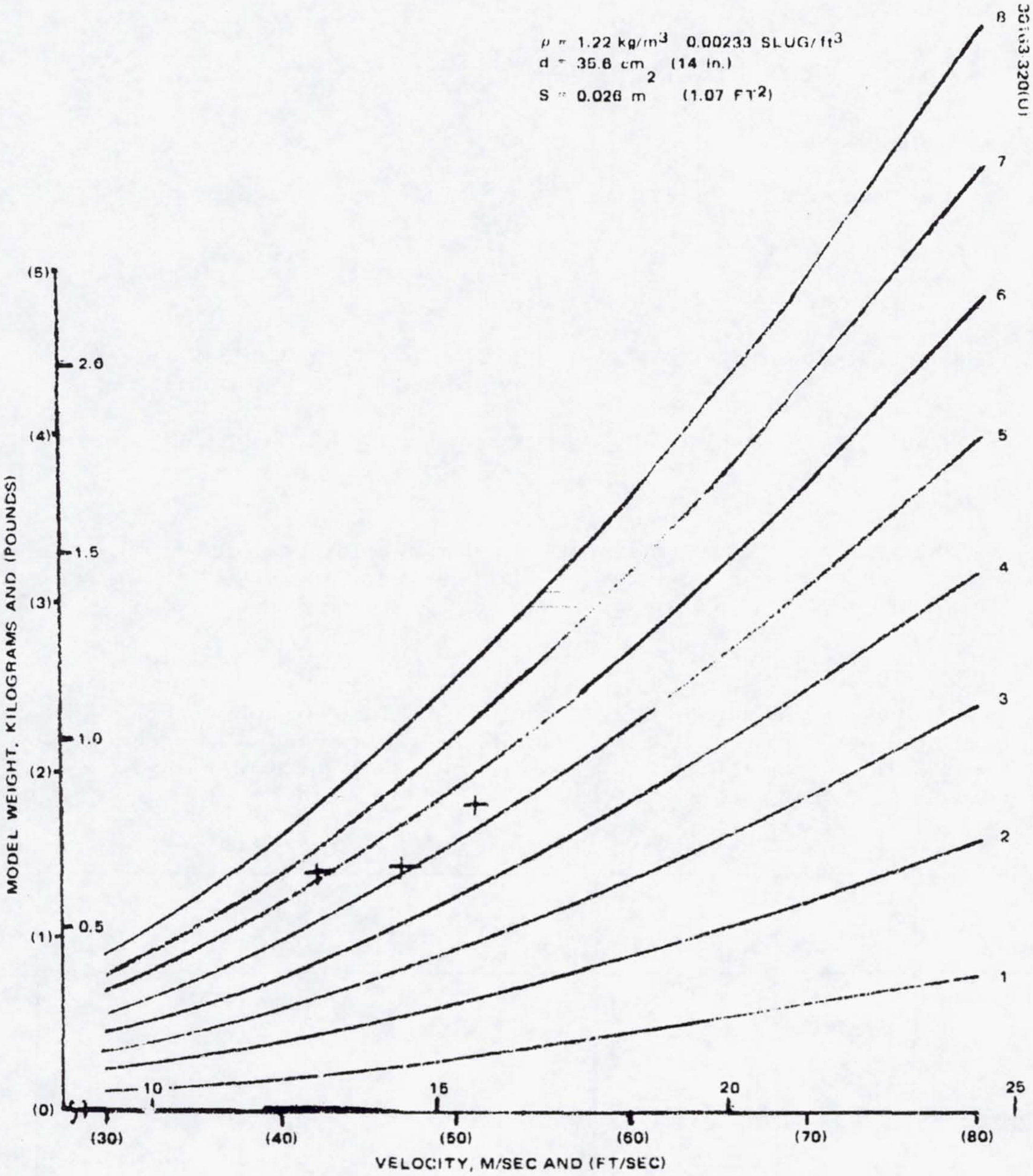

FIGURE 4.2-17. CONFIGURATION 7 MODEL DRAG CHARACTERISTICS

where

		Metric Units	English Units
m	model mass	kg	slugs } lbs
g	acceleration due to gravity	$9.81\ m/sec^2$	$32.2\ ft/sec^2$ } lbs
S	reference area $\frac{\pi d^2}{4}$	m^2	ft^2
d	outer ring diameter	m	ft
ρ	air mass density	$1.229\ kg/m^3$ (nominal)	$0.00238\ slug/ft^3$ (nominal)
V	velocity recorded on film strip	m/sec	ft/sec

The drag coefficient for configuration 7 has been determined from each run and presented in Figure 4.2-17. The drag coefficients of all configurations is tabulated in Table 4.2-3.

Stability Analysis. From the filmed records of the vehicles flight, the transient response to a pitch angle disturbance is derived. The technique used is to project the film frame by frame on a screen and measure the pitch and roll angles versus time. The velocity is also recorded at each frame. These data are plotted as functions of time. A typical plot for configuration 7 is given in Figure 4.2-18.

TABLE 4.2-3. AERODYNAMIC CHARACTERISTICS

Configuration	C. P.	C_{N_α}	C_D	C_{L_α}	Cm_q	C_{m_α} (c.g. at 0.51 cm (0.2 in.))
1	0	1.4	0.25	1.15		-0.02
1A	-0.0415	1.64	0.25	1.39		-0.09
2	-0.0322	1.4	0.40	1.0		-0.066
2A	-0.0443	1.724	0.42	1.304		-0.159
6	-------	-----	0.41			-0.126
4	-0.030	1.285	0.68	0.605		-0.057
4A	-0.057	1.459	0.68	0.779		-0.108
7	-0.01214	1.60	0.55	1.05	-.052	-0.042
9	---------	-----	0.65			-0.042

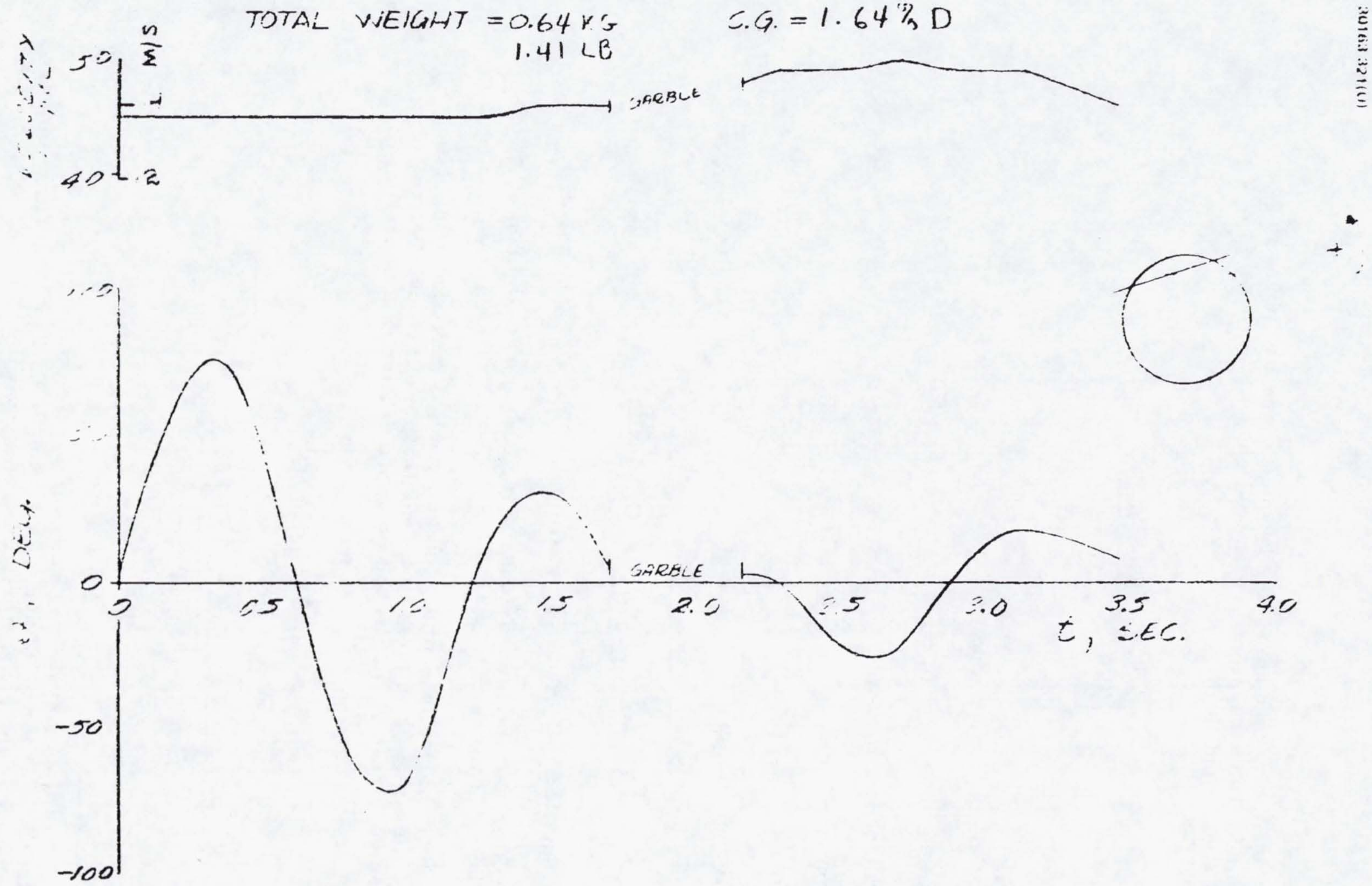

FIGURE 4.2-18. CONFIGURATION 7 STABILITY ANALYSIS PLOT

30163.321(U)

From the plot of θ versus time, the frequency and damping are measured. Assuming a linear system in steady flight with zero roll rate, the static stability coefficient is then given by: *

$$Cm_\alpha = \frac{\omega_n^2 I_y}{1/2\rho V^2 Sd}$$

where

ω_n = pitch natural frequency

I_y = moment of inertia in pitch

ρ = atmospheric density

V = tunnerl velocity

S = reference area, $\frac{\pi d^2}{4}$

d = reference length

Using the relations:

$$Cm_\alpha = \ell o\, C_{N_\alpha},\quad C_{L_\alpha} = C_{N_\alpha} - C_{D_o}$$

and the response data for different c. g. positions, C_{N_α}, C_{L_α} and the c. p. can be determined. From the measured damping coefficient, the combinations $Cm_q + Cm_\alpha$ can be determined.

When the model is rolling, the pitch and yaw motions are coupled and the response to a disturbance in pitch is a combination of two oscillations of different frequencies. This response can be approximated in a nonrolling coordinate system by:

$$\tilde{\theta} = B_1 e^{A_1 t} + B_2 e^{A_2 t}$$

$$A_{1,2} = -\eta \pm \frac{1}{2} \frac{P(Z\omega + \eta)}{\sqrt{\omega o^2 + \frac{P^2}{4}}} + i \left[\frac{P}{2} \pm \sqrt{\omega o^2 + \frac{P^2}{4}} \right]$$

---

*The assumption of a linear system is not valid for large disturbances, but for oscillations of the order of 10 deg it is reasonable. For large amplitudes, the technique results in the characteristic of an "equivalent" linear system.

where

$\tilde{\theta} = \theta + i\psi$

θ = pitch angle

ψ = yaw angle

$P = p \frac{Ix}{Iy}$

p = roll rate

Ix = roll moment of inertia

Iy = pitch moment of inertia

η = damping coefficient of nonrolling system

ωo = frequency of nonrolling system

Zw = damping in plunge coefficient of nonrolling system

To determine the aerodynamic coefficients from the motion, it must be viewed in two orthogonal planes (pitch and yaw), so that the actual roll axis motion can be identified as two oscillations. If only one plane is viewed, the combined oscillation appears as a single oscillation.

If the system is lightly damped and the roll rate is small compared to the pitch frequency, the transient oscillation following an initial disturbance in pitch appears as a high frequency oscillation of frequency, $\lambda = \sqrt{\omega o^2 + P^2/4}$ modulated at a frequency $P/2$.

where

$P = p \frac{Ix}{Iy}$

and

p = roll rate

The data can be reduced to pitching moment coefficient as before, using the relation:

$$\omega o^2 = \lambda^2 - \frac{P^2}{4}$$

where λ is the observed frequency.

Using the techniques described above, the data have been reduced and the aerodynamic characteristics obtained are tabulated in Tables 4.2-3 and 4.2-4 (only the data with zero or low roll rate have been used).

The results of the spin tunnel tests and dynamic analysis indicate that configurations 1, 2, 4, 6, 7, and 9 have satisfactory aerodynamic characteristics in that any of them can satisfy the design requirements. Hence, the baseline selection is not made on the basis of aerodynamic characteristics alone. The selection is made primarily on the basis of mechanical simplicity. The selected configuration is configuration 7, which is shown with typical instrument protuberances in Figure 4.2-16. This configuration was tested with and without protuberances and with various c.g. positions. The reduced stability data is shown in Figure 4.2-19, where Cm_α versus c.g. position is plotted. From this plot the following parameters are obtained.

$$C_{N_\alpha} = 1.60$$

$$C.P. = -.0125d$$

In Table 4.2-4 a large scatter in the measured values of the damping parameter, η, is noted. Accordingly, a conservative estimate of $\eta = 0.9$ is made which yields $Cm_q + Cm_\alpha = -0.052$.

Effect of Protuberances. The various protuberances which simulate scientific instruments protruding through the spherical body are shown in Figure 4.2-16. The protuberances were tested in various locations on the sphere. In general, the observed effect of all of these protuberances is negligible. Differences in dyanmic behavior with and without protuberances is well within the scatter of the data, with one exception: when a single protuberance A1 is installed, a pitch oscillation at the roll rate is observed. However, when the model is balanced by a small wad of clay diametrically opposite A1, the 'wobble" disappears. It is also noted that twisting A1 to a finite angle of attack produced a significant roll rate.

Analysis of Dynamic Behavior

A digital computer program entitled 6D-AESS has been developed to simulate the three-dimensional flight of a passive atmospheric entry system with 6-degrees-of-freedom. The primary purpose of the simulation is to describe the low subsonic dynamic behavior of a spinning atmospheric entry system subjected to initial disturbances and altitude variable winds. The simulation was employed in the analysis of the dynamic response of the large probe pressure vessel when subjected to initial disturbances and disturbances due to wind shear and sharp edged gusts. The analysis considered both symmetric and asymmetric configurations.

TABLE 4. 2-4. RESULTS OF STABILITY PLOT ANALYSIS

Configuration	Run	C. G., percent of	I_y		λ,	P,	V		η	Cm_α
			kg/m^2	Slug ft^2	rad/sec	rad/sec	m/sec	ft/sec		per radian
7 (clean)	78-1	1. 43	0. 00833	0. 00615	4. 83	0. 685	14. 5	47. 5	—	-0. 0425
	57-1			0. 00615	5. 93	0	17. 7	58	1. 10	-0. 043
	-1a			0. 00615	6. 28	0	17. 7	58	1. 10	-0. 049
	-2			0. 00615	6. 03	0	19. 0	62. 5	0. 53	-0. 038
	61-1		0. 00748	0. 00552	5. 61	0	18. 6	61. 0	1. 14	-0. 032
	64-1		0. 00763	0. 00563	6. 28	0. 66	16. 3	53. 6	—	-0. 052
7 (with protuberances	-2		0. 00763	0. 00563	5. 24	0. 57	16. 1	52	—	-0. 038
	63-3		0. 00767	0. 00566	5. 9	0	15. 8	52	0. 53	-0. 049
	65-1		0. 00772	0. 00570	5. 7	0	16. 5	54	0. 76	-0. 043
	-2		0. 00772	0. 00570	6. 02	0. 51	16. 5	54	—	-0. 048
	-3		0. 00772	0. 00570	6. 55	1. 16	16. 1	53	—	-0. 056
	-5		0. 00772	0. 00570	5. 46	0	16. 5	54	0. 91	-0. 039
	66-1		0. 00786	0. 0058	5. 24	0	16. 1	53	0. 55	-0. 038
	-3	1. 43	0. 00786	0. 0058	5. 82	0	16. 5	54	0. 66	-0. 045
	37-1	5. 77	0. 00673	0. 00497	7. 85	3. 92	14. 9	49	—	-0. 083
7 (clean)	43-1	5. 97	0. 00734	0. 00541	7. 85	2. 26	14. 6	48	—	-0. 096
	51-1	-0. 715	0. 00671	0. 00495	4. 13	2. 47	15. 5	51	—	-0. 021
	38-2	-0. 715	0. 00605	0. 00446	2. 86	1. 3	12. 2	40	—	-0. 012
	49-1	0	0. 00671	0. 00495	4. 49	2. 6	16. 5	54	—	-0. 021

REPRODUCIBILITY OF THE ORIGINAL PAGE IS POOR.

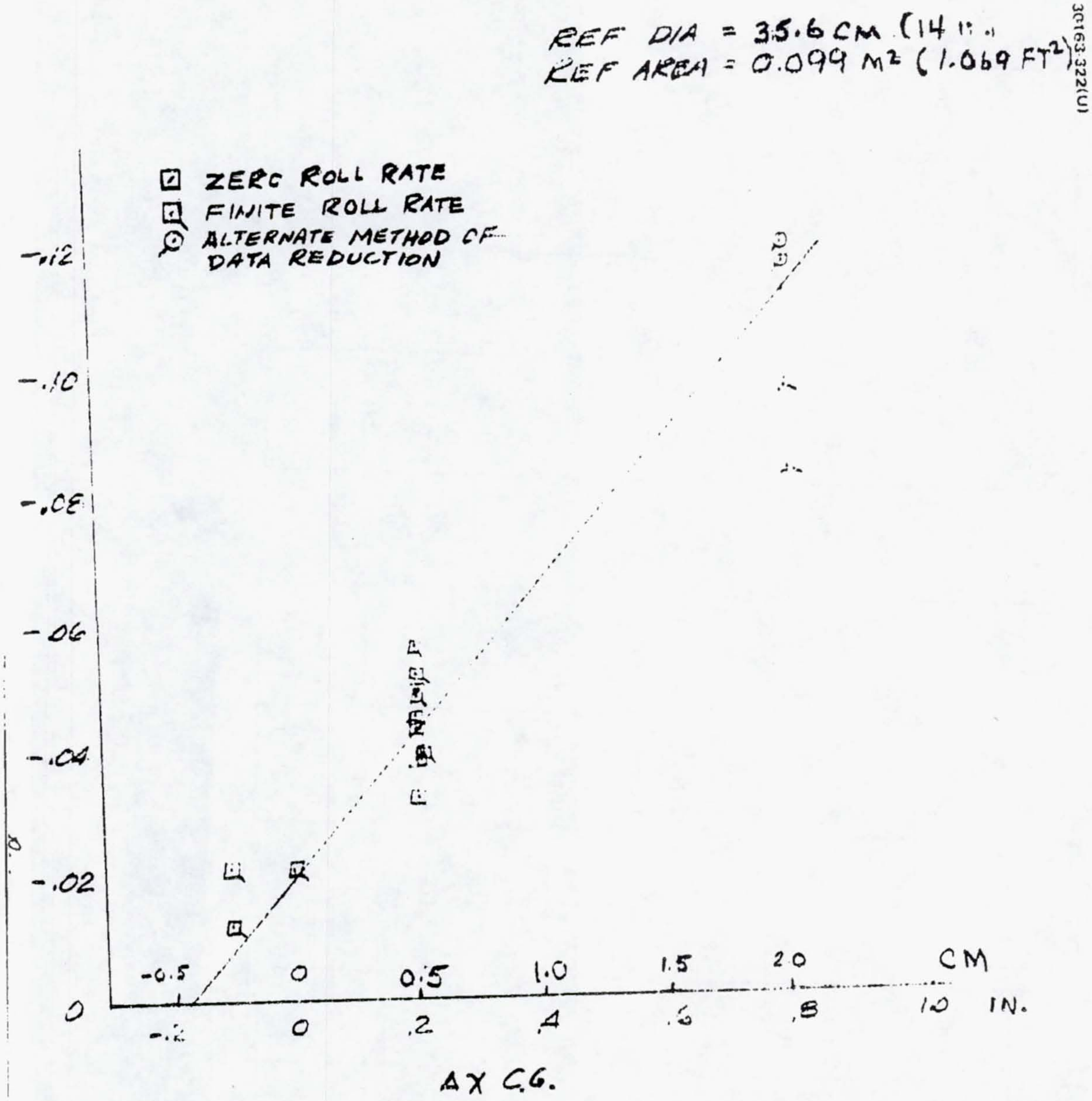

FIGURE 4.2-19. BASELINE CONFIGURATION PITCHING MOMENT COEFFICIENT VERSUS CG POSITION

REPRODUCIBILITY OF THE ORIGINAL PAGE IS POOR.

Computer Simulation Description. The computer simulation is programmed in the FORTRAN IV language for use on the GE-635 computer. The body linear acceleration components of the equations of motion are derived from aerodynamic, gravitational and buouyancy forces. The body angular acceleration components are derived from aerodynamic moments. Magnus forces and moments are assumed insignificant for low spin rates considered herein. The simulation considers a symmetric atmospheric entry system with the body axes aligned with the principal axes. The products of inertia of the system are therefore equal to zero and the moments of inertia are inputs to the simulation. The aerodynamic coefficient expansion employed in the simulation is linear. Small configurational asymmetries which induce non-zero trim angles of attack may be introduced into the equations of motion through the aerodynamic moment coefficient expansion inputs. Three coordinate systems are employed in the simulation:

1) Inertial system

2) Body fixed system

3) Nonrolling body fixed system

The atmospheric density and winds are described in the inertial system. The equations of motion are developed in the body fixed system and several simulation outputs are presented in a nonrolling body fixed system to render the dynamic behavior more discernible. Appropriate Euler angle transformations relate the three systems.

Simulation Results. The dynamic analysis was conducted for the large probe pressure vessel entering the Venusian atmosphere (GSFC No. 3609 Venus model atmosphere), at an altitude of 40 km (approximately 131,200 ft). It is assumed that the pressure vessel is separated from the drag chute at this altitude, rapidly speeds up, and then descends at very nearly constant dynamic pressure. The variations of spin rate and velocity during this near constant dynamic pressure descent for typical configurations are presented in the discussion of the baseline configurations.

The dynamic analysis discussed herein is especially concerned with the configuration response to a disturbance as measured by the total angle vertical offset, between the configuration centerline (spin axis) and the vertical.

The allowable vertical offset excursion of an atmospheric entry system is dictated by the system's antenna characteristics. The dynamic behavior analysis of several configurations has been conducted using this simulation to determine:

1) Maximum amplitude and time response of vertical offset due to an initial disturbance

2) Trim vertical offset due to small configuration asymmetries

3) Maximum amplitude and time response of vertical offset due to wind shear and sharp edged gusts

Small configurational asymmetry effects on trim angle of attack and vertical offset have been evaluated by the introduction of a constant amplitude moment term, Cm_o, into the linear aerodynamic moment coefficient expansion. A laterial c.g. offset from the body centerline, $\Delta \ell$ will result in a moment due to the axial drag force and can be related to Cm_o:

$$\Delta CG = Cm_o \frac{\Delta \ell}{CD}$$

The trim angle of attack induced by a lateral c.g. offset is essentially invariant with altitude. The effects of this c.g. offset on the dynamic behavior of the spinning pressure vessel are presented in the discussion of the baselines.

The response of an atmospheric entry system to a sharp edged gust at various altitudes is primarily a function of the system's stability and damping characteristics and its velocity at the time the gust is encountered. The higher the static stability the more rapidly it weathercocks into the relative wind and the larger the excursion of the vertical offset. To reduce the maximum vertical offset excursion due to winds, a lesser static stability margin is desirable. On the other hand, a large static stability margin is desirable to reduce the trim vertical offset due to initial disturbances and configurational asymmetries.

Selection Criteria

The baseline aerodynamic configuration is selected using the following criteria:

1) The system aerodynamic requirements must be met:
    a) Spin axis deviation from vertical must be less than 10 deg
    b) Spin rate must be less than 15 rpm
2) The configuration must adapt easily to a spherical pressure vessel
3) Minimum system cost
4) Minimum system weight
5) High reliability

30163-323(U)

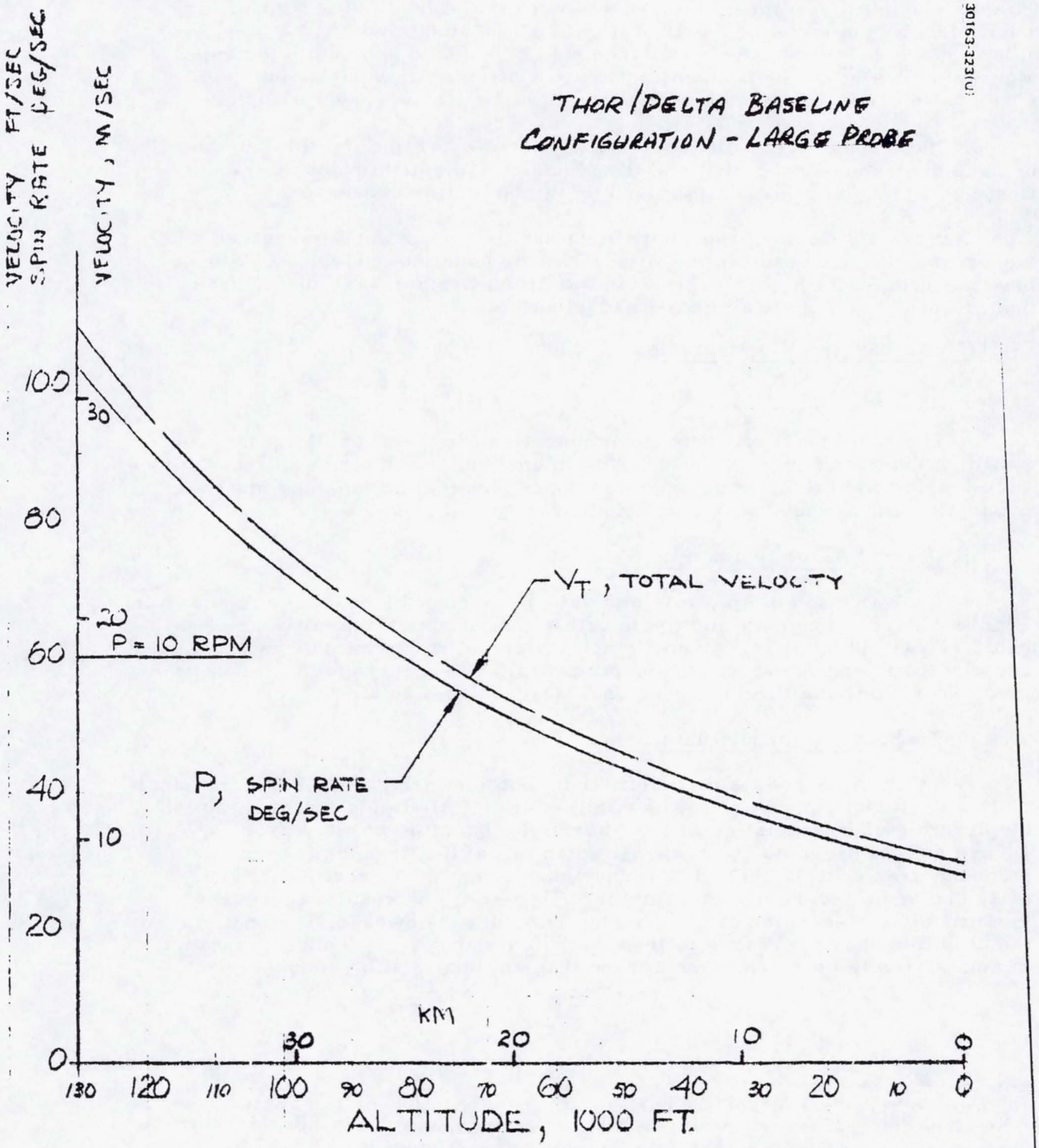

FIGURE 4.2-20. VELOCITY AND SPIN VARIATION WITH ALTITUDE

THE ORIGINAL PAGE IS POOR.

The system aerodynamic requirements dictated the static stability, damping, sensitivity to c.g. offset (both lateral and longitudinal), roll torque alignment, and moment of inertia ratios. All candidate configurations were able to meet the aerodynamic requirements. The selected baselines rated high in the desirable aerodynamic characteristics. All were based upon spherical shapes and so adapted readily to the pressure vessel design.

The highest reliability was obtained by eliminating the folding vane designs and choosing the ring stabilized designs for further consideration. Cost and weight were also minimized by this selection process.

In the selection of the Thor/Delta baseline, low weight received a higher priority than it did in the Atlas/Centaur baselines selection. Similarly, low cost received a higher priority in the Atlas/Centaur baseline selection than it did in the Thor/Delta baseline selection.

Thor/Delta Baseline Configuration

Configuration Description

The baseline aerodynamic configuration for the Thor/Delta launched probe is shown in Figure 4.2-16. All dimensions are in terms of the reference length which is the ring diameter. The physical dimensions and mass properties and aerodynamic coefficients are shown in Table 4.2-2.

Descent Velocity and Spin Rate

The variation of spin rate and velocity during the descent are shown in Figure 4.2-20. The maximum spin rate which occurs at the altitude of parachute release (40 km) is 17 rpm, which is determined primarily by the vane angle settings and is directly proportional to the descent velocity. It falls below 15 rpm by the time the probe has descended to 36 km.

Response to Initial Disturbance

Using the aerodynamic coefficients obtained from the LRC spin tunnel test, a series of runs were made with the 6D digital simulation to establish the dynamic characteristics of the Thor/Delta baseline reentry probe. Figure 4.2-21 presents the response to an initial disturbance (separation from the drag chute). The disturbance used is an initial vertical offset* of 20 deg and a diverging body rate of 30 deg/sec, and results in a large vertical offset excursion of approximately 40 deg. However, it is noted that the amplitude has decreased to less than 10 deg in 5 sec. This disturbance is considered to be much more severe than any that will be encountered.

---

*The term "vertical offset" is used in this report to define the angle between the body centerline and the local vertical. The maximum allowable vertical offset is dictated by the system's antenna characteristics.

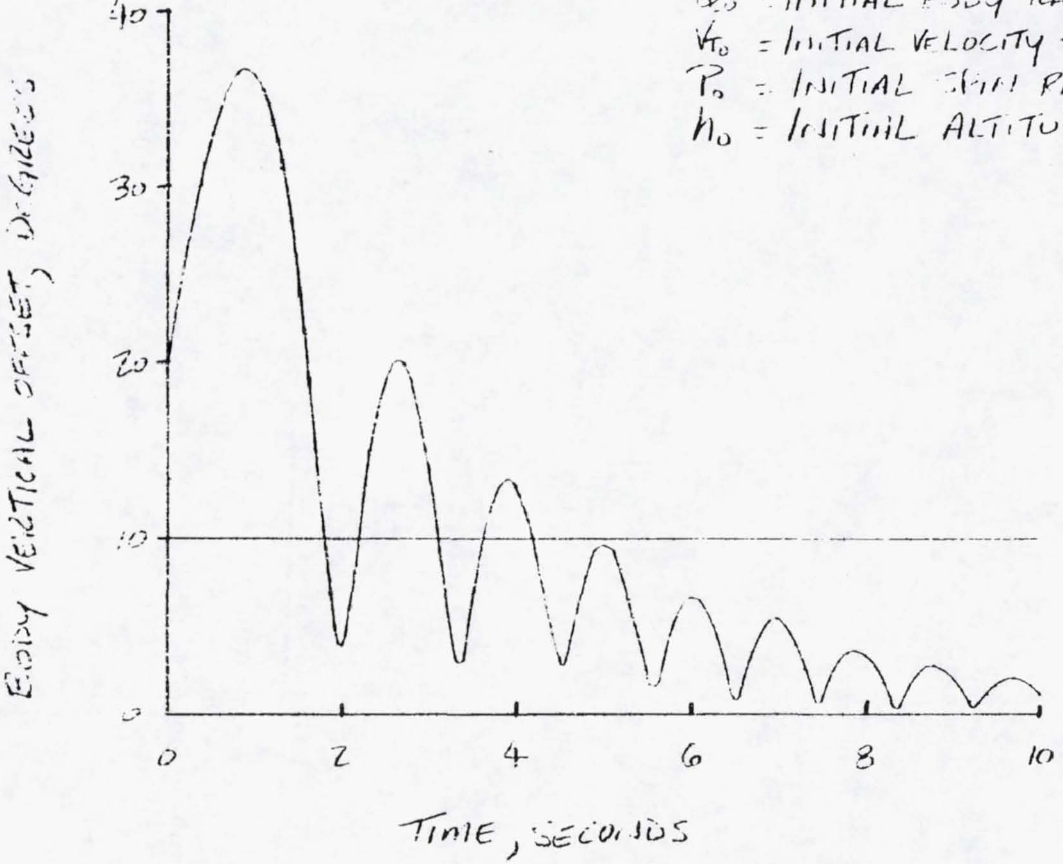

THOR/DELTA BASELINE CONFIGURATION

α_0 = INITIAL ANGLE OF ATTACK = 20°
Q_0 = INITIAL BODY RATE = 30°/SEC
V_{T_0} = INITIAL VELOCITY = (20 FT/SEC) 6.10 M/SEC
P_0 = INITIAL SPIN RATE = 27.5°/SEC
h_0 = INITIAL ALTITUDE = (131,200 FT) 40KM

30163.324(U)

FIGURE 4.2-21. RESPONSE TO INITIAL DISTURBANCE

Effect of Configuration Asymmetries

The trim angle of attack induced by a lateral c. g. offset is essentially invariant with altitude and spin rate due to the relatively low spin rates and the small differences between the moments of inertia. However, the trim angle relative to the local vertical (trim vertical offset) varies with altitude due to the variation in spin rate. Spin rate has a generally stabilizing effect on vertical offset increases with decreasing altitude for a given c. g., offset and non-zero C_{ℓ}. The maximum trim vertical offset occurs with zero spin rate and is invariant with altitude. These effects are clearly illustrated in Figures 4. 2-22 and 4. 2-23. For a maximum allowable vertical offset of 10 deg, the c. g. lateral offset from the centerline must be limited to approximately 0. 43 percent diameter.

Response to Gusts

The response to a step gust of 9. 15 m/sec (30 ft/sec) at various altitudes is shown in Figure 4. 2-24. Figure 4. 2-25 illustrates the variation of the maximum vertical offset angle excursions as altitude is decreased and gust velocities are varied. This figure indicates the gust profiles that can be tolerated as a function of altitude to assure the peak vertical offset excursions do not exceed 10 deg.

Effect of Wind Shear

Figure 4. 2-26 presents the effect of wind shear on the maximum body attitude excursion as a function of altitude. Two wind shear profiles are postulated:

1) A constant wind shear initiated at zero wind velocity and terminated when the wind velocity builds up to 9. 14 m/sec (30 ft/sec). The 9. 14 m/sec wind velocity is then maintained constant.

2) A constant wind shear initiated at zero wind velocity without termination.

As indicated by Figure 4. 2-26, the latter shear profile generally results in the larger vertical offset excursion. The two profiles result in identical maximum vertical offsets at low shear values where the maximum vertical offset excursion occurs prior to the wind velocity reaching 9. 14 m/sec (30 ft/sec).

Atlas/Centaur Baseline Configuration

The addition of the wind drift/altitude radar to the science payload and its planar antenna on the nose of the large probe pressure vessel requires a modification of the configuration. The addition of this large flat plate to the nose of the probe is expected to cause a forward shift in the center of pressure. Consequently, a spherical aerodynamic fairing and radome has been placed over it. This results in a geometrically similar configuration, except that the aft hemisphere is relatively smaller. The differences are

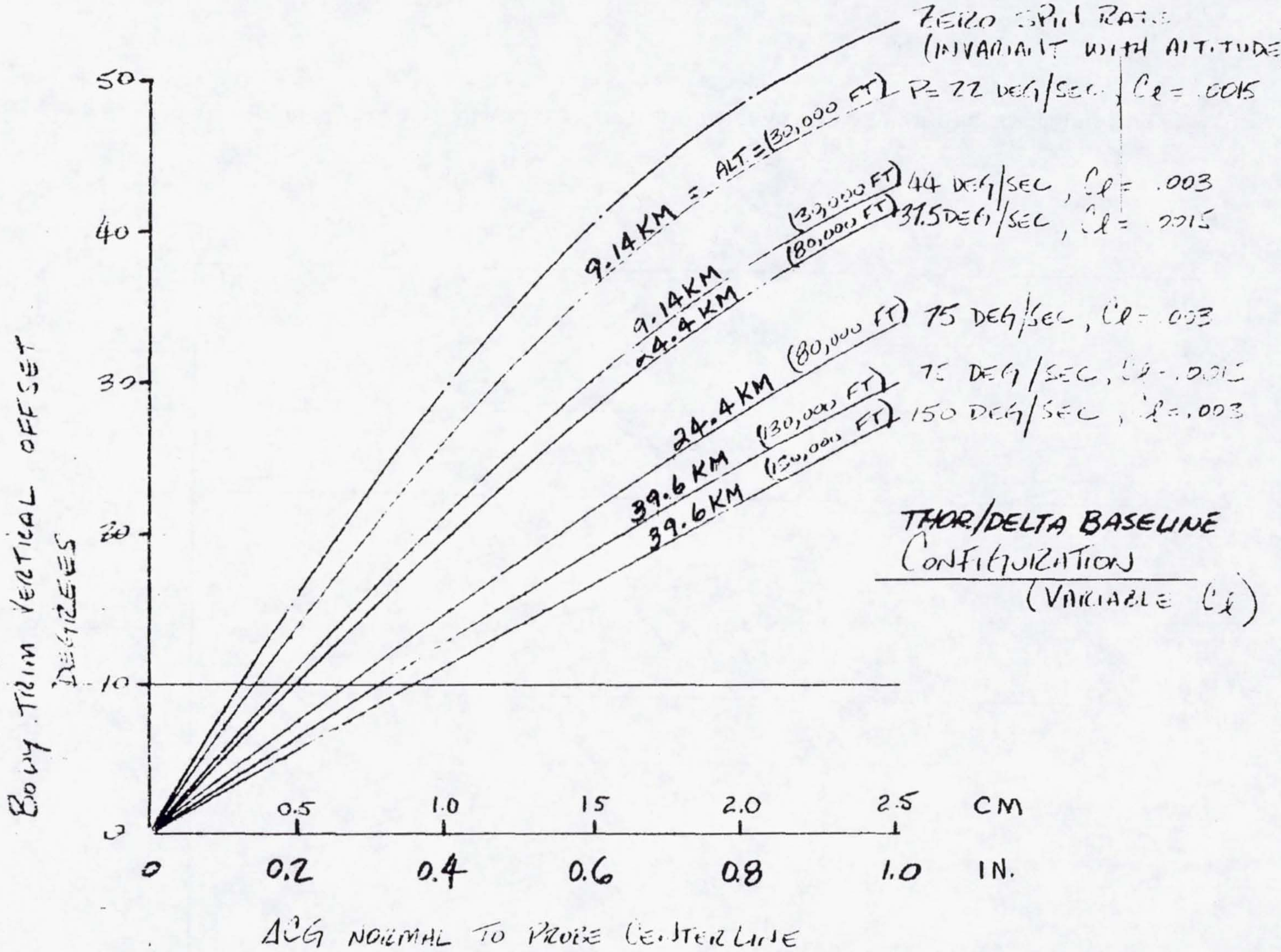

FIGURE 4.2-22. TRIM VERTICAL OFFSET DUE TO DRAG FOR ASYMMETRIC CONFIGURATION – LATERAL CG OFFSET

30163 325(U)

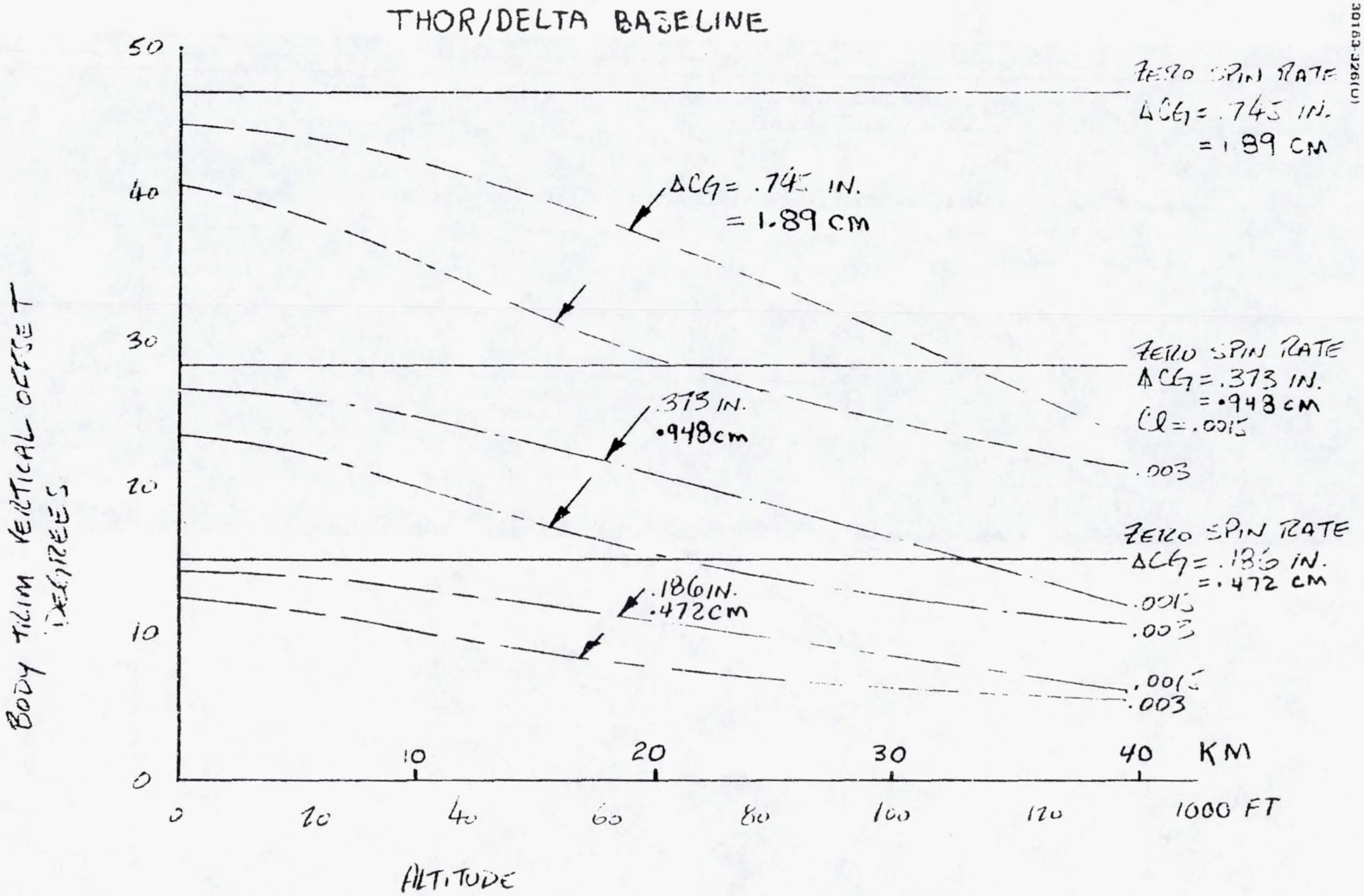

FIGURE 4.2-23. TRIM VERTICAL OFFSET DUE TO DRAG FOR ASYMMETRIC CONFIGURATION

30163-326(U)

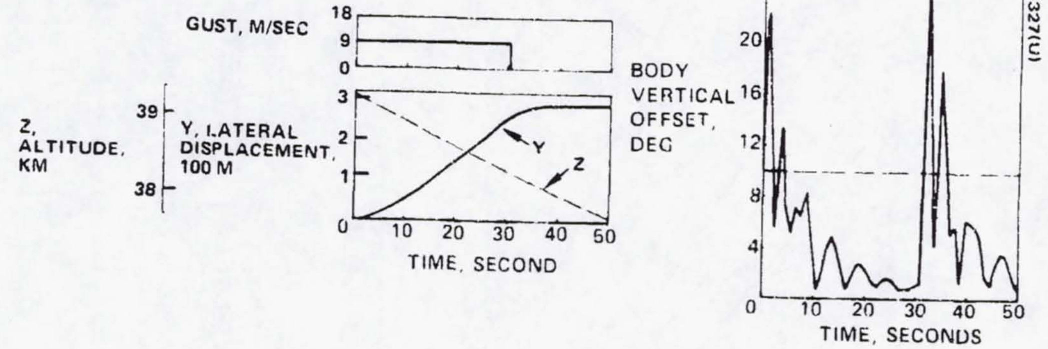

FIGURE 4.2-24. RESPONSE TO GUST

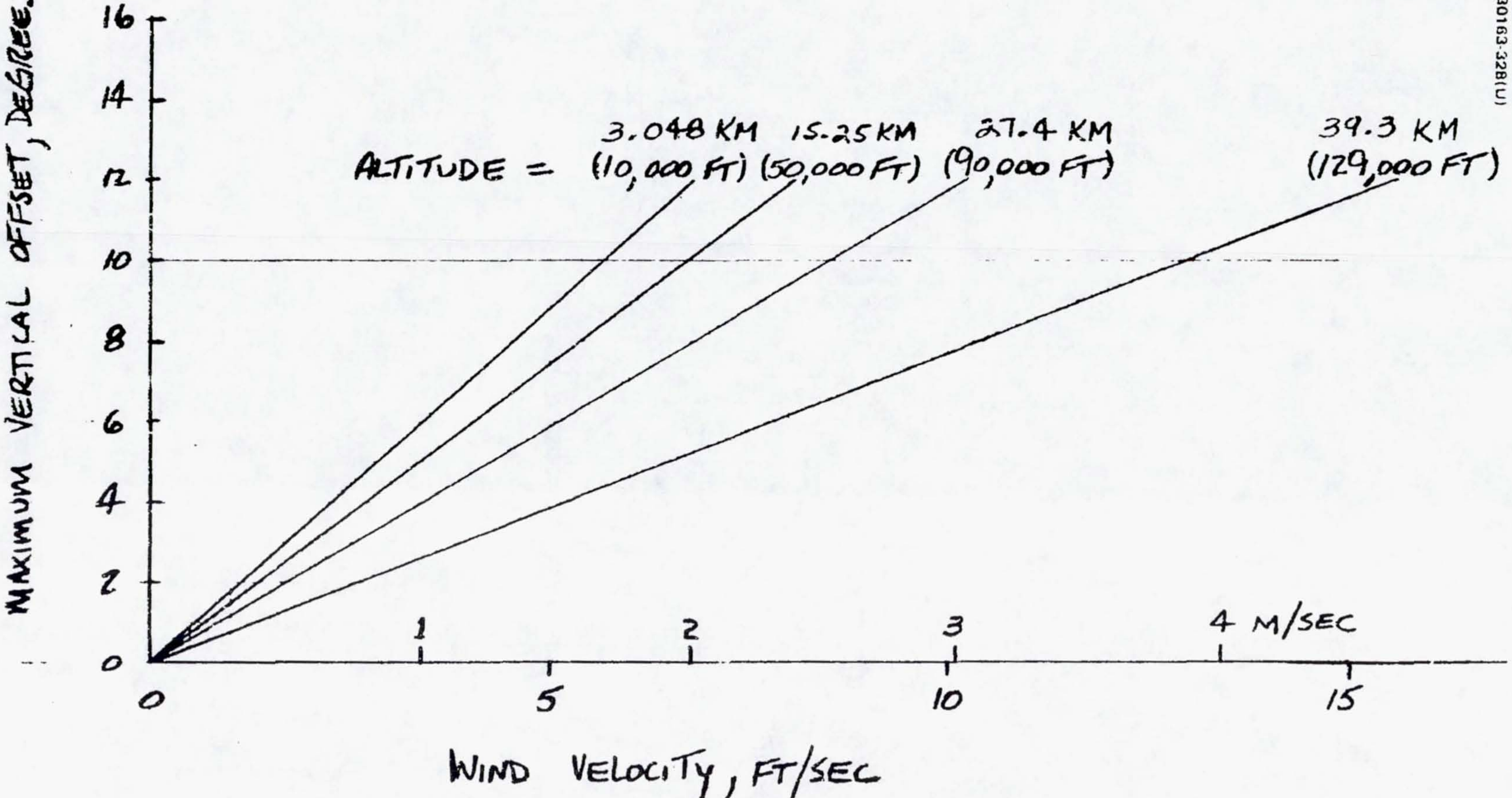

FIGURE 4.2-25. MAXIMUM BODY EXCURSION DUE TO SHARP EDGED GUST

30163-32B(U)

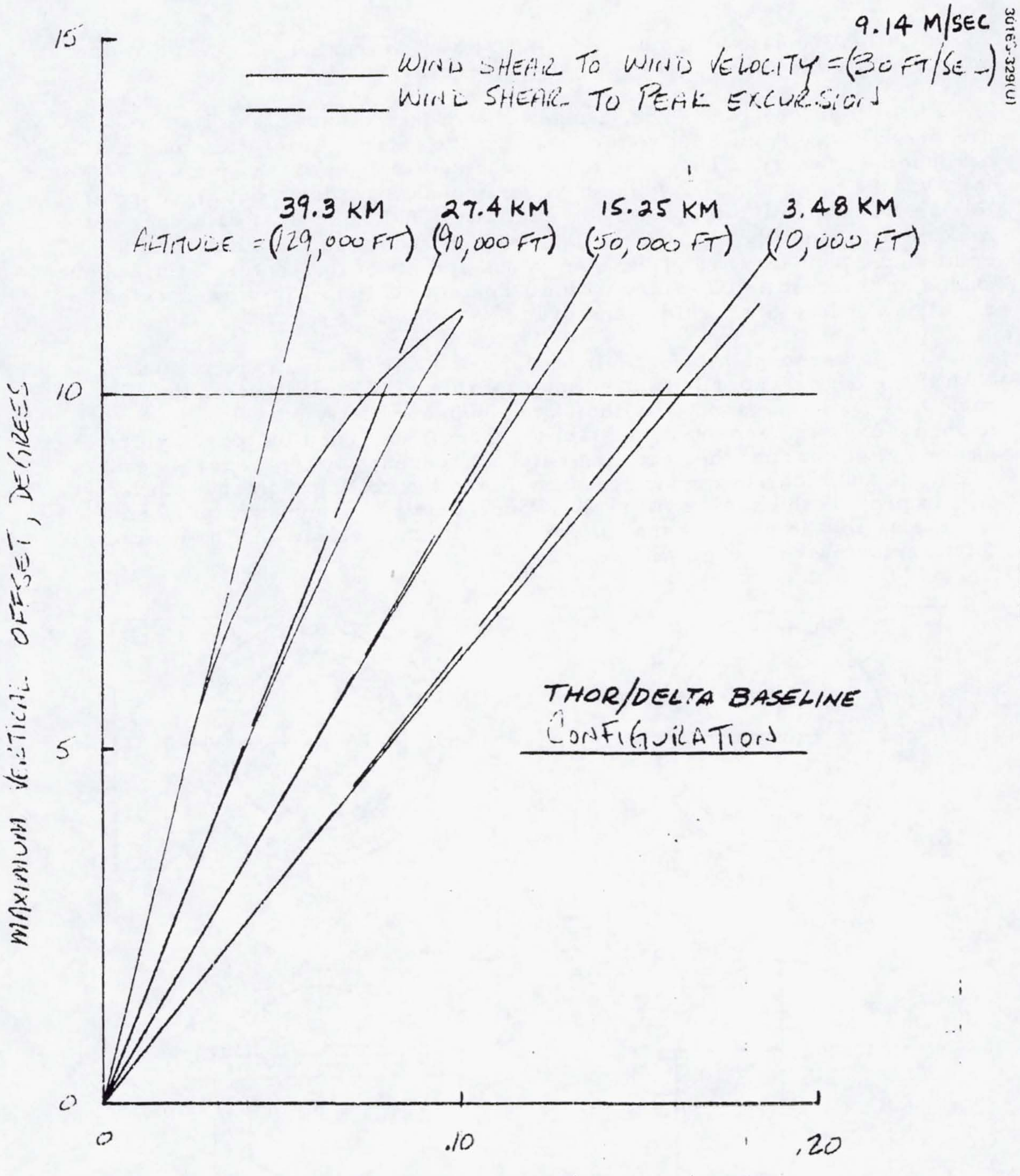

FIGURE 4.2-26. MAXIMUM BODY EXCURSION DUE TO WIND SHEAR

shown in Figure 4.2-27. Since this is in the wake region, it is expected to have a negligible effect on the aerodynamic characteristics.

In addition, two minor changes shown in sections A and B of Figure 4.2-27 have been required to transfer the entry deceleration load to the aeroshell structure. They result in reducing the span of the spin vanes and locating them farther aft, which have compensating effects but are expected to slightly change the pitch and yaw stability. Sufficient test data does not now exist to quantify this effect. The second change is the addition of a conical segment forward of the spin vanes and aft of the center of the sphere. Based on the results of sphere with aft conical sections, this is expected to slightly increase the stability and drag.

The aerodynamic coefficients for the Atlas/Centaur are compared with those of the Thor/Delta baseline in Table 4.2- It is noted that the ratio of W/C_DA is essentially the same, hence the descent velocity is unchanged. Furthermore, the stability margin has been increased but so has the pitch inertia; the resulting natural frequency is increased 4 percent. The vane angle has been changed to increase the rolling moment coefficient, C_{ℓ_0} to provide the same spin rate. Consequently, the dynamic performance is essentially the same as that of the Thor/Delta baseline and the characteristic performance curves will be very similar.

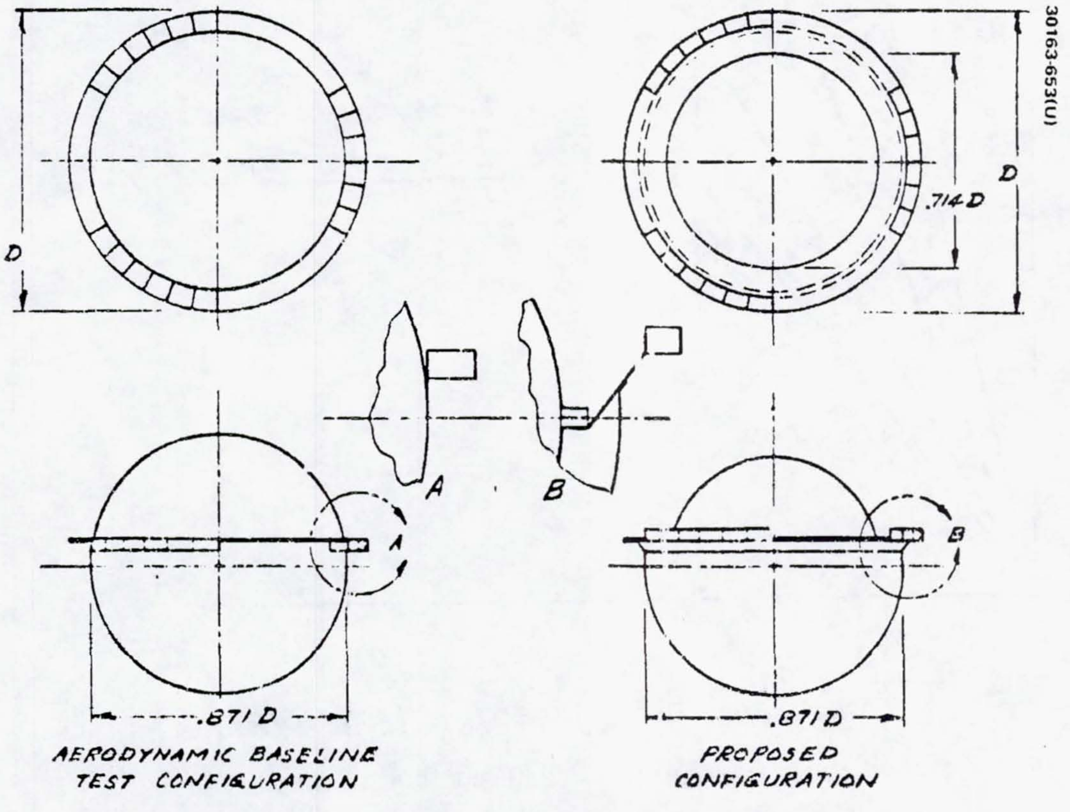

AERODYNAMIC BASELINE
TEST CONFIGURATION

PROPOSED
CONFIGURATION

FIGURE 4.2-27. ATLAS/CENTAUR AERODYNAMIC CONFIGURATION

TABLE 4.2-5. PARAMETERS USED IN DYNAMIC ANALYSIS

Configuration	Thor/Delta	Atlas/Centaur
C_{D_o}	0.55	0.58
C_{N_α}	1.60	1.60
Cm_α	-0.0382	-0.041
Cm_q	-0.052	-0.052
$Cm_{\dot{\alpha}}$	0	0
C_{ℓ_o}	0.002	0.0025
C_{ℓ_p}	-0.10	-0.10
ℓ ref, m (ft)	0.736 (2.416)	0.965 (3.167)
S ref, m^2 (slug-ft^2)	0.466 (4.581)	0.731 (7.877)
Ixx, Kg-m^2 (slug-ft^2)	2.97 (2.191)	7.43 (5.48)
Iyy, Kg-m^2 (slug-ft^2)	2.69 (1.983)	7.31 (5.39)
Izz, Kg-m^2 (slug-ft^2)	2.99 (2.207)	7.31 (5.39)
m, Kg (slug)	74.22 (5.186)	152.8 (10.47)

REFERENCES

4.2-1 "Pressure Vessel Subsonic Stability Analysis Report," Hughes Aircraft Co., HS507-0022-142, Task No. PB11, dated 23 M 23 March 1973.

4.2-2 S. F. Hoerner, "Fluid Dynamic Drag," 1965, pp. 3-7 and 3-8.

1.3 STRUCTURE

The structure of the pressure vessel module consists of the following major items:

1) The pressure vessel's thin spherical metal shell constructed by joining two hemispheres
2) The main flange and seal used to join the shell's hemispheres
3) The equipment support shelves
4) The shelf support flanges
5) The pressure vessel/aeroshell adapter assembly

The key design goal in the selection of the design concept, materials, thicknesses, gauges, and other structured parameters for these items was to produce a structural design that would adequately sustain, with minimum weight and cost, the critical loads associated with the Pioneer Venus mission. The key technical problem was the selection of the buckling coefficient or knock down factor that could be used in the design of the pressure vessel shell. (In thin spherical shells loaded by external pressure, the mode of failure is buckling and the buckling pressure is always less than the classical failure pressure calculated from linear theory. The ratio of the actual to the classical buckling pressure is defined as the knock down factor.)

During the first half of the Pioneer Venus Phase B, Systems Design Study, prior to the midterm review, the Thor/Delta was assumed to be the launch vehicle for the spacecraft. The boosted payload weight limitations of this vehicle required an emphasis on minimum weight design consistent with reasonable though not necessarily minimum cost. Later, however, after the midterm review, the Atlas/Centaur was selected as the launch vehicle. With the much higher payload weight capability of the Atlas/Centaur, the structural design objective was shifted to one in which the emphasis was on minimum cost consistent with reasonable but not necessarily minimum weight.

For purposes of summary, the following is a chronological review of the evolution of the structural design that is now the Atlas/Centaur baseline. The tests, analyses, and trade studies which are mentioned in this summary are described in greater detail in the subsections which follow.

During the Thor/Delta phase of the study, the probe configuration utilized a relatively thick thermal insulation external to the pressure vessel shell. The resulting bulk temperature of the pressure vessel's metallic shell was initially calculated to be on the order of 93°C (200°F) for both probes at maximum Venus atmospheric pressure (near the surface). In the vicinity of pressure vessel windows, or feedthroughs, the insulation was necessarily penetrated and interrupted, resulting in local hot spots. The local hot spot temperatures on the shell were preliminarily calculated to be

REPRODUCIBILITY OF THE ORIGINAL PAGE IS POOR.

on the order of 204°C (400°F). Based on these initial temperature estimates, and assuming a buckling coefficient or knock down factor of 0.4, a trade study was performed to select the material that would result in the lowest weight pressure vessel shell consistent with reasonable cost. Using the results of this trade study, the shell material was tentatively chosen to be titanium, and an unstiffened or monocoque construction was selected for the structural concept. This trade study is described in greater detail in a following subsection. The selection of titanium was tentative, pending the results of a parallel effort in which the chemical compatibility of this and other materials with the Venus atmosphere was being examined.

Test data then became available which indicated that a buckling coefficient in excess of the 0.4 initially assumed was in fact achievable in pressure vessel shells fabricated in titanium with the same radius-to-thickness ratio and in a manner identical to that selected for the Pioneer Venus application. The test data further substantiated the tentative selection of the titanium monocoque design as the least weight, reasonable cost alternative. The shell was subsequently redesigned to a knock down factor of 0.7.

A structural design study was then performed on the entire large and small probe pressure vessel modules. The purpose of this study was to derive, by the methods of stress analysis, a first estimate of the detailed thickness, gauges and other structural parameters, to enable the pressure vessels to sustain the critical design loads. Initial estimates of the structural weight of the Thor/Delta design were then based on the dimensions derived in this study. The design details which evolved from this study resulted in a pressure vessel module constructed entirely from titanium with the exception of the equipment shelves which were made from aluminum honeycomb.

A more detailed thermal analysis of the performance of the insulation system then became available. This analysis indicated that the bulk temperature of the shell could be hotter than previously predicted (about 204°C [400°F]) and that significant temperature gradients, other than those produced by penetrations, would be present in the shell. A structural analysis was then performed to determine the affect of these temperatures and gradients on the pressure vessel's design. The results of this analysis indicated the need for a lower knock down factor and the predicted weight of the pressure vessel shell was thus increased. However, titanium continued to be the material that resulted in the lowest weight design. This was the status of the Thor/Delta based structural design when the decision to change to the Atlas/Centaur launch vehicle was made.

At the same time, material studies were indicating that titanium may be chemically incompatible with the Venus environment. In fact, the data indicated that oxide free titanium would probably ignite spontaneously and burn at the CO_2 pressure/temperature combinations of the Venus atmosphere. Further, various acids that will quickly remove oxides from titanium are thought to be present in the Venusian atmosphere. In view of this data, the risk associated with the use of titanium as a primary structural material in the Venus atmosphere was considered excessive, even with a protective coating, and the use of this material was abandoned. As a substitute material for titanium, maraging steel was selected with 17-4 PH stainless steel as an alternate. The selected steel has no known incompatibility with the Venus environment. It is relatively inexpensive, readily available, and Hughes has had extensive experience with it. It has good machinability, workability, and weldability. In the structural design that existed at the midterm review, the substitution of steel for titanium was found to produce an increase in structural weight of approximately 33 percent in both pressure vessel modules. The weight of the structure in the titanium pressure vessel modules at that time was 23.6 kg (52 lb) in the large probe and 6.82 kg (15.05 lb) in the small probe.

In addition to the selection of steel as the primary structure, other significant changes in the structure occured as a result of configuration changes, load changes, and design philosophy changes due to the Atlas/Centaur decision. Principal among these changes was an increase in the diameter of the pressure vessel to accommodate increased equipment volume, an increase in the Venus entry deceleration loads caused by increased entry velocities associated with the 1978 mission, and the selection of a more conservative knock down factor of 0.4. This necessitated gauge and thickness increases from those calculated in the Thor/Delta structural design study, which resulted in further increases in the structural weight. Table 4.3-1 is a summary of the changes in the structural weight that resulted from the change to steel followed by the change to Atlas/Centaur.

The final change to the Atlas/Centaur baseline structure resulted from a trade study comparing an internally insulated pressure vessel with the externally insulated configuration which was the then current baseline. The trade study concluded that the internally insulated design would result in a small weight penalty but a significant cost savings. The lower cost internally insulated design was thus adopted. From a structural standpoint only, the major impact of the internally insulated design was to permit the temperature of the pressure vessel shell to essentially reach the ambient temperature of the Venus atmosphere at each altitude which results in a maximum shell temperature near the surface of about 483°C (900°F). To provide for the degradation in strength and stiffness properties that occur at this temperature, increases in skin gauges and thicknesses, and thus, the structural weights were required. In addition, some structure was added and some deleted in this design. The added structure includes an external aerodynamic fairing to provide a smooth surface over the wind/altitude radar antenna (on the large pressure vessel only) and an internal insulation retainer. The deleted structure includes the external insulation retainer and on the small pressure vessel module only, the aeroshell adapter. In addition, the pressure vessels were increased in diameter to provide volume for the internal insulation. All of these changes contributed to the net change in the total structural weight of each pressure vessel module.

Table 4.3-2 summarizes the combined effect on structural weight of all changes due solely to the adoption of the internal insulation design which is the current Atlas/Centaur baseline.

TABLE 4.3-1. CHRONOLOGICAL CHANGES IN PRESSURE VESSEL MODULE STRUCTURAL MASS, EXTERNALLY INSULATED CONFIGURATION

	Thor/Delta		Atlas/Centaur
	Midterm	Post Midterm	Current
	Titanium kg (lb)	Steel kg (lb)	Steel kg (lb)
Large probe	23.6 (52)	31.5 (69.4)	61.7 (136.04)
Small probe	6.82 (15)	9.2 (20.3)	14.6 (32.23)

The pressure vessel module structure consists of: Pressure vessel shell,
Flanges,
Equipment shelves,
Aeroshell adapter,
External insulation retainer.

TABLE 4.3-2. CHANGES IN MASS OF PRESSURE VESSEL MODULE STRUCTURE DUE TO ADOPTION OF INTERNALLY INSULATED DESIGN

Atlas/Centaur	Mass of Structure Only	
	Steel design	
	External Insulation Configuration, kg (lb)	Baseline Internal Insulation Configuration, kg (lb)
Large probe	61.7 (136.04)	74.6 (164.75)
Small probe	14.6 (32.23)	16.2 (35.64)

Function and Requirements

The pressure vessel structure for both the large and small probes serves the general function of physically supporting the science experiments and subsystems in an integral package with an appropriate shape and volume, while simultaneously protecting the contents from the pressure extremes of the space environment and the Venusian atmosphere.

The pressure vessel structure must be capable of sustaining without failure, the static and dynamic loads associated with rocket engine boost, the space environment and entry and descent through the Venusian atmosphere. It must further provide internal mounting surfaces and supports for the contained equipment. These must have sufficient rigidity to minimize the response of the contents to the structural loads imposed by each event contained within the mission requirements. In addition, electrical, mechanical, and optical penetrations must be provided in the pressure vessel for the science instruments, and such penetrations must not compromise the structural integrity of the pressure vessel or its intended function.

The most critical structural loads for the pressure vessel as well as for its rings, flanges, equipment shelves and penetrations are those which occur during entry and descent in the Venusian atmosphere. Loading conditions, which occur during boost ascent and space flight, are essentially noncritical for most items of the structure, but they do design some portions of the adapter cone which is the interface structure between the probe pressure vessel and the aeroshell.

A summary of all significant loading conditions from which the critical load cases were taken for use in the preliminary design analysis is given in Table 4.3-3.

To assure adequate structural reliability with a minimum impact on the structural weight, the pressure vessel structure is designed to be capable of withstanding ultimate loads 1.25 times greater than the maximum anticipated loads (limit loads) during Venus entry and descent. A factor of 1.5 is used on all other loads. These factors are not applied to the predicted temperatures.

It is also necessary to assure the absence of permanent structural deformations after loading. Such deformations, if permitted, could have a detrimental effect on the alignment of instruments. The absence of such deformations will be assured by designing so that the yield strength of all elements are not exceeded at limit load.

Tests, Analysis and Trade Studies

Pressure Shell Trades

During the Thor/Delta phase of the program, a trade study was performed for the purpose of selecting the optimum design for the pressure vessel structure. The results of this trade study indicated that the least weight design for both the large and small pressure vessels was a monocoque construction of titanium. On the basis of least weight only, the

TABLE 4.3-3. DESIGN ULTIMATE LOADS (LIMIT LOAD X SAFETY FACTOR)

Load Source	Loading Condition *	Large Probe		Small Probe	
		Axial **	Lateral ***	Axial	Lateral
Thor/Delta or Atlas/Centaur booster Quasi-static and dynamic	Maximum axial acceleration, g	T/D 21.0 A/C 10	T/D 1.15 A/C 0	T/D 25.0 A/C 40.0	T/D 0 A/C 0
	Maximum lateral acceleration, g	T/D 0 A/C 0	T/D 8.2 A/C 8.0	T/D 0 A/C 0	A/C 10.5 A/C 12.0
	Other combined accelerations, g	T/D 4.35	T/D 8.2	T/D 4.34 T/D 21.0	T/D 7.0 T/D 1.15
Venus environment	Maximum entry deceleration	T/D -625.0 A/C -715	T/D 31.25 A/C 31.25	T/D -700.0 A/C -745.0	T/D 31.25 A/C 31.25
	Maximum descent pressure(external) N/cm^2 (psi)	1200 (1740)		1200 (1740)	

*At each condition, lateral and axial loads shown are applied simultaneously

**Positive axial accelerations result in loads away from aeroshell; negative axial accelerations result in loads toward the aeroshell

***Lateral accelerations can be in any lateral direction

Note: Loads are given in g's. One g = 9.807 N/kg

Thor/Delta loads are taken from Reference 4.3-1

Atlas/Centaur loads are taken from Reference 4.3-18 runner up designs were beryllium monocoque second, aluminum third and steel last. Using the results of this study, titanium was chosen as the pressure vessel material for the Thor/Delta design.

The results of this study, so far as rank ordering of the materials by least weight is concerned, are equally applicable to the Atlas/Centaur design. However, titanium, the lightest choice, was eliminated because recent studies indicated a chemical incompatibility with the Venus environment. The runner up, beryllium, was eliminated because of its high cost. The next lightest, aluminum, was eliminated when a decision to use a hot wall design (no external insulation) was made and its usable temperature range was exceeded. This left steel as the next lightest material, and steel was ultimately chosen for the Atlas/Centaur design.

Selection of Buckling Coefficient

This analysis led to the selection of the optimum design for the Thor/Delta spherical pressure vessels. For a spherical shell under external pressure, two possible modes of failure exist; buckling and material yield or rupture. For each material considered, the minimum shell thickness required to prevent each of these modes of failure was found. Using the maximum of these two thicknesses (the one to prevent buckling or the one to prevent material failure), the weight of the shell in that material and thickness was calculated. The resulting weights for all of the candidate materials were then compared. The critical buckling pressure P_{cr}, for a spherical shell is given by (Reference 4.3-2):

$$P_{cr} = K \frac{2}{\left[3(1-\mu)^2\right]^{1/2}} E_c \cdot \left(\frac{t}{R}\right)^2$$

where

E_c - compressive modulus of elasticity of material, N/cm^2 (psi)

t - shell thickness, cm (in.)

R - shell radius, cm (in.)

μ - Poisson's ratio of material

K - experimental buckling coefficient or knock down factor

For steel, aluminum, titanium, and magnesium, Poisson's ratio, μ, is approximately equal to 0.3; for beryllium, $\mu = 0.024$. Equation 1 then reduces to

$$P_{cr} = 1.21\, K\, E_c \left(\frac{t}{R}\right)^2$$

TABLE 4.3-4. THICKNESS TO PREVENT BUCKLING

Material	Thickness, cm (in.)	
	Large Probe R = 27.9 cm (11 in.)	Small Probe R = 15.88 cm (6.25 in.)
Titanium	0.312 (0.123)	0.177 (0.070
Steel	0.231 (0.091)	0.132 (0.052)
Aluminum	0.419 (0.165)	0.226 (0.089)
Magnesium	0.531 (0.209)	0.302 (0.119)
Beryllium	0.193 (0.076)	0.109 (0.043)

TABLE 4.3-5. THICKNESS TO PREVENT YIELD

Material	Compressive Yield Allowable at 204°C N/cm^2 (psi)	Thickness, cm (in.)	
		Large Probe	Small Probe
Titanium 6AL 4V	67,000 (97,000)	0.248 (0.098	0.142 (0.056)
Steel 17-7 (PH)	99,300 (144,000)	0.167 (0.066)	0.096 (0.038)
Aluminum 7075-T6	26,200 (38,000)	0.640 (0.252)	0.363 (0.143)
Magnesium ZK60A	8,000 (11,600)	2.09 (0.825)	1.19 (0.470)
Beryllium (hot pressed block)	17,600 (25,500)*	0.952 (0.375)	0.540 (0.213)

*Taken from the results of the room temperature tests of Reference 4.3-3, and adjusted to 204C (400° F) using data from Reference 4.3-4.

for common structural material or

$$P_{cr} = 1.15\, K\, E_c \left(\frac{t}{R}\right)^2$$

for beryllium.

Setting $P_{cr} = 1200\ \mathrm{N/cm^2}$ (1740 psi), the design pressure, the minimum thickness required to sustain this pressure without buckling is computed from either of the two preceding equations as appropriate.

A knock down factor of K = 0.7 is used as a result of pressure vessel tests which are described and evaluated in Reference 4.3-3. Results from the pressure vessel tests described and evaluated in Reference 4.3-3 indicate that carefully manufactured titanium pressure vessels buckle at pressures which are 78 percent of the theoretically predicted values (K = 0.78). In view of these test results, the recommended knock down factor of 0.15 given in Reference 4.3-2 does not appear to be reasonable for the pressure vessel design. The knock down factor K = 0.15 of Reference 4. -2 is based on a compilation of all available test results including very thin shells (large r/t) and shells with large imperfections. Since the proposed Pioneer Venus shells will be manufactured in a manner similar to that used for the test specimens, a K = 0.7 was chosen for preliminary design purposes. E_c is selected for each material at the bulk temperatures of 93°C (200°F). In this manner, the minimum thickness required to prevent buckling is given in Table 4.3-4.

The maximum compressive stress, σ_c, in a spherical shell subjected to external pressure is given by the membrane equation:

$$\sigma_c = \frac{P_{cr}\, R}{2t}$$

Setting P_{cr} equal to the design pressure of $1200\ \mathrm{N/cm^2}$ (1740 psi) and setting σ_c, equal to the yield allowable for the material at the design temperature, the minimum thickness required to prevent yielding is shown in Table 4.3-5. For each design in contention, the resulting weight of the shell alone, based on the maximum required thickness, is shown in Table 4.3-6.

A titanium waffle stiffened design was also considered. The optimum configuration relative to rib size and spacing and shell thickness was derived using the method and equations of Reference 4.3-5. A hemispherical shell, built to this configuration, was tested as part of Task PB-28. The results of the tests indicated that the appropriate knock down factor to use with such a design is on the order of 0.4. That is, such a design is equivalent to an unstiffened monocoque shell of the same weight with a knock down factor of 0.4. Therefore, it was concluded that a rib stiffened design was not weight

TABLE 4.3-6. FINAL SHELL MASS COMPARISONS

Design	Failure Mode	Maximum Required Shell Thickness, cm (in)		Shell Weight, kg (lb)	
		Large Probe	Small Probe	Large Probe	Small Probe
Titanium Monocoque R = 27.9 (11.0) large probe R = 15.88 (6.25) small probe	Buckling (K = 0.7)	0.312 (0.123)	0.177 (0.070)	13.83 (30.5)	2.58 (5.7)
Aluminum monocoque	Yielding	0.640 (0.252)	0.363 (0.143)	17.38 (38.3)	3.18 (7.0)
Beryllium monocoque	Yielding	0.953 (0.375)	0.541 (0.213)	17.05 (37.6)	3.12 (3.9)
Steel monocoque	Buckling	0.231 (0.091)	0.132 (0.052)	18.8 (41.5)	3.44 (7.6)
Magnesium monocoque	Yielding	2.09 (0.825)	1.19 (0.470)	35.4 (78.0)	6.5 (14.4)

competitive with monocoque shells exhibiting knock down factors on the order of 0.7. Rib stiffened designs would also tend to be an order of magnitude more costly.

From the results of the tradeoff procedure described, which are shown in Table 4.3-6, the choice of a titanium monocoque design was made for the Thor/Delta version.

Structural Sizing of the Thor/Delta Pressure Vessel Module.

After the selection of titanium 6AL-4V as the optimum pressure vessel material, a relatively detailed structural design analysis of the large and small probe pressure vessel modules was performed (Reference 4.3-6). The purpose of the study was to derive by the methods of stress analysis a first estimate of the required thicknesses, gauges, and other structural parameters to enable these structures to adequately sustain with minimum weight and cost, the critical loads associated with the Pioneer Venus mission. Initial estimates of the structural weight were then based on the dimensions derived in this study. In addition to the structural sizing of the main pressure vessel shell itself, the study included analysis leading to the first estimate of sizing requirements for:

1) The internal equipment shelves

2) The shelf support flanges

3) The main flange and pressure seal

4) The probe to aeroshell adapter assembly

Although the stress analysis presented in Reference 4.3-6 is relatively detailed, the analysis did not treat every conceivable structural failure mode but rather was limited to those failure modes which on the basis of engineering judgement and experience were considered most likely to have an appreciable affect upon the design, the sizing of the structure and, hence, its weight. For example, fatigue as a potential failure mode was not investigated. The engineering judgement which led to this omission was based on the following reasoning. The maximum inertial loading condition for these structures occurs during deceleration and is of the order of 625 g ultimate for the small probe. These loads are essentially static or nonrepetitive and, hence, not part of a fatigue environment. In future structural analysis, however, fatigue will be evaluated in detail as will other failure mode considerations that have been omitted to date.

At the time of the analysis, the design of the probe pressure vessels was based on the use of an external insulation which strongly limited the pressure vessel shell temperatures and temperature gradients. However, parametric curves were derived and presented in Reference 4.3-6 which show the effect that more severe temperature levels and gradients would have on the required pressure vessel wall thickness and thus, on its weight. These curves were used for probe weight trade studies in which the total weight of internally and externally insulated designs were compared.

All material strength allowables used in the study were "A" value statistical minimums as defined in and taken from the MIL-HDBK-5A (Reference 4.3-4). A few strength allowables, such as those for the aluminum honeycomb core, preliminary choice for the equipment shelves, were taken from other sources. In those cases, the minimum allowables were chosen and then arbitrarily reduced to account for anticipated scatter.

Typically, the procedure followed in analyzing each structural element was to determine the most probable modes (often a judgement factor) in which the element could fail, and then for each of these modes of failure to:

1) Determine the type and direction of internal load that would be required to produce this failure

2) Determine the most critical ultimate load condition or combination of conditions from the Pioneer Venus mission that could produce this type of internal load. (The ultimate loads include an appropriate margin of safety).

3) Determine the magnitude of the internal load produced by the external Pioneer Venus load conditions.

4) Determine the minimum thickness or gauge of the structural element that would be just sufficient to prevent the failure at this internal load magnitude.

The minimum required thickness so derived, considering all failure modes, were compared and the maximum selected as the required size for that element. In many instances, because of St. Venant's principal or other load redistribution effects, the thickness required in a region adjacent to a point of load transfer is much greater than that which is required a short distance removed from the load point. For some elements, this fact enabled a variable thickness design to be evolved for minimum weight. The large probe to aeroshell adapter structure was sized for minimum weight in this manner.

The effect of reinforced penetrations on the buckling strength of the pressure vessel shell was determined by the tests of reference 4.3-3. These tests also verified the strength adequacy of the doubler design selected to reinforce the penetrations. The minimum doubler thickness selected was that which would effectively replace, locally, the material mass removed by the penetration. Another design criteria chosen for the thickened area was that the neutral axis of the thickened cross section should coincide with the neutral axis of the adjacent pressure shell. The tests indicated that penetrations so designed did not reduce the buckling pressure for the pressure vessel and did not produce local stresses significantly higher than the shell membrane stresses.

A summary of the structural sizing requirements for the major structural elements as derived in the analysis of Reference 4.3-6, is hown in a following subsection.

Chemical Incompatibility of Titanium With the Venus Atmosphere.

The following is a summary of data which became available after titanium was chosen as the optimum structural material for the large and small probe pressure vessel modules. The data strongly indicates that:

1) Titanium oxides could be removed from titanium surfaces by acids present in the Venus atmosphere

2) Oxide-free titanium will probably ignite spontaneously and burnin CO_2 (th primary constituent of the Venus atmosphere) at the pressure/temperature conditions of Venus.

As a result of this data, Grade 250 maraging steel was substituted for titanium as the primary structural material on the Atlas/Centaur probes.

Evidence of the ignition and combustion of titanium components in air and oxygen has been extensively reported upon in the published literature. It is known that ignition is the critical step in this process, and that combustion requires far less stringent conditions. There is no experimental data directly defining the ignition temperature of oxide-free titanium surfaces in CO_2 environments. However, evidence does exist which suggests that the behavior of oxide-free titanium in CO_2 is significantly parallel to its behavior in O_2 to allow one to extrapolate from data available for O_2.

This study first assumes an ignition temperature range for oxide-free titanium in a CO_2 environment of 1 atm and then approximates, where possible, the change in this temperature when increased atmospheric pressure, velocity, and stress conditions are considered.

Ignition Temperatures of Oxide-Covered Titanium in O_2 and CO_2 at 1 Atm Pressure. Large specimens of titanium have been shown to ignite in the range of 1300 to 1600°C (2372-2912°F), when resistance heated in static oxygen environments (Reference 4.3-7). Titanium, when heated in CO_2 under similar conditions, will ignite at 1510°C (2750°F), which is in the same temperature range (Reference 4.3-8).

Ignition Temperatures of Oxide-Covered Titanium in O_2 and CO_2 at High Pressures. An increase in oxygen pressure to 207-345 N/cm^2 (300-500 psi) will lower the ignition temperature of titanium to 870-1100°C (1598-2012°F) (References 4.3-8 and 4.3-9). Similar data is not available for titanium in CO_2 atmospheres, but one would expect similar decreases from 1510°C.

Ignition Temperatures of Oxide-Free Titanium at Various Pressures in O_2. Large shapes of oxide-free titanium will ignite in oxygen at room temperature in an atmospheric pressure of 241 N/cm^2 gage (350 psig), and at 1200°C (2192°F) at a pressure of 34.4 N/cm^2 gage (50 psig) (Reference 4.3-10). This is shown for other oxygen pressure/temperature combinations as well, in solid curve of Figure 4.3-1. This curve is based on test data reported upon in Reference 4.3-10. All of the preceding test data on the combustion of titanium in oxygen and CO_2 is summarized in Table 4.3-7.

Ignition Temperature of Oxide-Free Titanium in CO_2 at High Pressures. Data is available only on the effects of increasing oxygen pressure on the ignition of oxide-free titanium surfaces in oxygen environments. To extrapolate from this data, one must assume a value for the relative effectiveness of CO_2 and O_2 as oxidizing agents at high pressures. Titanium will ignite in air in the high end of the same temperature range as in oxygen, both environments being at a pressure of 1 atm (Reference 4.3-7). Ignition temperatures of titanium powder in CO_2 are from 10 to 25 percent

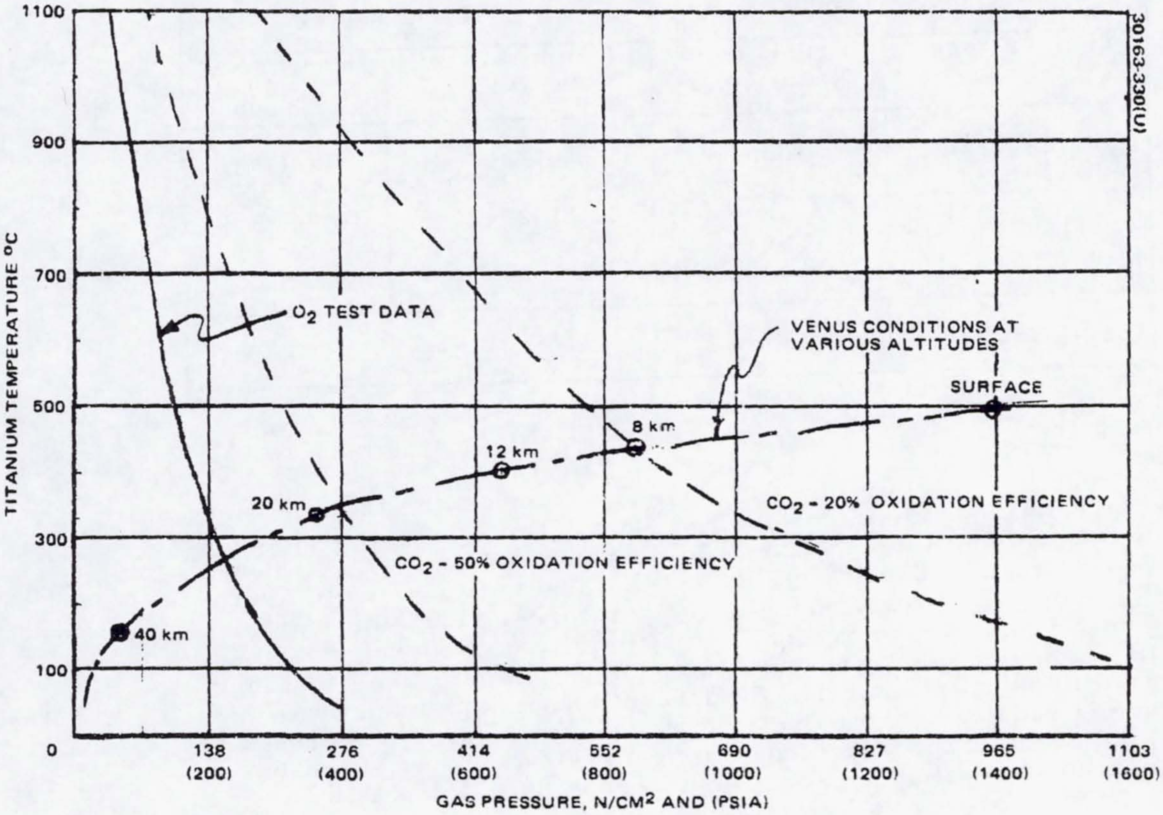

FIGURE 4.3-1. PRESSURE/TEMPERATURE CONDITIONS FOR AUTOIGNITION AND COMBUSTION OF SOLID OXIDE-FREE TITANIUM

TABLE 4.3-7. SUMMARY OF AVAILABLE TEST DATA FOR TEMPERATURE/PRESSURE CONDITIONS FOR SPONTANEOUS IGNITION AND COMBUSTION OF SOLID TITANIUM

	Oxide-Covered		Oxide-Free	
Test Gas	Temperature, °C (°F)	Pressure, N/cm^2 (psi)	Temperature, °C (°F)	Pressure, N/cm^2 (psi)
O_2	1300 (2372) to 1600 (2912)	Room	Room	241 (350)
	870 (1598) to 1100 (2012)	207 to 345 (300 to 500)	1200 (2912)	34.4 (50)
CO_2	1510 (2750)	Room	(No Data)	

higher in CO_2 than in air (Reference 4.3-11). To demonstrate the importance of the value for relative oxidizing efficiency, calculations have been made for assumed values of this efficiency of 50 and 20 percent. Figure 4.3-1 shows the pressures that would be required for each of these efficiencies to ignite oxide-free titanium in CO_2 for a range of temperatures. The solid curve shows actual test data for pure oxygen. An efficiency of 20 percent for CO_2 means that five times as much pressure is required to ignite the titanium as was required in pure oxygen. The 50 percent efficiency means twice as much pressure is required. Note that when these curves are compared with the expected temperature/pressure conditions of CO_2 on Venus, it becomes apparent that oxide-free titanium would be unacceptable. Even with an assumed oxidation efficiency as low as 20 percent, the titanium could ignite at 8 km Venus altitude.

Effect of Other Factors on the Ignition Temperature of Titanium. Effects of dynamic flow conditions, created by a descending probe, on the ignition temperature, are less documented. Figure 4.3-2 (Reference 4.3-10) illustrates the effects of a dynamic flow rate of oxygen on the total oxygen pressure necessary to ignite titanium at room temperature. Specific flow rates were not given. At a 60 percent oxygen environment, for example, a dynamic flow rate of that environment lowers the oxygen pressure necessary for ignition from 538 to 221 N/cm^2 gage (780 to 320 psig), a reduction of 59 percent. There exists fragmentary data that stress decreases the temperature necessary to ignite titanium in various atmospheres (Reference 4.3-12). This stress can be either physical, due to increased atmospheric pressure, or chemical. No data are available, however allowing the approximation of this factor. A third consideration, somewhat related, is the effect of corrosive agents in the environment. They might either increase or decrease the ~~oxidation rates of titanium in high pressure CO_2 environments.~~

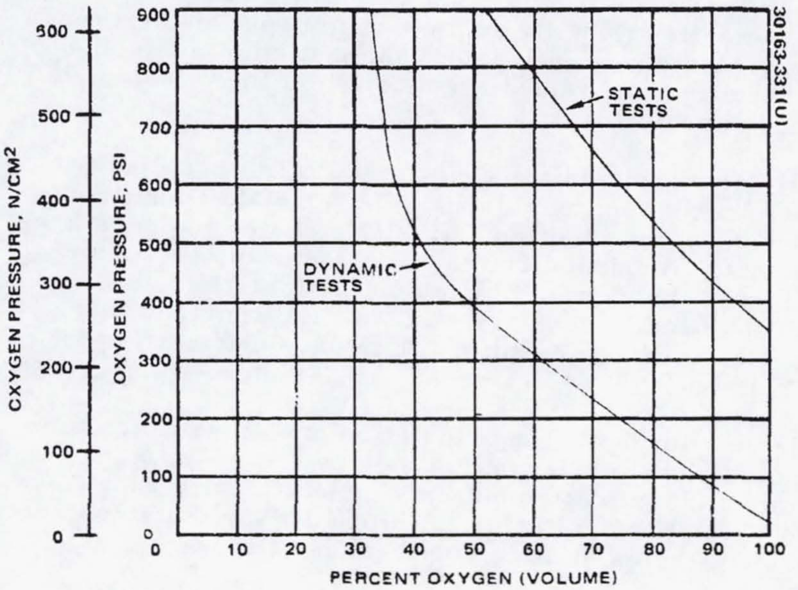

FIGURE 4.3-2. EFFECT OF DYNAMIC FLOW CONDITIONS ON IGNITION PRESSURE AT ROOM TEMPERATURE OF TITANIUM IN VARIOUS OXYGEN ATMOSPHERES

Removal of Titanium Oxides in the Venus Atmosphere. The precondition for occurrence of ignition and combustion of titanium in the Venus temperature-pressure profiles is the exposure of an oxide-free surface. Such surfaces have been produced on titanium in Earth ambient environments by etching in acidic solutions or by sand and vapor blasting. Etching times are typically 1 to 20 min in acid concentrations of 5 to 80 percent, although treatments less than 1 min in duration have been used (References 4.3-13 and 4.3-14). Times for vapor or sand blasting are also a few minutes in duration. Some typical etching conditions are given in Table 4.3-8.

The environment of Venus is believed to include clouds of the acids used in titanium etchants. It is also thought to include more particulate matter moving at higher velocities than does Earth's atmosphere (Reference 4.3-15). With such an environment, ignition and combustion of a titanium descent probe, with the resulting premature termination of the mission, is thought to be a very serious possibility.

Mercury Embrittlement. An additional incompatibility problem with Ti-6Al-4V is its rapid embrittlement by mercury, a possible constituent of the environment of Venus. At ambient and slightly elevated temperatures and in earthly environments, embrittlement can occur in minutes. A precondition for embrittlement is the wetting of titanium with mercury. In Earth environments, wetting usually requires an oxide-free surface; for Venusian environments, other surface conditions may be sufficient for wetting.

Data is not available allowing the extrapolation of failure times to the atmospheric conditions to be experienced by the descent probe. It is thought, though, that times for embrittlement may be sufficiently rapid to cause premature failure of the titanium shell. While steels are also subject to embrittlement in mercury, rates of attack on ferrous alloys are much slower than rates on titanium.

Conclusion. In view of the severe chemical incompatibility problems with the Venus environment, it was concluded that titanium is an unacceptable material for primary probe structure.

Steel Selection Trades.

With the elimination of titanium as an acceptable material for the pressure vessel module structure, a suitable substitute material was required. In the pressure vessel design trade studies described in a previous subsection, the lightest designs other than titanium were derived. Beryllium results in the next lightest design after titanium, with aluminum and steel in that order. For the Atlas/Centaur design, beryllium was eliminated because of its high cost. Aluminum was also eliminated because, with no external insulation, pressure vessel wall temperatures were on the order of 483°C (900°F), far beyond the structural capability of aluminum. A decision was made, therefore, to use steel as the primary structural material.

TABLE 4.3-8. TYPICAL ETCHANTS FOR TITANIUM ALLOYS
(Based on Tests)

Bath		Temperature $^{\circ}C$ ($^{\circ}F$)	Time
Solution	Percent		
HF HNO_3 H_2O	2 20 78	25.6 (78)	30 sec.
H_2SO_4 H_2O	25 75	Hot	5-10 min.
H_2SO_4 H_2O	30 70	93.3 (200)	?
HCl H_2O	50 50	48.4-79.5 (119-175)	5-15 min.
HNO_3 HF H_2O	10 1-2 88	25.6 (78)	1-2 min.

A trade study considered the following factors in evaluating three candidate steels; producibility, cost and compatibility with the Venus environment. The three candidate steels considered were D6AC, 17-4 PH and maraging (250 grade). Producibility factors were:

1) Forming of hemispherical shell with mounting flange

2) Machinability

3) Weldability

4) Heat treatment

Forming. Options for forming are forging, deep drawing, or spinning. Tooling for forging or deep drawing is more costly than tooling for spinning. Deep drawing a part with a heavy flange or forging the part will result in a heavy wall that will require more machining than if the part is made by spinning. However, it may not be possible to spin a hemisphere with both an external main flange and an internal equipment flange. Therefore forging appears to be the most practical method of forming prior to machining. The cost of forging is about equal for all the candidate steels.

Machining. The differences in machinability of alloy steels, and precipitation hardening stainless steels are not sufficient to favor one material over the other for the low quantities involved.

Welding. All materials under consideration are readily weldable. D6AC steel requires close control over preheat and postheat which increases the cost. It is estimated that in the order of increasing cost of welding, the materials are rated as follows:

1) Maraging steel and 17-4 PH steel

2) D6AC

Heat Treatment. For an internally insulated pressure vessel design, the steels require heat treatment after welding to develop the required properties. The heat treatments to optimize mechanical properties after welding are:

1) Maraging steel – age at 900°F

2) 17-4 PH steel – solution anneal at 1900°F, air cool, age at 900°F.

3) D6AC steel – austenitize at 1650°F, air quench (sections less than 1 in. thick), temperature at 1100°F.

From the producibility standpoint, the heat treatment of the maraging steel has advantages over those of the other two steels in that the part is subject to less distortion from the lower temperature heat treatment. However, since the other two steels can be air-quenched, they should not experience severe distortion.

The cost of the raw materials for low quantities is not very significant in the overall cost. In order of increasing cost, these materials are rated (1) D6AC, (2) 17-4 PH, (3) maraging steel.

Conclusions. In summary, relative ratings for the various factors* are:

Forming	Machining	Welding	Heat Treat	Raw Material
1) D6AC, 17-4 PH Maraging	Approximately equivalent	1) Maraging, 17-4 PH 2) D6AC	1) Maraging 2) 17-4 PH, D6AC	1) D6AC 2) 17-4 PH 3) Maraging

---

*No. 1 is the most favorable.

TABLE 4.3-9. CORROSIVE ENVIRONMENTS OF MARAGING AND STAINLESS STEELS ON EARTH

Medium	Stainless Steel	Maraging Steel
CO_2	No	No
HCl	Yes	Yes
H_2SO_4	Yes	Yes
H_2S	Yes	Yes
Cl_2	Yes	Yes
H_2O_2	No	No
HF	Yes	Yes
NH_3	No	No
Fl_2	Yes	Yes
Hg	No	Yes
$HgCl_2$	Yes	Yes
NH_4Cl	No	Yes
NH_4SO_3	No	Yes
S	Yes	Yes
SO_2	No	Yes
SCl_2 S_2Cl_2	No	Yes
$H_2SO_4 + HNO_3 + OH$	Yes	Yes

Without obtaining exact cost estimates, it is not obvious that there is a significant saving in the use of one material over another. Based solely on manufacturing considerations, maraging steel is favored.

Material Corrosion in the Venus Environment. Earth-based, IR spectroscopic measurements, aided by the Venera probe data, indicate that the environment of Venus is composed principally of CO_2 (95 ± 5 percent), with small amounts of CO, HCl, HF, Hg, and HgCl. Other data, as well as constituent interactions, indicate the possibility of appreciable amounts of H_2O_2, H_2SO_4, NH_3, Cl_2, Fl_2 and further byproducts. Due to lack of specific data, all of these products must be assumed present, even if only in trace amounts. The ability of most of these products to corrode both low alloy and stainless steels at ambient pressures and a range of temperatures is detailed in Table 4.3-9. The effects of a high pressure, high temperature CO_2 atmosphere on the various corrosive interactions are unknown.

Although maraging steel is somewhat more susceptible to corrosion than is stainless steel, the difference between them is not considered significant for the exposure times involved during Venus descent. However, based on manufacturing considerations and heat treatment advantages, maraging steel was chosen as the most appropriate material. Due to the corrosive nature of the Venus environment, even for short time exposures, a protective coating will be considered for the descent probe shell. Commercial porcelain enamels are available with low firing temperatures; thickness as low as 1 mil may be suitable. Another alternative is inexpensive, high temperature paints. Sperex VHT is one possibility. It will withstand 982°C for short periods of time and has a continuous service temperature of 650°C. Its adhesion to maraging steel is excellent, and it is resistant to thermal shock, fuels, humidity and salt spray, and most other corrosives. The paint is space qualified and has withstood direct exposure to rocket plume impingement. It is normally applied to a thickness of 0.005 cm and requires a cure of 1 hour at 425°C, which is compatible with the heat treatment of maraging steel.

Main Seal Selection - Atlas/Centaur

During the pressure vessel tests described in reference 4.3-3, some experimental data was obtained on various methods of providing a pressure seal in the main assembly flange. It was found that solid elastomer O rings are simple, reusable and very effective in providing a perfect seal under high external pressures comparable to Venus surface pressure also, they do not require tight tolerance glands. However such O rings have limited temperature capability and could therefore only be considered for an externally insulated pressure vessel design. For application with elevated temperatures equal to Venus surface conditions, metal seals are required. In the tests

REPRODUCIBILITY OF THE ORIGINAL PAGE IS POOR.

of Reference 4.5-5, various size hollow vented metal C rings were tested to pressures considerably in excess of Venus design pressures. It was found that such seals, which are qualified to temperatures higher than Venus surface temperatures, provide an effective seal but require a high preload, extreme cleanliness, careful handling, and precision tolerance in the gland dimensions. Another metal seal, which will be effective even during and after flexing of the main flange under thermal stresses or vibration is a V ring seal. Such a seal has a V shaped cross section oriented with the open end of the V toward the direction of the highest pressure against which sealing is required. The main advantage of this seal is that it operates well under relatively low preload, permitting the design of a light flange with fewer clamping screws. The high strength base metal of this ring is coated with a soft metal sealing material (such as silver). When squeezed between the flat surfaces of the gland, the soft metal coating material is forced into the mating surface roughness blocking all potential leak paths. Once initiated, the intimate contact is maintained by the seals resiliance and the gas pressure which tends to spread the V and compensate for relative motions. Such a seal is the tentative choice for the Atlas/Centaur design. Although intended to seal only against high pressure from the open end of the V, low pressure seal capability in the opposite direction is also achieved. Should this low pressure capability be inadequate for the 1 atmosphere of internal pressure during the transit stage from earth to Venus, an X shaped seal (or back to back V seals) can be employed, or the pressure vessel can be evacuated to a lower pressure of 4 psi (2.5 N/cm^2) prior to launch.

Structural Sizing -- Atlas/Centaur.

The required thicknesses for some items on the Atlas/Centaur baseline design were calculated by simply ratioing the Thor/Delta results up or down as necessary to account for differences in size, loads, material or other parameters between the Atlas/Centaur and the Thor/Delta. The method by which this was done is described in a previous subsection. However, this technique is only applicable to those elements on the Atlas/Centaur which have identically the same configuration as the corresponding element in the Thor/Delta design. The elements in this category include the pressure vessel shell, the main circumferential flange, the shelf support flange, and the adapter ring. The upper and lower equipment support shelf and shelf attachment structure on the Atlas/Centaur are of an entirely different configuration than the corresponding elements on the Thor/Delta. Therefore, an original design analysis was performed on these Atlas/Centaur items to determine the required structural sizing.

Thermal requirements dictate that both the upper and lower shelf on the Atlas/Centaur be constructed from solid aluminum since these shelves act as a heat sink mass for the equipment they support. (On the externally insulated Thor/Delta design, these shelves were constructed from aluminum honeycomb). To prevent heat conductance to the upper shelf from the hot steel pressure vessel shell wall, the shelf is not attached to the shell (as is the case in the Thor/Delta design). Instead, it is supported on 12 thin titanium columns or stringers, which are, in turn, supported by a titanium lower shelf support ring, which also supports the aluminum lower shelf. The titanium lower shelf support ring is fastened to a pressure vessel flange by thermal isolators. A sketch of this arrangement is shown in Figure 4.3-3A. The following subsection is a description of the design analysis of these shelf items on the Atlas/Centaur baseline.

Large Probe

Upper Shelf. Thermal considerations dictated that the upper shelf on the Atlas/Centaur Large probe be constructed from a solid aluminum plate. This plate acts as a heat sink mass in addition to supporting its equipment as a shelf. The total mass of equipment and upper shelf which must be supported is:

Equipment	12.34 kg (27.2 lb)
Required shelf thermal mass	13.15 kg (29.0 lb)*
Total =	25.49 kg (56.2 lb)

During the critical loading condition of Venus entry, the deceleration factor of 715 g produces a total vertical force of 179,000 N (40,000 lb). Due to the relatively uniform distribution of the equipment on the top shelf, it is reasonable to assume that the inertia force on the shelf is also uniformly distributed. Based on the dimensions from the sketch of Figure 4.3-3, the distributed force is

$$W_F = \frac{F}{A} = \frac{F}{\pi R^2} = 58.8 \text{ N/cm}^2 \text{ (85 psi)}$$

To provide adequate heat sink mass, the weight of the shelf must be 13.15 kg (29 lb). This requires a minimum shelf thickness in aluminum of t = 1.56 cm (0.62 in). The maximum bending stress in the shelf, assuming that it is supported at the edges, occurs at the center and for the above thickness is found to be (reference 6)

---

*Minimum required for heat sink effect.

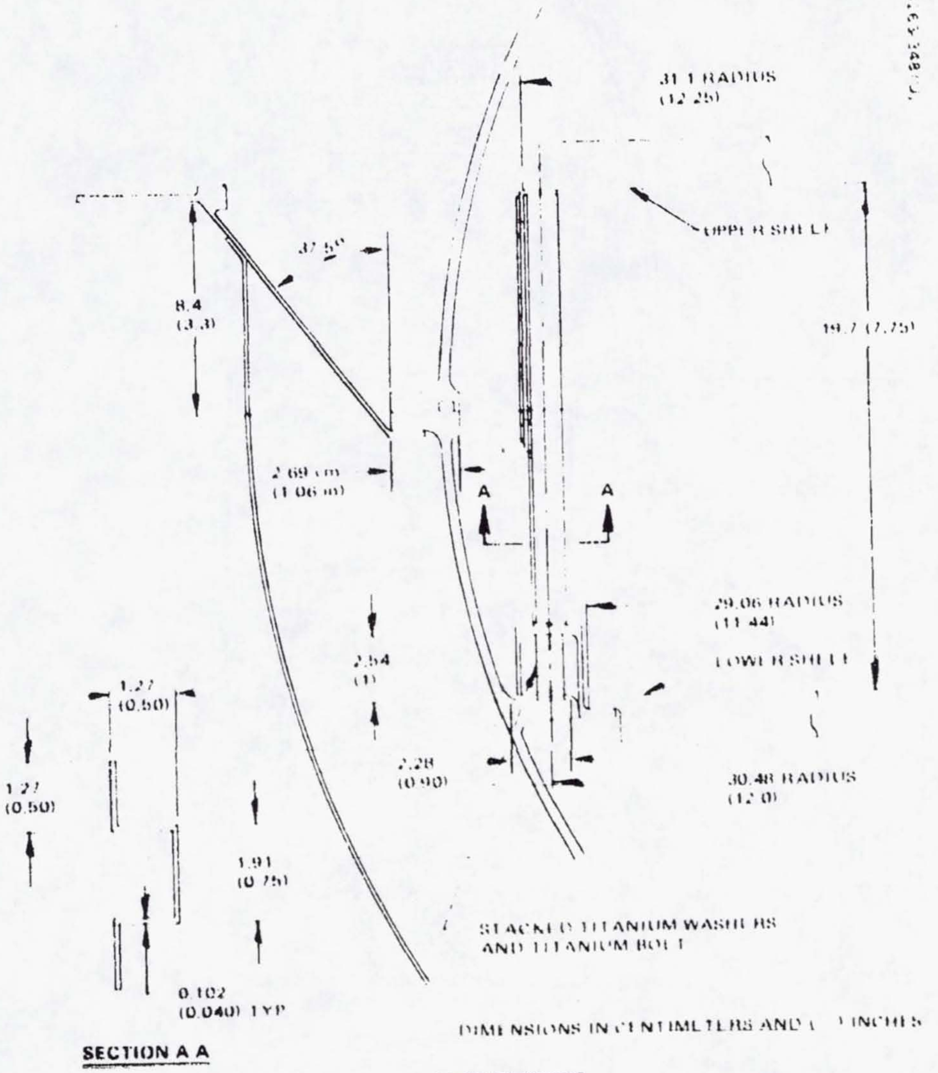

a) LARGE PROBE

FIGURE 4.3.3. PRESSURE VESSEL STRUCTURE a) LARGE PROBE

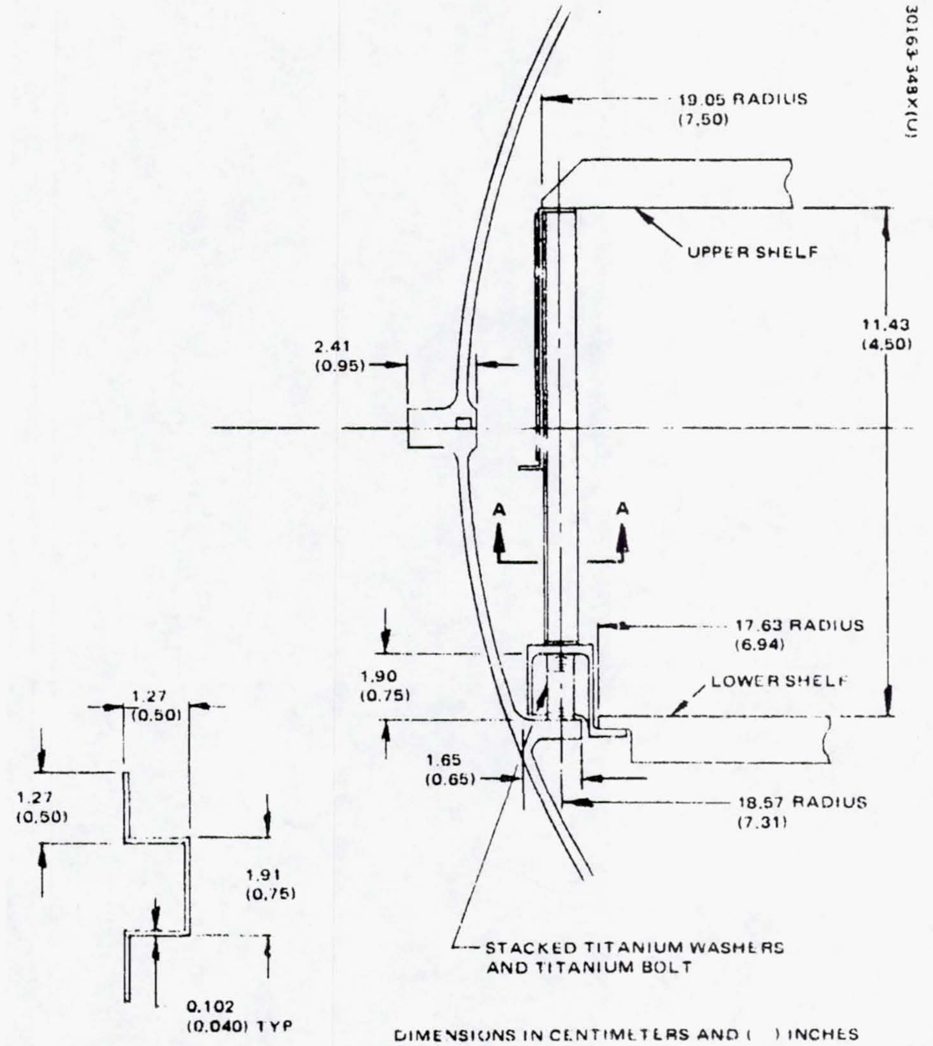

SECTION A-A

b) SMALL PROBE

FIGURE 4.3-3. PRESSURE VESSEL STRUCTURE b) SMALL PROBE

$$f_b = \frac{0.375\ W_f\ R^2\ (3 + \mu)}{t^2} \quad \text{where} \quad \mu = \text{Poisson's ratio (0.33 for aluminum)}$$

$$f_b = 28,570\ \text{N/cm}^2\ (41,436\ \text{psi})$$

Since this is less than the tensile yield allowable for numerous structural aluminum alloys, the minimum thickness required for thermal considerations is adequate for strength.

Upper Shelf Support Columns. Twelve titanium upper shelf support columns transmit the loads on the upper shelf to the lower shelf support flange. These columns are in the shape of hat sections. Dividing the total load on the upper shelf among the 12 stringers and assuming some additional inertia force from the upper shelf attach ring, the total load per stringer is

$$P_s = 16,600\ \text{N}\ (3735\ \text{lb})$$

Using assumed dimensions of the stringer as shown in Figure 4.3-3, the allowable load to prevent local crippling of each titanium stringer was found to be

$$P_{AL} = 63,000\ \text{N}\ (14,200\ \text{lb})$$

This was calculated using conventional stress analysis techniques. Since $P_{AL} > P_S$, the assumed dimensions are more than sufficient to prevent local crippling as a mode of failure. Next, the mode of failure of overall column buckling was checked (Euler Buckling). Using conventional methods, the load to induce the failure was found to be

$$P_{AE} = 57,800\ \text{N}\ (13,000\ \text{lb})$$

Again, the assumed stringer dimensions are more than adequate.

Lower Shelf. The lower shelf was analyzed in identically the same manner as previously described for the upper shelf. The weight supported by the lower shelf is

Equipment = 47.40 kg (104.5 lb)
Required shelf thermal mass = 9.30 kg (20.5 lb)
Total = 56.7 kg (125.0 lb)

At 715 g, the resulting total vertical force is

$$F = 398,000 \text{ N } (89,000 \text{ lb})$$

The minimum thickness required to prevent bending failure of the shelf was found to be

$$t_B = 1.42 \text{ cm } (0.560 \text{ in.})$$

The thickness required to cause the shelf to have the minimum required heat sink mass is

$$t_{HS} = 1.27 \text{ cm } (0.50 \text{ in.})$$

Therefore, the governing thickness for the lower shelf is t_B.

Lower Shelf Support Ring. A titanium lower shelf support ring is required to transmit the forces from the lower shelf to 12 thermal isolating washer stacks on the inner flange of the shell's lower hemisphere. The rings configuration and important dimensions are shown in the sketch of Figure 4.3-4. The load per unit length of circumference transmitted by the bottom shelf to the support ring is shown in Figure 4.3-5.

$$N_X = \frac{F}{2 R}$$

The flange thickness required at point A is

$$t = \sqrt{\frac{6M}{f_y}}$$

where M = limit moment at A
f_y = yield allowable for titanium

$t = 0.267$ cm (0.105 in.) required.

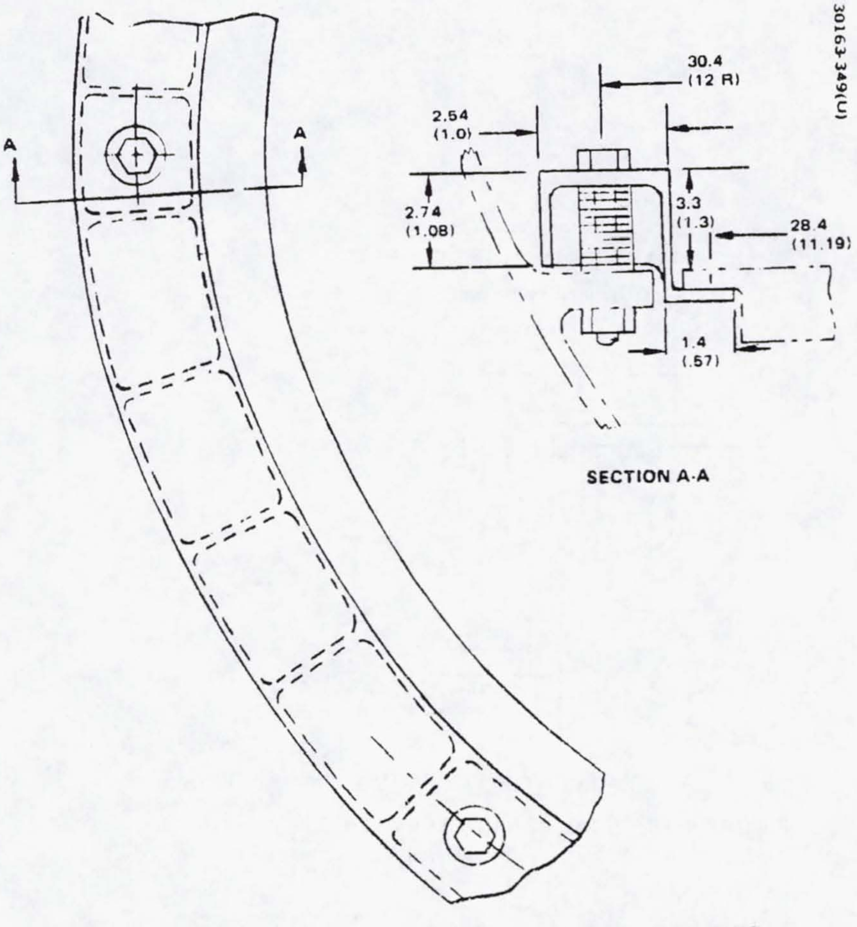

FIGURE 4.3-4. LARGE PROBE SHELF SUPPORT RING

$N_x = \frac{F}{2\pi R} = 2264 \frac{N}{cm}$ (1293 lb/in.) AT ULTIMATE

OR $N_x = 1811 \frac{N}{cm}$ (1034 lb/in.) AT LIMIT

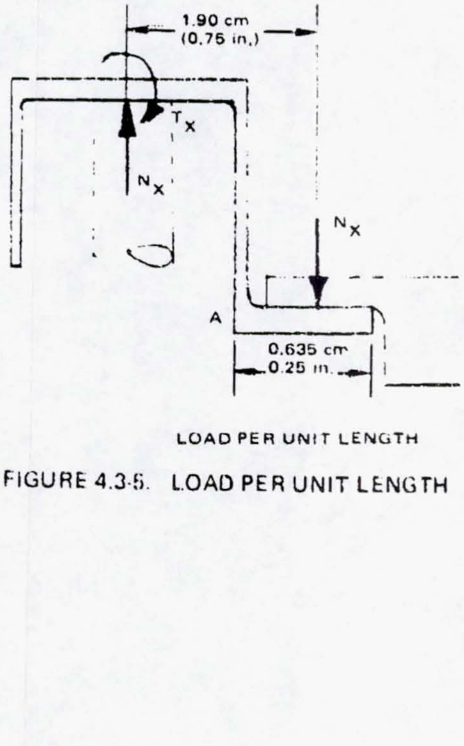

FIGURE 4.3-5. LOAD PER UNIT LENGTH

The force, N_x is transmitted to the ring to shell attach point producing a distributed torque, T_x, about the rings circumference. As shown in Reference 4.3-16, this produces a constant bending moment of

$$M_x = T_x R \quad \text{where } R = \text{radius of ring to center of rings cross section}$$

$$M_x = 105{,}000 \text{ Ncm } (9{,}300 \text{ in lb}) \text{ limit}$$

In addition, a moment M_c is also created when N_x is spanned between each of the 12 attach points. M_c is found to be

$$M_c = 18{,}700 \text{ Ncm } (1664 \text{ in-lb})$$

The maximum moment that must be resisted by the rings cross section without yielding is

$$M_{MAX} = M_x + M_c$$

$$M_{MAX} = 124{,}000 \text{ Ncm } (11{,}000 \text{ in-lb})$$

The cross section of the ring is closely approximated by a hollow square tube of thickness, t, and width 2.54 cm (1.00 in.). The maximum stress in this cross section under the moment, M_x, is given by:

$$f_{MAX} = \frac{6M}{1 - (1 - 2t)^4}$$

setting f_{MAX} equal to the yield allowable for the titanium and solving for the required thickness, gives

$$t = 0.185 \text{ cm } (0.073 \text{ in}) \text{ required}$$

To assure that a portion of the vertical force, N_x, is transferred to the outer leg of the ring as assumed, and to ensure sufficient transverse stiffness of the cross section, radial ribs are provided as shown in Figure 4.3-4.

Local stresses in the ring in the vicinity of each washer stack attachment point were also investigated. The behavior of the ring face at an attachment may be idealized as a clamped circular plate, clamped in the center (by the washer stack and bolt head) as shown in Figure 4.3-6. A solution to the idealized model is given in Reference 4.3-16. The maximum stress occurs at the inner edge and is given by

$$f_{MAX} = \frac{3W}{2\pi t^2}\left[1 - \frac{2a^2}{a^2 - b^2}\left(\ln \frac{a}{b}\right)\right]$$

where

W = load per washer stack

a, b, and t are as shown in Figure 4.3-6.

Setting f_{MAX} equal to the yield allowable for the titanium ring, and using the maximum limit load per washer stack, the required local ring thickness was found to be

$$t = 0.356 \text{ cm } (0.140 \text{ in}) \text{ local thickness required}$$

It should be noted, that the load W per washer stack that is transferred through the ring comes from the force on the bottom shelf only. The top shelf load is transmitted directly to each washer stack by the support columns without going through the ring.

Thermal Isolating Washer Stacks. As explained in the thermal control section of this volume, the titanium washer stacks shown in Figures 4.3-3 and 4.3-4, are required to provide insulation from thermal conductance between the hot pressure vessel wall to the equipment support shelves. The critical loading condition for this stack occurs at Venus entry and puts the washers in compression. The total ultimate load per washer stack is seen from the previous discussion to be

$$P = 49,700 \text{ N } (11,200 \text{ lb})$$

Assuming a washer outside diameter of 1.04 cm (0.41 in.) and an inside diameter of 0.508 cm (0.20 in.), the ultimate compressive stress in a washer is

$$f_c = 76,600 \frac{N}{cm^2} \ (111,000 \text{ psi})$$

This is less than the compressive yield stress for the material and is therefore safe.

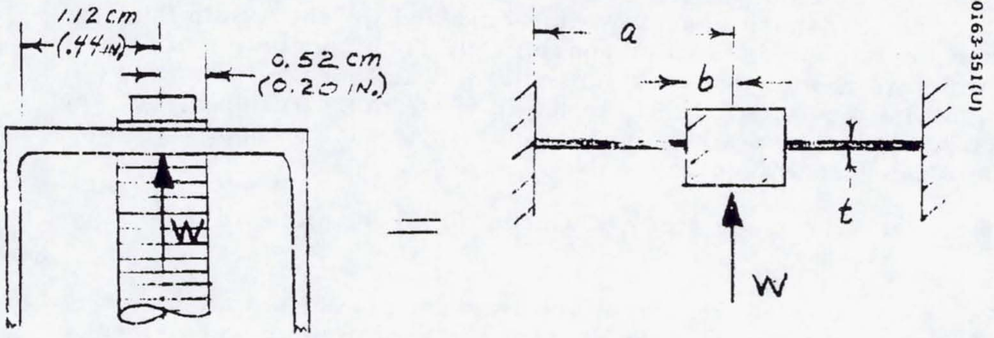

FIGURE 4.3-6. CLAMPED CIRCULAR PLATE

REPRODUCIBILITY OF THE ORIGINAL PAGE IS POOR.

Small Probe. The structural configuration of the small probe pressure vessel module is identical to that for the large probe. Therefore, the analysis techniques used to size the various structural elements were identical to those described for the large probe in the preceding subsections. The results of the sizing procedure for both the large and the small probes are given in a following subsection, Baseline Description – Atlas/Centaur.

Internally Versus Externally Insulated Structure Trade

In subsection 4.4 of this volume, a study is summarized which indicates that acceptable thermal protection of all on board equipment can be accomplished using either external insulation or internal insulation design approaches. These design approaches can have a profound affect on the cost and weight of the structural design. Accordingly, a trade study was performed to determine which of these design approaches was superior from the standpoint of overall pressure vessel module cost and weight. Both the Thor/Delta and Atlas/Centaur designs were considered. The conclusion of this trade study, which is reported in this subsection, was that the internally insulated design would be significantly lower in cost, more reliable, and yet not significantly heavier. As a result, the internal insulation approach was chosen for the Atlas/Centaur design.

Trade Study. The trade study was accomplished in the following manner:

1) For each concept, (external and internal insulation) all major structural elements of the pressure vessel module were sized and their weights calculated.

2) The weight of all nonstructural pressure vessel module items and other probe items which are affected by the insulation concept were calculated. These include:

    a) Thermal insulation and retaining hardware

    b) Heat sink mass required in shelves

    c) Aerodynamic fairing required on one design, but not on the other. (The Thor/Delta design may also have required a fairing if the wind altitude radar antenna had been specified in that payload).

    d) Deceleration module (size change).

3) For each design, the total weight of all affected items was obtained (from 1 and 2, above). Items, such as onboard equipment, whose weights would not be affected by the insulation design approach, were not included in the totals.

REPRODUCIBILITY OF THE ORIGINAL PAGE IS POOR.

4) The resulting design concepts of both were compared to determine:

   a) The design with the lowest anticipated cost of development, testing and fabrication

   b) The design with the least weight

Structural Size Effects. Detailed structural sizing for an externally insulated Thor/Delta design had already been accomplished in Task PB-27 (Reference 1.5-6). In that analysis, the effect on required thickness of primary dimensions, such as pressure vessel diameter, as well as the effect of load, material properties, etc., were derived. Therefore, the effect of changes to these parameters could be quickly determined by ratios. For example, since the analysis of Task PB-27, the pressure vessel material had changed from titanium to steel. The effect of converting to an internally insulated design was to increase structural temperatures, thereby decreasing certain material properties. In addition, the diameter of the Atlas/Centaur pressure vessel is greater than the Thor/Delta diameter used in the original analysis. Further diameter increase is necessitated to provide space for internal insulation in the case of that design. Inertia loads for Atlas/Centaur are greater than those used for Thor/Delta. By multiplying the Thor/Delta thicknesses by ratios of these parameter changes, the Atlas/Centaur thickness requirements were obtained. This was done for both the externally insulated and the internally insulated designs. As an example of this process, the required thickness of the large probe upper shelf support flange was derived as follows: The thickness of this flange for the titanium Thor/Delta design was found to be $t_{T/D}$ = 0.262 cm (0.103 in.).

In the derivation, this thickness was shown to be proportional to

$$\sqrt{\frac{WGb}{R\sigma}}$$

where

W	total mass of top shelf and equipment
b	flange width
G	acceleration load factor
R	shelf radius
σ	yield stress allowable for the flange material

The critical load for this flange occurs during Venus entry deceleration when the temperature is low. Therefore, the flange thickness is not affected by internal versus external insulation. The Atlas/Centaur parameter changes are:

W changed from 11.15 kg (31.2 lb) to 25.6 kg (56.5 lb)

E remained unchanged

Q changed from 625 to 715

R changed from 23.4 cm (9.2 in.) to 29.8 cm (11.75 in.)

σ changed from 82,800 N/cm² (120,000 psi) for titanium to 117,200 N/cm² (170,000 psi for 17-4 PH H900 steel

The required thickness for the flange on the Atlas/Centaur design is then obtained from

$$t_{A/C} = 0.262 \text{ cm} \sqrt{\frac{25.6}{11.15} \cdot \frac{715}{625} \cdot \frac{23.4}{29.8} \cdot \frac{(120,000)}{(170,000)}}$$

$$t_{A/C} = 0.280 \text{ cm } (0.110 \text{ in.})$$

This process was repeated in like manner for every major item of Atlas/Centaur structure in both an external and internal insulation design. The weight of each of these items of structure was then calculated.

To minimize weight in the Thor/Delta based structural design, a buckling coefficient of 0.7 was assumed in determining the required pressure vessel shell thickness. However, for the Atlas/Centaur design, a less optimistic coefficient of 0.4 was assumed. To achieve 0.4, fabrication tolerances can be somewhat looser, thus lowering machining costs, but the weight will be somewhat higher. The following is a summary of an analysis, which shows that the conservative value of 0.4 is a suitable choice for either an external or internal insulation design approach.

In recent tests conducted by Hughes, it was shown that accurately fabricated spherical shells with the same radius to thickness ratio as required on Pioneer Venus will buckle under external pressure that is 78 percent of the calculated theoretical maximum. This is equivalent to a buckling coefficient (or knock down factor) of 0.78. These tests are reported upon in detail in Reference 4.3-3. The tests also proved that there would be no reduction in this coefficient because of a reinforced window penetration or a rigid flange. However, the tests also revealed that imperfections in the sphericity of the shell's surface would substantially reduce the coefficient. Increases in shell temperatures that would occur due to an internally insulated design, would reduce the buckling pressure by reducing the modulus of elasticity of the shell material. However, the elevated temperature alone should have no effect on the buckling coefficient. On the other hand, thermal gradients, if present, will give rise to distortions of the shell's surface, which are in effect, imperfections in sphericity. Thus, thermal gradients should be expected to reduce the knock down factor.

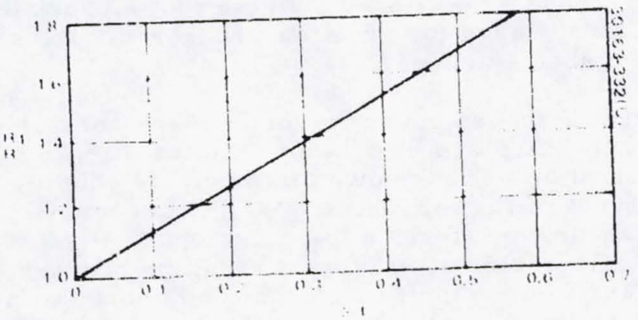

FIGURE 4.3-7 LOCAL RADIUS CHANGE DUE TO OUT OF ROUNDNESS

Information on the effect of distortions or imperfections in the shell surface geometry is available in the published literature. In Reference 4.3-17, it is shown that the buckling coefficient or knock down factor for a near perfect sphere is reduced by a local flat spot. If the radius of the sphere is R and the local radius of the flat spot is R_1, Reference 4.3-17 shows that the buckling coefficient will be reduced by a factor of

$$\frac{1}{(R_1/R)^2}$$

In Reference 4.3-17, a method is proposed by which any "out-of-roundness" imperfection may be converted to an equivalent flat spot radius. If the local deviation from sphericity is δ, the ratio of δ to the shell thickness, t, is related to R_1/R by the curve of Figure 4.3-7, which is taken from Reference 4.3-17.

The tests of Reference 4.3-17 also indicate that a knock down factor of 0.7 is a reasonable lower bound for spheres whose radii are accurate to within 2.5 percent of the shell thickness.

Tests conducted at Hughes appear to verify these conclusions. In particular, spheres which failed at a knock down factor of 0.78 when near perfect in geometry, failed at a knock down factor of 0.4 when local radius imperfections of 21 percent of the thickness were introduced. Using the above curve, the 21 percent imperfection is equivalent to $R_1/R = 1.3$ (Enter curve with $\frac{\delta}{t} = 0.21$). The factor of 0.78 would then be reduced by the factor $1/(1.3)^2 = 0.59$ and would result in a predicted knock down factor of $0.59 \times 0.78 = 0.46$, which correlates well with the Hughes results.

As a conservative first approximation to the effect of thermal gradients on the knock down factor, K, assume that the local radius of the sphere will increase by an amount equal to ΔR, where

$$\Delta R = R \alpha \Delta T \quad ,$$

where

α = coefficient of linear expansion

R = nominal shell radius

ΔT = local temperature change

This is conservative because it assumes a stress free uninhibited expansion which is, of course, not the case.

If the difference between the maximum and minimum shell temperature is ΔT_0, the resulting deviation from perfect sphericity would be

REPRODUCIBILITY OF THE ORIGINAL PAGE IS POOR.

$$\Delta R = R \alpha \Delta T_o$$

For either design with a given R and α, and shell thickness, t, this can be converted to values of $\Delta R/t$ as a function of ΔT_o and, therefore, by the method previously described, the knock down factor, K, can be determined as a function of ΔT_o.

For the Atlas/Centaur externally insulated steel design, the maximum ΔT_o has been estimated to be on the order of 177°C (350°F). By the method described above, this results is a predicted knock down factor of 0.5. On the other hand, when this is converted to an internally insulated design, a gradient of only 60°C (140°F) is estimated. This converts to a knock down factor of 0.64. Thus, the selection of 0.4 as the factor on the Atlas/Centaur design is more than adequate, regardless of the insulation concept. 0.4 Was therefore used in calculating the required thickness for the pressure vessel shell in both the external and internal design concepts.

Table 4.3-10 shows the weight of each insulation design dependent item for the large probe. Columns 1 and 2 permit a weight comparison to be made for a titanium Thor/Delta design in either a hot wall (internal insulation) or a cold wall (external insulation). Note that the total system weight of the hot wall design would be 3.62 kg (7.98 lb) heavier than the cold wall design. This represents about 3 percent weight increase for the total probe system. Note that an aerodynamic fairing is required when the external insulation is removed. The fairing gives the pressure vessel module the same external shape that it had with the external insulation. This is necessary to assure that the aerodynamic stability of the hot wall design will be the same as that for the cold wall design; the cold wall design having already been proven by wind tunnel tests. Thermal protection of the equipment on the hot wall design was accomplished by using 1.27 cm (0.5 in.) of fiberglass insulation on the inside wall of the shell and also by incorporating some beryllium plates into the equipment shelves to serve as heat sink or heat absorbing mass.

Columns 3 through 6 allow comparable comparisons to be made on the Atlas/Centaur design. These are 2 Atlas/Centaur cold wall designs. One for a nominal insulation thickness, column 3, and one for a double insulation thickness, column 4. The double insulation thickness design was being considered to increase reliability of the thermal protection system in the less weight sensitive Atlas/Centaur application. However, both concepts are included for comparison. Note that the nominal insulation weight of column 3 is significantly less than required on the Thor/Delta, column 1. This was caused by refinements in thermal calculations after the Atlas/Centaur decision was made. Similarly, two hot wall designs are shown. One using beryllium as the heat sink mass, column 5, and one using aluminum for this purpose, column 6. Both hot wall designs utilized 1.27 cm (0.5 in.) of fiberglass insulation on the inside wall surface. Again, the hot wall designs are eavier than the cold wall designs. However, the increase in weight as a ercentage of the total probe system weight is only 9 percent at most to percent at least, depending upon which two of the four designs are compared. 'he overall conclusion from Table 4.3-10 is that the weight penalty for a hot all design, large probe, is minimal.

Table 4.3-11 allows similar weight comparisons to be made for the mall probe hot and cold wall designs. Two notable differences in the list of esign affected items are these. First, no aerodynamic fairing is required pon removing the external insulation from the small pressure vessel, since ıe vessel always remains in the aeroshell. Second, removal of the external ısulation reduces the external diameter of the pressure vessel module. This ermits it to be pushed deeper into the aeroshell, giving a lower probe c.g., 'hich permits a smaller aeroshell base diameter. Thus, the deceleration ıodule decreases in weight. (This same weight savings could not be realized n the large probe because of the presence of the external wind/altitude radar ntenna). These two differences from the large probe result in weight ecreases for a hot wall design in one instance (compare columns 4 and 5),and very slight weight increase in another instance (compare columns 3 and 6). ı either case, the conclusion is that the weight penalty (or advantage) for a ot wall design, small probe, is not significant.

From a weight standpoint, the difference between the external or ıternal insulation designs is not significant so the designs are considered omparable. However, from a total cost and reliability standpoint, the ıternally insulated design is clearly superior. The external insulation Vin-K) requires considerable development. It must be designed to function uring direct exposure to the somewhat unknown and hostile Venus environ-ıent. It must be assembled in many pieces, yet the slightest leak at any of ıe seams would render the insulation nearly useless. Also, access to the ıterior after assembly requires disassembly of some of these seams. On ıe other hand, the internal insulation concept is straightforward and does ot require extensive development. The insulation is protected from the enus atmosphere by the pressure vessel. Insulation seams are easier to eal and small seam leaks are not significant. Clearly, the elimination of ıe external insulation system in the hot wall design will result in extensive ost savings in development testing, qualification testing and fabrication. he overall conclusion from this trade study is that the internally insulated esign is superior.

escription of Thor/Delta Pressure Vessel Structure

The following is summary of the structural sizes derived by the ıalysis described in a previous subsection.

REPRODUCIBILITY OF THE ORIGINAL PAGE IS POOR.

TABLE 4.3-16. LARGE PROBE MASS COMPARISONS BETWEEN HOT AND COLD WALL DESIGNS, *IN KG(LB)

Design Concept Dependent Mass Items	Thor/Delta			Atlas/Centaur, Steel		
	Titanium		Steel			
					Hot Wall	
	Cold Wall	Hot Wall	Cold Wall, (Nominal Thickness Insulation	Cold Wall, (Double Thickness Insulation	Beryllium Heat Sink	Aluminum Heat Sink
External insulation	7.25 (16.0)	0	3.72 (8.20)	7.61 (16.80)	0	0
External insulation retainer	1.31 (2.90)	0	3.11 (6.86)	3.35 (7.36,	0	0
Internal insulation plus retaining devices	0	1.63 (3.60)	0	0	2.42 (5.34)	2.42 (5.34)
Added heat sink mass for temperature control	0	2.13 (4.70)	0	0	6.44 (14.20)	12.59 (27.78)
Pressure vessel shell	13.20 (29.10)	20.70 (45.67)	37.7 (83.27)	37.7 (83.27)	47.3 (104.35)	47.3 (104.35)
Main flange plus shelf flanges	3.58 (7.90)	3.75 (8.27)	9.51 (20.98)	9.51 (20.98)	9.89 (21.80)	9.89 (21.80)
Equipment shelves	4.12 (9.10)	4.12 (9.10)	7.34 (16.17)	7.34 (16.17)	7.34 (16.17)	7.34 (16.17)
Probe/aeroshell adapter	1.36 (3.00)	1.42 (3.14)	3.74 (8.26)	3.74 (8.26)	3.89 (8.59)	3.89 (8.59)
Aerodynamic fairing	0	0.68 (1.50)	0	0	3.85 (8.50)	3.85 (8.50)
Affected items in deceleration module	0	0	0	0	0	0
Total items affected	30.8 (68.00)	34.4 (75.98)	65.2 (143.74)	69.0 (152.04)	81.0 (178.7)	87.3 (192.53)

* Hot wall – internal insulation design
Cold wall – external insulation design

REPRODUCIBILITY OF THE ORIGINAL PAGE IS POOR.

TABLE 4.3-11. SMALL PROBE MASS COMPARISONS BETWEEN HOT AND COLD WALL DESIGNS, * IN KG (LB)

Design Concept Dependent Mass Items	Titanium		Steel			
			Cold Wall		Hot Wall	
	Cold Wall	Hot Wall	(Nominal Thickness Insulation)	(Double Thickness Insulation)	Beryllium Heat Sink	Aluminum Heat Sink
External insulation	4.62 (10.20)	0	5.21 (11.50)	10.65 (22.80)	0	0
External insulation retainer	.544 (1.2)	0	1.43 (3.16)	1.62 (3.58)	0	0
Internal insulation plus retaining devices	0	0.725 (1.60)	0	0	0.95 (2.10)	0.95 (2.10)
Added heat sink mass for temperature control	0	7.03 (15.5)	0	0	3.90 (8.6)	7.63 (16.83)
Pressure vessel shell	2.76 (6.10)	4.78 (10.54)	7.42 (16.36)	7.42 (16.36)	10.07 (22.21)	10.07 (22.21)
Main flange plus shelf flanges	1.16 (2.55)	1.24 (2.74)	2.66 (5.86)	2.66 (5.86)	2.82 (6.22)	2.82 (6.22)
Equipment shelves	1.59 (3.50)	1.59 (3.50)	2.32 (5.11)	2.32 (5.11)	2.32 (5.11)	2.32 (5.11)
Probe aeroshell adapter	0.77 (1.70)	0	0.60 (1.32)	0.60 (1.32)	0	0
Aerodynamic fairing	0	0	0	0	0	0
Affected items in deceleration module	9.48 (20.90)	7.75 (17.10)	17.00 (37.50)	21.6 (47.70)	14.32 (31.60)	14.32 (31.60)
Total items affected	20.9 (46.15)	23.1 (50.98)	36.6 (80.81)	46.6 (102.73)	34.4 (75.84)	38.1 (84.07)

*Hot wall = internal insulation design
Cold wall = external insultion design

REPRODUCIBILITY OF THE ORIGINAL PAGE IS POOR.

Pressure Vessel Shell - Titanium 6AL-4V annealed

Large probe: Inside diameter = 55.9 cm (22 in.)

Shell thickness = 0.312 cm (0.123 in.)

Critical load = Venus atmospheric pressure
1200 N/cm^2

Mode of failure - buckling

Maximum compressive shell stress at failure =
53,500 N/cm^2 (77,600 psi)

Compressive yield stress allowable = 67,000 N/cm^2
(97,000)

Small probe: Inside diameter = 31.8 cm (12.50 in.)

Shell thickness = 0.177 cm (0.070 in.)

Failure mode, stresses, etc.: same as large probe

Main Separation Flange - Titanium 6 AL-4V annealed

Both probes:

Thickness each hemisphere: 0.635 cm (0.25 in.) large probe
0.47 cm (0.185 in.) small probe

Mode of failure: Tensile yield due to bending

Critical load: Venus entry deceleration 625 - 700 g

Tensile yield allowable: 82,600 N/cm^2 (120,000 psi)

Top Shelf Support Flange - Titanium 6AL-4V annealed

Large probe: Thickness = 0.262 cm (0.103 in.)

Small probe: Thickness = 0.167 cm (0.066 in.)

Both probes: Failure mode - yield due to bending
Critical load = Venus entry deceleration
Allowable = 82,600 N/cm^2 (120,000)

Bottom Shelf Support Flange - Titanium 6 AL-4V annealed

Large probe: Thickness = 0.508 cm (0.20 in.)

Small probe: Thickness = 0.277 cm (0.109 in.)

Both probes: Failure mode = yield due to bending
Critical load = Venus entry deceleration
Allowable = 82,600 N/cm^2 (120,000 psi)

ottom Shelf - Aluminum honeycomb sandwich

Small probe: Core thickness = 1.27 cm (0.5 in.)

Large probe: Core thickness = 2.54 cm (1 in.)

Both probes: Core material = 5056 Al, 0.397 cm (5/32 in.) cell size specification
Density 110 kg/m^3 (6.9 lb/ft^3)

Small probe: 7075-T6 aluminum face sheet, 0.076 cm (0.030 in.) thick

Large probe: 7075-T6 aluminum face sheet, 0.127 cm (0.050 in.) thick

Both probes: Failure mode = yield due to bending

Critical load: Venus entry deceleration

op Shelf - Aluminum honeycomb sandwich

Small probe: Core thickness = 1.27 cm (0.5 in.)

Large probe: Core thickness = 2.54 cm (1.0 in.)

Both probes: Core specification = 5056 al, 0.397 cm (5/32 in.) cell size, density 110 kg/m^3 (6.9 lb/ft^3)

Small probe: 7075-T6 Al face sheet, 0.046 cm (0.016 in.) thick

Large probe: 7075-T6 Al face sheet, 0.053 cm (0.021 in.) thick

Both probes: Failure mode = yield due to bending

Critical load = Venus entry deceleration

ressure Vessel to Aeroshell Adapter - 6AL 4V titanium, solution treated nd aged. Compressive yield allowable: 96,500 N/cm^2 (140,000 psi)

Large probe: Minimum skin thickness - 0.038 cm (0.015 in.)
Failure mode - buckling of conical shell
Critical load axial acceleration, Thor/Delta boost

REPRODUCIBILITY OF THE ORIGINAL PAGE IS POOR.

Maximum skin thickness = 0.208 cm (0.082 in.)
Failure mode = local bending
Critical load = axial acceleration, Thor/Delta boost

Small probe: Constant skin thickness = 0.051 cm (0.020 in.)
Failure mode = local bending
Critical load = axial acceleration, Thor/Delta boost

Description of Atlas/Centaur Pressure Vessel Structure

Tables 4.3-12 and 4.3-13 summarize, for the primary structural items, the sizes (thicknesses or gages) derived by the analysis described in a previous subsection.

TABLE 4.3-12. LARGE PROBE STRUCTURAL DESCRIPTION - ATLAS/CENTAUR

ructural Item	Material	Critical Load Condition	Failure Mode	Dimensions	Thickness
ressure vessel hell	Maraging steel	Maximum pressure and temperature at Venus surface	Buckling (k 0.4)	Inside diameter 68.1 cm (26.8 in.)	0.432 cm (0.170 in.)
ain assembly ange	Maraging steel	Venus entry deceleration	Yield due to bending	See Figure 4.3-3A	0.76 cm (0.30 in.) Each hemisphere
ner shell ange, bottom emisphere	Maraging steel	Venus entry deceleration	Yield due to bending	See Figure 4.3-3A	0.76 cm (0.30 in.)
pper equip-ent support helf	Aluminum 7075-T6	Venus entry deceleration	Yield due to bending	See Figure 4.3-3A	1.56 cm (0.62 in.)
ower equip-ent support helf	Aluminum 7075-T6	Venus entry deceleration	Yield due to bending	See Figure 4.3-3A	1.42 cm (0.56 in.)
pper shelf upport columns	Titanium 6 al-4V	Venus entry deceleration	Local crippling	See Figure 4.3-3A	0.102 cm (0.040 in.)
ower shelf upport ring	Titanium 6 al-4V	Venus entry deceleration	Yield due to bending	See Figure 4.3-3A	0.185 cm (0.073 in.) Skin gauge excep 0.267 cm (0.105 in.) Shelf support lip 0.356 cm (0.140 in.) Local thickness in vicinity of each washer stack
hermal solation washer tack	Titanium 6 al-4V	Venus entry deceleration	Compressive yield	Outside diameter 1.04 cm (0.41 in.) Inside diameter 0.508 cm (0.20 in.)	Not critical
PVM/DM dapter ring	17-4PH H900 steel	Atlas/Centaur launch thrust	Yield due to bending and tension	See Figure 4.3-3A	0.051 cm (0.020 in.) Skin gauge except 0.211 cm (0.083 in.) Aeroshell attach lip and aeroshell end of cone

REPRODUCIBILITY OF THE ORIGINAL PAGE IS POOR.

REPRODUCIBILITY OF THE ORIGINAL PAGE IS POOR.

TABLE 4.3-13. SMALL PROBE STRUCTURAL DESCRIPTION – ATLAS/CENTAUR

Structural Item	Material	Critical Load Condition	Failure Mode	Dimensions	Thickness
Pressure vessel shell	Maraging steel	Maximum pressure and temperature at Venus surface	Buckling (k = 0.4)	Inside diameter 40.6 cm (16.0 in.)	0.25 cm (0.100 in.)
Main assembly flange	Maraging steel	Venus entry deceleration	Yield due to bending	See Figure 4.3-3B	0.31 cm (0.125 in.) Each hemisphere
Inner shell flange, bottom hemisphere	Maraging steel	Venus entry deceleration	Yield due to bending	See Figure 4.3-3B	0.41 cm (0.160 in.)
Upper equipment support shelf	Aluminum 7075-T6	Venus entry deceleration	Yield due to bending	See Figure 4.3-3B	1.52 cm (0.60 in.)
Lower equipment support shelf	Aluminum 7075-T6	Venus entry deceleration	Yield due to bending	See Figure 4.3-3B	1.55 cm (0.61 in.)
Upper shelf support columns	Titanium 6 al-4V	Venus entry deceleration	Local crippling	See Figure 4.3-3B	0.102 cm (0.040 in.)
Lower shelf support ring	Titanium 6 al-4V	Venus entry deceleration	Yield due to bending	See Figure 4.3-3B	0.058 cm (0.023 in.) Skin gauge except 0.157 cm (0.062 in.) Shelf support lip 0.160 cm (0.063 in.) Local thickness, vicinity of each washer stack
Thermal isolation washer stack	Titanium 6 al-4V	Venus entry deceleration	Compressive yield	Outside diameter 0.76 cm (0.30 in.) Inside diameter 0.414 cm (0.163 in.)	Not critical

References

4.3-1. "Dynamic Loads Analysis: Multiprobe and Orbiter Spacecraft," Task No. VI-4, Hughes Aircraft Company Report No. HS 507-0022-88, 23 February 1973.

4.3-2. "Buckling of Thin Walled Doubly Curved Shells," NASA SP-8032, August 1969.

4.3-3. "Strength Tests of Spherical and Hemispherical Shells Under External Pressure," Hughes Aircraft Company TIC 4112.01/338, February 1973 (contained in Volume 15).

4.3-4. "Metallic Materials and Elements for Aerospace Vehicle Structures," Military Standardization Handbook, MIL-HDBK-5B, Dept. of Defense, Washington, D. C., 1 September 1971.

4.3-5. R. F. Crawford and D. B. Schwartz, "General Instability and Optimum Design of Grid-Stiffened Spherical Domes," AIAA Journal, Volume 3, No. 3, March 1965.

4.3-6. "Probe Pressure Vessel Structural Design Analysis," Task No. PB-27, Hughes Aircraft Company Report No. HS 507-0022-121, 17 April 1973.

4.3-7. E. L. White and J. J. Ward, "Ignition of Metals in Oxygen," DMIC Report 224, February 1, 1966, Defense Metals Information Center, Battelle Memorial Institute, p. 6.

4.3-8. L. E. Dean and W. R. Thompson, "Ignition Characteristics of Metals and Alloys," J. American Rocket Society, 31 (1961), pp. 917-923.

4.3-9. P. R. Hill, D. Adamson, D. H. Foland, and W. E. Bressett, "High-Temperature Oxidation and Ignition of Metals," NACA Memorandum RM L55L23b, Langley Aeronautical Laboratory, Langley Field, Virginia, for the National Advisory Committee for Aeronautics (March 26, 1956).

4.3-10. F. E. Littman, F. M. Church, and E. M. Kinderman, "A Study of Metal Ignitions I. The Spontaneous Ignition of Titanium," J. Less-Common Metals, 3 (1961), pp. 367-378.

4.3-11. R. A. Rheims, "The Utilization of Powdered Metals as Fuels in the Atmospheres of Venus, Earth, and Mars," Jet Propulsion Laboratory Technical Report TR-32-1073, February 28, 1967.

4.3-12. R. B. Smith, "Pyrophoricity - A Technical Mystery Under Vigorous Attack," Nucleonics, 14 no. 12, December, 1956, pp. 28-33.

4.3-13. E. S. Indira, S. Sampath, and K. S. G. Doss, "Preparing Titanium for Plating," Metal Finishing, July 1969, pp. 50-55.

4.3-14. L. Domnikov, "Electroplating on Titanium," Metal Finishing, 60, March 1962, pp. 59-62.

4.3-15. A. D. Anderson, "Dust Particle Terminal Velocities in the Venus Atmosphere From 0 to 100 Kilometers," Lockheed Missiles and Space Co. Report LMSC-6-77-67-18, May 1967.

4.3-16. R. J. Roark, Formulas for Stress and Strain, McGraw Hill Book Company, Incorporated, 4th Edition, 1965.

4.3-17. T. J. Kiernan, et al. "The Buckling Strength of Fabricated HY-80 Steel Spherical Shells," David Taylor Model Basin, Washington, D. C., July 1966.

4.3-18. "Pioneer Venus Environmental Test Specification," Hughes Aircraft Company SS 31639-002.

4.4 THERMAL CONTROL

The thermal control design for the Pioneer Venus probes is determined by the environmental and operational parameters of the entire mission. The mission, however, can be broken into three distinct thermally significant phases as follows:

1) Transit to Venus

2) Entry

3) Descent

Diagrams showing the sequence of events for the three phases of the mission are presented in Figures 4.4-1, 4.4-2, and 4.4-3. Differences between the Thor/Delta and Atlas/Centaur missions are noted where they are significant.

Details of the probes thermal control design and associated trades for the transit and entry portions of the mission are presented in other sections of this report. This section deals with the descent phase and with the thermal design of the pressure vessel module. The pressure vessel module is the portion of the probe that must survive exposure to the Venusian environment and operate until impact with the planet's surface. A brief description of the transit and entry thermal design considerations follows to set the stage for the detailed discussion of the descent phase thermal design.

Thermal Control Design Summary

Transit Phase

During the period of transit to Venus, the probes are mounted to the probe bus until approximately 20 days prior to entry (see Figure 4.4-1). At this time the probes are separated from the bus to achieve the desired dispersion in impact sites.

The primary thermal design objective for the transit phase of the mission is to achieve probe temperatures at entry which are at the minimum allowable limit for equipment operation. This is important because the probe pressure vessel module thermal design relies on heat capacity to minimize the temperature rise during the descent through the hot Venusian atmosphere. In addition to achieving minimum temperatures at entry, the transit thermal design must also maintain temperature limits over a broad range of environmental conditions.

Prior to separation from the bus, the probes must withstand the nearly twofold increase in solar intensity during the transit from Earth to Venus. During this time the spacecraft spin axis is maintained normal to the ecliptic plane except for transient trajectory corrective maneuvers (TCM).

REPRODUCIBILITY OF THE ORIGINAL PAGE IS POOR.

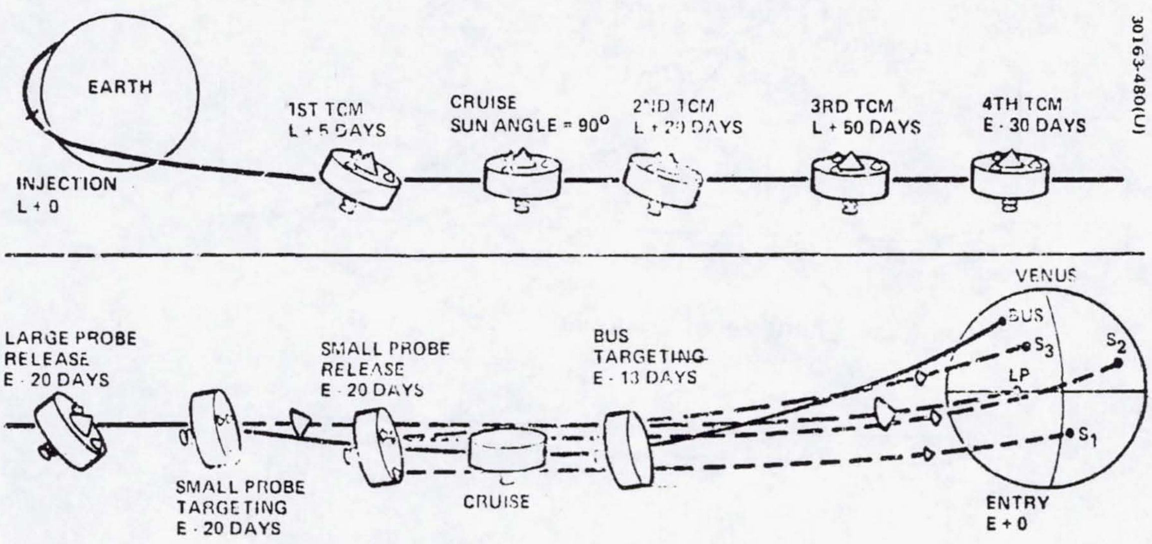

FIGURE 4.4-1. MULTIPROBE TRANSIT PHASE

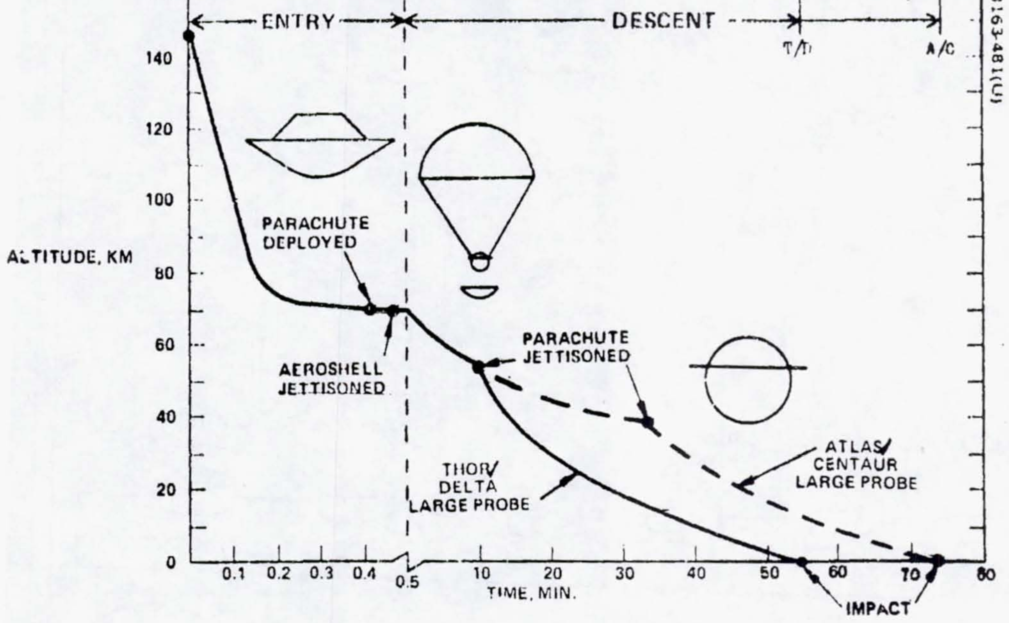

FIGURE 4.4-2. LARGE PROBE ENTRY AND DESCENT PHASE

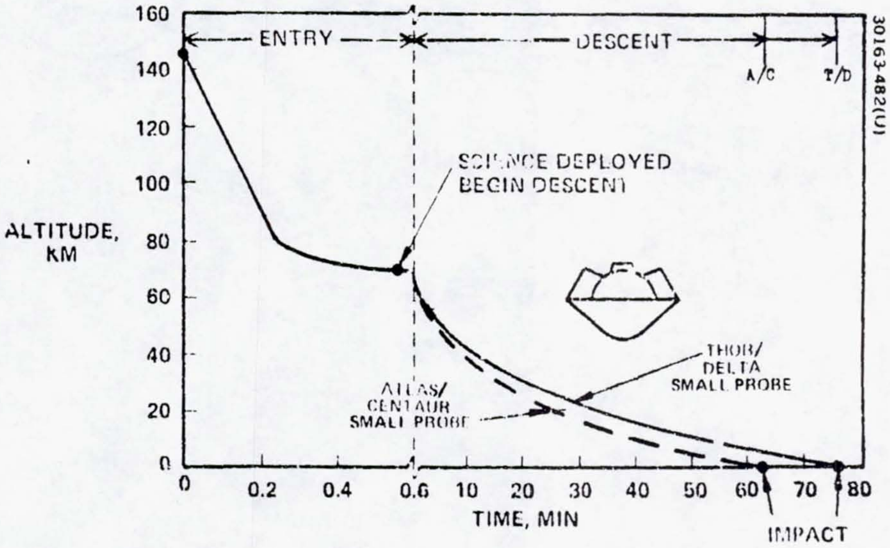

FIGURE 4.4-3. SMALL PROBE ENTRY AND DESCENT PHASE

The probes will be thermally isolated from the spacecraft because the probes and spacecraft must be thermally controlled independently during the 20 day period between separation and entry.

Since the probes are inactive until preseparation checkout, they can be subjected to a rather broad temperature range. The nonoperating pressure vessel module temperature limits during transit are -40°C (-40°F) to 52°C (125°F). These limits are set by the batteries. The minimum heatshield bondline temperature is -73°C (-100°F). Because the design is constrained to provide low temperatures at entry, the temperatures prior to separation also tend to be low. The present baseline design includes probe heaters powered by the spacecraft to maintain the batteries above the -40°C (-40°F) limit during the early periods of the transit phase. These heaters will also be utilized to warm up the batteries to their lower operating temperatures limit of -7°C (20°F) for the preseparation checkout.

Probe targeting requires a separation orientation which results in increased solar illumination of the probes. Because of this, temperatures are above the minimum operating limits at separation. Aside from brief checkouts, only the probe timers will be operating during the period between separation and entry. As the probes approach the planet, the sunline moves towards the spin axis normal resulting in decreased heat loads and, hence, decreased temperatures. The preentry thermal design has been selected to provide a nominal battery temperature of -1°C (30°F). This allows for a ±5°C (10°F) performance uncertainty which must be considered because of the passive nature (i.e., surface finishes) of the design. The minimum battery temperature at entry will be -7°C (20°F), which represents its lower operating limit. The passive design approach has been shown to provide adequate temperature control with a minimum of weight and hardware complexity.

Entry Phase

The prime thermal consideration during entry is the temperature rise created by the high deceleration heat loads. The deceleration module is the main portion of the probes affected by the heat pulse generated during this approximate 0.5 min phase. The upper temperature limit of the bondline between the heatshield and the aeroshell structure sets the deceleration module thermal requirements. This limit is 316°C (600°F). Heatshield thicknesses have been sized to insure that this temperature is not exceeded during entry.

Base heating on the probes is controlled by the addition of ESM. For the large probe, ESM is added to the aft cover which encloses the pressure vessel module within the deceleration module. On the small probes, the ESM is bonded directly to the aft hemisphere of the pressure vessel module.

Because of the short duration of the entry heat pulse and the insulated design of the pressure vessel module equipment, temperatures inside the modules increase an insignificant amount (less than 1°C (2°F) during the entry.

Descent Phase

The thermal design of the Pioneer Venus pressure vessel modules uring descent is dominated by the heat loads imposed by the Venusian tmosphere. The design must isolate the internal science and support payoad from atmospheric temperatures that may reach 770°K at the surface f the planet and permit the equipment to operate for approximately 1 hour n the Venusian atmosphere. Descent profiles for the large and small robe pressure vessel modules are presented in Figures 4.4-2 and 4.4-3.

Two distinct thermal control design concepts have been evaluated to rotect the pressure vessel modules during descent. Both have advantages, ut the choice is constrained by the alternate launch vehicles; the Thor/Delta nd the Atlas/Centaur. For the Thor/Delta design, the primary criterion s the minimization of weight. This lead to a thermal control design which tilized an external insulation system and the inherent heat capacitance of he equipment to achieve acceptable temperatures during descent. For the tlas/Centaur configuration, the minimization of costs through the use of roven and conservative design techniques is the prime criterion. This remise lead to a thermal design which utilized a hot pressure vessel with n internal insulation system augmented by equipment heatsinks to control he descent temperature rise.

Both designs will adequately control the temperatures inside the ressure vessel modules during descent while meeting the detailed requirements and basic criterion specified for the particular launch vehicle. The etailed analytical and test results reported in the following sections are resented in chronological order starting with the Thor/Delta design and rogressing to the Atlas/Centaur design. The Atlas/Centaur design epresents the current system baseline.

Pressure Vessel Module Thermal Control Requirements During Descent

Thor/Delta Design

The basic requirement for the entire Thor/Delta design is the minimization of weight. This translates into requiring some increases in the upper emperature limits for the probe equipment. In addition to equipment baselate upper temperature limits, the thermal design for the pressure vessel modules is determined by the masses, power dissipations, and the environment. For the descent phase of the mission, the baseplate upper temperature limits determine the design. These limits for all probe equipment, along with their respective masses and power dissipations, are presented n Tables 4.4-1 and 4.4-2.

The baseplate upper temperature limit is the maximum allowable emperature that can exist on the unit side of the unit/shelf mounting interface and still achieve acceptable unit performance. In predicting emperatures to compare to these limits, the thermal resistance due o the unit/shelf interface is included in the thermal model. However, no unit internal thermal resistances are considered. This means that an

REPRODUCIBILITY OF THE ORIGINAL PAGE IS POOR.

TABLE 4.1-1. THOR/DELTA LARGE PROBE PRESSURE VESSEL MODULE INTERNAL THERMAL REQUIREMENTS DURING DESCENT

Equipment	Mass, kg (lb)	Power Dissipation, Watts	Baseplate Upper Temperature Limits K (°F)
Science subsystem			
Temperature sensor electronics (two)	0.59 (1.3)	1.0	363 (194)
Pressure sensor electronics (two)	0.82 (1.8)	1.0	353 (176)
Cloud particle size analyzer	3.63 (8.0)	20.0	398 (257)
Solar flux radiometer	1.81 (4.0)	4.0	325 (125)
Planetary flux radiometer	2.27 (5.0)	4.0	325 (125)
Hygrometer sensor electronics	0.40 (0.89)	0.3	373 (212)
Accelerometers	1.13 (2.5)	2.3	363 (194)
Aucreole extinction detector	1.81 (4.0)	2.0	NA
Nephelometer: Source	0.45 (1.0)		
Detector	0.23 (0.5)		333 (140)
Electronics	0.45 (1.0)	2.0	333 (140)
Mass spectrometer	7.71 (17.0)	18.0/24.0	338 (149)
RF subsystem			
Filter (three)	0.77 (1.7)	0	
Receiver	0.91 (2.0)	3.0	338 (149)
Exciter	0.91 (2.0)	4.0	
Hybrid (two)	0.04 (0.1)	0	
Circulator	0.11 (0.25)	0	
Preamplifier	0.11 (0.25)	0.5	
Power amplifier/drive (two)	0.91 (2.0)	33.4	344 (160)
Power subsystem			
Battery packs (three)	6.67 (14.7)	44.2/45.8/44.9	333 (140)
Regulator/current sensor	2.72 (6.0)	20.5/21.6/21.6	339 (150)
Power interface	1.13 (2.5)	1.8	339 (150)
Pyro switch	0.68 (1.5)	0	339 (150)
Command/data subsystem			
Command/data	1.13 (2.5)	4.5	325 (125)
PCU	1.00 (2.2)	Transient only	NA
Equipment subsystem			
Pressure, strain gauge	0.09 (0.2)	1.5	
G-switch	0.45 (1.0)		
Total	38.93 (85.9)	168.0/176.7/175.6	

Switches at 55 km
Switches at 55 km, 20 km
NA = Not applicable

REPRODUCIBILITY OF THE ORIGINAL PAGE IS POOR.

TABLE 4.4-2. THOR/DELTA SMALL PROBE PRESSURE VESSEL MODULE INTERNAL THERMAL REQUIREMENTS DURING DESCENT

Equipment	Mass, kg (lb)	Power Dissipation, Watts	Baseplate Upper Temperature Limits, °K (°F)
Science subsystem			
Nephelometer	0.45 (1.0)	1.0	333 (140)
Magnetometer	0.50 (1.1)	1.0	
Pressure sensor electronics	0.41 (0.9)	0.5	353 (176)
Accelerometer	0.18 (0.4)	1.0	363 (194)
Temperature sensor electronics	0.34 (0.75)	0.5	363 (194)
RF subsystem			
Power amplifier	0.45 (1.0)	17.7	334 (160)
Exciter	0.45 (1.0)	4.0	
Stable oscillator	0.34 (0.75)	0.25	
Command/data subsystem			
Command/data	1.0 (2.2)	3.1	325 (125)
PCU	0.23 (0.5)	Transients only	NA
Power subsystem			
Battery	4.13 (9.1)	9.1	333 (140)
Discharge regulator	1.59 (3.5)	5.2	339 (150)
Power Interface	0.68 (1.5)	0.4	
Pyro switch	0.68 (1.5)	Transients only	339 (150)
Equipment subsystem			
G switch	0.23 (0.5)		
Total	11.66 (25.7)	43.75	

NA – Not applicable

TABLE 4.4-3. ATLAS/CENTAUR LARGE PROBE PRESSURE VESSEL MODULE INTERNAL THERMAL REQUIREMENTS DURING DESCENT

Equipment	Nominal Mass,* kg	(lbs)	Nominal Power Dissipation,** Watts	Baseplate Upper Temperature Limit, K	(°F)
Science					
Temperature sensor electronics	0.3	(0.65)	0.5	325	(125)
Pressure sensor electronics	0.4	(0.9)	0.5	325	(125)
Cloud particle size analyzer	3.65	(8.0)	20.0	325	(125)
Solar flux radiometer	2.25	(5.0)	4.0	325	(125)
IR flux radiometer	2.25	(5.0)	3.0	325	(125)
Hygrometer	0.5	(1.1)	0.25	325	(125)
Accelerometer	1.15	(2.5)	2.3	325	(125)
Mass spectrometer	9.07	(20.0)	12.0	325	(125)
Gas chromatograph	3.6	(8.5)	6.0	325	(125)
Wind/altitude radar	4.0	(8.8)***	0/40.0****	325	(125)
RF subsystem					
Exciter/receiver	2.0	(4.4)	7.0	325	(125)
Filter TXBP	0.45	(1.0)	2.0	325	(125)
Filter harmonic	0.05	(0.1)	0	325	(125)
Circulator	0.11	(0.25)	1.0	325	(125)
Transmitter					
Driver	0.20	(0.45)	9.2	333	(140)
Isolator	0.11	(0.25)	0	325	(125)
Output amplifiers (four units) (per unit)	0.54	(1.2)	18.5	333	(140)
Three-way summer divider (two units) (per unit)	0.09	(0.2)	2.0	325	(125)
Power subsystem					
Battery packs	11.98	(26.4)	67.6 73.6****	325	(125)
Power electronics (discharge regulator and power interface)	6.35	(14.0)	36.0 44.5****	325	(125)
Command/data subsystem					
Command/data box	1.9	(4.1)	6.6	325	(125)
Pyro control unit (PCU and pyro switch)	1.18	(2.6)	Transient only	325	(125)
Equipment subsystem					
Pressure gauge	0.09	(0.2)	0.5	325	(125)
G switch	0.45	(1.0)	0	325	(125)

For science — thermal design mass 90 percent of nominal mass

For science — thermal design power dissipation - 120 percent of nominal power dissipation

Antenna mass of 0.68 kg (1.5 lb) included

Switches at 40 km

internal electrical component will operate at a higher temperature which depends on the dissipation within the component, its thermal mass, and the component to baseplate thermal path. Maximum baseplate temperatures will occur at impact.

Because the descent design relies on the heat capacitance of the internal equipment to control the temperature rise, it is desirable to start the descent at as low a temperature as is possible. The lower operating temperature limit for all pressure vessel module internally mounted equipment is -7°C (20°F). This limit is set by the batteries. The preentry design described above provides equipment temperatures between -7°C (20°F) and 4°C (40°F) at the start of descent. The effect of the entry phase on internal equipment temperatures is insignificant. Considering these factors, the descent design analyses assume that all internal equipment starts the descent at 4°C (40°F), thus allowing for the uncertainties in the preentry analyses. For the small probe, which retains its deceleration module during descent, aeroshell/heat shield initial temperatures are based on the entry analyses. These vary between 38°C (100°F) and 316°C (600°F), depending upon the area of the structure in question.

The descent environment is defined by Venus Atmosphere Model I described in Reference 4.4-1. The descent phase for both probes begins at an altitude of 69 km. The descent ends at zero altitude or at a nominal planet radius of 6050 km. The descent profiles for the large and small probe pressure vessel modules are presented in Figures 4.4-2 and 4.4-3. The initial and final atmospheric temperatures and pressures are 228°K, 0.06 atm, and 767.5°K, 93.7 atm, respectively. The atmospheric composition is assumed to be 100 percent CO_2.

Atlas/Centaur Design

Conservatism and minimum cost are basic requirements for the entire Atlas/Centaur probe design. The temperature limits for the pressure vessel module internal equipment during descent reflect this requirement. All internally mounted equipment will be maintained at less than or equal to 52°C (125°F) during the descent phase, with the exception of the transmitter driver and output amplifiers which are allowed to rise to 60°C (140°F). These numbers reflect design limits which do not require the implementation of special high temperature equipment designs and the associated electrical component qualification testing. Tables 4.4-3 and 4.4-4 present the internal thermal requirements for the large and small probe pressure vessel modules, respectively. In addition to the upper baseplate temperature limits outlined above, unit masses and power dissipations are presented. The definition of upper baseplate temperature limit was presented in the previous section.

The thermal environment for both probes prior to descent is established by the cruise and preentry operations and spatial orientation. As with the Tor/Delta design, it is desirable to start the descent at as low a temperature as is possible. Based on the preentry analyses, 4°C (40°F) has

REPRODUCIBILITY OF THE ORIGINAL PAGE IS POOR.

TABLE 4.4-4. ATLAS/CENTAUR SMALL PROBE PRESSURE VESSEL MODULE INTERNAL THERMAL REQUIREMENTS DURING DESCENT

Equipment	Nominal Mass,* kg	(lb)	Nominal Power Dissipation,** Watts	Baseplate Upper Temperature Limit, °K	(°F)
Science					
Nephelometer	0.45	(1.0)	1.0	325	(125)
Pressure gauge	0.4	(0.9)	0.5	325	(125)
Accelerometer	0.18	(0.4)	1.0	325	(125)
Temperature gauge	0.3	(0.65)	0.5	325	(125)
IR flux detector	0.5	(1.2)	1.0	325	(125)
Stable oscillator	0.34	(0.75)	0.25	325	(125)
RF subsystem					
Exciter	0.64	(1.4)	4.0	325	(125)
Transmitter					
Driver	0.20	(0.45)	9.2	333	(140)
Isolator	0.11	(0.25)	0	325	(125)
Output amplifier	0.54	(1.2)	16.0	333	(140)
Command/data subsystem					
Command/data box	1.54	(3.4)	4.6	325	(125)
Pyro control unit	0.54	(1.2)	Transient only	325	(125)
Power subsystem					
Battery	3.67	(8.1)	16.6	325	(125)
Power electronics (discharge regulator and power interface)	3.18	(7.0)	9.8	325	(125)
Equipment subsystem					
G switch	0.23	(0.5)	0	325	(125)

* For science — thermal design mass 95 percent of nominal mass

** For science — thermal design power dissipation 120 percent of nominal power dissipation been selected as the initial internal equipment temperature at the start of descent. This allows for uncertainties in the preentry analyses. Small probe initial aeroshell/heat shield temperatures are based on the entry analyses and vary between 38°C (100°F) and 316°C (600°F), depending upon the area of the structure in question.

The descent environment is defined by Venus Atmosphere Model I described in Reference 4.4-1. The descent phase for both probes begins at an altitude of 67 km and ends at zero altitude or at a nominal planet radius of 6050 km. The descent profiles for the large and small probe pressure vessel modules are presented in Figures 4.4-2 and 4.4-3. The initial and final atmospheric temperatures and pressures are 235°K, 0.09 atm, and 767.5°K, 93.7 atm, respectively. The atmospheric composition is assumed to be 100 percent CO_2.

Thermal Control Trade and Test Results

The thermal control design of the probe pressure vessel modules during descent (from ~70 km to the surface) is based on the results of a number of trades and tests performed during the study. A chronology of these trades and tests is presented in Figure 4.4-4. This figure will aid the reader in understanding the evolution of the design for both the Thor/Delta and Atlas/Centaur baselines.

The Thor/Delta design was established following the completion of all but one of the trades and tests. This occurred shortly after the midterm review. Because of this, the design reported herein represents a refined version of the design presented at the midterm review.

The Atlas/Centaur probes thermal design for the descent phase of the mission was established based on the results of the final trade. This trade reanalyzed the concepts examined in an earlier trade using a set of more detailed and updated design information. The conclusions that were reached totally revised the probes thermal design. By implementing this major revision, the thermal design helped to achieve the basic Atlas/Centaur requirement of cost minimization.

Insulation Material Selection

This study investigated possible external insulation materials for the large and small probes. The insulation would be used to maintain the probe pressure vessel and payload within an acceptable temperature range during the atmospheric descent phase. The Venusian surface conditions were taken as 100 percent CO_2 at 93.7 atmospheres and 494.3°C. This environment represents a set of requirements that are unique to the Pioneer Venus program; thus, performance data is scarce and material development (towards this application) has not been done.

The activity included a review of the mission requirements, a literature search, a review of previous efforts in this area, and the

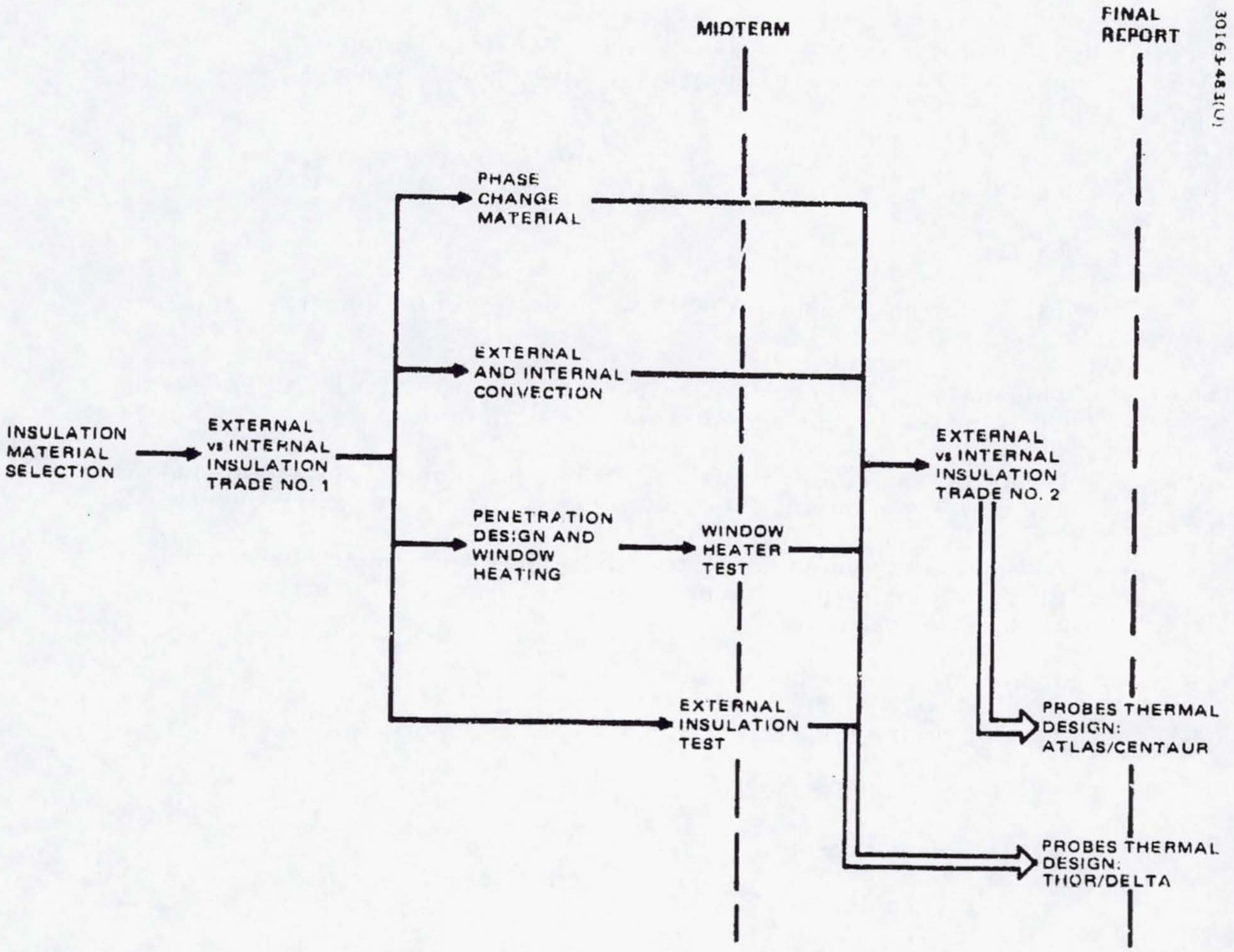

FIGURE 4.4-4. PROBES THERMAL CONTROL DESIGN CHRONOLOGY

collection of information on the materials which were recommended. The materials suggested as candidates in order of preference were:

1) Min-K TE 1400

2) FA Fiberglass

3) Palarite

The following set of requirements were defined for the insulation materials:

- Thermal - The thermal requirements are dictated by the descent phase pressure and temperature time histories
- Dynamic - Various vibration, shock and acoustic environments are generated during the launch, separation, and entry events
- All generic types of insulation materials were considered with the exception of multilayer, which requires a vacuum for efficient performance
- Desirable properties are:

1) Low thermal conductivity

2) Low density

3) Low outgassing

4) Mechanical stability

5) Fabricability

6) Dimensional stability

7) Long term vacuum compatibility

8) High bearing strength

9) High shear strength

10) High specific heat

11) Low cost

The significant properties for the thermal insulation are the same for the Atlas/Centaur and the Thor/Delta launch vehicle.

The search for candidate insulations began in January 1970 and has continued since. Direct contacts were made with approximately 15 vendors and the Defense Ceramic Information Center.

TABLE 4.4-5. CANDIDATE INSULATIONS

	Min-K TE 1400	FA Fiberglass	Paralite
Description	Opacified, fibrous-reinforced submicron molded silica	Felted unbonded fiberglass batt	Carbon-bonded silica fibers
Supplier	Johns-Manville	HITCO	Union-Carbide (AEC)
Chemical composition	>83.2 percent SiO_2 >15.8 percent TiO_2 (computed)		13 percent carbon 87 percent silica (variable)
Maximum operating temperature, °C	760	650	1095
Fabrication technique	Machine or have molded, or both	Wrap	Machine or have molded, or both
Porosity	85 to 88 percent (TE 1200)		75 to 95 percent
Outgassing	Weight loss <2 percent (water only)	Weight loss <2 percent after 10 min at 649° C	
Free standing ρ, g/cc	0.320	0.061	0.112 to 0.512
Conductivity (W/m/°K) at T = 427°C, P = 1 atm	0.0332 ρ= 0.320	0.0779 ρ= 0.096	0.0562 (in argon) ρ= 0.160
ρk	0.0106	0.0075	0,0090
Specific heat, J/kg/°K	0.96×10^3 at 250° C (1301)		0.98×10^3 at 250° C (19.2 percent carbon)
Strength	Composite strength 10 percent — 123 kg/cm^2 J-M data	Not load bearing. Bearing strength — 150 g	Composite strength (ρ = 0.184) 10 percent — 63 kg/cm^2
Dynamic load resistance	Some J-M data		Tested: Vibration 500 Hz Shock 70 g Acceleration 200 g

C-3

Three formal literature searches were employed for this survey:

1) NASA Literature Search No. 20221, "Insulating Materials For Venus Probes", 110 citations

2) NASA Literature Search No. 19426, "Venus Probes", 243 citations

3) DDC Report Bibliography No. 09007, "Venus Probes"

In addition, other library sources such as the "Engineering Index", "Scientific and Technical Aerospace Reports", "International Aerospace Abstracts", and "Applied Science and Technology" were examined.

The only applicable thermal conductivity test data reported in the public literature are the Avco results from the Planetary Explorer program (Reference 4.4-2). In this test program, Min-K TE 1200 was tested in N_2 and CO_2, but the results were brief and inconsistent. In addition, a small amount of conductivity testing was done by Hughes during the Pioneer Venus proposal effort, namely Min-K TE 1400 in N_2.

Based on the past and present literature surveys and the limited test data available, the materials which were recommended and studied in detail are shown in Table 4.4-5, along with a summary of the available information of interest. All materials were initially screened on the basis of their density (ρ) - conductivity (k) product, after which considerations such as installation and important chemical and physical properties were judged. One difficulty with this approach is that the ρk products cannot be evaluated at a representative pressure and temperature condition because virtually all the available data were taken in a vacuum or at one atmosphere of air.

The Min-K and Pararite materials have similar configurations and properties with the Pararite having the lower ρk for the test conditions. The Pararite can be molded in different varieties, all having different densities, porosities and conductivities. The Min-K is opacified so its conductivity should be superior at elevated temperature. The fiberglass, although easier to install, would require care to insure homogeneity because it would be layered.

The conclusion of this study was that Min-K and FA Fiberglass should be given further consideration as possible external insulation materials for the probes. Of these two, Min-K was considered the prime candidate, based principally on its lower expected thermal conductivity.

External Versus Internal Insulation Trade 1

The two basic options of internal versus external insulation protection for the probe equipment were studied in this trade. The two configurations both include a titanium pressure vessel, in one case covered with Min-K TE 1400 and in the other case containing multilayer insulation (MLI), around the internal payload. A vacuum would be provided for the MLI so that its insulating properties far exceed that of the porous Min-K, which is exposed to the high pressure, high temperature CO_2. The advantage in favor of the external insulation is that the shell weight is much lower, due both to the better structural properties at the lower temperatures and the decreased diameter. The advantage in favor of the internal insulation is that insulation weight is lower, due both to the lower density and the smaller thickness required. The tradeoff was based entirely on the resultant weight totals of the shell and insulation, and the combined penetration conductance was parameterized. Cost comparisons and differences in the uncertainties were ignored. The critical assumptions affecting the results and the interpretation of those results are the MLI effective emittance, the shell weight for the internal insulation design, and the penetration conductance.

This configuration tradeoff was done early in a study; the thermal models were very simple. The external model had seven nodes, five of them representing the insulation, one the atmosphere and one combining the capacitance of the equipment payload and the shell. The internal model had only three nodes, including separate nodes for the payload and shell. The probe's initial temperature was 4°C (40°F) and the upper temperature limit was assumed as 52°C (125°F). These values represented the descent operating temperature limits in effect at the time of the trade. The descent profile was 72.4 min long from an altitude of 68 km. The example used was the large probe with a payload weight (including internal structure) of 44.0 Kg (96.9 lb), a power dissipation of 155 W, and a pressure vessel or MLI inner diameter of 53.8 cm (21.2 in.).

The external convection was modeled using the semiempirical relationship

$$Nu = 2 + .60\, Re^{1/2}\, Pr^{1/3}$$

where:
Nu = Nusselt number
Re = Reynolds number
Pr = Prandtl number

The penetration conductance terms (G_p) were handled in a simplified manner. The design concepts for the penetrations for either model were not defined at the time of the study. Consequently, the conductance terms for both models were varied from:

$$0 \le G_p \le \frac{2.64}{X}\, \frac{\text{watts}}{^{o}C} \left(\frac{5}{X}\, \frac{\text{Btu}}{\text{m} - {^{o}F}}\right)$$

where: X = insulation thickness in centimeters (inches)

A conductance value of zero represents a completely insulated sphere. The latter value was assumed to be the upper bound for this trade.

The MLI was characterized by computing an effective emittance based on thickness of the blanket and the interface temperature. The emittance was calculated from a correlation found in the literature which, when appropriately modified, compared well with Hughes empirical data. This function was assumed to hold for layer densities between 16 (40) and 39 (100) layers per centimeter (inch). The corresponding mass densities were 0.03 g/cc (1.92 lb/ft^3) and 0.08 g/cc (4.8 lb/ft^3) respectively. The density of the Min-K was 0.32 g/cc (20 lb/ft^3).

Terminal internal payload temperatures as a function of insulation thickness and penetration conductance are shown in Figures 4.4-5 and 4.4-6 for the external and internal insulation configurations, respectively. Over the selected range of penetration conductances, the thickness requirements are 0.13 to 5.08 cm (0.05 to 2.0 in.) for the MLI and 2.54 to 5.08 cm (1.0 to 2.0 in.) for the Min-K. Figure 4.4-7 shows the sum of the shell and insulation masses as a function of insulation thickness. Masses for both MLI layer densities are shown.

To determine the relative masses of the two candidate configurations, it was necessary to make an assumption of the relative penetration conductances. The penetration designs are different for the two configurations because of different installation and window heater requirements. To simplify matters, only the structural attachment was considered because it was the largest heat path. For the external model the payload was assumed to be attached directly to the penetration at the closure flange, ignoring the resistance through the pressure vessel wall. The resultant conductance was:

$$0.23 \frac{W}{^oC} \left(0.44 \frac{Btu}{hr^oF} \right)$$

which falls within the parameter range:

$$0 \le G_p \le \frac{0.53}{X} \frac{W}{^oC} \left(\frac{1}{X} \frac{Btu}{hr^oF} \right)$$

in Figure 4.4-5, and requires an insulation thickness between 2.54 cm (1.0in.) and 3.05 cm (1.2 in.). The corresponding total mass is between 23 kg (51 lb.) and 25 kg (55 lb.).

For the internal model the penetration was assumed to consist of similar adapter rings extending through the MLI from the closure flange to the equipment shelves. This results in a 15 cm (6 in.) path with an 0.05 cm (0.02 in.) ring thickness for minimum conductance. For maximum conductance, this term was computed by assuming the ring length was equal to the insulation thickness. The parameter range is then between:

$$\frac{1.32}{X} \frac{W}{^oC} \left(\frac{2.5}{X} \frac{Btu}{hr^oF} \right) < G_p \le \frac{2.64}{X} \frac{W}{^oC} \left(\frac{5}{X} \frac{Btu}{hr^oF} \right)$$

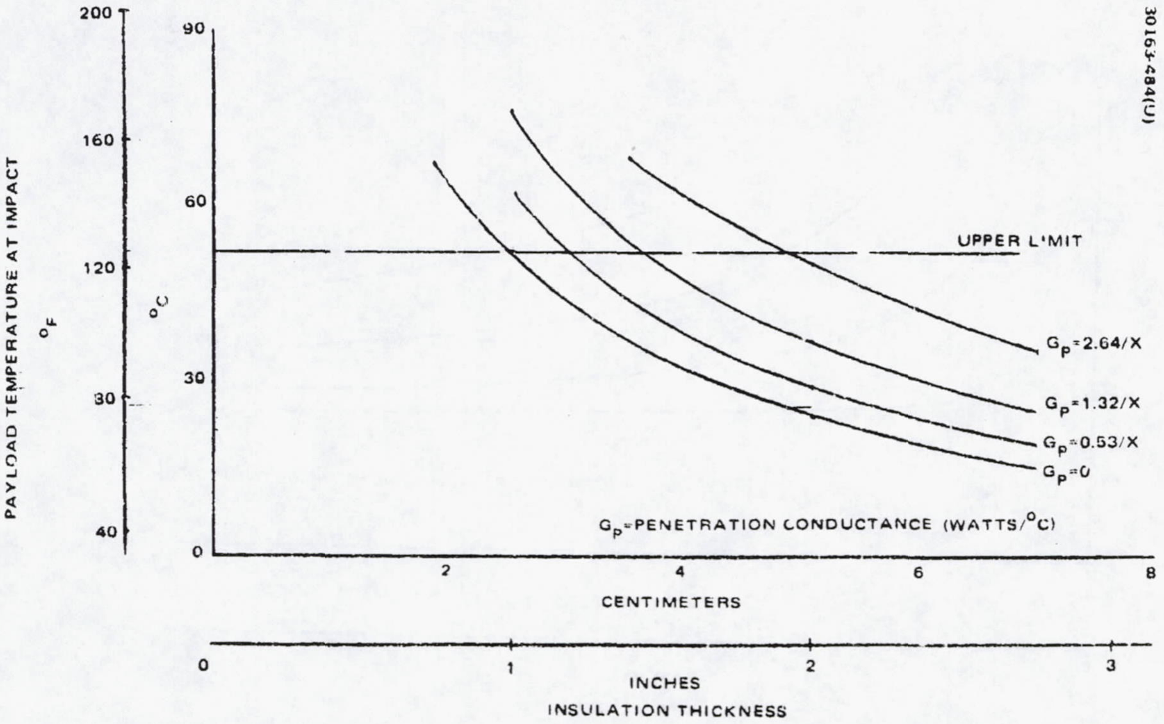

FIGURE 4.4-5. EXTERNAL INSULATION CONFIGURATION – PAYLOAD TEMPERATURES AT IMPACT VERSUS INSULATION THICKNESS

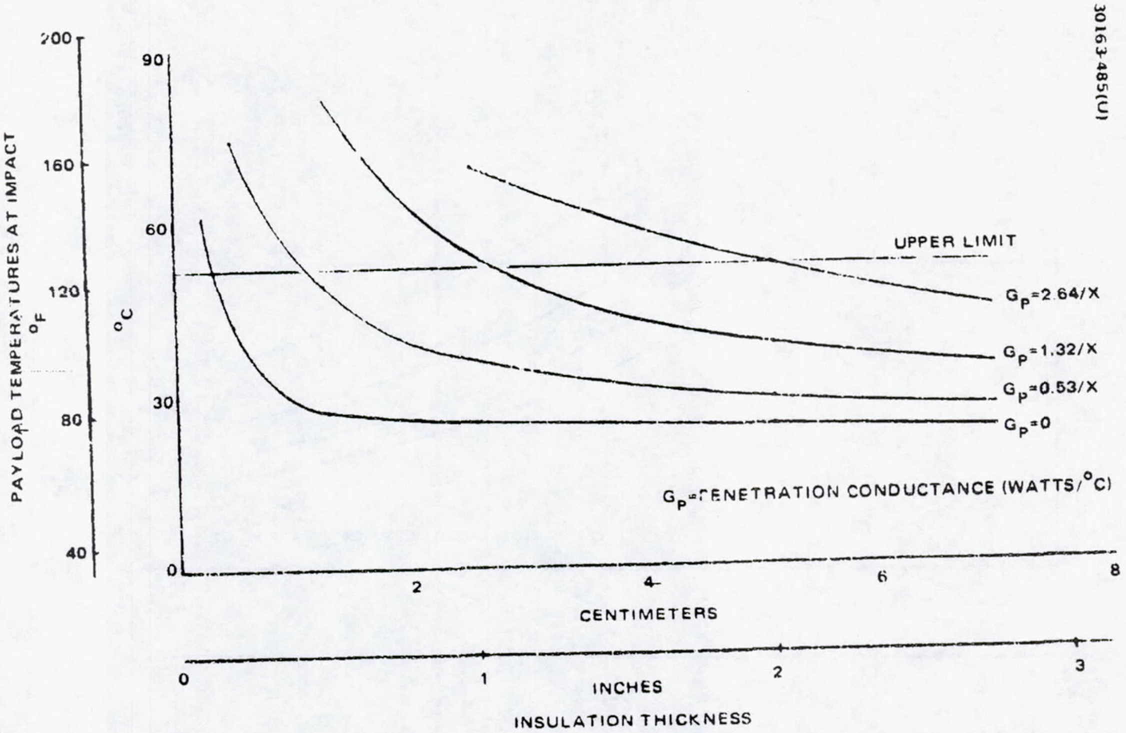

FIGURE 4.4-6. INTERNAL INSULATION CONFIGURATION -- PAYLOAD TEMPERATURES AT IMPACT VERSUS INSULATION THICKNESS

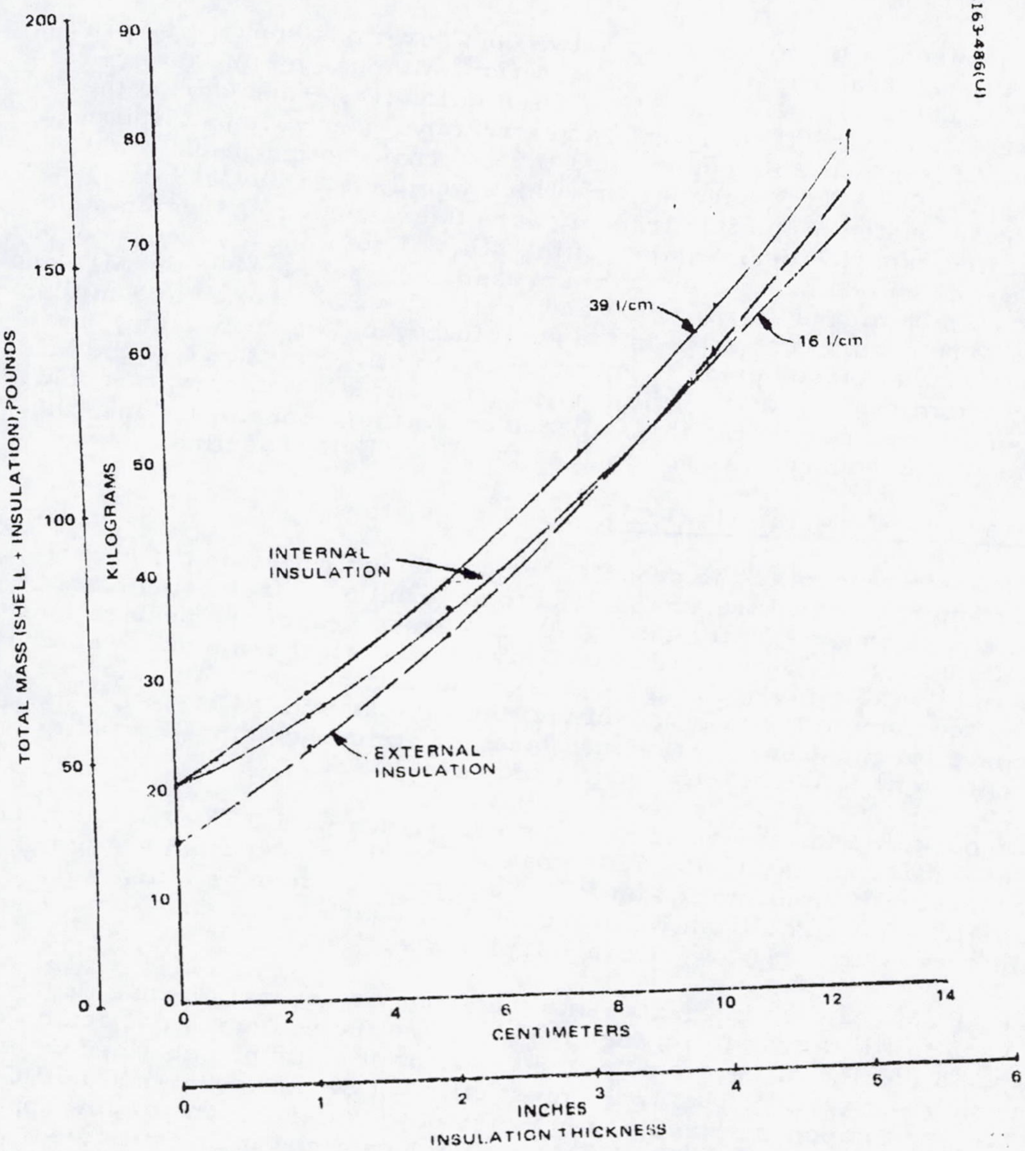

FIGURE 4.4-7. TOTAL MASS (SHELL AND INSULATION) VERSUS INSULATION THICKNESS

ich, from Figure 4.4-6 requires between 2.79 cm (1.1 in.) and 5.08 cm 2.0 in.). The range of total weights is between 28 kg (61 lb.) and 26 kg (79 lb.) or the lower MLI density.

Comparison of the masses of the two configurations shows a favorable nargin for the externally insulated configuration, although for the lower enetration conductance values the MLI design is lighter. Considering the arge number of scientific, electrical, and structural penetrations required n the probe, it is reasonably certain that the external configuration would ave the lower mass. Two other factors which would effect the MLI design ut were not accounted for in this tradeoff were the vacuum requirement and he as-installed expected performance of the MLI. Providing a vacuum could e accomplished by adding a second, thin pressure vessel between the MLI and he payload, which means extra weight and seals. It could also be accomplished y adding a pyrotechnic vent valve in the shell that would be open during the ruise phase and be closed prior to entry. The effective emittance of the MLI s probably optimistic because of the small surface area, high curvature and igh ratio of seams and penetrations. Based on all these considerations, the xternal insulation concept was selected as the Thor/Delta baseline.

Phase Change Materials (PCM).

The basic concept of the probe's thermal design relies on the capacitance of the internal structure and payload to absorb the energy being dissipated by the payload and coming through the pressure vessel and penetrations from the atmosphere. The approach is designed to limit the amount of entering energy to an allowable level through the use of insulation. An alternate approach is to augment the heat capacity of the payload with PCM. PCM has been proposed for most of the previous planetary atmospheric probe studies because of its very efficient technique to add capacitance.

Although there has been some flight experience with PCMs, it has been with the less efficient materials and the package designs have been heavier than necessary. The information on PCMs and package designs which was used in this tradeoff came from Reference 4.4-3, which documents some development work directed towards this application.

The PCM could be integrated into the probe by several means. It could be used to fill the voids between the shell and the equipment, it could be contained along the inboard side of the shell, or it could be contained within the honeycomb shelves. Probably the most efficient design would use the PCM only for the few components having either high power dissipations or low upper temperature limits, or both. The PCM could be contained in an integrated package with the component, sharing the base plate.

This analysis assumed that the PCM was attached to specific internal components. The PCM was incorporated into the large probe thermal model including a program subroutine which accounted for the specific and latent heat of the material. PCM was only used on the top shelf, because of its higher power to mass ratio.

The PCM selected for the tradeoff was lithium nitrate trihydrate ($LiNO_3 \cdot 3H_2O$), which appears to be the best material for this application. Its significant properties are as follows:

Melting temperature	29.9°C (85.8°F)
Heat of fusion	$3.02 \times 10^4 \frac{J}{kg}$ (127.3 BTU/lb)
Density (solid/liquid)	1.55/1.43 g/cc (96.8/89.3 lb/ft^3)

The criterion for the tradeoff was the sum of the masses of the pressure vessel insulation and PCM required to limit the inside of the probe to 52°C (125°F) at impact. The PCM mass includes an estimate of the container and metallic filler material requirements. Because of the small volumes of PCM involved, there is no need to include a mass penalty for extra volume in the pressure vessel. For estimation purposes the PCM interface area used was 7.62 by 20.32 cm (3 by 8 in.), which was representative of the power amplifier.

The baseline design used for comparison was the one used at the mid-term review, which had 7.5 kg (16.5 lb.) of insulation. Adding various incremental masses of PCM yielded the results shown in Table 4.4-6. No mass was allocated for filler material because of the small PCM thickness. The optimum combined mass appears to be at slightly over 0.9 kg (2 lb.) of PCM, and represents a weight savings of approximately 2.7 kg (6 lb.) over the baseline design.

PCM was considered on the Thor/Delta probes because of the mass savings indicated above. However, significant developmental costs are expected if PCM is used. Because of this PCM was not made part of the baseline Thor/Delta design but remained a possible alternative control technique. With the adoption of the Atlas/Centaur launch vehicle and the associated low cost design philosophy, PCM was dropped from further consideration because of the high expected costs.

TABLE 4.4-6. PCM AND INSULATION MASS, kg(lb)

PCM	0.45 (1.0)	0.90 (2.0)	1.36 (3.0)
Filler	0	0	0
Container	0.16 (0.36)	0.19 (0.41)	0.21 (0.46)
Total	0.61 (1.36)	1.09 (2.41)	1.57 (3.46)
Insulation	5.31 (11.7)	3.90 (8.6)	3.58 (7.9)
Total	5.92 (13.06)	4.99 (11.01)	5.15 (11.36)

External and Internal Convection

Convection is a prime mode of heat transfer during the descent phase of the mission. Determining the appropriate methods of quantifying these convection parameters was an important part of the analytical effort. This section reports on how the ~~external~~ and internal convection terms were calculated for the analytical models.

External Convection. The Venusian atmosphere represents the primary heat load on the probes. The convection heat transfer between the atmosphere and the probes must be quantified. For the large probe, the convection coefficient was predicted using the semi-empirical relationship

$$Nu = \frac{hd}{k} = 2. + 0.60 \, Re^{1/2} \, Pr^{1/3}$$

where

Nu = Nusselt number
h = convection coefficient
d = sphere diameter
k = gas conductivity
Re = Reynolds number
Pr = Prandtl number

which is for forced convection over a sphere submerged in an infinite fluid. In this application the coefficient gets as high as $17.6 \times 10^{-3} W/cm^2 - {}^{o}C$ (31 $BTU/hr\text{-}ft^2 - {}^{o}F$). This average coefficient was used for all positions on the probe surface.

For the small probe, the external areas of the heatshield and the aeroshell, as well as the pressure vessel, must be convectively coupled to the atmosphere. For the heatshield and aeroshell, the heat transfer coefficient to the Venusian atmosphere was assumed to vary linearly with time from 0.57×10^{-3} to $28.3 \times 10^{-3} W/cm^2\text{-}{}^{o}C$ (1 to 50 $BTU/hr\text{-}ft^2\text{-}{}^{o}F$). The coefficients between the aeroshell, the lower pressure vessel hemisphere, and the enclosed gas, as well as between the enclosed gas and the atmosphere, were assumed to vary linearly with time from 0.57×10^{-3} to $2.83 \times 10^{-3} W/cm^2\text{-}{}^{o}C$ (1 to 5 $BTU/hr\text{-}ft^2\text{-}{}^{o}F$). These values were based on the average coefficients calculated for the large probe. The coupling for the upper pressure vessel hemisphere was determined using the semi-empirical relationship for a sphere.

Internal Convection. The baseline design has assumed an internal atmosphere of air at 1 atm pressure. This condition exists because it is the local environment when the probe is sealed prior to launch. Although this is a free convection environment and the probe is very densely packaged, the temperature differences between the pressure vessel and the components get large enough to make convection significant.

Because the geometry inside the probe is a variety of flat and curved surfaces at different angles to one another, the coefficients cannot be predicted very accurately. The applicable correlations have one of three forms:

1) $Nu_x = 1 \; (Gr_x \lesssim 10^3)$

2) $Nu_x = C_1 \, Gr_x^{1/4} \, Pr^{1/4} \; (10^3 \lesssim Gr_x \lesssim 10^5)$

3) $Nu_x = C_2 \, Gr_x^{1/3} \, Pr^{1/3} \; (10^5 \lesssim Gr_x \lesssim 10^7)$

where

Nu_x = Nusselt number, based on separation distance, $\underline{\underline{x}}$

Gr_x = Grashof number, based on separation distance, $\underline{\underline{x}}$

Pr = Prandt number

C_1 and C_2 = constants or functions of characteristic lengths

The subscript x refers to the separation distance between the surfaces. The appropriate correlation is selected based upon the value of the Grashof number (Gr_x) and the orientation of the surfaces with respect to the gravity field. The first relationship (i.e., $Gr_x \lesssim 10^3$) applies to surfaces that are close together (compared to the characteristic length of the surfaces). Here the mode of heat transfer is actually gas conduction rather than free convection. The third relationship applies to surfaces that are separated by a large distance. The second relationship holds for the majority of cases where an intermediate amount of separation exists compared to the characteristic length. This represents the conditions which are usually found within the probes. A notable exception is the hot insulation retainer over top shelf. This condition results in only gas conduction without free convection.

A number of coefficients have been computed for different orientations, separation distances, characteristic lengths, and temperature differences. The results indicated a range of convection coefficients between two surfaces (h_x) of 0.03×10^{-3} W/cm^2-°C $\leq h_x \leq .57 \times 10^{-3}$ W/cm^2-°C (0.06 BTU/hr-ft^2-°F $\leq h_x \leq 1.0$ BTU/hr-ft^2-°F). The convection coefficient between a surface and the internal air (h) can be represented as twice the coefficient between two surfaces (h_x).

For most of the descent phase the coefficients would be close to zero because the temperature differences between surfaces are small. Because of this, most values of h_x fell in the lower middle portion of the range. For purposes of analysis, one value of $h = 2 \, h_x$ was conservatively selected for use in the models. This value was $h_x = 0.28 \times 10^{-3}$ W/cm^2-°C (0.5 BTU/hr-ft^2-°F) which is equivalent to an $h = 0.57 \times 10^{-3}$ W/cm^2-°C (1.0 BTU/hr-ft^2-°F). This could be considered to be a one sigma high value.

The effect of varying the internal convective coefficient (h) has been investigated using the Thor/Delta large probe model. The effect of increasing and decreasing the value of h on the thickness and mass of external insulation needed is shown in Table 4.4-7. Details of the baseline design using an h .57 X 10^{-3} W/cm^2-°C (1.0 BTU/hr-ft^2-°F) can be found in the Thor/Delta and Atlas/Centaur description Sections.

Two additional design considerations are imposed by the presence of the warm air atmosphere inside the probes during descent. The first of these is that all equipment must be capable of operating under conditions of 1 to 2 atm of pressure during descent. The increase in internal pressure will be caused by the heating of the air during descent. At this time, this condition does not appear to create any problems.

The second effect which must be considered is the heating of low mass (i.e., approximately zero thermal capacitance) pieces of hardware by the air. Low mass items (such as single wires or electrical components) which are not heatsunk to structure or equipment will tend to track the air temperature. This could induce high temperature failures near the end of descent when the internal air temperature reaches approximately 232°C (450°F). The design will insure that all internal pieces of equipment are well heatsunk so that this problem can be totally avoided.

Penetration Design and Window Heating

Penetration. The penetrations, or heat shorts through the insulation, fall into three categories: science, structure, and electrical connectors and electrical connectors and leads. The effect of these penetrations on the shell and ~~com~~component temperatures is a strong function of the insulation thickness, since the thickness largely determines the ratio of heat entering the probe. These penetrations were designed and integrated to minimize their heat transfer as much as possible.

TABLE 4.4-7. INSULATION MASS VERSUS INTERNAL CONVECTION COEFFICIENT

h, W/cm^2-°C Btu/hr-ft^2-°C	Insulation Thickness, cm (in.)	Insulation Weight, kg (lb.)
0	0.51 (.20)	1.6 (3.6)
0.57 X 10^{-3} (1.0)	1.14 (.45)	3.7 (8.1)
0.85 X 10^{-3} (1.5)	1.42 (.56)	4.6 (10.2)

Modeling of the penetration heat transfer was based on conduction only. Although some heat will be transferred by convection and radiation from the windows, the amount is negligible by comparison. Also, some energy will enter through the pressure taps and mass spectrometer inlet, but this is considered to be insignificant. The penetration values used in the models varied with insulation thickness, external convection coefficient, conductivity, and altitude.

Windows and Window Heating. A substantial analytical effort was directed toward the design of the various scientific instrument windows and the determination of their heating requirements. From a thermal control standpoint, the two prime concerns were: 1) limiting the heat transfer through the insulation cutouts caused by the windows, and 2) minimizing the power requirements for maintaining the outer windows surfaces at a high enough temperature to prevent condensation from the atmosphere. Because no firm requirement existed, it was decided to maintain the windows 6°C (10°F) higher than the local atmospheric temperature. These two objectives are interrelated, and they were treated jointly.

The two general window mounting configurations considered in the analyses were:

1) Windows mounted in the plane of the pressure vessel
2) Windows mounted on short tubes extending outboard into the atmosphere.

A window mounted directly in the plane of the pressure vessel has a relatively good heat conduction path to the high thermal capacitance of the pressure vessel wall. Because of this, window heater requirements are large and heat loss reduction is important. To reduce losses and heater size, a window is designed to have a minimum diameter, a thin inner window is added to minimize the convection and radiation to the internal payload, the window support flange is coupled to the external environment to raise its sink temperature, and a small annulus of insulation is added inside the pressure vessel doubler area. Additional structural thickness is also required around pressure vessel mounted windows to handle the temperature gradients which exist.

Mounting a window on short tubes extending outboard into the atmosphere thermally decouples it from the pressure vessel. This lowers the heater power requirements. Another benefit from this approach is the lowering of the temperature gradients in the pressure vessel which minimizes the thickness required to meet structural criteria. As a result, most of the windows are designed in this fashion, although each has a unique design.

Window heater power must be sufficient to raise the temperature of the window mass and account for the losses. The losses consist of the following:

1) Convection and radiation to the atmosphere

2) Convection and radiation to the payload

3) Conduction to the support structure

Detailed computer models of the window were constructed for four different designs which represent the Thor/Delta baseline configurations:

1) Nephelometer source; sapphire, 0.89 cm (0.35 in.) total diameter, 0.15 cm (0.06 in.) thick, brazed window, O-ring seal at fitting (Figure 4.4-8)

2) Planetary flux; CVD Zn Se, 2.79 cm (1.1 in.) total diameter, 2.03 cm (0.8 in.) thick, brazed window, O-ring seal at fitting (Figure 44.-9)

3) Solar flux; sapphire, 7.62 cm (3.0 in.) by 2.54 cm (1.0 in.), 0.32 cm (0.125 in.) thick, O-ring seal, sapphire inner window (Figure 4.4-10)

4) "Typical" remote window, similar to small probe nephelometer, cloud particle, and aureole windows; sapphire, 3.56 cm (1.4 in.) total diameter, 0.51 cm (0.2 in) thick, O-ring seal, sapphire inner window (Figure 4.4-11)

An important model parameter is the conductance across the O-ring and seat interface. Test results indicate a value of 0.02 W/°C (0.04 BTU/hr-°F) per circumferential inch of O-ring should be used in the model. The effect on the required window heater power of doubling this conductance was also evaluated. Another parameter which was examined was the effect of an atmosphere whose temperature was 11°C (20°F) higher at all altitudes. Table 4.4-8 presents the results of these analyses. The heater powers shown are constant values rather than varying with altitude because there was no appreciable power savings realized by incorporating variable heaters into the design.

Window heating requirements for the Atlas/Centaur configuration (hot pressure vessel and internal insulation) are expected to be less severe than for the Thor/Delta configuration (external insulation and warm pressure vessel) presented above. This is because conduction losses to the pressure vessel sink are reduced significantly since the vessel tracks the atmospheric temperature. The window design will be similar to that outlined above except some of the conduction isolation (i.e., the protruding mounting tubes) will be eliminated. The current Atlas/Centaur baseline budgets the same amount of power per window for the heaters as the Thor/Delta baseline for the sake of conservatism.

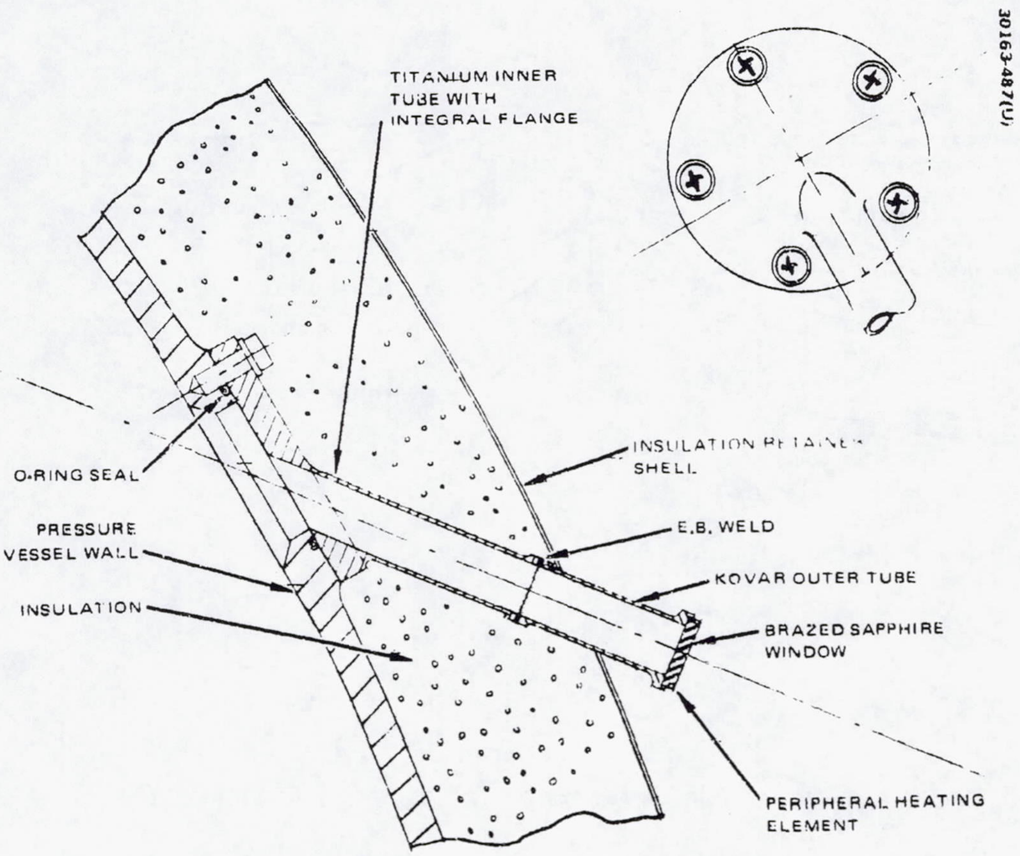

FIGURE 4.4-8. NEPHELOMETER SOURCE WINDOW

REPRODUCIBILITY OF THE ORIGINAL PAGE IS POOR

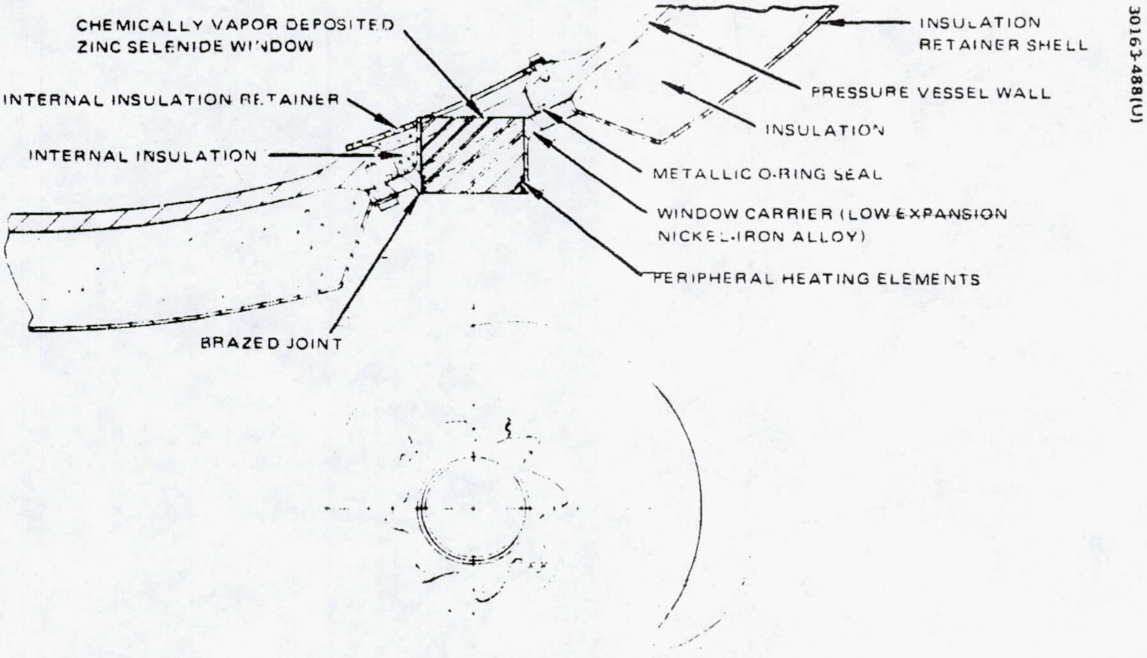

FIGURE 4.4-9. PLANETARY FLUX WINDOW

REPRODUCIBILITY OF THE ORIGINAL PAGE IS POOR.

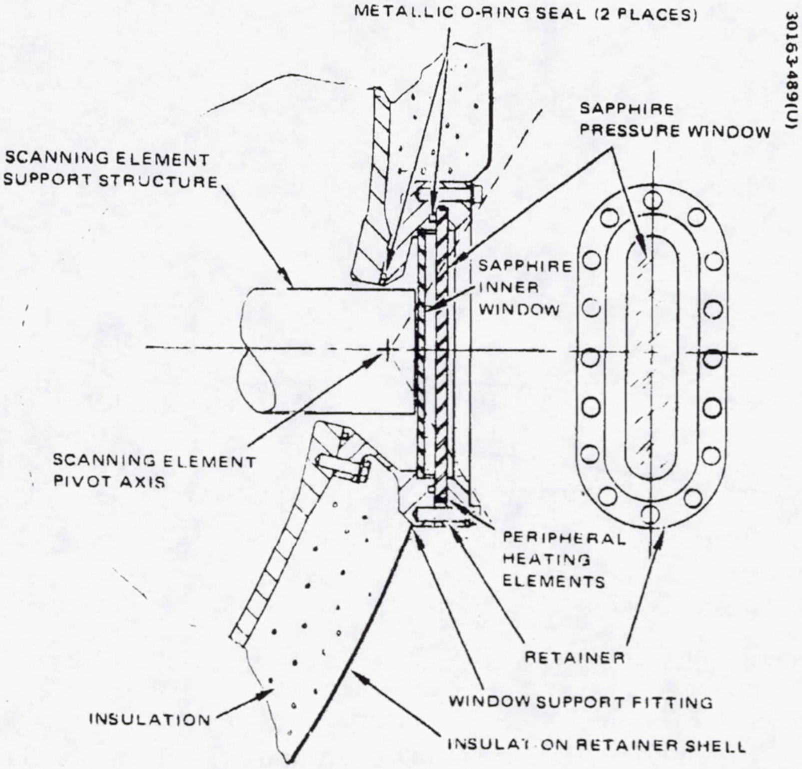

FIGURE 4.4-10. SOLAR FLUX RADIOMETER WINDOW

REPRODUCIBILITY OF THE ORIGINAL PAGE IS POOR.

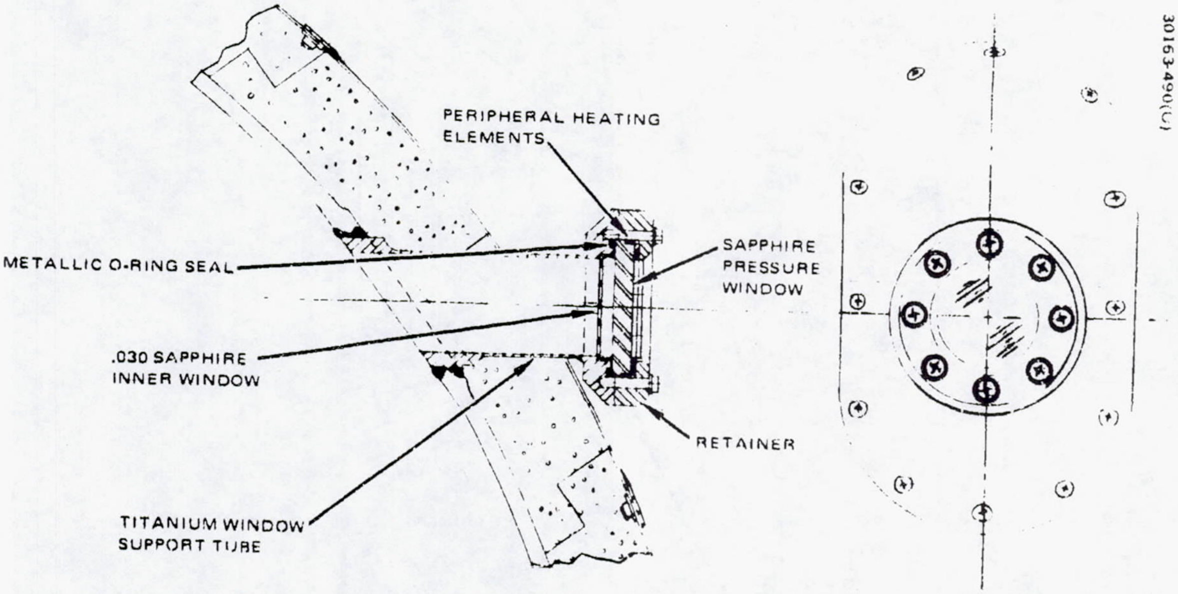

FIGURE 4.4-11. TYPICAL REMOTE WINDOW

REPRODUCIBILITY OF THE ORIGINAL PAGE IS POOR.

TABLE 4.4-8. SUMMARY OF LARGE PROBE WINDOW HEATER REQUIREMENTS — THOR/DELTA BASELINE

Window	Baseline Heater Power, W	Atmosphere 11°C (20°F) Hotter, W	Two Times O-Ring Conductance, W
Nephelometer source	2.2	~2.2	~2.2
Solar flux	24.3	25.1	30.9
Planetary flux	27.0	27.3	33.3
Typical remote window	12.5	13.0	14.0

Window Heater Test

A series of tests was run with a science instrument window and window heater in a simulated Venusian descent environment. The objectives of the tests were to verify the structural design of the window, to verify the integrity of the pressure seal, and to determine the thermal conductance between the windows and the mounting fixture. The conductance was an important parameter in the estimation of the power requirements for the probe window heaters.

The window which was built and tested was an early design of a pressure vessel-mounted concept. A 1.91 cm (0.750 in.) diameter, 0.32 cm (0.125 in.) thick sapphire window was mounted to a titanium fixture, which was mounted to an aluminum heat sink. The window was held in place with five screws and had a metallic O-ring. The heater was constructed by wrapping about six turns of constantan wire around the edge of the window. Two thermocouples were located on the surface of the window, and 13 other thermocouples were located in the gas, on the heat sink, etc. The assembly was surrounded with Min-K insulation to reduce heat losses, and was tested in a pressure chamber.

Seven steady-state tests with three heater power levels each were run, followed by four transient tests using the same descent profile used in the insulation tests. The steady-state test conditions varied from 1 atm and 66°C (150°F) to 56 atm and 432°C (810°F). The power levels varied from zero to 40 W. The transient tests had power levels of zero, 40, and 60 W.

The structural design of the window assembly withstood repeated descent profiles with no damage, verifying adequate design. The seal design needs some refinement, since a small amount of leakage was observed in the last two transient tests. This leakage occurred just as the tests were completed when the heaters were being turned off.

The O-ring conductance was estimated from the steady-state data only, because in the transient tests the heater appeared to expand faster than the window and thus the actual heat input is unknown. A heat balance of the test fixture was made, accounting for radiation and convection from the window, conduction from the screws, conduction to the adjoining structure, and convection to the surrounding gas. The estimation of the last term was approximate and was significant to the computed conductance. The resulting values ranged between 0.005 W/°C (0.01 Btu/hr -°F) and 0.06 W/°C (0.12 Btu/hr -°F). A similar series of tests with an updated window design is in work.

External Insulation Test

A series of tests was run with the objective of measuring the transient response of two candidate insulation materials in a simulated Venusian descent environment. The two materials were Min-K TE 1400 and FA fiberglass, which for these tests were applied to a solid aluminum sphere (separately) and exposed to a typical large probe descent profile. The test specimen were each tested twice in a pressure chamber whose walls were also insulated on the inside. CO_2 was bled into the chamber and heated, reaching a nominal environment of 768°K and 93.7 atm.

These tests were defined as critical early in the program because the thermal performance, or effective thermal conductivity, of the insulation in this environment and in this configuration was not known with any confidence. This knowledge was important to both weight and size estimates, particularly for the Thor/Delta version.

The size of the test specimen was dictated by the usable internal diameter of the chamber, which was approximately 25 cm (10 in.). A pretest analysis was performed to estimate the diameter and material of the sphere, and thickness of the insulation required to give approximately the same temperature gradient in the ~~test~~ insulation as in the large probe. A 17.8 cm (7.0 in.) diameter aluminum 6061-T6 sphere was selected, with a Min-K thickness of 3.2 cm (1.25 in.). The fiberglass was to be tested at the same thickness, with a test density of 0.16 g/cc (10 lb/ft^3). The Min-K was machined into two hemispheres from blocks which were bonded together, and then fitted over the sphere with a step joint in the seam. The fiberglass was layered over the sphere in gores and compressed and held in place with fiberglass cord.

The gaseous CO_2 was manually regulated into the chamber from high pressure bottles and heated with firerod heaters. The gas temperatures were automatically controlled for the fiberglass tests but manually controlled for the Min-K tests. The descent profile had a time of 72.4 min from 68 km. Each specimen was instrumented with nine thermocouples, which were located near the top, bottom, and side of the sphere and measured the inner surface, midpoint, and outer surface temperatures of the insulation. Five thermocouples measured the gas temperatures around the specimen, and two pressure transducers with different ranges were used. Most of the data was recorded on magnetic tape and reduced by computer.

The tests were started at room temperature. The pressure simulation was generally within 3.45×10^4 N/m^2 (5 psi) of the desired value. The temperatures were generally too high during the first phase of the tests, and would fluctuate ±28°C (±50°F) during the second phase. For the fiberglass specimen the density and thickness were difficult to control because of the configuration and the compression of the material. The Min-K was carefully machined but did not fit tightly around the sphere because of the instrumentation leads.

The Min-K sphere temperature reproducibility was excellent, but the temperatures were much higher than expected. The average temperature rise was 48°C (87°F). Analysis predicted only an 18°C (32°F) rise. Inspection of the Min-K after the test showed a discoloration pattern around the seam, indicating the possibility that it was partially open and that a heat short of the gas developed through the insulation. The fiberglass sphere temperature rose an average of 60°C (108°F), but the fiberglass density for the test was only about 20 percent of the Min-K and, hence, a greater rise was expected. The lack of success in correlating the analytical data with the empirical data and the apparent sensitivity of Min-K to seam construction makes the use of Min-K risky. These data were not considered usable, and if the tests were repeated a great deal of attention would have to be given to the attachment of the insulation to the test specimen, the instrumentation, and the environmental simulation.

External Versus Internal Insulation Trade 2

The evolution of the thermal control design for the probes during descent eventually led to a reexamination of the external versus internal insulation concepts originally studied in the trade reported in an earlier subsection. The major motivation was to save the developmental and fabrication costs associated with the external insulation system which appeared to be much higher than originally expected. The objectives of this second trade were to determine the weight and cost implications of considering an internal insulation design concept. Detailed thermal models of the large and small probes for each concept were analyzed under a consistent set of performance ground rules. Results were compared on the basis of the mass required to achieve acceptable temperatures.

The details of the design were more fully developed and understood than they were in the earlier trade and multilayer superinsulation had been discarded as an internal candidate because of the vacuum requirements necessary for adequate performance. Evacuating the probes was undesirable because of possible corona generation during descent, reliability problems with the evacuation schemes, and the additional unit and science requirement of vacuum operation capability. A vacuum surrounding the superinsulation could be provided by adding a thin pressure vessel between the multilayer insulation and the payload. This was not considered because of the additional weight requirements and the complexity of joining and integrating two concentric spherical pressure vessels. FA fiberglass was selected for the internal insulation material because of its low, 1 atm conductivity values, its relatively low weight, and the fact that it is a flexible rather than a rigid material. Min-K remained as the external insulation material because of its superior performance under conditions of high temperature and pressure.

The earlier trade had shown that the pressure vessel weight increased dramatically when the vessel radius was increased to provide room for the internal insulation (the increase is by the square of the radius). Because of this, it was decided that temperature control for the internal equipment would be accomplished by a combination of two techniques. These were:

1. A fixed amount of internal FA fiberglass insulation
2. Beryllium heatsinks to provide additional internal thermal capacitance

The heatsinks could be fit into the void areas of ~~the~~ probe without further increases in the pressure vessel size. Beryllium heatsinks were proposed because of the high thermal capacitance of ~~the~~ material which makes it ideal for this application. Fine tuning of the design would be accomplished by the addition or subtraction of heatsink material. Hence, the internal insulation/heatsink design was conceived.

Several parameters determined by the thermal design hardware were held constant throughout the trade. The first of these was shelf to pressure vessel isolation. An isolation mount was designed which conductively decoupled the shelves from the pressure vessel. Details of the design can be found in a later subsection describing the Thor/Delta baseline thermal design. For the sake of the analysis, it reduced the shelf to pressure vessel conductance by approximately 85 percent, thus minimizing a prime heat leak into the equipment. This isolation was incorporated into both the external and internal insulation models.

The second constant hardware parameter applied only to the internal insulation/heatsink models. As was pointed out earlier, the pressure vessel weight increases rapidly with increasing radius. To fix the maximum size of the vessel, a maximum internal insulation thickness of 1.27 cm (0.05 in.) was selected as a baseline. Beryllium heatsink mass, rather than additional internal insulation thickness, would be added to decrease the temperatures at impact within the desired limits.

The trade was done using the detailed computer models. These models were made up of between 50 and 100 nodes, depending upon the configuration being studied; accounted for conduction, convection, and radiation coupling; and had variable input parameter capability.

The Thor/Delta probes were analyzed first. The launch vehicle dependent design parameters were held constant for comparing the external and internal insulation systems. These included:

1. The internal power dissipation
2. The internal equipment masses
3. The descent profile

The equipment baseplate upper temperature limits were assumed to be 52°C (125°F) for all equipment and science, with the exception of the output amplifiers and drivers which had an upper limit of 60°C (140°F). These limits could not be exceeded prior to impact.

The four Thor/Delta thermal models (large and small probes; external sulation and internal insulation/heatsink) were run to determine the thermal ontrol mass required to meet the upper temperature limits. Table 4.4-9 resents the Thor/Delta results. It can be seen that for a slight mass penalty n the large probe and approximately twice the thermal control mass on each mall probe an internal insulation/heatsink design could be implemented into e Thor/Delta baseline. The results of this study were consistent with the arlier trade. The external insulation concept remained the baseline since ass minimization was the key requirement for the Thor/Delta design.

The basic concepts for the Atlas/Centaur design were different, owever. Here, the minimization of cost and the use of proven and conser-ative design techniques were of paramount importance. Internal insulation/eatsink computer models for the Atlas/Centaur probes were constructed. These models reflected the Atlas/Centaur power dissipations, masses, and escent profiles. External insulation models were not constructed. Instead, he Thor/Delta insulation thickness values were used directly and the insula-ion masses were scaled to account for the larger Atlas/Centaur pressure essel size. Hand calculations indicated that the use of the Thor/Delta nsulation thicknesses for the Atlas/Centaur probes were reasonable estimates onsidering the descent profile changes and the increased mass of the probes.

The results for the Atlas/Centaur probes are presented in Table 4.4-10. Approximately twice as much total thermal control mass is needed in the large robe if an internal insulation/heatsink system is used. A 15 percent mass lecrease is realized on the small probes by using the internal concept. If he total probe compliment is considered (i.e., one large and three small), he total weight penalty resulting from the use of the internal insulation/heat sink design for all probes is 1.2 kg (2.6 lb) or approximately 6 percent of the otal external insulation design thermal control mass.

Any direct comparison of the two tables presented in this section must be done with care and an understanding of the input parameters involved in the analyses. Each set of results was devised using the internal masses, heat dissipations, and descent profiles that were dependent on the particular launch vehicle. For the Atlas/Centaur probes, internal masses and power dissipation are larger than for the Thor/Delta probes. Because of a lower parachute drop altitude, the descent time for the Atlas/Centaur large probe is longer than for the Thor/Delta large probe. The opposite is true for the small probes where the Atlas/Centaur descent time is shorter due to a heavier probe and a different aerodynamic configuration. The combined effects of all these parameters are:

1. The required external insulation thickness remains approximately the same for the two baseline designs but the Atlas/Centaur external insulation mass increases due to the increased size of the probes. This holds true for both the large and small probes.

REPRODUCIBILITY OF THE ORIGINAL PAGE IS POOR.

TABLE 4.4-9 EXTERNAL INSULATION VERSUS INTERNAL INSULATION/HEATSINK TRADE RESULTS - THOR/DELTA BASELINE

Trade Item	Large Probe		Small Probe	
	External Insulation	Internal Insulation/ Heatsink	External Insulation	Internal Insulation/ Heatsink
External insulation weight, kg (lb), and thickness, cm (in.)	2.5 (5.5) 0.79 (0.31)	-	3.9 (8.6) 3.00 (1.18)	-
Internal insulation weight, kg (lb), for 1.27 cm (0.5 in.) thickness	-	0.7 (1.6)	-	0.3 (0.6)
Beryllium heatsink weight, kg (lb)	-	2.1 (4.7)	-	7.0 (15.5)
Totals, kg (lb)	2.5 (5.5)	2.8 (6.3)	3.9 (8.6)	7.3 (16.1)

TABLE 4.4-10 EXTERNAL INSULATION VERSUS INTERNAL INSULATION/HEATSINK TRADE RESULTS - ATLAS/CENTAUR BASELINE

Trade Item	Large Probe		Small Probe	
	External Insulation	Internal Insulation/ Heatsink	External Insulation	Internal Insulation/ Heatsink
External insulation weight, kg (lb), and thickness, cm (in.)	3.8 (8.4) 0.79 (0.31)	-	5.2 (11.4) 3.00 (1.18)	-
Internal insulation weight, kg (lb) for 1.27 cm (0.5 in.) thickness	-	1.1 (2.5)	-	0.4 (0.9) s
Beryllium heatsink weight, kg (lb)	-	6.4 (14.2)	-	3.9 (8.6)
Totals, kg (lb)	3.8 (8.4)	7.5 (16.7)	5.2 (11.4)	4.3 (9.5)

2. On a weight comparison basis, the internal insulation/heatsink design is more sensitive to changes in integrated heat load on the probe (i.e., the internal dissipation plus the environmental heat inputs over the duration of the descent) than is the external insulation design. For the Atlas/Centaur large probe the increased integrated heat load accounts for the significant increase in the amount of heat sink material needed. For the Atlas/Centaur small probes, the higher power level is more than offset by the lower environmental loads (because of a shorter descent), thus creating a condition requiring less heat sink material.

For the Atlas/Centaur design, the weight penalty seemed a small price to pay for the potential cost savings that could be realized by implementing the internal insulation/heatsink design into the Atlas/Centaur baseline. Cost savings are expected to be realized for the following reasons:

- Fewer thermal developmental tests on the insulation will have to be run. This is because the internal insulation is exposed to only 1 to 2 atm of air (or inert gas) within the probe rather than the severe Venusian atmosphere. Thermal data on insulation exposed to this benign internal environment is well known and will not have to be totally derived by experiment. The same cannot be said for the external Min-K insulation and the extensive testing that would be required to insure an adequate design.

- Less design integration and manufacturing time will be required with the internal insulation system. This is because the internal insulation is a flexible batt which can be easily worked while the external insulation is constructed of rigid pieces which must be machined and dimensionally accurate.

- The internal insulation is easier to repair. A piece of batt can be patched in whereas repairing the Min-K requires the replacement of an entire piece. The Min-K is also more susceptible to damage due to its brittle consistency.

- Complicated seam sealing processes will not be needed with the internal insulation design. With an external insulation, seam sealing is critical since direct hot gas leaks through the insulation must be eliminated.

- The internal insulation/heatsink approach is easier to test thermally at the systems level. The effects of atmospheric pressure and the chemical constituents of the atmosphere on the thermal performance of the insulation need not be simulated. Only the appropriate temperature profiles need be imposed on the exterior of the pressure vessel.

From the data presented in Table 4.4-10 one could conclude that the lightest weight combination would be the use of external insulation for the large probe and internal insulation/heatsink for the three small probes. However, such an arrangement would encounter all of the difficulties mentioned above for the external insulation plus incurring the cost of two thermal insulation development programs instead of one. Hence, a substantial cost increase would result.

A structural mechanics tradeoff was performed in conjunction with this thermal trade. Both trades used the same configurations and ground rules. The results of the structural trade (see Section 4.3) indicated that the internal insulation/heatsink design was superior from the standpoints of cost and reliability and comparable to the external insulation design on the basis of weight. Based on the results of both studies, the internal insulation/heatsink concept was selected for the Atlas/Centaur baseline.

~~Several~~ alternative configurations for the internal insulation/heatsink design were also considered during this trade. The first of these was the use of foam to fill up the void areas between the equipment and the internal insulation retainer. The purpose of the foam was to minimize the convective and radiative heat transfer between the insulation retainer and the equipment. This approach immediately created several problems. First, the foam had to withstand temperatures on the order of 316°C (600°F) at the interface with the insulation retainer. This meant the use of a high temperature foam. These foams are relatively heavy and, hence, a fairly significant mass penalty would be incurred. Second, the foam complicated the assembly of the probes. The third and decisive problem became apparent when the thermal parameters of the foam were input into the thermal analytical models. The foam conductance terms were approximately equivalent to the replaced radiation and convection coefficients. The resulting temperatures showed little or no improvement. This idea was therefore discarded.

A second, more fruitful, alternative dealt with the mounting arrangement for the top shelf. All previous designs had shown both the top and bottom shelves mounted to the pressure vessel. This arrangement was particularly detrimental to the thermal performance of the top shelf on both the large and small probes. This was because of the low thermal capacitance of the equipment mounted in this area. The heat leak from the vessel plus the high power dissipation created a condition that made it highly desirable to totally decouple the top shelf from the vessel. To accomplish this, the feasibility of mounting the top shelf off the bottom shelf was investigated. The configuration was checked from the systems, hardware integration, and structural standpoints and found to be acceptable. Thermally, it was found that the design could potentially save about a kilogram of heatsink material. Since all the trades yielded positive results, the mounting of the top shelf off the bottom shelf was incorporated into the Atlas/Centaur baseline design, for both large and small probes.

A third alternative of adding another 1.27 c, (0.5 in.) of internal insulation (total thickness 2.54 cm (1.0 in.)) was also examined. This change significantly lowered the amount of heatsink material needed for each probe by about 2 kg. To do this, however, would require an increase in probe diameter, and the associated increase in shell and insulation mass more than cancelled the heatsink mass savings. This alternative was not incorporated into the baseline design. It will be considered again should the heatsink requirements force an increase in pressure vessel volume. Under these cirmumstances, the addition of a combination of insulation plus heatsinks will result in a lighter design than only the addition of heatsinks. The use of a combination approach will lessen the total mass increase.

Thor/Delta Pressure Vessel Module Thermal Design and Performance for the Descent Phase

Thermal Design for the Descent Phase

The primary criterion for the entire Thor/Delta design is the minimization of mass. This served as the basis for the selection of thermal design which utilized external insulation and the inherent heat capacitance of the internal structure and equipment to achieve acceptable descent temperatures.

The Thor/Delta external insulation design utilizes the following hardware items to achieve the desired thermal environment within the probes.

- External insulation. Min-K TE 1400 retained by an external titanium shell. This shell is porous and allows the atmosphere gas to penetrate the Min-K.
- Shelf to pressure vessel mounting isolation. Stacked titanium washers and titanium screws. This was implemented into only the small probe design.

As mentioned earlier, this design is a refined version of the midterm design. Studies subsequent to midterm indicated the desirability of shelf isolation from the pressure vessel on the small probe. This refinement has not been integrated into the structural baseline since direction has since been shifted to the Atlas/Centaur version. However, no implementation problems are anticipated.

Figure 4.4-12 presents an exploded view of the external insulation subsystem. The various pieces of Min-K must be accurately fitted over the entire pressure vessel to avoid direct exposure of the vessel to the atmosphere. Windows and ports are the only external surfaces of the vessel that interface directly with the atmosphere. Since the Min-K is a rigid material, each piece must be machined accurately to insure a good fit. Each mating joint between pieces will be sealed to minimize the gas leaks through these cracks. Special pieces of Min-K will be fitted around each penetration protuberance to minimize the heat leak into the vessel at these points. The entire insulation assembly will be retained by a titanium shell (not shown in the figure). This shell is not a pressure vessel and allows the gas to penetrate the Min-K during descent.

Figure 4.4-13 shows a stacked washer arrangement that is proposed for the small probes. This arrangement provides isolation between the top and bottom shelves and the pressure vessel. The stack is made up of approximately 25 titanium washers and will create a standoff distance of 2.54 cm (1.0 in.) between the shelf flanges and the vessel flanges. A #10 titanium screw (approximately 0.48 cm (3/16 in.) OD) is used to attach the shelves to the vessel flange. Sixteen attachment points are proposed for each shelf. Oversized holes would be drilled in the shelf and vessel flanges, as well as the washers, to minimize any circumferential conductance within the joint which could cause a thermal short.

Good unit-to-shelf thermal conductance is desired to get the maximum benefit from the thermal capacitance of the internal equipment. For most units, a good conduction tie to the structure can be accomplished by filling the interface joint with a thermal filler material such as RTV or indium foil. For those units which do not have sufficient contact area with the structure, thermal straps could be added. No such units were identified during the Thor/Delta design study.

Internal radiation isolation from the warm pressure vessel wall is desirable and is accomplished by providing all internal surfaces with low emittance finishes. Cleaned titanium (the vessel) can provide a hemispherical emittance (ϵ_H) in the range of 0.10 to 0.20. Equipment boxes, which are normally constructed of aluminum, can either be cleaned or given a finish of vapor deposited aluminum with resulting hemispherical emittances (ϵ_H) between 0.03 and 0.06.

A summary of the specific thermal control hardware requirements is presented in Table 4.4-11. The insulation thickness requirements represent minimum weight designs that will provide temperatures within the probes consistent with the requirements presented in a previous subsection. This design data was derived using the computer models described in Reference 4.4-4.

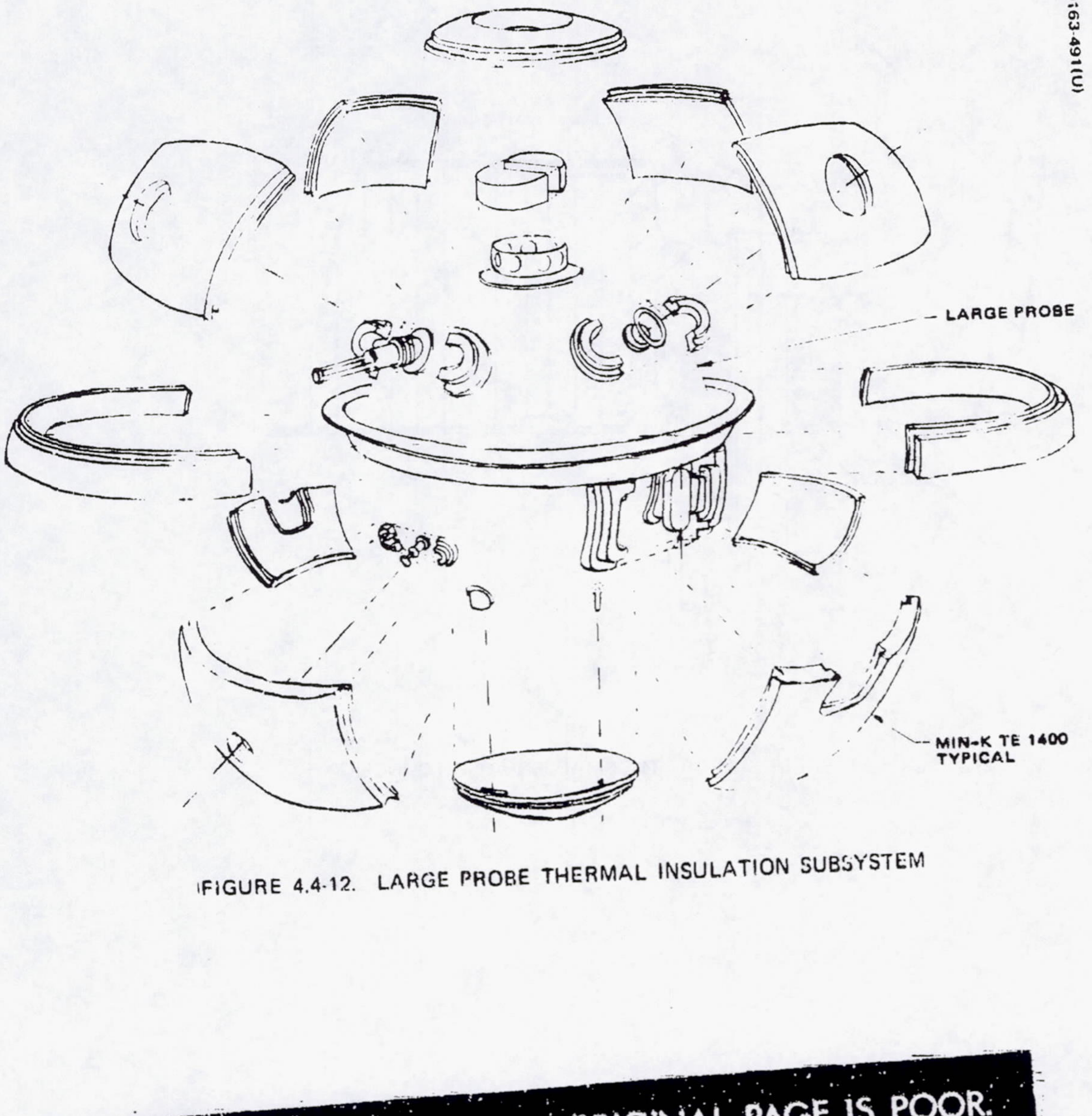

FIGURE 4.4-12. LARGE PROBE THERMAL INSULATION SUBSYSTEM

REPRODUCIBILITY OF THE ORIGINAL PAGE IS POOR.

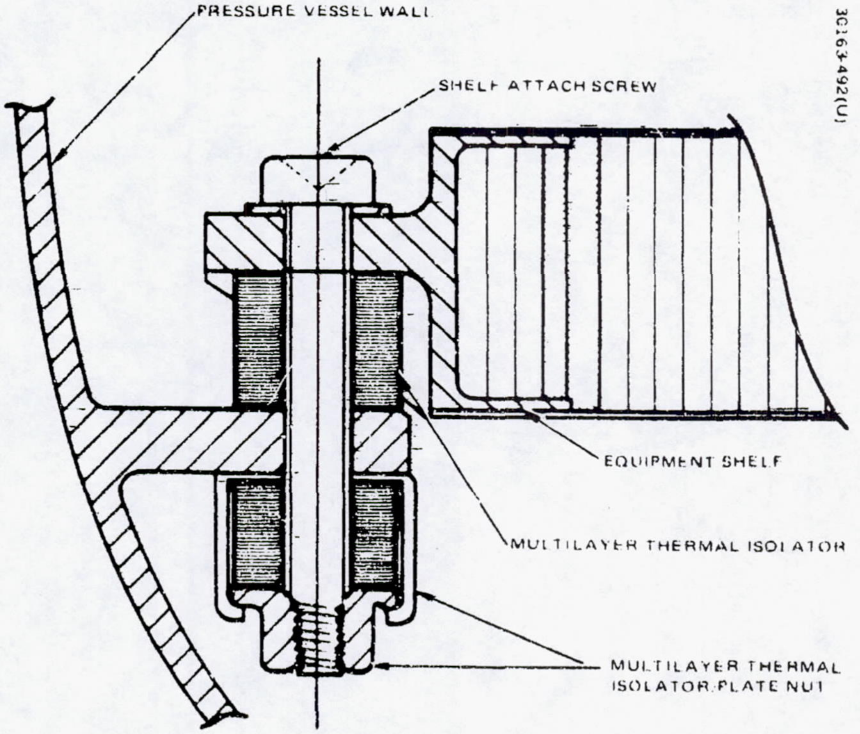

FIGURE 4.4-13 SHELF SUPPORT THERMAL ISOLATION CONCEPT

TABLE 4.4-11. THOR/DELTA THERMAL CONTROL HARDWARE REQUIREMENTS

	Large Probe	Small Probe
External insulation	1.14 cm (0.45 in.) of Min-K TE 1400 3.7 kg (8.1 lb) of insulation	2.90 cm (1.14 in.) of Min-K TE 1400 on the upper hemisphere 2.34 cm (0.92 in.) of Min-K TE 1400 on the lower hemisphere 3.3 kg (7.3 lb) of insulation
Shelf isolation mount*	Not used	16 mounting points, both shelves Standoff distance = 2.54 cm (1.0 in.) No. 10 titanium screw Minimum number of washers = 25 Washer OD = 0.90 cm (0.354 in.)

*Hardware change from midterm baseline

Thermal Performance for the Descent Phase

Temperature predictions for the Thor/Delta baseline design described in the preceding section were obtained for both pressure vessel modules using large multimode computer programs (Reference 4.4-4). Equipment, shelf, pressure vessel, and insulation temperatures were predicted for the entire descent phase for each probe. However, equipment temperatures at impact are the most important results of these analyses, since this is where the maximum temperature is experienced. By an iterative process, the thermal control hardware parameters are varied and temperature predictions obtained. The iteration proceeds until a favorable comparison is obtained between the predicted baseplate temperatures at impact and the allowable baseplate upper temperature limits for the critical components. The input parameters to the analytical model at this iteration then become the basis for the thermal control hardware design. A direct comparison of predicted and permissible baseplate temperatures without allowance for prediction tolerance is justifiable due to the transient nature of the mission and the fact that worst case parameters are used in the analytical model.

Equipment temperatures at impact for the large pressure vessel module are shown in Figure 4.4-14. Corresponding pressure vessel temperatures are shown in Figure 4.4-15. The constraining component is the command/data box, which is the only component at its temperature limit. Although limits were not shown for some of the RF components, their temperature predictions should be acceptable. The bulk temperature of the pressure vessel is 242°C (468°F).

Equipment and pressure vessel temperatures for the small pressure vessel module are presented in Figures 4.4-16 and 4.4-17. The command/data box sized the insulation thickness on the upper hemisphere and the stable oscillator sized the lower hemisphere insulation thickness. The bulk temperature of the pressure vessel is 193°C (380°F).

Atlas/Centaur Pressure Vessel Module Thermal Design and Performance for the Descent Phase

Thermal Design for the Descent Phase

The pressure vessel module thermal design for the Atlas/Centaur configuration is based on the premise of minimizing costs through the use of proven and conservative design approaches. This premise has led to a baseline thermal design which utilizes a hot pressure vessel with an internal insulation system agumented by equipment heatsinks to control the descent temperature rise. This contrasts with the external insulation system and relatively cooler pressure vessel presented for the Thor/Delta configuration.

The decision to proceed with an internal insulation/heatsink design was made after reviewing the earlier trade between internal and external insulation systems made for the Thor/Delta design. The results of this

UPPER SHELF

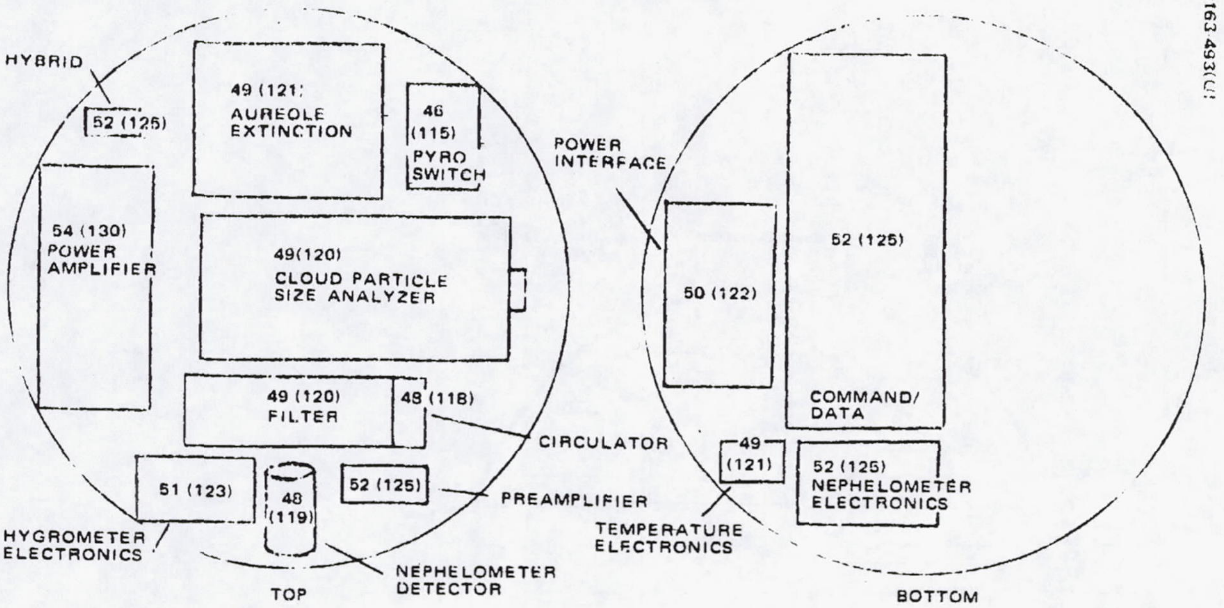

LOWER SHELF

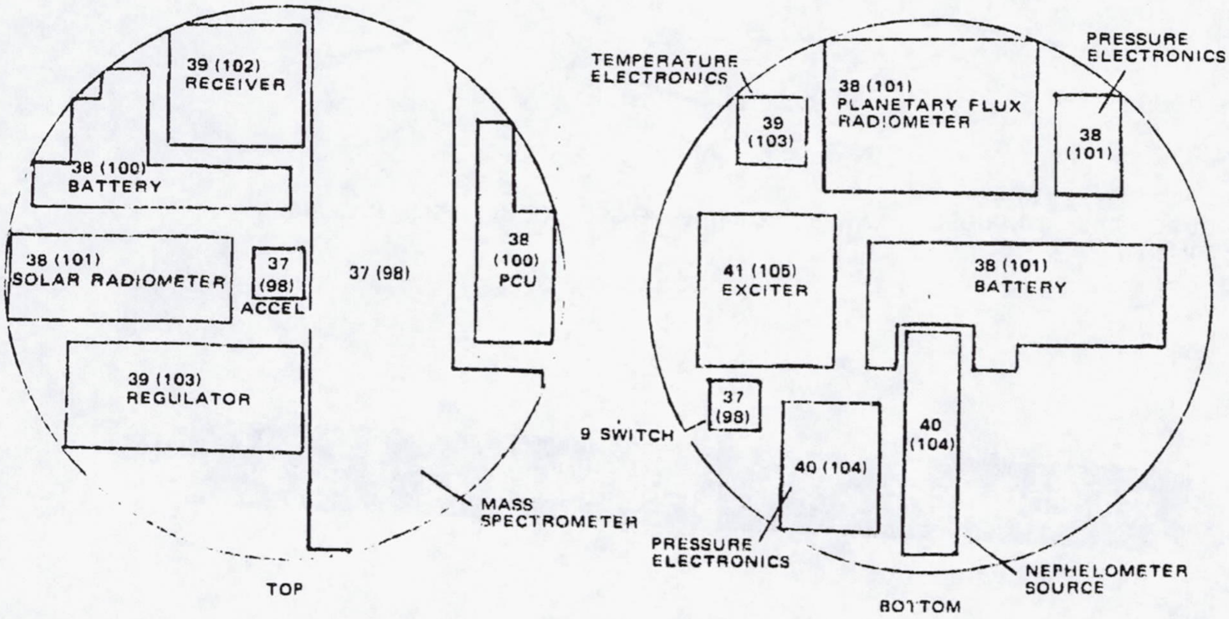

FIGURE 4.4-14. THOR/DELTA LARGE PRESSURE VESSEL MODULE EQUIPMENT TEMPERATURES AT IMPACT - °C (°F)

30163-493(U)

CE IS POOR.

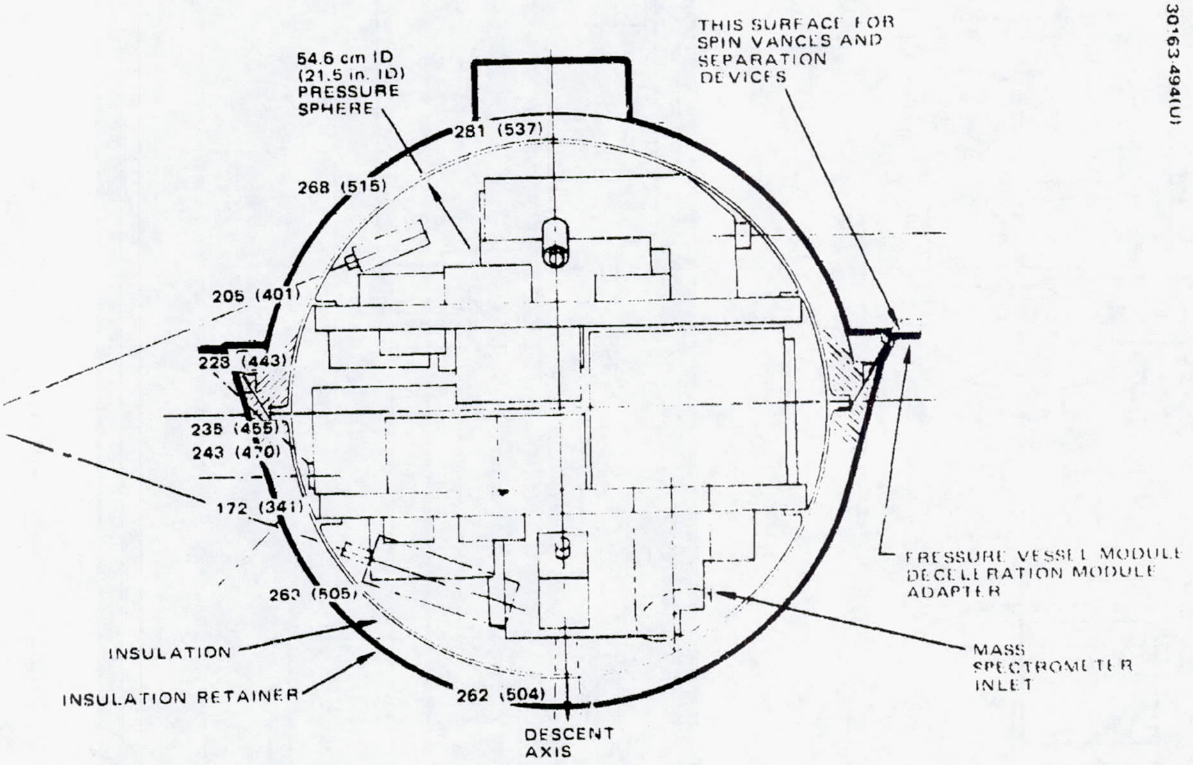

FIGURE 4.4-15. THOR/DELTA LARGE PRESSURE VESSEL MODULE TEMPERATURES AT IMPACT - °C (°F)

REPRODUCIBILITY OF THE ORIGINAL PAGE IS POOR.

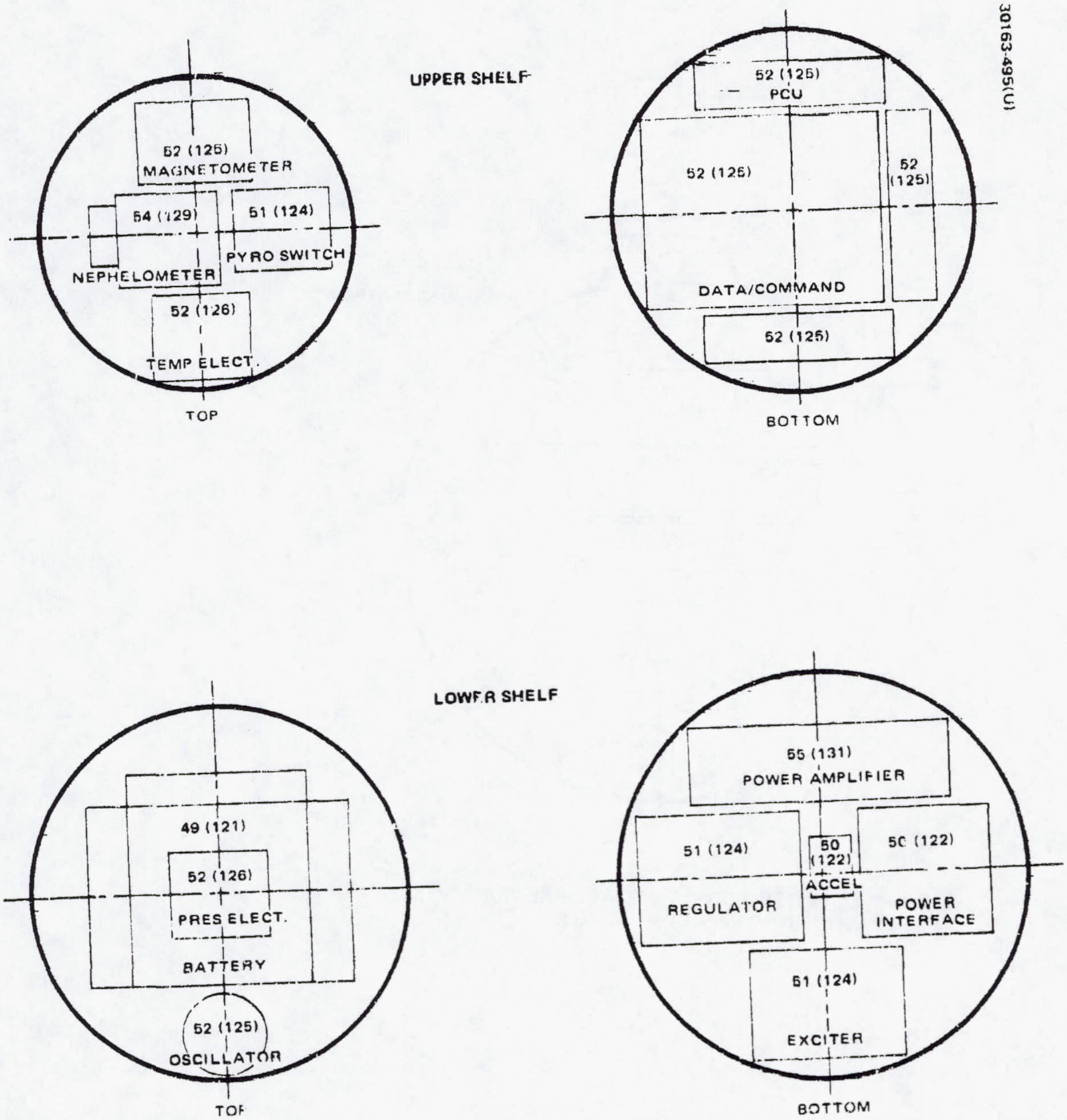

FIGURE 4.4-16. THOR/DELTA SMALL PRESSURE VESSEL MODULE EQUIPMENT TEMPERATURES AT IMPACT – °C (°F)

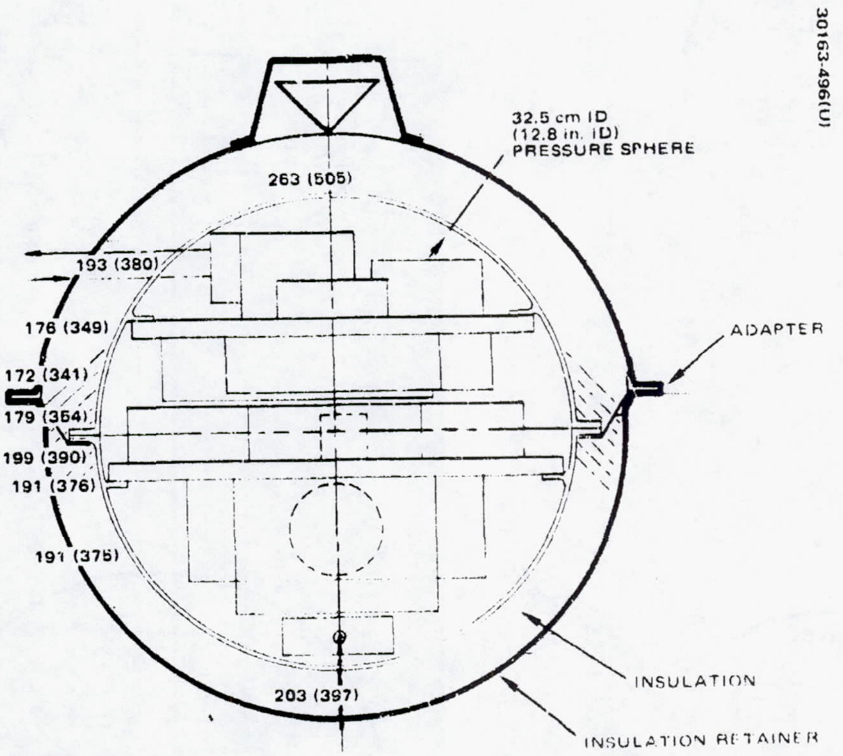

FIGURE 4.4-17 THOR/DELTA SMALL PRESSURE VESSEL MODULE TEMPERATURES AT IMPACT – °C (°F)

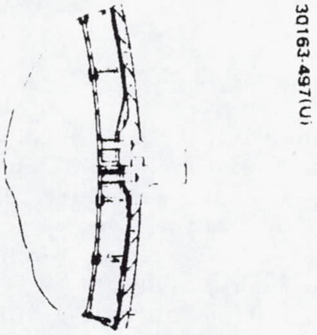

BATTING INSTALLED IN PRESSURE VESSEL AT CLOSURE FLANGE

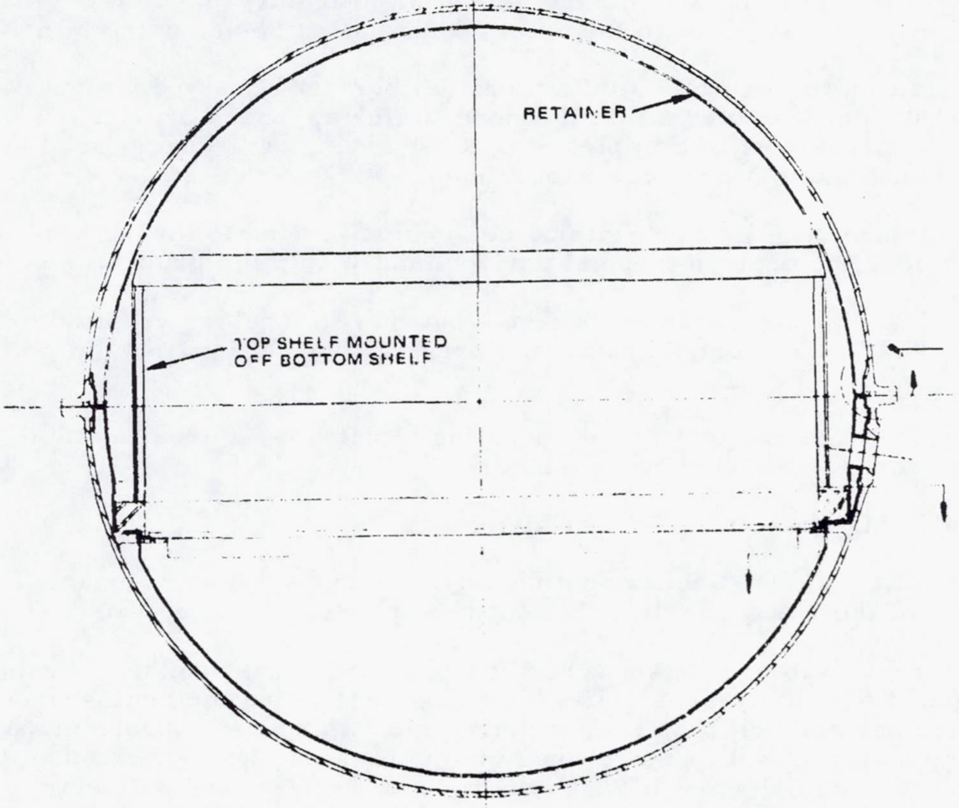

INTERNALLY INSULATED PRESSURE VESSEL

FIGURE 4.4-18. INTERNAL INSULATION AND TOP SHELF MOUNTING SCHEMATIC trade and the review are presented in previous subsections. The earlier trade considered only multilayer superinsulation for the internal insulation system. In addition to increasing the probe weight (based on the design parameters in effect at that time), this system required insulation evacuation to achieve efficient performance. Evacuation schemes were unacceptable based on other design considerations (weight, corona generation, reliability, and unit requirements). In updating the trade, an internal insulation system using fiberglass batt was considered instead of the multilayer superinsulation. Equipment heatsinks were considered to augment the internal insulation and the appropriate combination of these two control techniques were analyzed in detail. It was found that the internal insulation/heatsink design could provide acceptable unit temperatures within the probes and that the hot pressure vessel created no difficult structural problems. It was also determined that the internal insulation/heatsink design did not significantly penalize the mass of the system when compared to the external insulation design using Min-K.

In addition to providing similar thermal performance and a more predictable design, the internal insulation/heatsink approach provides a design which is less costly to implement. Cost savings will be realized for the reasons outlined in a previous subsection.

The internal insulation/heatsink design utilizes the following hardware items to achieve the desired thermal environment within the probes:

- Internal insulation - fiberglass batt (FA fiberglass supplied by HITCO) supported against the pressure vessel by a retainer shell
- Shelf to pressure vessel mounting isolation - stacked titanium washers and titanium screws
- Heatsinks - beryllium or aluminum
- Alternate top shelf mounting arrangement - top shelf mounted off the bottom shelf rather than the pressure vessel wall

Figure 4.4-18 presents a schematic of the internal insulation design that is planned for both probes. The fiberglass batt is packed against the internal retainer and held in place by short captive pins which protrude part way into the batting. Full penetration by the pins is not desired because this would create a thermal short between the pressure vessel and the retainer. The retainer is fabricated of thin sheets of titanium or steel which are attached to the pressure vessel in the areas of the flanges. The heat leak from the vessel to the retainer is minimized by constructing the retainer from low conductivity materials with minimum thicknesses. Special provisions will have to be made in the area of the pressure vessel closure flange to insure insulation integrity when the vessel is closed. This will be accomplished by forming a lip in the retainer that will enclose the insulation and minimize the heat leak at the crack.

A stacked washer arrangement, similar to the design proposed for the Thor/Delta small probes, will provide isolation between the bottom shelf and the pressure vessel for both large and small probes (Figure 4.4-13). The stack will be made up of approximately 25 titanium washers and will create a standoff distance of 2.54 cm (1.0 in.) between the shelf flange and the vessel flange. A #10 titanium screw (approximately 0.48 cm (3/16 in.) OD) will be used to attach the shelf to the vessel flange. Sixteen attachment points are currently planned around the shelf. Oversized holes will be drilled in the shelf and vessel flanges, as well as the washers, to minimize any circumferential conductance within the joint which could create a thermal short.

Additional mass will be added to each shelf as needed to maintain temperatures within the desired equipment limits during the descent transient. Beryllium is the most efficient heat sink material on a per unit of mass basis because of its high specific heat. However, beryllium is difficult to machine and relatively expensive. Because of this, aluminum may be substituted if the associated mass penalty is accepted. Since the design philosophy is to create an isothermal mass of equipment and shelf, heatsink material can be added either to the structure (shelf) or directly to the equipment boxes. It is of course always more efficient to add the material directly to the box which is predicted to overheat, but this may not always be practical. The isothermal concept minimizes the inefficiencies of adding mass to the structure adjacent to an overheating package and thus allows for greater design flexibility.

An alternative top shelf mounting arrangement has been devised which allows the top shelf to be entirely conductively decoupled from the pressure vessel. The top shelf is mounted off the bottom shelf on a cylindrical strut and shear skin structure (Figure 4.4-18). This is a desirable arrangement because it minimizes the heat flow from the vessel to the communications transmitter which is mounted on the top shelf. The components of the transmitter are generally low mass and high dissipation items and thus require significant heatsinking. This shelf mounting arrangement will minimize the needed heatsink mass for the top shelf.

As mentioned above, creating an isothermal mass of equipment and structure on each shelf is a prime part of the internal insulation/heatsink design concept. For most units, a good conductive tie to the structure can be accomplished by filling the interface joint with a thermal filler material such as RTV or indium foil. For those units which do not have sufficient contact area with the structure, thermal straps may be needed. At this time, no such units have been identified. This may become necessary, however, when detailed alignment and associated shimming requirements are completely understood.

Internal radiation isolation will be accomplished by providing all surfaces with low emittance finishes. For the insulation retainer, cleaning processes for either titanium or steel can provide hemispherical emittances (ϵ_H) in the range of 0.10 to 0.20. Equipment boxes, which are normally constructed of aluminum, can either be cleaned or given a finish of vapor deposited aluminum with resulting hemispherical emittances (ϵ_H) between 0.03 and 0.06.

A summary of the specific thermal control hardware requirements is presented in Table 4.4-12. Required heatsink masses are presented for both beryllium and aluminum. This design data has been derived using the computer models developed for the revised internal versus external insulation trade outlined in a previous subsection. Appropriate revisions of these Thor/Delta models have been accomplished to simulate the Atlas/Centaur configuration.

Thermal Performance for the Descent Phase

Temperature predictions for the Atlas/Centaur pressure vessel module designs described above are presented in the Tables 4.4-13 and 4.4-14. As with the Thor/Delta analyses, large multimode computer models of both probes were used to predict equipment, shelf, insulation, and pressure vessel temperatures for the entire descent phase of the mission.

An iterative process permits the selection of thermal control parameters which produce acceptable baseplate temperatures for the critical components. These input parameters become the basis for the thermal control hardware design. A direct comparison of predicted and permissible baseplate temperatures without allowance for prediction tolerance is justifiable due to the transient nature of the mission, the use of worst case parameters in the analytical models, and the conservative nature of the design limits.

Several components within each probe reached the 52°C (125°F) upper temperature limit. This was expected due to the isothermal nature of the internal design. Only the power amplifiers (and associated drivers) were allowed to exceed the 52°C (125°F) limit. These units were maintained below their 60°C (140°F) limit in both probes.

The pressure vessel temperatures for both probes tracked the atmospheric temperature profiles closely during the descent. Each hemisphere of the vessels was approximately isothermal at any time during the descent.

At impact the bulk temperature of the large probe pressure vessel was 482°C (899°F) and the bulk temperature of the small probe pressure vessel was 472°C (882°F). The maximum temperature gradient within any vessel hemisphere for either large or small probes at impact was 22°C (40°F).

TABLE 4.4-12. ATLAS/CENTAUR THERMAL CONTROL HARDWARE REQUIREMENTS

	Large Probe	Small Probe
Internal insulation	1.27 cm (0.5 in) of FA fiberglass 1.1 kg (2.5 lb) of insulation	1.27 cm (0.5 in) of FA fiberglass 0.4 kg (0.9 lb) of insulation
Shelf isolation Mount	16 mounting points, bottom shelf only Standoff distance = 2.54 cm (1.0 in) No. 10 titanium screw Minimum number of washers = 25 Washer OD = 0.90 cm (0.354 in.)	16 mounting points, bottom shelf only Standoff distance = 2.54 cm (1.0 in) No. 10 titanium screw Minimum number of washers = 25 Washer OD = 0.90 cm (0.354 in.)
Heat sink material required	Top shelf (in addition to 2.0 kg [4.5 lb] shelf): In beryllium = 6.4 kg (14.2 lb) In aluminum = 13.2 kg (29.0 lb) Bottom shelf (in addition to 2.8 kg [6.2 lb] shelf): No heatsink required	Top shelf (in addition to 0.7 kg [1.5 lb] shelf): In beryllium = 2.1 kg (4.7 lb) In aluminum = 4.4 kg (9.6 lb) Bottom shelf (in addition to 0.9 kg [2.0 lb] shelf): In beryllium = 1.8 kg (3.9 lb) In aluminum = 3.6 kg (8.0 lb)

TABLE 4.4-13. ATLAS/CENTAUR LARGE PRESSURE VESSEL MODULE INTERNAL EQUIPMENT TEMPERATURES AT IMPACT

Equipment	Temperature °C	(°F)
Cloud particle size analyzer	49	(121)
Hygrometer	52	(125)
Filter	49	(120)
Hybrid	43	(109)
Circulator	47	(117)
Preamplifier	52	(125)
Power amplifiers	59	(138)
Pyro switch	47	(116)
Temperature sensor electronics	51	(123)
Power interface	48	(118)
Command data box	52	(125)
Solar flux radiometer	52	(125)
Accelerometer	49	(121)
Mass spectrometer	48	(119)
Receiver	52	(125)
PCU	51	(123)
Battery pack	47	(117)
Discharge regulator	52	(125)
Pressure sensor electronics	52	(125)
Wind/altitude radar	51	(124)
IR flux radiometer	52	(125)
Gas chromatograph	48	(118)
Exciter	52	(125)
Battery pack	50	(122)
G switch	50	(122)

TABLE 4.4-14. ATLAS/CENTAUR SMALL PRESSURE VESSEL MODULE INTERNAL EQUIPMENT TEMPERATURES AT IMPACT

Equipment	Temperature °C (°F)
IR flux detector	49 (121)
Pyro switch	48 (118)
Temperature electronics	49 (120)
Nephelometer	52 (125)
Command/data box	50 (122)
PCU (three locations)	50 (122)
Power amplifiers	57 (134)
Power interface	51 (124)
Exciter	52 (125)
Discharge regulator	51 (124)
Accelerometer	51 (123)
Battery	51 (123)
Stable oscillator	52 (125)
Pressure sensing system	50 (122)

References

4.4-1 "Models of Venus Atmosphere (1972)", NASA SP-8011, Sept. 1972, NASA.

4.4-2 D. P. Crowley and P. Levine, "Insulator Testing Under Venus Environmental Conditions", AVCO Systems Division, AIAA Paper 72-368, April 1972.

4.4-3 B. G. Shelden and J. O. Golden, "Development of a Phase Change Thermal Control Device", Journal of Spacecraft and Rockets, Vol. 10, No. 2, February 1973, pp. 99-100.

4.4-4 Hughes Aircraft Company, HS507-022-156, "Thor/Delta Pressure Vessel Thermal Analysis", Task No. PB-4, dated 11 May 1973.

4.5 SCIENCE AND HOUSEKEEPING STRUCTURAL PENETRATIONS

The probe structural subsystem must provide access to and communication with the science and housekeeping systems within the pressure vessel. The science payload requires windows for atmospheric observations in the visible and infrared, and ports for atmospheric sampling by the pressure sensor, mass spectrometer, and gas chromatograph. Housekeeping requirements include access ports and electrical feedthroughs operating at dc and at rf frequencies.

In addition to the functional requirements established by science and housekeeping, structural, thermal and producibility requirements were defined for design purposes. Using these as constraints, preliminary designs were developed to meet the particular requirements shown in Table 4. 5-1 of instrument and housekeeping subsystems carried on both large and small probes. Designs were carried out in enough detail to allow meaningful comparisons between characteristics such as weight, structural integrity, and development risk. These figures were used in trade studies, the results of which were evaluated to yield recommended baseline approaches for both Thor/Delta and Atlas/Centaur baselines.

The remainder of this section is divided into sections concerning requirements, trade studies, and descriptions of the respective Thor/Delta and Atlas/Centaur baseline configurations for each area studies. A summary of the areas studied and some of the conclusions of the study are also shown in Table 4. 5-1.

The requirements section describes the general requirements applying to all penetrations in order to survive the mission environment; individual instrument requirements such as fields of view or location with respect to the stagnation point are described in the sections on trade studies and baseline configurations.

Tradeoffs were conducted to optimize the configuration of many of the systems considered. Candidate configurations, requirements, and factors involved in baseline selection are described in detail in the trades section.

Two sections are devoted to describing the structural penetration approaches evolved for the Thor/Delta and Atlas/Centaur mission, respectively. Descriptions in the Atlas/Centaur section are limited to those areas where the design approach used differed from that used for Thor/Delta.

Penetration Requirements

Requirements to be satisfied by pressure vessel penetrations and associated hardware are governed primarily by the mission environment and by subsystem functional requirements. Environmental factors important in penetration design are the planetary entry deceleration loads and the pressure, temperature, and composition of the Venus atmosphere. Entry deceleration loads of 575 g for the large probe and 595 g for the small probe were multiplied by a factor of 1. 25 to obtain the values of 720 and 745 g, respectively, used for the design.

TABLE 4.5-1. PRIMARY STRUCTURES/INTEGRATION AREAS STUDIED

Item	Configuration Selected	Primary Reason for Selection
Science Integration		
Visible wavelength window material selection	Sapphire (AL2O3)	Good optical properties, superior strength
IR wavelength window material selection	Chemically vapor deposited zinc selenide	Excellent optical properties
Window seal configuration	Braze or metallic O-ring, depending on application	Both are well proven techniques
Window heater configuration	Sheathed element or film type depending on application	Both are well proven configurations
Instrument window configuration	Separate configuration selected for each instrument	Instrument requirements differ widely
Window contaminate removal system	Transparent jettisonable protective cover	Lightweight; simplicity
Large probe pressure sensor inlet system	Welded tubular feedthrough	Simple, reliable
Small probe pressure sensor inlet system	Welded tubular feedthrough; jettisonable plug for protection during entry	Minimize possibility of inlet blockage
Mass spectrometer inlet system installation	Installation from inside pressure vessel	Avoid removal of inlet system from analyzer
Gas chromatograph inlet system installation	Flanged, O-ring sealed tubular feedthrough	Ease of installation and removal
Large probe temperature sensor installation	Mount to pressure vessel wall	Allows checkout of all-up system
Small probe temperature sensor installation	[illegible] deployable [illegible] entry	Entry protection provided by swing-arm
[illegible] sensor installation	Recess inside aerodynamic fairing	Minimize interference at aeroshell separation
Cloud particle size spectrometer mirror support installation	Mirror support mounted to instrument for mechanical isolation from pressure vessel	Satisfied alignment requirements
Wind drift altimeter radar antenna installation	Mounted in bottom of probe [illegible] radome	Satisfies field of view and aerodynamic [illegible] requirements
[illegible]		
Large or small [illegible] shell [illegible]	[illegible]	Lightweight, highest survivability
[illegible]	[illegible] sheath antenna	Minimize RF losses
[illegible]	Ceramic [illegible] metal [illegible] header welded [illegible] pressure vessel	Superior structural and seal integrity
[illegible]	[illegible]	Access for systems test
[illegible]	[illegible]	Best highest survivability
[illegible]	[illegible]	Best highest survivability

REPRODUCIBILITY OF THE ORIGINAL PAGE IS POOR.

Venus surface temperature and pressure values of 757.5°K and 94.9 atmospheres were used as baseline values for penetration design. Atmospheric composition used in evaluating materials exposed to the Venus environment is based on the Young model, which predicts aerosols of sulfuric and fluosulfonic acid in the cloud layers.

General functional requirements include optical, structural, seal, thermal, and producibility factors. A summary of these requirements and the approaches taken to implement them are shown in Table 4.5-2.

The primary factor in window design is assuring satisfactory optical qualities in the wavebands of interest, and low in-band emissivity at high temperatures. Internal scattering should be minimized. Optical system design should provide for a minimum of surfaces in the line-of-sight. The angle of incidence should be kept as close as possible to normal and internal path length should be minimized.

Window sizing is governed primarily by experiment field-of-view requirements and window material mechanical properties. Window diameter is sized to satisfy experiment requirements for fields of view, and the thickness is then chosen as a minimum consonant with maintaining a safety factor of four at the temperatures and pressures characteristic of the Venus surface environment.

Seal integrity must be maintained by all pressure vessel penetrations against both the long duration internal 1 atm pressure differential of trans-Venus trajectory and the relatively short duration external pressure of approximately 100 atm encountered at the surface of Venus. Seal temperatures will range from -40°C during interplanetary coast to 482°C at the termination of the descent.

Thermal requirements on penetrations include minimization of heater power required for window defrosting during the descent, and minimization of heat input to the interior of the probe. Integration with the pressure vessel insulation layers and insulation retaining shell is required for all pressure vessel penetrations, without compromising the efficiency of the insulation or access to the pressure vessel. Heaters, if used, must also be integrated into the window assembly, and contamination removal systems, if used, must be closely integrated with both window, pressure vessel, and outer shell.

Maximum use of common materials, off the shelf hardware, and straightforward designs and methods of fabrication is required to minimize cost and risk. Other cost sensitive design considerations include ease of assembly, ease of optical alignment where required, and ready access for inspection and repair.

In addition to general requirements, most instruments have special requirements not shared by others. Special requirements of this type are summed up in Table 4.5-3. More detailed descriptions of individual instrument requirements are contained in the sections on trades and baseline descriptions.

TABLE 4.5-2. PENETRATION REQUIREMENTS/APPROACHES

	General Requirements	Approach
Optical	Good transmissivity at required wavelengths Low index of refraction High transmissivity at elevated temperatures Low emissivity at elevated temperatures	Selection of window material
	Low internal scattering Field of view	Vary size and shape of window
	Normal angle of incidence between window surface and line of sight Minimize number of optical surfaces in line of sight	Window mechanical design
Structural	Provide accurate alignment for cloud particle size spectrometer mirror	Mount mirror support directly to instrument
	Maintain pressure vessel structural integrity	Provide doublers around penetrations
	Provide window structural integrity	Size window thickness
	Provide for structural integrity of internal lines carrying external ambient pressure	Size tubing thickness
Seal	Provide hermetic seal for all penetrations during trans-Venus cruise	Use O ring or brazed seals, depending on application
Thermal	Minimize heat flow through insulation to interior Minimize window anticondensation heater power Minimize pressure vessel hot spots around penetration (Thor/Delta only)	Insulate windows and external protuberances from pressure vessel and probe interior
Producibility	Minimize cost of installing penetration doublers in pressure vessel wall	Study
	Minimize cost of detail parts	Use well proven materials and fabrication techniques
	Facilitate installation, checkout, test, and repair	Provide complete access to penetrations even after installation of insulation layer

TABLE 4.5-3. PRIMARY PENETRATION REQUIREMENTS

Item Studied	Primary Individual Requirements
Windows	
Nephelometer source window	2 deg conical field of view line of sight must intersect that of sensor. Visible wavelengths
Nephelometer sensor window	10 deg conical field of view visible wavelengths
Cloud particle size spectrometer window	2.5 cm (1.0 in) cylindrical field of view visible wavelengths. Line of sight perpendicular to descent axis
Planetary flux radiometer window	5 deg conical field of view: IR wavelengths (8.3 and 10.6μ) line of sight parallel to descent axis
Solar flux radiometer window	±15 deg field of view horizontal ±65 deg vertical; visible wavelengths. Line of sight perpendicular to descent axis
Aureole extinction detector window	±7.5 deg in verticle plane; ±9.25 deg horizontal plane. Visible wavelengths. Line of sight aft solar zenith
Small probe IR radiometer window	0.5 diameter window; deployable mirror; line of sight scanned vertically up and down; 8.3 and 10.6μ
Small probe nephelometer window	1.5 diameter window; visible wavelengths; line of sight perpendicular to descent axis
Ports	
Large probe pressure sensor inlet system	Location within 30 deg of stagnation point. Size to minimize blockage by condensation
Small probe pressure sensor inlet system	Locate at stagnation point
Mass spectrometer inlet system installation	3.0 diameter penetration
Gas chromatograph inlet system installation	Size to minimize blockage by condensation
Cloud particle size spectrometer mirror support	Alignment within 1 mr required throughout mission
RF feedthrough	Minimize co-ax line length
DC and low frequency feedthrough	Approximately 60 pins required. Separate feedthroughs for pyro and signal and power
Access and inspection ports	2.0 diameter; access must be possible with probe mounted in aeroshell
Other	
Large probe temperature sensor installation	Sensor must protrude into boundary layer
Small probe temperature sensor installation	Sensor must be housed for protection during entry. Deployment into free stream after entry
Hygrometer sensor installation	Sensor must be located in free stream
Wind drift altimeter radar antenna installation	Antenna must have unobstructured downward view. Influence on aerodynamic stability should be minimized
Large probe pressure vessel aeroshell IFD	Approximately 60 conductors must be opened. High g survivability essential
Small probe nephelometer windoe entry protection	Fail safe operation
Insulation subsystem integration and insulation	High g survivability and minimum interference with access to probe interior
Window contamination removal system	Minimize weight and power. Some capability should remain if system fails
Window heater system	Minimize weight and power

REPRODUCIBILITY OF THE ORIGINAL PAGE IS POOR.

Trade Studies

Most trade studies were conducted in the science integration area. At least two candidate configurations were considered for each of the following items:

1) Window material selection
2) Window seals
3) Window configuration
4) Window heater mechanical design
5) Window contamination removal systems
6) Large probe pressure sensor inlet system
7) Small probe pressure sensor inlet
8) Cloud particle size spectrometer mirror
9) Small probe nephelometer protective cover
10) Small probe altimeter for antenna installation
11) Small probe temperature sensor deployment
12) Wind/altitude radar antenna installation

A number of trades were also conducted in the housekeeping category, such as:

1) Large probe pressure vessel module/aeroshell in-flight disconnect
2) Umbilical to spacecraft
3) Communications antenna rf feedthrough configuration and location

The remainder of this section contains brief descriptions of the studies conducted in the areas mentioned above. Configurations not covered in this section are described in detail in the Thor/Delta and Atlas/Centaur configuration descriptions.

Window Material Selection

Factors to be considered in selecting window materials that will function properly in the Venus surface environment are:

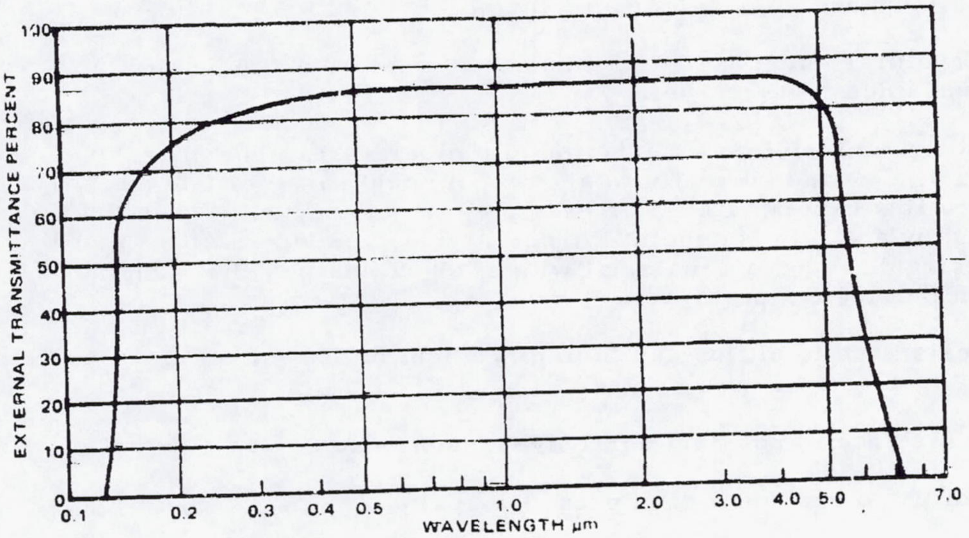

a) TRANSMISSION BAND OF SAPPHIRE

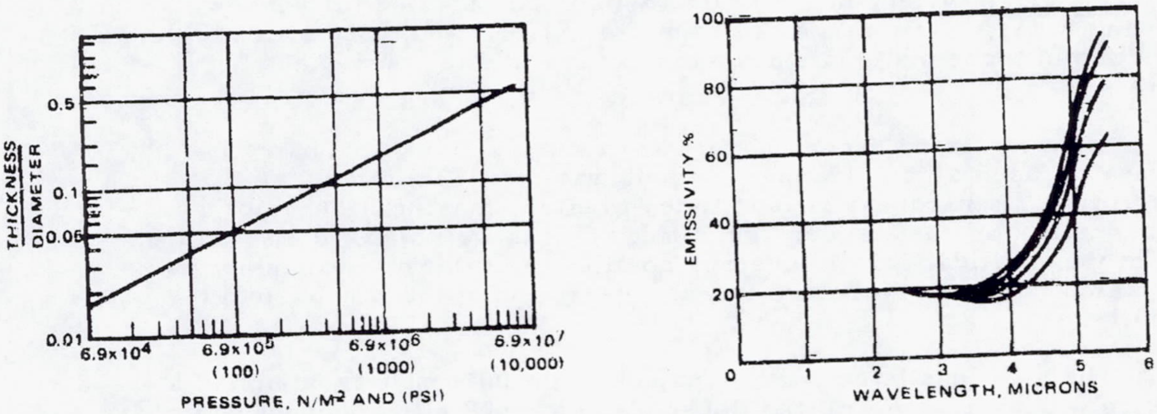

b) EXPERIMENTALLY DERIVED BURST STRENGTH DATA FOR SAPPHIRE WINDOWS – SAFETY FACTOR OF 4 INCLUDED

c) EMISSIVITY OF SAPPHIRE AS A FUNCTION OF WAVELENGTH AND TEMPERATURE

FIGURE 4.5-1. OPTICAL AND MATERIAL PROPERTIES OF SAPPHIRE

1) Maintenance of good transmission at elevated temperatures

2) Structural integrity; i. e. , modulus of rupture and possible change in flatness due to deflection

3) Inband emissivity as a function of temperature. The energy emitted by the window adds directly to signal and could cause problems in the planetary flux experiment. For example, the energy emitted in the (5 to 10) band by a 1. 0 in. diameter window at $500^{\circ}C$ is emissivity x 4. 0 W. Thus, it is desirable to have a material with a low emissivity that does not change with increasing temperature.

4) Resistance to pitting due to impingement of dust or other abrasive particles (hardness)

5) Resistance to possible corrosive condensation

6) Ability to provide a good pressure seal

7) Optical quality; i. e. , low internal scattering. This is especially important for imaging systems.

Visible Wavelengths. Candidate materials studied for windows operating in the visible range are sapphire ($AL_2 0_3$) and fused silica ($S_i 0_2$). properties of these materials are summarized in Table 4. 5-4 and Figure 4. 5-1.

In every factor except density and transmissivity, sapphire is superior to fused silica. Sapphire's long wave limit is lower than that of fused silica; its hardness is four times greater, making it superior in dust and abrasion resistance; its melting point is well above the softening point of fused silica, and its average coefficient of thermal expansion is a good match to that of invar facilitating integration of the window into the structure.

The high tensile strength of sapphire at $500^{\circ}C$ allows design of a sapphire window of one-half the thickness of a fused silica window while maintaining a comparable safety margin. As a result of the reduced thickness, the sapphire window possesses a higher uncoated transmittance because of the reduced optical path length, and it is only 90 percent as heavy, despite sapphire's greater density.

The high compressive strength and smooth surface finish of sapphire make it easily adaptable to sealing methods using hollow metallic O rings, with, their high initial preloads. There is also considerable experience in making sapphire to metal seals for windows in high pressure gas discharge devices operating at pressures of 20 atm and temperatures approaching $482^{\circ}C$.

Structurally, fused silica softens rather than melts. The normal service limit for this glass in the annealed condition is $900^{\circ}C$, well over the

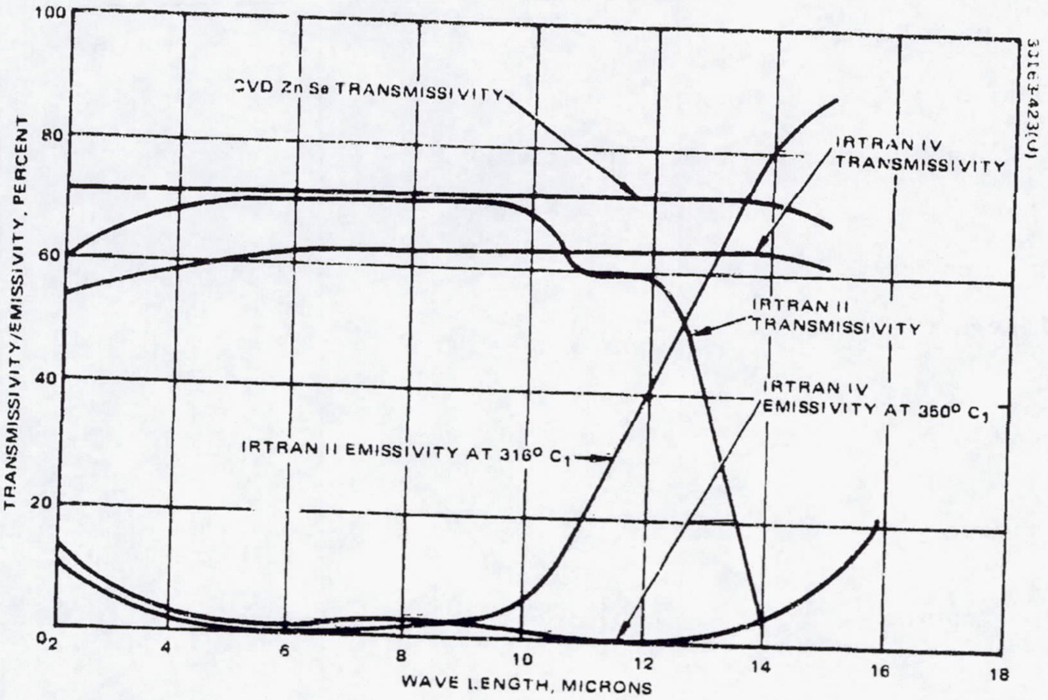

1) PLOTTED FROM KODAK DATA -- REF. 2
2) PLOTTED FROM HUGHES DATA -- REF. 6
3) EMISSIVITY OF CVD ZnSe NOT SHOWN; REF. 6 INDICATES IT SHOULD COMPARE FAVORABLY WITH IRTRAN IV.
4) ALL TRANSMISSIVITIES FOR 6mm MATERIAL THICKNESS

FIGURE 4.5-2. TRANSMISSION AND EMISSIVITY CHARACTERISTICS OF CANDIDATE MATERIALS FOR WINDOWS OPERATING AT IR WAVELENGTHS

TABLE 4.5-4. PROPERTIES OF CANDIDATE MATERIALS FOR WINDOWS OPERATING IN THE VISIBLE WAVELENGTHS

Properties	Sapphire ($AL_2 0_3$)	Fused Silica ($Si\ 0_2$)
Long wave limit (μ)	5.5	3.5 to 4.5
Transmissivity at 2μ, 0.2 thick	82 percent	93 percent
Hardness (Knoop)	1600 to 2200	470
Melting point	2030°C	
Softening point	---	1500 to 1700°C
Average thermal exponent 20 to 500°C	7.7×10^{-6} °C	0.55×10^{-6} °C
Tensile at 500°C	2.76×10^{8} N/m^2 (40,000 psi)	6.9×10^{7} N/m^2 (10,000 psi)
Young's modulus	$3.5 - 3.9 \times 10^{11}$ N/m^2 ($50\text{-}56 \times 10^{6}$ psi)	7.25×10^{10} N/m2 (10.5×10^{6} psi)
Modulus of rupture	$4.5 - 6.9 \times 10^{3}$ N/m^2 (65-100,000 psi)	---
Density, gm/cc	3.98	2.2
Index of refraction 2.2μ	1.73	1.43

Venus surface temperature. The relatively low tensile strength of 6.9×10^7 N/m^2 (10,000 psi) at 537°C however, and the low modulus of 7.25×10^{10} N/m^2 (10.5×10^6 psi) require a relatively thick window to maintain structural integrity and minimize deflections.

As a result of its overall superiority in all factors related to window material selection, sapphire has been selected as the baseline material for windows operating in the visible wavelengths.

Infrared Wavelengths. Candidate materials studied for windows operating in the infrared (2.5 to 14) wavelength are hot pressed zinc sulfide (IRTRAN II), hot pressed zinc selenide (IRTRAN IV) and chemically vapor deposited zinc selenide (CVD ZnSe). Properties of these materials are summed up in Table 4.5-5, and the transmission and emissivity characteristics are shown in Figure 4.5-2.

TABLE 4.5-5. PROPERTIES OF CANDIDATE MATERIALS FOR WINDOWS OPERATING IN IR WAVELENGTHS

Material Properties	Chemically Vapor Deposited Zinc Sulfide (CVD ZnSe)	Hot Pressed Zinc Selenide (IRTRAN IV)	Chemically Vapor Deposited Zinc Selenide (CVD ZnSe)
Hardness (Knoop)	354	Approximately 250	Approximately 250
Melting point (°C)	–	1,500	1,500
Average thermal exponent ($^\circ C^{-1}$)	6.9×10^{-6}	7.4×10^{-6}	7.4×10^{-6}
Young's modulus N/M^2 (Annealed) (psi)	9.65×10^{10} (14.0×10^{6})	7.2×10^{10} (10.3×10^{6})	7.2×10^{10} (10.3×10^{6})
Modulus of rupture N/M^2 (Annealed) (psi)	1.03×10^{8} (15,000)	4.14×10^{7} (6,000)	4.14×10^{7} (6,000)
Density gm/cc	4.1	5.4	5.4
10.6μ absorption coefficient	~0.05 cm^{-1}	0.015 cm^{-1}*	0.005 cm^{-1}
Effect of 200° F on 10.6μ absorption coefficient	~0.16 cm^{-1}	Unknown, but believed to be small	No change
Index of refraction: 10μ	2.20	2.40	2.40

* Extinction coefficient: takes scattering into account

It is possible to make a high temperature (700°C) rigid ceramic pressure seal between IRTRAN II and a nickel iron compound using a ceramic frit. Alternatively, the mechanical properties of the material would allow use of a hollow metallic O ring bearing on the material surface as a high temperature seals. —

Sealing a window of IRTRAN IV can be accomplished by brazing, using a ceramic frit to braze the material to a nickel iron compound collar which would interface with the pressure vessel. An alternate sealing method would use a hollow metallic O ring bearing directly on the face of the material.

Particle impingement may be a problem for each of the IR window materials considered. While they ~~all~~ pass the MIL-E-5272C sand and dust erosion tests, these tests involve particle impingement at low velocities. During the probe descent mission, aeroshell separation occurs at parachute deployment at a velocity of Mach 0.7. After the parachute is jettisoned, terminal descent speed may approach 75 m/sec. Tests of germanium, which is a harder material than any studied here (6.5 moh as compared to 4.5 for ZnS and 3 to 4 moh for the ZnSe), indicated chipping and pitting occur at rain impingement velocities approaching Mach 1.0. Thus, Zns or ZnSe could be expected to degrade at lower impingement velocities, and some form of protection for the planetary flux radiometer during the period immediately following parachute deployment may be required. Further incentive for some form of continuous protection is protection from attack by acids and bases. ZnS and ZnSe do not possess the exceptional chemical inertness of sapphire or fused silica, and while they will withstand dilute acids and bases at room temperature, concentrated acids and bases will destroy the surface. It is possible that at elevated temperatures, even dilute acids and bases will etch the surface of these materials.

Zinc sulfide has the best material properties; however, ZnS has a lattice absorption band which begins at about 10.5μ, causing the emissivity of the material to increase with increasing temperature (Figure 4.5-2). Thus, both the transmission and the emitted energy of the window in a band centered at 10.3 are strongly temperature dependent, effectively precluding the use of ZnS as a window material in the waveband of 8.3 to 10.3 required by the planetary flux radiometer.

IRTRAN IV and CVD ZnSe are mechanically identical, as shown in Table 4.5-5. Either material, when used in a 1 in. diameter window designed to withstand 1.38×10^7 (2,000 psi) at a temperature of 480°C with a safety factor of four, requires a window thickness of 31 mm (1.21 in.). This is a fairly thick window, but due to the extremely low scattering in the CVD ZnSe material, its 10.6 absorption coefficient is only 0.005 cm^{-1}, yielding an absorption through the window in the 3.5 to 10.3 waveband of approximately 1.5 percent, compared to 8 to 10 percent for IRTRAN IV.

Thus, CVD ZnSe is the selected infrared science instrument window material. When provided with some degree of protection from particle impingement, a requirement shared by all candidate materials, CVD ZnSe meets all criteria for the planetary flux radiometer window.

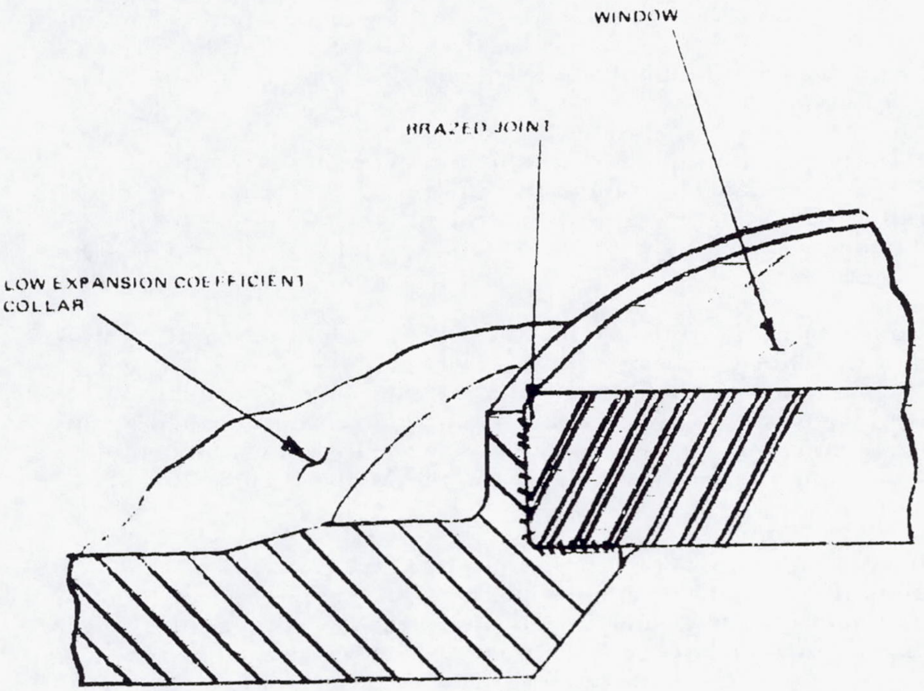

BRAZED SEAL

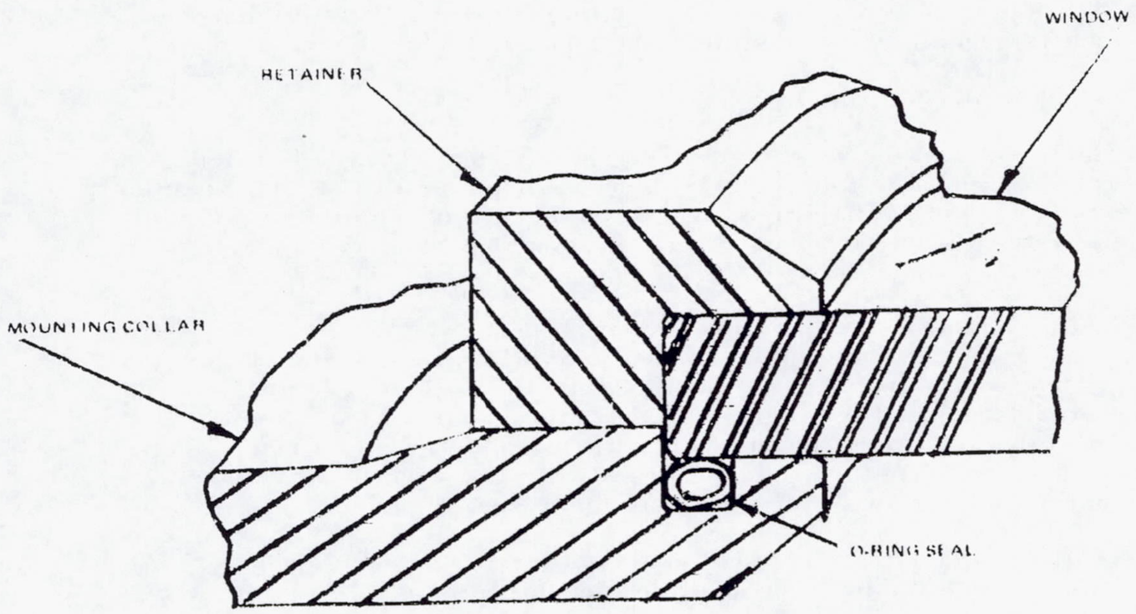

O RING SEAL

FIGURE 4.5.3. CANDIDATE SEAL CONFIGURATIONS

Antireflective Coatings. Preliminary investigation indicates that the [illegible] of either visible range or IR range windows can be improved with antireflective (AR) coatings that can withstand the high temperature and potentially abrasive conditions encountered during probe descent through the Venus atmosphere.

Their use is not recommended on sapphire windows except where experiment considerations make it mandatory, as the low refractive index of sapphire in the visible wavelength (approximately 1.75) keeps losses by reflection at the window surfaces very low for single element optical systems without the use of coatings.

Coatings are also available for the CVD ZnSe selected for IR transparent probe windows. These coatings routinely survive exposure to temperatures of 537°C in air for periods of 20 min during brazing operations performed on coated windows. These capabilities would be increased in the low oxygen dry atmosphere of Venus. Hughes experience shows abrasion resistance to be good, and the coatings will pass the MIL-M-13508B tests for adhesion and hardness.

The relatively high refractive index (approximately 2.4) of the CVD ZnSe material makes the use of coatings appear attractive. High efficiency multilayer IR wavelength coatings such as the IR H.E.A.* series supplied by Optical Coating Labs, Inc. can provide efficiencies of 98.5 percent per surface in the 8 to 11.7 wavelengths, for a total transmittance of over 95 percent compared to slightly over 70 percent for an uncoated sample.

Testing of these coatings to verify their survivability in the Venus environment is recommended, as their use appears highly desirable.

Window Mechanical Design

Seals. All probe window penetrations must maintain a hermetic seal under external conditions ranging from hard vacuum at -40°C to approximately 100 atm at over 480°C. High pressure exposure is limited to approximately 1 hour, while the vacuum encountered during Earth-Venus transit lasts for several months.

Two types of seal capable of operating under the specified temperature and pressure conditions were evaluated (Figure 4.5-5). Hollow, metallic O-ring seals are used in many extremely high temperature and pressure applications. Rigid brazed seals between windows and mounting surfaces perform well, but require very careful selection of paired window/mount materials with coefficients of thermal expansion that match closely over the entire temperature range to be encountered.

Both brazed and O-ring seal concepts offer well developed and effective solutions to the probe window seal requirements. Brazing is the preferred sealing method for windows mounted remotely from the pressure vessel, as this allows simple integration of the Kovar mount, which can be sealed to the pressure vessel with an O-ring. This method takes advantage

---

*High efficiency antireflective.

3C163-425/C

INTEGRALLY MACHINED
DOUBLER INSTALLATION

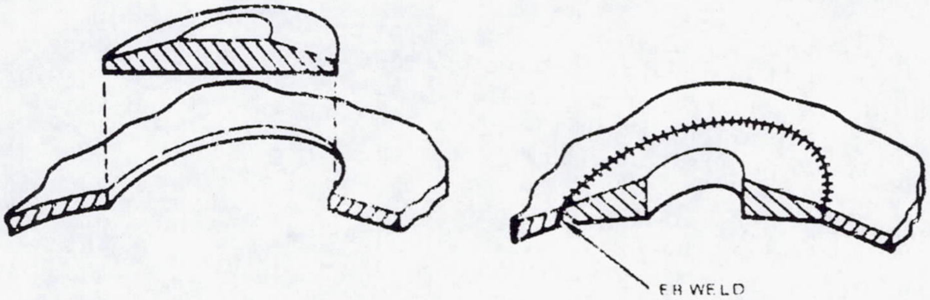

ELECTRON BEAM WELDED
DOUBLER INSTALLATION

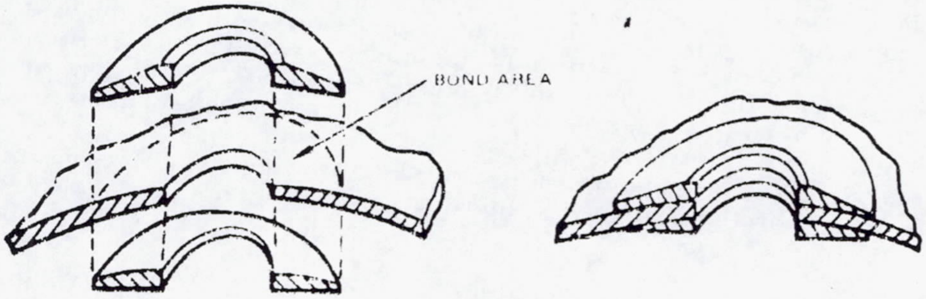

BONDED DOUBLER
INSTALLATION

FIGURE 4.5.4 PENETRATION REINFORCEMENT – DOUBLER FABRICATION CONCEPTS of the low [illegible] [illegible] reliability of the braze [illegible] [illegible] will allow separate [illegible] [illegible] O-ring seals [illegible] interface with the pressure vessel wall, [illegible] provide flexibility in material compatibility and of the seal [illegible] with an O-ring sealed joint. Representative [illegible] [illegible] O-rings (14 [illegible] diameter) have been tested at [illegible] pressures and temperatures which simulate Venus conditions at the surface. No measurable leakage was observed during the test.

Careful selection and use of both seal concepts in a complementary manner allows optimization of the entire seal system for minimum weight while maintaining access and ease of integration.

Doublers, or locally thickened areas of the pressure vessel wall, are required around penetrations to maintain structural integrity. These doublers have been made axisymmetric where possible to facilitate fabrication.

Three methods have been studied for incorporation of doublers into the pressure vessel wall: 1) integral mechining of the doubler directly into the wall, 2) fabrication of doubler and penetration as an axisymmetric plug to be welded into a hole machined in the pressure vessel wall, and 3) bonding of doublers around penetrations (Figure 4.5-4).

Electron beam welding of axially symmetric plugs which incorporate the doubler configuration into a shell of uniform thickness has been selected as a baseline fabrication method. The cost of this approach is low with respect to integral machining of shell and doublers, and its effect on pressure vessel structural integrity is minimal. Evaluation of bonded doublers is also continuing pending better definition of pressure vessel wall temperatures. No other difficulties are anticipated in fabrication of window configurations typical of those studied.

Experiment Window Detail Design

The diversity of large probe window requirements prevented design of one baseline window suitable for all experiments. Instead, each window was considered on an individual basis, taking into account the experiment requirements and the seal, structure, thermal and productibility constraints already covered. Two, and sometimes three configurations were generated in some detail for each window to allow a quantitative comparison of weight and integration characteristics. Comparison of the candidate configurations using the data generated in the study then allowed selection of baseline designs for each window.

Nephelometer Windows. The nephelometer source window provides a 1 deg. conical field of view centered about a line of sight lying in the -X, -Z quadrant of the X-Y plane at an angle of 21 deg. with respect to the negative X-axis. The nephelometer light source operates in the visible wavelengths, allowing use of sapphire as a window material. The window must be heated throughout the descent to prevent condensation of Venus atmosphere constituents. Two configurations considered for the source window are shown in Figure 4.5-5.

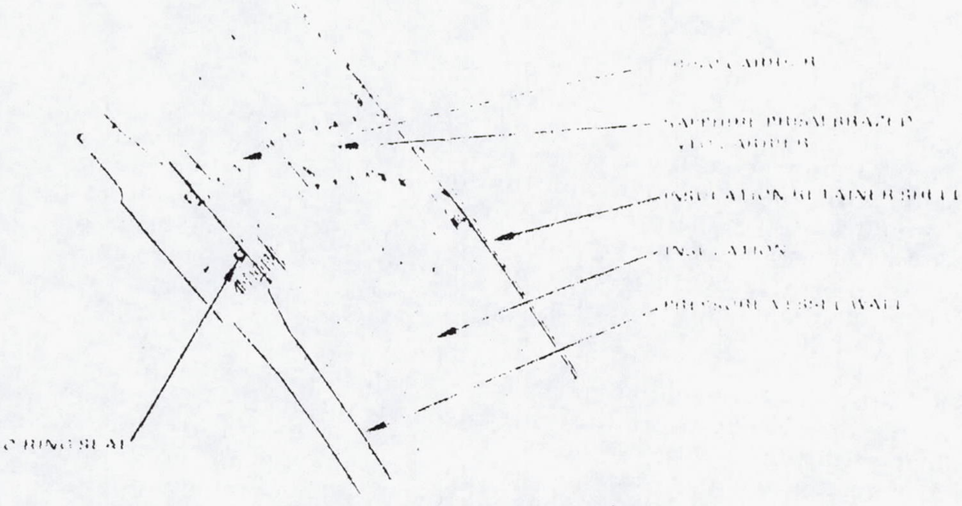

a) PRISM CONFIGURATION 4.54 x 10^{3} kg (0.01 lb)

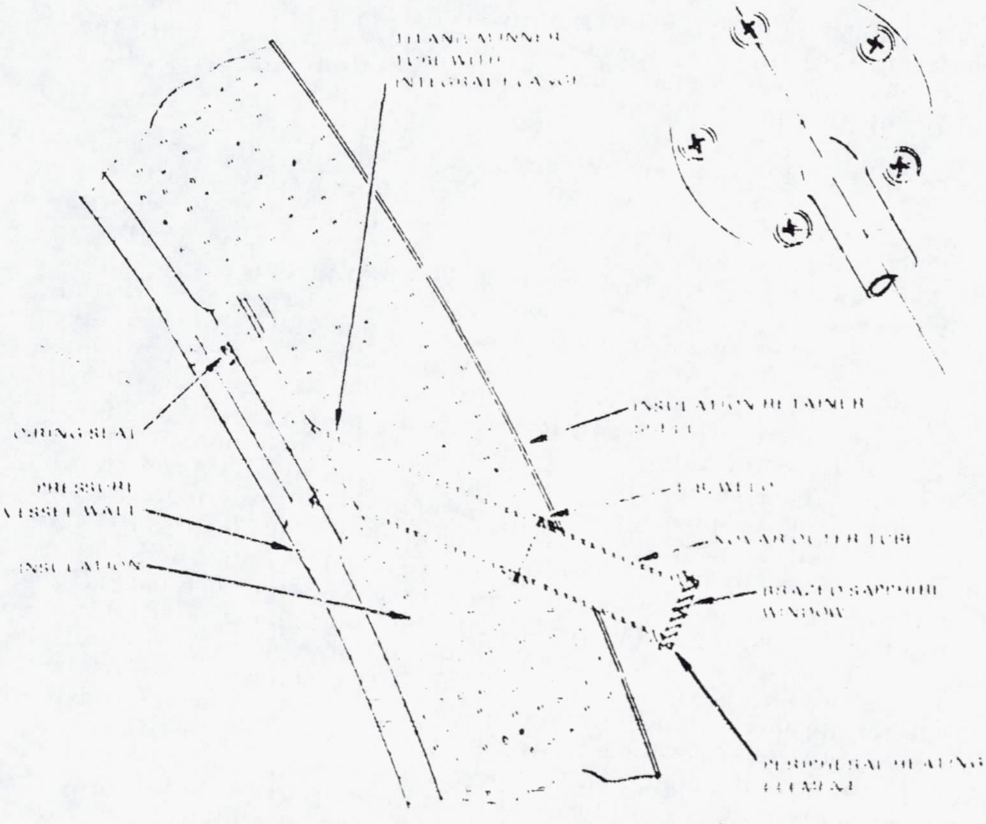

b) REMOTE WINDOW CONFIGURATION 4.54 x 10 10^{3} kg (0.01 lb)

FIGURE 4.5-5 NEPHELOMETER WINDOW CANDIDATE CONFIGURATIONS

In terms of weight, the candidate configurations are closely matched. The remote window, however, requires less heater power, as the internal location of the window and its exposed position act to decrease power requirements by isolating the window from the relatively cool pressure vessel wall. The easire integration with the external insulation offered by the prism configuration with its mounting normal to the pressure vessel surface, is offset by the slightly power weight and complexity and superior optical properties of the remote window configuration with its brazed window. Accordingly, configuration two has been chosen as the baseline configuration for the large probe nephelometer source window.

The nephelometer sensor window provides a 10 deg. conical field of view centered on a line of sight lying in the -X, +Z quadrant of the X-Z plane at an angle of 21 deg. with the negative X-axis, intersecting it at a distance of 635 mm (25 in.) from the probe Z-axis. The sensor operates in the visible wavelengths, and sapphire is used as a window material. The window must be heated to prevent condensation.

The sensor window configuration is similar to the source window, except that the window optical diameter is one half inch to accommodate the wider field of view requirement. The support tube inside diameter is also increased to 12.7 mm (0.5 in.).

Aureole Extinction Experiment Window. The aureole window provides a field of view of 7.5 deg. vertically and ±10.25 deg. horizontally centered on a line of sight lying in the -X, -Z quadrant of the X-Z plane 25 deg. from the negative X-axis. The aureole extinction detector operates at wavelengths from 0.3 to 0.9 M allowing use of sapphire as a window material. Heat must be supplied to prevent condensation on the window surface down to an altitude of 40 km, where the experiment is shut off. Figure 4.5-6 shows the two configurations studied for the aureole window. The first configuration uses a 35 mm diameter, 5 mm thick window remotely mounted at the end of a tube welded to the pressure vessel wall to minimize heater power. The window is retained by a ring bolted to the tube, which also serves to preload the metallic O-ring seal. Figure 4.5-6a shows the first configuration, which is heated by a sheathed element heater wrapped around the periphery of the window. The heater is electrically switched off at 40 km. The second configuration (Figure 4.5-6b) utilizes a pressure vessel mounted pressure window contained with an outer window on tempered glass, which is hermetically sealed to the retaining ring by a silicone rubber O-ring. The area between the window is filled with a dry, inert gas, which prevents condensation on the inner window, eliminating the need to heat it. The outer window is heated by a transparent conductive film heater deposited on the window surface (see Section 3). The outer window withstands the external pressure down to an altitude of 40 km, where the pressure lead becomes great enough to fracture the window. The residual stresses induced by tempering cause the window to disintegrate into powder like particles which are remoded by the airstream. This disintegration cuts off the heater power at the electrical film is disinegrated.

Heater power consumption for both concepts is approximately equal. The remotely mounted window is heavier than the pressure vessel mounted

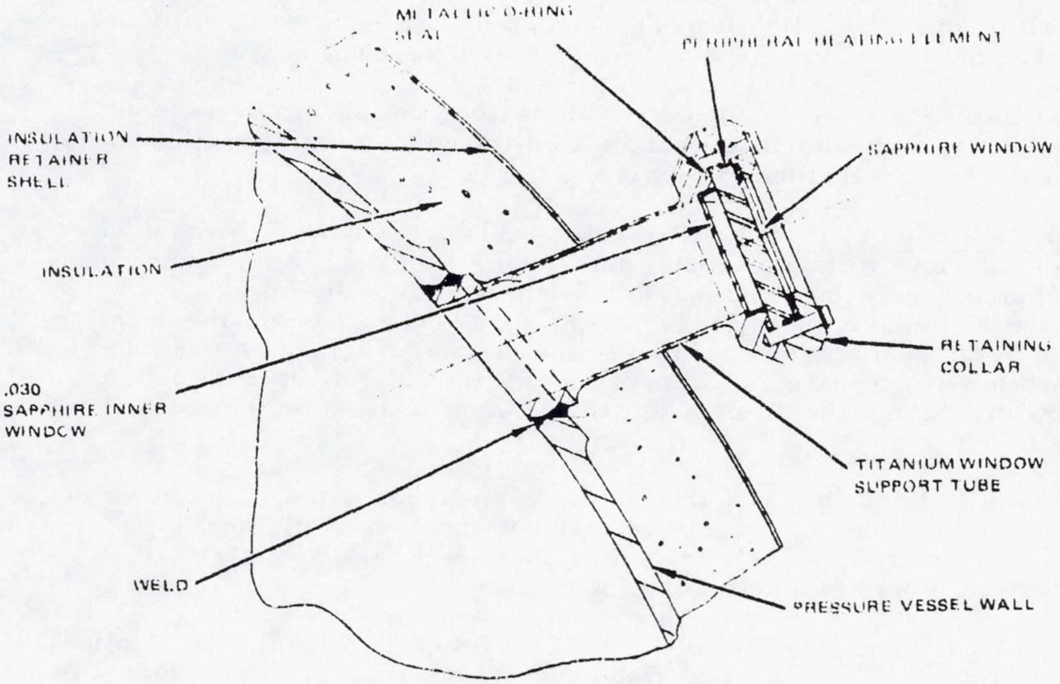

a) REMOTELY MOUNTED WINDOW 0.1 kg (0.22 lb)

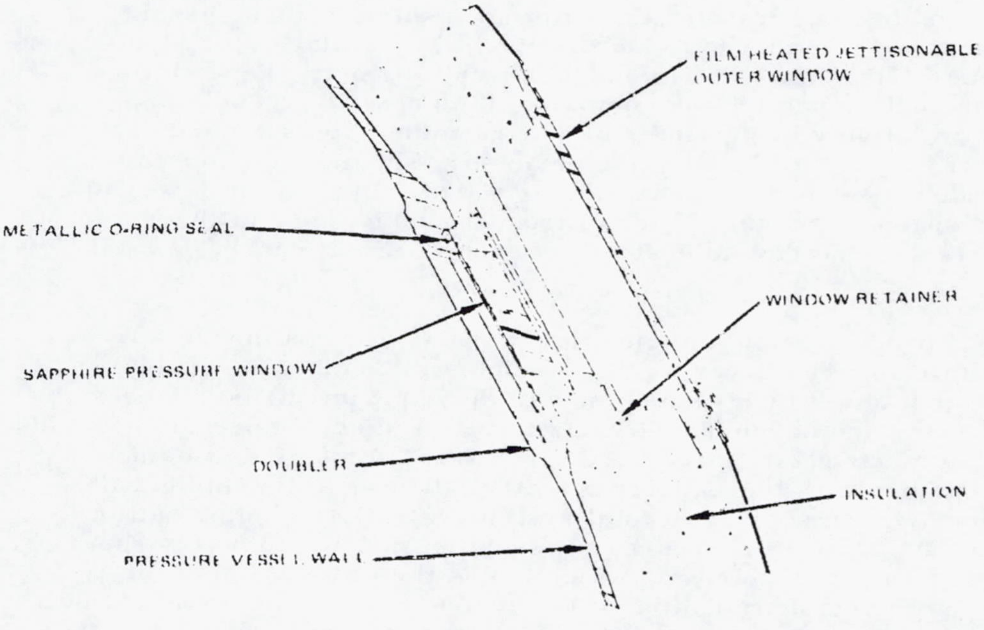

b) PRESSURE VESSEL MOUNTED WINDOW 0.082 kg (0.18 lb)

FIGURE 4.5-6. AUREOLE EXTINCTION DETECTOR WINDOW CANDIDATE CONFIGURATIONS

3G163 427(U)

window, and it requires added weight for electrical switching if heater power is to be cut at 40 km. The slightly decreased optical transmissivity of the film heated window can be compensated for in instrument calibration.

Accordingly, the double window, film heated configuration has been chosen on the basis of minimum weight as baseline window configuration for the aureole extinction detector experiment.

Solar Radiometer Window. The solar radiometer window provides a ± 15 deg. field of view in the horizontal plane and a ± 65 deg. field of view in the vertical plane, centered about a line of sight contained in the -X, +Z quadrant of the X-Z plane, parallel to 64 mm and (2.50 in.) below the negative X-axis. The solar radiometer operates in the visible wavelengths from 0.3 to 3 μ, allowing use of sapphire as a window material. Heat must be supplied to the window throughout the descent to prevent condensation on the window surface.

The wide field of view required in the vertical plane requires either a large window in the pressure vessel wall, or some means of placing the scanning prism or mirror outside the pressure vessel, allowing a relatively small penetration. Both methods were investigated.

Concept 1 (Figure 4.5-7b) uses 64 by 12.7 mm (2.5 km 0.5 in.) optical size window, 3 mm (0.125 in.) thick, mounted in a boss integrally machined in the pressure vessel wall. Concept 2 (Figure 4.5-7a) is designed to minimize the penetration size required in the pressure vessel wall. Temperature protection for the motor is provided by the heat sinking it to the relatively cool pressure vessel, and burying it under the external insulation. The weight penalty for the motor is considered to be minimal, as it replaces the scanning motor incorporated in the experiment. Concept 3 (Figure 4.5-7c) also brings the scanning optics outside the contour of the pressure vessel, but keeps them in the relatively benign interior environment. This reduces heat flow to the pressure vessel wall aiding the peripheral sheathed element heater in heating the window. Heater power is further reduced by a 0.75 mm (0.030 in. thick) window spaced 3 mm (0.125 in. h) from the inside face of the heated window, which acts as a barrier to heat losses from thermal convection and radiation.

The optical properties of configuration 3 are as good as those of any configuration examined. The lower weight of configuration 2 (valid in any case only if stepper motor weight is assigned to the experiment) is balanced by the increased risk, and development costs involved in developing the precise externally mounted mechanization required for scanning prism positioning. These factors, together with the inferior optical qualities of this configuration led to its rejection. A comparison of total system weights (including battery weight required to supply heater power) shows configuration 3 to be far superior to configuration 1. This superiority in weight, plus the elimination of the window hot spot due to remote mounting of the heated window, led to selection of this concept as baseline configuration for the solar radiometer window.

FOLDOUT FRAME

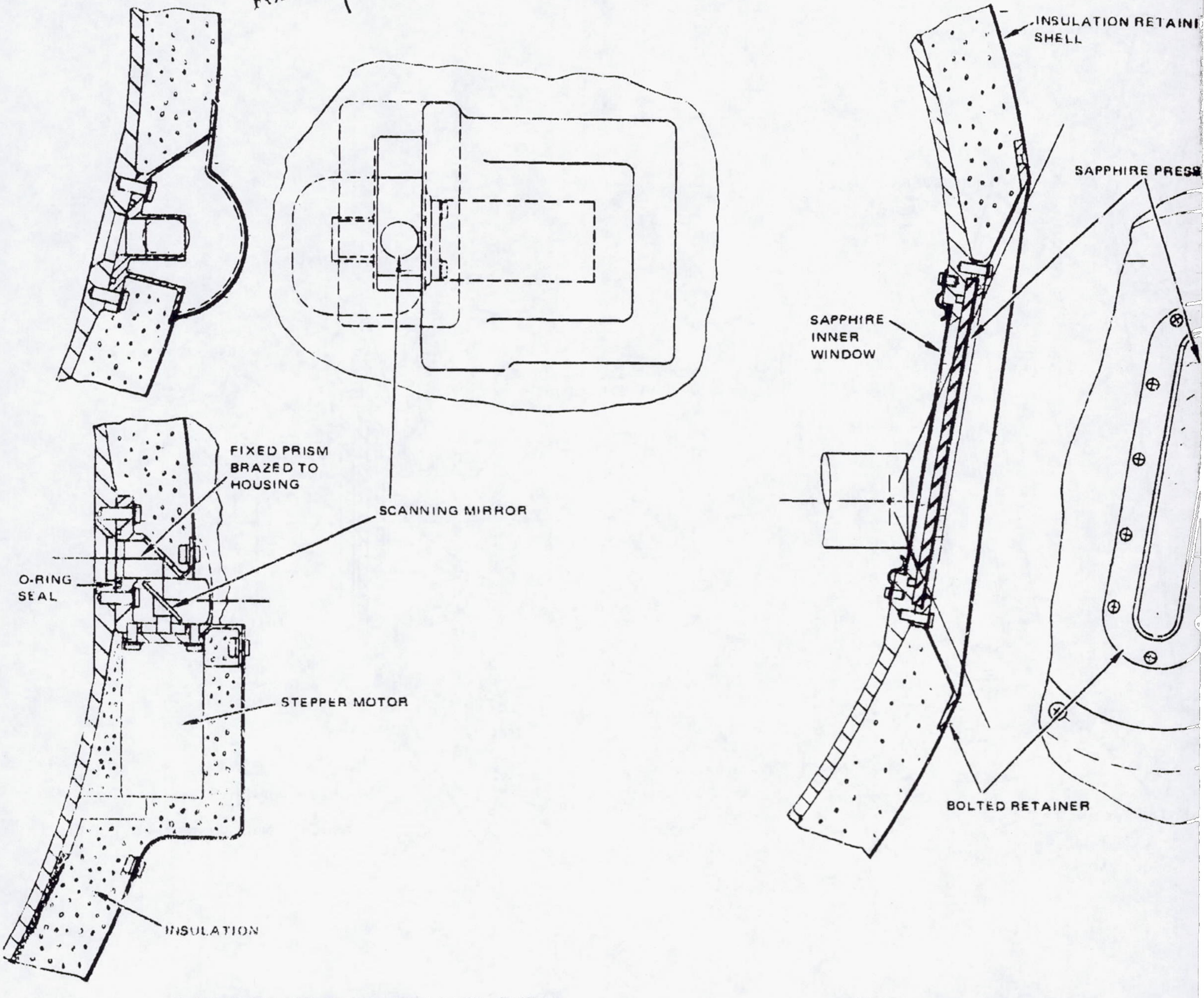

a) EXTERNAL SCANNING MIRROR 0.068 kg (0.15 lb)
(WEIGHT OF STEPPER MOTOR NOT INCLUDED)

b) PRESSURE VESSEL MOUNTED WINDOW 0.

FIGURE 4.5-7. SOLAR FLUX RADIOMETER WINDOW CANDIDATE CONFIGURATIONS

PRECEDING PAGE BLANK NOT FILMED

FOLDOUT FRAME

2

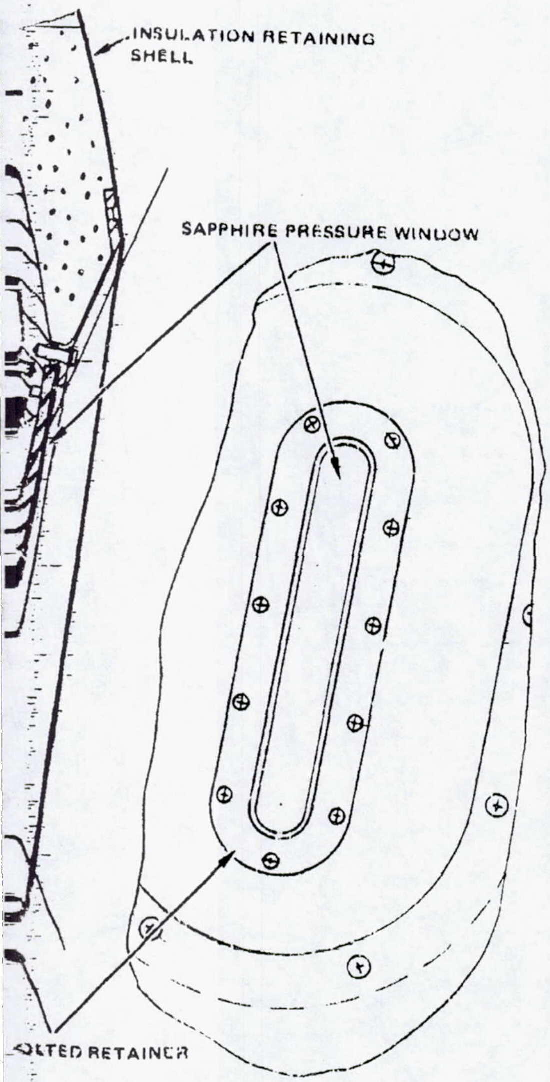

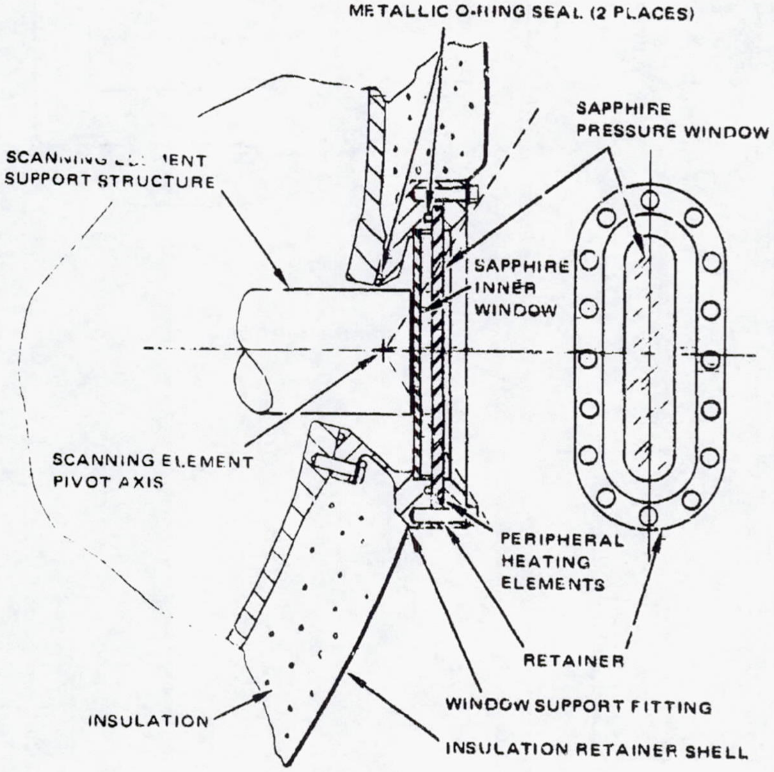

30163-428(U)

VESSEL MOUNTED WINDOW 0.14 kg (0.3 lb)

c) REMOTE MOUNTED WINDOW EXTERNAL SCANNING ELEMENT 0.13 kg (0.27 lb)

Planetary Flux Radiometer Window. The planetary flux radiometer window provides a 5 deg. conical field of view centered about a line of sight contained in the +Y, +Z quadrant of the Y-Z plane, parallel to and 171 mm (6.75 in.) from the Z-axis. Operating wavelengths range from 3 to 11 μ, well into the infrared, and CVD ZnSe has been selected as the window material. Heat must be supplied throughout the descent profile to prevent condensation on the window surface.

Two configurations were studied for the planetary flux radiometer window, allowing comparison of brazing versus mechanical retention. Configuration 1 (Figure 4.5-8a) uses a 25.4 mm (1.0 in.) optical diameter 21.6 mm (0.85 in.) thick window fabricated of CVD ZnSe.

Configuration 2 (Figure 4.5-8b) uses a mechanical retention system with 35.6 mm (1.4 in.) total diameter 21.5 mm (0.85 in.) thick CVD ZnSe window.

The mechanical simplicity and resulting lighter weight associated with the brazed window of configuration one, when combined with equal or lower heater power requirements make this the logical choice for the baseline solar radiometer window configuration.

The somewhat lower heat conductance into the pressure vessel of the mechanically retained window, caused by the O-ring type seal, is negated by the requirement of continually raising the temperature of a much larger window mass, resulting in a heater power consumption approximately equal to that of the relatively high conductance brazed window.

Cloud Particle Size Spectrometer Window. The cloud particle size spectrometer window provides a constant 25.4 mm (1.0 in.) diameter view field extending between the pressure vessel and an externally mounted mirror. The view field is centered on a line of sight contained in the +X, -Z quadrant of the X-Z plane, parallel to and 172 mm (6.75 in.) from the probe X-axis. The experiment operates in the visible region of the spectrum, and sapphire has been chosen as the window material. Heat must be applied to the window throughout the descent profile to eliminate condensation.

Two different experiment optical configurations were considered. The first possesses a single 25.4 mm (1.0 in.) diameter aperture, the second one 6.3 mm (0.25 in.) diameter, and one 12.7 mm (0.5 in.) diameter aperture on 1 inch centers. Window concepts were developed for both configurations.

Three configurations (Figure 4.5-9) were considered for the cloud particle size spectrometer window; a dual window, for the experiment concept using separate source and sensor lenses; a remote mounted window 25.4 mm (1.0 in.) in diameter for the single lens experiment concept; and a concept incorporating an integral mirror mount to evaluate one method of maintaining good mirror alignment throughout the mission.

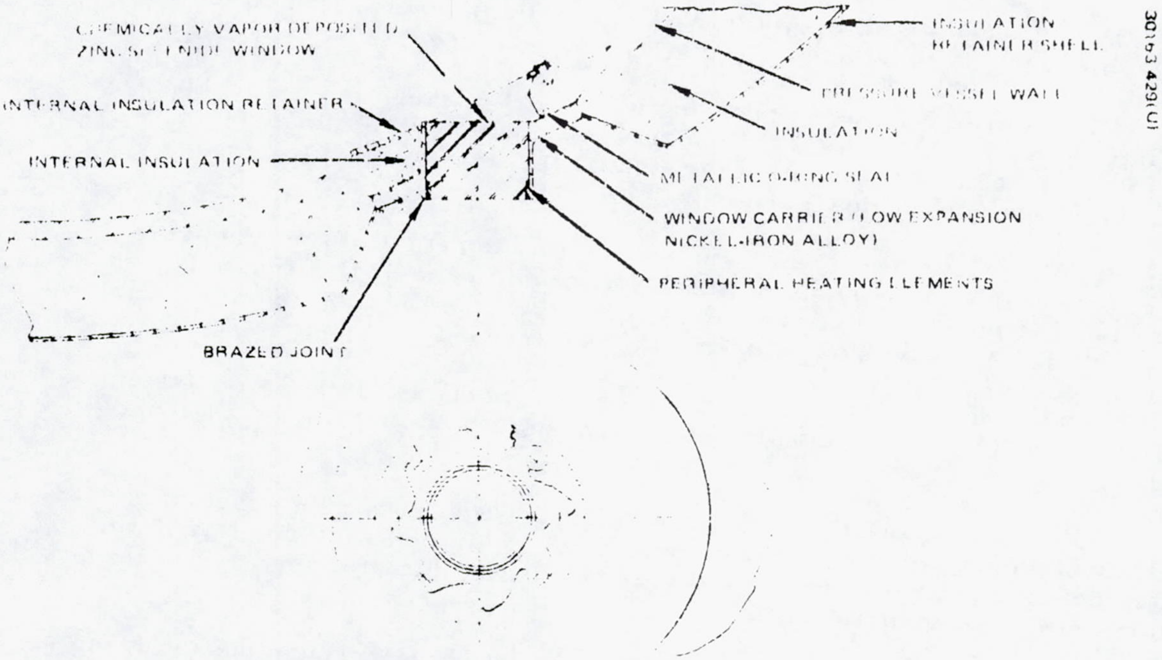

a) **BRAZED WINDOW 0.14 kg (0.31 lb)**

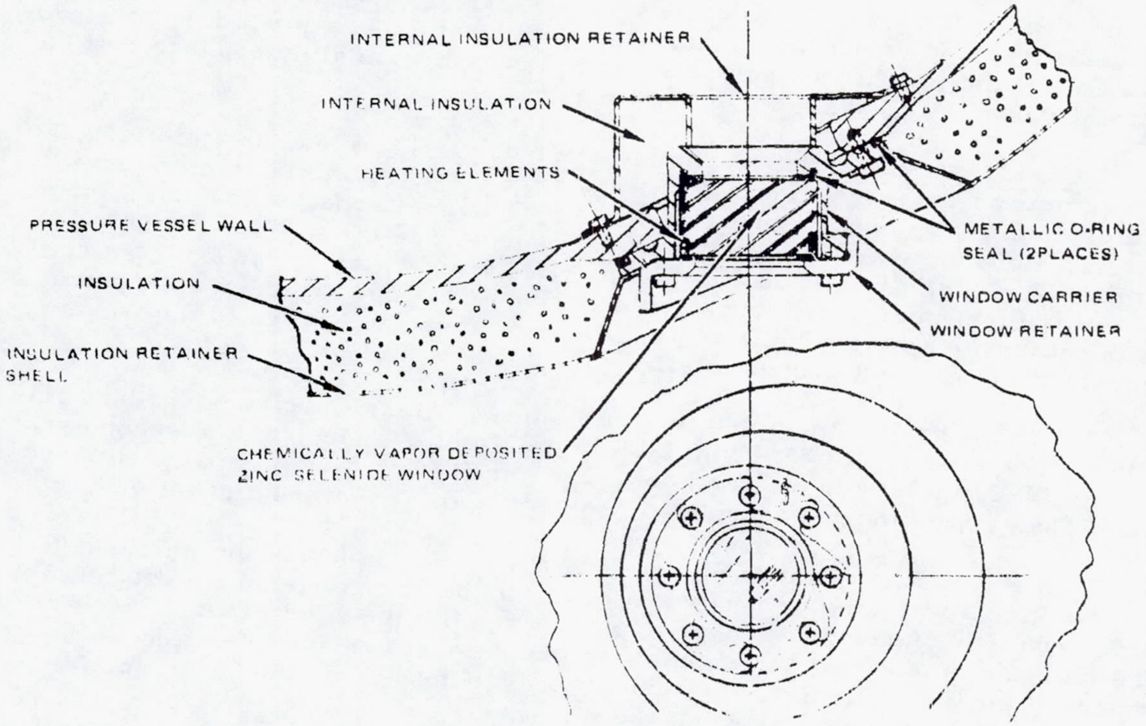

b) **O RING SEALED WINDOW 0.22 kg (0.49 lb)**

FIGURE 4.5.8 – PLANETARY FLUX RADIOMETER WINDOW CANDIDATE CONFIGURATIONS

REPRODUCIBILITY OF THE ORIGINAL PAGE IS POOR.

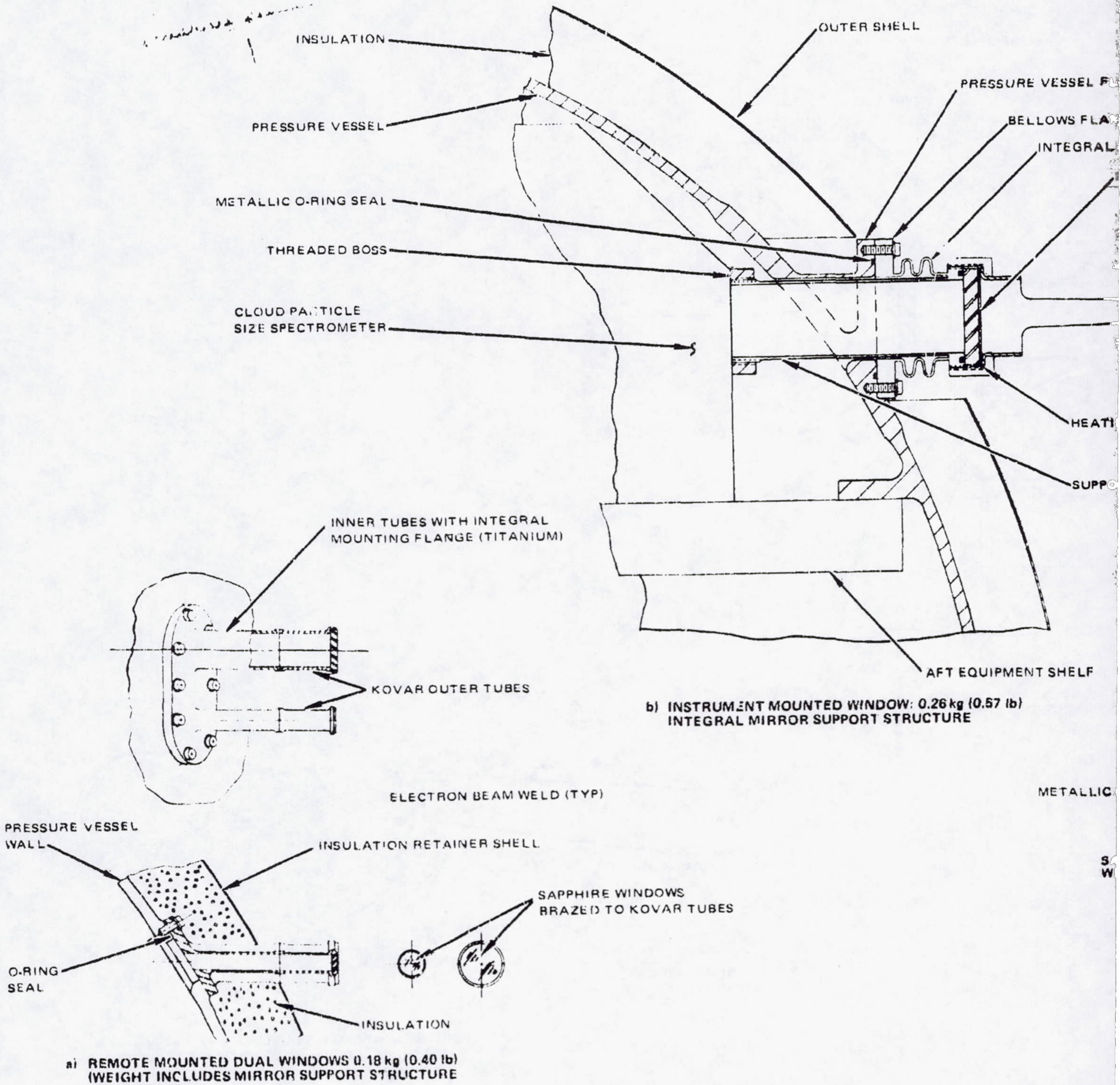

b) INSTRUMENT MOUNTED WINDOW: 0.26 kg (0.57 lb) INTEGRAL MIRROR SUPPORT STRUCTURE

a) REMOTE MOUNTED DUAL WINDOWS 0.18 kg (0.40 lb) (WEIGHT INCLUDES MIRROR SUPPORT STRUCTURE NOT SHOWN)

FIGURE 4.5-9. CLOUD PARTICLE SIZE SPECTROMETER WINDOW CANDIDATE CONFIGURATIONS

FOLDOUT FRAME

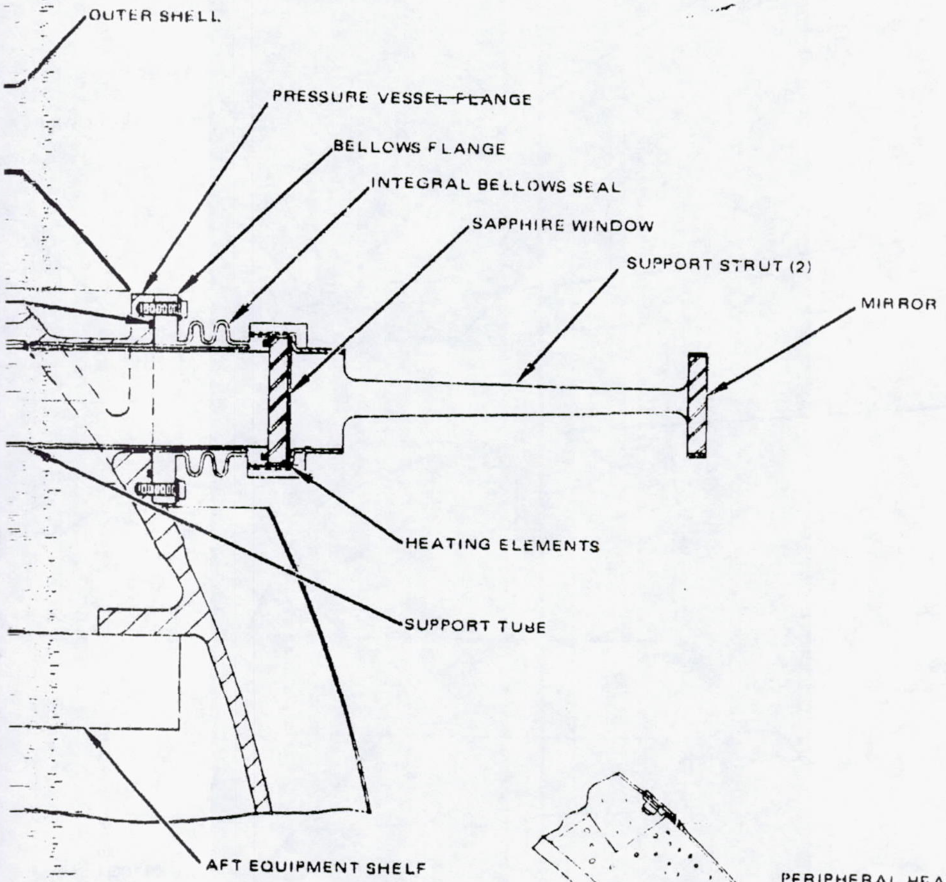

UNTED WINDOW: 0.26 kg (0.57 lb)
R SUPPORT STRUCTURE

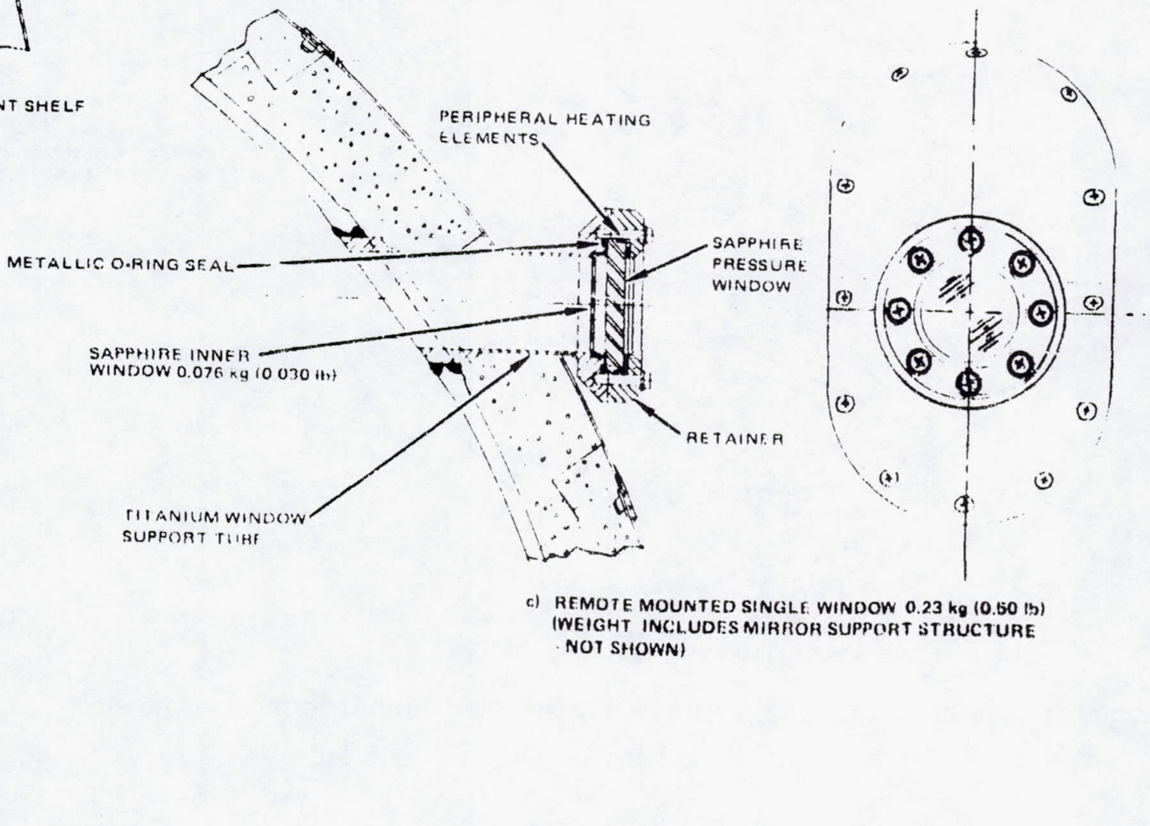

c) REMOTE MOUNTED SINGLE WINDOW 0.23 kg (0.50 lb) (WEIGHT INCLUDES MIRROR SUPPORT STRUCTURE NOT SHOWN)

30163-430(U)

Concept 2 (Figure 4.5-9c) uses a single 25.4 mm (1.0 in.) diameter pressure window mounted on a titanium support tube to minimize heat conduction to the pressure vessel wall. Concept 3 (Figure 4.5-9b) combines window, support tube, and mirror support into a single structure cantilevered from the experiment enclosure.

Weights for the three concepts studied were compared by adding mirror support structure weight figures to the window weights of concepts 1 and 2 to arrive at a total system weight for each. Heater power requirements were also compared for each concept, with mirror heater power consumption assumed to be the same for all.

Configuration 1 is clearly the lightest system, and uses the least power, leading to its selection, with associated mirror support structure as baseline window configuration for the cloud particle size spectrometer.

REPRODUCIBILITY OF THE ORIGINAL PAGE IS POOR.

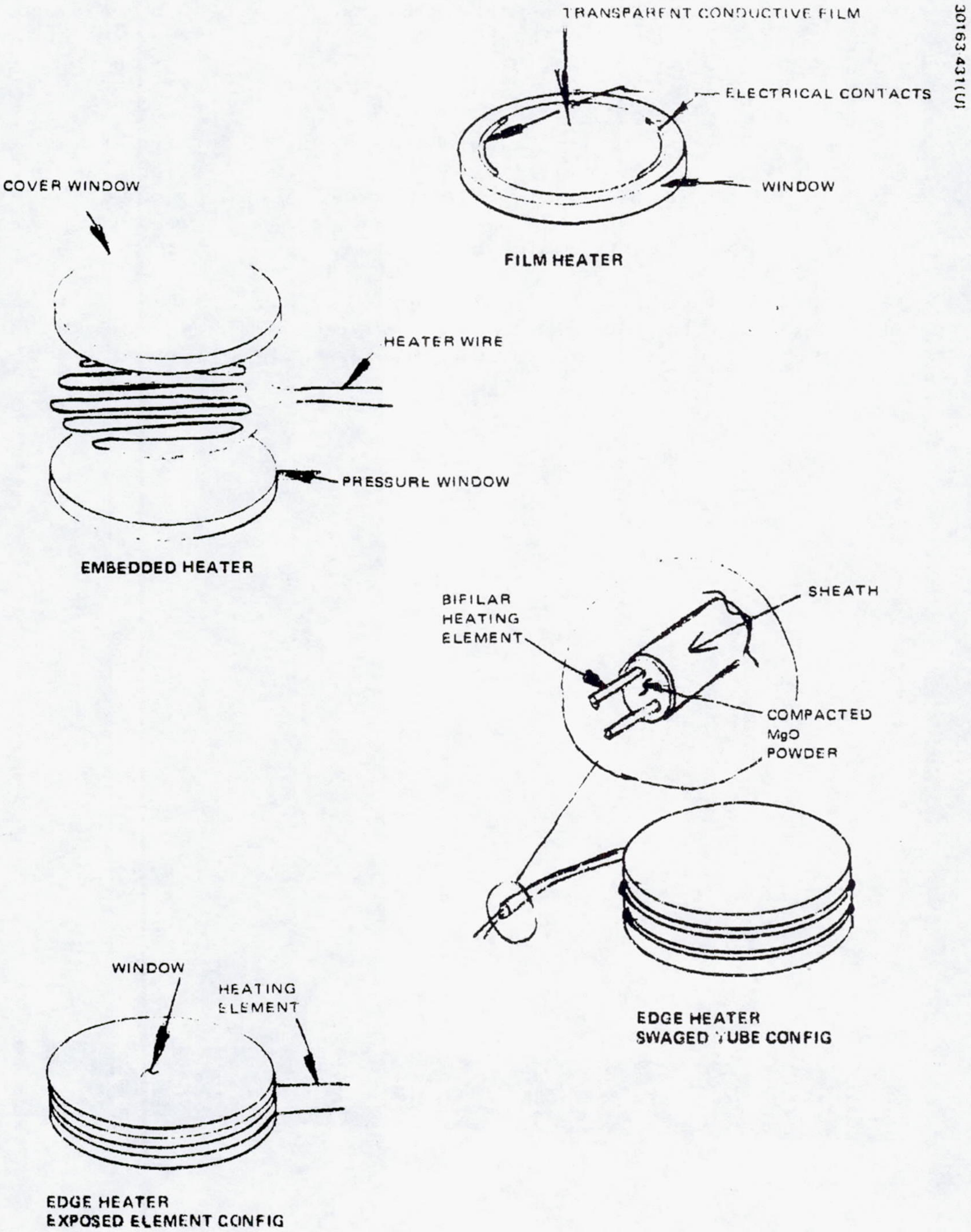

FIGURE 4.5 10. CANDIDATE WINDOW HEATER CONFIGURATIONS

REPRODUCIBILITY OF THE ORIGINAL PAGE IS POOR.

Window Heater Design

Preliminary analyses using the baseline windows as models have been performed to define heater power requirements. At Venus surface conditions the 0.25 in. diameter windows of the nephelometer require 6 W each. The 1 in. diameter windows of the cloud particle size analyzer and the planetary flux radiometer require 12 W and the 2 in. oval window for the solar flux radiometer requires 20 W. Heater power scheduling methods studied were: 1) using a controller to keep the windows at a set temperature differential with respect to ambient; 2) turning the heaters on at full power when the aft cover is jettisoned; and 3) using two power levels, initiating low power mode when the after cover is jettisoned and switching to high power at parachute release. As a result of these studies the single power level approach was determined to be a minimum weight system and was selected as a baseline.

Three window heater configurations were studied for windows exposed to the full differential between Venus atmosphere ambient and probe internal pressure: 1) film heaters using a thin layer of a proprietary conductor deposited on the window surface, 2) heating elements consisting of thin wires sandwiched between layers of sapphire. Grooves would be etched into the surface to mechanically retain the heating elements, 3) edge heating by means of electrical heating elements wrapped around the window periphery in direct contact with the window edge, 4) edge heating by means of electrical heating elements enclosed in a metallic sheath which contacts the window edge (see Figure 4.5-10).

An evaluation of these configurations led to rejection of the film heater for pressure windows for reasons of power density and the difficulty of integrating electrical contacts into the small window sizes used. The "sandwich" heater approach is an efficient system, but the extra thickness of sapphire required as a retainer (the pressure window must retain its full thickness, as no bonding material can exist at the required temperatures to form the two windows into an integral structure), as well as the unavoidable optical losses at the extra interface, led to rejection of this approach. Bare electrical heating elements represent the highest efficiency for edge heater configurations, and are potentially the lowest weight method, but fundamental difficulties in maintaining electrical isolation in extremely compact window configurations and at the high temperatures under investigation as well as generation of stray magnetic fields make this a high risk approach. Heating elements enclosed in a metallic sheath and heating the window around its periphery were selected as a baseline because they are well developed, space qualified, and available in a wide variety of shapes and power ratings, yielding a very flexible and low risk approach. In addition, the bifilar nature of the heating element current flow eliminates stray magnetic fields.

For nonpressure windows, with their much smaller ratio of thickness to diameter, film heaters save considerable power compared to edge heating, resulting in the selection of film heaters as a baseline configuration for all external windows operating in the visible range.

Contaminant Removal Systems

Contamination of probe window surfaces by liquid or solid particles suspended in the atmosphere of Venus may significantly degrade the experiment data obtained through the windows.

Several processes by which window contamination could occur were examined to determine which constituted the greatest threat to window optical properties.

Gases and solids present relatively minor problems. Condensation of gases, or freezing of liquids or slurries, is prevented easily by window heaters, and abrasion caused by solid particles is prevented by selecting abrasion resistant window materials, such as sapphire. Etching of window surfaces by the chemical action of acids or bases is also best dealth with by selection of window materials which are chemically inert.

Accordingly, as window heaters are already carried, consideration of contamination removal systems was limited to those capable of dealing with formation of a liquid film or adherence of particles or droplets.

Window contaminants of particulate nature (dust, sand, liquid droplets) could significantly degrade experiment data. Accordingly six candidate methods of contaminant removal have been studied:

1) Frangible, squib actuated tempered glass protective covers

2) Transparent, jettisonable protective cover

Both of the preceding methods would have the instruments reading through the cover down to a preset altitude. At this point the covers are either destroyed or jettisoned, removing accumulated contaminants (accumulation of which would be indicated by a sudden change in readings following cover removal).

3) Transparent rotary shutter. This shutter could be operated in two modes: rapid continuous rotation (at least several thousand rpm) would sling contaminants off by centrifugal force; alternatively, slower, stepped rotation would bring a clear area of shutter into view prior to each reading.

4) Mechanical shutter. Solenoid actuated, the shutter minimizes the amount of time that the window is exposed to contamination.

5) Mechanical wiper. Also solenoid actuated, the mechanical wiper requires a double window as the wiped window should be flush with the wiper surface. Development of a wiper material capable of providing both effective, nonsmearing wiping action and withstanding the Venus surface environment is a high risk item, but potential effectiveness is very good if such a material can be developed.

6) Gas Jet. A gas jet system using a squib actuated valve to bleed gas from an internal reservoir to nozzles adjacent to each window requires relatively little development effort and is adaptable to sunken windows; but it is by far the heaviest and bulkiest system considered. An alternate gas jet system using filtered ram air was evaluated and appears attractive because of its low weight and completely passive nature, but considerable testing would be required to determine system effectiveness.

A preliminary analysis has been conducted to yield weight, power consumption and other characteristics for each configuration considered. The results of these studies are summarized in Table 4.5-6.

On the basis of these studies, jettisonable protective covers are recommended as a baseline contaminant removal system for windows operating in the visible range because of their low weight, low power consumption, and low development risk.

Pressure Sensor Inlet System

The primary function of the pressure sensor inlet system is to provide ambient pressure to the internally mounted pressure sensor. In addition, the inlet system must satisfy the following requirements:

1) Location: The inlet system must sample pressure at locations in the forward hemisphere 30 deg either side of the descent axis

2) Length: To minimize line pressure loss, the sensor assembly should be located as close as possible to the ports. Overall line length should be under 150 mm (6.0 in.)

3) Structural: The feed through aperture in the pressure vessel should not affect pressure vessel structural integrity. The lines carrying ambient pressure inside the pressure vessel will be sized to a safety factor of four

4) Seals: The feed through the internal pressure lines, and the fitting which joins the pressure sense lines to the pressure sensor will maintain a hermetic seal throughout all phases of the mission

5) Blockage: The pressure lines are required to be large enough (≥ 6.3 mm (0.25 in.) diameter) to be self-clearing in the event of internal condensation

6) Installation: Access must be provided for connection of the internal pressure line to the fitting on the pressure sensor assembly during experiment installation

Two inlet system configurations were considered, one of which allowed the pressure sensor to be mounted on the equipment shelf, and the other

FOLDOUT FRAME

FOLDOUT FRAME

TABLE 4.5-6. COMPARISON OF CANDIDATE CONFIGURATIONS--CONTAMINANT REMOVAL SYSTEMS

	Approach					
	Continuously Acting Systems				[illegible]-Shot	
	High Pressure Gas Jet	Ram Air Gas Jet	Rotary Shutter	Mechanical Wiper	Mechanical Shutter	[illegible] Cover
Characteristics	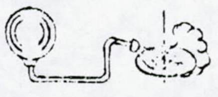		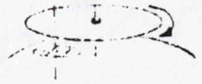			
Operation	Fixed nozzle directs gas flow over window, blowing contaminants off	Ram air collected by scoop and filtered, then ducted across window shielding window from contaminants	Rapidly rotating transparent cover slings contaminants off	Wiper mechanically removes contaminants from outer of double window configuration	Mechanical shutter opens only during readings, minimizing window exposure to contaminants	Transparent cover shatters, carrying away accumulated contaminants
Removes contaminants	Yes	No	No	Yes	No	Yes
Shields window	Yes	Yes	Yes	No	Yes	Yes
Effectiveness	Difficult to assess without testing	Very difficult to assess without testing	Potentially good; testing required for evaluation	Potentially excellent if suitable wiper material available	Depends on nature of contaminants. Some protection inherent with respect to unprotected window	Very effective for all types of contamination, but can only be used once
Droplet/particle accumulation	Potentially fair to good	Very difficult to assess without testing	Potentially good	Excellent		
Liquid film	Potentially fair to good	Very difficult to assess without testing	Potentially excellent	Excellent		
Acid etch	Difficult to assess	Very difficult to assess without testing	Cover susceptible	Depends on wiper material and contaminant		
Abrasion	Could increase abrasion (sandblast)	Good	Good, but cover susceptible to abrasion	Could increase abrasion		
Mechanization	Solenoid actuated valve periodically bleed gas from reservoir. Regulator required to lower gas consumption	Completely passive	Electric motor drives rotating disc shaped cover – continuous or stepped rotation	Solenoid sweeps wiper spring return	Solenoid opens shutter against return spring	Squib driven pin impacts cover. Residual stresses tempered glass cover cause total disintegration
Mass per window	5.7 kg (12.5 lb)	91 g (0.2 lb)	0.68 kg (1.5 lb)	0.68 kg (1.5 lb)	0.45 kg (1.0 lb)	45 g (0.1 lb)
Commands required	1 squib actuation pulse for system start 1/10 duty cycle pulses for solenoid	None	1 command required system actuation	1/10 duty cycle pulses required for switching power to solenoid	Command required prior to each instrument reading to switch solenoid and open shutter	1 squib actuation pulse required for cover disintegrat
Power required for window	Squib pulse plus 7 W average continuous	None	15 W	17 W	13 W	1 squib pulse
Relative reliability	Good due to simple mechanization	Very high due to passive nature of system	Potentially low due to complex mechanization	Good, as mechanization is simple redundancy provided by spring return	Good, mechanization very simple. Redundant actuation provided by spring cartridge	Very high due to straightforward mechanization
Relative development effort required	Low – primarily testing to evaluate performance and optimize design	High – extensive development required to define system and evaluate performance	High – extensive development required to qualify high temperature motor and drive mechanism	High – development required to define and qualify suitable wiper material	Low – mechanical development limited to high temperature qualification of drive mechanism	Lowest – similar system operatio on AF-Hughes "Maverick" mi
Easily acceptable to different window configurations	Yes	No	No	No	No	Yes

PRECEDING PAGE BLANK NOT FILMED

FOLDOUT FRAME

IGURATIONS–

Systems			One-Shot Systems	
ur	Mechanical Wiper	Mechanical Shutter	Frangible Cover	Jettisonable Cover
			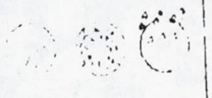	
trans- ngs f	Wiper mechanically removes contaminants from outer of double window configuration	Mechanical shutter opens only during readings, minimizing window exposure to contaminants	Transparent cover shatters, carrying away accumulated contaminants	Transparent cover jettisoned, carrying away accumulated contaminants
	Yes	No	Yes	Yes
	No	Yes	Yes	Yes
for	Potentially excellent if suitable wiper material available	Depends on nature of contaminants. Some protection inherent with respect to unprotected window	Very effective for all types of contamination, but can only be used once	Very effective for all types of contamination but can only be used once
	Excellent			
llent	Excellent			
ate	Depends on wiper material and contaminant			
sus- sion	Could increase abrasion			
drives aped ous or	Solenoid sweeps wiper spring return	Solenoid opens shutter against return spring	Squib driven pin impacts cover. Residual stresses in tempered glass cover cause total disintegration	Hot wire retiator unlocks cover which is jettisoned by springs
	0.68 kg (1.5 lb)	0.45 kg (1.0 lb)	45 g (0.1 lb)	45 g (0.1 lb)
uired	1/10 duty cycle pulses required for switching power to solenoid	Command required prior to each instrument reading to switch solenoid and open shutter	1 squib actuation pulse required for cover disintegration	1 squib actuation pulse required for cover jettison
	17 W	13 W	1 squib pulse	1 squib pulse
due to niza-	Good, as mechanization is simple redundancy provided by spring return	Good, mechanization very simple. Redundant actuation provided by spring cartridge	Very high due to straightforward mechanization	Very high due to straightforward mechanization
quired tem- and	High – development required to define and qualify suitable wiper material	Low – mechanical development limited to high temperature qualification of drive mechanism	Lowest – similar system operational on AF-Hughes "Maverick" missile	Low – mechanization easy to implement
	No	No	Yes	Yes

REPRODUCIBILITY OF THE ORIGINAL PAGE IS POOR.

Page intentionally left blank

mounting the pressure sensor directly to the wall of the pressure vessel (Figure 4.5-11).

The shelf mounted sensor is desirable from an integration standpoint, as it allows all up installation and checkout of units on a single shelf outside the pressure vessel, and does away with the need for brackets inside the shell, or extension of the shelf electrical harness to non-shelf mounted units.

The wall mounted unit is more difficult to integrate, but does not need the long pressure lines required by a shelf mounted unit.

As the functional requirements of the science payload are considered to have highest priority in evaluation of design approaches, the wall mounted sensor has been chosen as the baseline approach to inlet system integration because it minimizes pressure sensor line length compared to the shelf mounted configuration.

Stagnation Point Pressure Sensor Inlet System

The small probe pressure sensor inlet system must provide a pressure port at the small probe stagnation point while minimizing total line length to reduce line pressure losses. In addition, the following requirements must be satisfied:

1) Structural: The feedthrough aperture in the pressure vessel wall must not affect pressure vessel structural integrity. The lines carrying ambient pressure inside the probe, because of the mission critical nature of their failure will be sized to a safety factor of four. The resulting weight penalty is negligible due to the small size and short length of internal lines.

2) Seals: The feedthrough, internal pressure lines, and all internal fittings in the system will maintain a hermetic seal throughout all phases of the mission.

3) Blockage: The pressure lines must be large enough (≥ 6.3 mm (0.25 in.)) to be self-clearing in the event of internal condensation.

4) Installation: Access must be provided for connection of the internal pressure line to the fitting on the pressure sensor assembly during experiment integration. Access may also be required for inlet system/aeroshell integration.

Design considerations involved in pressure vessel/sensor integration were solved in the manner evolved for the large probe. Three inlet system designs capable of meeting these objectives were considered: A passive "suvivable" probe, a mechanically jettisoned ablatable plug, and a pyrotechnic cutter system (Figure 4.5-12). A comparison of the candidate pressure sensor inlet system characteristics is presents in Table 4.5-7.

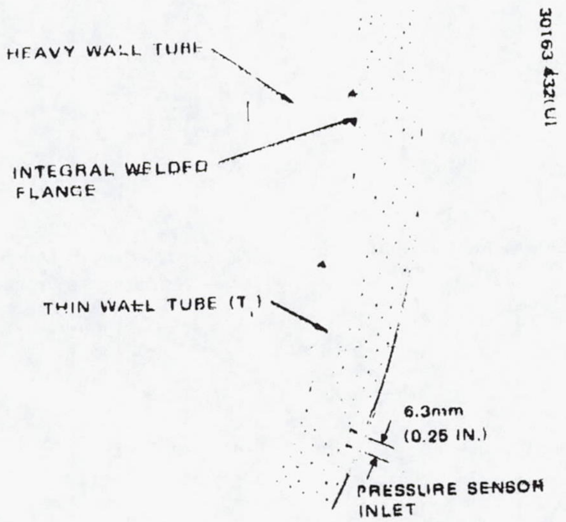

b) WALL MOUNTED SENSOR

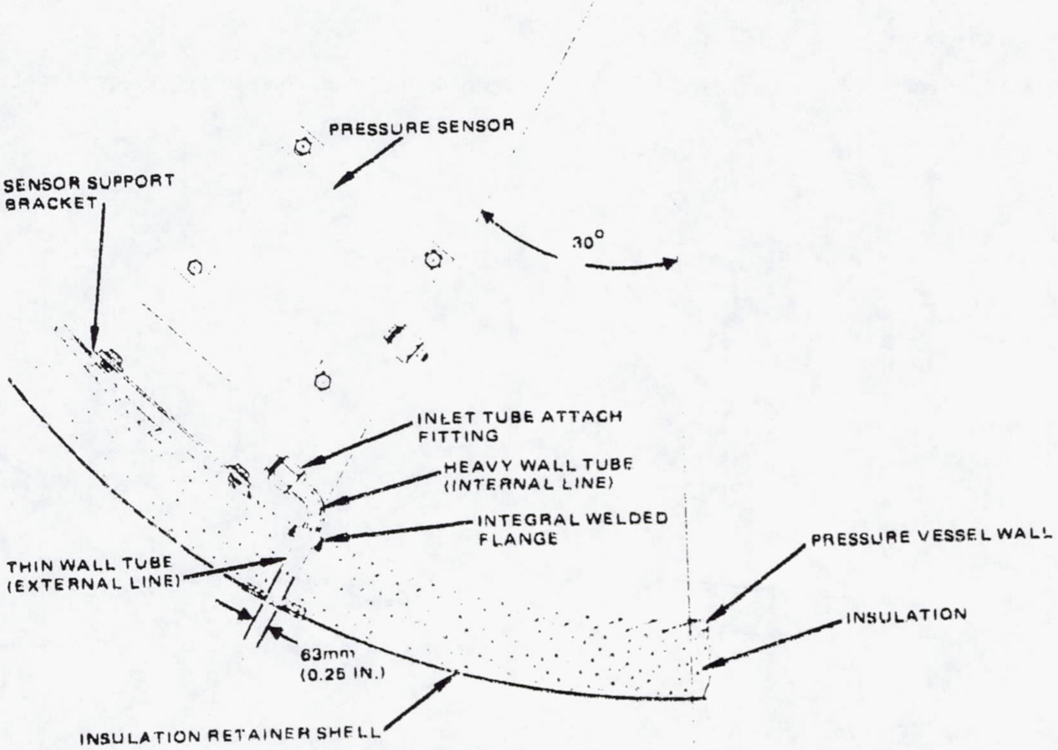

a) SHELF MOUNTED SENSOR

FIGURE 4.5-11. LARGE PROBE PRESSURE SENSOR INLET INSTALLATION CANDIDATE CONFIGURATIONS

REPRODUCIBILITY OF THE ORIGINAL PAGE IS POOR.

FOLDOUT FRAME 1

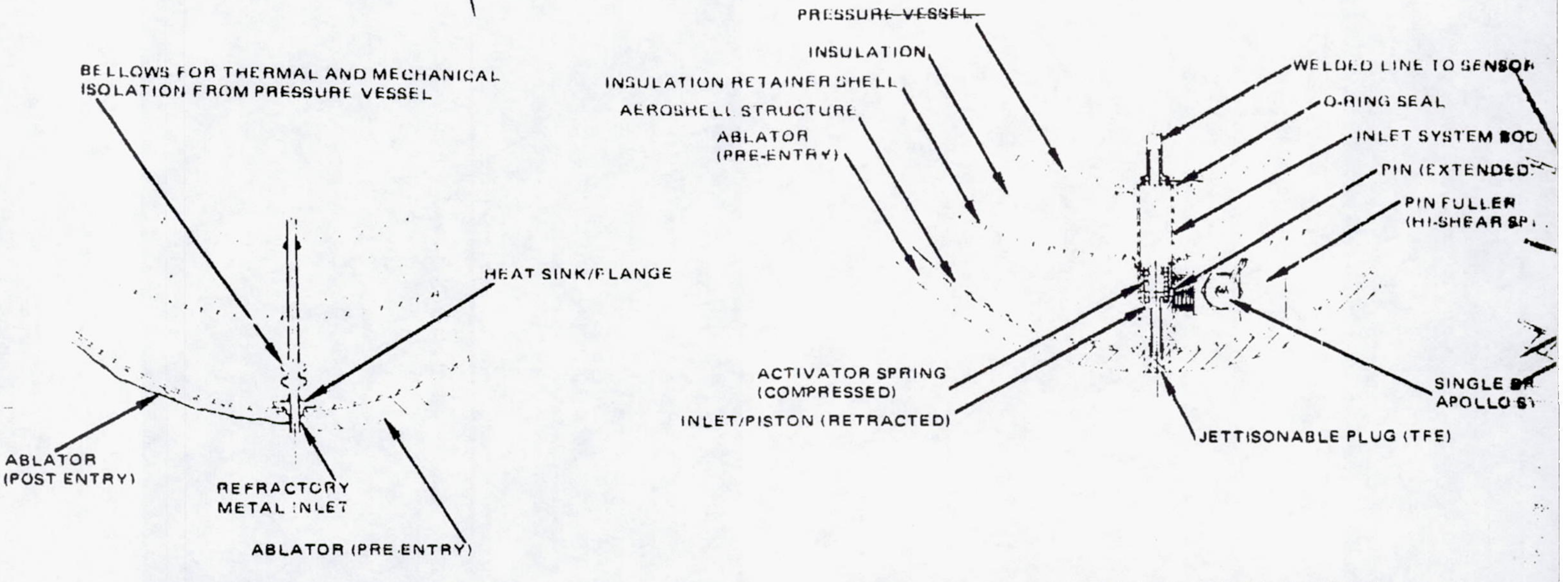

b) SURVIVABLE PROBE INLET SYSTEM

c) JETTISONABLE PLUG INLET SYSTEM: INLET RETRACTED

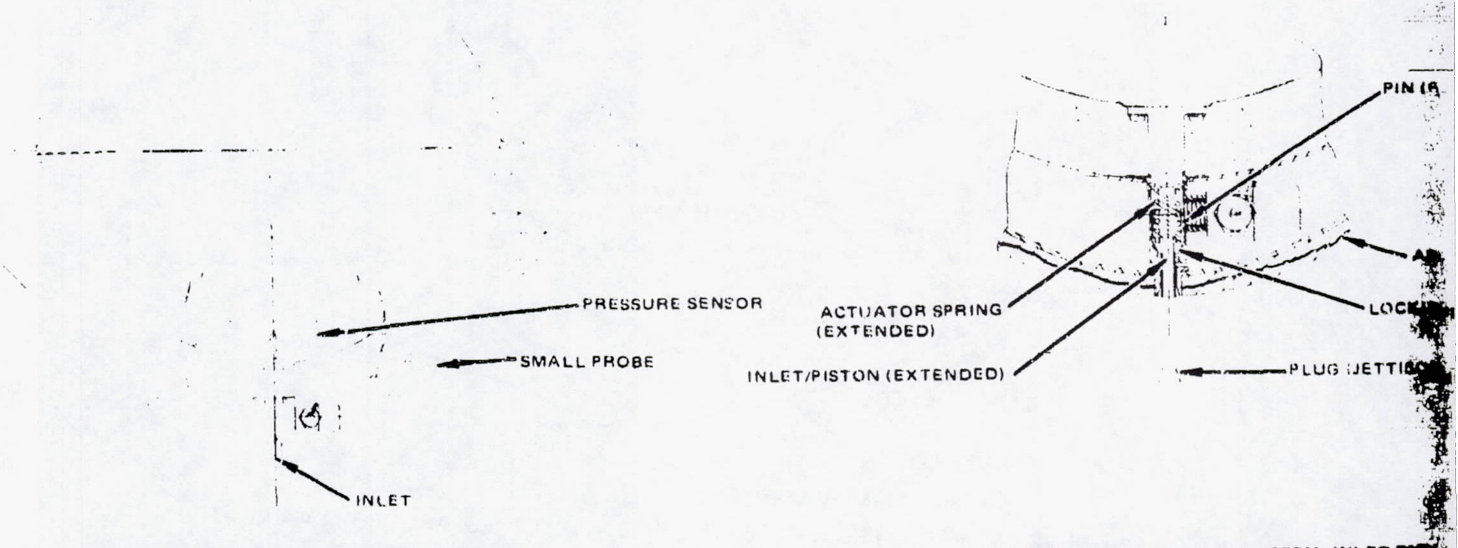

a) PRESSURE SENSOR INLET SYSTEM LOCATION

d) JETTISONABLE PLUG INLET SYSTEM: INLET

FIGURE 4.5-12. SMALL PROBE STAGNATION POINT PRESSURE SENSOR INLET SYSTEMS CANDIDATE CONFIGURATIONS

FOLDOUT FRAME

30163-433(U)

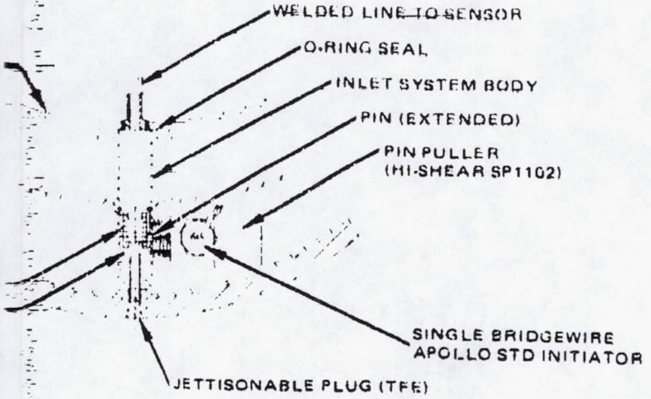

NLET SYSTEM: INLET RETRACTED

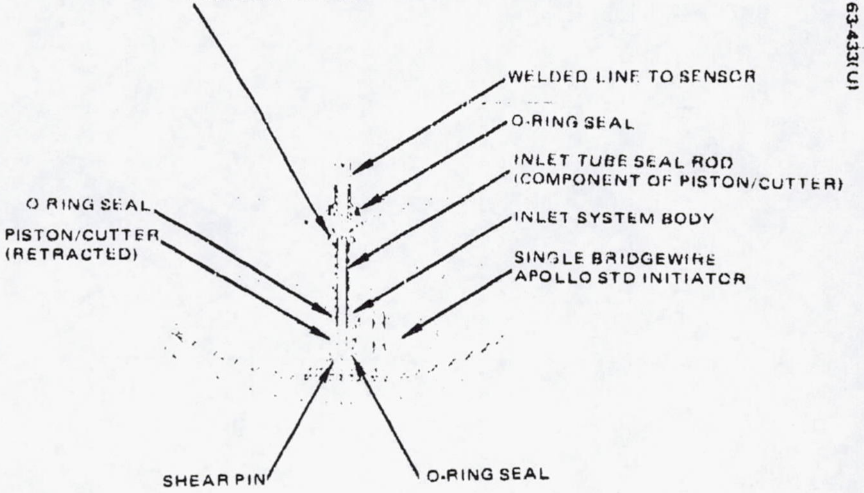

e) PYROTECHNIC CUTTER INLET SYSTEM: BEFORE ACTIVATION

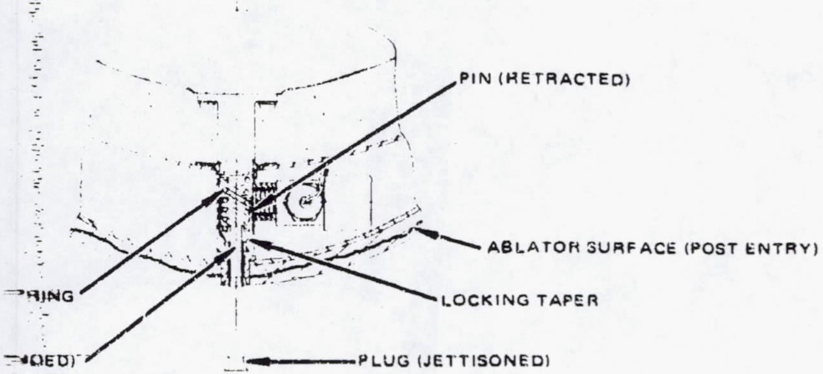

JETTISONABLE PLUG INLET SYSTEM: INLET DEPLOYED

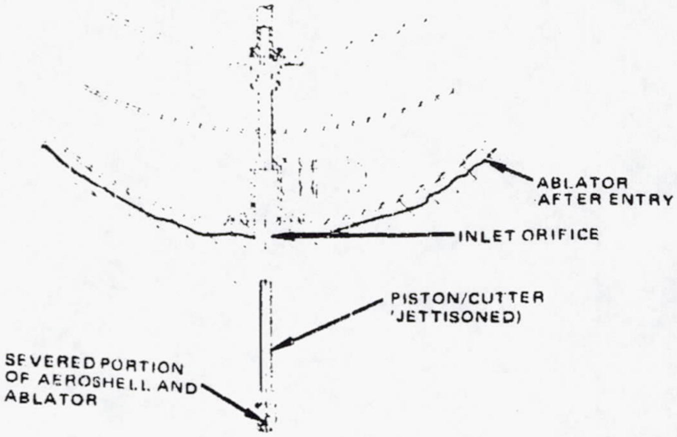

f) PYROTECHNIC CUTTER INLET SYSTEM: INLET DEPLOYED

TABLE 4.5-7. COMPARISON OF CHARACTERISTICS: PRESSURE SENSOR INLET SYSTEM

[illegible]	[illegible] Plug	Perforated [illegible]
Advantages	Advantages	Advantages
1) [illegible] simple	1) Operation is straightforward	1) Simple
2) [illegible]	2) [illegible] hardware [illegible]	2) [illegible]
3) [illegible]	[illegible]	3) [illegible]
	3) [illegible] temperature compensation	
	4) No integration problem	
Disadvantages	Disadvantages	Disadvantages
1) [illegible]	1) [illegible] (0.25 Pa)	1) Potential [illegible]
2) [illegible]	2) [illegible]	2) Perforation [illegible] aeroshell [illegible]
3) [illegible]	3) [illegible] with surrounding [illegible] testing	3) Cleanliness [illegible] testing
4) [illegible]	4) [illegible] aeroshell structure [illegible] required	4) Susceptible to damage [illegible]
5) [illegible]		5) Access and installation [illegible] difficult [illegible] aeroshell required

REPRODUCIBILITY OF THE ORIGINAL PAGE IS POOR.

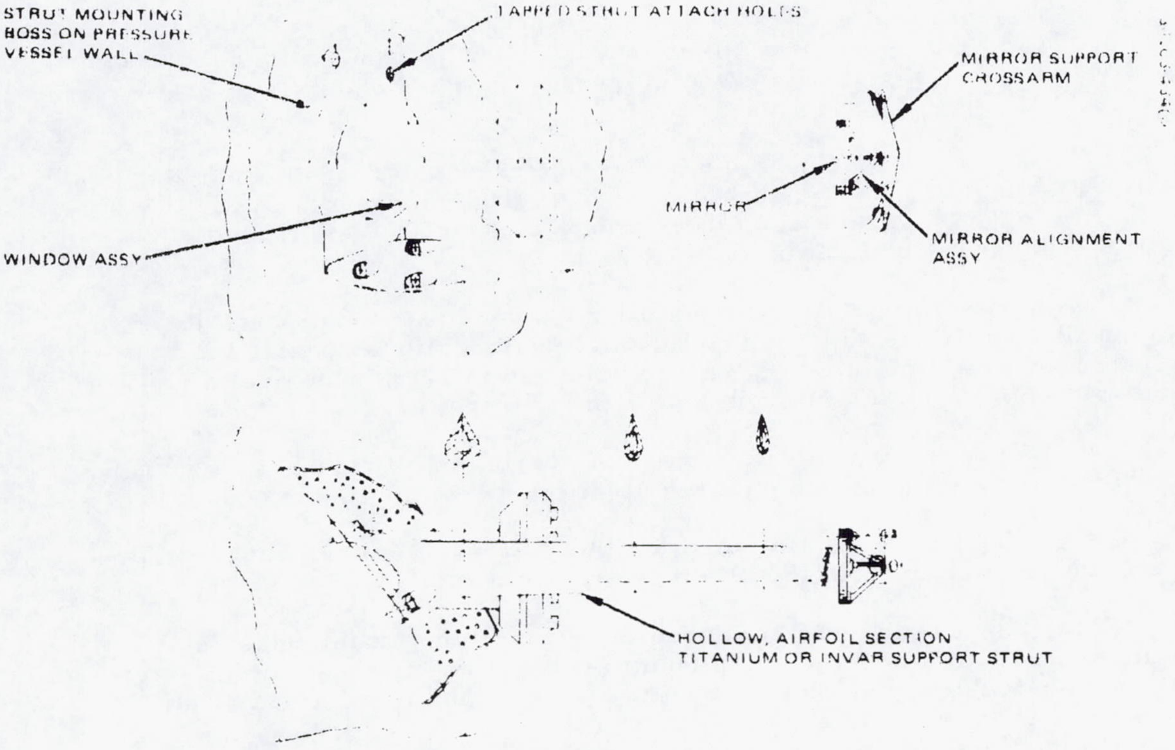

13a) "BRIDGE" TYPE SUPPORT STRUCTURE

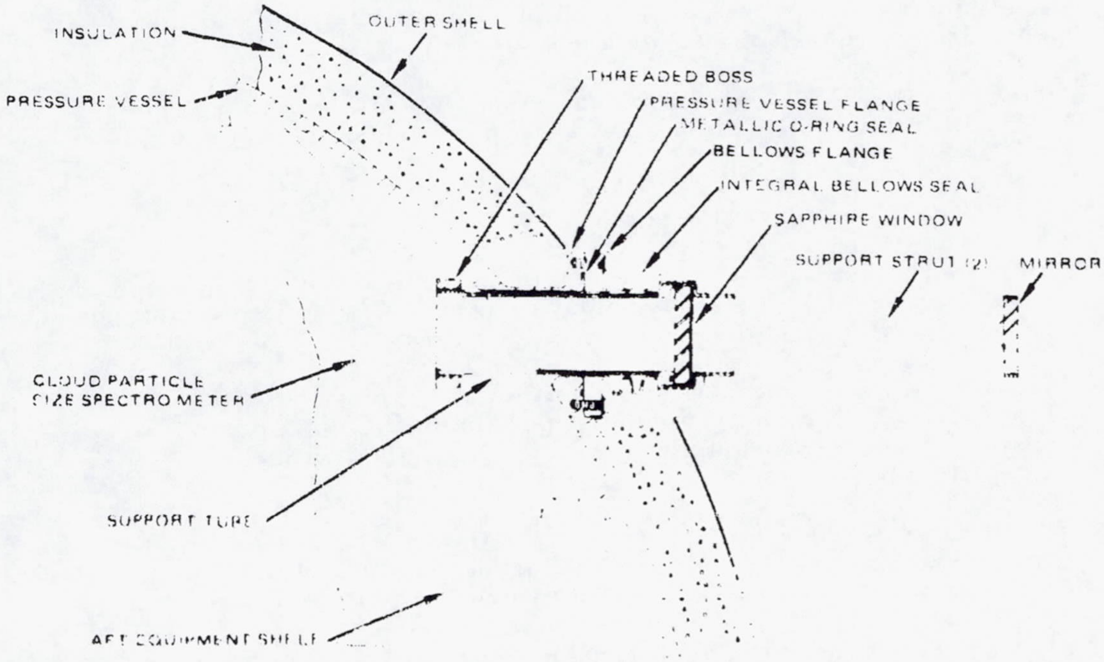

13b) MIRROR SUPPORT INTEGRAL WITH EXPERIMENT

FIGURE 4.5-15 CLOUD PARTICAL SIZE SPECTROMETER MIRROR SUPPORT STRUCTURE CANDIDATE CONFIGURATIONS

REPRODUCIBILITY OF THE ORIGINAL PAGE IS POOR.

The primary factors to be considered in evaluation of the three designs studied are probe survival and experiment function. Other criteria include weight, development effort required, integration, and flow obstruction through the inlet body.

None of the approaches considered represent a threat to probe survival; but the jettisonable plug configuration, with its protruding inlet system is far less susceptible to blockage and offers a better chance of experiment success than the other two configurations.

Development effort and testing for all three system are considered to be approximately the same. The thermal qualifications required for the survivable probe and the teflon plug are balanced by the mechanical and structural qualification tests required by the pyro cutter.

The maximum weight differential of approximately 0.059 kg (0.13 lb) between the systems is not considered significant in selection.

Integration is straightforward for the jettisonable plug, but could present a definite problem with the other two configurations.

Flow blockage is not considered to be a problem in the quasi-static situation encountered in the large plenum area of the jettisonable plug inlet body; the survivable probe and pyro cutter present no obstructions at all.

Proportionately greater weight must be given to consideration of successful experiment function in the final concept selection. The jettisonable plug has a clear superiority in this area, combined with inherently simpler integration and relative equality in other areas of comparison.

Accordingly, the jettisonable plug has been chosen as the baseline approach to design of the small probe stagnation point pressure sensor inlet system.

Cloud Particle Size Spectrometer Mirror Mount

The cloud particle size spectrometer utilizes an externally mounted condensing mirror as part of its optical subsystem. The mounting structure for this mirror must satisfy the following requirements:

1) The mirror must maintain its position and alignment with respect to the internally mounted portion of the optical system. Angular alignment must be maintained with ±1 milliradian

2) The mirror support structure must maintain alignment after exposure to the 510 g acceleration load of Venus entry and to Venus surface temperature and pressure

Two configurations were considered: mounting the mirror support structure to the pressure vessel wall, and keeping the mirror mount integral with the instrument (Figure 4.8-13).

[illegible] support [illegible] Figure 4. [illegible] indicate that if the arms are [illegible] thermal conductivity [illegible] for angular misalignment [illegible] bottom of the support arms will be [illegible].

The integral mirror support structure (Figure 4.5-13b) [illegible] mirror, [illegible] into a single unit. As in the pressure vessel [illegible], low expansion coefficient high thermal conductivity alloys are used to minimize thermal gradient induced deflections. The bellows seal decouples the [illegible] from the deflections of the pressure vessel, helping to maintain alignment. As pressure loads on the window are not reacted by the pressure vessel wall, the instrument case must be sized to accommodate an axial load of approximately 71[illegible] N (1600 lb) at the surface of Venus, as well as the shear and moment induced in the support tube by the entry deceleration loads.

The pressure vessel mounted mirror support structure is a lighter, simpler system. Its seal integrity is better than that of the integral mirror mount, as it has only one interface to seal. Integration difficulties are minimal, as no direct connections are made between shelf mounted components and the pressure vessel wall. Initial alignment can be easily accomplished using methods in everyday use at Hughes.

By way of contrast, the integral system is bulky and heavy. It has two interfaces to seal instead of one, and it presents integration difficulties, as the mirror and support assembly, once installed, would have to be disconnected and removed to allow removal of the equipment shelf. Its primary advantage over the other [illegible] the entire optical system of the experiment into one [illegible] unit, [illegible] independent of both shelf and pressure vessel.

The primary [illegible] factor in the trade, however, must be the assurance of uninterrupted [illegible] operation. The uncertainty of relative motion between shelf and pressure vessel as the probe is subjected to the steadily increasing temperatures and pressures of the descent profile render the pressure vessel mounted mirror unable to satisfy the requirement for uninterrupted precise alignment of the [illegible] mirror. Accordingly, despite its disadvantages, the integral [illegible] mirror support concept is recommended as baseline, as it offers the best approach to fulfilling all mission requirements.

Pressure Vessel Module/Deceleration Module In-Flight Disconnect

The primary function of the pressure vessel module/deceleration module in-flight disconnect (IFD) is to provide reliable electrical connection for the two twisted, shielded pairs, four number 22, and 37 number 28 insulated wires of the [illegible] (PVM) [illegible] during all phases of the mission until PVM aeroshell separation; and then to provide a clean and complete electrical and mechanical break to allow unimpeded separation. Additional requirements include:

1) Interference. The post disconnect configuration of the IFD must preclude any possibility of interference with the aeroshell during separation.

2) High g survivability. The IFD must function reliability after exposure to the high g levels encountered during planetary entry (610 g design).

3) Reliability. The IFD must meet reliability criteria for mission-critical equipment.

4) Electrical isolation. Isolation is required between the high current leadwires connecting the squib drivers to the pyrotechnic initiators and the relatively low current wires carrying bus power and signal voltages.

5) Integration. The IFD must provide a positive, easily accessible disconnect between PVM and aeroshell to allow their separation for assembly and ground handling purposes.

Two fundamentally different methods of implementing the in-flight disconnect function were studied: an electrically released plug and receptacle disconnect, and a pyrotechnically activated guillotine type cable cutter (Figure 4.5-14). Table 4.5-8 summarizes the comparison of characteristics for the two candidate approaches.

The primary criteria for selection of the configurations studied is the ability to function successfully during all phases of the mission. Other criteria include weight, reliability, and development effort required.

Both pyrotechnically activated cutters and mechanical in-flight disconnects have compiled large amount of time in the space environment. The requirement for operation after a high g planetary entry, however, is a new one for both types of device, and represents the largest single obstacle to successful function of the IFD system. The extremely rugged nature of the cutter, its low parts count, and its use of the well proven Apollo standard initiators make it inherently more resistant to high g loadings than the relatively large and complex mechanical disconnect. It eliminates the need for a slack service loop to allow for plug retraction. and its low mass, close coupled to the probe structure, reduces loads induced in the supporting structure and provides a high resonant frequency.

The cutter is free from any possibility of interference caused by hang-up of mechanically retracted components, always a possibility with plug and receptacle designs.

TABLE 4.5-8. COMPARISON OF CHARACTERISTICS

Mechanical IFD	Mechanical Cutter
Advantages:	Advantages:
1) Long history of [illegible] discoverer reentry [illegible] space qualified 2) Available off-shelf 3) Easily disconnected for servicing	1) Low mass 0.635 kg (1.4 lb) saving on mechanical IFD for entire installation 2) Rugged – high survivability should be good 3) No service loop required – umbilical bundle can be securely tied at all points 4) Available off-shelf 5) Good electrical isolation – separate connectors and wire bundles throughout 6) Minimal impact on aeroshell structure 7) All initiators are on pressure vessel side of interface 8) Zero tipoff impulse
Disadvantages:	Disadvantages:
1) Successful operation after 600 exposure uncertain 2) Contact bounce or separation during high g exposure likely 3) IFD initiation must go through IFD if receptacle is probe mounted 4) Electrical isolation – pyro, power, and signal conductors in same connector 5) Loose service loop required – high g survivability doubtful 6) Requires relatively large access cover	1) Dual initiator configuration has no space experience. (Single initiator version used on Thor-Delta)

FOLDOUT FRAME

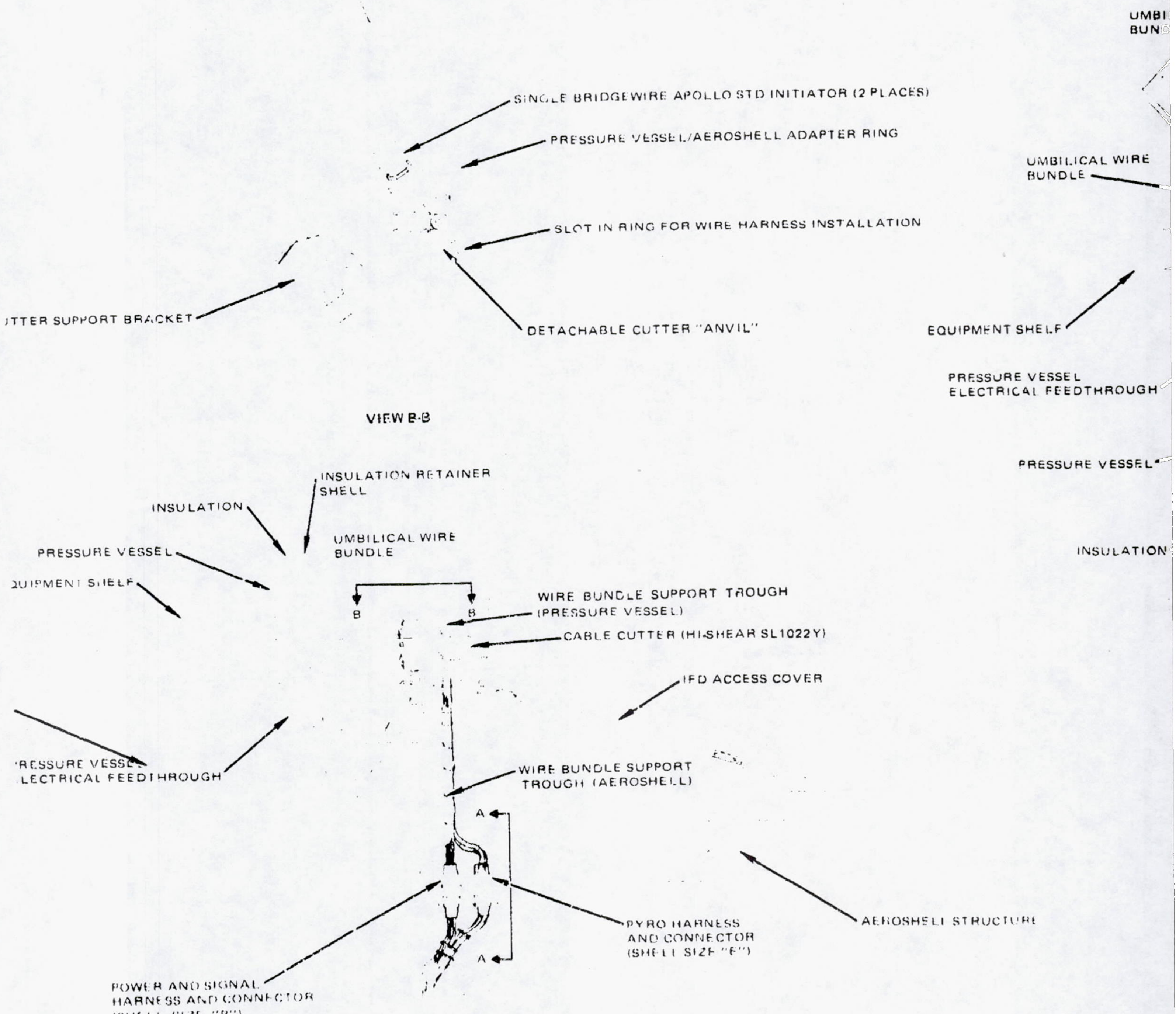

a) CABLE CUTTER IN-FLIGHT DISCONNECT

FIGURE 4.5-14. LARGE PROBE PRESSURE VESSEL/AEROSHELL IN-FLIGHT DISCONNECT CANDIDATE CONFIGURATIONS

FOLDOUT FRAME

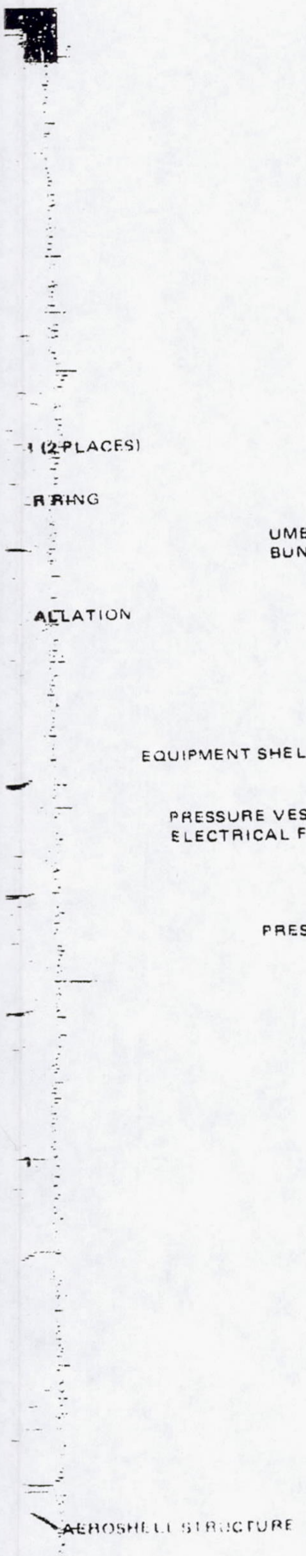

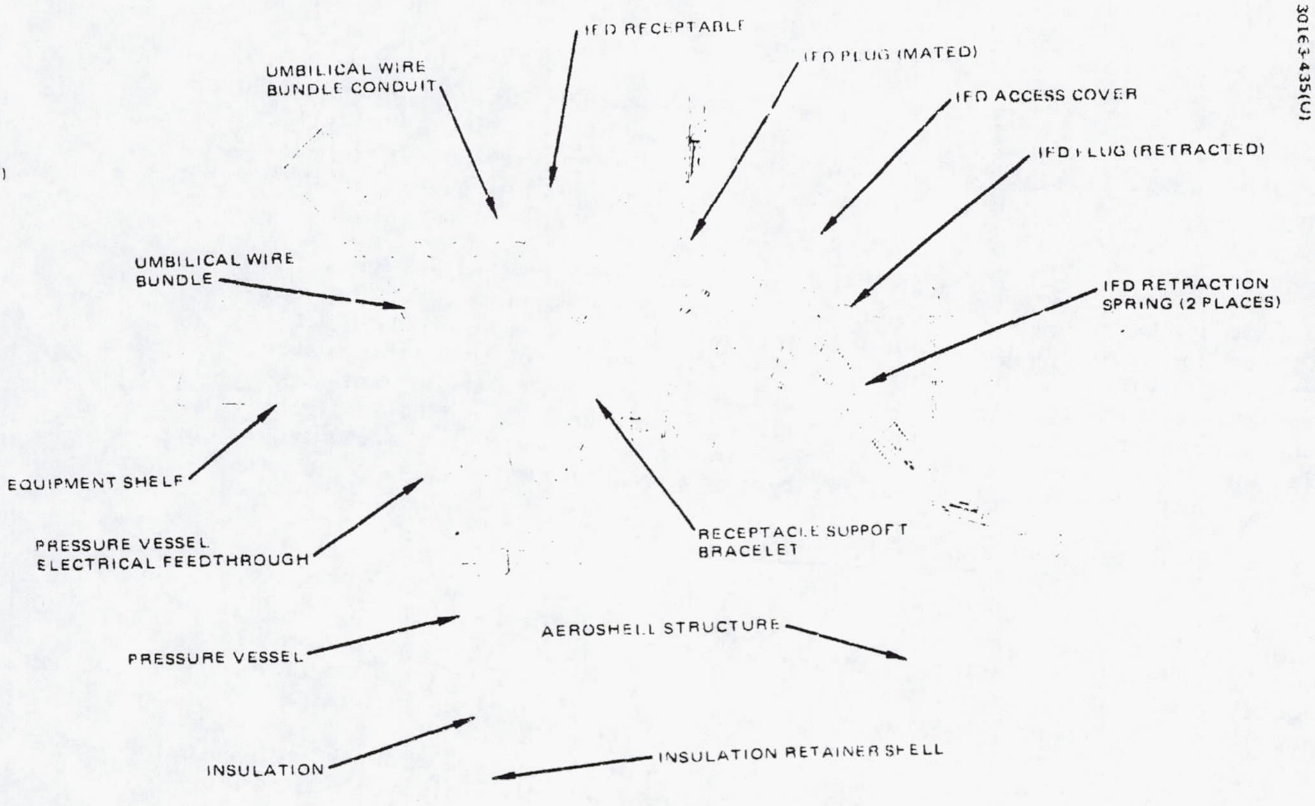

13b) CONNECTOR IN FLIGHT DISCONNECT (G&H TECHNOLOGY INC. MODEL 740E ELECTRICALLY RELEASED IN-FLIGHT DISCONNECT)

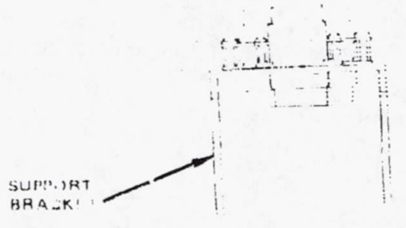

VIEW A-A

REPRODUCIBILITY OF THE ORIGINAL PAGE IS POOR.

Reliability is considered to be approximately equal for both systems, as both use highly reliable space proven initiators for actuation. The cutter, however avoids the requirement for activation across the disconnect interface which the mechanical disconnect requires.

The 0.635 kg (1.4 lb) mass difference between the two concepts, the simpler integration provided by the cutter IFD, and the superior electrical isolation provided by providing separate connectors for pyro and signal and power harnesses are additional areas in which the guillotine concept is advantageous.

The single area in which the mechanical IFD system enjoys a clear superiority is in space experience. This experience, however is not considered applicable to the probe mission, which requires separation after entry, not before. The pyrotechnic cutter is considered to be the system best able to withstand the critical high g entry condition; its advantages in other areas are clear cut. Accordingly, the pyrotechnic cutter in-flight disconnect is recommended as the baseline IFD design for the pressure vessel/ aeroshell separation subsystem on the large probe.

Nephelometer Window Protective Cover

The small probe nephelometer window is mounted on the aft hemisphere of the small probe, a location which is exposed to a high thermal flux during Venus entry. In order to prevent damage to the window, a cover is required which will protect the window during entry and which can subsequently be opened or jettisoned to allow operation of the experiment.

Two nephelometer window protective cover configurations were evaluated; a mechanically latched door and a pyrotechnically activated jettisonable cover (Figure 4.5-15). Table 4.5-9 compares the characteristics of the two approaches.

The protective door assembly (Figure 4.5-15a) consists of two parts: The movable door, and a fixed hood, which mates with the aft hemisphere insulation retainer shell. Both hood and door consist of formed and machined titanium structures: all exterior surfaces except the hinge fittings are covered with G.E. ESM ablator. The door is retained in the closed position by a two-ball latching assembly which is actuated by G + H technology series 800A non-explosive initiator. Upon latch release, the door is opened and retained in the open position by dual redundant torsion springs, providing a clear field of view for the instrument. Total calculated mass for the system is 0.15 kg (0.34 lb).

The pyrotechnically actuated jettisonable cover also uses a fixed hood, attached to the aft insulation retainer shell; but the jettisonable cover mounts directly to the hood. Circumferential slots surround the jettisonable portion of the cover, leaving it attached at seven points. Both hood and cover, as in the previous configuration, are completely covered with G.E. ESM ablator. Cover jettison is accomplished by firing the pyrotechnic initiator. The hot gas that results is used to abruptly change the cross section of the actuator

TABLE 4.5-9. COMPARISON OF CHARACTERISTICS

Mechanically Latched Door	Blow-Off Cover
Advantages:	Advantages:
1) Lighter weight (0.15 kg vs. 0.18 kg)	1) Effectively solid state - no moving parts (high g)
2) Method of operation straightforward	2) Very simple
3) Door positively retained after activation	3) Reliable seal during entry - no gap
Disadvantages:	Disadvantages:
1) Gap around door required	1) Heavier
2) Complex - high parts count	2) Testing required to establish repeatability
3) High g susceptibility (str. deformation?)	3) Possible damage caused by door impact
4) Susceptible to jamming by charred ablator	4) Possible window contamination if tube ruptures

tube from flat to tubular, displacing the cover outward far enough to fracture the seven retaining links, and delivering an impulse which flings the cover away at high velocity. All gases caused by initiator firing are contained, lessening the risk of window contamination. The pyrotechnic shock of actuator tube expansion is attenuated by a titanium backup ring, and further reduced by transmission through the hood structure. As there is no direct structural tie between the cover-hood assembly and the window, pyro shock is not considered to be a problem. Total calculated mass for this sytem is 0.18 kg (0.41 lb).

Due to the mission critical nature of window protection during entry, the ability of the cover assembly to provide this protection with highest possible reliability under the high entry g loading condition encountered by the small probes becomes the primary criteria for system evaluation. Accordingly, the positive seal and superior high g survivability of the blow-off cover are considered to outweight the advantages of lighter weight and conceptually simpler operation possessed by the door. In addition, the types of failure likely to be encountered by the blow-off cover primarily affect operation of the nephelometer only; failure of the door latch, or opening of the door-hood gap as a result of structural deformation during high entry g-loads could cause

REPRODUCIBILITY OF THE ORIGINAL PAGE IS POOR.

FOLDOUT FRAME

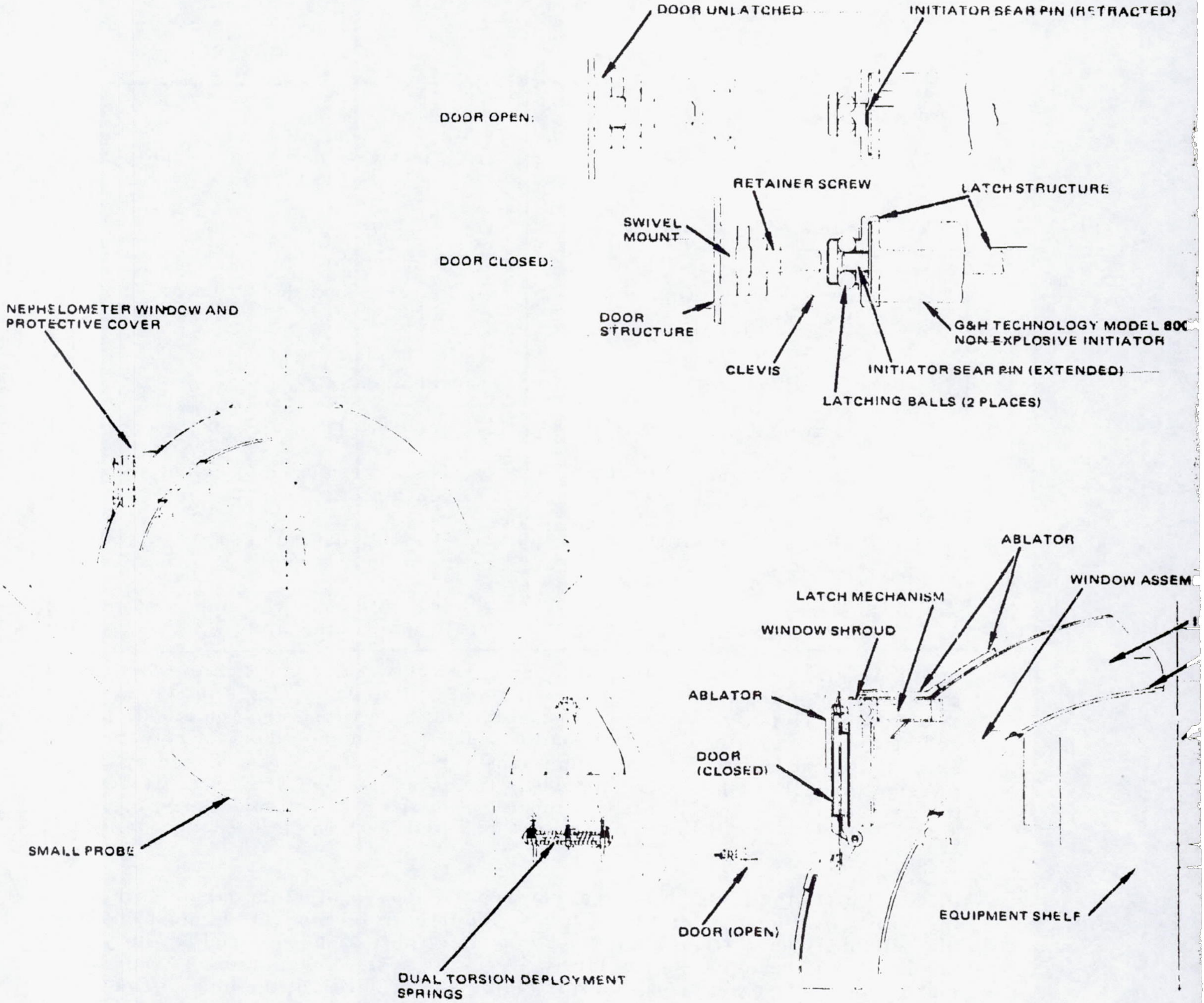

15a) MECHANICAL LATCH-HINGED DOOR

FIGURE 4.5-15. SMALL PROBE NEPHELOMETER WINDOW PROTECTIVE COVER CANDIDATE CONFIGURATIONS

REPRODUCIBILITY OF THE ORIGINAL PAGE IS POOR.

FOLDOUT FRAME 2

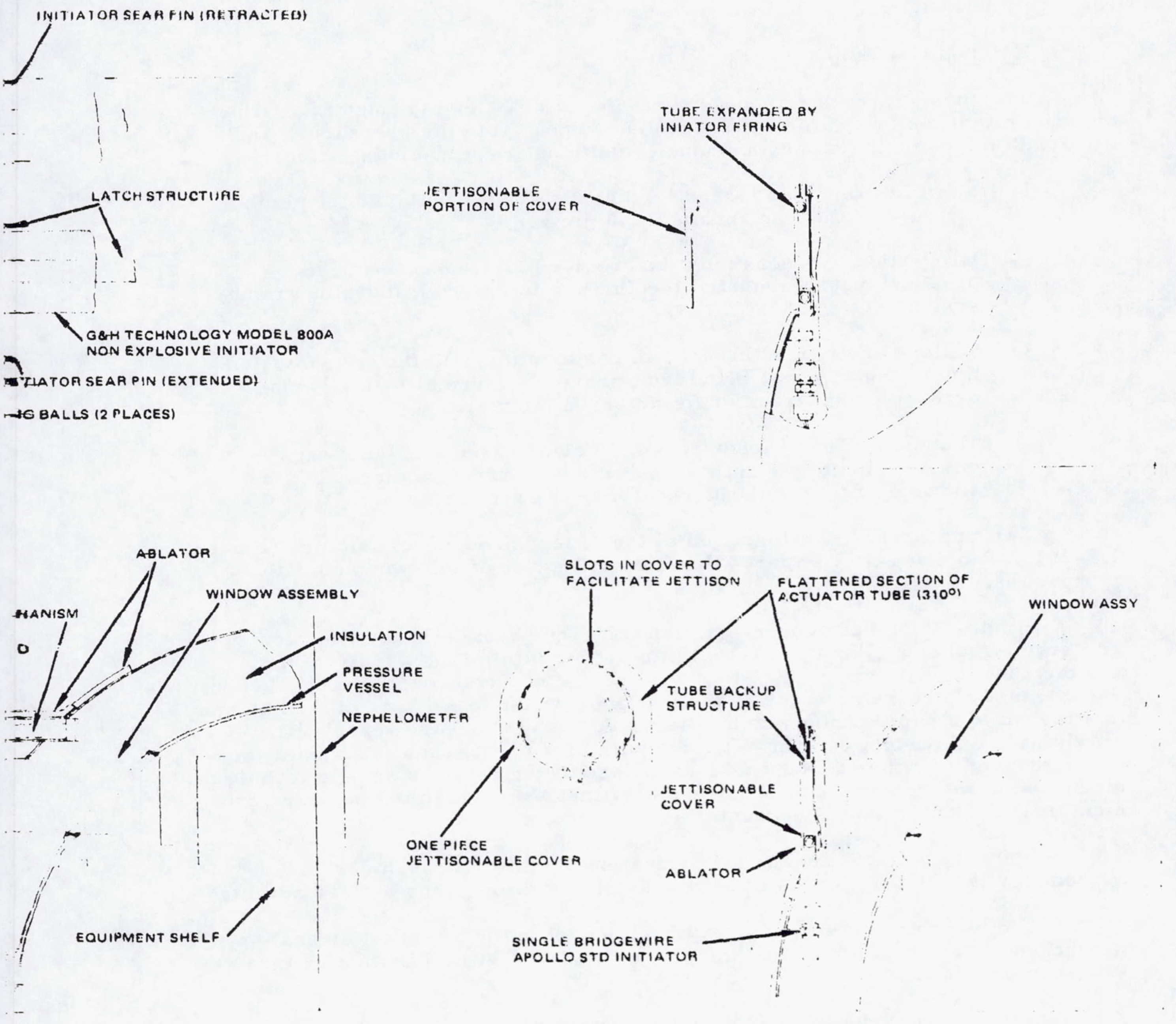

15b) PYROTECHNIC ACTIVATED JETTISONABLE COVER

REPRODUCIBILITY OF THE ORIGINAL PAGE IS POOR.

30163-436(U)

failure of the window and the entire probe. Effectively in mission terms the blow-off cover is "fail-safe"; the door is not, leading to selection of the pyro-activated blow-off cover as the baseline method for nephelometer window entry protection.

Antenna Co-Axial Lead Feedthrough

The primary requirement of the antenna coax feed through is to allow the rf current from the probe rf subsystem to penetrate the pressure vessel and reach the communications antenna. Additional requirements include:

1) Minimization of rf losses. Total coax line length and the number of bends in the line should be minimized

2) Integration. Access must be provided for connection of the pressure vessel mounted feedthrough to the shelf mounted rf subsystem

3) Seals. The rf feedthrough, in combination with the transmission line to the antenna, should not provide a thermal path allowing excessive heat transfer to the probe interior.

4) Thermal. The rf feedthrough, in combination with the transmission line to the antenna, should not provide a thermal path allowing excessive heat transfer to the probe interior.

Two approaches to integration of the rf feedthrough were studied (Figure 4.5-16). Table 4.5-10 compares the characteristics of the two candidate approaches.

Simplicity and ease of integration were emphasized in the first concept. The second concept (Figure 4.5-16a) attempts to minimize total line length and the number of bends required by locating the rf feedthrough directly below the antenna. In both concepts a circular flange on the lower face of the antenna is attached to a support ring which is fastened to the pressure vessel wall, providing a lightweight and very stiff mounting for the antenna. Co-axial feedthroughs used in either concept take advantage of the ceramic sealing techniques discussed in the subsection that follows to withstand the high temperature and high pressure environment encountered.

Primary criteria chosen for evaluation of rf feedthrough design approaches is rf loss. In this area, the axial feedthrough has a clear advantage.

The two concepts are approximately equal in the areas of integration, weight, and structural impact on the pressure vessel wall, eliminating these as selection criteria.

Criteria in which the remote feedthrough enjoys superiority are sealing, with only one interface to seal instead of two, simplicity, and thermal conduction to the probe interior. None of these areas, however, are considered

[illegible]

Remotely Mounted Feedthrough	Axial Feedthrough
Advantages:	
1) Mechanical simplicity	1) Low rf [illegible] bends
2) Good thermal [illegible]	
3) Hermetic welded seal	
4) Good access to inside of feedthrough	
Disadvantages:	
1) RF losses relatively high: long cable run, several right angle bends	1) Seals - two interfaces to seal pin to fitting and fitting to pressure vessel
	2) Thermal - relatively direct thermal path to probe interior
	3) Complex - relatively high parts count

critical. Though the remote feedthough has a lower parts count, both systems are relatively simple. Similarly, thermal input from each concept is minor enough to be accepted despite the advantage possessed by the simpler system. The added metallic O-ring seal possessed by the axial feedthrough is acceptable in terms of seal integrity, though not as advantageous as the welded seal of the remote feedthrough.

Accordingly, as the disadvantages of the axial location are minor and as it possesses lower rf losses than the remote concept, the axial mounted rf feedthrough is recommended as the baseline configuration for both large and small probes.

FOLDOUT FRAME

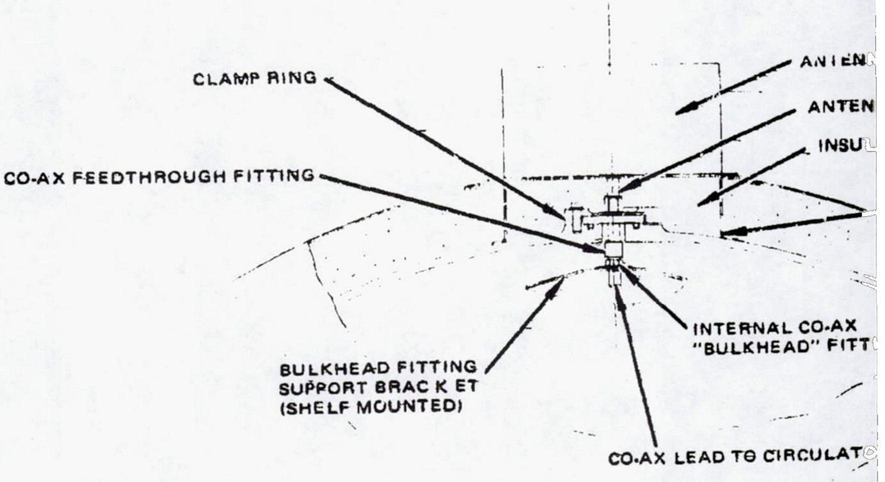

DETAIL A AXIAL R.F. FEEDTHROUGH CONFIGURA

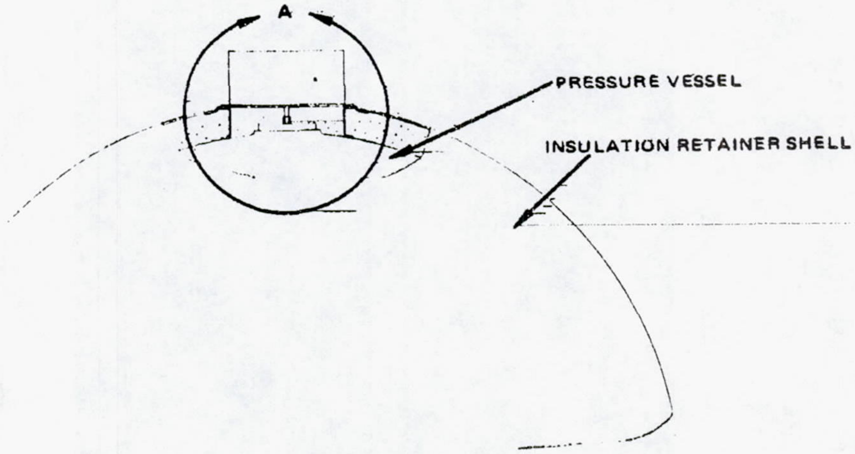

a) CO-AX FEEDTHROUGH ON PRESSURE VESSEL AXIS

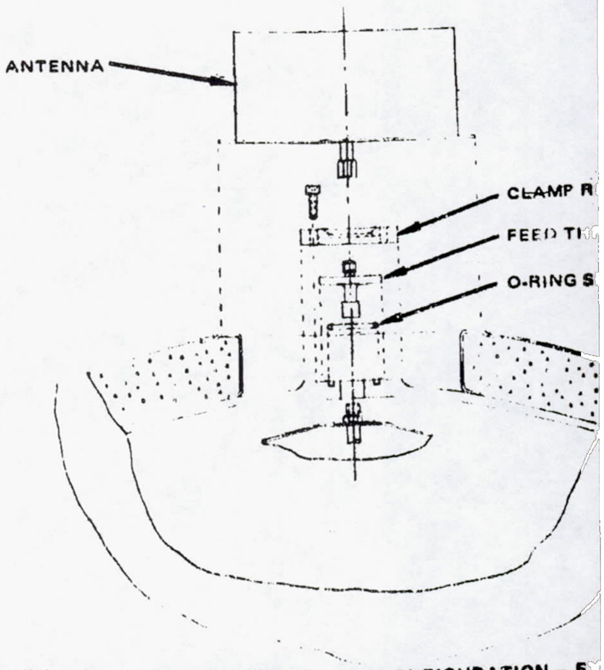

DETAIL B AXIAL RF FEEDTHROUGH CONFIGURATION – E

FIGURE 4.5-16. ANTENNA COAXIAL LEAD FEEDTHROUGH CANDIDATE CONFIGURATIONS

FOLDOUT FRAME 2

30163-437(U)

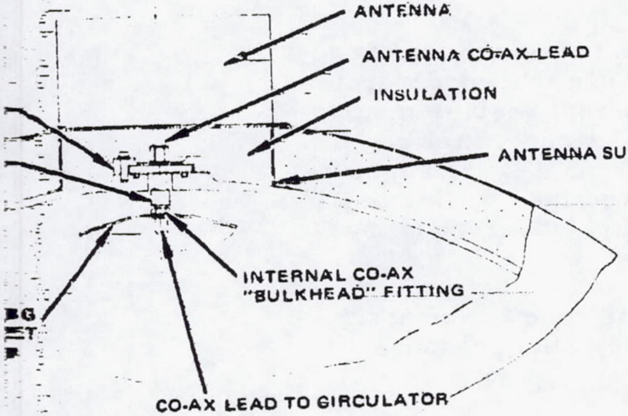

A AXIAL R.F. FEEDTHROUGH CONFIGURATION

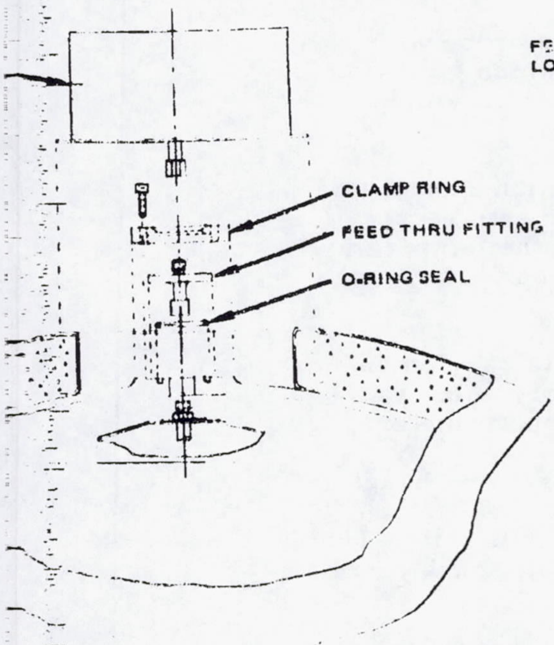

RF FEEDTHROUGH CONFIGURATION – EXPLODED VIEW

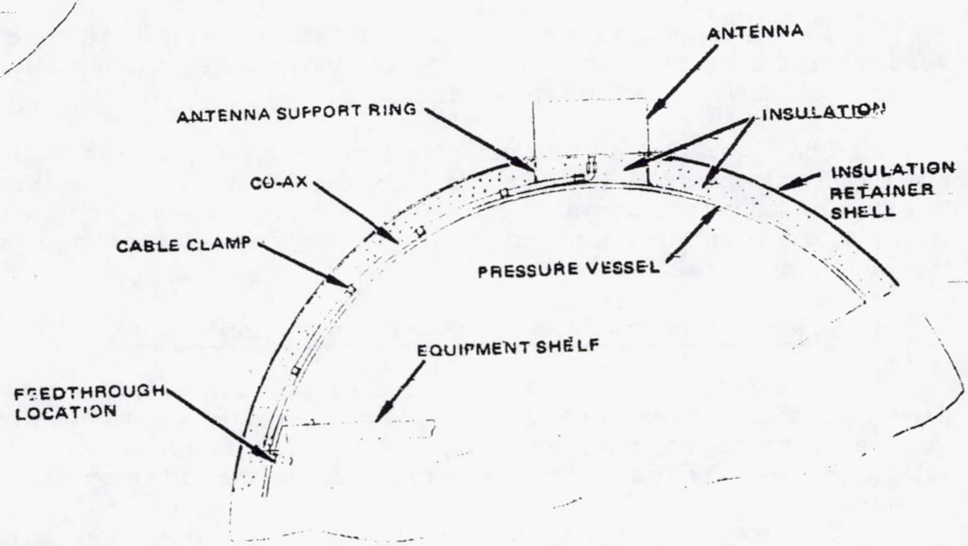

b) CO-AX FEEDTHROUGH BELOW SHELF

REPRODUCIBILITY OF THE ORIGINAL PAGE IS POOR.

Thor/Delta Baseline Configuration Description

This section describes the design approaches used in integrating the penetrations with the Thor/Delta large and small probe structures. Design of items used for this study's baseline definition is based on the configuration presented at the January 1973 midterm review. No attempt has been made to incorporate revisions to the payload subsequently received.

This configuration is based on a 550 mm (21.5-in.) inside diameter spherical pressure vessel which splits at a horizontal flange that incorporates a metallic O-ring pressure seal. Two disc shaped equipment shelves mount all of the science and housekeeping subsystems; one shelf mounts in each hemisphere. Insulation is solid and is mounted externally in a layer approximately 25.4 mm (1.0 in) thick. The insulation layer is retained by thin metal hemispheres which form an outer skin. All windows and protuberances must interface with both skin and insulation.

Six windows accommodate five optical experiments, and two pressure sensors and a mass spectrometer inlet system pass through the pressure vessel wall. No radar antennas are carried.

The Thor/Delta baseline small probe configuration is in almost every respect a miniature [325 mm (12.3 in) dia.] version of the large. However, the amount of instrumentation is much reduced. Only one window is carried, in the aft hemisphere, and only a single pressure sensor line passes through the pressure vessel wall.

Science Penetrations – Thor/Delta Large Probe

Penetrations providing the science payload of the large probe with direct physical access to the atmosphere of Venus and those which give optical access to the probe exterior (windows) are described in the sections which follow, as well as the components mounted on the outer surface.

Two experiments require direct access to the Venus atmosphere: the mass spectrometer and the pressure sensors. Three experiments require that components be mounted exterior to the pressure vessel: the temperature and hygrometer sensors and the condensing mirror or the cloud particle size spectrometer.

Optical windows are required by five of the instruments carried on the large probe: the nephelometer, aureole extinction detector, solar radiometer, planetary flux radiometer, and cloud particle size spectrometer.

Table 4.5-11 provides a summary of the selected Thor/Delta baseline window configurations for each experiment and their important characteristics. Figure 4.5-17 shows the location of each window on the baseline Thor/Delta large probe. Contamination protection is provided by jettisonable protective covers over each window.

Jettisonable Cover. Contaminants accumulate on a transparent, heated, cover which protects the window until it is jettisoned at a set altitude,

FOLDOUT FRAME

TABLE 4.5-11. SUMMARY OF CHARACTERISTICS: LARGE PROBE BASELINE WINDOW CONFIGURATIONS

		Instruments				
		Nephelometer Source	Nephelometer Sensor	Aureole Extinction Detector	Solar Radiometer	Planetary Flux Radiometer
	Configuration	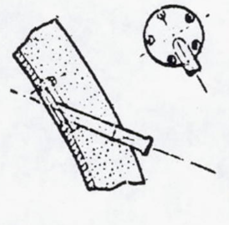	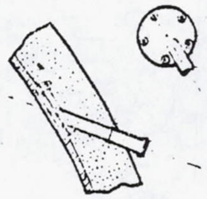	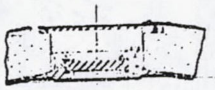	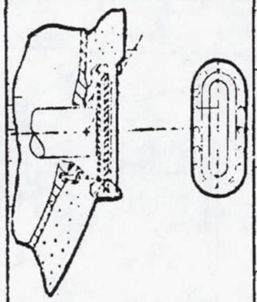	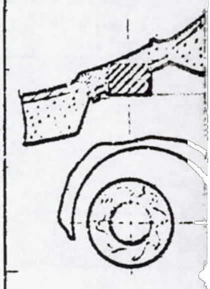
Window Characteristics	Quantity	1	1	1	1	1
	Field of view	1 deg conical	5 deg conical	In vertical plane ±15 deg In horizontal plane ±1/2 deg	In vertical plane ±60 deg In horizontal plane ±15 deg	5 deg conical
	Aperture size	0.64 cm (0.25 in.) diameter	1.3 cm (0.50 in.) diameter	2.5 cm (1.0 in.) diameter	Vertical 5.1 cm (2.0 in.) Horizontal 1.3 cm (0.50 in.)	2.5 cm (1.0 in.) diameter
	Window material	Sapphire	Sapphire	Sapphire	Sapphire	CVD ZnSe*
	Long wave cutoff	3.5	3.5	3.5	3.5	13.5
	Type heater	Sheathed element	Sheathed element	Film heater – outer window only	Sheathed element	Sheathed element (if required)
	Heater power	2 W	6 W	4 W (Off at 40 km)	22 W	18 W
	Type seal	Braze	Braze	O-ring	O-ring	Braze
	Window assembly mass	4.5 g (0.01 lb)	18 g (0.04 lb)	82 g (0.18 lb)	118 g (0.26 lb	141 g (0.31 lb)
	Contamination removal	Jettisonable cover	Jettisonable cover	Jettisonable cover	Jettisonable cover	Jettisonable cover
	Comments	Lightest weight configuration examined. Remote mounting for window thermal isolation	Window larger than source window to accommodate wider field of view. Same general configuration	Space between inner and outer window hermetically sealed	O-ring seal used to provide increased thermal isolation for window	Thick window due t modulus of rupture IR transparent win material

*Chemically vapor deposited zinc selenide

REPRODUCIBILITY OF THE ORIGINAL PAGE IS POOR.

PRECEDING PAGE BLANK NOT FILMED

FOLDOUT FRAME

2

ARGE PROBE

Instruments			
ole Extinction Detector	Solar Radiometer	Planetary Flux Radiometer	Cloud Particle Size Spectrometer
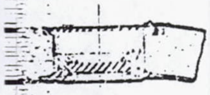	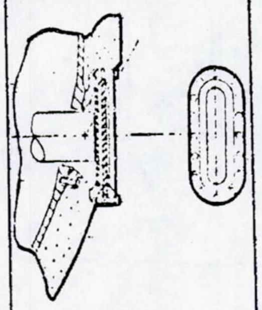	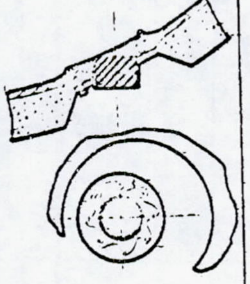	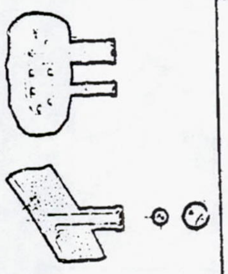
	1	1	2
ertical plane ±15 deg orizontal plane ±1/2 deg	In vertical plane ±60 deg In horizontal plane ±15 deg	5 deg conical	1.3 cm (0.50 in.) constant diameter 0.64 cm (0.25 in.)
cm (1.0 in.) meter	Vertical 5.1 cm (2.0 in.) Horizontal 1.3 cm (0.50 in.)	2.5 cm (1.0 in.) diameter	1.3 cm (0.50 in.) ~~diameter~~ 0.64 cm (0.25 in.)
phire	Sapphire	CVD ZnSe*	Sapphire
	3.5	13.5	3.5
heater – outer dow only	Sheathed element	Sheathed element (if required)	Sheathed element
(Off at 40 km)	22 W	18 W	8 W (total)
ing	O-ring	Braze	Braze
([illegible]8 lb)	118 g (0.26 lb	141 g (0.31 lb)	45 g (0.10 lb)
isonable cover	Jettisonable cover	Jettisonable cover	Jettisonable cover
ce between inner and er window hermetic- y sealed	O-ring seal used to provide increased thermal isolation for window	Thick window due to low modulus of rupture of IR transparent window material	Dual window configuration is lightest configuration and uses the least heater power of [illegible] examined

LANK NOT FILMED

REPRODUCIBILITY OF THE ORIGINAL PAGE IS POOR.

FOLDOUT FRAME

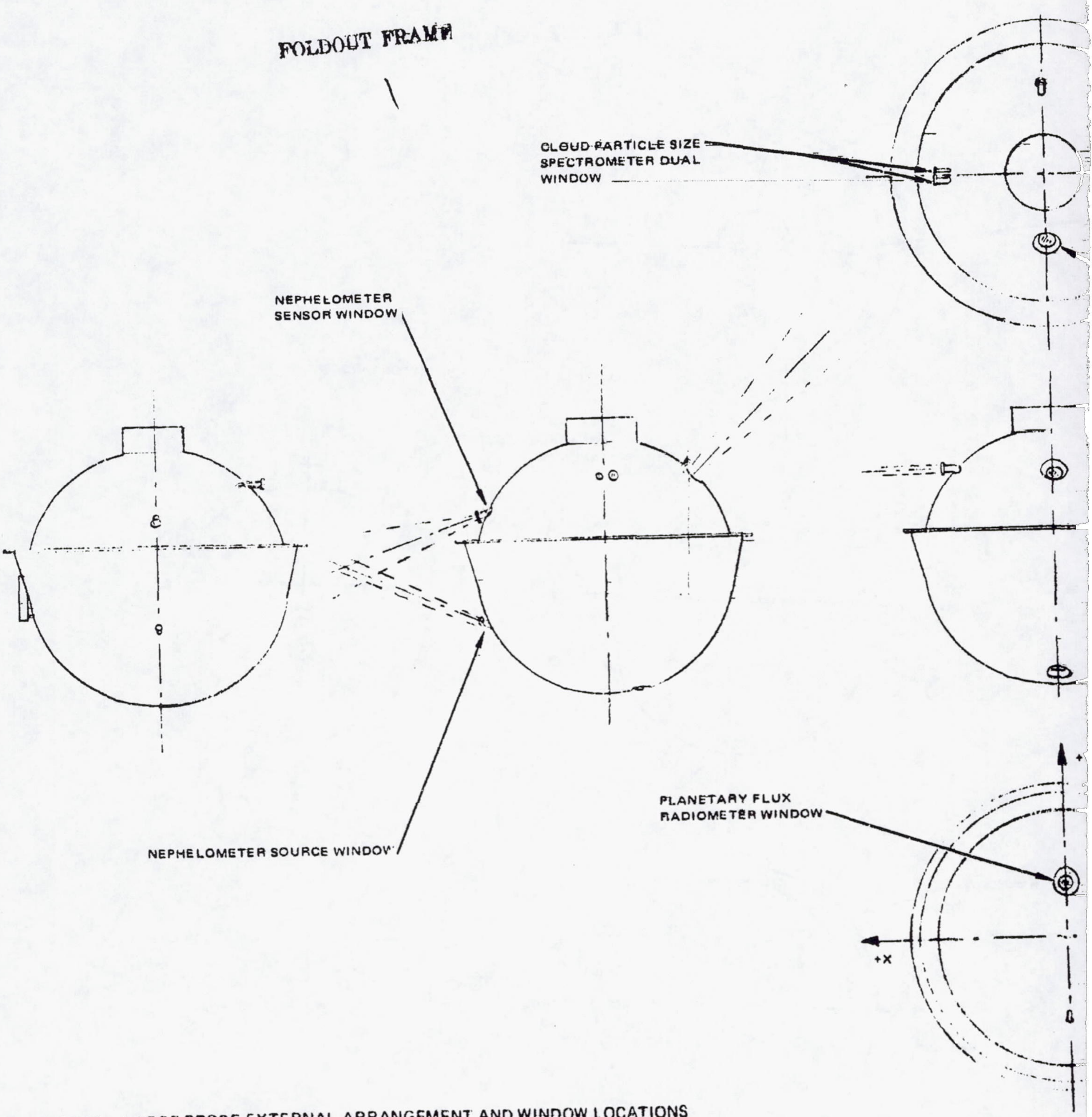

FIGURE 4.5-17. LARGE PROBE EXTERNAL ARRANGEMENT AND WINDOW LOCATIONS

REPRODUCIBILITY OF THE ORIGINAL PAGE IS POOR.

FOLDOUT FRAME 2

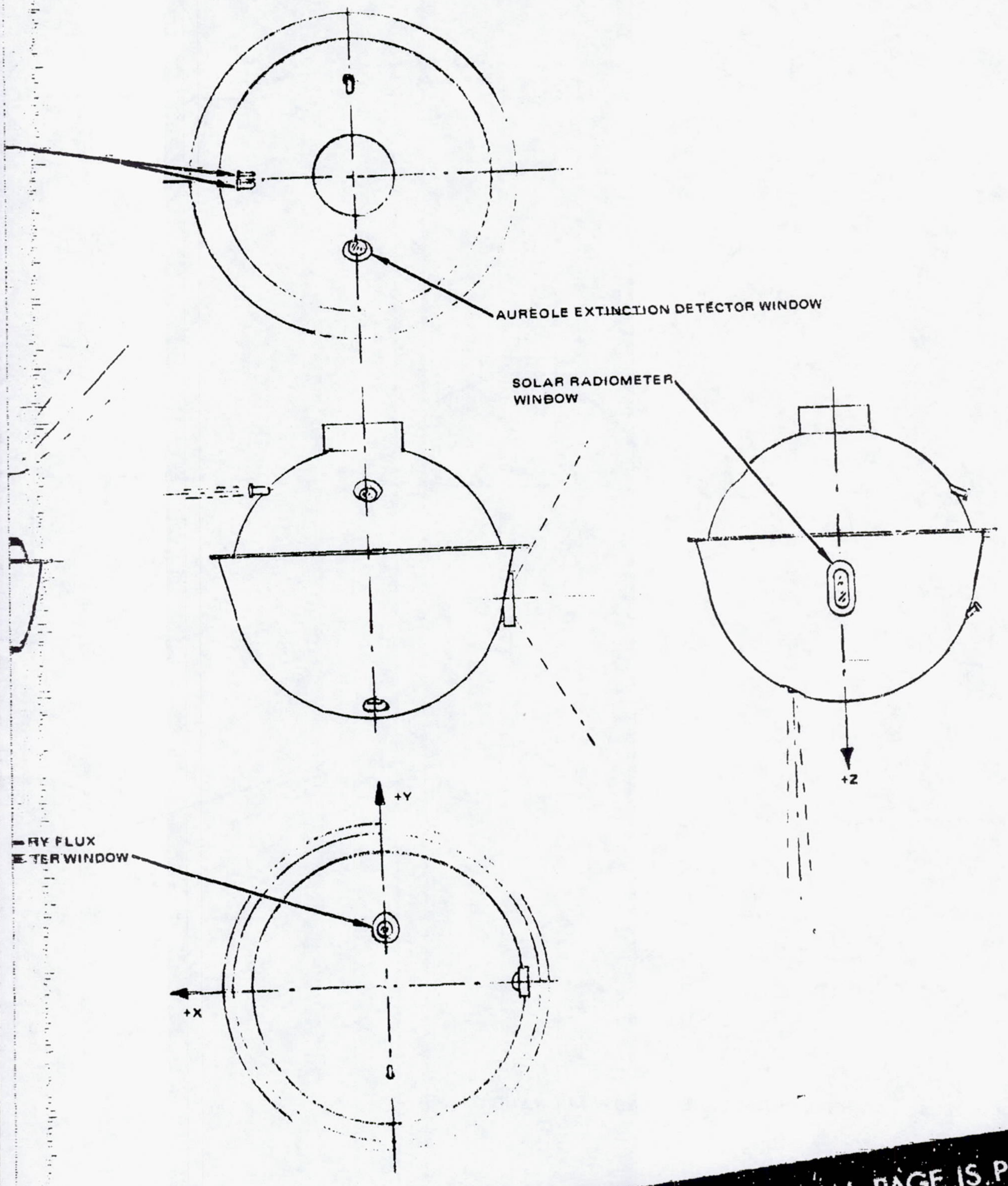

REPRODUCIBILITY OF THE ORIGINAL PAGE IS POOR.

Page intentionally left blank

arrying away contaminants and exposing the clean inner window. Eight ollets retained by a split metal band hold the cover in place against the orce of eight spring loaded plungers (Figure 4. 5-18). When the band is eleased by a hot wire initiator, the cover is ejected and carried away by the lipstream. Window heating is provided by a transparent film heater similar o that used on the frangible window configuration. Spring type electrical onnectors to the window heater are designed not to hinder window jettison. Temperature limitations on the squib operated configuration limit minimum ltitude for window jettison to something about 40 km. A properly thermally nsulated solenoid could probably operate to lower altitudes.

A slightly modified approach is used for the hermetically sealed window of the aureole extinction detector experiment (Figure 4. 5-6), otherwise the pressure differential across the outer window could prevent jettison. Accordingly, a burst diaphragm is provided in the structure separating the windows. When the pressure differential across the diaphragm equals a preset amount corresponding to the altitude of window jettison, it ruptures, equalizing pressure across the outer window and allowing jettison to be accomplished. Exact timing of the rupture with respect to initiator firing is not important; either the initiator will not have been fired before pressure equalization, and a normal jettison will result, or else the retaining collets will have been released prior to diaphragm rupture, and jettison will occur immediately upon pressure equalization.

Instruments looking through the cover would probably have to be calibrated both with and without the cover. A sudden change in reading after cover disposal would indicate the presence of a contaminant buildup. This approach could be adapted to the planetary flux radiometer's IR wavelength requiprements, but the modulus of rupture of suitable IR transparent cover materials is very low, making use of a positive ejection mechanism difficult. In addition, the film heater configuration proposed for the visible wavelength covers is not transparent in the IR wavelengths of interest, and alternate methods of heating the relatively thin cover window are prohibitively inefficient.

Due to the relatively simple mechanization, this is a light system, with mass of 0.023 to 0.045 kg (0.05 to 0.10 lbm) per window for a squib operated system and approximately 0.18 to 0.36 kg (0.4 to 0.8 lbm) for a solenoid actuated system.

Power required for the cover jettison is limited to a single squib or solenoid actuating current pulse. Maximum window hwater power required just prior to window jettison is 4 W.

Reliability of the squib actuated system is very high because it is simple and the reliability of the squibs high. Reliability of the solenoid actuated system depends on development of a suitable space-qualified high temperature solenoid and is potentially very good. Transparency of the cover provides some capability in event of actuator failure.

REPRODUCIBILITY OF THE ORIGINAL PAGE IS POOR.

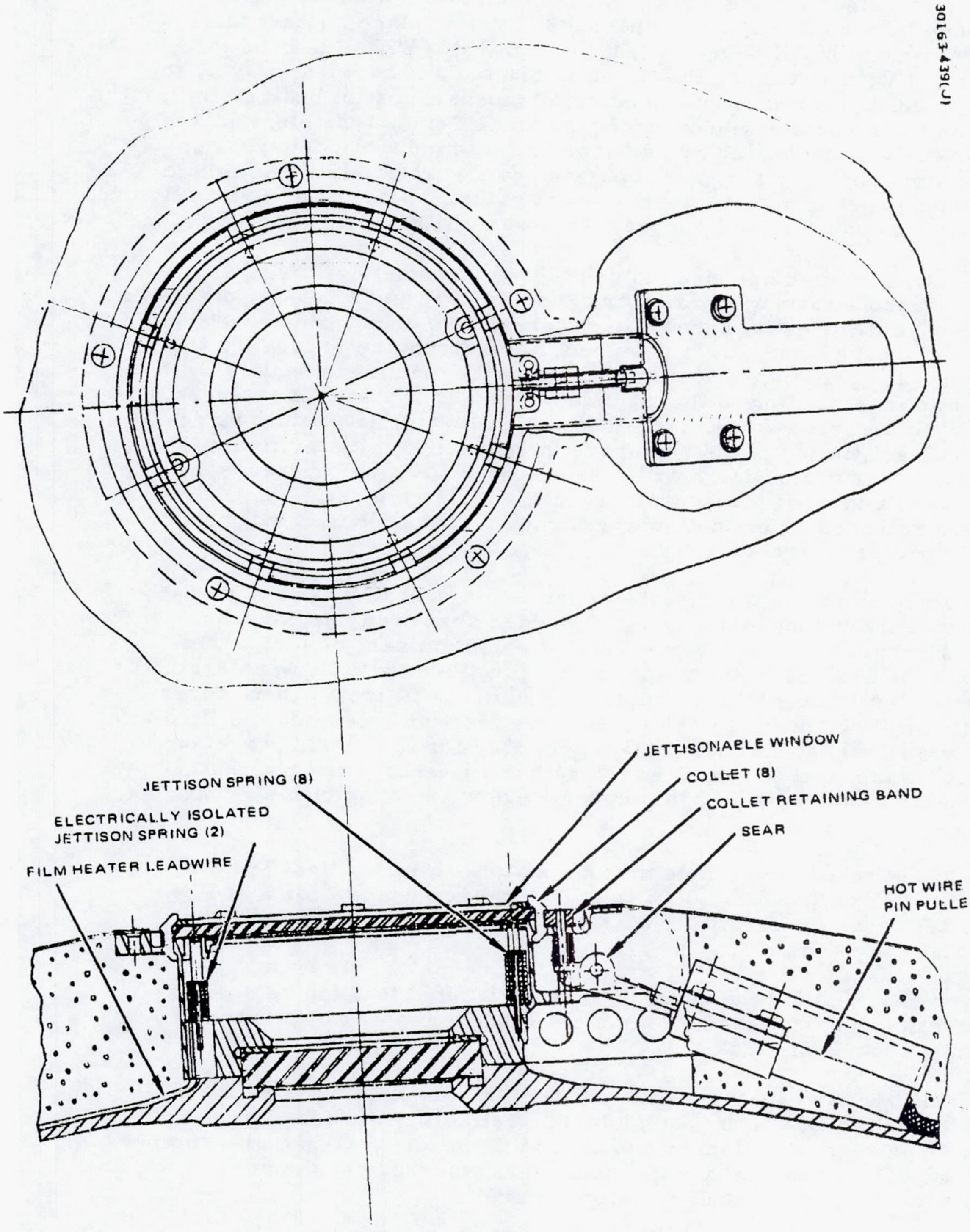

FIGURE 4-5-18. JETTISONABLE WINDOW

REPRODUCIBILITY OF THE ORIGINAL PAGE IS POOR.

The cover is effective against all modes of contamination when used, and overall effectiveness is high if contaminants are concentrated above window disposal height, but one shot operation limits use.

Development of the jettison mechanism is straightforward. Interaction of the jettisoned cover with the probe slipstream is an unknown quantity, requiring testing to evaluate. Solenoid activation would require development and qualification of a suitable high temperature solenoid.

Mass Spectrometer. The double focusing type of spectrometer does not lend itself to installation from the outside, as the analyzer assumes a somewhat wide, flat layout with a number of rather bulky components separated by high-vacuum plumbing. This layout is well suited for shelf mounting, with the inlet assembly protruding out through the pressure vessel wall radially at an angular distance of approximately sixty degrees from the probe stagnation point. For the purposes of design, a 3 in diameter inlet system was assumed, although this is felt to be quite conservative (Figure 4.5-19). To insure that the rigidly shelf mounted inlet system does not constrain the pressure vessel wall, sealing is accomplished by means of a bellows in addition to the metallic O-ring. Additional flange bolts are required to overcome the adverse pressure load caused by internal installation of the flange. The squib-driven guillotines must be mounted after assembly so the hat can be fitted through the relatively small aperture.

This design is somewhat bulky and adequate room must be allowed on the shelf to give the analyzer room for installation. This type of spectrometer requires final installation after the other components and equipment shelves are installed in the pressure vessel in order to maintain the integrity of their vacuum systems.

Cloud Particle Size Spectrometer Mirror Mount. The cloud particle size spectrometer utilizes an externally mounted condensing mirror as part of its optical subsystem (Figure 4.5-20). The instrument mounted mirror support structure joins mirror, pressure window, and instrument into a single unit. A support tube mounted to the instrument case protrudes through the pressure vessel wall and incorporates a seat for a metallic O-ring seal in a boss machined into its outer end. The tube is sealed to the pressure vessel wall with a welded metal bellows which incorporates a metallic O-ring sealed flange that bolts to the wall, completing the hermetic seal. A sapphire window and metallic O-ring mount to the outer end of the tube, and the threaded retainer ring that holds the window in place also retains the mirror support struts at their inboard end. At their outboard end, the struts support the mirror directly; no provision for final adjustment is required, as the entire assembly is machined as a unit to provide built-in alignment. As in the pressure vessel mounted struts, low expansion coefficient high thermal conductivity alloys are used to minimize thermal gradient induced deflections. The bellows seal decouples the instrument from the deflections of the pressure vessel, helping to maintain rigid alignment. As pressure loads on the window are not reacted in the pressure vessel wall, the instrument case must be sized to accommodate an axial load of approximately 7200 N (1600 lbf) at the surface

REPRODUCIBILITY OF THE ORIGINAL PAGE IS POOR.

FOLDOUT FRAME

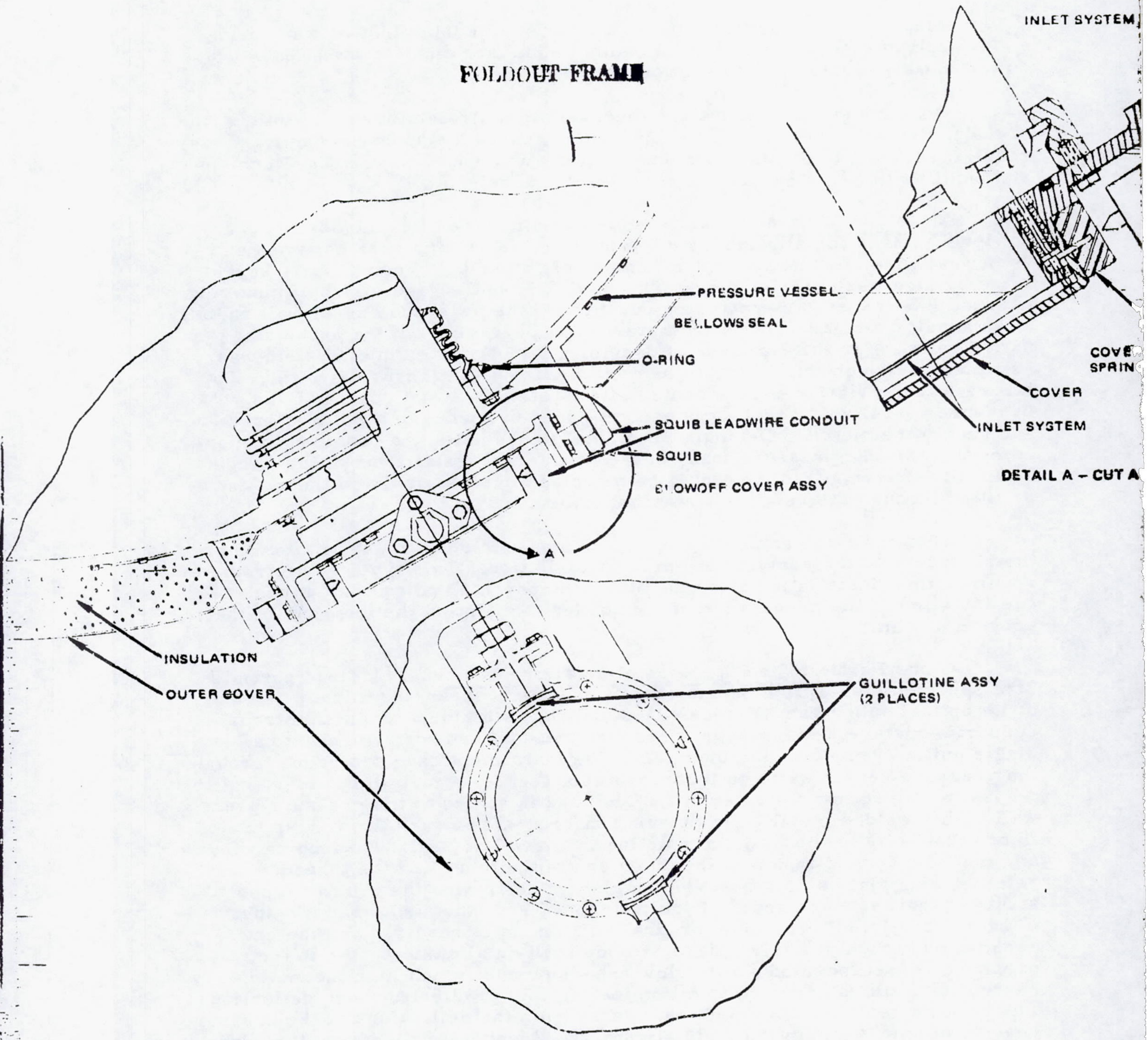

a) INSIDE MOUNTED INLET ASSY – BELLOWS SEAL

Figure 1. Mass Spectrometer Inl

FIGURE 4.5-19. MASS SPECTROMETER INLET SYSTEM

PRECEDING PAGE BLANK NOT FILMED

FOLDOUT FRAME 2

30163-440(U)

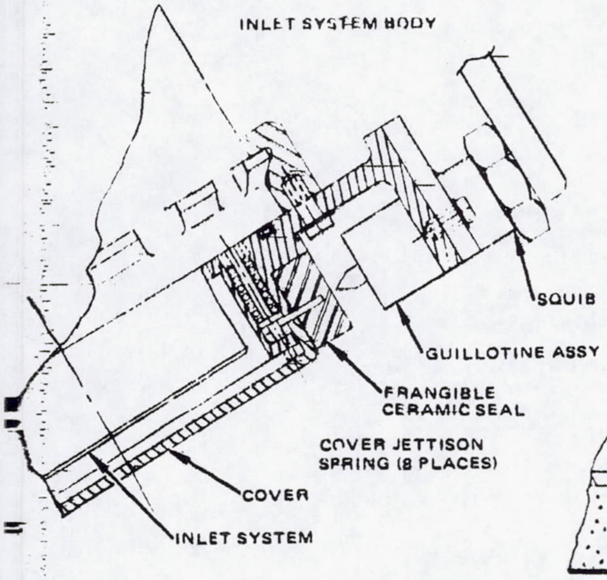

DETAIL A – CUT AWAY

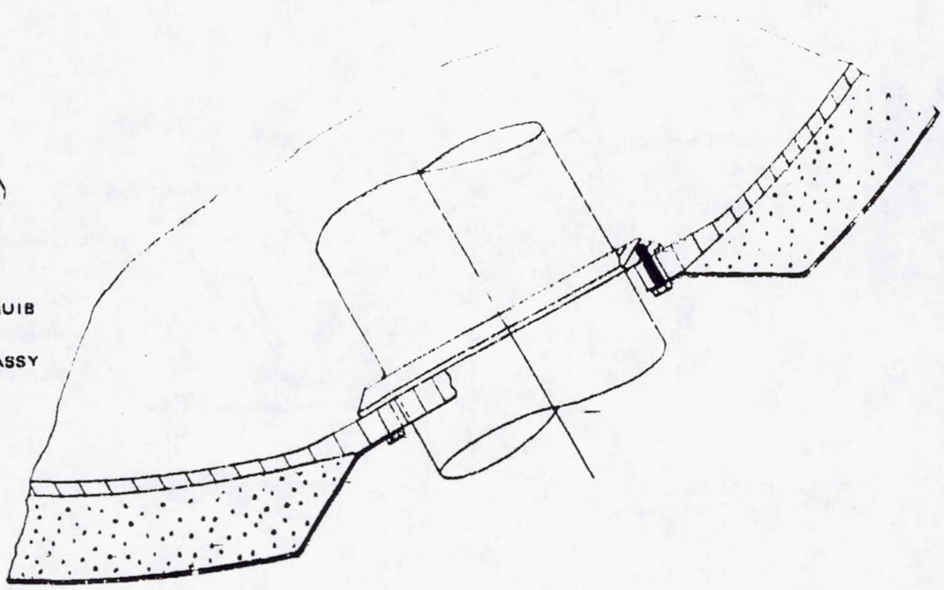

b) INSIDE MOUNTED INLET ASSY – SOLID FLANGE

GUILLOTINE ASSY (2 PLACES)

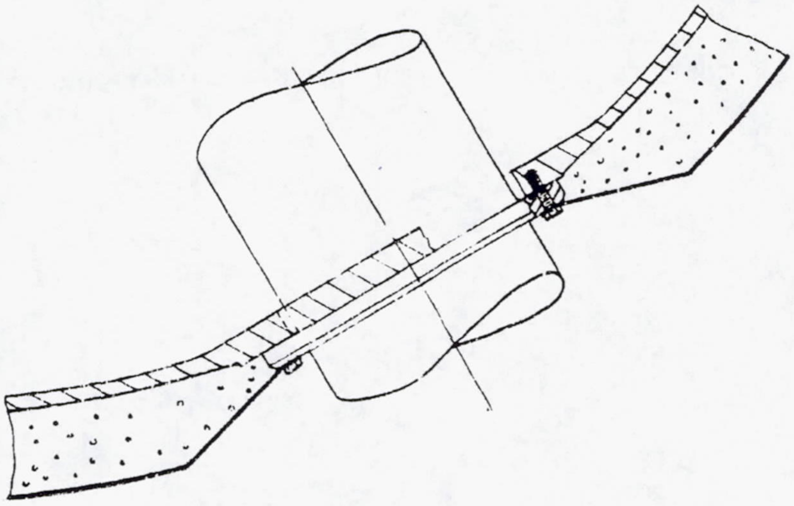

c) EXTERNALLY MOUNTED INLET ASSY – SOLID FLANGE

Mass Spectrometer Inlet System

MED

REPRODUCIBILITY OF THE ORIGINAL PAGE IS POOR.

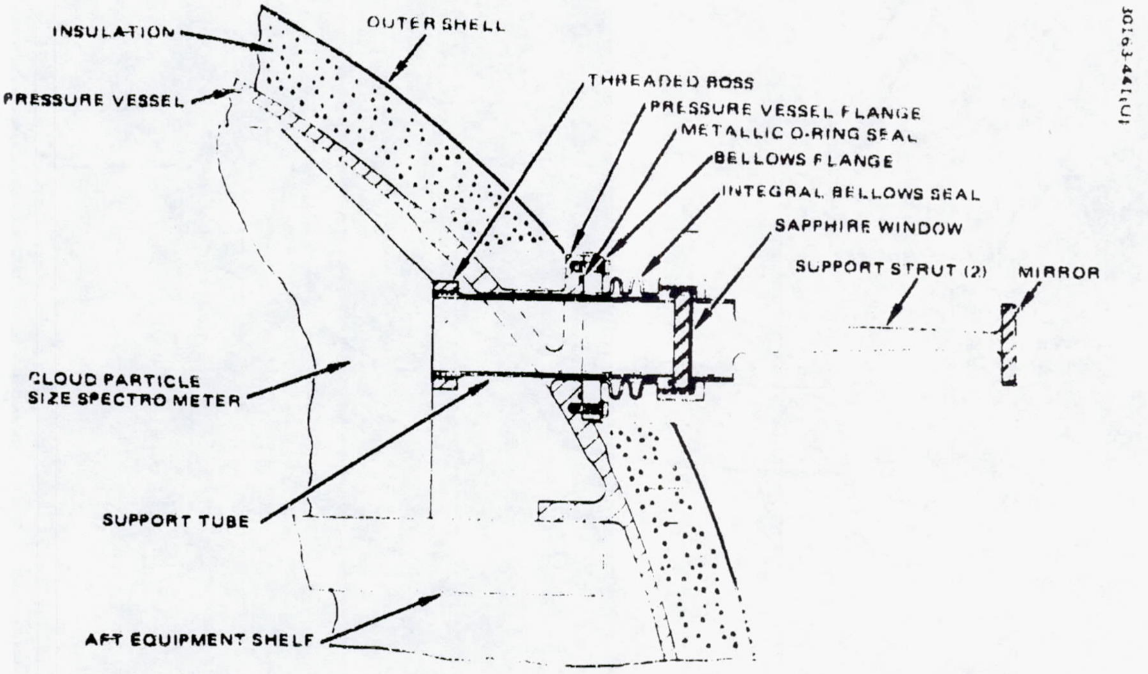

FIGURE 4.5-20. MIRPOR SUPPORT INTEGRAL WITH EXPERIMENT

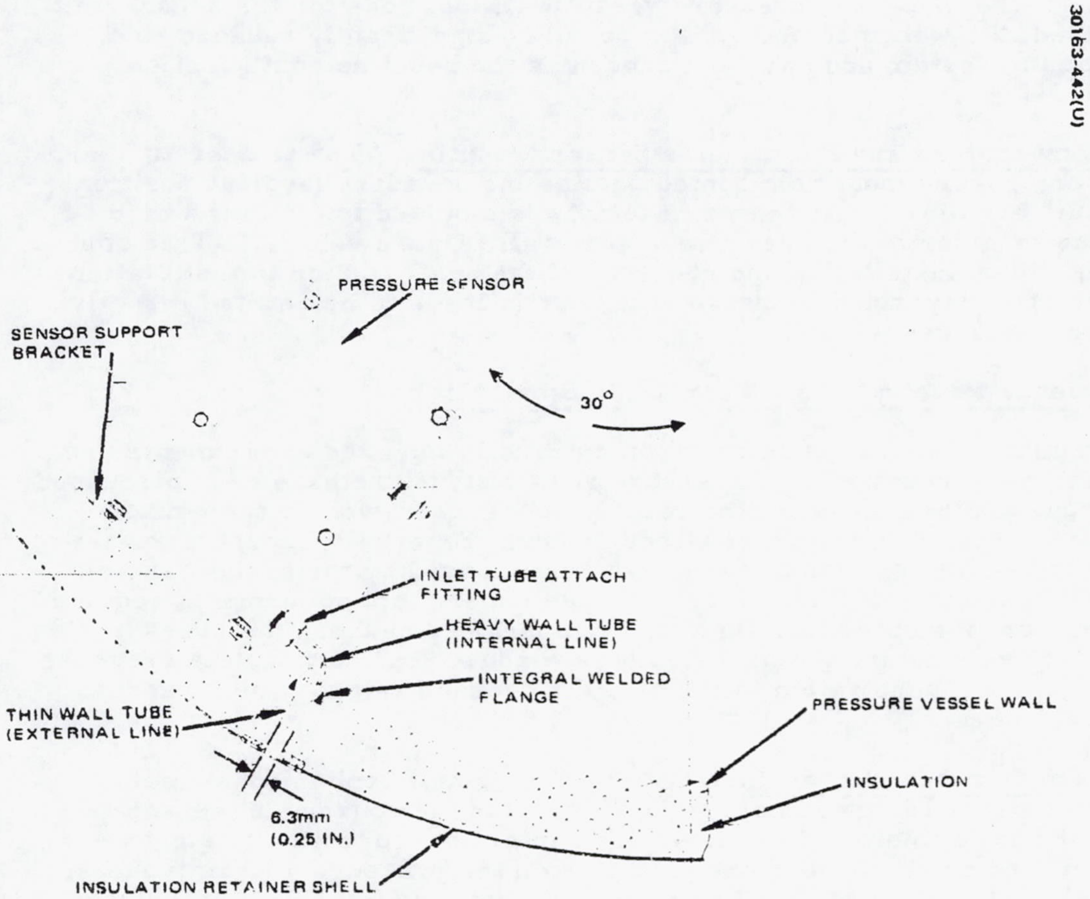

FIGURE 4.5-21. WALL MOUNTED SENSOR

REPRODUCIBILITY OF THE ORIGINAL PAGE IS POOR.

of Venus, as well as the shear and moment induced in the support tube by the entry deceleration loads.

Pressure-Sensor Inlet System. The primary requirement to be satisfied in design of the inlet system for the pressure sensor is keeping the inlet within 30 deg of the probe stagnation point while minimizing line length to the internal sensor. Shelf and pressure vessel wall locations for the sensor unit were studied; the wall mounted sensor provides significantly reduced line lengths for the system and has been chosen as the baseline configuration (Figure 4.5-21).

Temperature and Hygrometer Sensor Mounting. The temperature and hygrometer sensors must be mounted outside the boundary layer at positions of maximum air flow. The sensor assembly is mounted to a fitting which bolts to the exterior of the pressure vessel wall (Figure 4.5-22). This configuration allows installation and checkout of the sensor prior to installation of the insulation layer and allows sensor inertia loads to be reacted directly into the pressure vessel.

Science Penetrations – Thor/Delta Small Probe

Primary constraints imposed on externally mounted experiments and those which must penetrate the pressure vessel structure have been discussed in a previous section. These constraints apply equally well to the small probe, but another requirement has been added: Externally mounted experiments must be able to withstand the heat flux imposed by the probe wake on the aft half of the probe during entry. Three experiment components require protection from the entry heat flux: the temperature sensor, the pressure sensor inlet system, and the nephelometer window. In addition, the pressure sensor requires a penetration in the pressure vessel wall to provide access to the atmosphere.

Nephelometer Window Installation. The small probe nephelometer window provides a 15 deg conical field of view for the source and sensor lenses of the instrument. Both fields are centered about a line of sight located perpendicular to the probe spin axis on the pressure aft hemisphere. The nephelometer operates in the wavelengths between 0.3 to 3 μ, allowing use of sapphire as a window material. Heat must be supplied to the window throughout the descent to prevent condensation on the window surface, and the window must be configured such that the outgoing beam from the light source is isolated from the returning reflected light.

Field of view requirements are satisfied by a 37. mm (1.5 in) optical size pressure window, 6.35 mm (0.25 in) thick. A secondary internal, nonpressure window 0.8 mm (0.030 in) thick is spaced 0.32 mm (0.125 in) from the inner surface of the pressure window to block thermal convection and radiation. Both windows are mounted at the outboard end of a tube welded into the pressure vessel wall to further reduce the thermal input to the probe interior (Figure 4.5-23). The window is heated by a sheathed element heater wrapped around the window periphery; sealing is provided by a metallic O-ring bearing on the inboard surface of the pressure window.

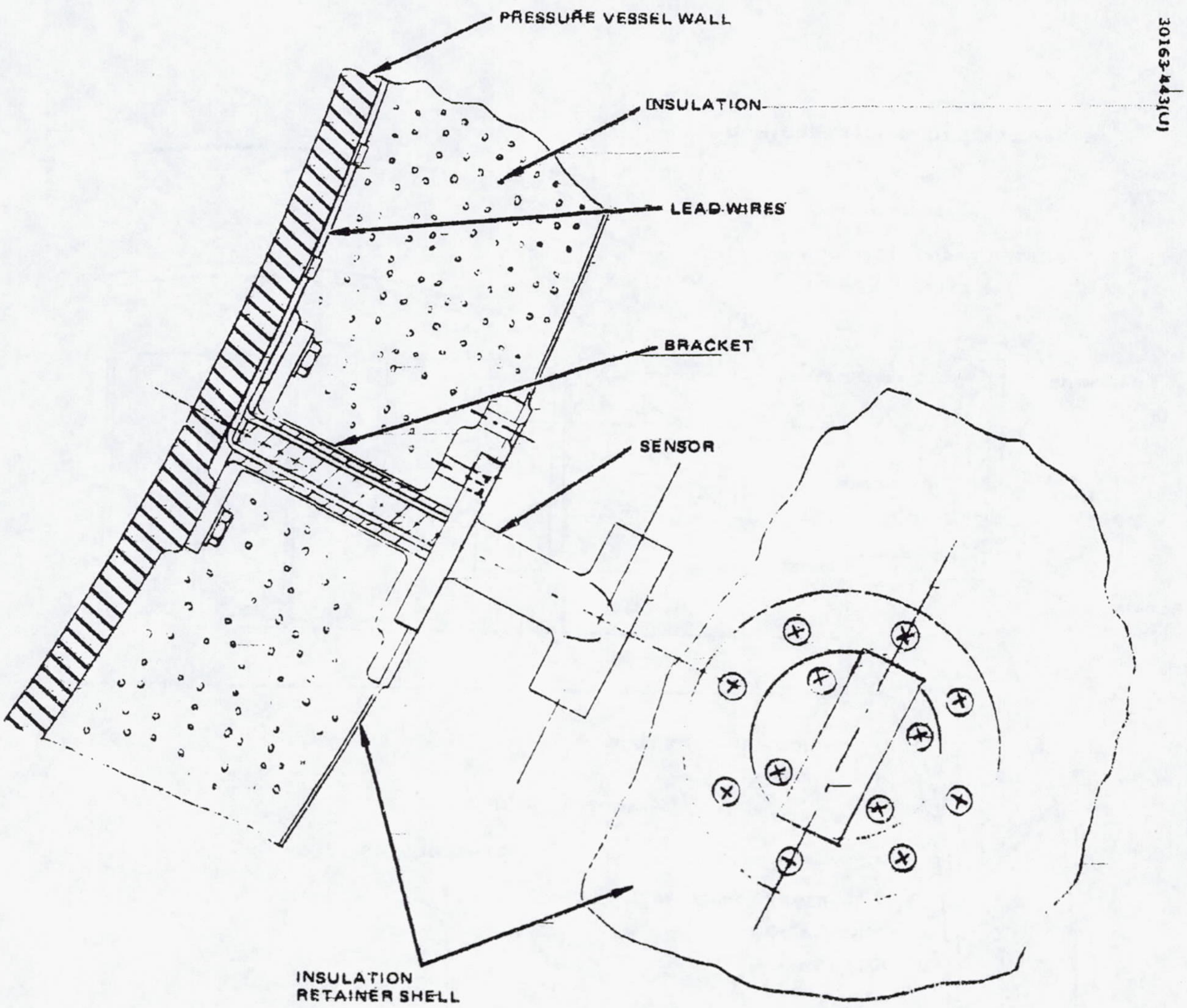

FIGURE 4.5-22. LARGE PROBE TEMPERATURE SENSOR MOUNTING

REPRODUCIBILITY OF THE ORIGINAL PAGE IS POOR.

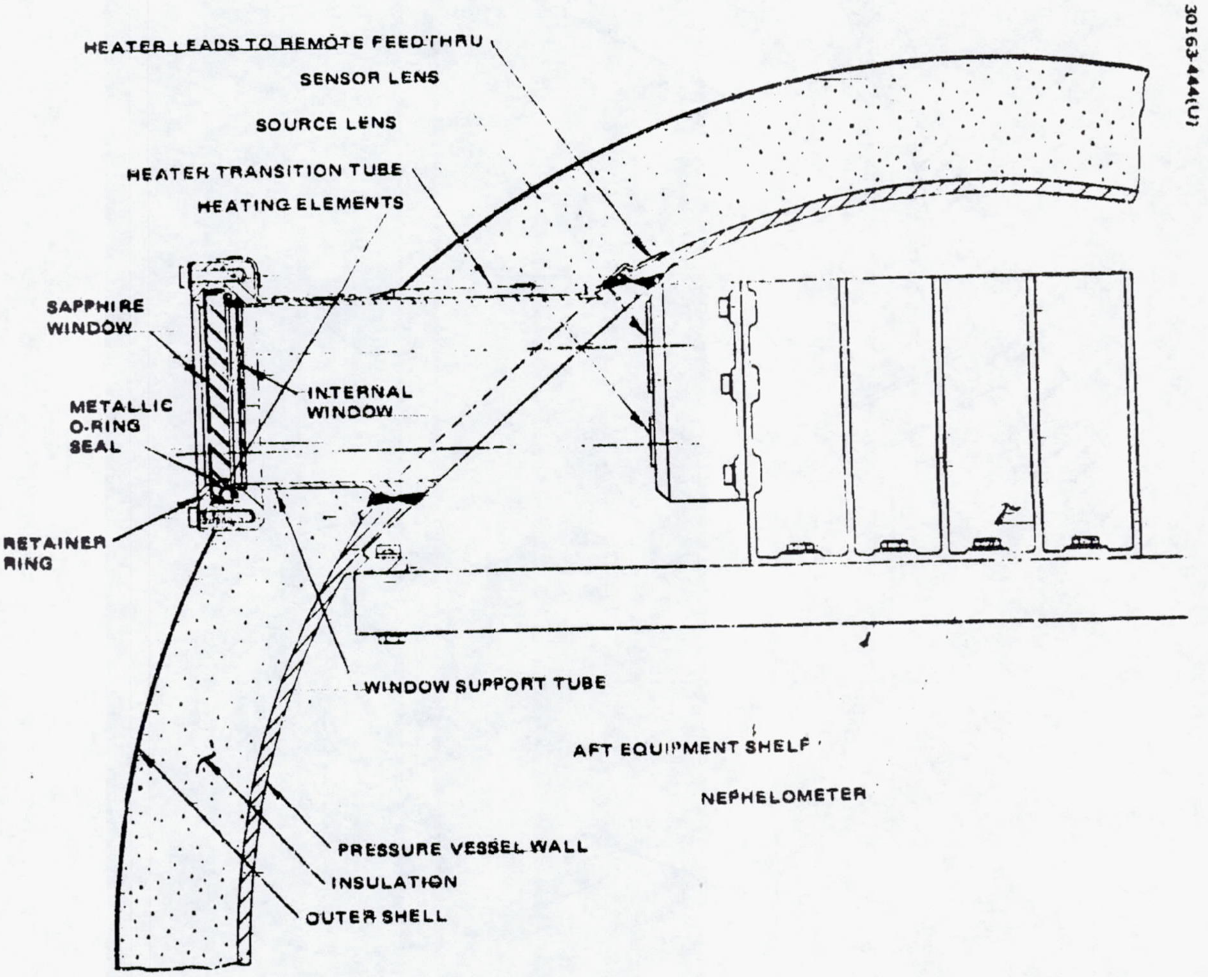

FIGURE 4.5-23. SMALL PROBE NEPHELOMETER INSTALLATION

REPRODUCIBILITY OF THE ORIGINAL PAGE IS POOR.

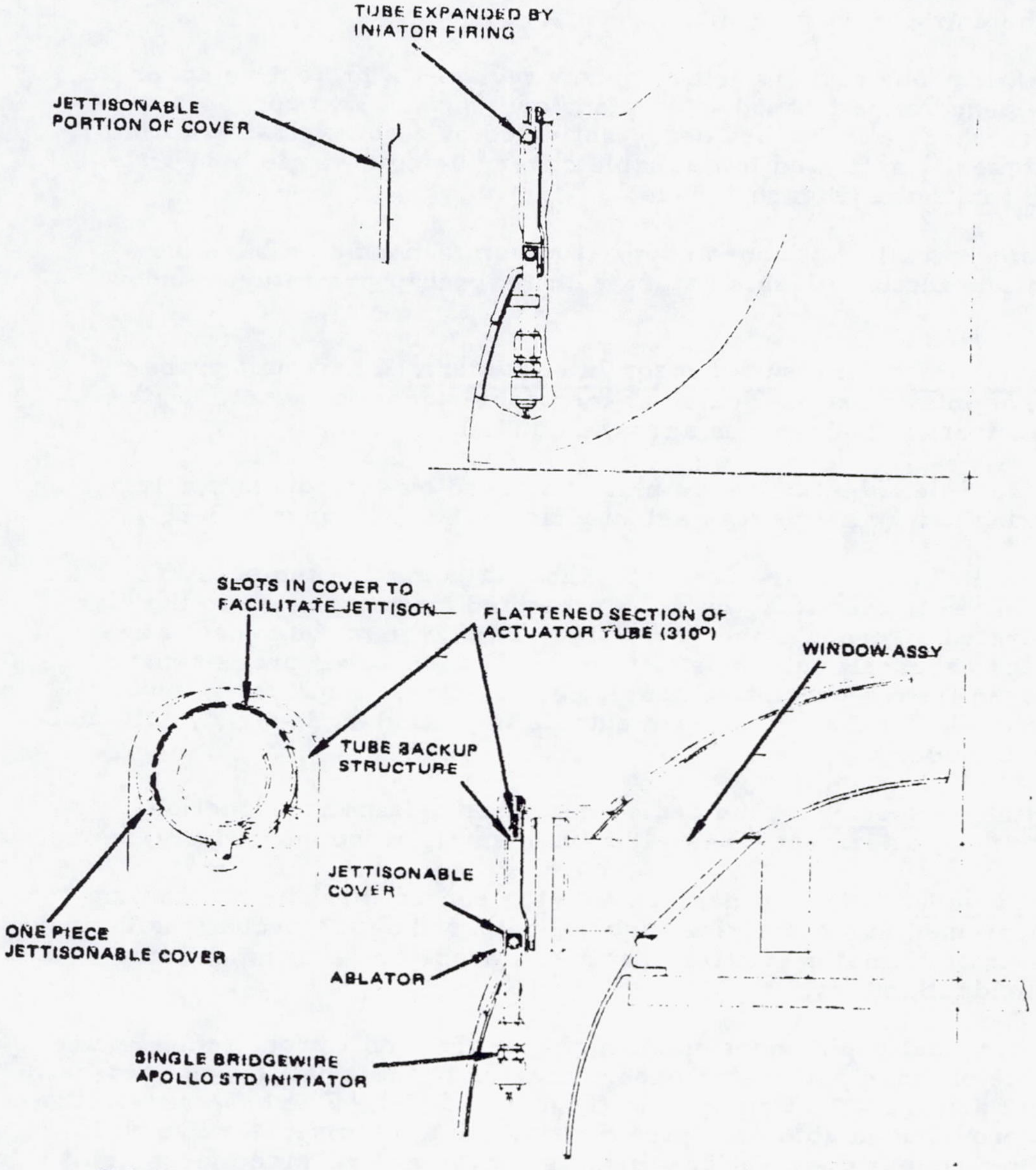

FIGURE 4.5-24. PYROTECHNIC ACTIVATED JETTISONABLE COVER

REPRODUCIBILITY OF THE ORIGINAL PAGE IS POOR.

No provisions for contamination removal are made beyond heating the window, but a jettisonable protective cover is provided to enable the window to withstand the entry heating condition.

The small probe nephelometer window requires a protective cover which can be opened or jettisoned after planetary entry. Two concepts were examined: a mechanically latched door, activated by a nonexplosive initiator, and a pyrotechnically activated jettisonable cover, using a single bridgewire apollo standard initiator (Figure 4.5-24).

A pyrotechnically jettisoned cover is recommended as a baseline because of its inherently fail-safe nature with respect to premature window exposure.

Stagnation Point Pressure Sensor Inlet System. The small probe pressure sensor inlet must be located at the probe stagnation point. This requires a penetration in the probe aeroshell and ablator.

A jettisonable, ablating teflon plug, removed by a pyrotechnically activated, spring driven piston was selected as baseline (Figure 4.5-25).

Deployable Temperature Sensor. The platinum wire temperature sensors considered in this study must be protected from exposure to the high heat flux generated by probe planetary entry. The large probe sensors are protected by the aeroshell until it is jettisoned, but the small probe sensor must be deployed from a protective housing after entry. Deployment must locate the sensor in the free airstream outside the boundary layer. Additional requirements include:

1) High g exposure. The deployment mechanism must function reliably after exposure to the 700 g small probe entry deceleration.

2) Envelope. Prior to deployment, the sensor mechanism must be contained in a cylindrical volume centered on the probe longitudinal axis of diameter equal to that of the probe bus attachment ring inside diameter.

The swing-out deployment mechanism for the small probe temperature sensor consists of three parts: the base, mounted to the small probe aeroshell; the swing arm; and the actuation system (Figure 4.5-26). The base serves two functions: it provides an ablator coated housing for the temperature sensor during entry and houses the pivot bearings, springs, and release mechanisms comprising the activation system. The base is machined in one piece from aluminum alloy; all external surfaces are coated with ESM ablator. The swing arm provides a mount for the platinum wire temperature sensor (similar to the Rosemount Engineering Co. Model 101) and a conduit for the temperature sensor leads. Like the base, it is machined from aluminum alloy; all external surfaces are coated with ESM ablator.

Activation of the swing arm is carried out by a system composed of redundant springs, a redundant hot wire initiator release mechanism, and a

30163-446(U)

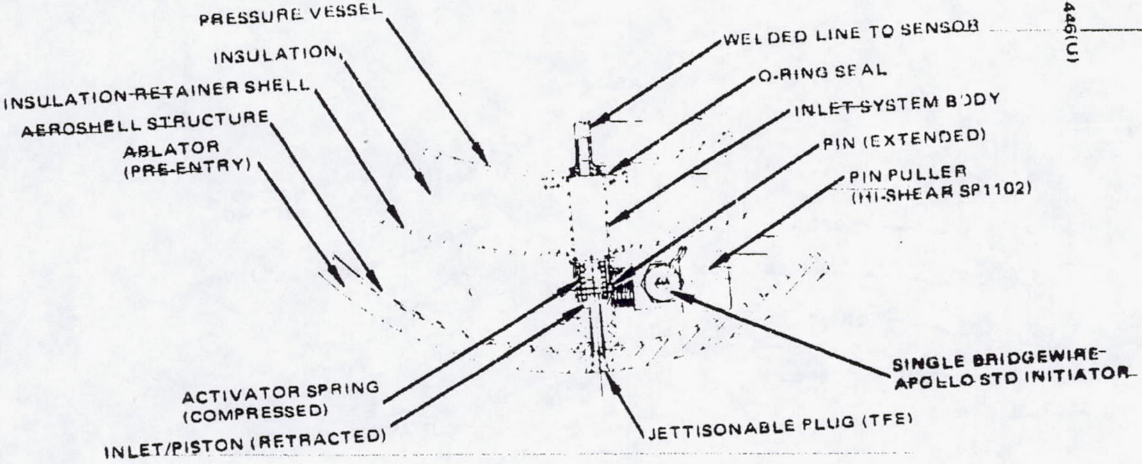

a) INLET RETRACTED

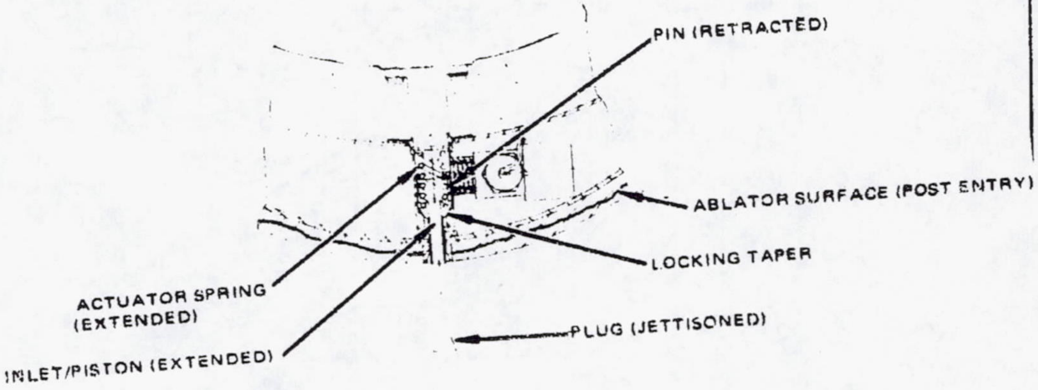

b) INLET DEPLOYED

FIGURE 4.5-25. JETTISONABLE PLUG INLET SYSTEM

REPRODUCIBILITY OF THE ORIGINAL PAGE IS POOR.

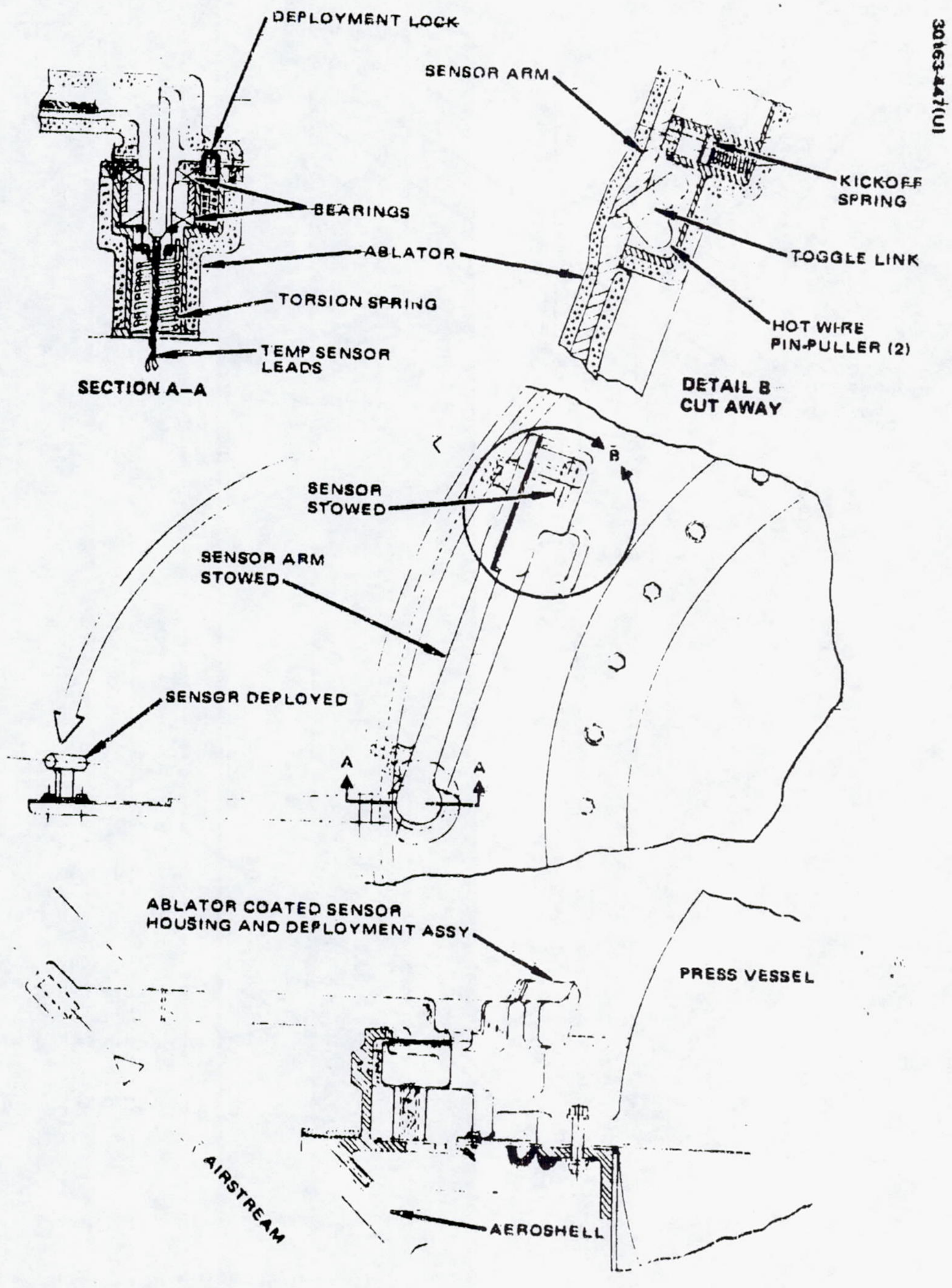

FIGURE 4.5-28. SWING ARM DEPLOYABLE TEMPERATURE SENSOR

REPRODUCIBILITY OF THE ORIGINAL PAGE IS POOR.

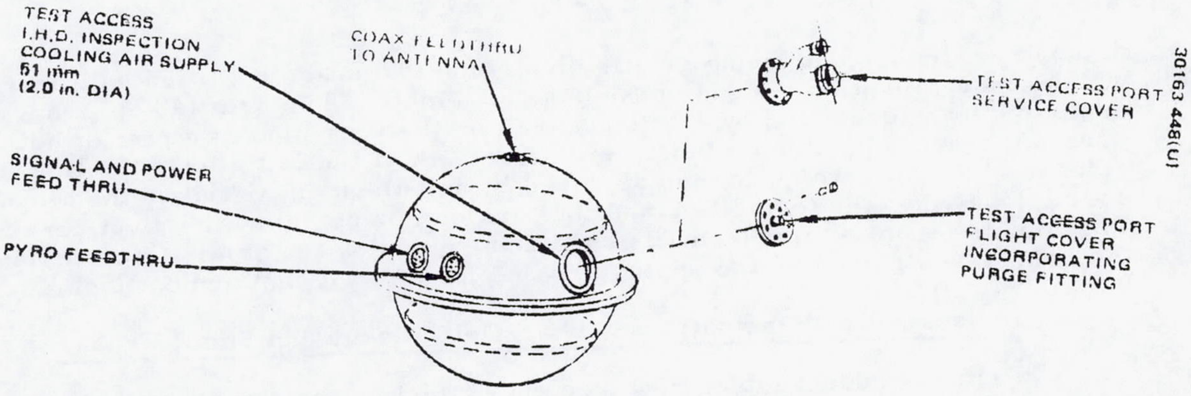

a) SMALL PROBE PRESSURE VESSEL

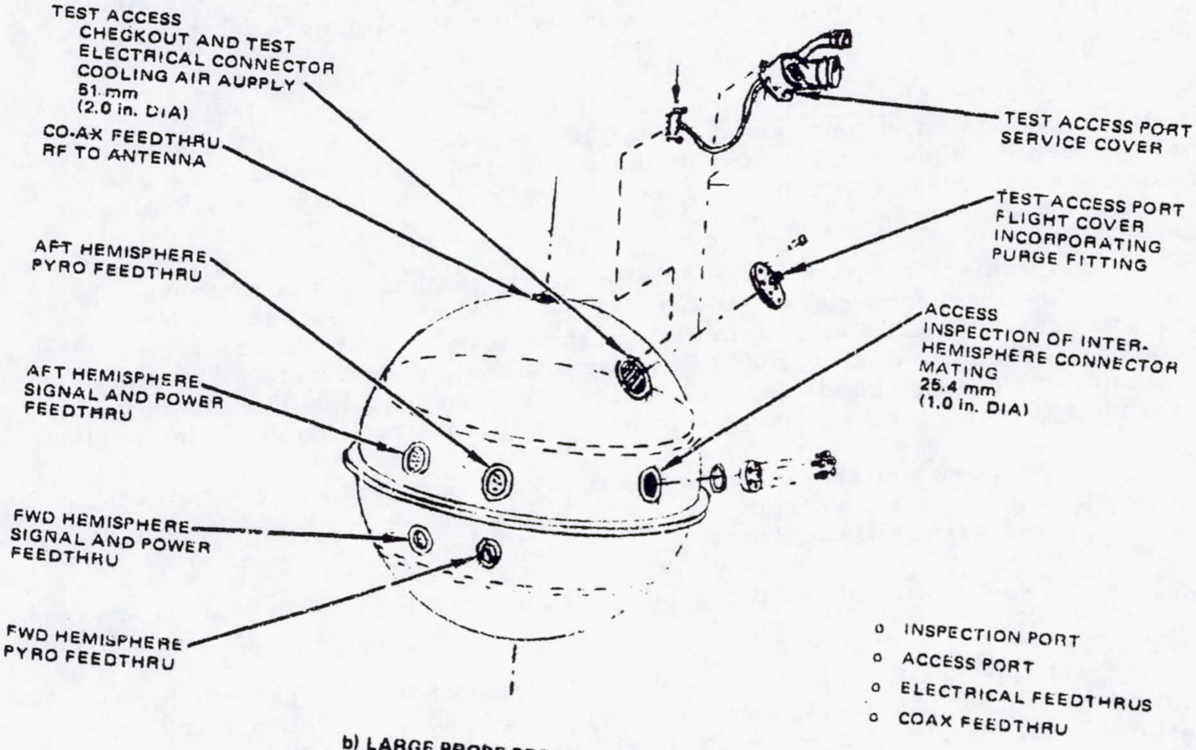

b) LARGE PROBE PRESSURE VESSEL

FIGURE 4.5-27. HOUSEKEEPING PENETRATIONS

REPRODUCIBILITY OF THE ORIGINAL PAGE IS POOR.

deployment lock. The swing arm is pivoted on two space qualified ball bearings which are retained in one end of the base assembly. The arm is kept from deploying by a toggle link which is secured by the sear pins of a pair of hot wire initiators. Upon actuation of either or both of the initiators, the link releases the arm, which is then deployed by impulses delivered by the kickoff spring located at the toggle link and the torsion spring below the pivot bearings. The impulse from either spring is sufficient to deploy the arm. Once deployed, the arm is restrained by the spring driven piston of the deployment lock.

Housekeeping Penetrations – Thor/Del Large and Small Probes

Primary housekeeping requirements affecting the structure integration task are first the requirement to bring electrical current, both dc and rf, into and out of the hermetically sealed pressure vessel, and second the providing of a limited amount of access to the interior of the pressure vessel after assembly to provide for electrical connections, cooling air supply and borescope inspection during pre-flight systems test activities. The third item considered in this section of the study was the in-flight disconnect for the pressure vessel module—deceleration module electrical umbilical. A general view of the housekeeping penetrations on large and small probes is shown in Figure 4.5-27.

DC Electrical Feedthroughs.

DC or low frequency electrical feedthroughs are located in four places on the large probe and two on the small probe. Feedthroughs carrying pyrotechnic initiation pulses from the squib drivers are separated from those carrying power currents to satisfy EMI requirements.

The primary function of the dc electrical feedthroughs is to convey the relatively low frequency signal, power and pyro firing currents through the pressure vessel wall. While maintaining a hermetic seal at Venus surface temperatures (approximately 500°C) and pressures (approximately 100 atm). This function requires good electrical properties, such as low resistance pins and high pin to pin breakdown voltage. Additional requirements include:

1) Number and size of pins. As many as 60 pins may be required. Pin sizes range from No. 28 for signal leads to No. 22 for power and pyro initiator leads.

2) Structural. Installation should not affect pressure vessel structural integrity.

The basic feedthrough (Figure 4.5-28) consists of a header machined as an integral part of a short, tubular body. The header is multiply drilled to allow use of individual compression ceramic seals for each pin. Compatibility problems between the high conductivity nickel ferrous alloy pins and the seal material are solved by brazing a collar made from a ceramic compatible metal around each pin. This arrangement provides the strongest possible header while maintaining excellent electrical properties; Venus surface conditions are easily withstood. Because of the rigorous environment, hermetic feedthroughs using all ceramic or all glass headers were rejected.

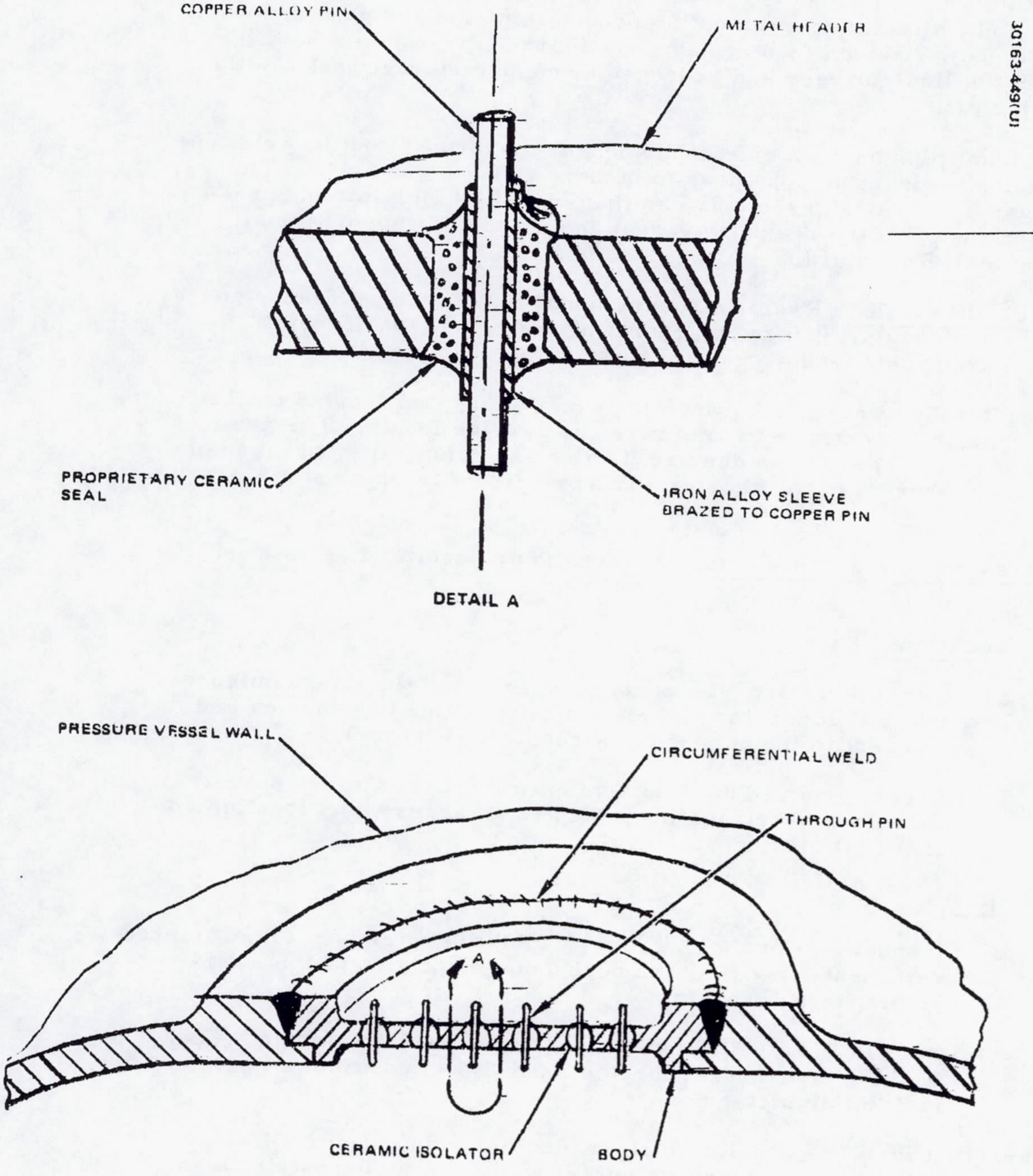

FIGURE 4.5-28. HERMETIC ELECTRICAL FEEDTHROUGH

Welding was chosen as the method of attaching the feedthrough to the pressure vessel wall as it minimizes the penetration size and provides the best possible seal. Welded feedthroughs are thoroughly space proven; they were used on the liquid oxygen and hydrogen cryogenic storage tanks in the Apollo service module.

Individual pins on each side of the header are brought out to weld type terminations, allowing a stub harness to be hardwired to each side. The entire harness/feedthrough assembly can then be potted, minimizing protrusion on the inside of the pressure vessel and providing support for all wires during high G loadings.

RF Feedthroughs. Radio frequency feedthroughs for both large and small probes use coaxial fittings incorporating the same type of metal/ceramic seal used in dc feedthroughs (Figure 4.5-29).

A feedthrough was chosen which uses an O-ring seal located on the probe axis beneath the antenna to minimize coaxial line length. The axial feedthrough location was chosen despire its relative complexity, because of lower rf losses inherent in the shorter and more direct transmission line routing.

Access and Inspection Ports. Requirements peculiar to each port include:

1) Location:

   a) Inspection Port. To enable inspection of the interhemisphere internal connector, a location between the two shelves and adjacent to the connector is required (Figure 4.5-27).

   b) Access Port. The requirement for access after pressure vessel aeroshell mating indicates an access port location aft of the aft shelf.

2) Size:

   a) Inspection Port. 25.4 mm (1.0 in) diameter port is considered sufficient for visual and borescope inspection of the interhemisphere connector.

   b) Access Port. Efficient exhausting of cooling air and access to the internal test receptable are satisfied with a 51 mm (2.0 in) diameter port.

Inspection Port (Figure 4.5-30a). A doubler reinforced 25.4 mm (1.0 in.) diameter hole in the pressure vessel wall is by a concentric O-ring groove and hole pattern. The 25.4 mm (1.0 in.) thick titanium cover bolts into place with eight fasteners; sealing is provided by a metallic O-ring.

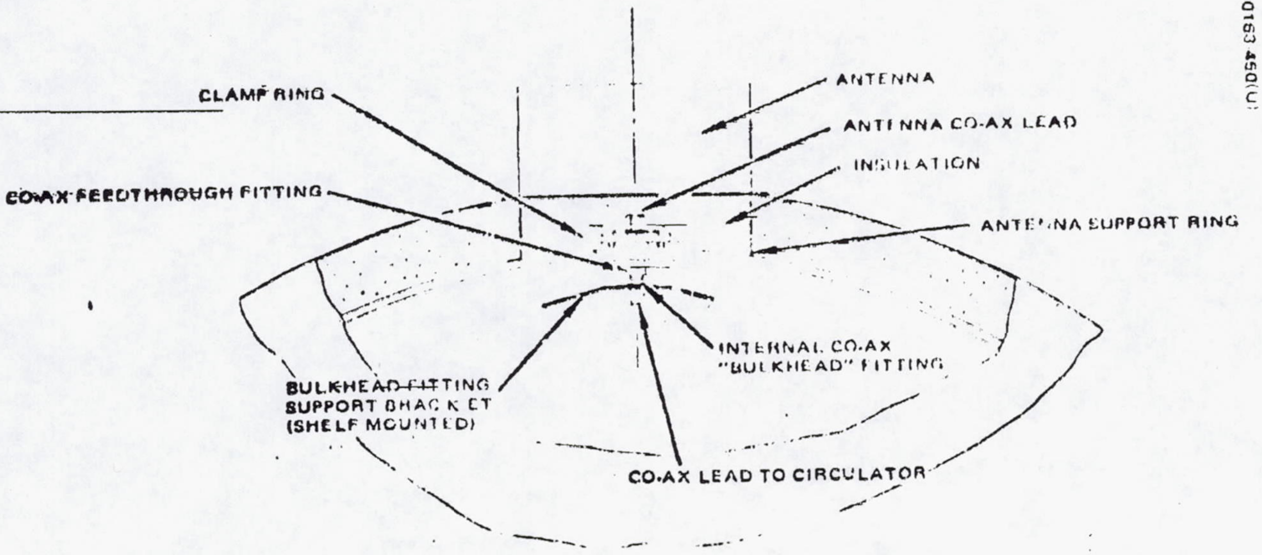

a) AXIAL RF FEEDTHROUGH CONFIGURATION

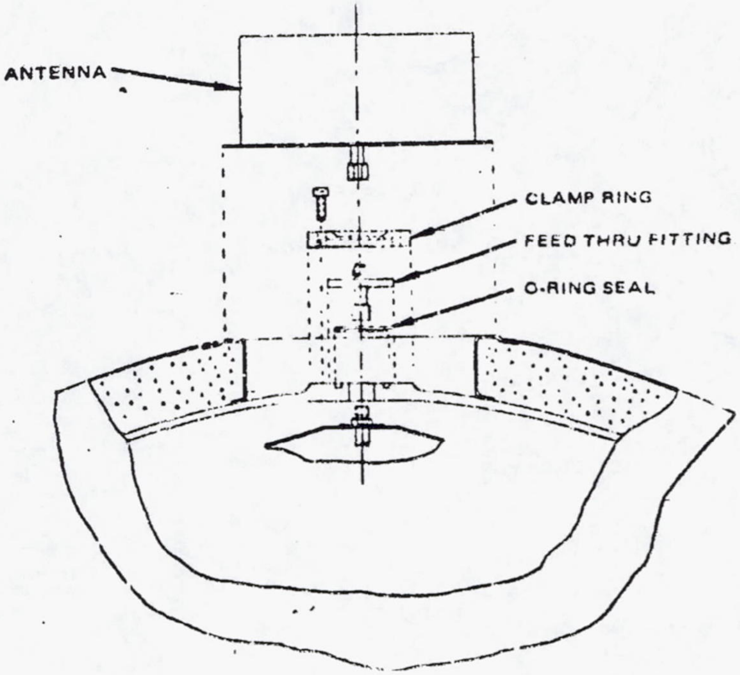

b) EXPLODED VIEW

FIGURE 4.5-29. AXIAL RF FEEDTHROUGH CONFIGURATION

30163 450(U)

REPRODUCIBILITY OF THE ORIGINAL PAGE IS POOR.

FOLDOUT FRAME

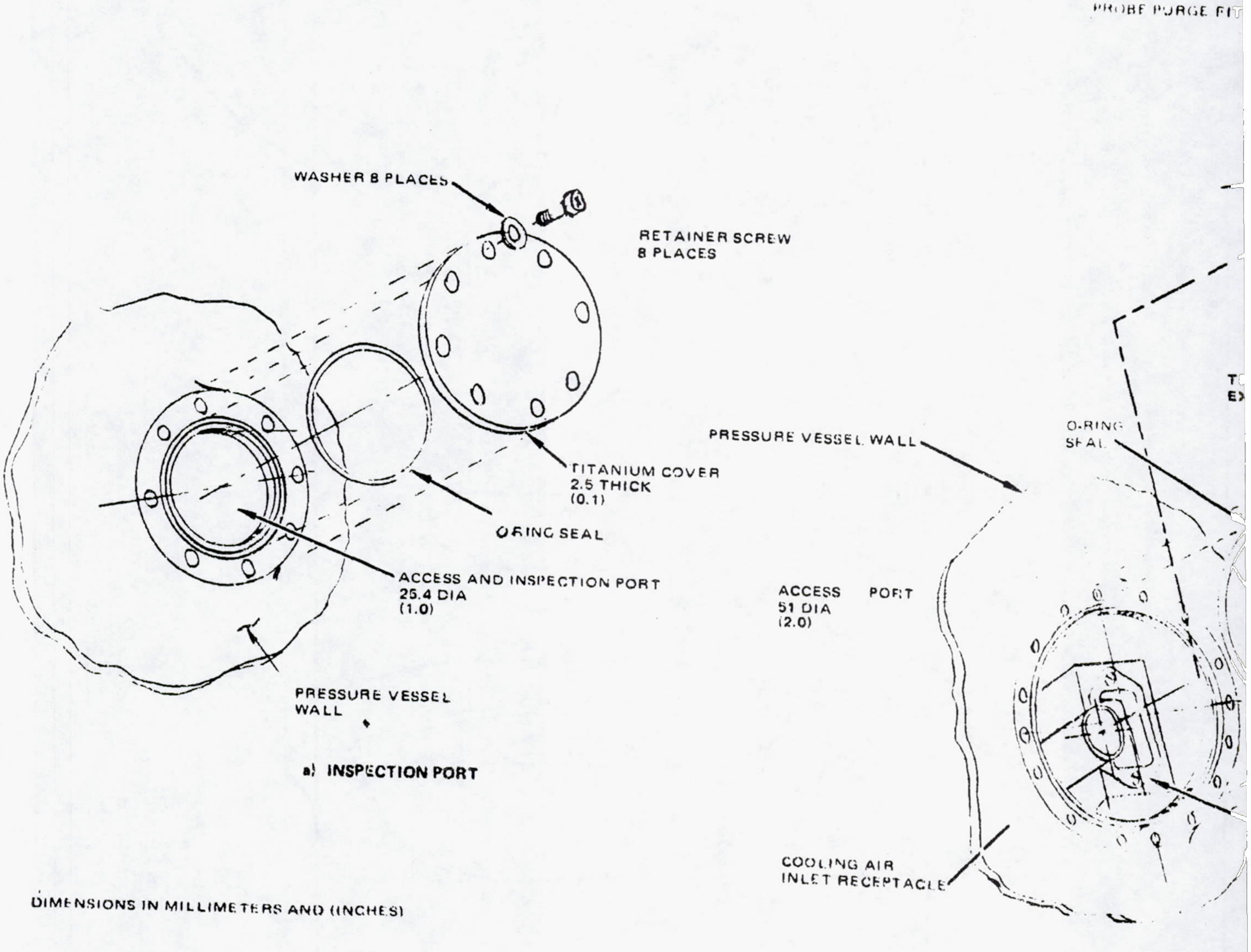

a) INSPECTION PORT

DIMENSIONS IN MILLIMETERS AND (INCHES)

FIGURE 4.5-30. ACCESS AND INSPECTION PORT CONFIGURATION

FOLDOUT FRAME

2

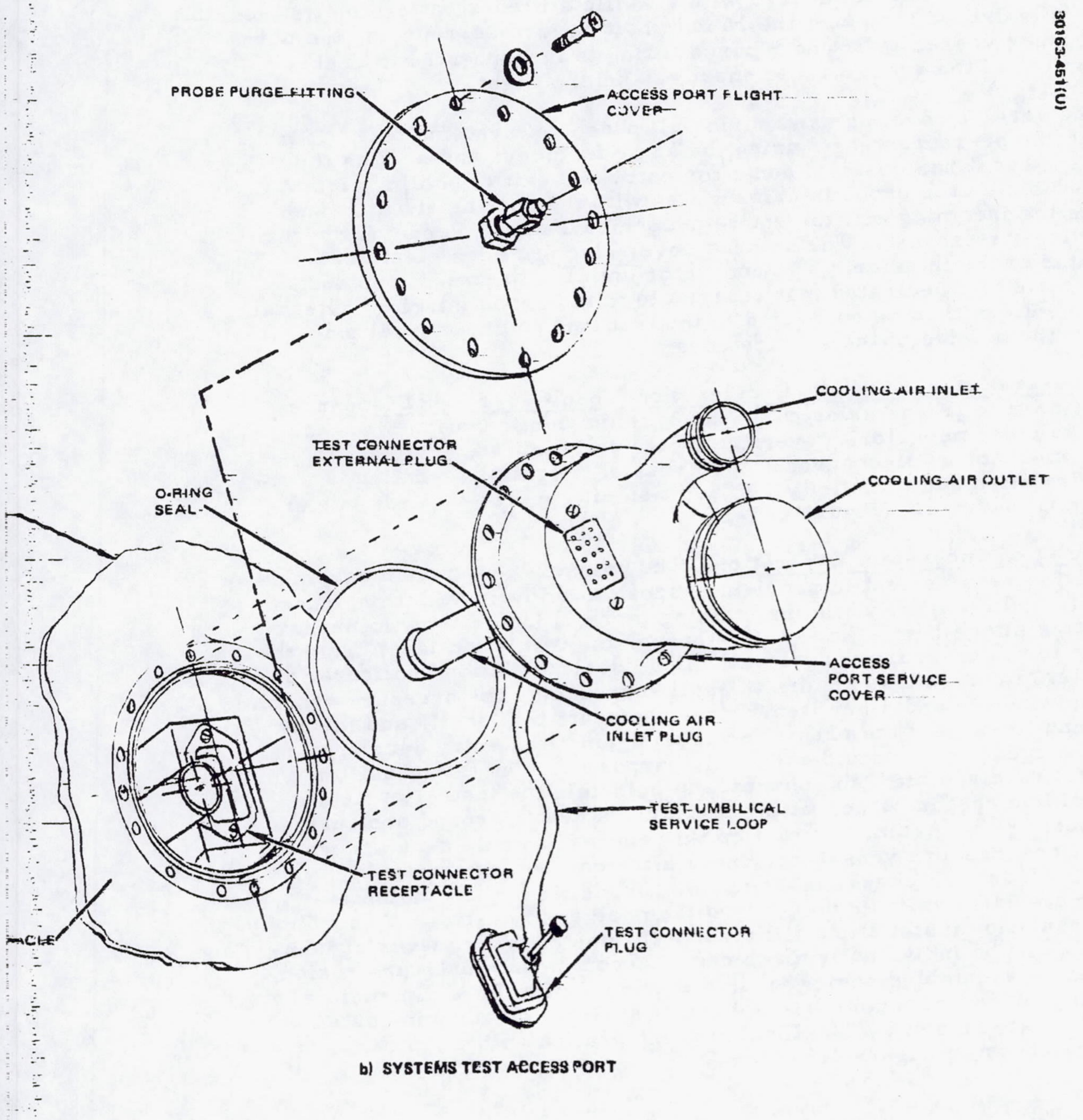

b) SYSTEMS TEST ACCESS PORT

Access Port (Figure 4-5-30b). Except for its larger size, the access port is identical in configuration to the inspection port. In order to accommodate system test requirements, however, two separate covers are used. Sealing for both covers is provided by a metallic O-ring.

The flight cover is used during the acutal mission. It is fabricated of 17-4 PH stainless and reinforced with a waffle-stiffener pattern on its inner surface. It is drilled to accept the 16 hole bolt pattern surrounding the port in the pressure vessel wall, and a purge fitting is incorporated to enable pressurization of the probe with an inert gas before flight.

The service cover is used during all phases of systems test. It is fastened to the pressure vessel using the same fasteners and seal as the flight cover, but it has co-axial ducts for entry and exit of cooling air. A system of ducts on the probe interior mates with the cooling air inlet and distributes the incoming air; the entire probe serves as a plenum for return of the cooling air exhaust. The service cover also provides electrical access to the probe interior. The connector umbilical service loop and connector mate to a dedicated test receptacle in the probe interior; external test equipment can then be connected to the test connector external plug mounted on the outside of the service cover.

Pressure Vessel Module/Deceleration Module In-Flight Disconnect. The guillotine type IFD is selected as the baseline configuration since the cutter shows clear superiority over the electrically initiated plug and receptacle mechanical disconnect in the areas of weight, integration, electrical isolation and simplicity. In addition, it appears far less vulnerable to high-G loadings. (Figure 4.5-31)

Insulation Subsystem Integration. The primary penetration assembly and integration requirement is providing access to allow installation, checkout and test, and repairs, while maintaining thermal integrity by minimizing or eliminating altogether leakage paths through the insulation layer from the atmosphere to the pressure vessel wall. The ideal insulation configuration would consist of a seamless spherical shell surrounding the pressure vessel. In practice, windows and other items must penetrate this shell, and means must be found to support the pressure vessel against the entry deceleration loads. The support ring provided for this purpose divides the insulation layer into forward and aft hemispheres. In principle the insulation hemispheres could be cast in place, fitting themselves neatly around protrusions and the support ring. Again, in practice this approach would deny access to the penetration-pressure vessel interfaces after casting, preventing operations such as leak checks or removal. In addition, the candidate insulation materials available do not lend themselves to casting. Accordingly, the actual insulation installation will involve the use of many pieces of insulation which will be individually machined to accommodate each protrusion, and will then be assembled somewhat in the manner of a three dimensional jigsaw puzzle to provide a complete spherical shell which accommodates all protrusions (Figure 4.5-32). Insulation integration with a typical protrusion is shown in Figure 4.5-33.

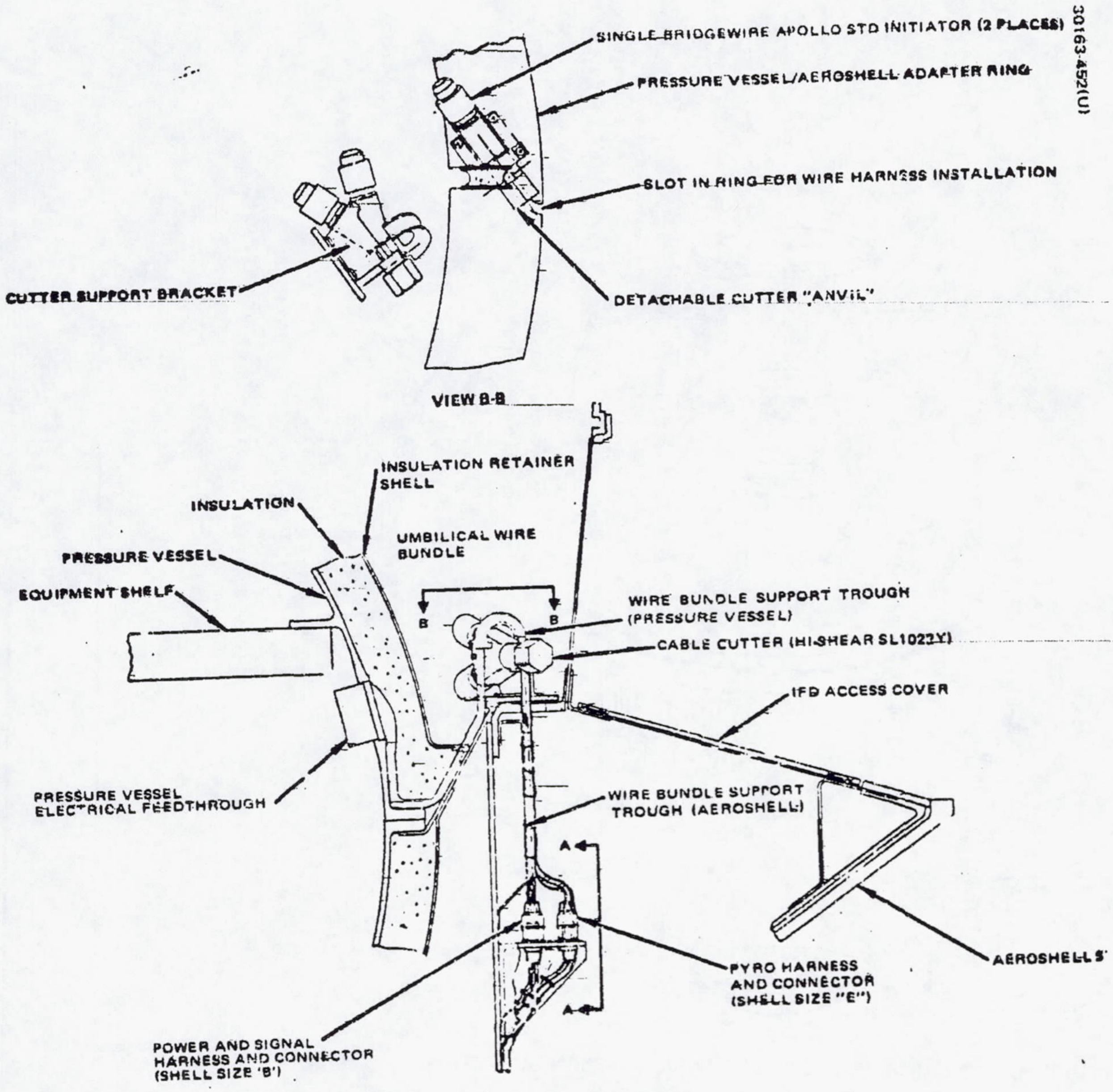

FIGURE 4.5-31. CABLE CUTTER IN-FLIGHT DISCONNECT

REPRODUCIBILITY OF THE ORIGINAL PAGE IS POOR.

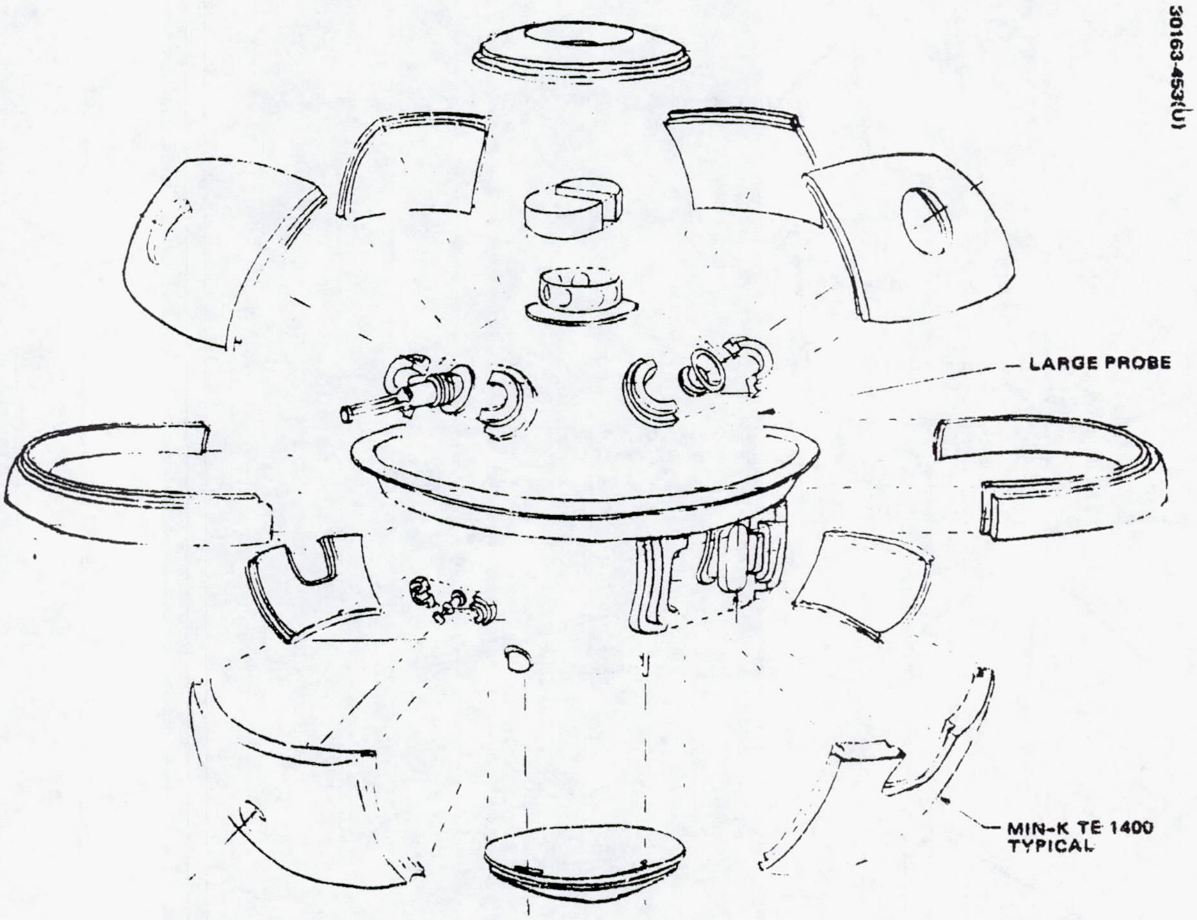

FIGURE 4.5-32. LARGE PROBE THERMAL INSULATION SUBSYSTEM

REPRODUCIBILITY OF THE ORIGINAL PAGE IS POOR.

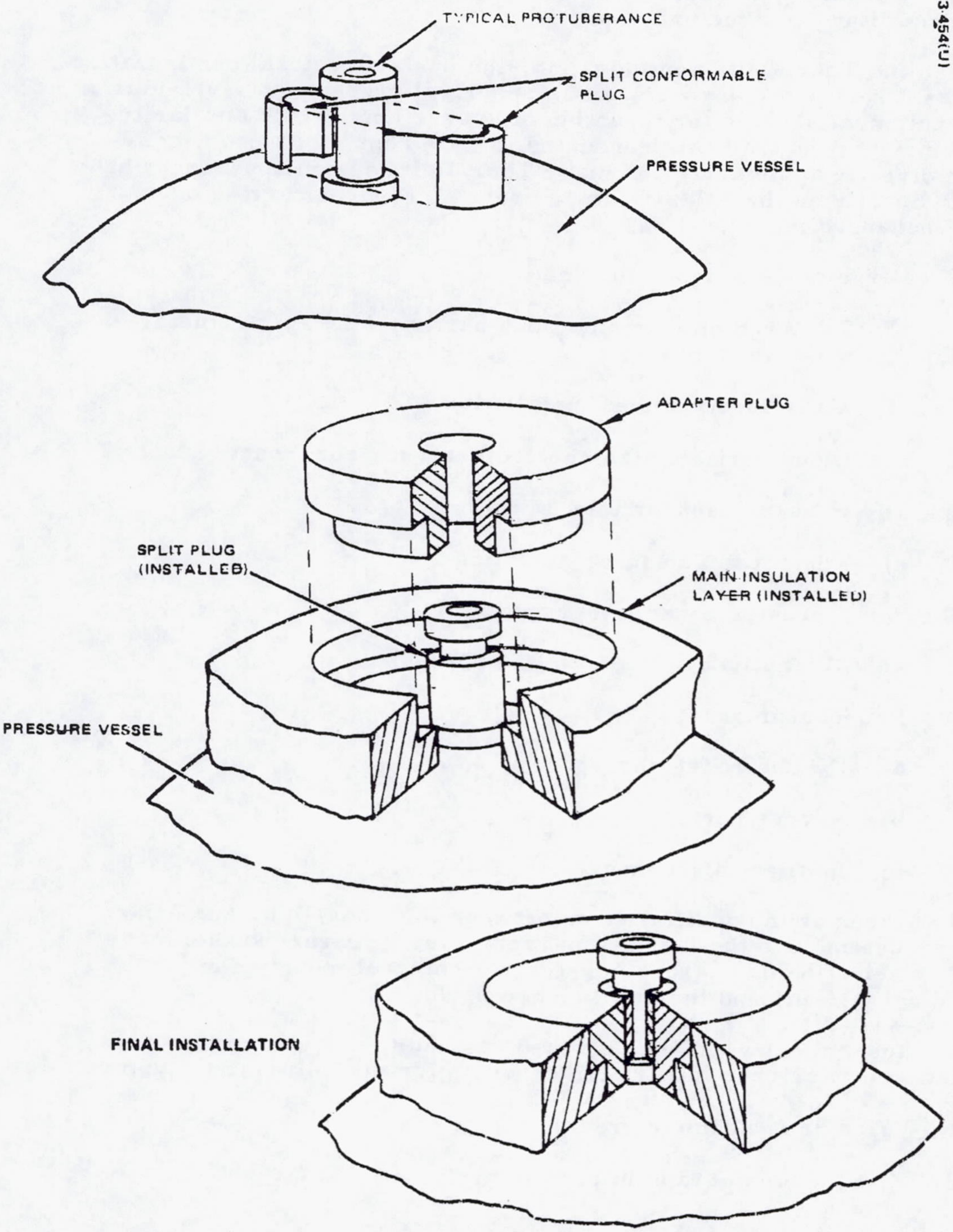

FIGURE 4.5-33. INTEGRATION OF INSULATION WITH PROTUBERANCES

Atlas/Centaur Baseline Configuration Description

This section describes the baseline design approaches used in integration of science and housekeeping subsystems with the Atlas/Centaur large and small probe structures.

Like the Thor/Delta configuration, the basic structural configuration of the Atlas/Centaur probe consists of a spherical pressure vessel and two internal equipment shelves for mounting of subsystems. This similarity has made many of the tradeoffs conducted for the Thor/Delta probe configuration directly applicable, and many Thor/Delta design approaches have been used directly on the Atlas/Centaur probes. Designs carried over virtually unchanged include:

1) Large probe science integration:
    a) Solar radiometer and cloud particle size spectrometer windows
    b) Mass spectrometer installation
    c) Cloud particle size spectrometer mirror mount
    d) Pressure sensor inlet system
    e) Temperature sensor mounting
2) Small probe science integration:
    a) All identical to Thor/Delta approach
3) Housekeeping:
    a) DC and rf feedthroughs
    b) Access ports
    c) In-flight disconnect

The three primary differences between the Thor/Delta and Atlas/Centaur probes include the larger, maraging steel pressure vessel made possible by selection of a larger booster; the internal mounting of the insulation subsystem, and the new science payload.

Of these, the new science payload has had the largest impact, necessitating new science integration concepts for the following instruments:

1) Wind drift/altimeter radar
2) Gas chromatograph inlet system

REPRODUCIBILITY OF THE ORIGINAL PAGE IS POOR.

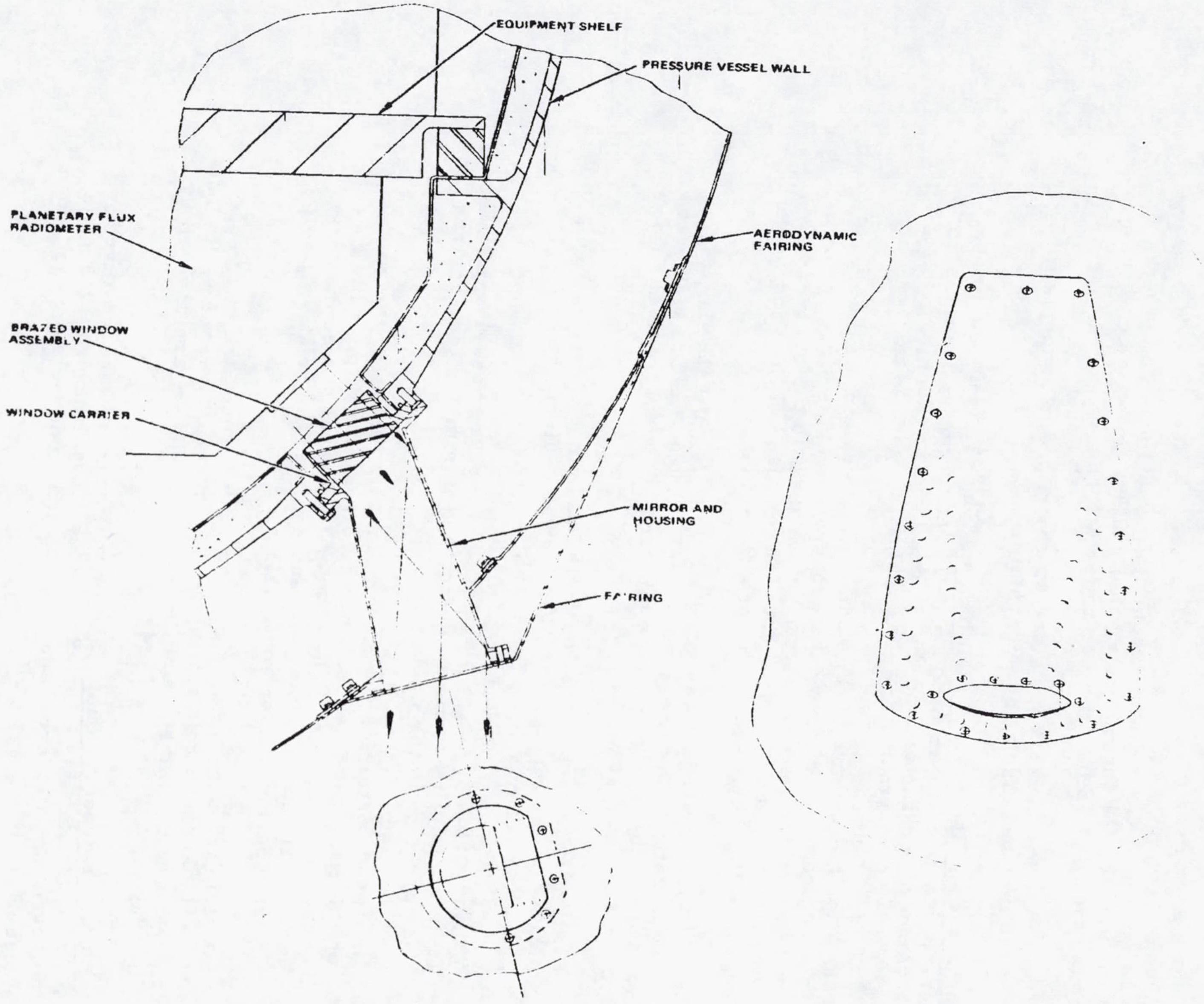

FIGURE 4.5-34. PLANETARY FLUX RADIOMETER WINDOW

3) Hygrometer mount

In addition to new instruments requiring accommodation, a new approach was developed for the planetary flux radiometer window to enable it to look around the wind drift/altimeter radar antenna.

New design in the housekeeping are as restricted to concepts for installation of the internal insulation subsystem.

Planetary Flux Radiometer Installation. The primary new impact on the planetary flux radiometer of the Atlas/Centaur probe configuration is the requirement of looking around the wind/altimeter radome. Optical, structural and seal requirements are identical with Thor/Delta.

In relocating the window of the radiometer to retain the downward vertical 5 deg. conical field of view, the concept of looking directly downward through a horizontal window oriented at an angle to the pressure vessel wall was dropped, as the angle between the plane of the window and the plane tangent to the wall becomes impractically large.

Accordingly, the window was designed with its optical axis passing through the center point of the pressure vessel, and the field of view was directed downward using a front surface mirror. This approach has three advantages over a horizontal window:

1) Flexibility of location. The entire radiometer may now be located on the top surface of the lower equipment shelf, providing ready access for service.

2) Window oriented in the plane of the pressure vessel wall. This feature simplifies window design and minimizes the required aperture size in the wall.

3) Improved contamination protection. By recessing the window, only the mirror is exposed to the direct flux of possible airborne contaminants. The mirror in general can be made far more resistant to pitting and erosion than the relatively soft IR transparent window material.

To maintain the aerodynamic contour of the probe, the mirror is buried between the aerodynamic fairing and the pressure vessel wall. The protruding portion of the mirror and its support structure are covered by a streamlined fairing (Figure 4.5-34).

Hygrometer Sensor Mount. The primary requirement involved in hygrometer sensor mounting is providing free stream flow to the sensor tube while preventing interference between sensor tube and aeroshell upon pressure vessel/aeroshell separation.

To minimize interference problems the sensor is recessed within the outer surface of the aerodynamic fairing. A scoop in the fairing surface

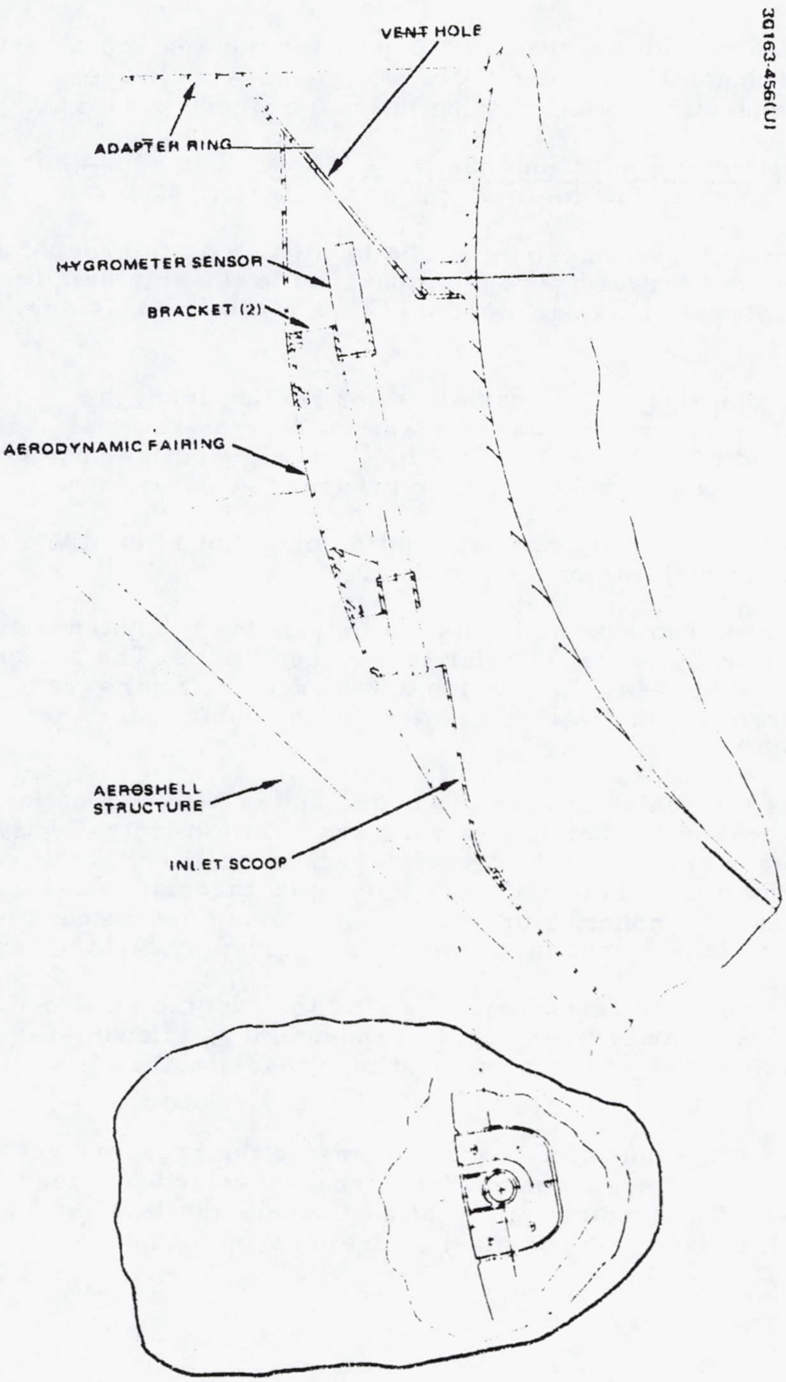

FIGURE 4.5-35. HYGROMETER SENSOR INSTALLATION

directs free stream air to the sensor inlet while bleeding off the low energy boundary layer.

The fairing also provides structural support for the sensor, allowing easy access for servicing. The fairing power and signal wire harness provides electrical connection with the probe interior (Figure 4.5-35).

Wind Drift/Altimeter Radar Antenna Installation. The wind drift altimeter radar requirements fall into three general classifications:

1) Field of view. The antenna must be located so as to provide an unobstructed downward view from parallel to the spin axis to a 10 deg. off axis plus half the 8 deg. beam width, or 14 deg. total.

2) Transmission line. The coaxial cables leading from the antenna to the internal radar package must be as short as possible and of equal length. Hermetic seals must be provided where the coaxial cables enter the pressure vessel.

3) Aerodynamic. The antenna installation must not affect the aerodynamic stability of the probe.

Field of view requirements are satisfied by locating the antenna at the forward end of the probe, perpendicular to the centerline. The antenna is supported by a ring shaped bracket, which also serves as a forward attach point for the aerodynamic fairing and a mounting surface for the radome (Figure 4.5-36).

The radome is fabricated of ceramic foam, and is held to a uniform half wavelength thickness in the antenna viewing arc to minimize reflective losses. Its edge flanges are clamped between layers of resilient "feltmetal" metal packing to allow for differential coefficients of thermal expansion between the antenna and its mounting bracket. The packing and antenna are both held in place by a circumferential clamp ring retained by eight screws.

In combination with the aerodynamic fairing the radome acts to minimize the impact of the antenna on probe aerodynamics, allowing the use of a wind tunnel proven aerodynamic configuration whose stability is well established.

Coaxial cables from the antenna are led outside the pressure vessel to hermetically sealed right angle coaxial feedthroughs welded into the pressure vessel shell. The feedthrough location is above the level of the lower equipment shelf to facilitate the making and breaking of internal connections.

REPRODUCIBILITY OF THE ORIGINAL PAGE IS POOR.

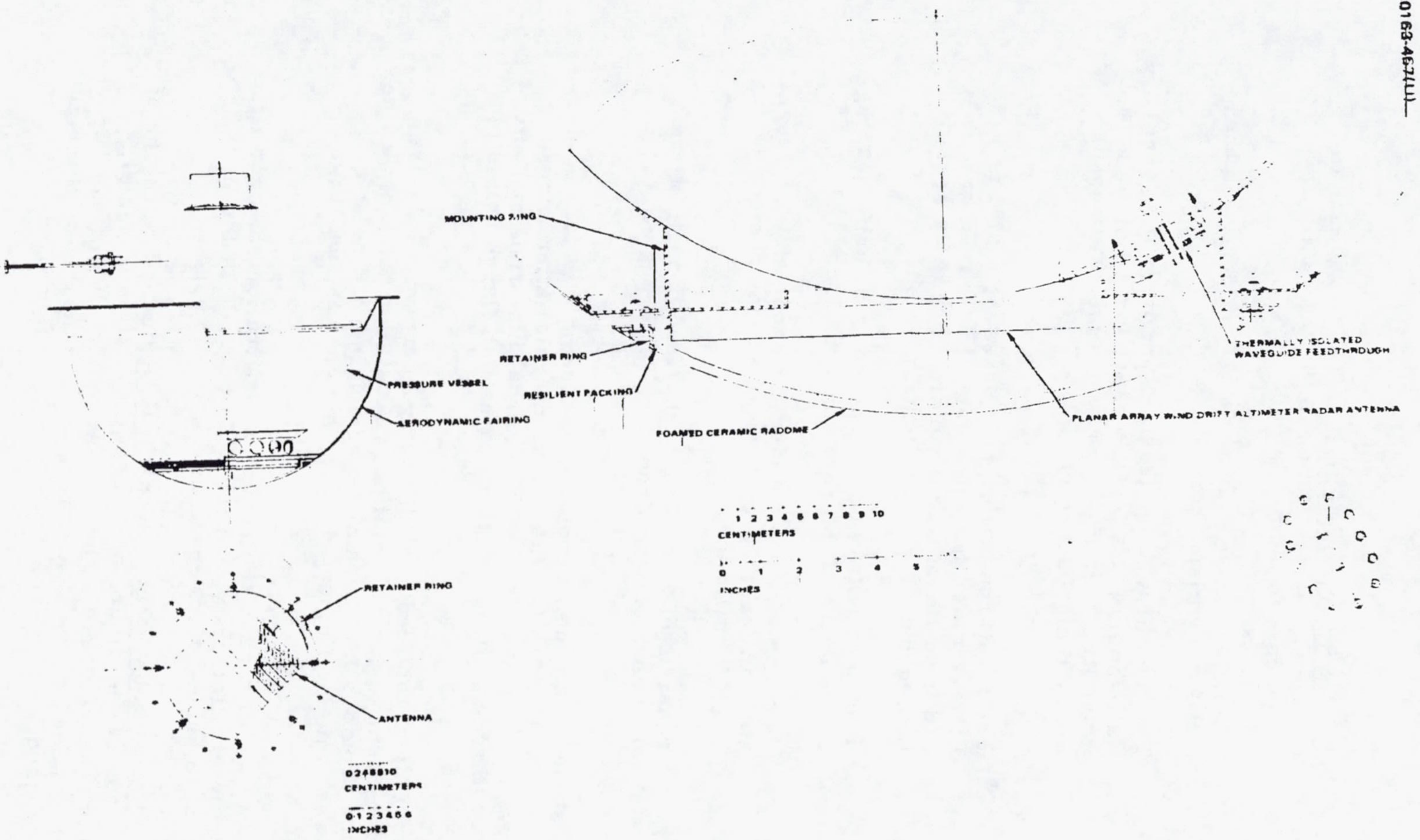

FIGURE 4.5-36. WIND DRIFT/ALTIMETER RADAR ANTENNA INSTALLATION

Gas Chromatograph Inlet System Installation. The gas chromatograph inlet system provides atmospheric samples to the internally mounted instrument; additional requirements to be met include:

1) Location. The inlet system orifice must be located in the forward hemisphere of the probe.

2) Structural. The feedthrough aperture in the pressure vessel wall should not affect pressure vessel structural integrity. The lines carrying ambient pressure inside the pressure vessel will be sized to a safety factor of four.

3) Seals. The feedthrough, internal pressure lines, and the fittings which join the intake line to feedthrough and instrument will maintain a hermetic seal throughout all phases of the mission.

4) Blockage. The lines will be large enough to be self-clearing in the event of internal condensation.

5) Installation. Access must be provided for connection of internal lines to feedthrough fittings and instrument during shelf installation.

The inlet system consists of an external tube/feedthrough fitting assembly, and an internal line which runs from the feedthrough to the instrument inlet fitting (Figure 4.5-37).

The O-ring sealed removable feedthrough assembly is located above the level of the equipment shelf to facilitate system installation access. The thin wall bellows isolated stainless steel external tube runs radially outward from the feedthrough fitting and terminates in a flange bolted to the aerodynamic fairing.

The internal side of the feedthrough fitting incorporates a flare fitting for connection to the heavy wall stainless steel internal sample line. A bellows in the line provides for thermal expansion induced relative displacements between the shelf mounted instrument and the wall fixed feedthrough.

The relatively small size of the required penetration does not affect pressure vessel structural integrity, but the 0.25 in. I.D. of the lines is considered sufficient to prevent condensation caused blockage.

Internal Insulation Subsystem: Mechanical Design. The choice of a lightweight, nonload bearing fiberglass batting insulation material, mounted inside the pressure vessel, requires a completely different approach to mechanical retention of the insulation layer when compared to the rigid Min-K TE 1400 proposed for the Thor/Delta probe configuration.

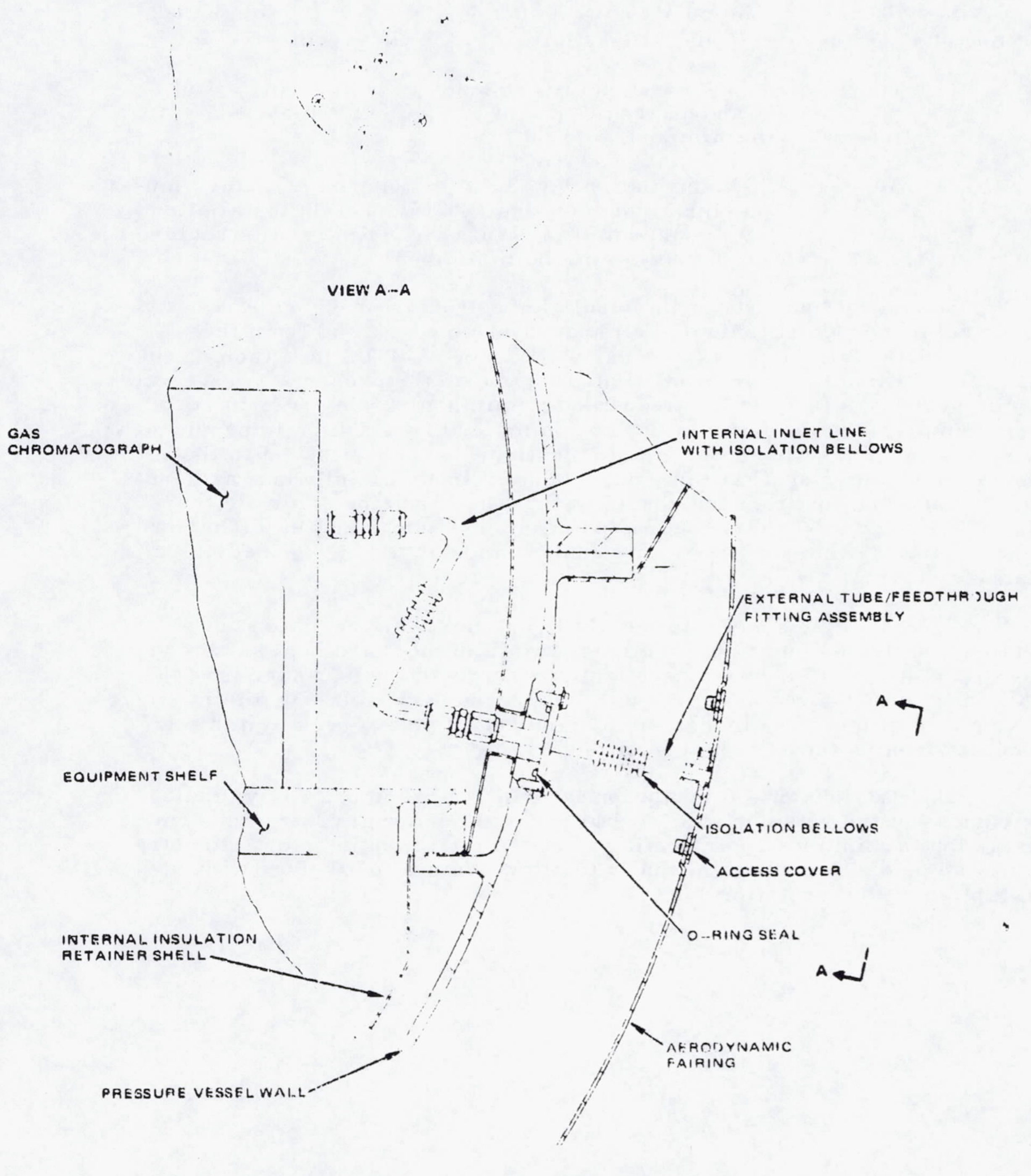

FIGURE 4.5-37. GAS CHROMATOGRAPH INLET SYSTEM INSTALLATION

REPRODUCIBILITY OF THE ORIGINAL PAGE IS POOR.

In addition to providing structural support for the insulation batts, the insulation support system must satisfy the following requirements:

1) Thermal. Conductive paths through the batting which tend to 'short circuit' the insulation layer must be minimized.

2) Access. The insulation layer and its support structure must be installed such that their impact on installation and removal of pressure vessel internal structure and subsystems is minimized.

Structural support for the insulation batting is provided by a spherical monocoque titanium shell spaced 11 mm (0.5 in.) from the interior surface of the pressure vessel (Figure 4.5-38). By attaching the insulation batting to the internal shell rather than the pressure vessel wall itself, heat leaks through the tiedowns are eliminated. In order to keep from compressing the felt-like insulation material, retention is provided by spikes fabricated from polimidide plastic; these are attached to the insulation retainer shell at their bases and protrude radially outward, not quite contacting the pressure vessel wall. These retainers impale the insulation layer at several hundred points in both upper and lower hemispheres, preventing shifting of the insulation under the high g loadings of planetary entry.

To maximize access to the probe interior, the insulation and retainer is divided into three sections, two in the forward hemisphere and one in the aft. All three sections fasten directly to the pressure vessel wall, and are removed as a unit with the pressure vessel. By minimizing the number of mounting faces, this configuration also serves to minimize conductive paths through the insulation.

Penetrations of the insulation layer are accommodated by tubular extensions of the retainer shell and by jacketing internal protrusions with insulation to minimize their heating effect on the probe interior. Penetrations can be disconnected internally to allow removal of shelves without disruption of the insulation layer.

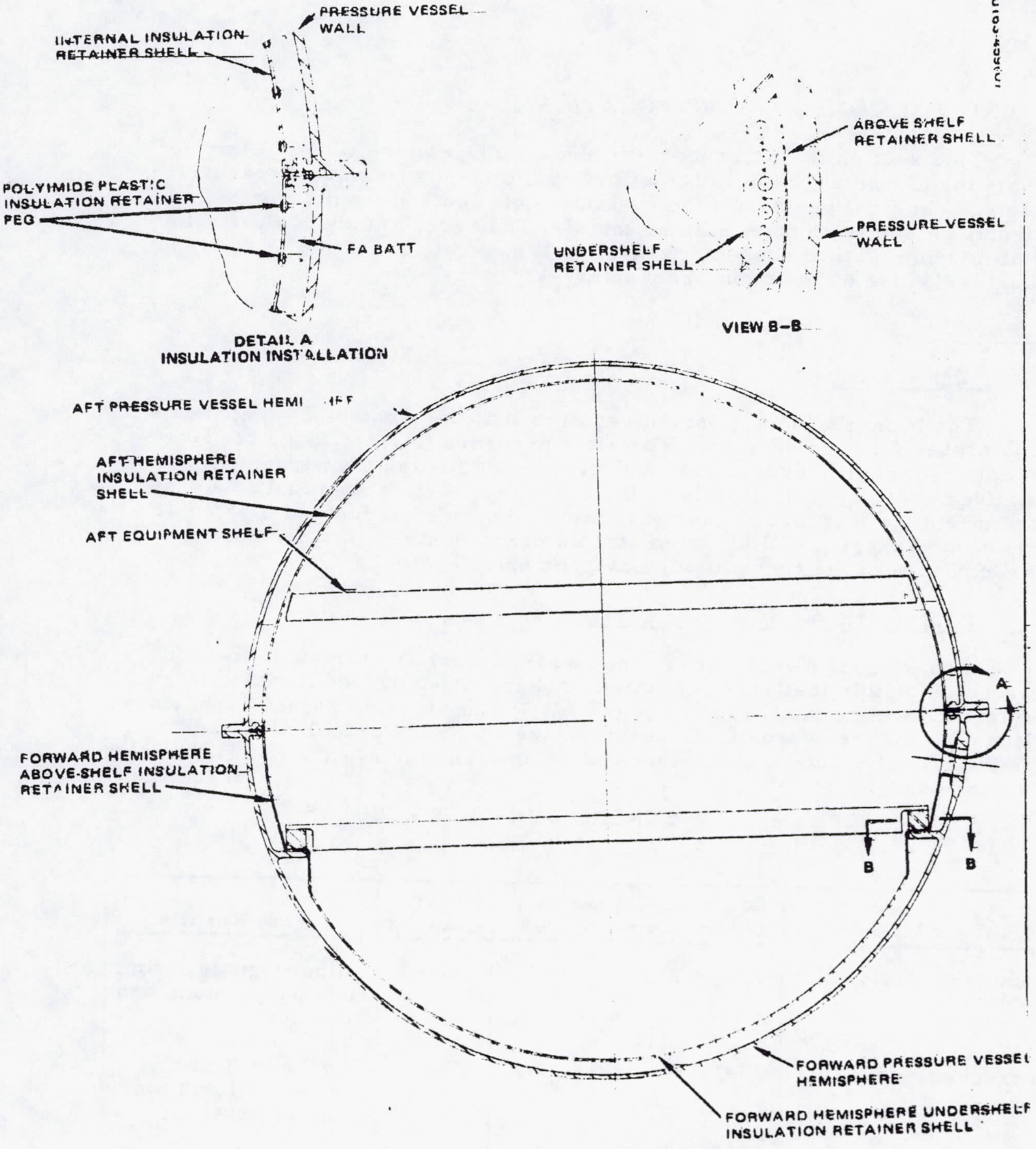

DETAIL A
INSULATION INSTALLATION

VIEW B–B

GENERAL ARRANGEMENT: INTERNAL INSULATION RETAINER SHELLS

FIGURE 4.5-38. INTERNAL INSULATION SUBSYSTEM INSTALLATION

REPRODUCIBILITY OF THE ORIGINAL PAGE IS POOR.

4.6 UNIT PACKAGING AND INTEGRATION

This section is concerned with three studies which were initiated to support the design and integration effort on the large and small pressure vessels. The first deals with the evaluation of electronic units in a high g environment and foam-packaging material. The second study evaluates the use of microminiature connectors and small gage wire, and the third study evaluates the use of conformal packaging.

Summary

High G Study

The Pioneer Venus mission requires that the electronic components in the probes function during and/or after exposure to entry loads of 650 g. Typical flight quality components were subjected to high g environment in a centrifuge. The overall results of the centrifuge tests shown in Table 4.6-1 substantiate the fact that Hughes Aircraft Company's methods of electronic component packaging will allow electronic components to function during and after exposure to the probe high g environments.

Connectors and Small Gage Wire

The Pioneer Venus harness subsystem consists of the unit-to-unit intercabling within the large and small probes. A study was initiated to evaluate the use of small gage wire (28 AWG) and microminiature connectors in lieu of the more conventional heavier gage wires (24 and 22 AWG) and subminiature connectors for weight and volumetric savings for the Thor/Delta mission.

TABLE 4.6-1. CENTRIFUGE TEST RESULTS

Test Unit	Component Assembly Technique Employed	Test Level, g	Test Results
Countdown chain	MICAM	804	Output signals strong and sharp during and after tests
Preregulator	Cordwood	508	Checked out during five of six tests and after all tests
Cross strap converter	Point-to-point	512	No frequency change or conversion loss after test
Quartz Oscillator (Hewlett-Packard off-the-shelf item)	Printed circuit	697	Frequency change after test. Fastener sheared off during test

The conclusion was that the decrement in this ratio for smaller gages is not significant, so that the weight/volume advantage remains the determining factor in wire gage selection. Results of the study indicate weight savings of 32 to 50 percent. This apparent advantage will be reduced somewhat when actual wire mixes (shielding and power lead requirements added) are established.

Because of this weight advantage, the small gage (28 AWG) wire is the choice for the probes on the Thor/Delta configuration. There will be, however, some increase in both design and manufacturing costs, resulting from the development of new processes, procurement of new tools, and greater difficulty in handling and terminating, particularly where shielded wires are involved. The major cost increment is in the area of manufacturing labor costs, estimated to increase by 20 to 30 percent.

Since the Atlas/Centaur application is addressed to cost savings, even at some weight expense, the conclusion here is that conventional gage wire (24 AWG) should be retained.

Conformal Packaging

In an effort to achieve the most efficient integration of the electronic components within the large and small pressure vessels, a study was made to evaluate the use of conformal packaging. Since Hughes did not have the details necessary to evaluate the scientific experiments packaging, the study was focused upon the conformal packaging of the power, digital and rf subsystems. The Thor/Delta configurations, where volume was most critical, were used as a basis for these studies. In this regard, the power subsystem group developed a semicircular element for small probe application at a total estimated cost increase over conventional packaging methods of less than $25,000.

The digital group (command and data handling) developed four conformal packaging schemes for use on the small probe. All of these schemes lend themselves to installation between the upper and lower shelves. The total cost increase over conventional packaging methods is estimated to be 20 percent.

For the large probe, the digital group developed a cylindrical segment (pie-shaped). This conformal package consisted of multilayer printed circuit cards, and would cost approximately 170 to 200 percent more than the conventionally packaged MICAM design approach.

The rf group has employed modular construction for its packaging scheme, and the need for conformal packaging of the rf units was reduced, and was not evaluated further in this study.

The conformal packaged units developed for the Thor/Delta configured pressure vessels are applicable to the Atlas/Centaur configured pressure vessels. However, for application to the various conformal shapes would be increased in volume.

Requirements

The unit and component packaging and integration requirements for the probes are derived from the mission requirements. These call for the probes to operate under very high entry acceleration, and meet the criteria of minimum size, weight and cost.

The following criteria for packaging and integration are thus established:

1) All units and components must operate with specified performance while subjected to an axial acceleration of 650 g

2) High packaging density is required to minimize the diameter of the probe pressure shells

3) Minimum weight

4) Minimum cost

Criterion 1 is a definite requirement which must be met in order to insure mission success. Criteria 2, 3, and 4 are all important criteria, but the emphasis on weight is more important for the Thor/Delta version, while cost is emphasized for the Atlas/Centaur probes.

Studies and Tests

High G Study

A MICAM assembly packaged in a flight quality chassis and encapsulated in foam was subjected to acceleration loads between 300 and 804 g. To assure practical application for space missions, the MICAM circuit was made similar to the timing countdown chain presently employed on the Orbiting Solar Observatory-I (OSO). A preregulator used on a Hughes classified space program and representative of typical electrical units employing cordwood component fabrication techniques was also centrifuge tested to a substained load of 508 g. This unit was also foam encapsulated, The third unit tested, a cross strap converter, was previously used on the Applications Technology Satellite experiments and employed the point-to-point component fabrication technique. The fourth unit was a Hewlett-Packard off-the-shelf quartz oscillator. This unit typified the use of printed circuit board applications. It is noted that all of these units incorporated foam encapsulation of the components.

Figure 4.6-1 illustrates the centrifuge test facility used for the subjecte tests. The units were mounted to the centrifuge arm in several positions. The MICAM and oscillator were tested together (see Figure 4.6-2) as were the preregulator and converter (see Figure 4.6-3).

The centrifuge test results and the subsequent foam compression test indicate that foam densities as low as two pounds per cubic foot are sufficient as a packaging agent to protect components against the rigors of high g

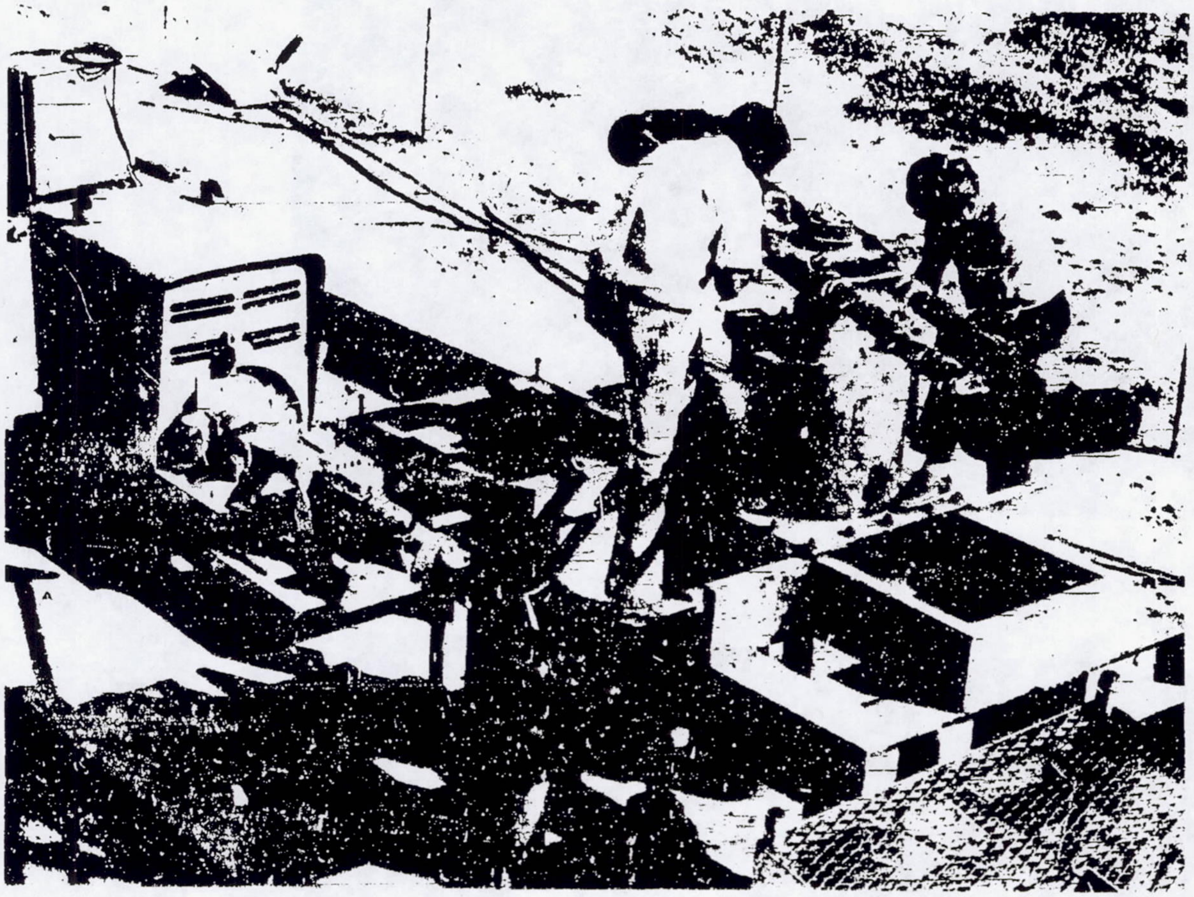

FIGURE 4.6.1 APPROVED ENGINEERING TEST LABORATORY 5 F. CENTRIFUGE (PHOTO 4R24803)

REPRODUCIBILITY OF THE ORIGINAL PAGE IS POOR.

FIGURE 4.6-2. HORIZONTALLY MOUNTED MICAM ASSEMBLY AND OSCILLATOR (PHOTO)4R29170)

FIGURE 4.6-3. INSTALLATION OF PREREGULATOR UNIT (LEFT) AND CONVERTER (PHOTO 4R 24806)

REPRODUCIBILITY OF THE ORIGINAL PAGE IS POOR.

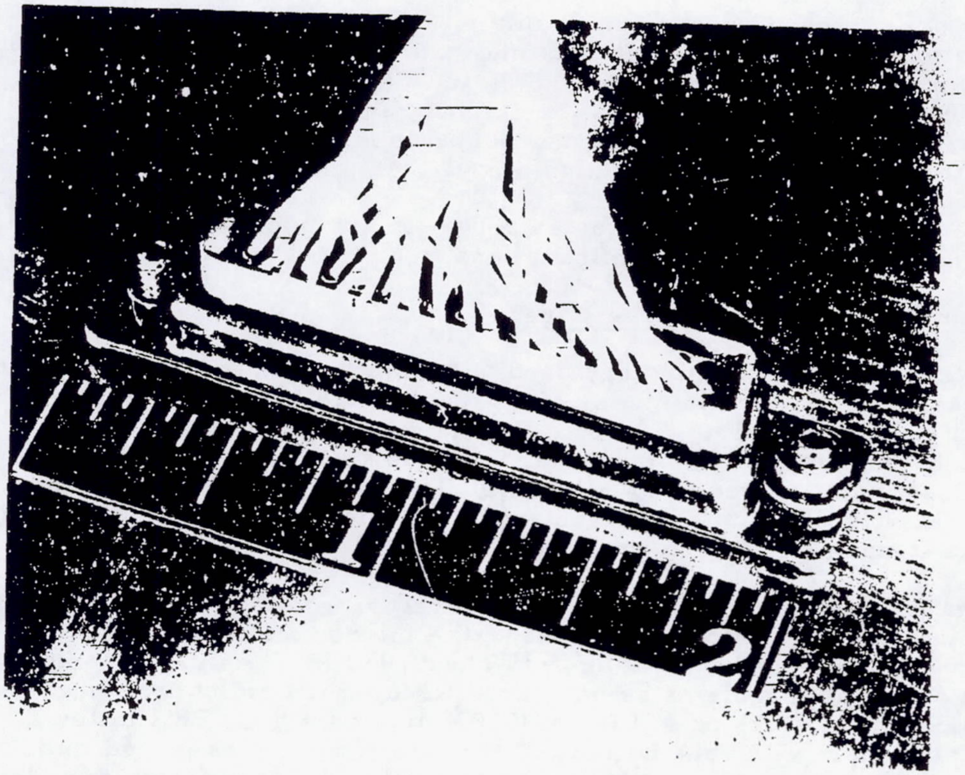

FIGURE 4.6-4. MATRIX DOUBLE-DENSITY-D CONNECTOR (PHOTO 30163-464)

REPRODUCIBILITY OF THE ORIGINAL PAGE IS POOR.

exposure. It is noted that three of ~~the four~~ test units (preregulator, converter and oscillator) components were encapsulated in 32 kg/m^3 (2 lb/ft^3) density foam. The fourth (MICAM circuit) was encapsulated in 128 kg/m^3 (8 lb/ft^3) density foam. Each unit to be employed on the Pioneer Venus mission will have to be evaluated on an individual basis, but based upon the result of these tests, it is anticipated that no new packaging techniques will have to be developed to meet the needs of the high g environment.

The conclusions of these studies and tests are applicable to both the Thor/Delta and Atlas/Centaur configurations.

Connectors and Small Gage Wire

In the connector terminology used herein, which is in agreement with vendor's data sheets, subminiature refers to connectors having number 20 contacts on 0.254 cm (0.100 in.) centers, and microminiature describes connectors having number 22 or smaller contacts spaced on centers substantially less than this, down to 0.13 cm (0.050 in.). Typical of the subminiature class is the Cannon DM rectangular; typical of the microminiature class is the Cannon MDM rectangular.

Conclusions from the company sponsored program to evaluate the use of microminiature connectors were these: the microminiature connector having wire form solder contacts on 0.13 cm (0.050 in.) centers presented significant assembly problems as compared to another candidate having insertable crimp contacts on 0.191 cm (0.075 in.) centers. This latter connector, the Matrix Double-Density-D (Figure 4.6-4), was judged to be an acceptable compromise between the subminiature and microminiature classes of connectors. As its name implies, it provides double the contact density in the same shell size as the corresponding standard subminiature, but can be readily wired using standard assembly and handling techniques. For these reasons, in addition to the fact that the Matrix design has been qualified and slated for use on the OSO program, this connector was selected as the standard for evaluation of wiring techniques in the Pioneer Venus probe.

The intent of the study was to demonstrate weight and volumetric savings possible by reduction in wire and connector size, but because of the high g environment to be encountered by the probes, it was also necessary to consider whether there was significant loss in reliability attributable solely to the use of smaller wire under inertial loads.

It appeared that, from a reliability standpoint, a larger wire gage might be preferable, since the breaking strength/weight ratio increases with gage. This is so, since, for any insulation type selected, insulation thickness remains constant over the whole range of conductor sizes. Using this ratio as a figure of merit, we have, for wire per MIL-W-81044 employing alloy conductor having a minimum breaking strength of 203 N/cm^2 (55,000 psi), the following:

REPRODUCIBILITY OF THE ORIGINAL PAGE IS POOR.

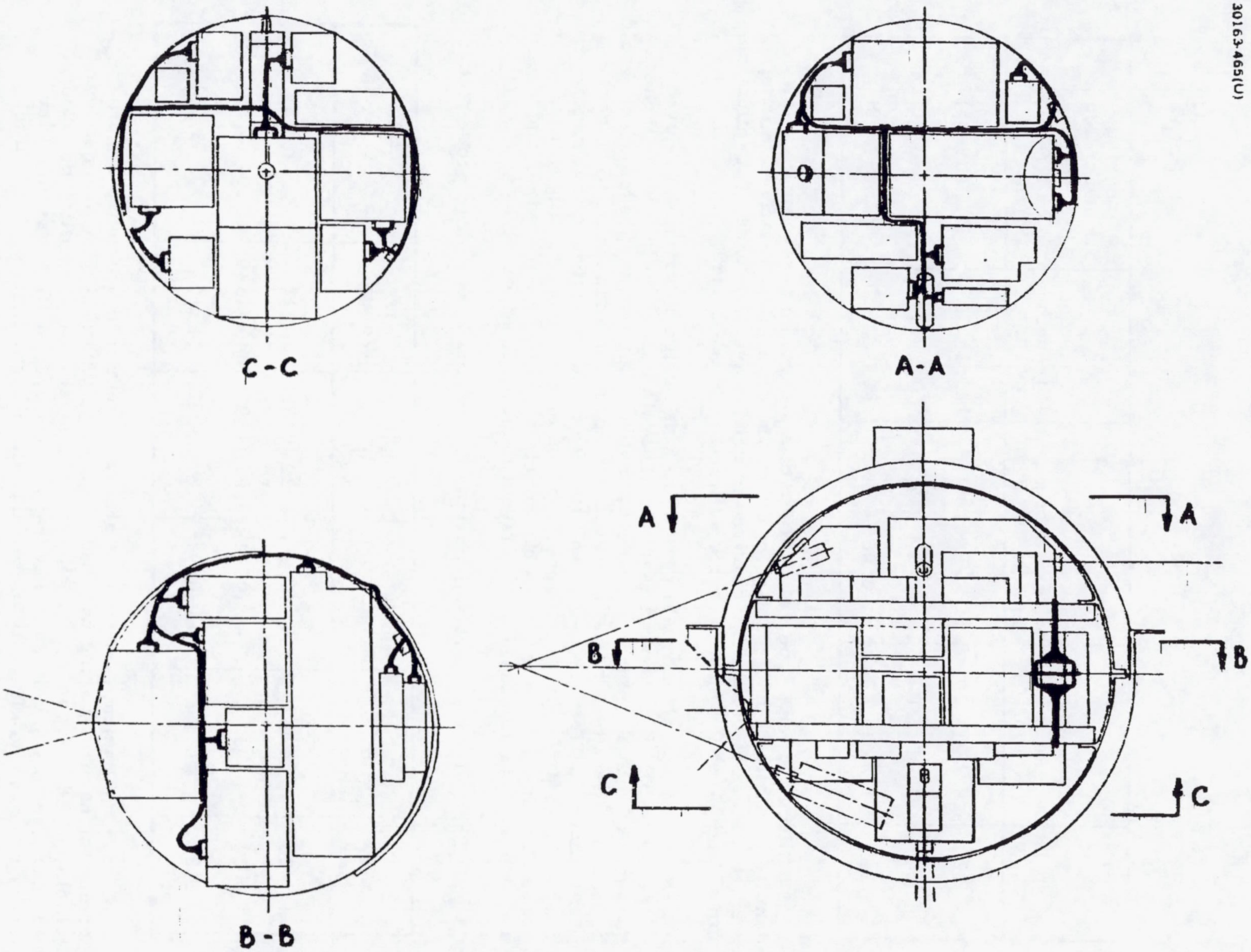

FIGURE 4.6-5. LARGE PROBE INTERCABLING DESIGN

Gage	Weight, kg/km (lb/1000 ft)	Cross Section, $cm^2 (in^2 \times 10^{-4})$	Breaking Strength N (lb)	Breaking Strength Weight Ratio N/kg/km (lb/lb/1000 ft)
22	4.46 (3.00)	32.5 (5.03)	123.1 (27.7)	27.6 (9.25)
24	2.98 (2.00)	20.5 (3.17)	77.3 (17.4)	25.9 (8.70)
28	1.37 (0.92)	8.08 (1.25)	30.7 (1.25)	22.4 (7.50)

Since the wire type selected for this study employs a thin wall low density insulation, the reduction in the figure of merit is relatively minor; i. e., the support provisions required to relieve inertial loads at terminations for 22 and 24 AWG would probably suffice for 28 AWG wire.

A conceptual intercabling scheme was designed for the large probe (Figure 4.6-5). This design assumes separate upper and lower hemisphere harnesses, with an interface connector between the two harnesses which would be mated at the time of final closure of the probe hemispheres. The schematic shown in Figure 4.6-6 is an estimate of the interconnections required for the large probe pressure vessel, based on the current configuration. Proposed routing paths are realizable for either 24 or 28 AWG wire, and weight and volume data are based on the layout depicted in Figure 4.6-5.

The following chart summarizes the results of the large probe study:

Wire Gage	Number of Connectors	Weight, Connectors kg (lb)	Weight, Wire kg (lb)	Wire Volume in^3	Total Harness Weight, kg (lb)
28	45	0.43 (0.94)	0.29 (0.65)	208 (12.7)	0.72 (1.59)
24	45	0.43 (0.94)	0.87 (1.91)	246 (15.0)	1.07 (2.35)
22	45	0.43 (0.94)	0.96 (2.12)	274 (16.7)	1.39 (3.06)

In the company-sponsored program mentioned previous, a multiconnector harness having wire runs averaging 0.9 m (3 ft) was constructed employing 28 AWG wire. To simulate the most severe handling conditions, the harness was subjected to several rework cycles. The assembly technicians reported no difficulty in working with the small gage wire, either during initial fabrication or rework at the crimp type connectors as proposed for Pioneer Venus, and no failure modes were encountered.

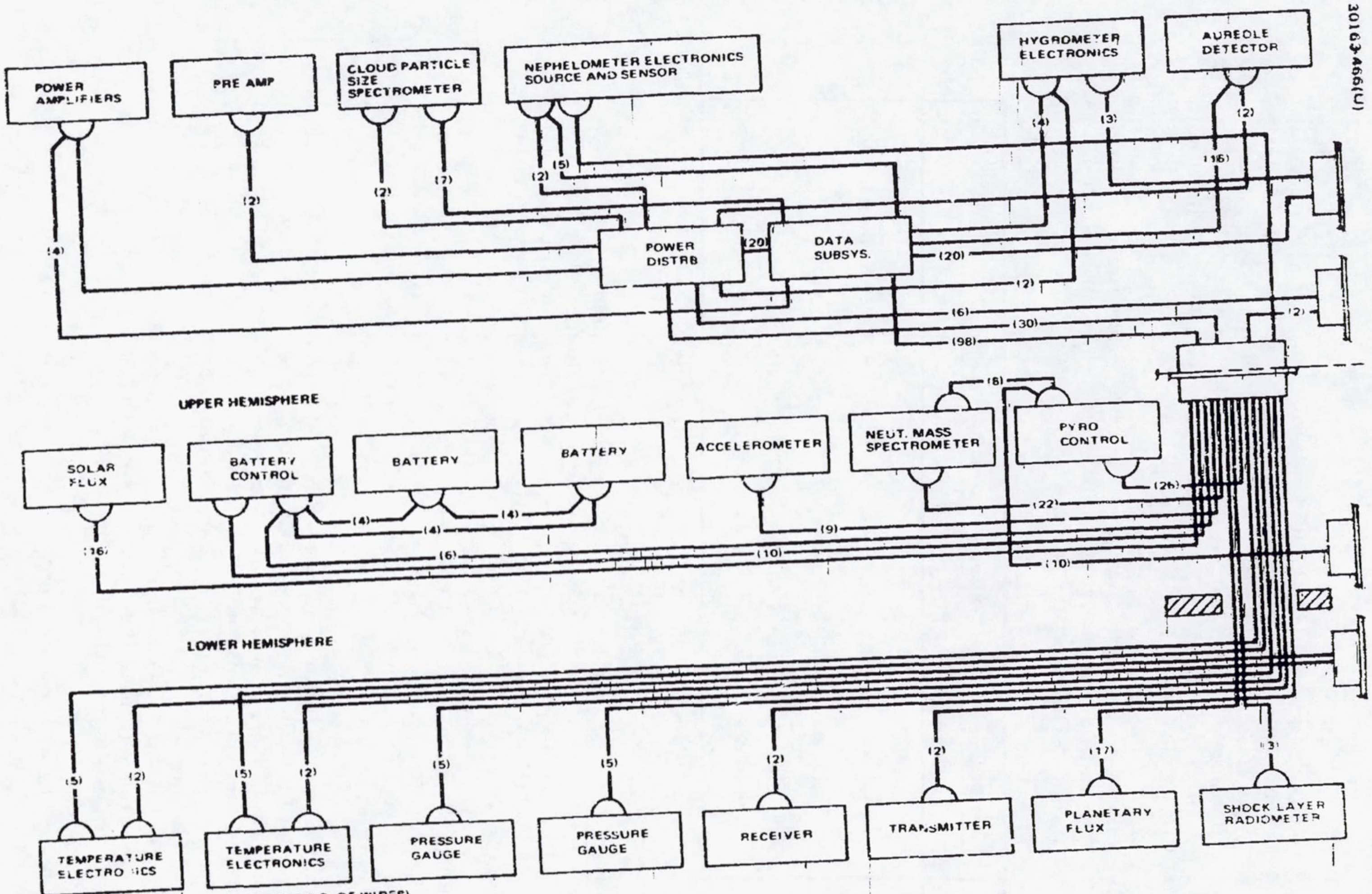

(FIGURES IN PARENTHESES DENOTE NO. OF WIRES)

FIGURE 4.6-6. LARGE PROBE PRESSURE VESSEL INTERCONNECTIONS

3016-466(U)

Since the 28 AWG wire provides a weight savings of nearly 0.68 kg (1.5 lb) in cabling the large probe, and since the greater strength of 22 AWG wire offers minimal improvement in resistance to acceleration loads, the choice of 28 gage has obvious merits. For those few leads where voltage drop considerations might negate 28 AWG, the connector can be provided with contacts as required to accept either 24 or 22 AWG wires.

The following chart summarizes harness weights, showing the comparison between 24 AWG and 28 AWG wire. Figures for the small probes were arrived at by using the scale factors derived from the large probe.

Wire Gage	Total Harness Weight, kg (lb)		
	Large Probe	Three Small Probes	Total
24 AWG	1.1 (2.4)	1.2 (2.7)	2.3 (5.1)
28 AWG	0.7 (1.6)	0.8 (1.8)	1.5 (3.4)
Weight Savings	0.4 (0.8)	0.4 (0.9)	0.8 (1.7)

Conformal Packaging

Power Subsystem. The small probe of the Pioneer Venus satellite contains three electronics units (battery discharge regulator, power interface unit, pyro switch). Two packaging configurations are being considered. The first alternative is to install each electronic unit into a separate rectangular chassis. The second alternative is to install all three units into a semicircular container with a 11.3 cm (5.25 in.) radius and a 3.8 cm (1.5 in.) height (Figure 4.6-7). In the first case, the three rectangular chassis have a combined volume of 1071 cm ($65.3\ in^3$) whereas the second alternative yields 1067 cm^3 ($65.0\ in^3$) of packaging space. The cost estimates for each packaging configuration are summarized in Table 4.6-2.

The table shows the estimated increase in cost to package the electronic hardware in a semicircular container over packaging the same hardware into three existing rectangular chassis which have been used in the past. It was estimated that the manufacturing cost due to fabricating the semicircular chassis would cost $1.6 K more than if the same hardware were put into rectangular chassis. It was also estimated that the engineering costs due to the thermal analysis and in-process testing of the semicircular chassis would cost $19.5 K more than the engineering costs associated with the rectangular packages. (These estimates were based on historical cost data).

The large probe of the Pioneer Venus satellite also contains three electronics units (battery discharge regulator, power interface unit, pyro switch). Two packaging alternatives are also being considered. As in the small probe, the first alternative is to install each electronic unit into a

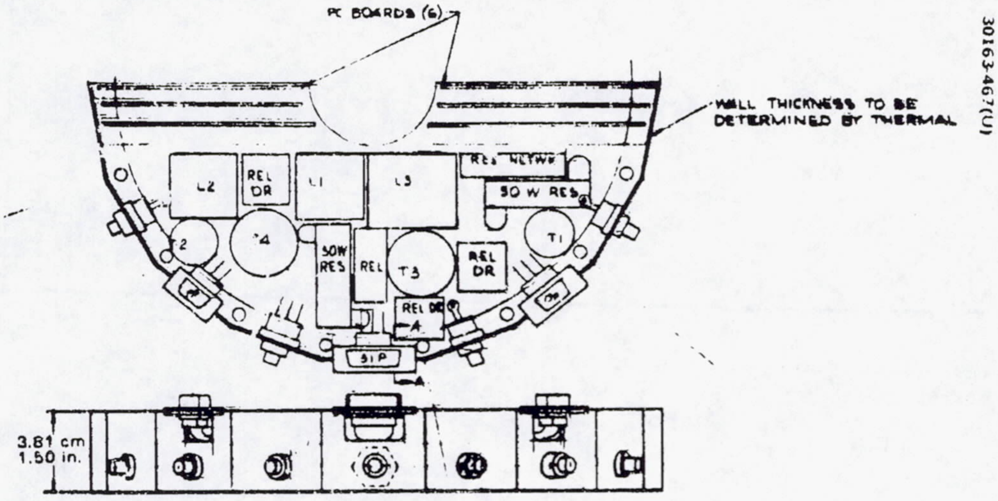

FIGURE 4.6-7. SMALL PROBE SEMICIRCULAR ELEMENT

REPRODUCIBILITY OF THE ORIGINAL PAGE IS POOR.

TABLE 4.6-2. PACKAGING COST ESTIMATES

Configuration	Delta Engineering Costs, $	Delta Manufacturing Costs, $
Small Probe		
First alternative (conventional)	-	-
Second alternative (semicircular element)	19,800 (increase)	1,600 (increase)
Large Probe		
First alternative (conventional)	-	-
Second alternative (cylindrical segment)	24,700 (increase)	2,200 (increase)
Third alternative (spherical section)	24,700 (increase)	2,200 (increase)

separate rectangular chassis. The second alternative is to install all three units into a cylindrical segment with legs 23.1 cm (9.10 in.) by 17.5 cm (6.75 in.) and a height of 8.1 cm (3.19 in.) (Figure 4.6-8). In the first case, the three rectangular chassis have a combined volume 2750 cm³ (167.5 in³) whereas the cylindrical segment described yields a volume of approximately 2380 cm³ (145 in³). Cost estimates are shown in Table 4.6-2.

Table 4.6-2 shows the estimated increase in cost to package the electronic hardware in a cylindrical segment over packaging the same hardware into three existing rectangular chassis which have been used in the past. It was estimated that the manufacturing cost due to fabricating the cylindrical segment shape of container and assembling the hardware into it would cost $2.2 K more than if the same hardware were put into rectangular chassis. It was also estimated that the engineering costs due to thermal analysis and in-process testing of the cylindrical segment package would cost $24.7 K more than the engineering costs associated with the rectangular packages. (These estimates were based on historical cost data.)

There is also a third alternative to the packaging of the above large probe electronics. This plan consists of packaging the above electronics units into a spherical section which conforms to the large probe in two degrees of curvature (Figure 4.6-9). The volume of this configuration is 4100 cm³ (250 in³). Cost estimates based on the same considerations as above for this configuration are shown in Table 4-6.2.

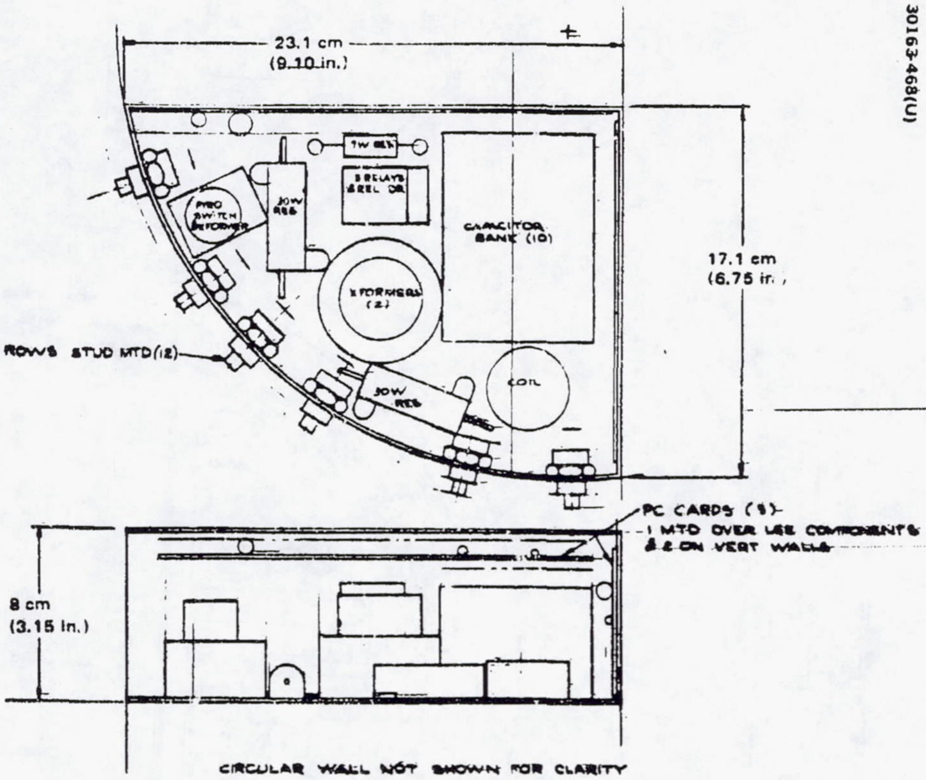

CIRCULAR WALL NOT SHOWN FOR CLARITY

FIGURE 4.6-8. LARGE PROBE CYLINDRICAL SEGMENT

30163-468(U)

REPRODUCIBILITY OF THE ORIGINAL PAGE IS POOR.

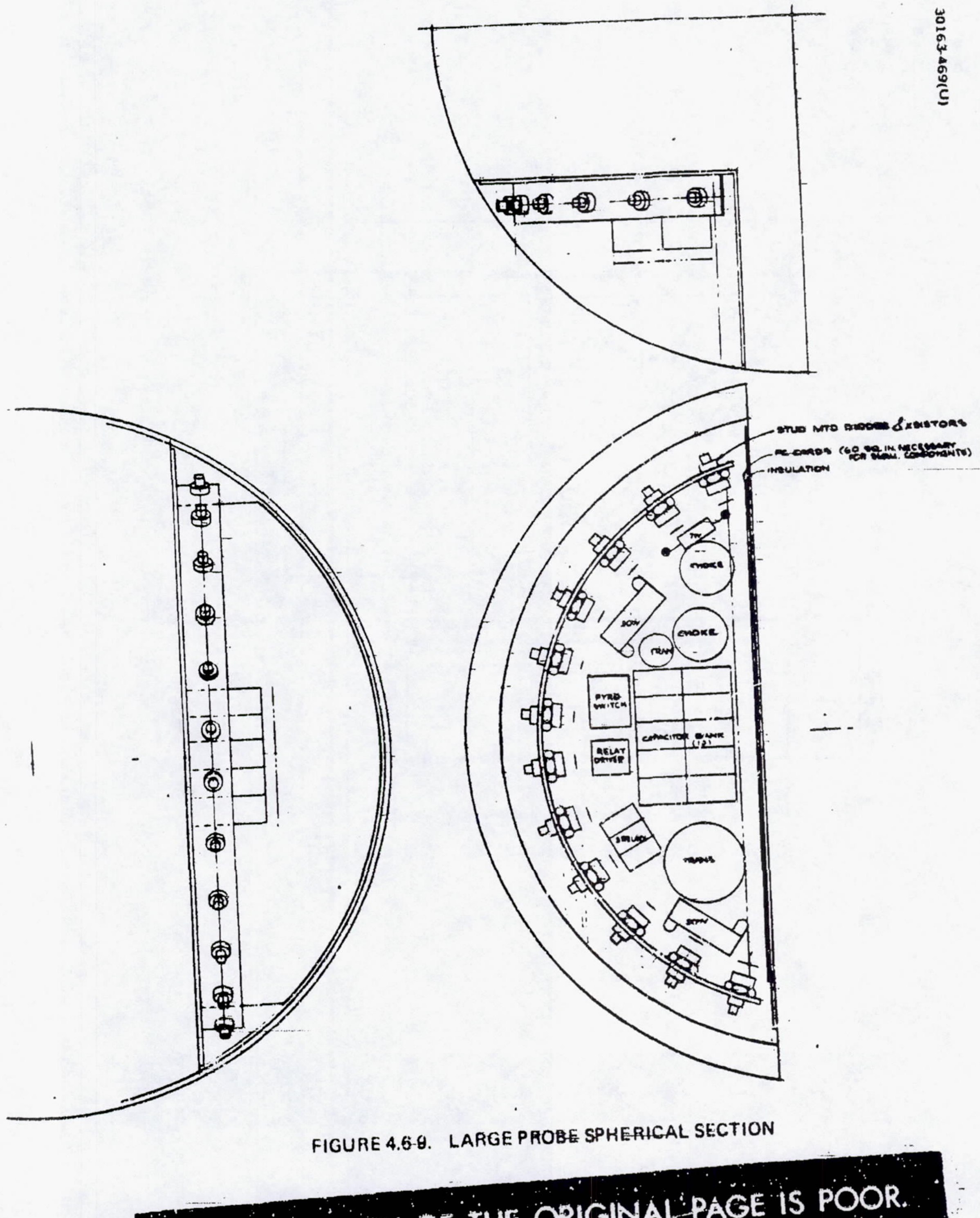

FIGURE 4.6-9. LARGE PROBE SPHERICAL SECTION

REPRODUCIBILITY OF THE ORIGINAL PAGE IS POOR.

Digital Components. For packaging the digital components, several alternative package sizes and shapes were considered for the probes. In these alternatives the command data and the pyro control are combined into one unit. A circuit design study will be required to verify that this approach is a reasonable one as regards noise pickup and interference between circuit functions. Figures 4.6-10 through 4.6-13 are applicable to the small probe command/data/pyro control. Figure 4.6-14 is applicable to the large probe command/data/pyro control. All of these printed circuit card designs are based on multilayer printed circuit packaging.

Product design costs for the multilayer printed circuit card approach are estimated to be 170 to 200 percent of a MICAM design approach. For the module concept made up of MICAM, LSI printed circuit boards, stud mounted power transistors, and welded pyro control unit modules (see Figure 4.6-10), the total cost increase over the conventional packaging methods is estimated to be 20 percent.

RF Components. The design of the rf subsystem has used modular construction for its packaging scheme. This enables systems engineering to lay out individual rf components to conform to the available space. In this sense the packaging is conformal.

Hughes' design goal has been to reduce the size of components as much as possible without reducing electrical performance. An example is the power amplifier. The design concept was to delete the dc regulator and use the power systems on the probes provided a regulated +28 V. At the same time, commonality with the probe bus and orbiter is maintained by using the same rf circuit. Since this microwave circuit uses distributed line lengths as circuit elements, it does not lend itself to further conformal packaging.

The largest component in the rf subsystem is the receiver/exciter. Hughes has tentatively selected the microminiature Viking transponder made by Philo-Ford. Although some overall system volumetric saving may be possible if this unit were to be repackaged with conformal packaging in mind, the ground rule set by the Hughes Pioneer Venus program management was to accept already developed vendors items essentially "as is" so as to minimize the program cost.

Size and weight estimates for the rf components have been made for both Thor/Delta and Atlas/Centaur configurations. For the latter case, the increased emphasis on low cost has led us to somewhat larger components in some instances. However, the above considerations regarding conformal packaging of the Thor/Delta rf subsystem could be equally applicable to the Atlas/Centaur.

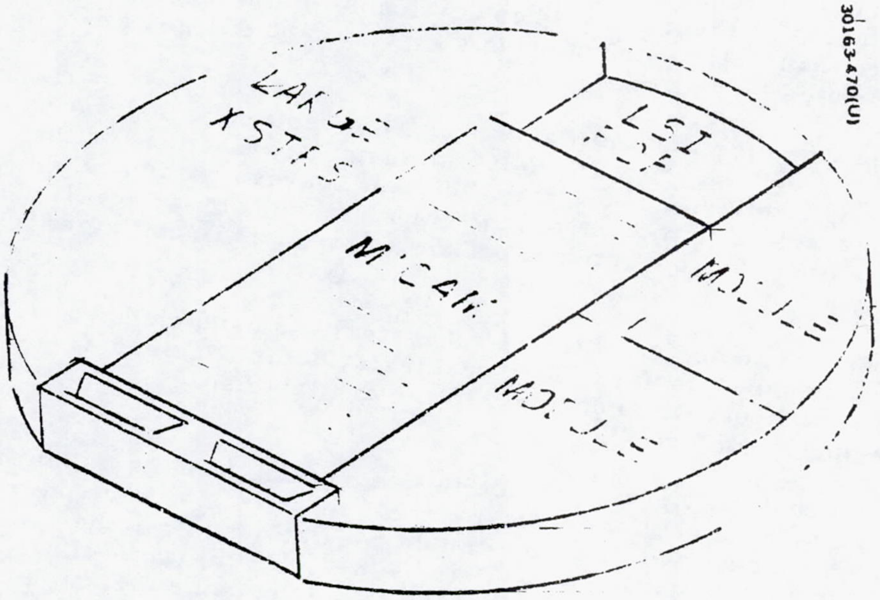

22.9 cm DIA. X 2.8 cm THICK (9.0 in. DIA. X 1.1 in. THICK)

WEIGHT: 1135 gm (2.5 lb.)

(COVERS NOT SHOWN)

FIGURE 4-6-10. MODIFIED MICAM DESIGN DISC

REPRODUCIBILITY OF THE ORIGINAL PAGE IS POOR.

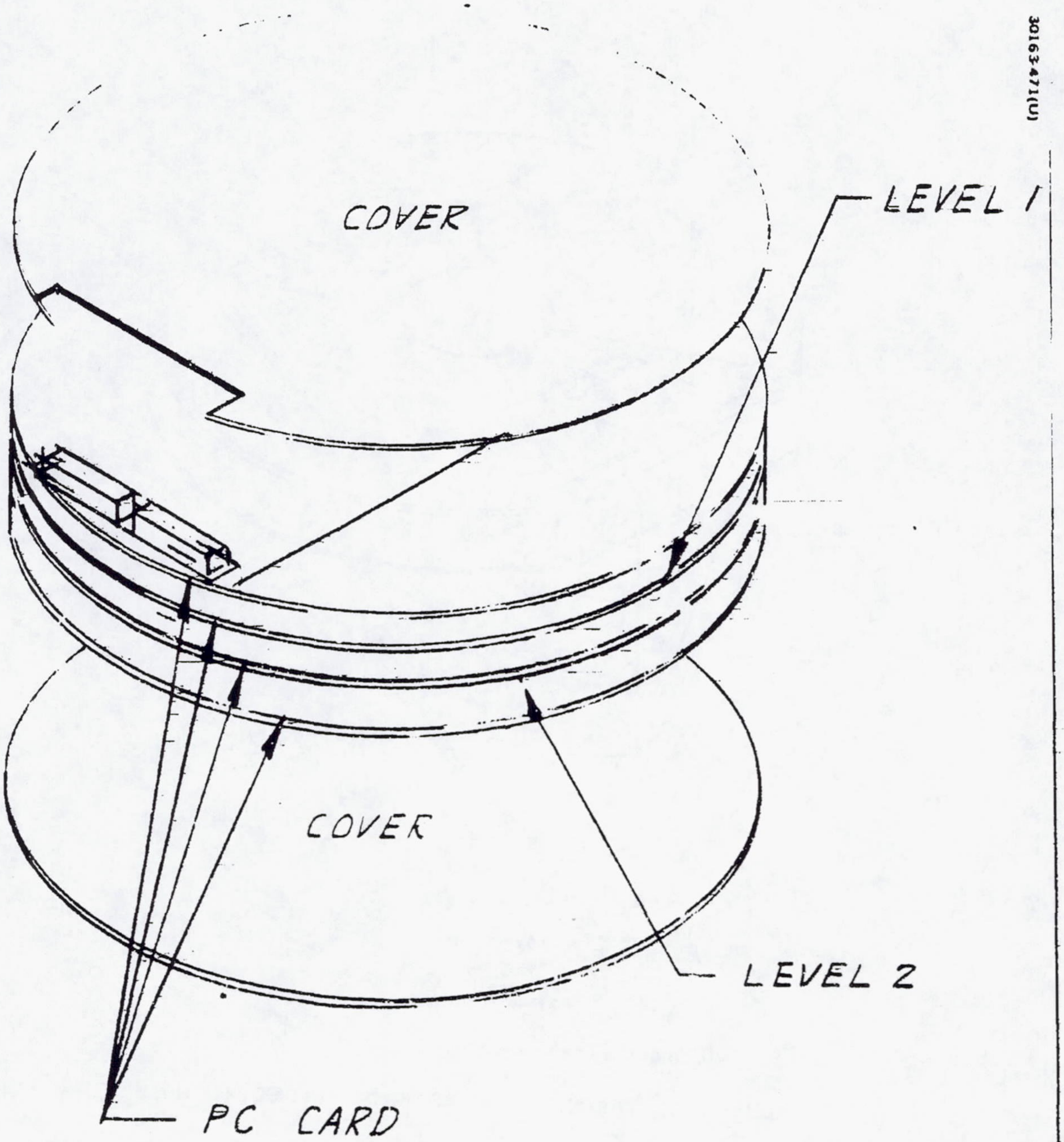

WEIGHT: 1000 gm (2.2 lb.)

19.3 cm DIA. X 3.2 cm THICK

(7.6 in. DIA. X 1.25 in. THICK)

FIGURE 4.6-11. PRINTED CIRCUIT BOARD DESIGN DISC

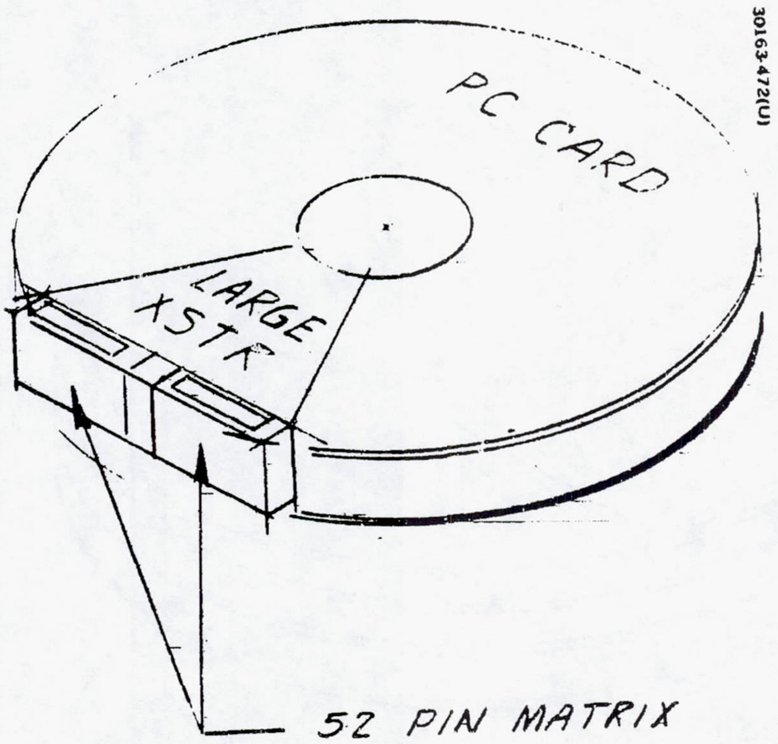

WEIGHT: 1135 gm (2.5 lb.)

2.8 cm ID
24.1 cm OD × 2.0 cm THICK

(1.12 in. ID
9.5 in. OD × 0.78 in. THICK)

(COVERS NOT SHOWN)

FIGURE 4.6-12. PRINTED CIRCUIT BOARD DESIGN DISC WITH HOLE

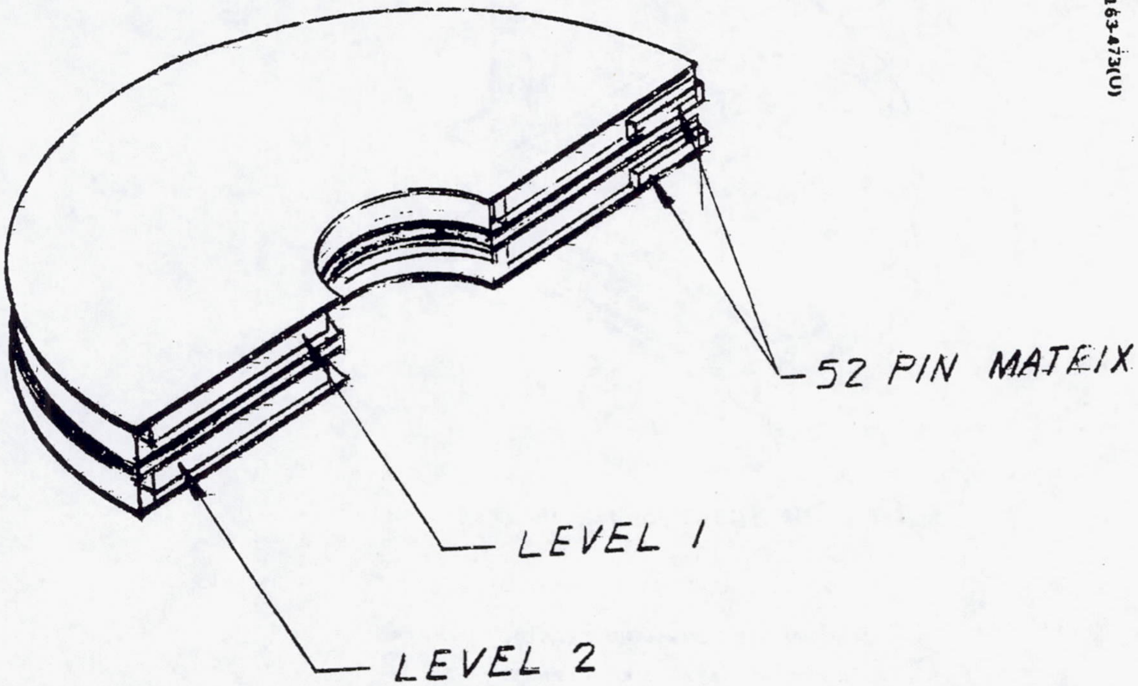

WEIGHT: 1000 grm (2.2 lb.)

2.8 cm ID
X 4.3 cm THICK (1.12 in. ID X 1.7 THICK)
(9.50 in. ID)
24.1 cm OD

COMMAND DATA	526 EQUIV PARTS
PYRO UNIT	60 EQUIV PARTS (3 STUD X STRS)
	586 EQUIV PARTS

FIGURE 4.6-13. PRINTED CIRCUIT BOARD DESIGN HALF DISC WITH HOLE

30163-473(U)

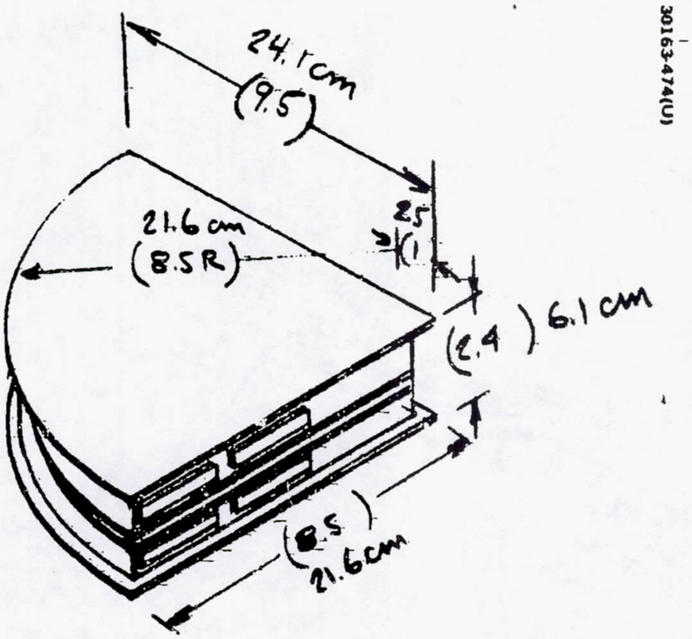

( ) DIMENSIONS IN INCHES

ESTIMATED WEIGHT 1861 grm (4.1 lb.)

LARGE PROBE – COMMAND/DATA UNIT AND PYRO

COMMAND DATA 719 EQUIV PARTS

PYRO 380 EQUIV PARTS (20 STUD X STRS)

1099 TOTAL PARTS

FIGURE 4.6-14. PRINTED CIRCUIT BOARD DESIGN QUARTER DISC

5. DECELERATION MODULE

The probe deceleration modules provide the vital functions of atmospheric braking and thermal protection from aerodynamic heating during entry into the Venusian atmosphere. For the large probe, the deceleration module must also perform a sequence of events, which includes ejecting a pilot parachute, separating an aft closure, deploying the main parachute, then disconnecting and jettisoning the aeroshell. These and other functions are illustrated in Figure 5-1.

For the small probe, the parachute and separation functions during descent are not required; instead, the aeroshell remains integrated with the pressure vessel module all the way to impact. Consequently, the deceleration module must provide subsonic aerodynamic stability and a predictable descent, as well as the entry braking and thermal protection.

In the process of designing the deceleration modules, it was necessary to conduct many trade studies and tests in order to evolve designs which could best meet the primary criteria of low cost and low weight. In meeting these criteria, the designs must provide adequately for the science experiments and meet the mission and interface constraints. A summary of the trades, tests and studies is presented in Table 5-1. These are grouped into the areas of configuration, aerodynamics, structure, heat shield, parachute, and separation and despin. Most of these studies emphasized the Thor/Delta configurations, but extensions of the studies were made in order to provide design data for defining the Atlas/Centaur baseline.

5.1 CONFIGURATION

Trade studies of the probes deceleration modules resulted in the identification of two cone angle configurations, 45 and 55 deg half cone angles, either of which will meet mission requirements. The 55 deg configuration has been selected as the large probe baseline design for Thor/Delta primarily because it is a flight proven configuration for a science mission of this type, results in an easily testable flight thermal environment, allows a higher parachute deployment altitude, and is more readily packaged in the bus configuration. With the Atlas/Centaur selection as the launch vehicle the bus packaging constraints have been eliminated. The selection therefore has been changed to the 45 deg configuration to achieve commonality between the probes, resulting in reduced cost for aero test and analysis.

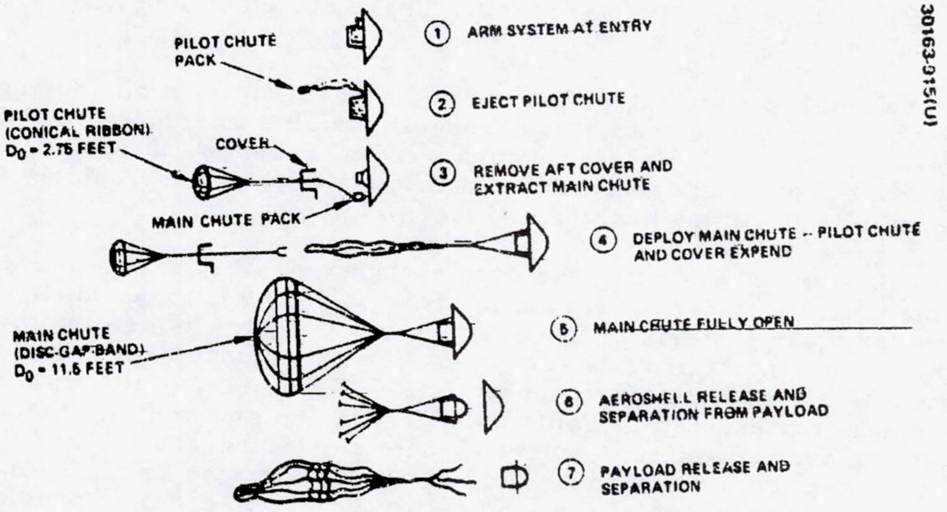

FIGURE 5-1. LARGE PROBE SEQUENCE

TABLE 5-1. SUMMARY OF DECELERATION MODULE TRADES, TESTS AND DESIGN STUDIES

Trades, Tests, Studies	Candidates	Selection and Rationale	Need for Trade
Basic configuration			
Large and small probes	Flight proven configurations Spherical nose + cone body Cone half angles: 45, 55, 60 deg	Large probe 55 deg for Thor/Delta - least weight readily packaged on bus 45 deg for Atlas/Centaur – lowest development cost, commonality with small probe, best stability Small probe 45 deg for both Thor/Delta and Atlas/Centaur – best subsonic performance	To establish basic external configuration for deceleration modules to maximize science, minimize cost, and weight
Aerodynamics			
Six degree of freedom aerodynamic characteristics	Flight proven configurations Spherical nose + cone Cone half angles: 45, 55, 60 deg	Selections as above – aero characteristics obtained from existing flight and wind tunnel data for range of expected flight conditions	Basic aerodynamic data for predicting trajectory and flight dynamic performance of candidate configurations
Entry motion predictions, Large probe	Large 55 deg Thor/Delta probe Nominal V_E, γ and p Varied γ_E, C_{l_o}, C_{l_p}, $X_{c.g.}$, $C_{mq} + C_{m_\alpha}$, α_E	Nominal design parameters provide well behaved entry. Dynamic angle of attack 1 to 10 deg	Determine stability characteristics through entry phase
Entry and descent predictions, Small probe	Small 45 deg probe with and without fin damping nominal V_E, and p varied γ_E, α_E, C_{l_o}, C_{mq}, $X_{c.g.}$	Nominal design parameters with fins provide satisfactory entry and descent motion. Spin well damped.	Determine stability characteristics through entry and descent, particularly motions induced by spin excursions.
Horizontal wind effects, descent phase	Small probe – Thor/Delta Large probe on parachute – Thor/Delta simulated descent subjected to knife edge and gradual wind shears	For both configurations communication angle is primarily affected by probe terminal descent velocity, virtually unaffected by amount of stability	To determine if "communication angle" is seriously affected by horizontal gusts
Aerodynamic tests Ames water tank	Thirteen sphere cone configurations matrix of 45, 55, 65 deg cone half angles; spherical forebodies; 0.7, 0.9, full dome and 45 deg conical afterbodies. Weights and c.g. varied	Smaller cone angles show better stability than larger angle for allowable c.g. location	To provide initial screening of deceleration module aerodynamic configurations for descent phase
Langley vertical spin tunnel	Four forebodies interchangeable with three afterbodies. 45, 51.5, and 55 deg half angles plus hemisphere. Later tests added fin and drogue configurations	45 deg sphere cone with fins provides suitable subsonic descent characteristics and meets entry requirements	To select deceleration module configuration for descent phase and provide aerodynamic characteristics

REPRODUCIBILITY OF THE ORIGINAL PAGE IS POOR.

REPRODUCIBILITY OF THE ORIGINAL

TABLE 5-1. (Continued)

Trades, Tests, Studies	Candidates	Selection and Rationale	Need for Trade
Structure			
Material trades	Aluminum alloy Beryllium Titanium Stainless steel	Thor/Delta Beryllium, ring stiffened monocoque for large probe Beryllium pure monocoque for small probe Lightest weight Atlas/Centaur Aluminum, ring stiffened monocoque, for large probe Stainless steel, pure monocoque for small probe Lowest cost	To establish structural concept and material selection that best meet principal criteria for Thor/Delta (lightest weight) and Atlas/Centaur (lowest cost)
Structural concepts	Monocoque Ring stiffened monocoque Honeycomb		
Heat shield			
Hypersonic entry heating	Thor/Delta and Atlas/Centaur	Extensive data bank available for sphere cone earth reentry bodies	To establish heating loads for design of heat shield
Heat shield weight trades	Phenolic nylon Carbon phenolic ESM-1004 Teflon	Carbon phenolic -- least ablation, most predictable weight, close second in lightness, acceptable cost	To establish preferred material for probe nose core protection
Bond selection	RTV-560 RTV-630 PD-200	PD-200 selected for phenolic nylon heat shield – best cold soak capability RTV-630 selected for carbon phenolic – high strength at elevated temperature	To select best bonding materials compatible with carbon phenolic and phenolic nylon heat shields
Ablation test program	Phenolic nylon Carbon phenolic ESM-1004 Teflon	Recession measurements verified analysis. Carbon phenolic least ablation	To verify analysis in selection of ablation material for heat shield
Parachute			
Pilot parachute sizing	Conical ribbon chute D_o varied above and below 1.0 m	D_o = 0.84 m conical ribbon chute selected for Thor/Delta. D_o - 0.84 m for Atlas/Centaur. Provides minimum size and weight with adequate drag.	To select minimum size pilot chute
Main parachute sizing	Disc-gap-band Ring slot Ribbon All with varied diameters, nylon versus dacron	D_o = 2.51 m disc-gap-band nylon for Thor/Delta. D_o = 4.6 m disc-gap-band nylon for Atlas/Centaur. Lowest weights consistent with other requirements. Most experience with nylon.	To select minimum weight main chute
Ejection device	Pyrotechnic-deployed cover Ejection mortar	Ejection mortar – highest reliability	Selection of preferred main chute ejection device

REPRODUCIBILITY OF THE ORIGINAL PAGE IS POOR.

TABLE 5-1. (Continued)

Trades, Tests, Studies	Candidates	Selection and Rationale	Need for Trade
Separation and Despin			
Large probe			
Bus/probe separation	Ejection spring rates varied to give various ΔV's	ΔV = [illegible] cm/sec for Thor/Delta probe. Increased for Atlas/Centaur	Determine ejection spring size for satisfactory separation of probe from bus
Aeroshell pressure vessel [illegible] separation	Separation time delay varied	2 sec selected. Prompt, yet adequate separation results	Select separation time delay
Parachute release method	One point attachment Two point attachment Three point attachment	Three point attachment — best aero stability	Select method of attachment
Small probe			
[illegible]	Various values of opening arm [illegible] velocity	100 deg/sec arm opening velocity, best clearance	Select parameters for design of separation system
Despin system	Yo-yo mechanism Small rockets	Small rockets — ease of installation, testing, minimum weight	Select optimum despin system

The 45 deg configuration has been selected for the small probe configuration based upon its subsonic performance characteristics for both Thor/Delta and Atlas/Centaur.

Requirements

Selection of entry vehicle configurations for the large and small probes involves many interrelated factors. Experiment requirements, stability, minimum weight, ballistic coefficients, bus and scientific payload packaging requirements, selection of the afterbody configuration, and thermal loads resulting from the configuration selection must all be considered. In addition, minimizing development costs by using previously tested aerodynamic shapes, maintaining commonality wherever possible in order to reduce testing, and designing the configuration to create thermal loads compatible with existing test facilities play a large part in the final design. These considerations have been traded off to arrive at a baseline design that meets both mission and program requirements. The resultant configurations and the rationale that led to their selection are discussed in the following sections.

Thor/Delta Configuration Trades

Science

The configurations must provide stable, protected platforms for scientific measurement. In essence, both the large and small probes are themselves calibrated instruments and perform best under constrained, simply predictable motion, as suggested by Seiff and Sommer and demonstrated by the PAET Program. Considered in the selection of optimal configurations must be the sensitivity of the effects of aerodynamic and motion tolerances on the measurements, their communication, and interpretation. Previous analyses have revealed the importance of accurate a priori knowledge of axial force coefficient (C_X) in particular, and the dynamic motion model in general, for both the high and low altitude atmosphere regimes. Minimization of the error is most efficiently achieved through selection of configurations that simplify the force and motion model; i.e., ensure circular, well bounded motion with minimal variation of C_X with angle of attack. This maximizes the individual data point value and thereby permits lower sampling rates and higher scientific value return for the available information system. General considerations relating the science objectives to configuration alternatives are shown in Table 5.1-1.

Aerodynamics

Aerodynamic characteristics of blunt cones in cone half angle range from 40 to 70 deg exist over a large range of Mach numbers and angles of attack. This data bank is compiled from wind tunnel, ballistic range, drop tests and flight experience. Most notable in the area of flight experience are the NASA-Ames PAET configuration, a 55 deg half-angle sphere cone, which successfully measured the earth's atmospheric properties, and the GE MK II, a 51.5 deg sphere cone.

TABLE 5.1-1. CONFIGURATION RELATION TO SCIENCE OBJECTIVES

GENERAL: Minimize cost and weight to maximize science. Provide delivery protection, stability, and predictability.

Science Objective	Dynamic Performance Requirements		Deceleration Module Configuration Implications						
				Specific Preference					
				Forebody θ_c				Afterbody Type	
	Large Probe	Small Probe	General	45^0	51.5^0	55^0	60^0	PAET	MK-2
Atmosphere reconstruction (ρ,p,T)	High Altitude ($M > 1$)								
	Minimum β Minimum α Circular	Minimum β Minimum α Circular	Maximum drag area (C_DA)			X	X		
			$I_R/I_p > 1$; S.M. > 20%; $\lambda < 0$	X	X	X			X
			Maximum roll momentum/ asymmetry		X	X	X	X	
	Known aerodynamics	Known aerodynamics	$C_X, C_N = f(\alpha, M, R_e, \gamma)$	X	X	X		X	X
	Low Altitude ($M < 1$)								
	No requirement	Minimum α	$\lambda < 0$; $\lambda = f(C_{L_\alpha}, C_{m_\alpha}, p)$	X	X	X		X	
		Predictable motion	Roll damping $\geq C_{l_0}$		X	X	X	X	
Cloud definition	Minimum dynamic effects during deployment of chute Minimum swinging on chute	No requirement	S.M. >20%; minimum asymmetry; $\lambda < 0$ Avoid res. spin; minimum chute side drag area	X	X	X		–	–
Winds	Minimum response (α)	Minimum response	Stable forward, $C_{M_{\alpha_w}} < 0$	X	X	X			X
	Maximum discernible	Maximum discernible	Stable for no winds, $\lambda < 0$	X	X	X		X	

SUMMARY

- Dynamic stability: lower cone angles better
- Aerodynamic predictability: MK-2 experience and lower cone angle advantages
- Motion simplicity: MK-2, PAET both good

20140-309T

REPRODUCIBILITY OF THE ORIGINAL PAGE IS POOR.

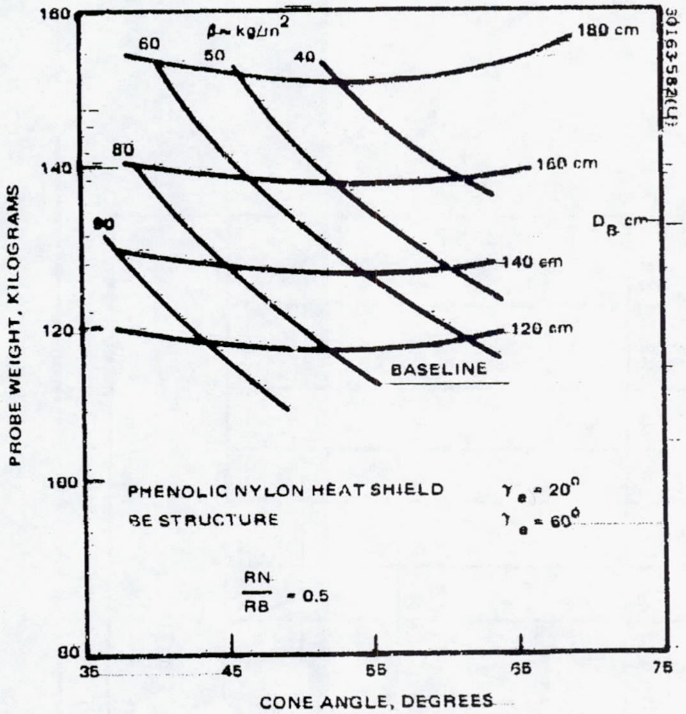

FIGURE 5.1-1. LARGE PROBE WEIGHT/CONFIGURATION TRADES (36036-437)

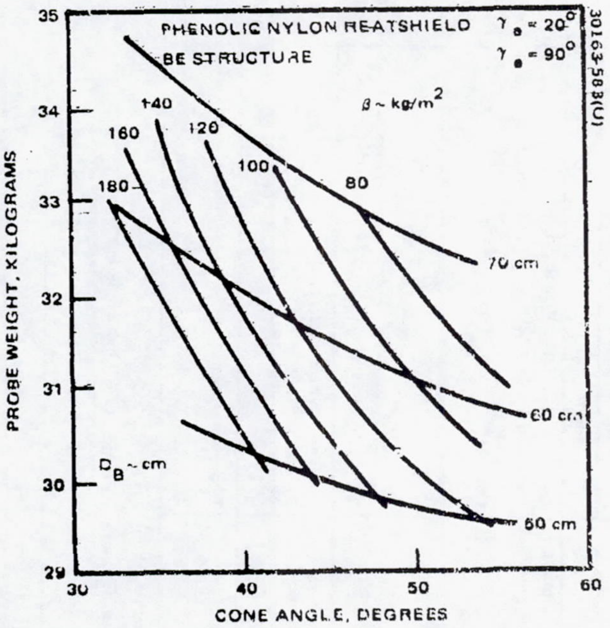

FIGURE 5.1-2. SMALL PROBE WEIGHT/CONFIGURATION TRADES (36036-438)

Beyond these flight proven configurations, the best characterized cone half angles are 60 and 70 deg. Data on these cone angles were developed on other programs which had a need for high drag bodies when entering a planetary atmosphere having very low density (e.g., Mars). Configurations with large cone angles (>60 deg) have dynamic stability problems in the hypersonic and transonic Mach number range which necessitate active attitude control systems and supersonic parachute deployment. Where high drag and associated low ballistic coefficients are not mandatory, therefore, it is desirable to decrease the cone-half angle below 60 deg. As mentioned previously, large aerodynamic data banks exist for 55 and 51.5 deg configurations with scattered additional data at various angles down to the slender cone regime. With these data and the theoretical flow field techniques available, aerodynamic characteristics can be defined for any selected cone angle in this regime.

In conclusion, both the 55 and 45 deg large probe and the 45 deg small probe provide acceptable aerodynamic characteristics for their science and mission objectives.

Weight

The variation of the large and small probe weights and resultant hypersonic ballistic coefficients with cone half angle, bluntness ratio and base diameter is shown in Figures 5.1-1 and 5.1-2. Although these curves were generated for a beryllium structure and phenolic nylon heat shield, they are representative of the trends for any heat shield/structure combination. The weight variation with cone half angle is minimal. However, it should be noted that vehicle weight is highly dependent upon the aeroshell base diameter. Therefore, the initial effort was directed towards packaging the science module in a minimum size vehicle base diameter to reduce weight. The minimum diameters considering packaging constraints were 1.17 m (46 in.) and 0.56 m (22 in.) for the large and small probes, respectively. The same minimum packaging diameters were obtained for both 55 and 45 deg configurations.

It was found necessary to increase the small probe base diameter to 0.61 m (24 in.) to enhance its subsonic stability characteristics as will be discussed below.

Effects of C.G. Location

Tests conducted at the NASA Langley Spin Tunnel indicated that the small probe will be dynamically unstable if the c.g. is not forward of the first maximum diameter of the aeroshell. Figure 5.1-3 presents c.g. location of typical small probe configurations as a function of cone angle and base diameter. The upper limit of the small probe (Thor/Delta) diameter is 0.61 m (24 in.) based upon geometrical limitations while attached to the bus. It can be seen from Figure 5.1-3 that in the 55 deg cone case, even if the base diameter were increased to 0.61 m (24 in.), the c.g. would still be slightly aft of the first maximum diameter. In the case of the 45 deg

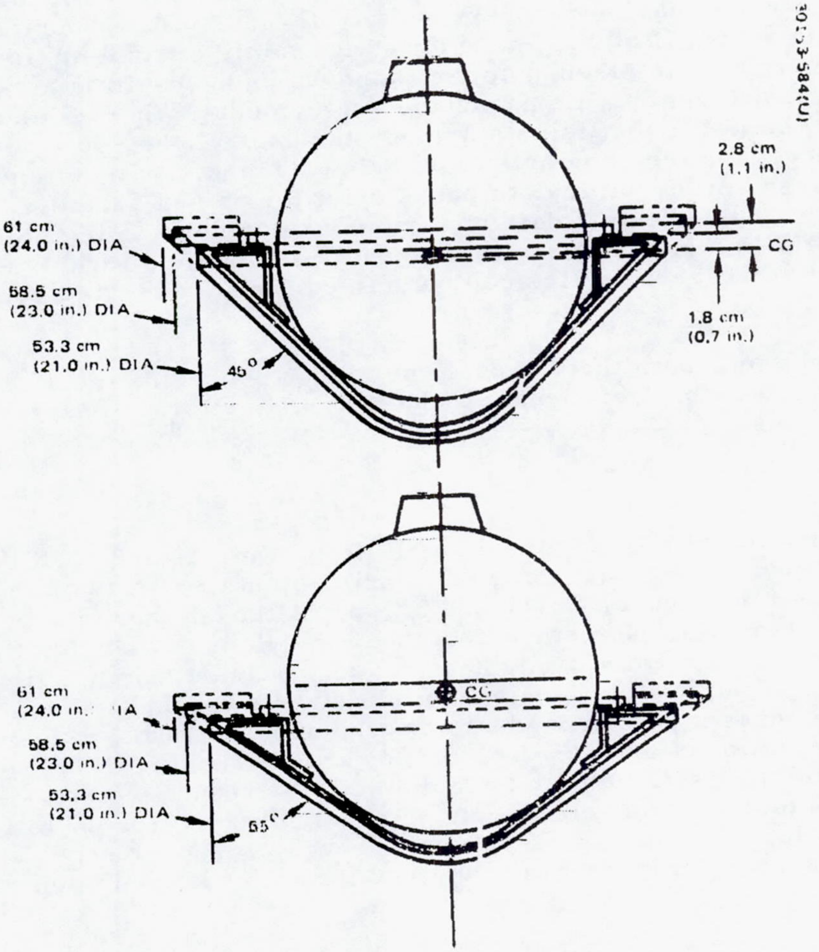

FIGURE 5.1-3. C.G. LOCATIONS FOR TYPICAL SMALL PROBE CONFIGURATIONS

nfiguration, a 0.61 m (24 in.) base diameter will result in a c.g. 2.80 cm .1 in.) forward of the first maximum diameter. To achieve this forward .g. location on the 55 deg cone would require 5.42 kg (12 lb) of ballast per robe, an unacceptable weight penalty. It was primarily for this reason at the small probe baseline has been selected as the 45 deg configuration ith a 0.61 m (24 in.) base diameter.

Figure 5.1-4 presents the c.g. location of the large probe as a unction of cone angle for a 1.17 m (46 in.) base diameter. Analysis to date as indicated that it is desirable although not mandatory to locate the c.g. t or forward of the probe first maximum diameter. Both the 45 and 55 deg onfigurations will meet this requirement. Although the location of the c.g. the 45 deg cone will be further forward than in the 55 deg configuration, tability for the 55 deg case is adequate, considering the hypersonic and ransonic regions (and times involved) in which the large probe must operate.

Parachute Deployment Altitude

The basic parachute deployment requirements are:

1) Pressure vessel will be deployed on parachute at an altitude no lower than 66 km

2) The parachute deployment will be subsonic to minimize the costs of development and proof testing

The variation in chute deployment altitude between the 60 and 55 deg robe configuration is less than 0.5 km for expected values of β and entry ngle. Selection of the 45 deg Atlas/Centaur configuration would mean a loss n deployment altitude of approximately 2.5 km from the 55 deg Thor/Delta esign due to the higher ballistic coefficient. However, all configurations eet the 66 km requirements.

Effects on System Packaging

Figure 5.1-5 depicts the arrangement of the probes on the bus for the Thor/Delta configuration. If the small probe base diameter were increased eyond the current 0.61 m (24 in.), the large probe base diameter would have o be decreased to avoid interference. Conversely, an increase in the large robe base diameter would require a corresponding decrease in small probe ase diameter. Since the large probe 1.17 m (46 in.) base diameter is inimum from the science module packaging requirements and the small robe 0.61 m (24 in.) diameter is minimum from the subsonic stability re-uirements, no reduction in these diameters is permissible. Any gain in he base diameter of either could only be accommodated by pushing the large robe position on the bus forward from that shown in Figure 5.1-5. The ajor effect of the shifting forward of the large probe would be to lower the roll to pitch moment of inertia ratio of the bus configuration during the transit phase.

REPRODUCIBILITY OF THE ORIGINAL PAGE IS POOR.

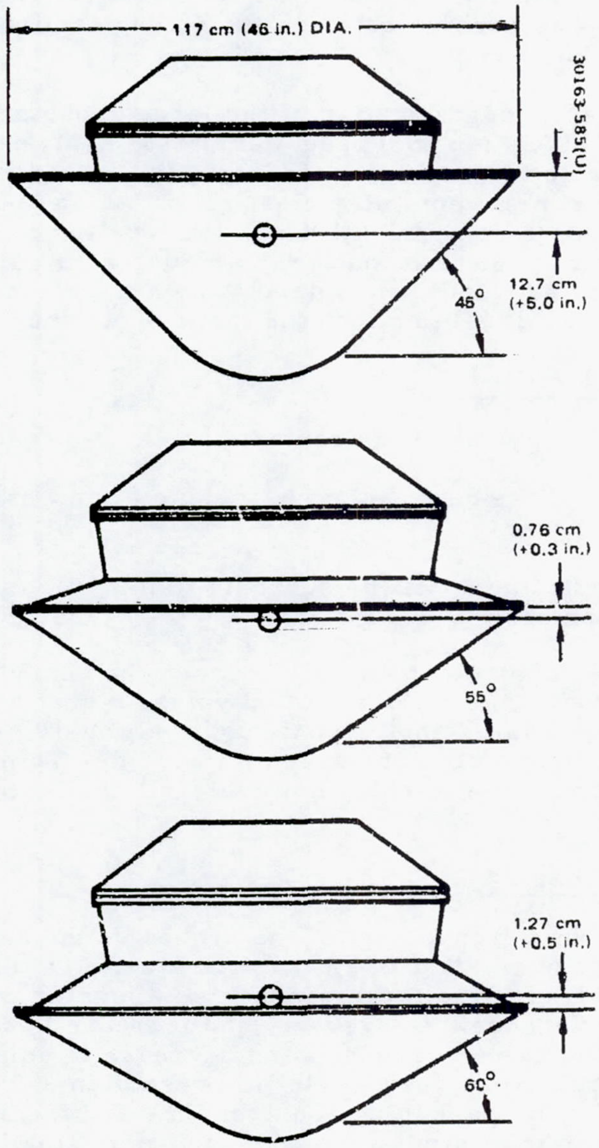

FIGURE 5.1-4. LARGE PROBE CONFIGURATION COMPARISON

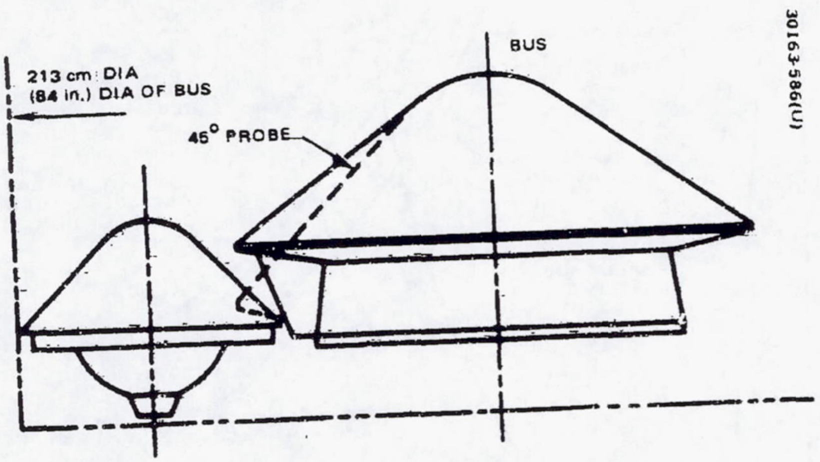

FIGURE 5.1-5. PROBES ON THOR/DELTA BUS

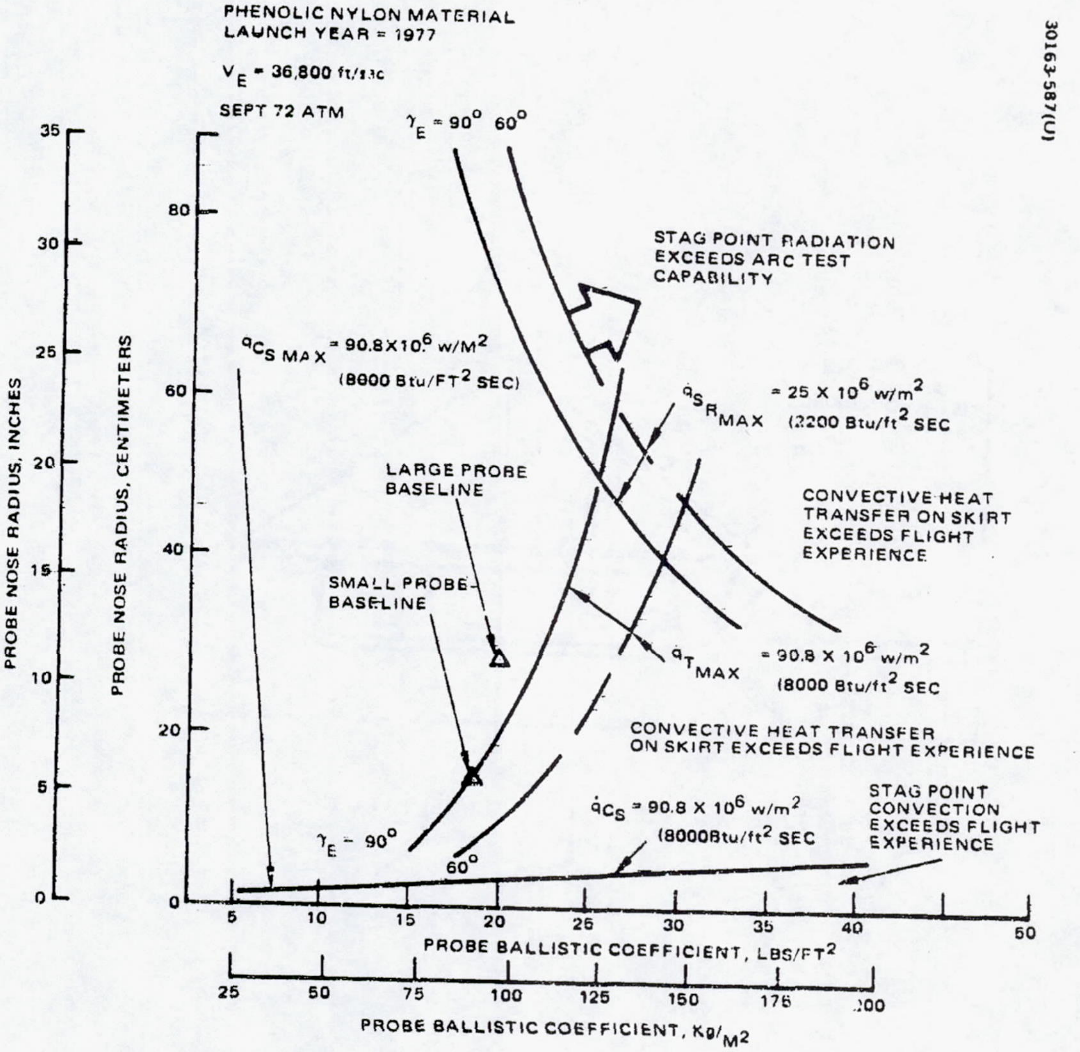

FIGURE 5.1-6. CONFIGURATION CONSTRAINTS TO MAINTAIN FLIGHT ENVIRONMENT WITHIN PREVIOUS FLIGHT EXPERIENCE AND CURRENT RADIATIVE TEST CAPABILITY

Preliminary investigations indicated that if the large probe were to be shifted forward by as much as 5.08 cm (2 in.), difficulties would arise in maintaining the required probe bus inertia ratio.

Also shown in phantom in Figure 5.1-5 is the large probe 45 deg, 1.17 m (46 in.) base diameter configuration with its nose apex at the same station as in the 55 deg baseline. It can be seen that the 45 deg configuration would have to be moved forward approximately 8.89 cm (3.5 in.) to eliminate interference with the small probes. This would result in the same inertia problem which was discussed above.

Effects of Descent Rate on Small Probe Configuration

Studies conducted have indicated no major impact on systems weight or science accommodation within the range of ballistic coefficients (β's) which were considered.

Thermal Effects

Heat transfer rates to the entry probes should be limited to fall within the bounds of previous flight experience and the current radiation test capability. Phenolic nylon, the selected baseline shield material, has been flight tested successfully on numerous occasions at GE. The maximum total heat transfer rates predicted for the Pioneer Venus probes have been used and approximate techniques employed to generate the limiting combinations of nose radius and hypersonic ballistic coefficient to maintain: 1) the maximum convective heat transfer at or below the flight experience levels, and 2) the maximum radiative heat transfer at or below the maximum test capability of the NASA Ames AEHS facility of 250 x 10^7 W/m^2 (2200 Btu/ft^2-sec) (see Figure 5.1-6).

With the cone angle of the large probe changed from 55 to 45 deg, the hypersonic ballistic coefficient is increased to about 156 kg/m^2 (32 lb/ft^2). The maximum turbulent heat transfer on the skirt then is increased from the current value of about 7.18 x 10^7 W/m^2 (6300 Btu/ft^2-sec) to about 9.12 x 10^7 W/m^2 (8000 Btu/ft^2-sec) for an entry path angle of 60 deg. The resultant thermal loads are therefore not a driving parameter in choosing between a 45 and 55 deg configuration.

Commonality

It would be desirable to have cone angle commonality between the large probe and small probe, thereby reducing the aerodynamic testing and number of wind tunnel models requiring design and fabrication. Preliminary estimates place this cost savings in the area of \$200 K.

Since the small probe cone angle is restricted to 45 deg (as discussed in subsection 5.2), the large probe cone angle would also have to be 45 deg. With the selection of the Atlas/Centaur, the weight constraints which led to the 55 deg configuration on the large probe are removed. As a result, the Atlas/Centaur baseline configurations for both large and small probes are defined as 45 deg cone angles.

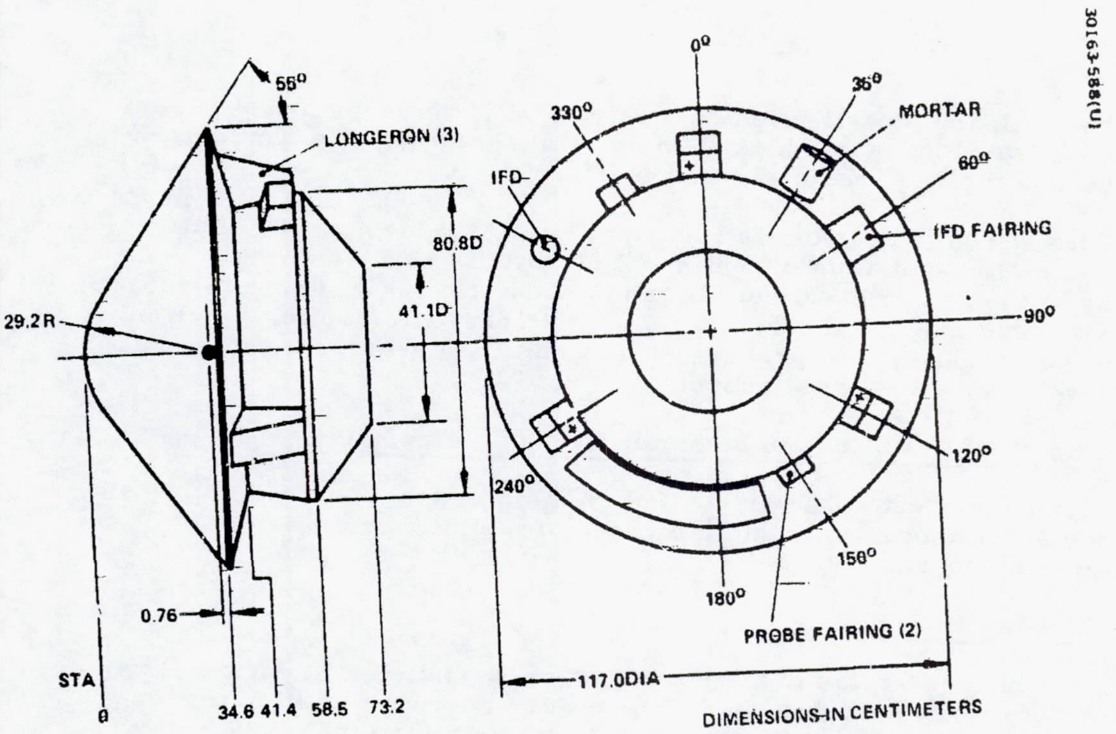

FIGURE 5.1-7. THOR/DELTA LARGE PROBE CONFIGURATION

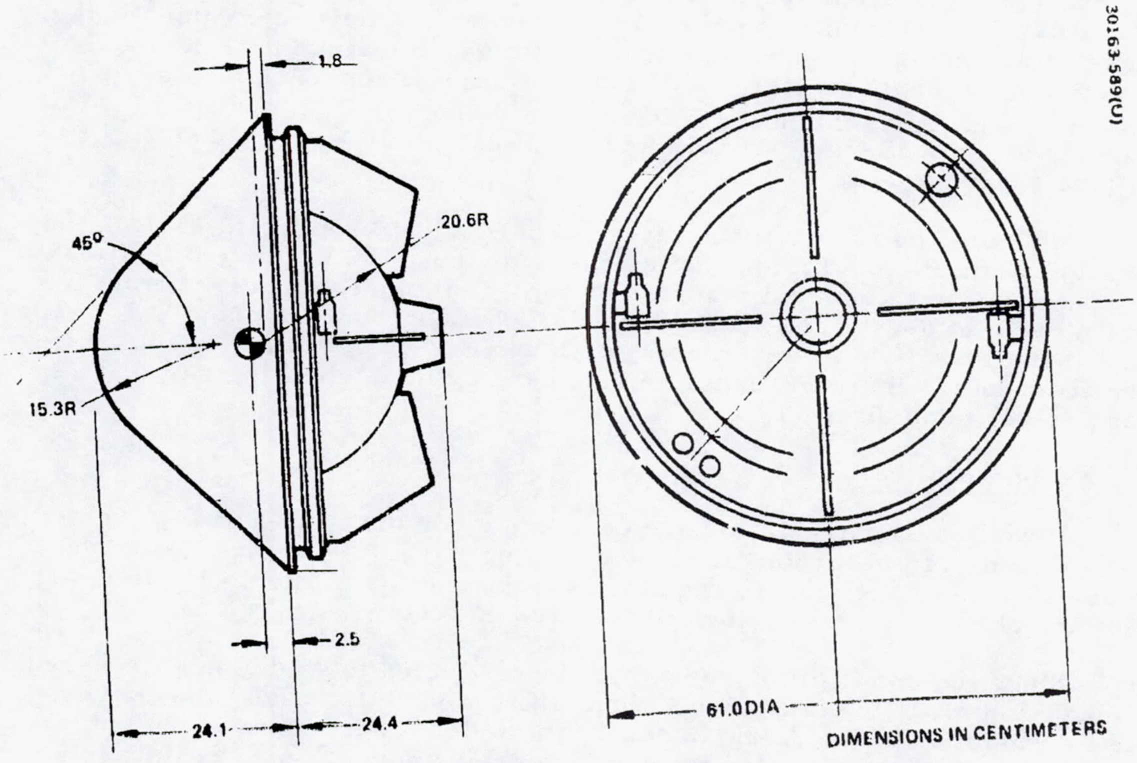

FIGURE 5.1-8. THOR/DELTA SMALL PROBE CONFIGURATION

Thor/Delta Configuration

The selected large and small probe configurations are shown in Figures 5.1-7 and 5.1-8.

As has been previously discussed, the large probe has a 55 deg cone angle, 1.17 m (46 in.) base diameter, and a bluntness ratio of 0.5. Adequate provision has been made for the packaging of all engineering and science equipment. The c.g. location is slight forward of the first maximum diameter to insure the dynamic stability of the vehicle.

The small probe has a 45 deg cone angle, 0.61 m (24 in.) base diameter, and a bluntness ratio of 0.5. To enhance dynamic stability, fins have been incorporated on the aft end. It should be noted that the c.g. is 2.54 cm (1 in.) forward of the first maximum diameter. This forward c.g. is adequate to maintain subsonic stability.

Atlas/Centaur Configuration

The large and small probe configurations selected for Atlas/Centaur and shown in Figures 5.1-9 and 5.1-10 are a result of extensions of the Thor/Delta trade studies discussed in the previous sections.

The large probe cone angle has been changed to 45 deg to achieve commonality with the small probes. Increases in the payload size have resulted in the base diameter being increased to 1.4 m (55 in.). Increased static and dynamic stability margin has been achieved by shifting the c.g. location further forward of the first maximum diameter.

The small probe configuration is basically the same as for the Thor/Delta with the exception that the base diameter has been increased to 0.67 m (26.5 in.). Changes in the science package, together with the requirement of maintaining a forward c.g., dictated the increase in the base diameter. The resultant c.g. location actually results in greater margin then was present in the Thor/Delta design.

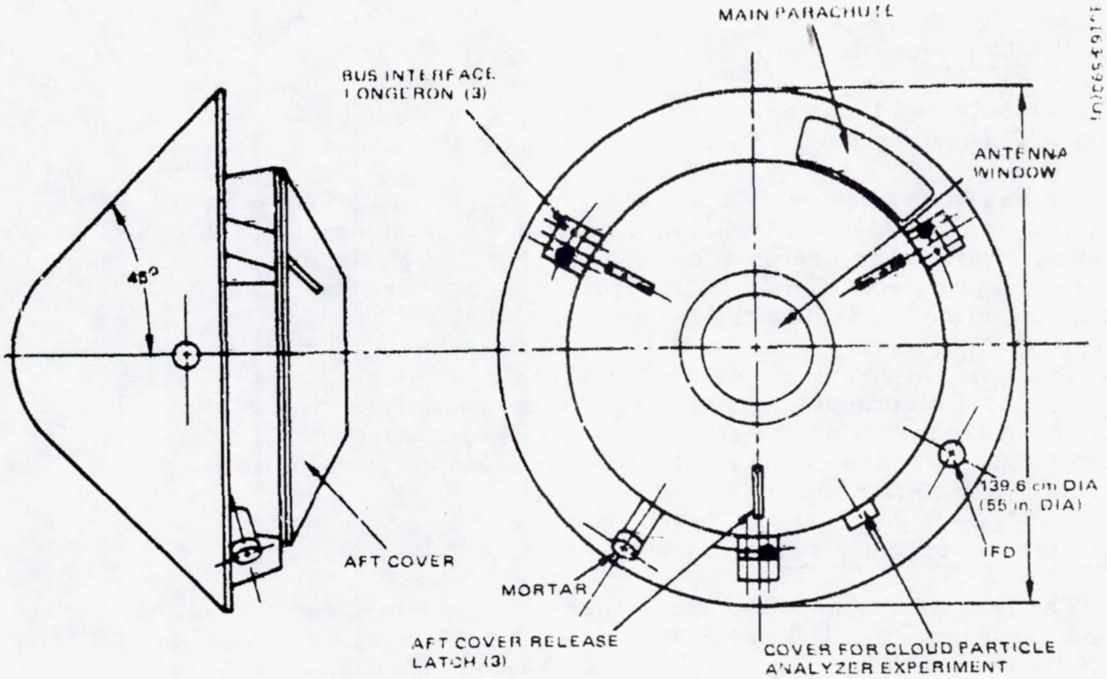

FIGURE 5.1-9. ATLAS/CENTAUR LARGE PROBE CONFIGURATION

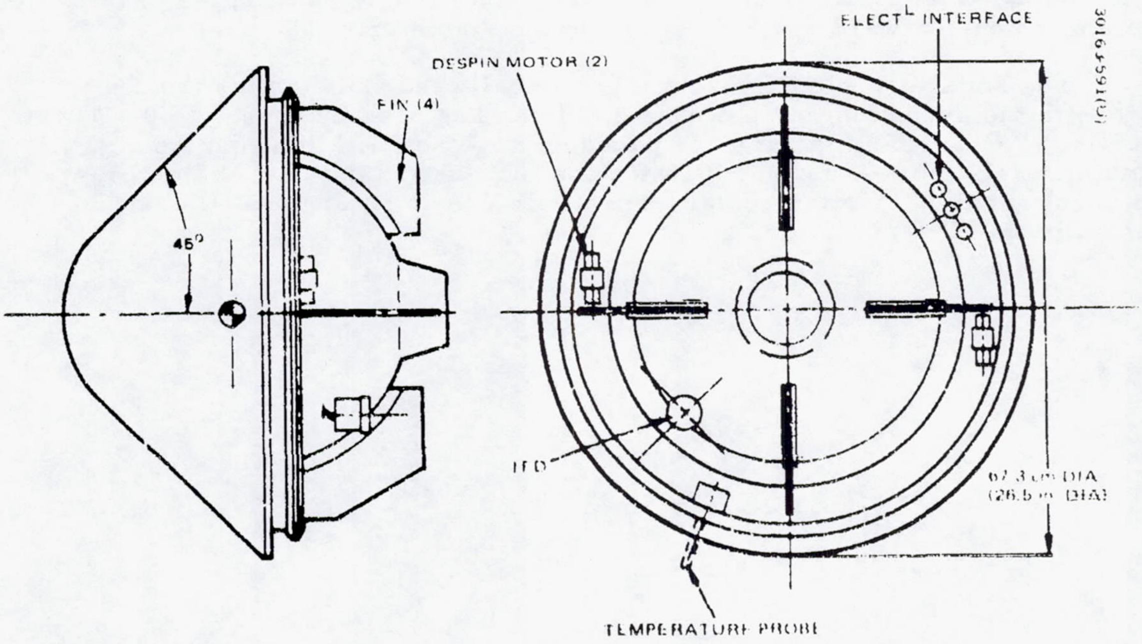

FIGURE 5.1-10. ATLAS/CENTAUR SMALL PROBE CONFIGURATION

5.2 AERODYNAMICS/FLIGHT DYNAMICS

Summary

In order to accomplish the mission defined for the Pioneer Venus program, the deceleration module must provide a platform sufficiently stable to allow retrieval of data. This section presents data and analyses performed during the study that permit evaluation of the characteristics of the probe designs.

Aerodynamic characteristics were generated for sphere-cone configurations with a bluntness ratio of 0.5 for cone angles of 45 and 55 deg. Since the bluntness ratio was held constant, overall dimensions are not a factor and the analyses, therefore were applicable to both Thor/Delta and Atlas/Centaur configurations.

Utilizing the aero characteristics, detailed analyses were conducted of the motion of the different configurations during entry. Results show that the dynamics of both the 45 and 55 deg configurations are acceptable, provided satisfactory center of gravity locations can be maintained.

Studies conducted of the deceleration characteristics of the large probe indicate that subsonic conditions, desired for parachute deployment, are reached at sufficiently high altitude to permit experiment initiation.

Tests were conducted in two different facilities to examine in detail the subsonic terminal fall characteristics of the small probe. These tests led to a change in configuration (from 55 to 45 deg) and affirmed the acceptability of the final small probe design.

Wind shear effects were examined to determine reaction of the small probe during the terminal fall portion of the trajectory. General results show that if the wind shear is not overly severe, attitude constraints (required for communications) will not be exceeded.

Requirements

Vehicle motion requirements are dictated by mission objectives that are ultimately aimed at successful atmospheric reconstruction. To meet these objectives, it is necessary to have a well characterized aerodynamic shape that can be packaged within the booster limitations and maintain a center of gravity position compatible with both static margin and dynamic damping requirements. Furthermore, and more specifically, the probes must be developed sufficiently that the scientific instrument payload may be put into operation above 66 km altitude. For the large probe, this requires subsonic parachute deployment conditions above about 67 km. Parachute deployment conditions are directly related to the vehicle ballistic coefficient and, hence, drag coefficient, which then dictates a relatively blunt shape.

For the small probes, evaluation must include not only the initial entry portion, but also the terminal descent region in which the major portion of the mission takes place.

In the Thor/Delta mission, an additional restriction was placed on angle of attack excursions, which were required to be less than 10 degrees. This was caused by the directional antenna used in an extremely weight-limited design. The Atlas/Centaur design uses a hemispherical coverage antenna and the restriction does not apply.

Analysis

Six degrees of freedom aerodynamic characteristics, including drag, normal force, center of pressure, and pitching moment variations with angle of attack, Mach number, and altitude were generated for both the 45 deg small probe and the 55 deg large probe compatible with the Thor/Delta booster. Available ground test data in air for 40 to 60 deg sphere cones were compiled for low Mach numbers. For hypersonic Mach numbers in CO_2 (to simulate the Venus atmosphere), both equilibrium transonic and unsteady flow computations were made. Theoretical variations with altitude were generated by using Newtonian and free molecular flow computer programs coupled with a slip flow correlation. Earlier studies of large cone angle bodies were used as guidelines in establishing coefficient trends.

The configurations studied were sphere cones with bluntness ratios of R_N/R_B 0.5 and reference c.g.s located at the first maximum base diameter. The configurations differ in forebody cone angle, base radius, and afterbody definition. Sketches of both probes and details of the aerodynamic coefficients developed for the configurations are given in Appendix A.

Large Probe Entry Motion Studies

The large probe configuration model used in this motion study has the following characteristics:

Cone angle, θ_c	55 deg
Base diameter, d_B	1.16 m (46 in.)
Nose radius/base radius, r_n/r_b	0.5
Weight, W	136 kg (299 lbs)
Roll moment of inertia, I_x	1080 kg-m^2 (7.21 slug-ft^2)

Transverse moment of inertia, I_y	821 kg-m^2 (5.52 slug-ft^2) (average)
C.G., X_{cg}	0.0213 m (0.84 in.) forward of base diameter point

The aerodynamic characteristics employed are described in Appendix A.

The nominal trajectory entry conditions used were:

Velocity, V	11.2 km/sec
Path angle, γ	41 deg (measured down from local horizontal)
Altitude, h	150 km

Basic motion performance was computed for bounding entry path angles of 35 and 60 deg.

The nominal motion initial conditions used are:

Total angle of attack, δ	10 deg
Roll rate, p	15 rpm

The variations in initial conditions, mass properties, and aerodynamic characteristics considered are:

Roll moment coefficient, C_{l_o}	0.5×10^{-4} for $h < 92$ km
Roll damping coefficient, C_{l_p}	$0 > C_{l_p} > -0.02$
Lateral c.g. offset, C_2	0.254 cm (0.1 in.)
Principal axis tilt, ϵ_3	1 deg
Trim angle of attack, α_o	1 deg
Longitudinal c.g. shift, X_{cg}	4.66 cm (0.84 in.) aft nominal location
Dynamic stability, derivative, $C_{m_q} + C_{m_{\dot{\alpha}}}$	reduced to -0.1 supersonically
Initial angle of attack	40 deg

These off-nominal conditions were investigated to ensure the adequacy of the large probe motion characteristics.

A very conservative 10-deg entry angle of attack was assumed based on an analysis of these contributors: separation tipoff rates, probe-bus spin axis misalignment, and probe transverse products of inertia. The assumptions (also quite conservative) for these contributors and resultant angle of attack errors are shown in Table 5.2-1. Even the worst case summation results in half the value used in the motion analysis.

The baseline trajectory and motion performance of the large probe was computed using nominal conditions described previously, nominal aerodynamic characteristics, and no mass or aerodynamic asymmetries. A set of trajectory and motion parameter histories for this case (case 1) is furnished in Figure 5.2-1. Angle of attack and roll rate histories for a maximum spin rate condition are shown in Figure 5.2-2. An angle of attack history is presented in Figure 5.2-2 for the defined worst case design condition. Figure 5.2-3 presents a composite plot of angle of attack from all conditions examined to show the expected bounds on angle of attack motion. Table 5.2-2 provides a tabulation of inputs to, and key results from a matrix of trajectories computed.

The motion simulations show that angle of attack converges rapidly from its 10-deg value at entry, to a minimum in the baseline case of about 0.2 deg by about 15 sec after entry. The divergence of motion, which occurs subsequently, is due to the transonic dynamic instability predicted for the large probe: $C_{m_q} + C_{m_{\dot{\alpha}}}$ is positive (destabilizing) for angles of attack less than about 10 deg between Mach numbers of 0.6 and 1.6. In the 60 to 70 km altitude range, terminal fall velocity is of the order of about Mach 0.6.

TABLE 5.2-1.—ANGLE OF ATTACK ERRORS

Error Source	Magnitude	Angle of Attack Error	
		Bias, deg	Coning, deg
Separation tipoff rates (with Pe = 15 rpm)	2 deg	1	1
Probe/spacecraft misalignment in spin axes	1 deg	0.8	0.8
Probe products of inertia	4.92 kg-m^2 (0.033 slug-ft^2)	0.8	0.8
	Sum	2.6	2.6
	RSS	1.54	1.54
Nominal (sum of RSSs) = 3.1 deg Worst case (total sum) = 5.2 deg			

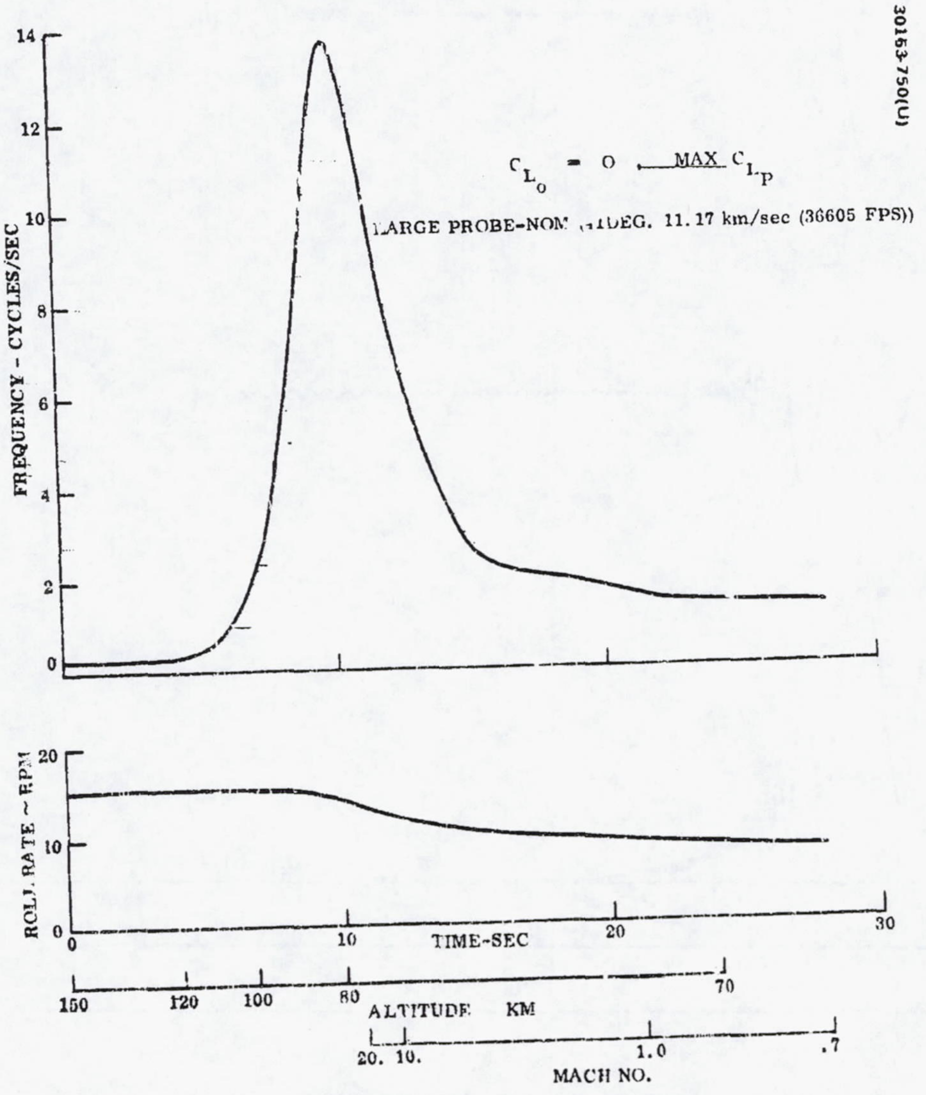

FIGURE 5.2-1. BASELINE HISTORY (CASE 1)

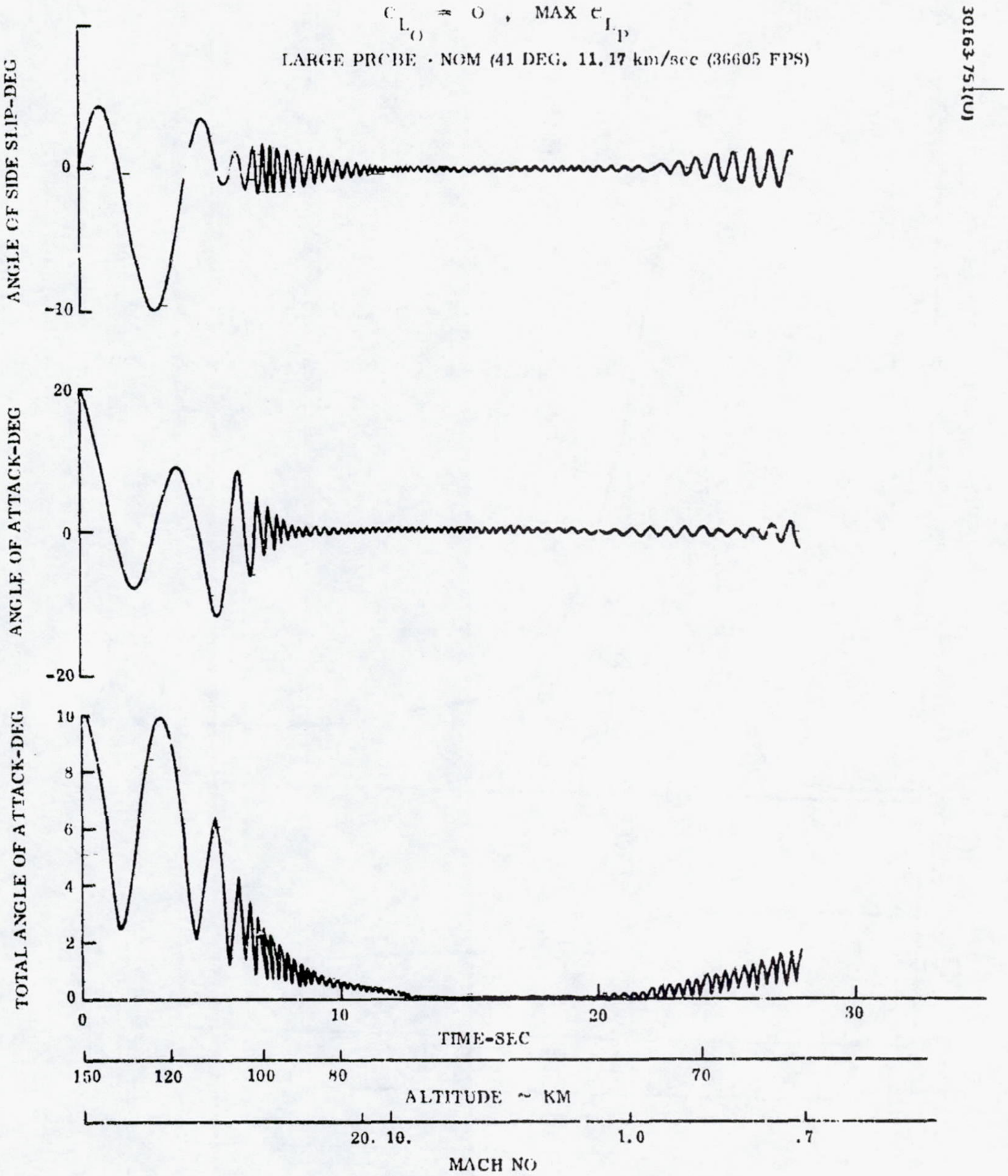

FIGURE 5.2-1. (CONTINUED) BASELINE HISTORY (CASE 1)

30163-75(U)

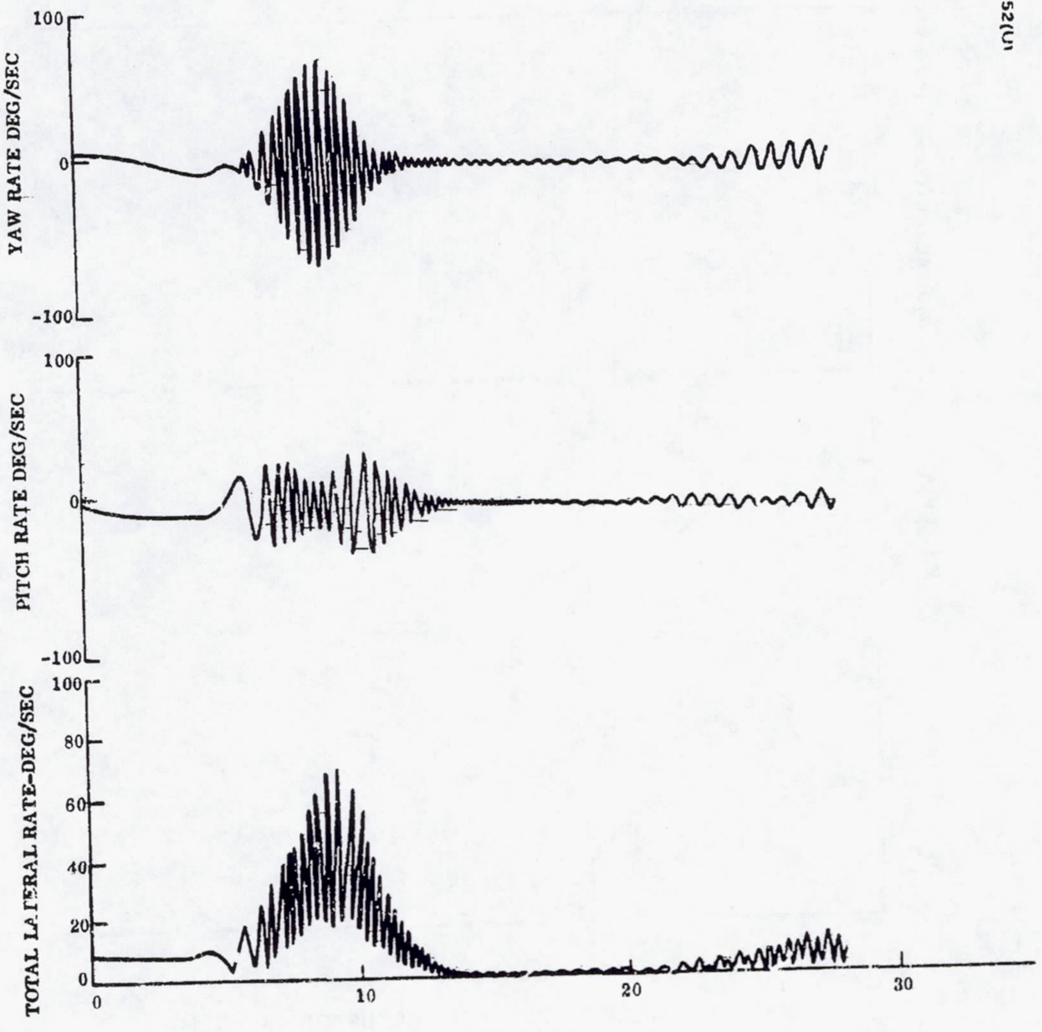
LARGE PROBE-NOM(41 DEG. 11.17 km/sec (36605 FPS))

30263-752(U)

FIGURE 5.2-1. (CONTINUED) BASELINE HISTORY (CASE 1)

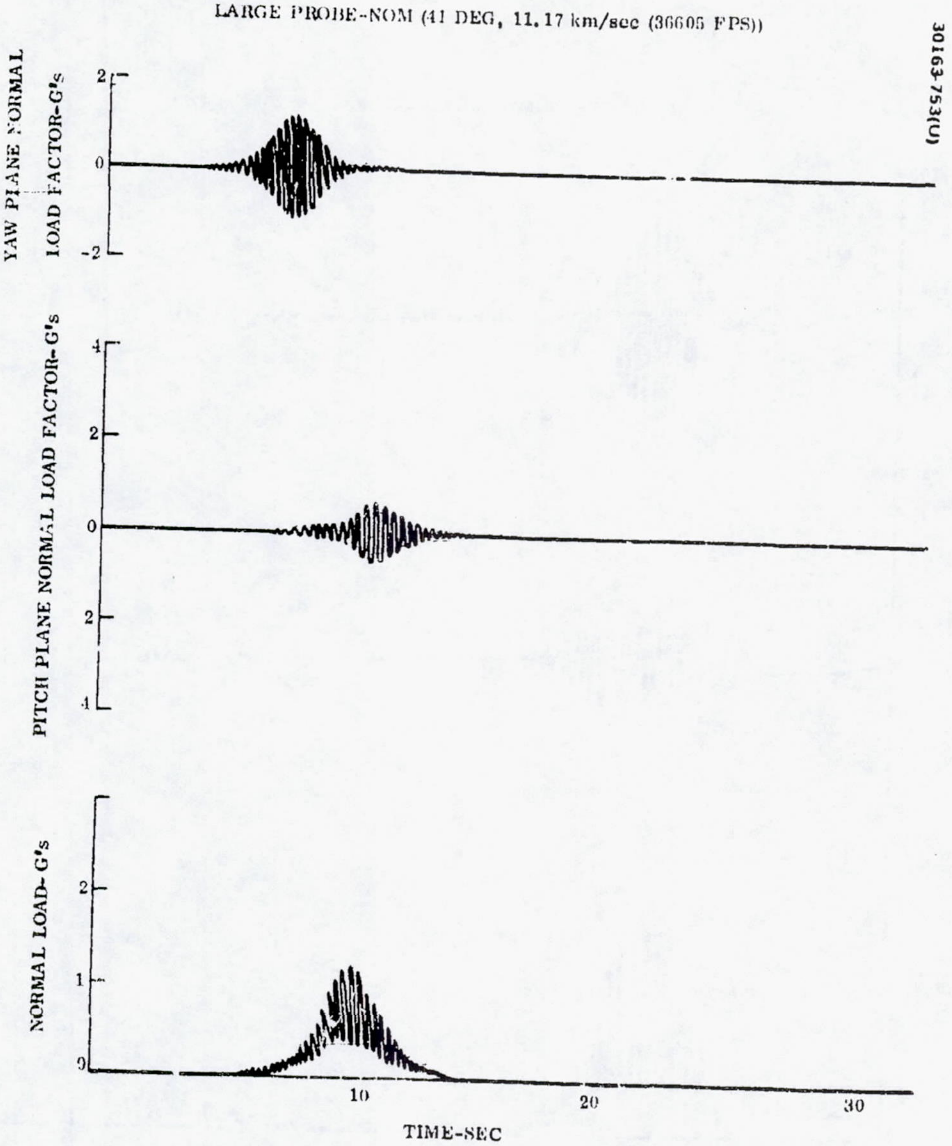

FIGURE 5.2-1. (CONTINUED) BASELINE HISTORY (CASE 1)

LARGE PROBE--ALFHA 0=40

30163-754(U)

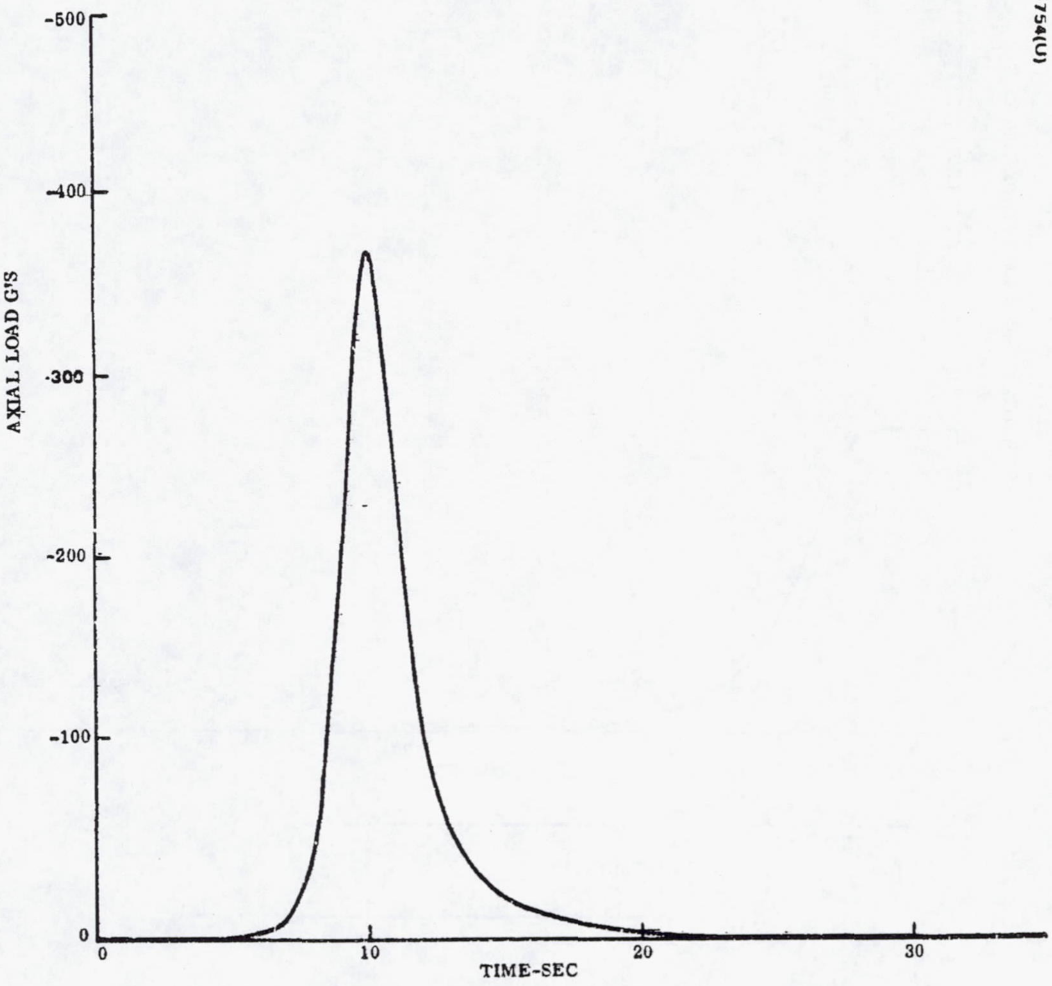

FIGURE 5.2-1. (CONTINUED) BASELINE HISTORY (CASE 1)

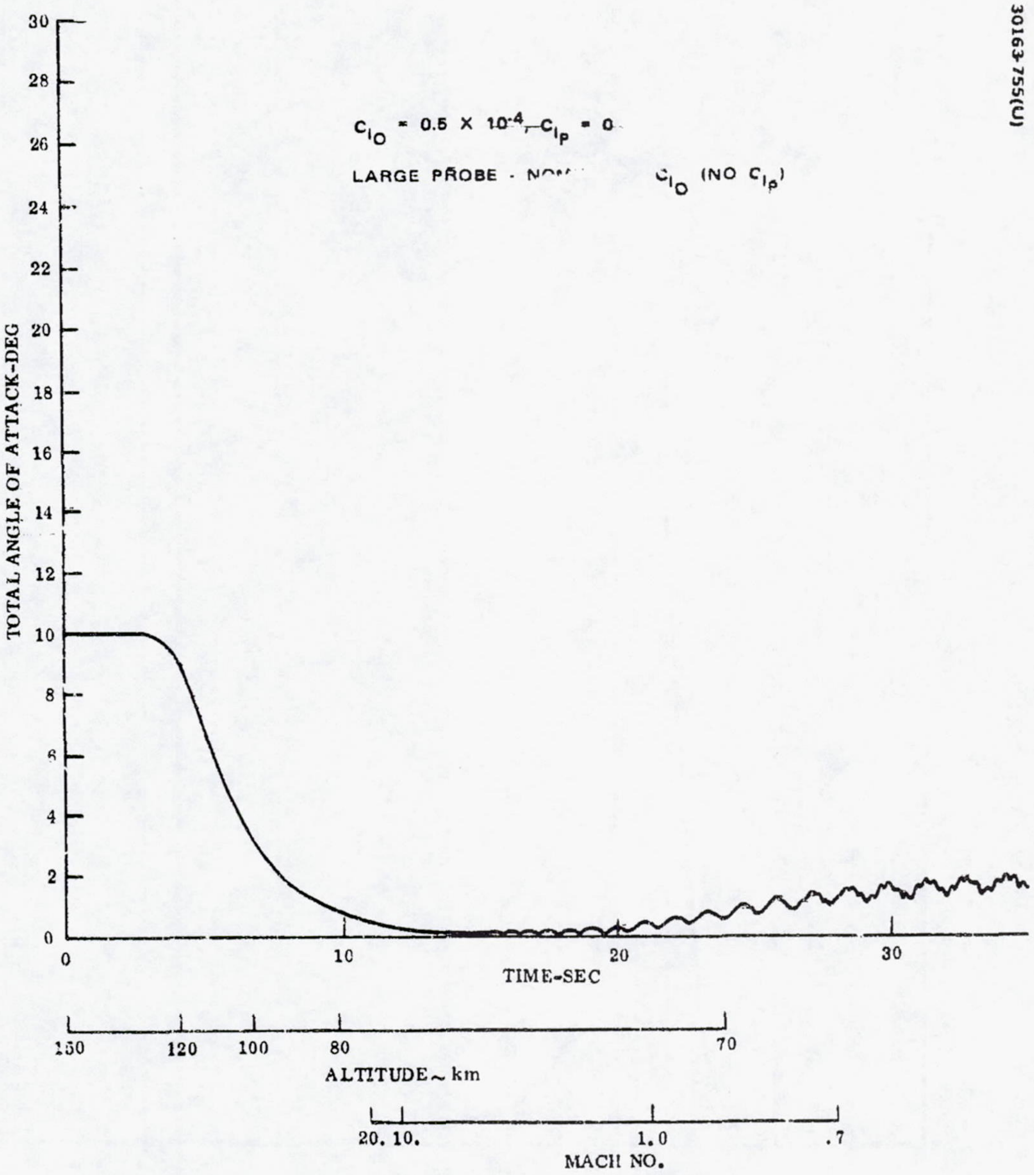

FIGURE 5.2-2. BASELINE HISTORY (CASE 4)

30163-755(U)

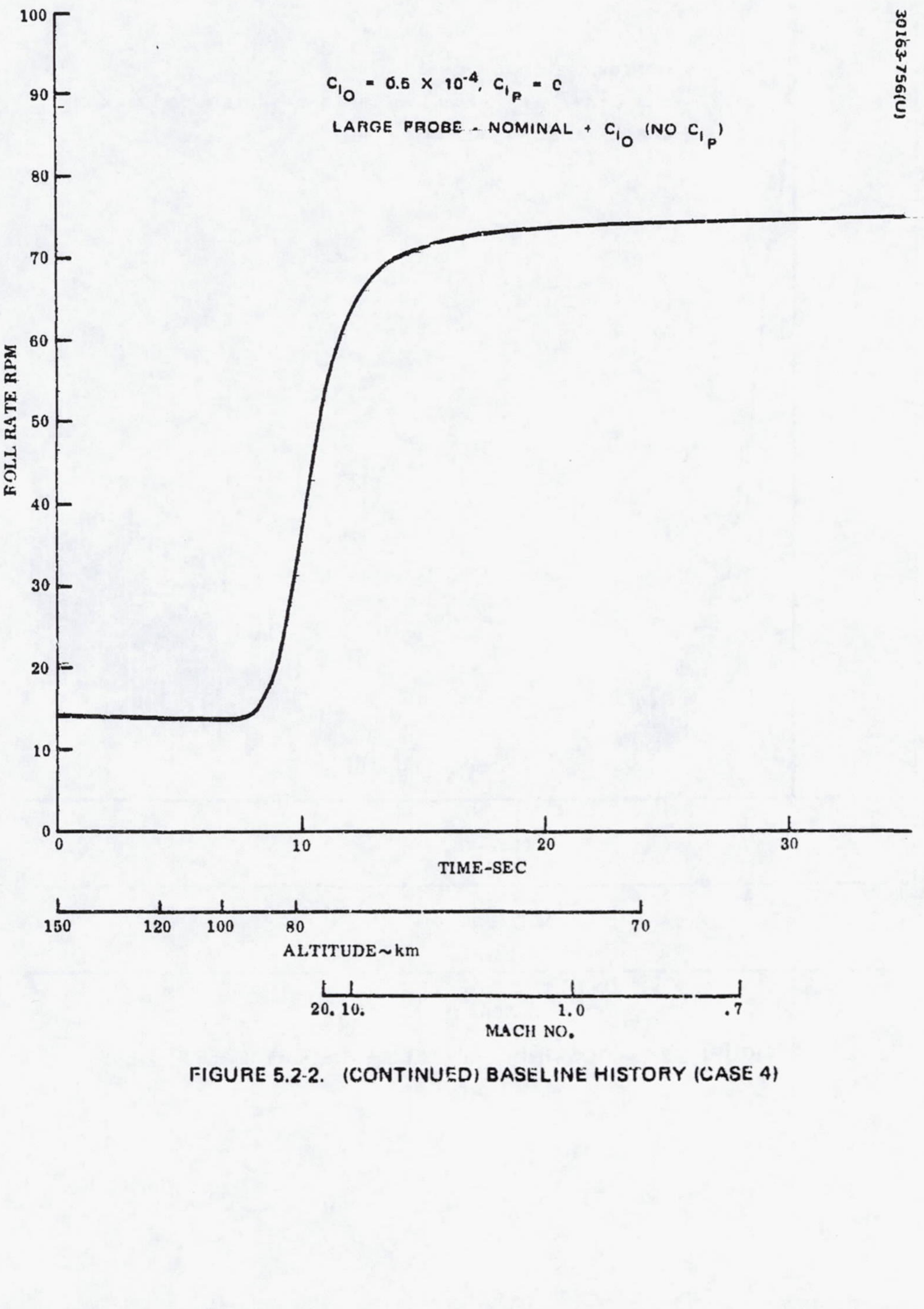

FIGURE 5.2-2. (CONTINUED) BASELINE HISTORY (CASE 4)

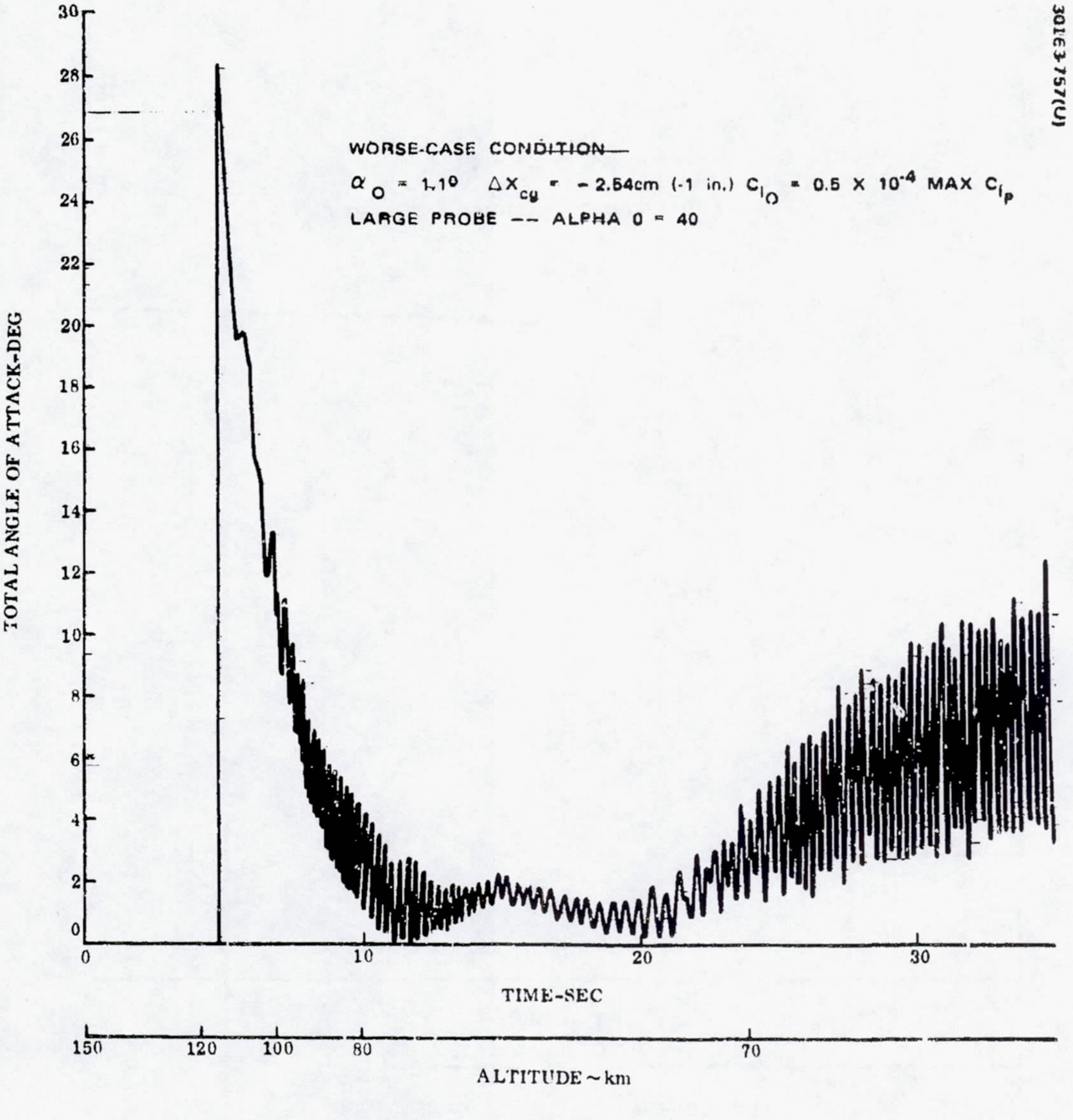

FIGURE 5.2-2. (CONTINUED) BASELINE HISTORY (CASE 4)

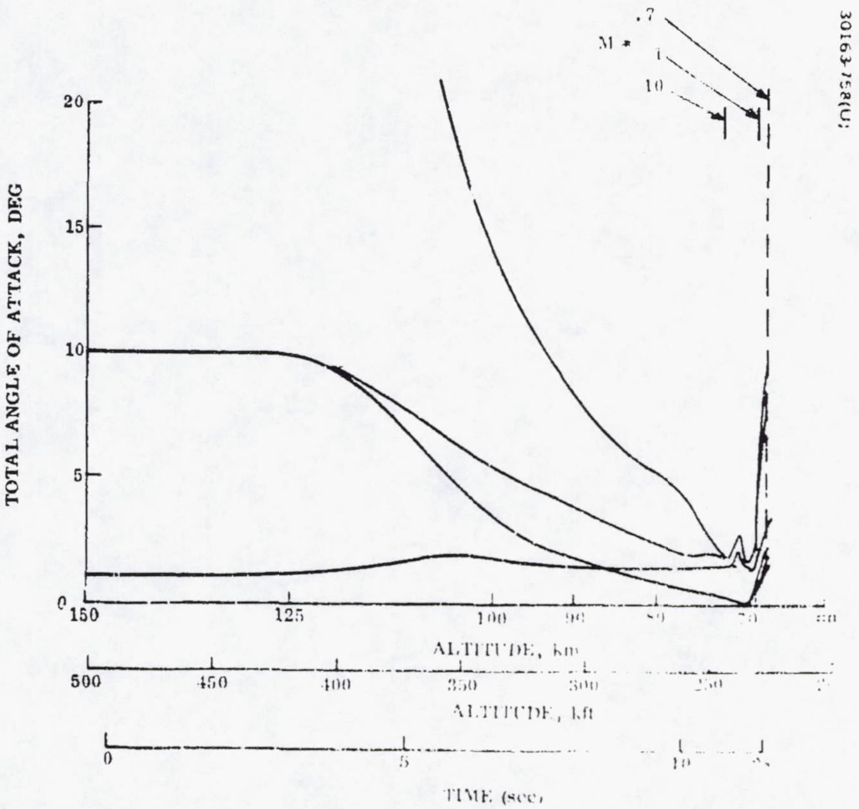

FIGURE 5.2-3. LARGE PROBE ANGLE OF ATTACK (UPPER ENVELOPE) HISTORIES

TABLE 5.2-2. PARAMETERS VARIED AND KEY RESULTS FROM LARGE PROBE MOTION COMPUTATIONS

[illegible]	[illegible]	[illegible]	[illegible]
[illegible]	Nominal	[illegible]	[illegible]
[illegible]	Nominal	[illegible]	[illegible]
[illegible]	Nominal	[illegible]	[illegible]
[illegible]	Nominal	[illegible]	[illegible]
[illegible]	Nominal	[illegible]	[illegible]
[illegible]	Nominal	[illegible]	[illegible]
[illegible]	Nominal	[illegible]	[illegible]
[illegible]	Nominal	[illegible]	[illegible]
[illegible]	Nominal	[illegible]	[illegible]
[illegible]	Nominal	[illegible]	[illegible]
[illegible]	[illegible]	[illegible]	[illegible]

For motion profiles that do not involve large angles of attack or traverse regions in which significant nonlinear aerodynamic coefficients exist, or aerodynamic, mass, or inertia asymmetries, then different entry angles of attack profiles can be estimated from any given one by simply rationing the two entry angle of attack values. Thus the baseline case (Case 1), which had an initial entry angle of attack of 10 deg and an angle of attack amplitude at Mach 0.7 of 1.7 deg, would have an angle of attack of only 3/10 x 1.7 deg or 0.5 deg at Mach 0.7 if its entry angle of attack were a more probable value like 3 deg rather than 10 deg. This observation applies to cases 1, 4, 5, and 6.

The potential for spin-induced dynamic instability associated with vehicles of the large probe configuration was of concern. From the motion computations, the effect of a roll rate excursion produced by an approximately worst-case C_{l_0} of 0.5×10^{-4} was found to have negligible effect on angle of attack amplitudes (case 4). Even without roll damping, the maximum roll rate obtained was 76 rpm at M = 0.7 (Figure 5.2-2). Comparison of the δ history from this case (Figure 5.2-2) with the baseline history (Figure 5.2-1) shows that the amplitudes are virtually the same. It may be observed, however, that the character of these two histories is different. The difference is due to the different initial amplitudes of the high and low frequency motion arms input to the motion computations. There is only a minor effect to be seen in varying the relative amplitudes of the motion arms on the total angle of attack amplitudes during re-entry.

The angle of attack history for the condition defined as worst-case for design (case 9) is presented in Figure 5.2-2. Inputs to it were:

δ_e 40 deg

α_0 1.1 deg

ΔX_{cg} 4.66 cm (-1.84 in.) (reduced static stability)

(Also included was C_{l_0} 0.5×10^{-4}, but as already shown, its effects on motion are negligible.)

This condition, with its 40 deg entry angle of attack, represents a failure situation, such as would result from a probe/spacecraft separation failure. Its inclusion does not imply that such a condition is considered probable, but rather to show that the resulting probe motion is acceptable, even under the combination of severe off-nominal assumptions.

The peak envelope value of δ obtained at M = 0.7 was about [illegible] deg. The apparent divergence from 13 to 15 sec is due to the predicted decrease in static stability in the supersonic Mach number regime (reaching a minimum at Mach = 3). Representation of aerodynamic trim by a constant trim moment results in a substantial increase in the resultant trim angle of attack. It can be seen that the δ increase is a trim angle increase and that motion amplitudes about trim are essentially unaffected.

In all cases studied, without exception, the peak amplitudes of [illegible] at Mach = 0.7 are bounded by about 1.7 and 9.6 deg. This can be seen by referring to Figure 5.2-[illegible] and Table 5.2-2.

Thus, it is seen that the motion is well-behaved throughout the entry phase. Dynamic angle of attack oscillations at parachute deployment are nominally of the 1 to 2 deg range, and are bounded under worst-case conditions by 10 deg.

Path angle variations within the 35 to 60 deg range considered have virtually no effect on initial motion convergence and on angle of attack amplitudes at Mach 0.7. Cases 5 and 6 were generated for γ of 35 and 60 deg, and key results are shown in Table 5.2-2.

Conclusions. The motion results show that the effects of a large lateral c.g. offset (0.1 in.), a large principal axis tilt (1 deg), a large trim angle of attack (1 deg), a large roll moment coefficient (0.5 x 10^{-4}), and a fairly far aft c.g. position 2.54 cm (1 in.) aft of base diameter point) can be tolerated. The observed tolerance for mass asymmetries and longitudinal c.g. position appears to allow for useful design flexibility within reason. The worst case angle of attack at Mach = 0.7 parachute deployment is 10 deg; deployment at Mach numbers as high as 1.0 can reduce this by about a factor of 5, but with a possible penalty to parachute design due to higher opening loads.

From this analysis it is therefore concluded that parachute deployment may take place as late as Mach 0.7 keeping (in the worst case) the deployment angle of attack motion within a ten-degree bound.

Small Probe Entry Motion Studies

Entry and descent motion have been simulated in six degrees of freedom for the small probes in which the nominal entry conditions were investigated, as well as combinations of off-nominal conditions. Of concern has been the adequacy of the dynamic stability characteristics aggravated by possible extraneous spin rate excursions during entry. In the following analyses, it is seen that the baseline small probe motion is indeed quite satisfactory.

The baseline small probe physical characteristics are shown in Table 5.2-3. Also shown are the entry conditions assumed in performing motion simulations. Aerodynamic characteristics as presented in Appendix A were used with additions made for simulating spin-damping as follows:

1) For simulations of the probe without spin-damping fins, a spin-damping parameter (C_{l_p}) value of -0.00[illegible] was used throughout the trajectory. This value was obtained from the Langley Spin Tunnel results.

TABLE 5.2-3. SMALL PROBE CONDITIONS SIMULATED

Configurational quantities	
Weight	26.1 kg (57.3 lb.)
Forebody cone half angle	45 deg
Bluntness ratio	0.5
Base diameter	0.585 m (1.917 ft)
Base area	0.268 m^2 (2.885 ft^2)
Roll moment of inertia	70 kg-m^2 (0.47 slug-ft^2)
Pitch moment of inertia	53.5 kg-m^2 (0.36 slug-ft^2)
Longitudinal c.g. location (forward of maximum diameter)	4.19 cm (1.65 in.)
Aerodynamic properties	Taken from Appendix A
Entry conditions	
Altitude	150 km
Velocity	11,150 m/sec (36,600 fps)
Flight-path angle	
Design range	20 to 90 deg
Value used in most of simulations	40 deg
Angle of attack	
Design range	0 to 35 deg
Value used in most of simulations	30 deg
Spin rate	15 rpm
Simulation techniques	
Numerical integration of the equations of motion in six degrees of freedom	

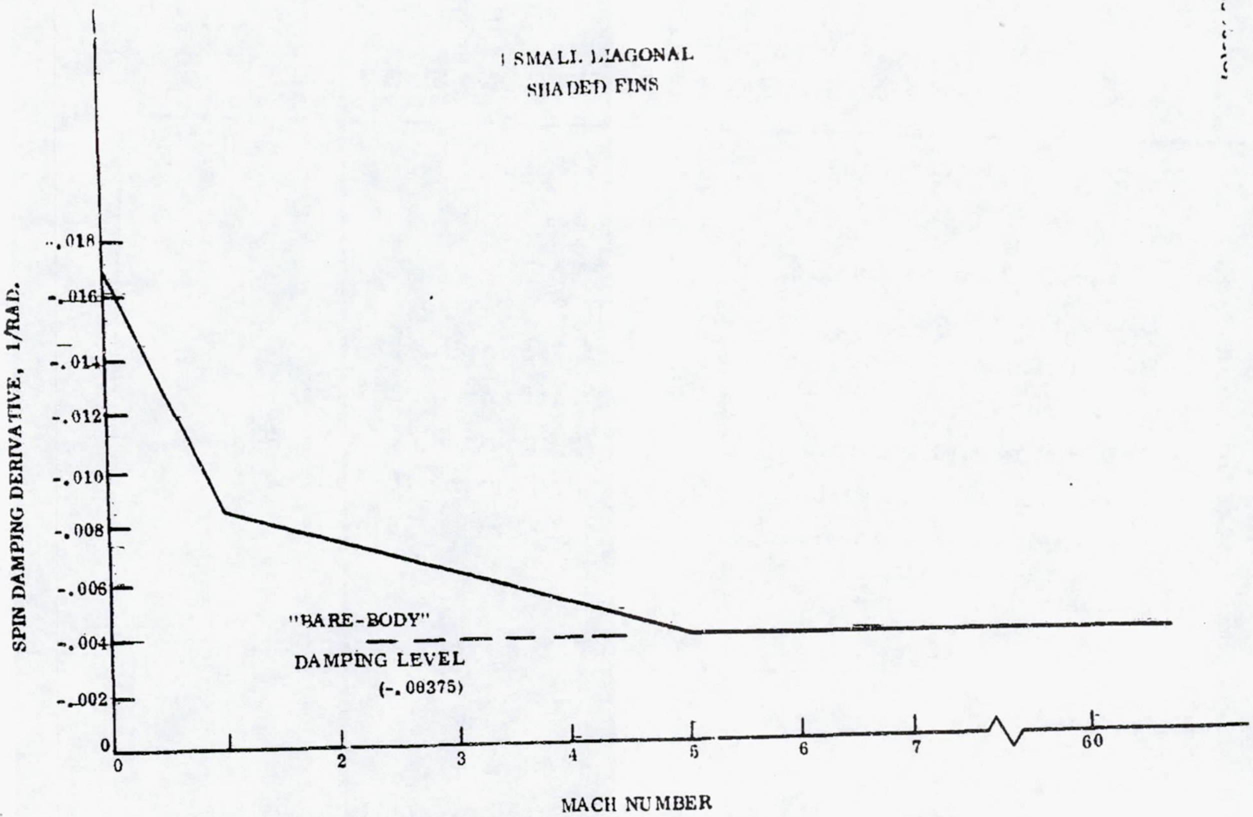

FIGURE 5.2-4. SPIN-DAMPING DERIVATIVES USED IN SIX DOF SIMULATIONS

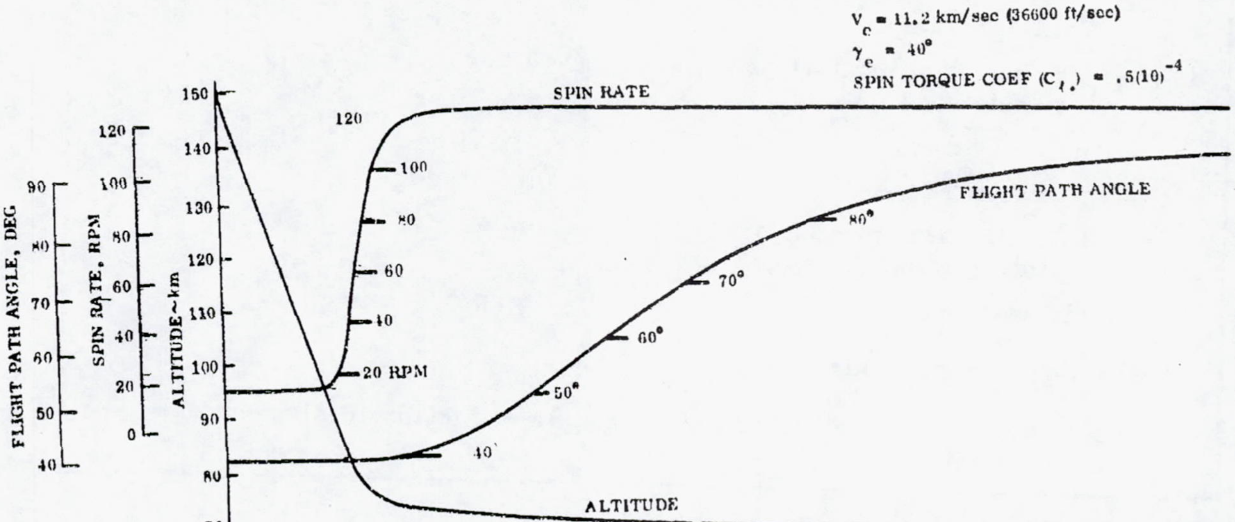

FIGURE 5.2-5. SMALL PROBE TRAJECTORY QUANTITIES

2) For simulations of the probe with spin-damping fins, spin damping data from the Langley results was again used. The configuration consisted of four diagonal fins mounted aft of the aeroshell. The C_{l_p} value derived was -0.0166, and the Mach number variation of C_{l_p} used in the simulations is shown in Figure 5.2-4.

Detailed trajectory and motion quantities during entry and into the beginning of the descent phase were computed. Typical results are provided in Figure 5.2-5.

The following observations are pertinent:

- Spin rate increases from its entry value of 15 rpm to about 120 rpm. The spin rate excursion results from the assumption of an ablation-induced spin torque coefficient of 0.5×10^{-4}. The spin rate excursion is contained by the influence of the aerodynamic spin-damping derivative, C_{l_p} whose value is -0.00375.
- Total angle of attack converges from its 30 degree entry value to about 0.2 degree at 18 seconds.
- A slight motion divergence (angle of attack increases from 0.2 to 0.9 deg) exists between the times of 18 and 30 sec. This is the transonic Mach number region where C_{m_q} is positive.
- The hypersonic stability is excellent.

Other brief observations are as follows:

Observation	Altitude, km	Time, sec
Maximum angular rates, 300 deg/sec	86.0	9
Maximum lateral loads, 8 g	83.0	9.5
Maximum dynamic pressure: (7000 psf) 335,000 N/m^2	80.5	10
Maximum axial loads: 360 g	80.5	10
Maximum pitching frequency: 25 Hz	80.5	10
Mach Number = 5.0	73.2	13.6
Mach Number = 1.3	71.0	19.2
Mach Number = 0.7	69.8	27.4

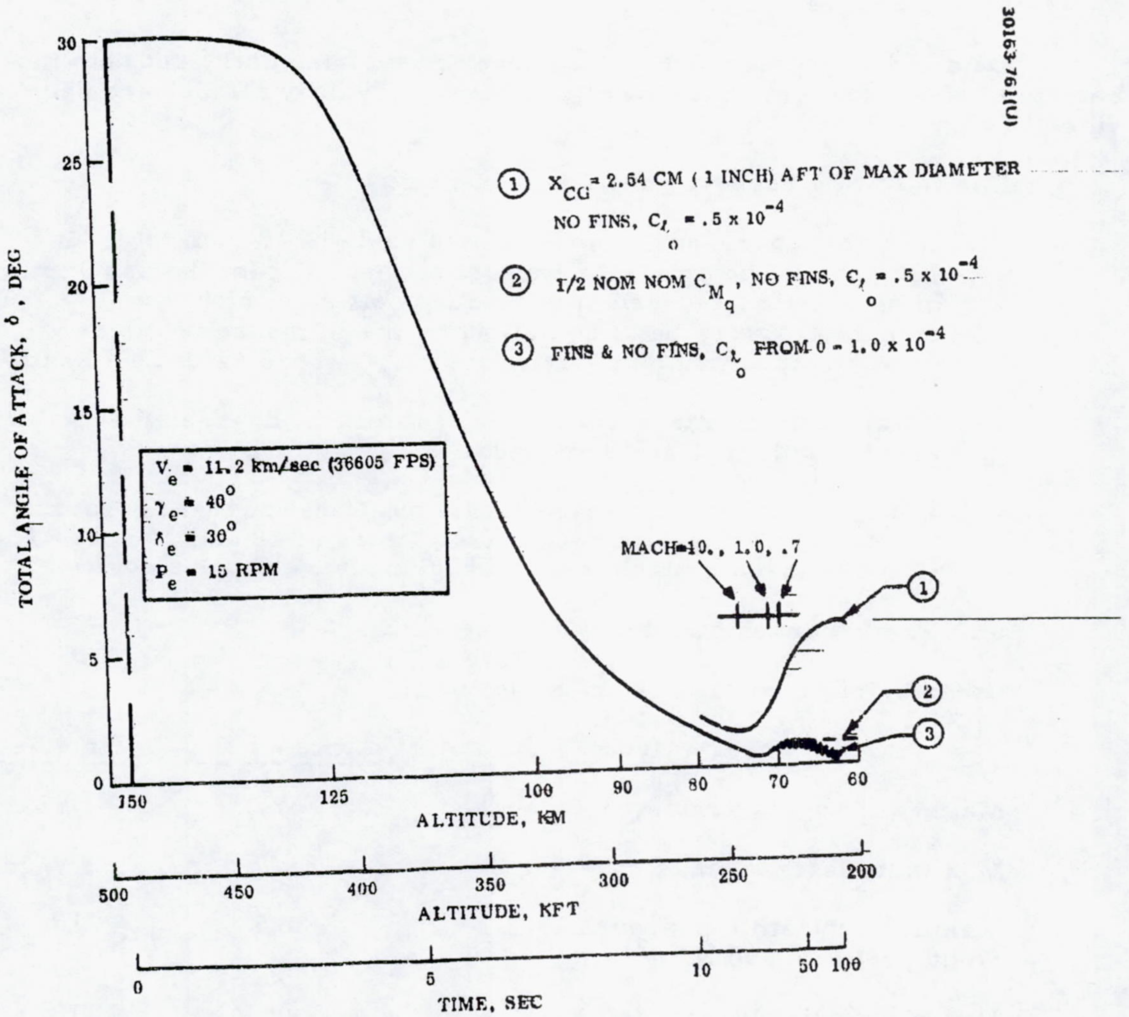

FIGURE 5.2-6. SMALL PROBE COMPOSITE UPPER ENVELOPE ANGLE OF ATTACK HISTORIES

The overall motion behavior of the simulation discussed is typical of all the simulations made. In particular, all featured a slight destabilization around 70 km altitude due to the effect of the predicted transient region of destabilizing C_{m_q}, aggravated in cases of high spin rates by spin-induced instability.

Simulations were made to determine the effect upon probe motion of entering at various other entry path angle conditions. Specifically, the conditions in Table 5.2-4 were used in the simulations.

The resulting behavior was very similar to that described earlier. The maximum angles of attack following the transonic divergence region were all small. Their differences resulted primarily from the fact that they all had different initial angles of attack at entry; the entry path angle itself had no dominating effect.

In addition to the 4 trajectory and motion simulations described thus far, 11 others were made wherein selected combinations of the following effects were investigated:

- Spin damping fins: (with and without)
- Spin torque coefficient: 0, 0.2, 0.5, and 1.0×10^{-4}
- Dynamic damping derivative: reduced by a factor of 2.0, subsonically, and throughout.
- C.G. location: nominal and 2.54 cm (1.0 in.) aft of base, 6.71 cm (2.65 in. aft of nominal).

A composite plot of total angle of attack envelope profiles for these cases is shown in Figure 5.2-6. The results of all but two cases fall nearly on top of each other, being very similar to the detailed case described earlier in this section. These include simulations with and without spin damping fins, and with roll torque coefficients up to 1.0×10^{-4} (five times the value taken as "design C_{l_o}"). Case 2 (note 2) in Figure 5.2-6 shows the

TABLE 5.2-4. SIMULATION CONDITIONS

γ_e, deg	α_e, deg	Spin Rate P_e, rpm	C_{l_o}	α_{max}, deg
70	9	15	0.2×10^{-4}	0.3
40	22	15	0.2×10^{-4}	0.6
20	31	15	0.2×10^{-4}	1.3

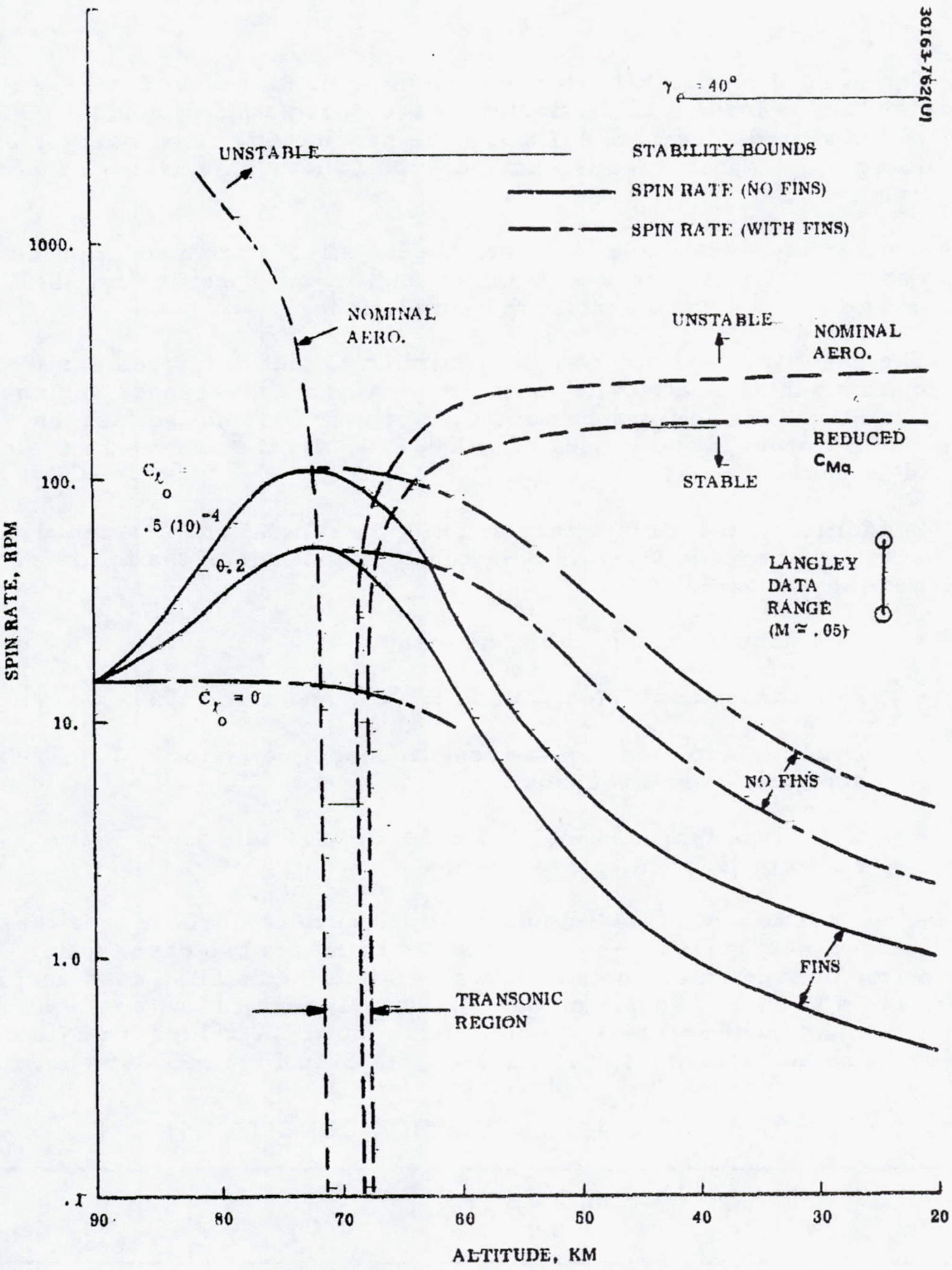

FIGURE 5.2-7. SMALL PROBE SPIN INDUCED STABILITY REGIONS

effect of reducing the subsonic damping parameter by a factor of 2.0 together with a C_{l_o} value of 0.5×10^{-4}. Here the angle of attack tends to "hang up" following the transonic region. However, its magnitude is small, namely 1.0 deg.

Finally, case 1 (note 1) in Figure 5.2-6 shows an angle of attack divergence to nearly 6 deg. This condition resulted from the assumption that the longitudinal c.g. was 2.54 cm (1.0 in.) aft of the base, and that C_{l_o} was 0.5×10^{-4}. In addition, the C_{m_q} value was halved throughout the entire trajectory, reflecting inferences obtained from the Langley tests.

While the latter behavior is undesirable, it is not catastrophic. More importantly, it should not be thought of as a design condition, since the current design c.g. location is ahead of the base. Rather, it shows what would happen <u>if the c.g.</u> were to be moved aft, and if there was a C_{l_o} of 0.5×10^{-4}.

More insight to the dynamic stability behavior as influenced by transonic aerodynamics and spin phenomena is gained from Figure 5.2-7. This figure consists of spin rate profiles corresponding to selected simulations discussed. Also shown are dynamic stability boundaries in the form of spin rate required to produce neutral stability. These boundaries were calculated from linear theory using the predicted (linearized) aerodynamic properties. The latter curves show that in a 3 km region around 70 km, the probe is unstable at all spin rates. This is the transonic region, wherein the dynamic damping derivative, C_{m_q}, is positive (destabilizing).

Spin rate profiles are shown with and without spin damping fins and for roll torque coefficient values up to 0.5×10^{-4}. Here it is seen that spin damping does not materially affect the spin rate until shortly before the transonic region is reached. Moreover, the effectiveness of the spin damping fins over that of the body alone is not realized to any great extent until after the transonic region has been traversed. (At altitudes below about 50 km, the fins produce a factor of about 4.5 reduction in spin rate compared to bare body results.) Therefore, at face value, the question of whether to use fins would seem unimportant.

Langley Data Implications

Results from the Langley Test Data, showed that spin rates corresponding to neutral dynamic stability were in the range 40 to 65 rpm — lower than the low subsonic Mach number predictions shown in Figure 5.2-6. Thus, the existence of a neutral stability roll rate is established qualitatively although the level is not correlated quantitatively. The LRC data do, however, indicate an area for concern as to the effect of lowering the stability levels.

Associated probe engineering design efforts have shown that the use of small aft-mounted, spin damping fins do not entail any serious design compromises. On the basis of the above discussions then, such fins are recommended for the base line design with prudence, conservatism and insurance providing the motivation.

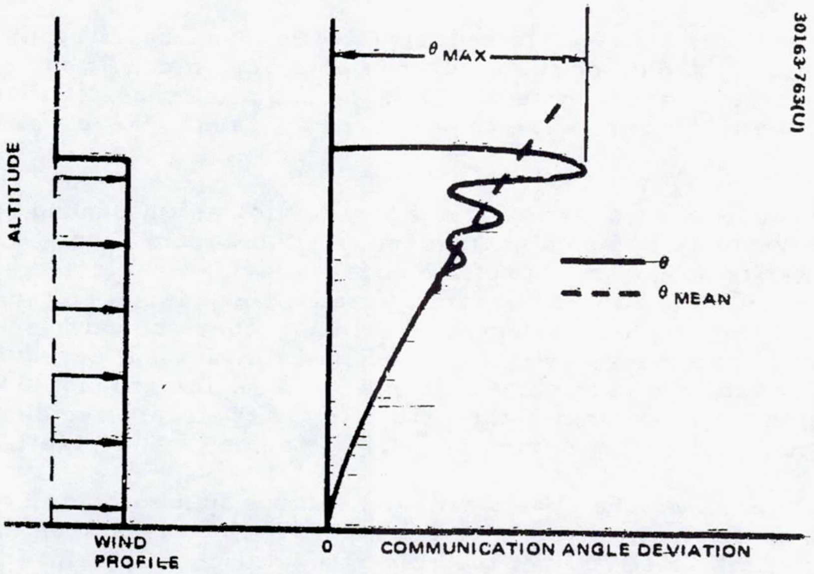

FIGURE 5.2-8. QUALITATIVE RESPONSE TO WIND SHEAR

Conclusions.

The small probe entry and descent motion behavior is good throughout the trajectory regime. The motion behavior is essentially insensitive to entry path angle over the design range, and is largely unaffected by off-nominal aerodynamic characteristics.

Effect of Atmospheric Horizontal Wind on Communication Angle Deviation.

This subsection evaluates the effects of atmospheric horizontal winds on the deviation of communication angles for the probes descent. Winds of two types are considered, "knife-edge shear" (discontinuous wind profile) and smooth wind gradients (wind linearly changing with altitude).

Knife Edge Shear. - The effect of a sharp wind shear is represented in this analysis as a time-discontinuity in the wind profile. The effect on communication angle of such a wind shear encounter is addressed. The vehicle (small probe or pressure sphere suspended on parachute) is assumed to be in stable terminal descent at the time of shear encounter. From this assumption, it follows that the effect on communication angle depends only upon the amount of wind velocity change, and not on the absolute wind velocity itself. Thus, the effects on communication angle response would be the same for a vehicle going from zero to 10 m/sec. horizontal wind, as it would going from 10 m/sec to 0, or from 40 to 30 m/sec. The resulting trajectory drift angles would of course be different. The qualitative response of communication angle (θ) to a knife-edged wind shear is illustrated in Figure 5.2-8.

The behavior of θ can be thought of as the sum of two constituents — a mean response profile and oscillations about the mean.

The mean profile is that which would result if the vehicle had pitch-damping, but had no pitching inertia, and as a result would trim into the relative wind instantly.

The oscillatory portion of the communication response profile is that generated by the static and dynamic pitching moment characteristics. Of special significance is the maximum value. In the limit, as the vehicle pitching moment of inertia and the dynamic damping characteristics approached zero, the communication angle would "overshoot" θ mean initial by exactly a factor of 2.0. The existence, however, of nonzero response time and damping produce an overshoot factor of about 1.8 (±0.1). This range applies both to the small probe as well as the pressure sphere/parachute system, and is in fact relatively insensitive to the actual pitching characteristics of the probes (moment of inertia, static and dynamic stability).

Using an average initial overshoot factor of 1.8, the maximum allowable wind shear was calculated for the small probe and the large probe/parachute. This information is shown in Figure 5.2-9.

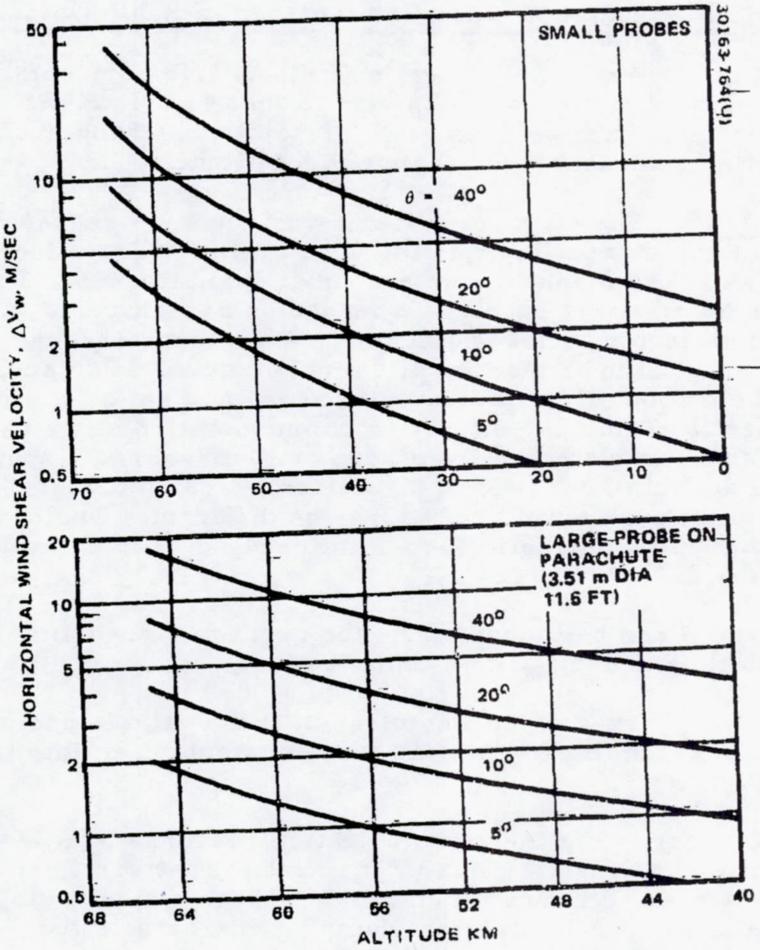

FIGURE 5.2-9. MAXIMUM ALLOWABLE HORIZONTAL WIND SHEAR FOR GIVEN COMMUNICATION ANGLE (θ) DEVIATIONS

The time to half damping of the oscillations can vary widely for the nall probe if the region of transonic instability just preceding terminal scent is considered. For regions of neutral dynamic stability (Mach mbers less than about 0.8) the time to half damping is bracketed by ± 2 sec at 65 km, decreasing somewhat exponentially with altitude to 5 ± 0.15 sec at the surface. Similar figures for the pressure sphere/ rachute system are approximately 2 ± 1 sec at 65 km, increasing to out 4 ± 2 sec by 45 km. This reversed behavior for the large probe is e primarily to the added mass characteristics of the parachute.

Wind Gradients. In a gradual wind gradient environment, the havior of the probes will be different from that in a wind shear vironment.

To the extent that the wind change is slow compared to the vehicle tching frequencies, rotational dynamics may be ignored; the vehicle effec- vely trims into the relative wind. This behavior is quantified as follows. efine the following quantities:

V_w horizontal wind velocity

V_p probe horizontal component of velocity

V_∞ probe descent velocity

The direction of the relative wind vector sensed by the probe, lative to the planet local vertical is given by

$$\theta = \frac{V_w - V_p}{V_\infty}$$

ssuming small angles.

The only horizontal component of force is drag assuming the vehicle ims instantly and writing the drag equation with altitude as the independent ariable, the communication angle is shown to be:

$$\theta = \frac{-\left(V_{po} - \frac{V'_w}{A}\right) e^{A(h-h_{ref})} + \frac{V'_w}{A}}{V_\infty}$$

REPRODUCIBILITY OF THE ORIGINAL PAGE IS POOR.

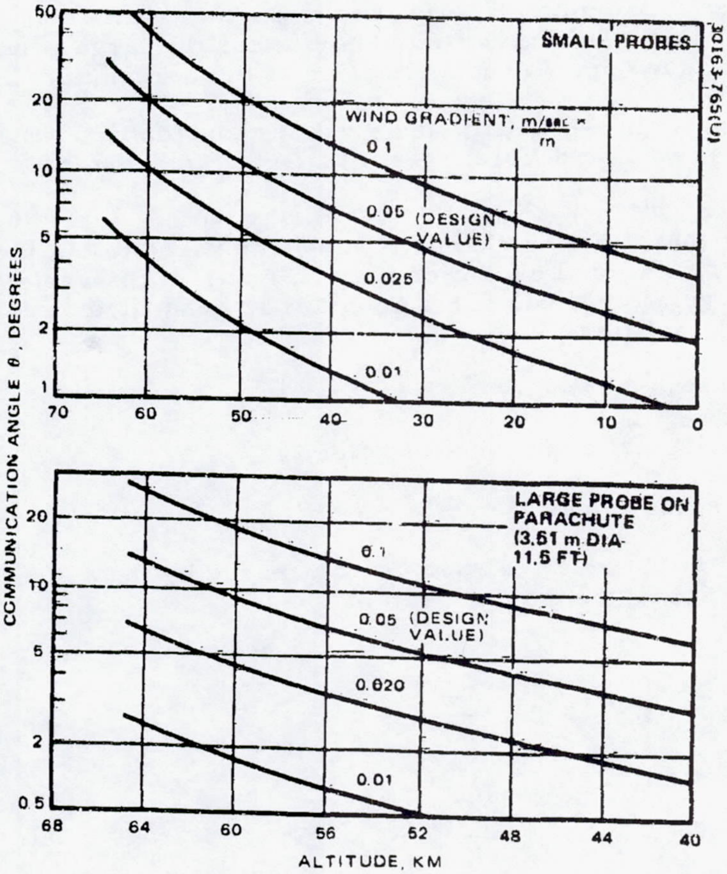

FIGURE 5.2-10. COMMUNICATION ANGLE DEVIATION DUE TO HORIZONTAL WIND GRADIENTS

where

V_{po} = arbitrary initial value of V_p

A = $S\rho C_D/2m$

h = altitude

h_{ref} = reference altitude

$'$ denotes derivative

The quantity "A" is also defined as:

$$A = \frac{C_D S \rho}{2\,m} = \frac{g_v}{V_T^2}$$

which yields a steady state solution for communication angle given by

$$\theta = \frac{-V'_w\,V_\infty}{g_v}$$

where g_v is the planetary gravitational acceleration.

Parametric curves of this steady state communication angle are shown in Figure 5.2-10 for the small probes and the large probe on the parachute.

According to Ainsworth and Herman* the maximum expected horizontal wind gradients are of the order 0.05 m/sec/meter altitude, occurring in the 40 to 50 km region. Figure 5.2-10 shows that with a gradient of 0.05, the resulting communication angle for the small probes is of the order 10 deg in this altitude region. The values are smaller by a factor of approximately 2.3 for the large probe, due to its lower descent velocity.

REPRODUCIBILITY OF THE ORIGINAL PAGE IS POOR.

---

*Ainsworth, J. E., and Herman, J. R., "An Analysis of the Venus Measurements," Published by Goddard Space Flight Center, December, 1972.

Conclusions. The orientation angle behavior of the descent probes due to atmospheric disturbances has been analyzed. General observations of the results are as follows:

1) The probe terminal descent velocity is a key parameter affecting the communication angle disturbance values. In the case of sharp wind shears, faster descent velocities produce smaller disturbances. Conversely, for linear wind gradients, faster descent velocities produce larger disturbances.

2) Little can be done through engineering design to alter the communication angle response characteristics shown. This is true because the response depends directly upon descent velocity, and descent velocity varies as the square root of probe ballistic coefficient. Thus, for instance, to change the communication angle sensitivity by a factor of 2.0 would require changing the ballistic coefficient by a factor of 4.0.

3) The communication angle response characteristics presented are virtually unaffected by the degree of static or dynamic stability or pitch moment of inertia values (the only assumption being that the configurations are both statically and dynamically stable).

4) When the term "communication angle deviation" is used, the word "deviation" is stressed. Specifically, the results shown in this section represent deviations from the nominal descent communication angle, which itself could be large (especially for the small probes, since they are targeted "a long way" away from the Venusian subearth point). This being true, a given deviation due to wind effects is not necessarily deleterious; and in fact could just as easily reduce the communication angle as increase it. The degree to which a wind induced deviation helps or hinders communications is determined by the direction (azimuth) of the wind with respect to the azimuth of the targeted point with respect to the subearth point.

Aerodynamic Test Summary

A series of tests have been conducted in the NASA Langley Vertical Spin Tunnel and the NASA/Ames Water Tank to evaluate qualitiative subsonic terminal fall stability for the small probe. Terminal stability is critical on the small probe due to the long time (approximately 1 hr) required to reach the planet surface after achieving terminal conditions and the 10 deg angle of attack limitation for communication. These tests have examined configuration variables, center of gravity locations, and the use of roll damping fins and their effects on the observed motion.

Initial and final wind tunnel test data are discussed in Appendix B with the analysis of that data and the water tank tests discussed in Appendix C and D, respectively.

REPRODUCIBILITY OF THE ORIGINAL PAGE IS POOR.

Thor/Delta Summary

As shown in six degree of freedom motion simulations in previous sections both 55 deg large and 45 deg small probes have acceptable entry characteristics compatible with mission requirements. Total angle of attack diversion on the large probe reaches a maximum at parachute deployment of <10 deg using worst case vehicle mass properties and entry conditions. Summary point mass plots for the large probe at a nominal entry path angle of 40 deg are shown in Figure 5.2-11. The altitude at which M = 0.7 occurs for a range of ballistic coefficients as a function of entry path angle is presented in Figure 5.2-12 for the large probe. As indicated in the figure significant altitude margin is available to deploy the parachute above the 66 km requirement.

Typical small probe entry trajectory parameters are presented in Figure 5.2-13. Maximum axial loads for both large and small probes as a function of path angle are provided in Figure 5.2-14. Since the large probe is designed for entry path angle variations between 20 and 60 deg the maximum loading will be limited by 500 g. Small probe entry path angles lie between 20 and 90 deg, which would indicate maximum loading of 535 g.

Atlas/Centaur Summary

Because of the change in cone angle of the large probe from 55 to 45 deg, the change in payloads, and vehicle mass properties brought about by the choice of the Atlas/Centaur booster, additional point mass trajectories were generated for both large and small probes. Results are provided in Figure 5.2-15 for the large probe and 5.2-16 for the small probe. Curve format has been changed from subsection 5.2.4 to permit direct comparisons between steep and shallow path angles. With the choice of the Atlas/Centaur, the small probe maximum axial g have increased from 535 to 590 while the large probe decelerations have gone from ≈490 to 510 g.

The altitude at which Mach = 0.7 is reached as a function of path angle for the Atlas/Centaur configuration may still be obtained from Figure 5.2-12 for a ballistic coefficient of 152 kg/m^2. At the nominal entry angle, 30 deg, the Mach 0.7 altitude is above 68 km, still sufficiently high to meet the requirements of reaching terminal velocity on the main parachute prior to 66 km.

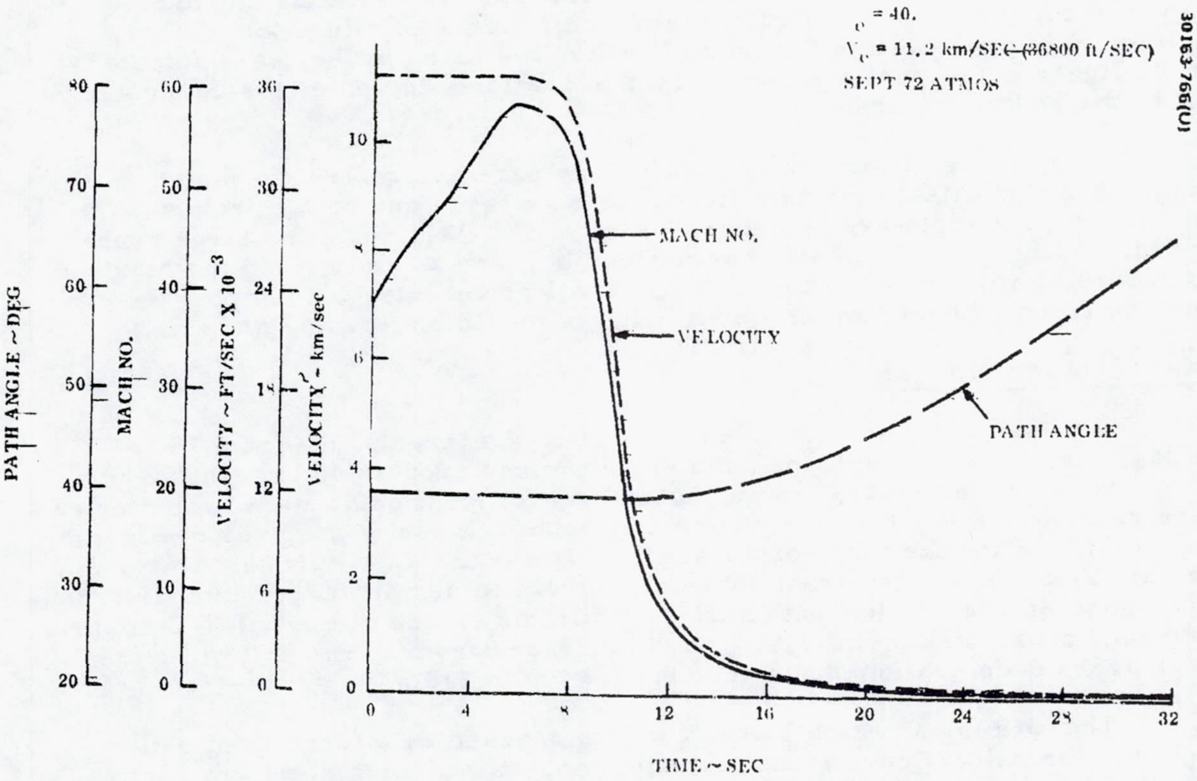

FIGURE 5.2-11. LARGE PROBE TYPICAL TRAJECTORY PARAMETERS

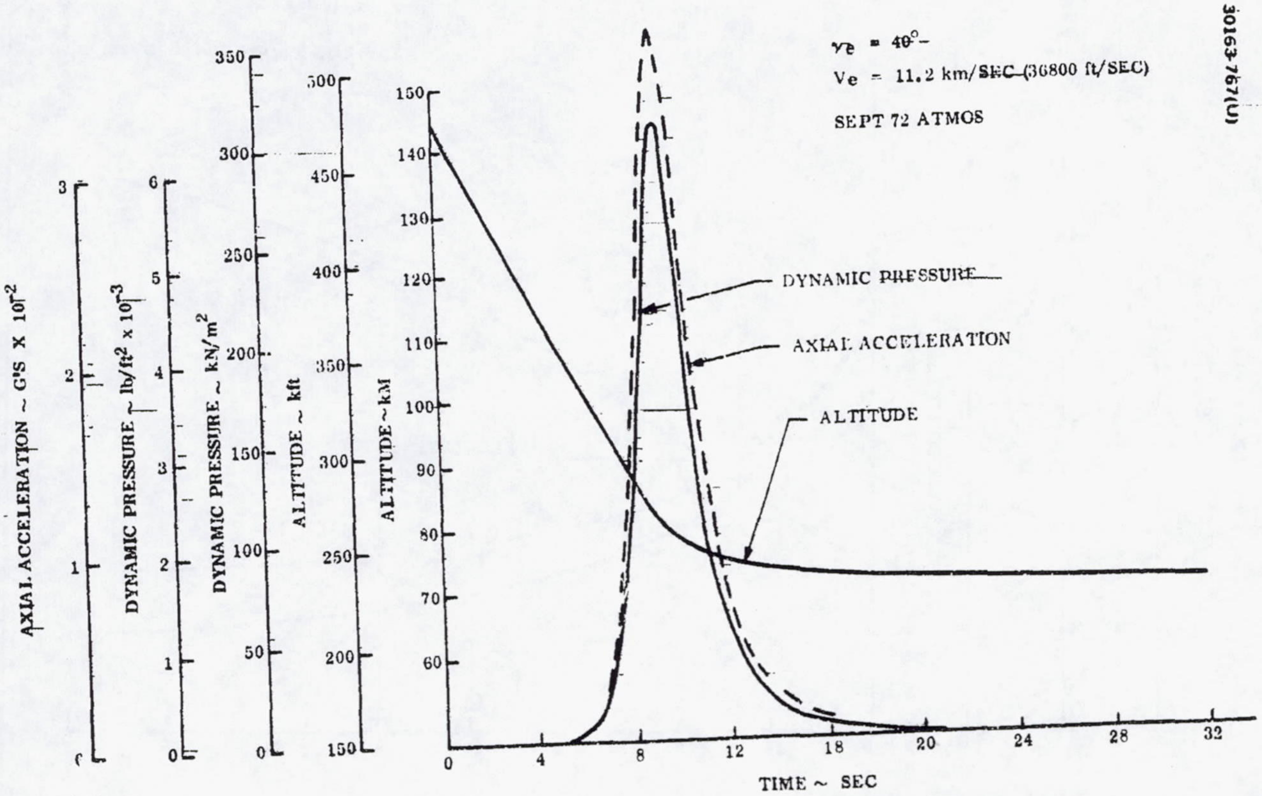

FIGURE 5.2-11. (CONTINUED) LARGE PROBE TYPICAL TRAJECTORY PARAMETERS

REPRODUCIBILITY OF THE ORIGINAL PAGE IS POOR

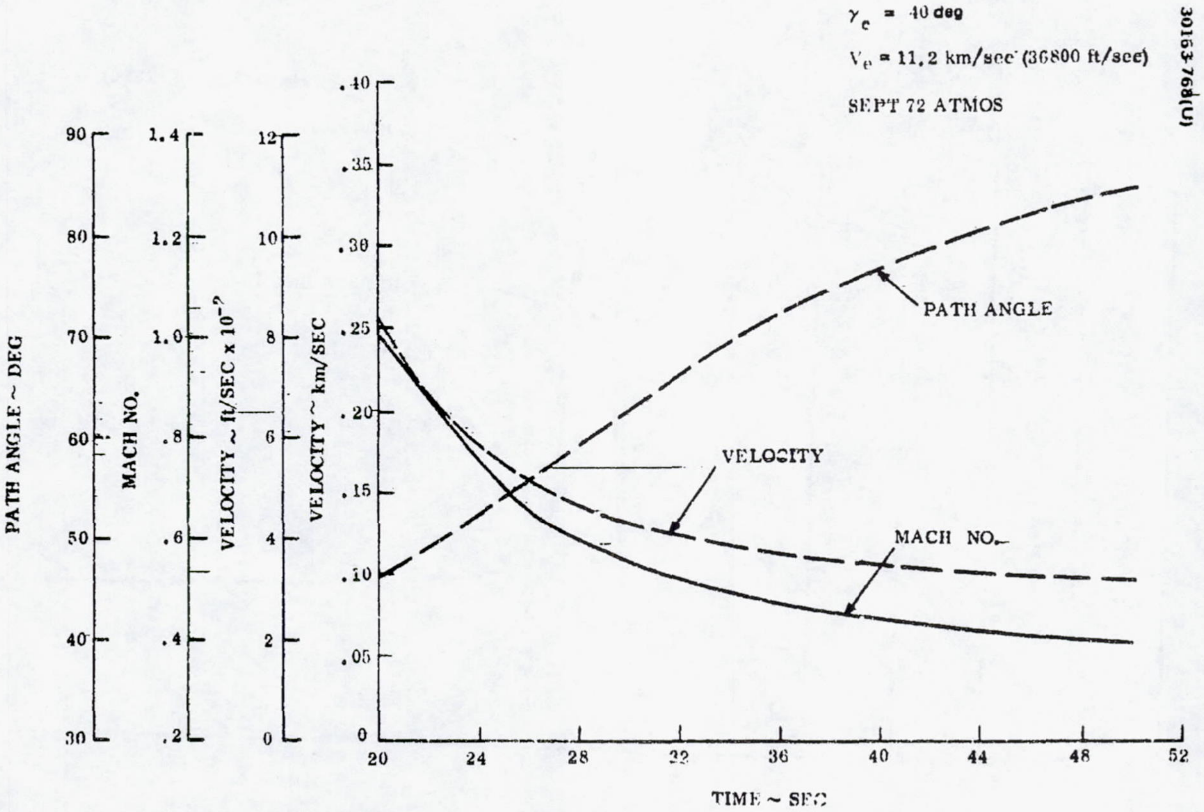

FIGURE 5.2-11. (CONTINUED) LARGE PROBE TYPICAL TRAJECTORY PARAMETERS

30163-768(U)

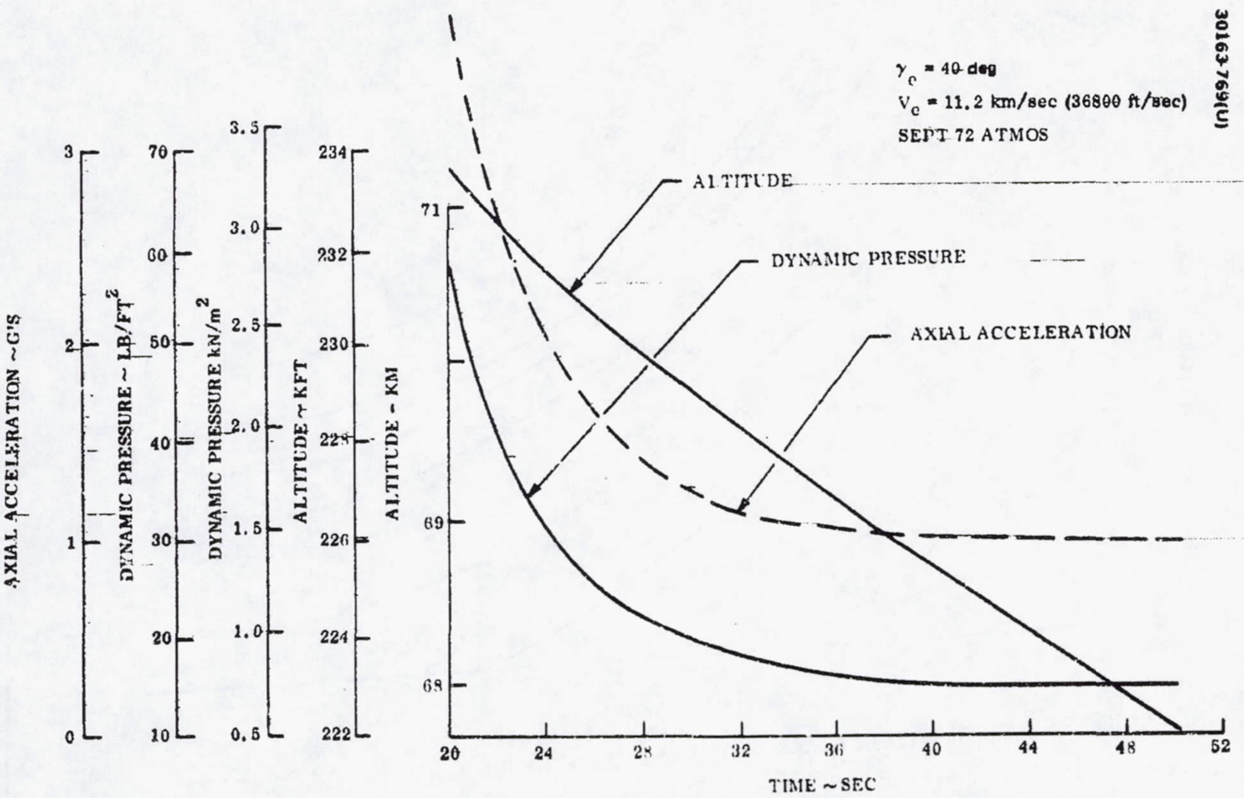

FIGURE 5.2-11. (CONTINUED) LARGE PROBE TYPICAL TRAJECTORY PARAMETERS

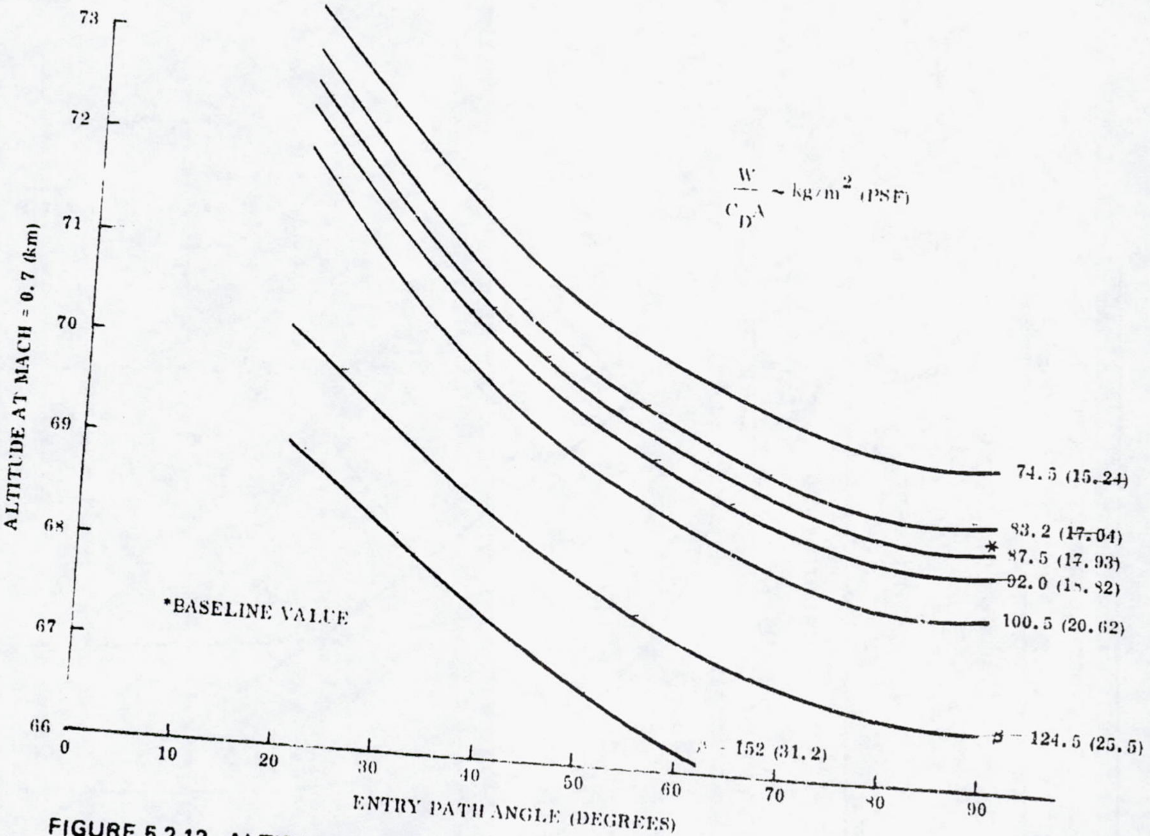

FIGURE 5.2-12. ALTITUDE AT MACH 0.7 VERSUS ENTRY PATH ANGLE FOR LARGE PROBE

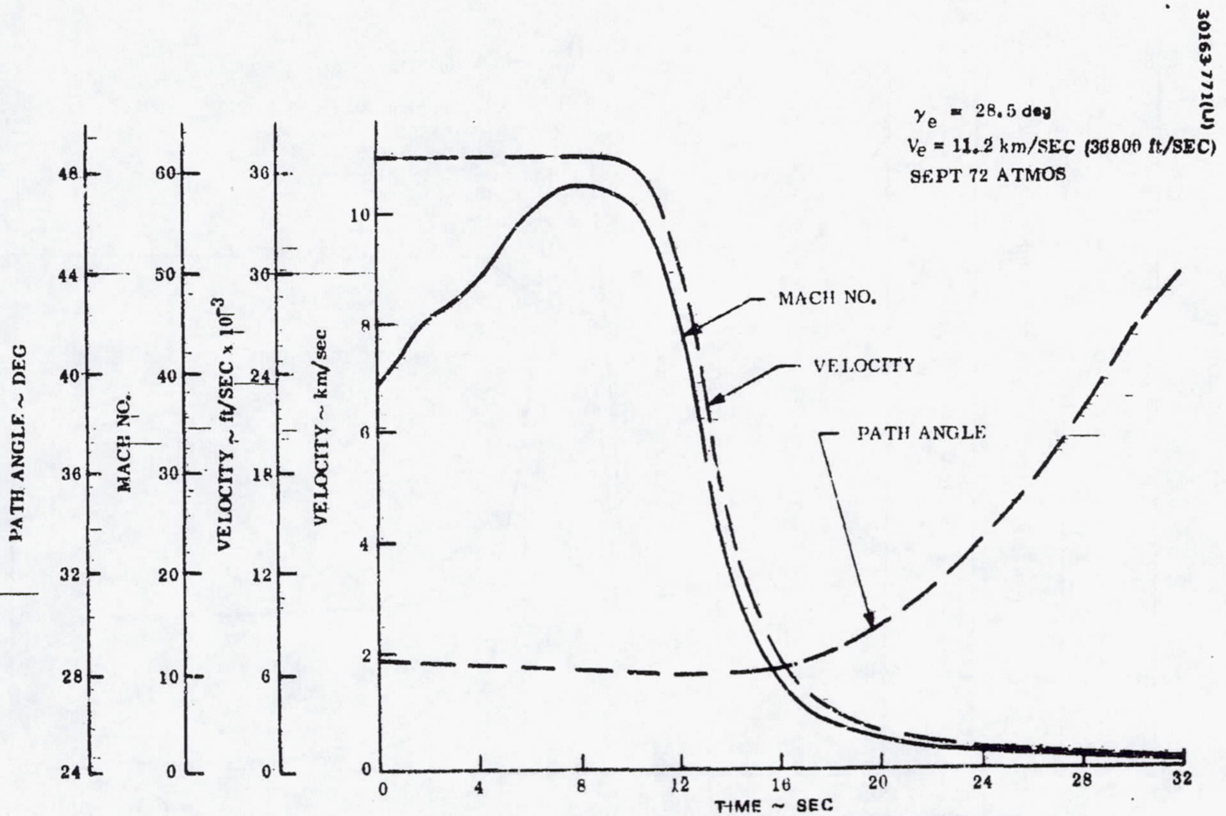

FIGURE 5.2-13. SMALL PROBE TYPICAL TRAJECTORY PARAMETERS

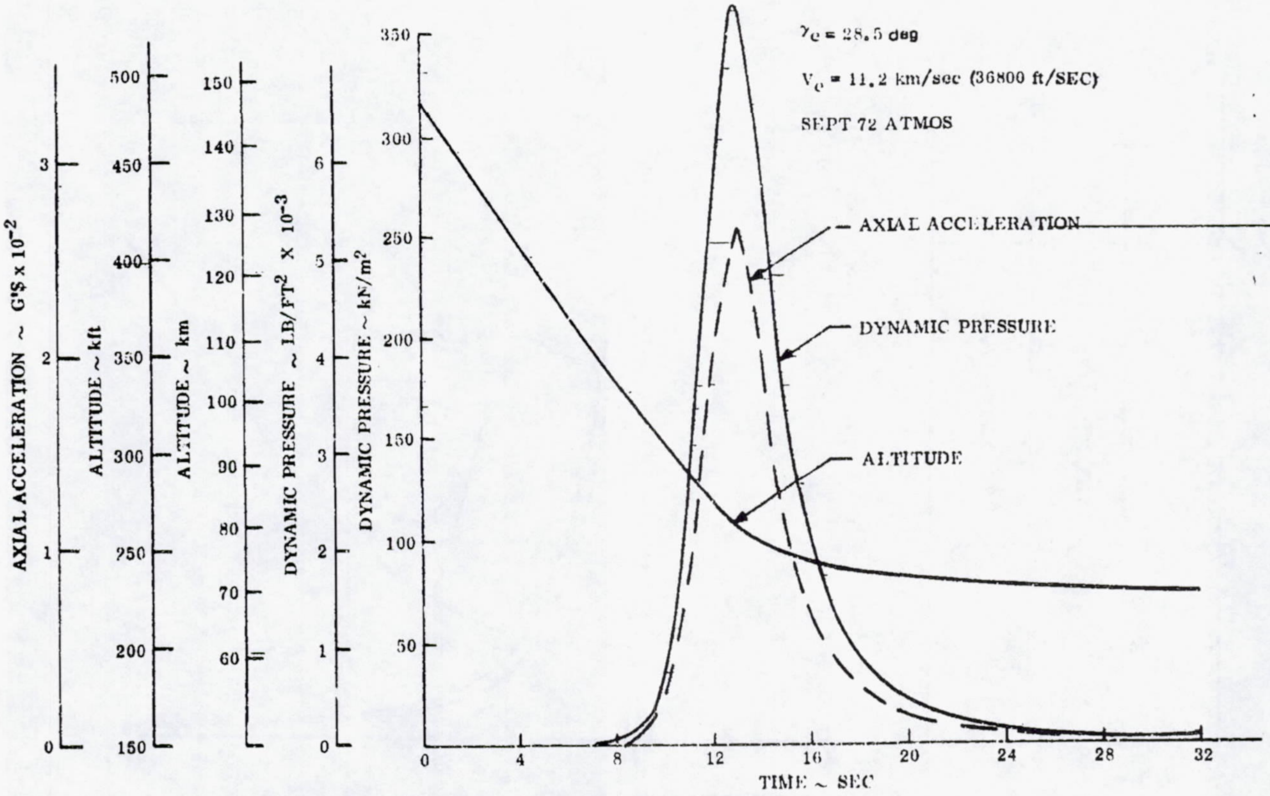

FIGURE 5.2-13. (CONTINUED) SMALL PROBE TYPICAL TRAJECTORY PARAMETERS

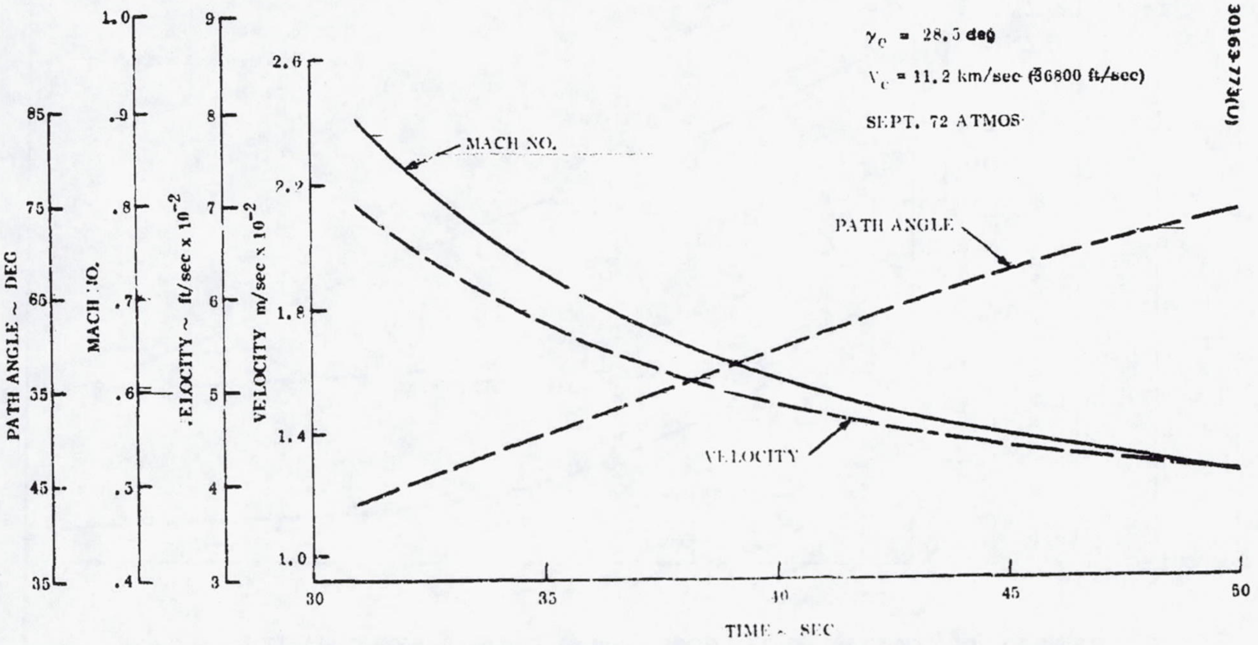

FIGURE 5.2-13. (CONTINUED) SMALL PROBE TYPICAL TRAJECTORY PARAMETERS

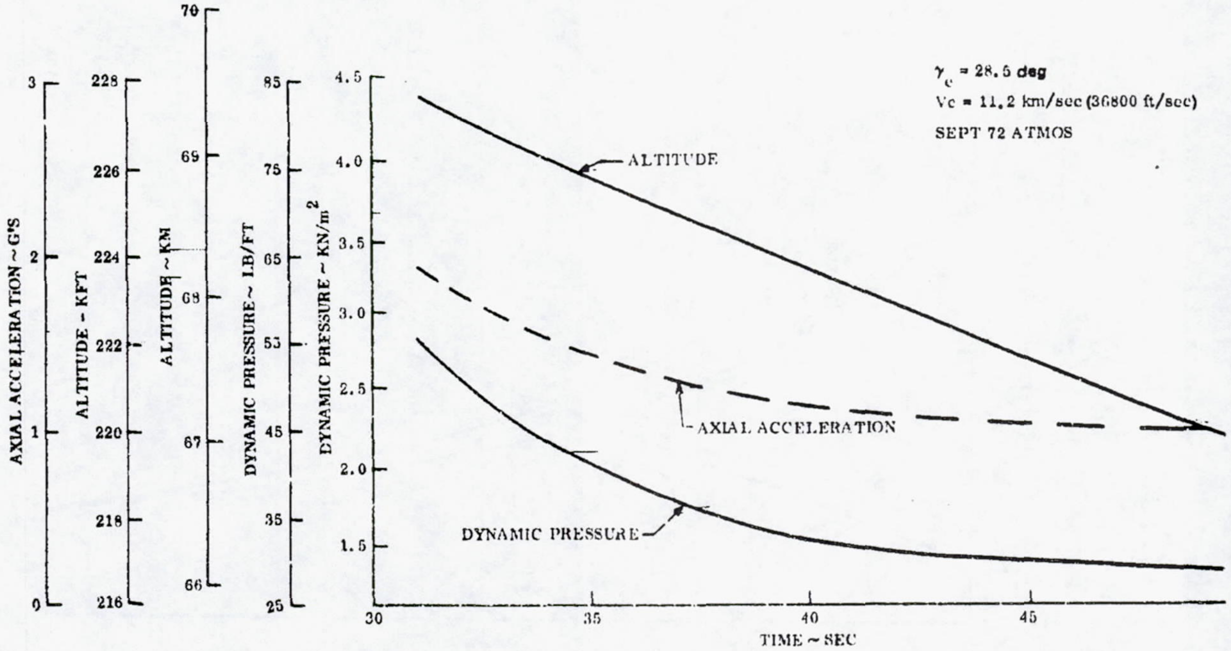

FIGURE 5.2-13. (CONTINUED) SMALL PROBE TYPICAL TRAJECTORY PARAMETERS

REPRODUCIBILITY OF THE ORIGINAL PAGE IS POOR.

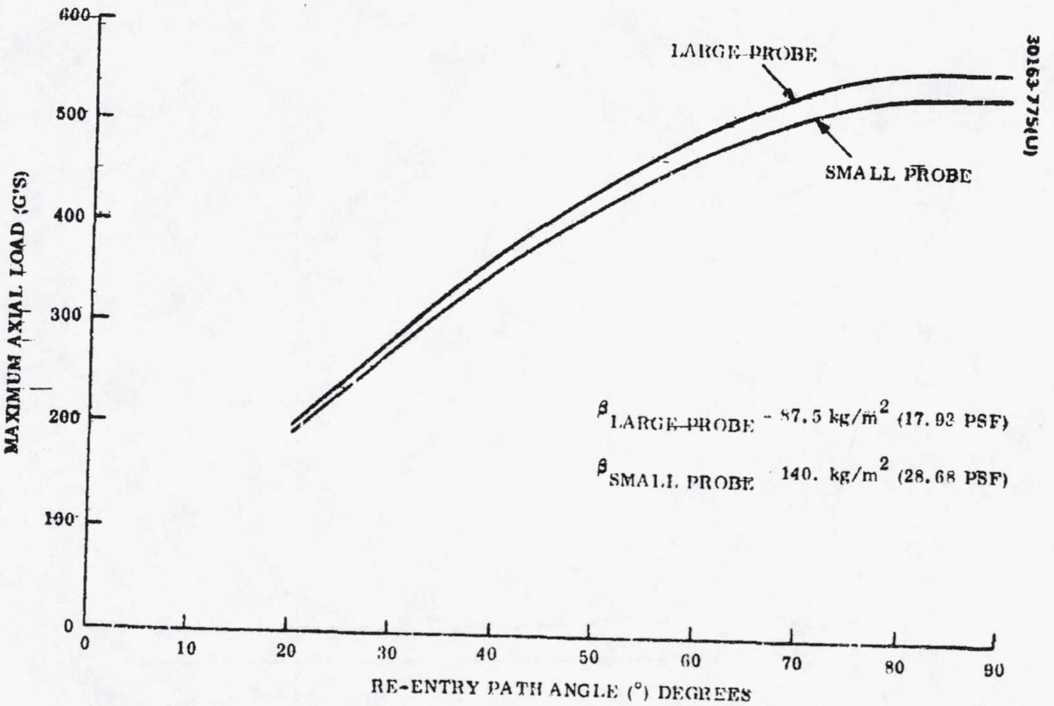

FIGURE 5.2-14. MAXIMUM AXIAL-ENTRY LOADS

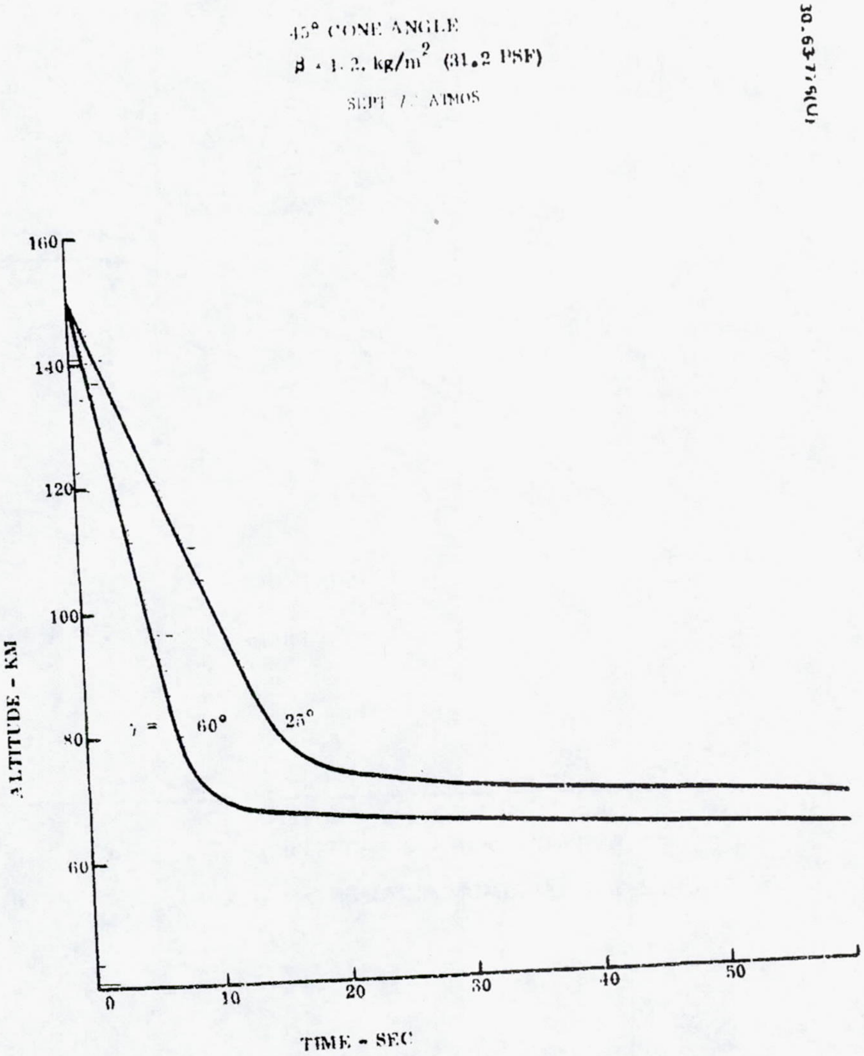

FIGURE 5.2-15. LARGE PROBE TRAJECTORY PARAMETERS

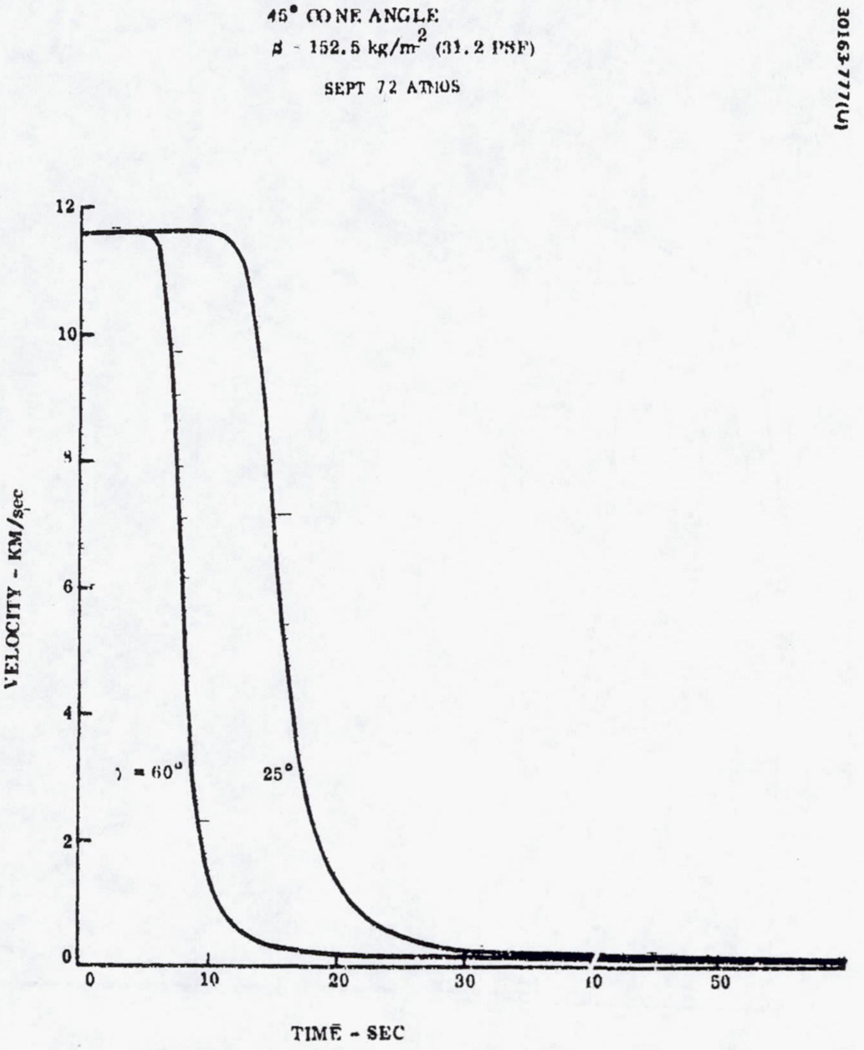

FIGURE 5.2-15. (CONTINUED) LARGE PROBE TRAJECTORY PARAMETERS

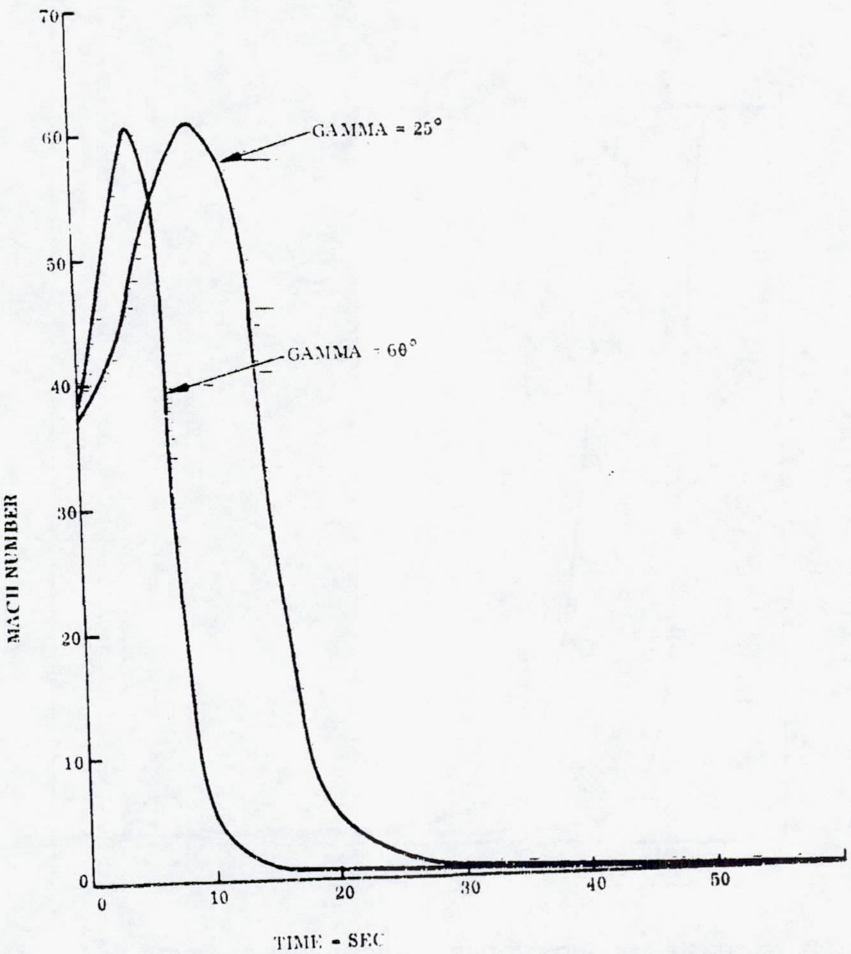
45° CONE
β = 152.5 kg/m^2 (31.2 PSF)
SEPT 72 ATMOS

3016З-778(U)

FIGURE 5.2-15. (CONTINUED) LARGE PROBE TRAJECTORY PARAMETERS

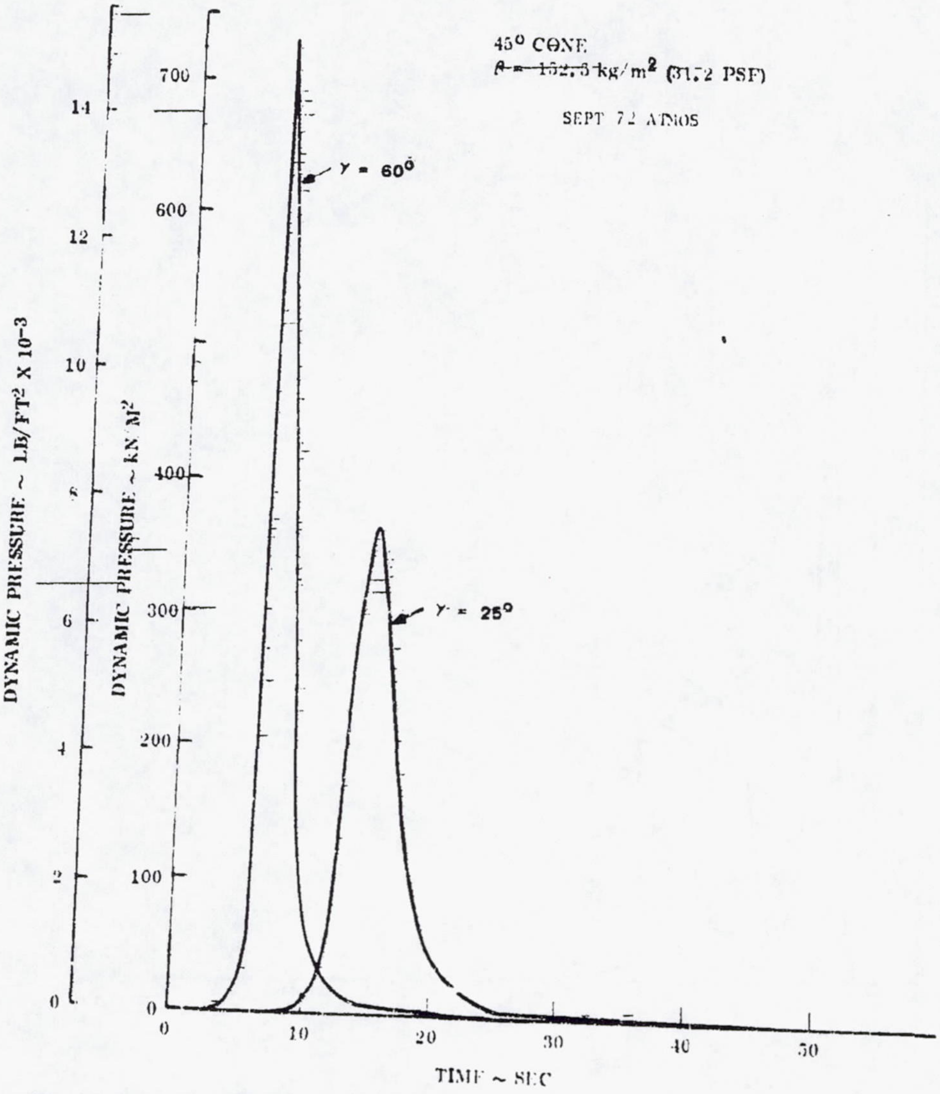

30163-779(U)

FIGURE 5.2-15. (CONTINUED) LARGE PROBE TRAJECTORY PARAMETERS

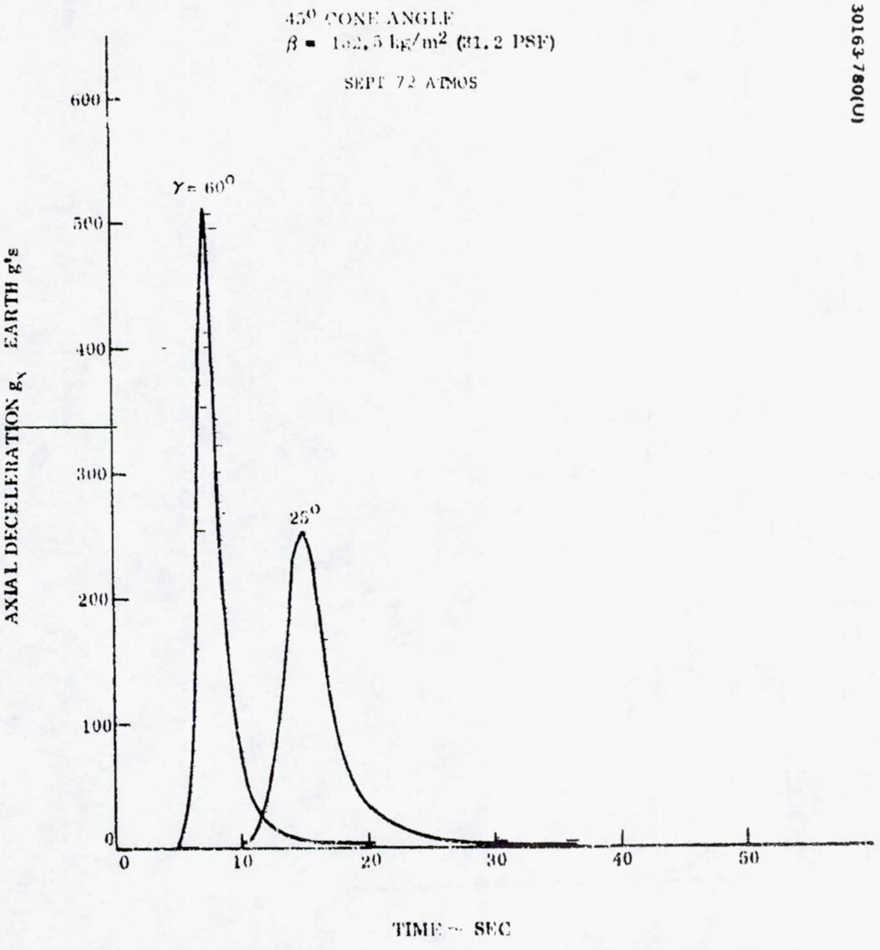

30163-780(U)

FIGURE 5.2-15 (CONTINUED) LARGE PROBE TRAJECTORY PARAMETERS

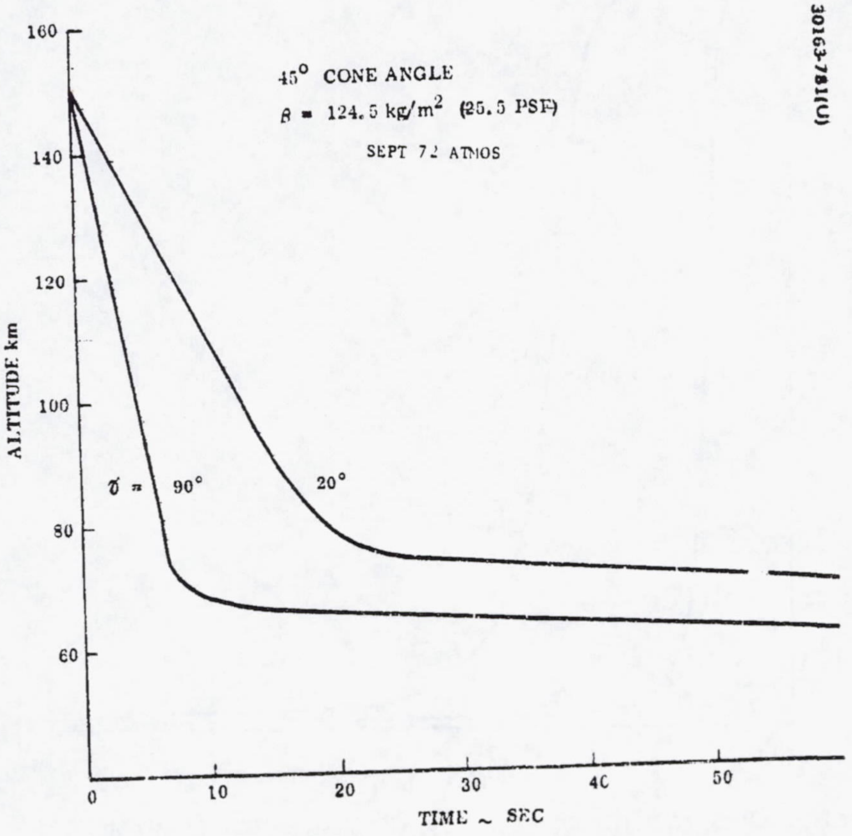

FIGURE 5.2-16. SMALL PROBE TRAJECTORY PARAMETERS

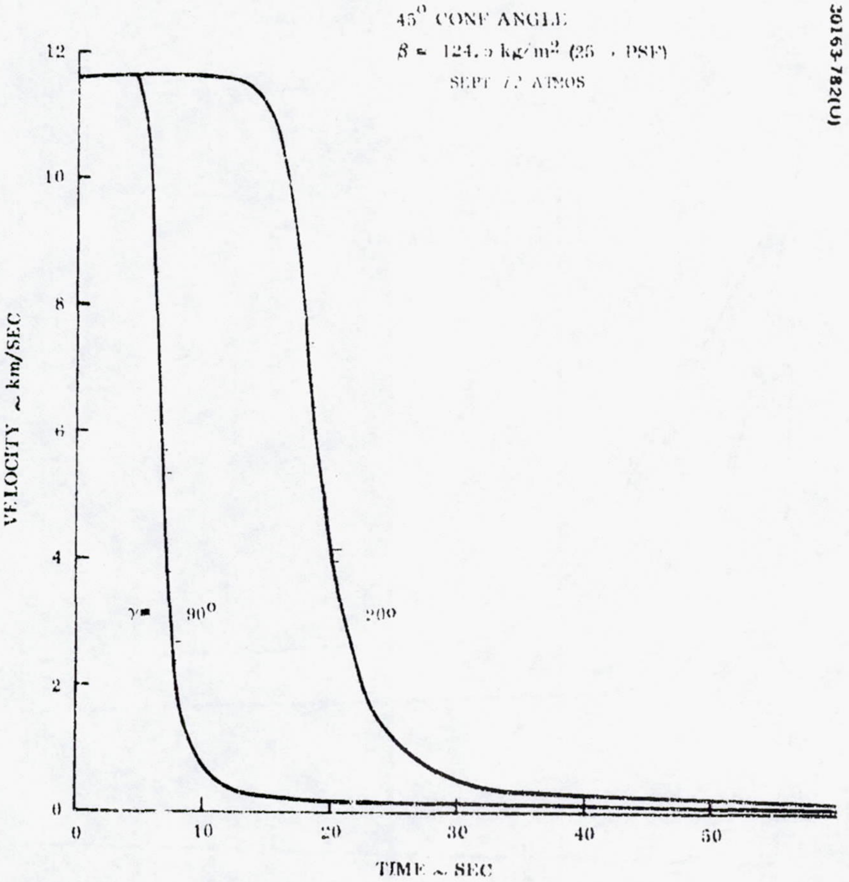

FIGURE 5.2-16. (CONTINUED) SMALL PROBE TRAJECTORY PARAMETERS

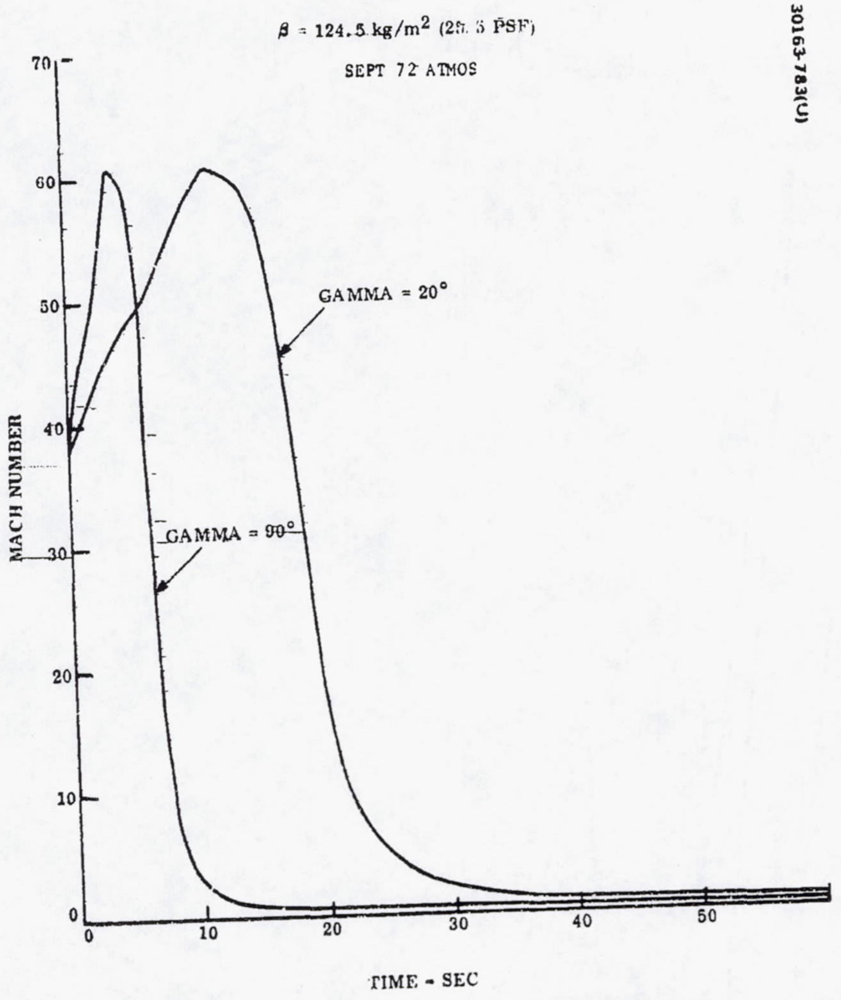

FIGURE 5.2-16. (CONTINUED) SMALL PROBE TRAJECTORY PARAMETERS

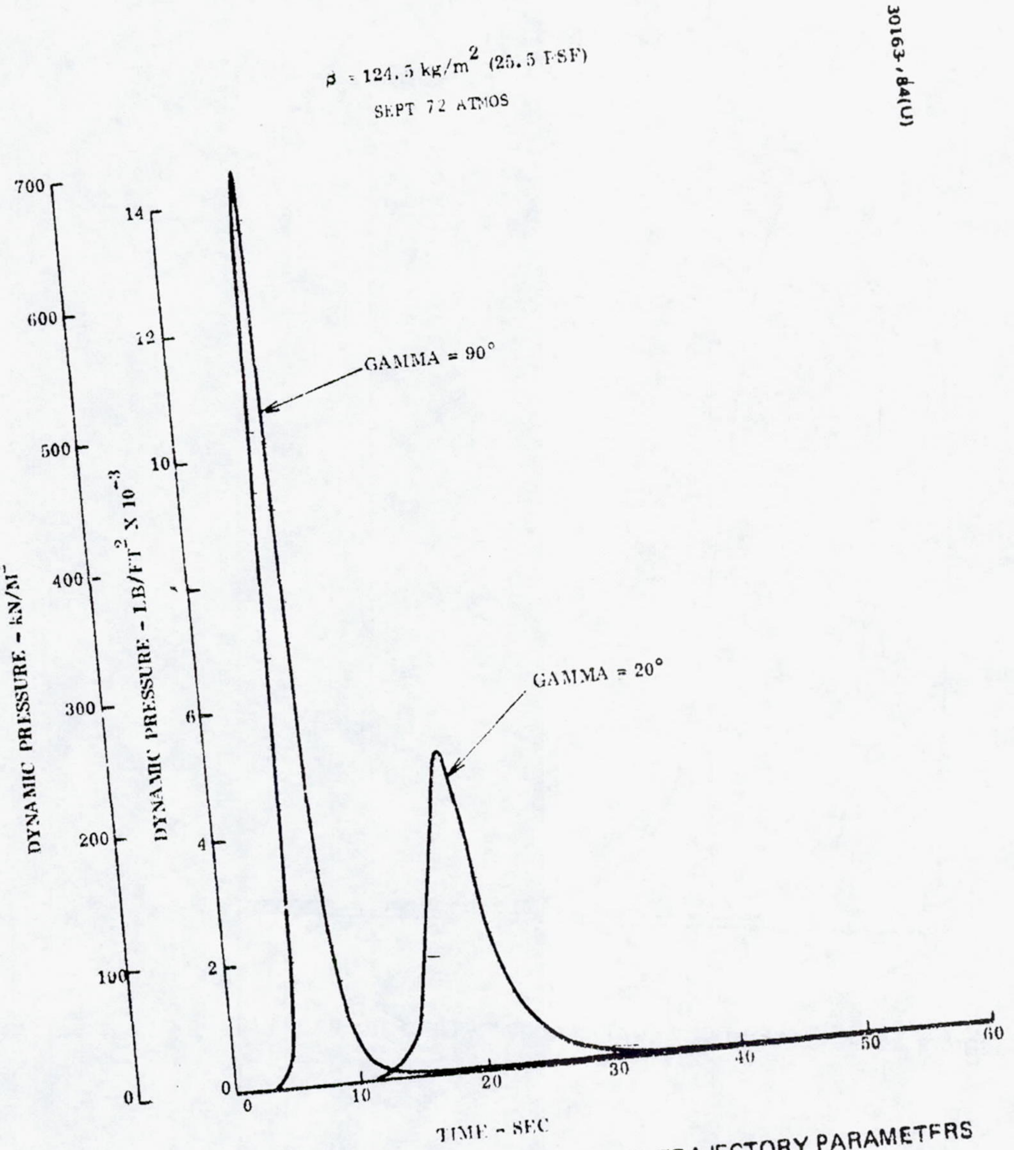

FIGURE 5.2-16. (CONTINUED) SMALL PROBE TRAJECTORY PARAMETERS

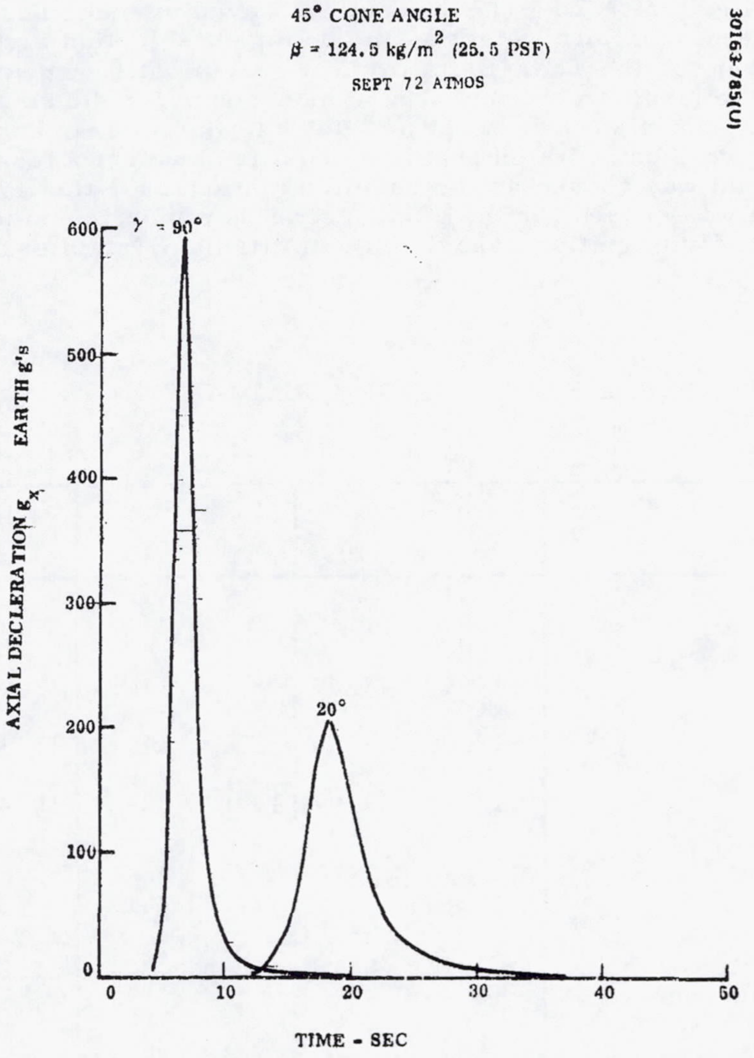

FIGURE 5.2-16. (CONTINUED) SMALL PROBE TRAJECTORY PARAMETERS

5.3 STRUCTURE

A structure trade study to determine the optimum structure in a variety of materials (aluminum alloy, beryllium, titanium, and stainless steel) and with various structural concepts (monocoque, ring stiffened monocoque, and honeycomb) indicated that 7.7 kg (17 lb) could be saved by using beryllium (see Table 5.3-1). Therefore, with weight as the dominant selection criteria, this material was chosen for the Thor/Delta probes. A ring stiffened monocoque was selected for the large probe, and a pure monocoque for the small. The use of beryllium imposes an added cost of $900 K to the progra, and so for the Atlas/Centaur version, with emphasis on cost (and weight a less critical problem), aluminum was chosen as the baseline material for the large probe. Initially, titanium was chosen for the small probe; however, considering the potential problem of autoignition associated with titanium, stainless steel was the final choice.

TABLE 5.3-1. WEIGHT SUMMARY

	Aluminum		Beryllium		Titanium	
Structure	kg	lb	kg	lb	kg	lb
Large Probe						
Monocoque	19.58	43.07	8.10	17.81	25.90	56.97
Ring-stiffened	12.86	28.30	5.13	11.28	15.38	33.84
Honeycomb	15.44	33.97	14.83	32.65	19.42	42.73
Small Probe	Stainless Steel					
58.4 cm diameter - 45 deg cone monocoque	4.12	9.10	1.25	2.75	3.75	8.26
Honeycomb	--	--	3.18	6.99	5.40	11.87
53.3 cm diameter - 55 deg cone monocoque	5.70	12.59	1.03	2.27	3.10	6.82
Honeycomb	--	--	3.00	6.61	4.36	9.58
58.4 cm diameter - 55 deg cone monocoque	5.10	11.21	1.32	2.91	4.31	9.49
Honeycomb	--	--	3.33	7.32	4.82	10.60

Requirements

The basic requirements for the descent module structure are to supply support for the pressure vessel and heat shield during powered flight and entry. The structural design loads for entry are shown in Table 5.3-2. Typical pressure distributions over the 45 and 55 deg cone aeroshells are shown in Figures 5.3-1 and 5.3-2. Design limit loads were increased by a factor of 1.25 for Thor/Delta and 1.5 for Atlas/Centaur to obtain ultimate design loads. The selected structural design temperature limit was 600 °K however, due to the heat shield thermal lag characteristics, the structural temperature at the time of the design loading would be 365°K

Tests/Trades

A structure trade study was made to determine the relative merits of various materials and structural concepts. The material properties assumed for the study are shown in Table 5.3-3, and the structural concepts in Figure 5.3-3.

The initial study considered only the main structural members of the basic frustum, and the only selection criteria was weight. The more detailed study considered the effects of the secondary structure (for weights, see Table 5.3-4), manufacturing problems, and program cost. From this data, the selection of a beryllium structure was made for the Thor/Delta probes (a ring stiffened monocoque being used for the large probe and pure monocoque for the small). For the Atlas/Centaur variant an aluminum ring stiffened monocoque was selected for the large probe and a stainless steel monocoque for the small probe. The choice was mainly determined by weight considerations for the Thor/Delta probes, and cost for the Atlas/Centaur.

Aluminum was not considered for the small probe because of the requirement to survive the maximum soak out temperature of 772°K at the surface of Venus. For the ring stiffened designs, it should be noted that the number of rings selected as the practical optimum is less than the optimum predicted from the curves shown in Figures 5.3-4 and 5.3-5. All three stiffened monocoque concepts (stringer stiffened, fabricated ring stiffened, and integrally machined) offer very similar solutions regarding weight. Integral machining was selected as the optimum concept for beryllium as it avoided the cost and problems of hotforming components and reduced the amount of

TABLE 5.3-2. DESIGN ACCELERATIONS

	Thor/Delta		Atlas/Centaur	
	Large Probe	Small Probe	Large Probe	Small Probe
Axial, g	500	560	510	590
Lateral, g	25	25	25	25

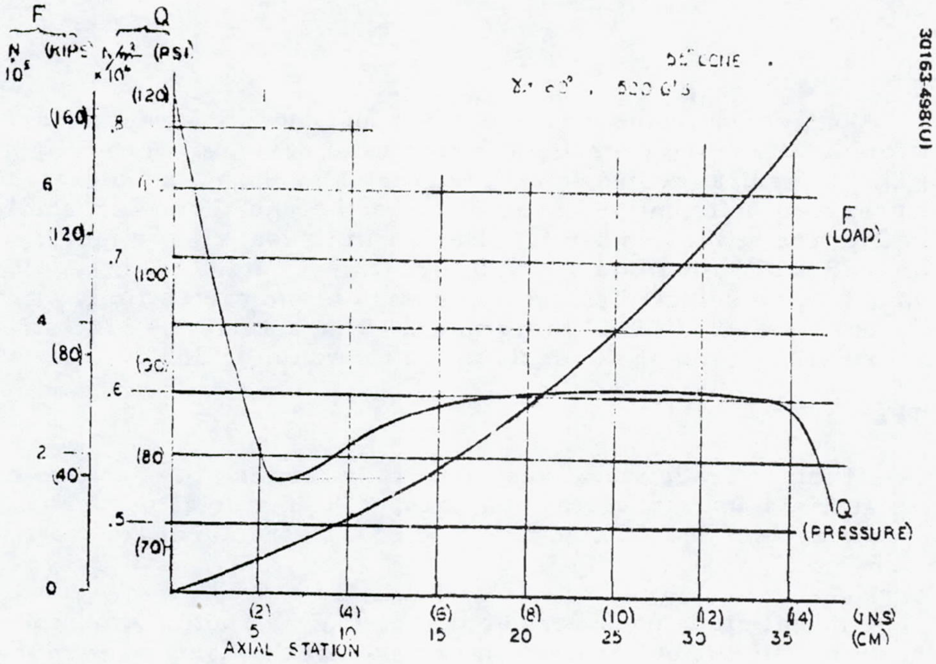

FIGURE 5.3-1. LARGE PROBE PRESSURE LOADING

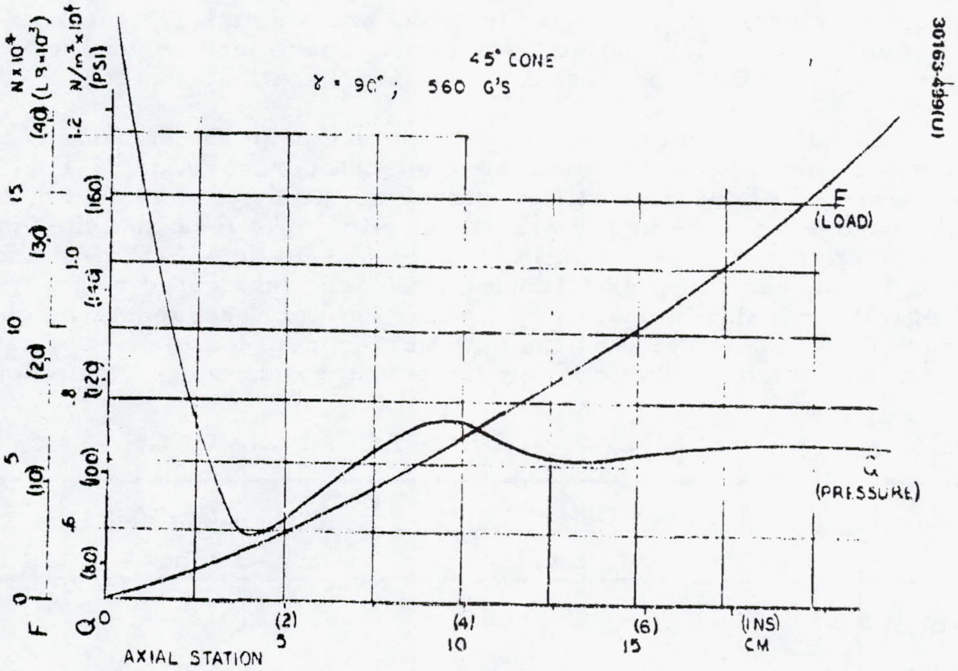

FIGURE 5.3-2. SMALL PROBE PRESSURE LOADING

TABLE 5.3-3. MATERIAL PROPERTIES

	F_{ty}		F_{tu}		F_{cy}		F_{su}		E				
Material	GN/m^2	Ksi	GN/m^2	Ksi	GN/m^2	Ksi	GN/m^2	Ksi	GN/m^2	lb/in^{2}x10^6	gm/cm^3	lb/in^3	
Aluminum 7075-T6*	0.44	64.0	0.52	75.0	0.43	62	0.30	43.0	72	10.5	2.8	0.10	0.33
Aluminum 2024-T861*	0.43	62.0	0.48	70.0	0.44	63	0.28	40.0	72	10.5	2.8	0.10	0.33
Titanium 6AL-4V*	0.86	126.0	0.92	134.0	0.91	132	0.53	79.0	11	16.4	4.45	0.16	0.31
Beryllium 2 percent BeO cross rolled sheet	0.41	59.0	0.47	69.0	0.40	58	0.48	70.0	290	42.0	1.86	0.067	0.25
Fiberglass 182; polyester resin**	0.19	28.1	0.29	42.5			0.06	8.7	17	2.5	2.55	0.092	
Stainless steel*	1.03	150.0	1.22	177.0	1.09	158	0.79	115.0	206	0.30	7.63	0.276	0.32

*Mil-5-B Handbook values

**Mil-17 Handbook values

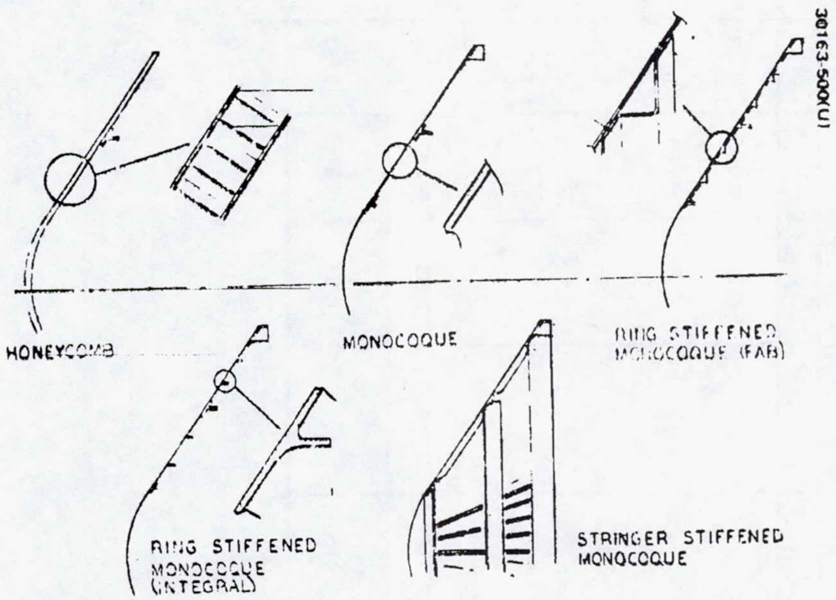

FIGURE 5.3-3. STRUCTURAL CONCEPTS

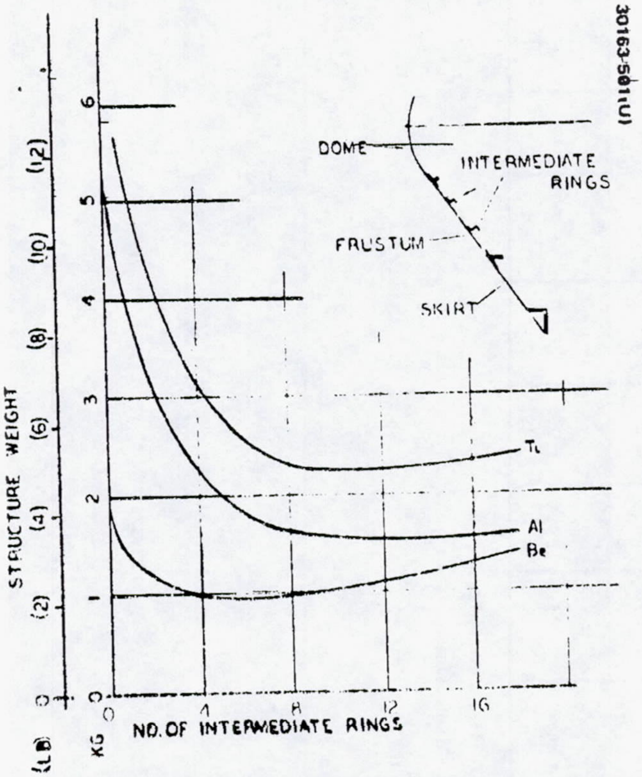

FIGURE 5.3-4. LARGE PROBE FRUSTUM STRUCTURE WEIGHT VERSUS NUMBER OF INTERMEDIATE RINGS

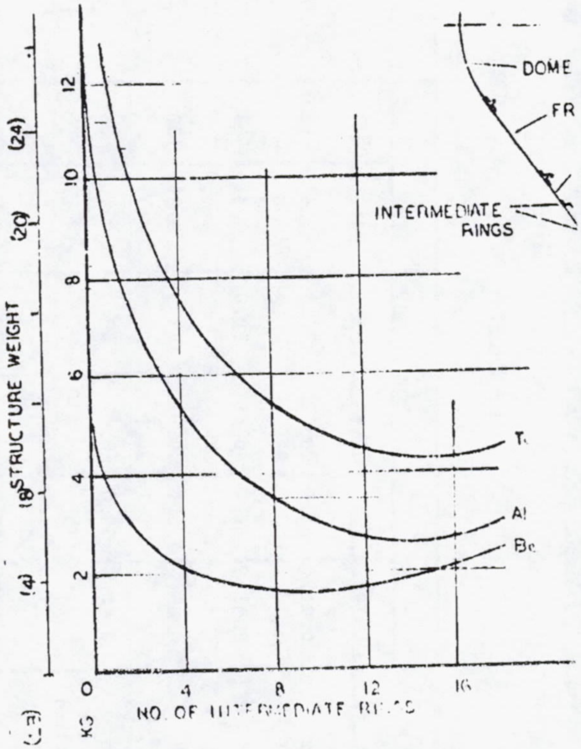

FIGURE 5.3-5. LARGE PROBE SKIRT STRUCTURE WEIGHT VERSUS NUMBER OF INTERMEDIATE RINGS

REPRODU

TABLE 5.3-4. COMBINED AEROSHELL AND INTERNAL STRUCTURE

Probe	Structure	Material	kg	lb
Large	Ring Stiffened Monocoque	Aluminum Alloy	24.3	53.6
Large	Stringer Stiffened Monocoque	Beryllium	12.7	28.0
Large	Ring Stiffened Monocoque	Beryllium	12.2	26.9
Large	Monocoque	Beryllium	15.3	33.8
Small	Monocoque	Beryllium	3.3	7.3
Small	Monocoque	Titanium	7.7	17.1

rivetting on the assembly. Integral machining was also found to be optimum for aluminum considering the small number of assemblies to be produced. Analysis also showed that a local thickening of the skin was needed in the region of the payload ring. With integral machining this could be accommodated without resorting to the complexity of doubler plates.

To keep the aft structure temperature within design limits, it is covered by 0.1 in. (2.5 mm) of low density ESM. This will give a considerable safety margin over the theoretical heat protection requirements presented in Figure 5.3-6.

Integrated Structure

As an alternative to the baseline design, an integrated structure concept was evaluated for the small probe. This is shown in Figure 5.3-7, and the weight statement (Table 5.3-5) provides a comparison with the baseline design. With this concept the pressure vessel is shaped to given an acceptable aerodynamic configuration, and hence no separate aeroshell is required; the thermal protection for entry is applied directly to the shell. The pressure vessel is made in two parts, the forward one being a hemisphere and the aft section having the same spherical radius as the fore section but is somewhat less than a hemisphere so that when the two sections are joined an aft facing step is produced. The resulting body is somewhat smaller in base diameter than the baseline design, thus making it easier to package the bus, but more aerodynamic data is required to support the configuration. The main structure must be run hot in this design, and this has several undesirable con-

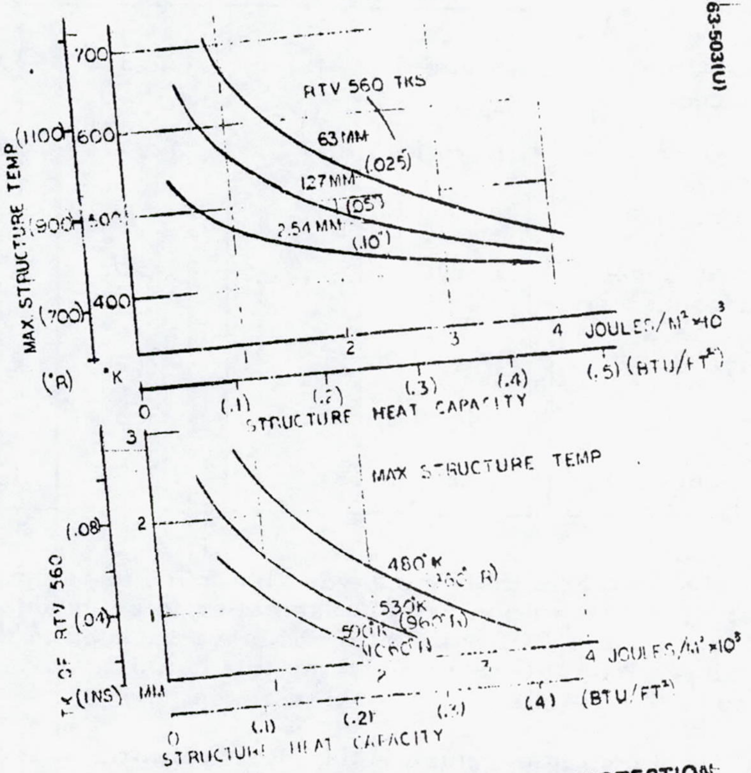

30163-503(U)

FIGURE 5.3-6. AFT COVER THERMAL PROTECTION REQUIREMENTS

REPRODUCIBILITY OF THE ORIGINAL PAGE IS POOR.

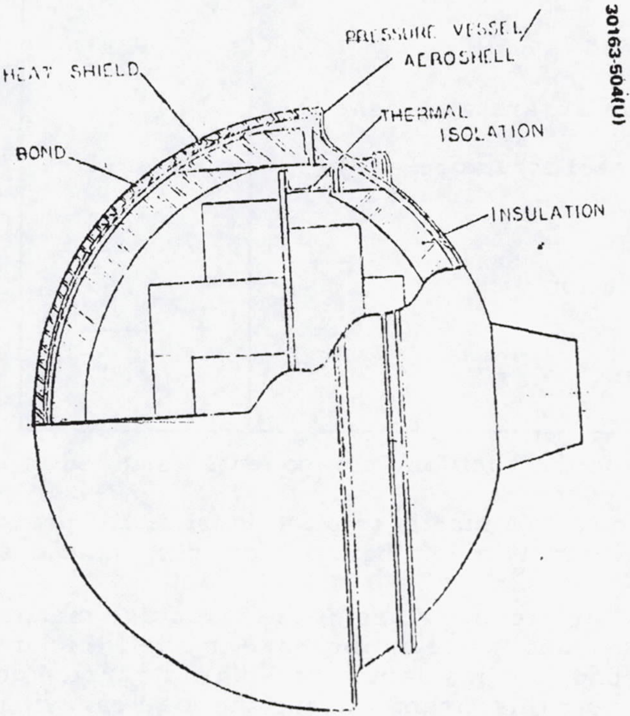

FIGURE 5.3-7. INTEGRATED STRUCTURE CONCEPT

REPRODUCIBILITY OF THE ORIGINAL PAGE IS POOR.

TABLE 5.3-5. MASS PROPERTIES COMPARISON - INTEGRATED DESIGN VERSUS BASELINE

	Mass Difference	
	kg	lb
Shield and bond	-1.18	- 2.6
Elimination of separate aeroshell	-3.35	- 7.4
Pressure vessel structure	4.71	10.4
Insulation	.45	1.0
Thermal isolation	.45	1.0
Total difference	1.0	2.2

NOTES:
1) Equipment shelf and components assumed to be same for both concepts
2) Ratio of roll inertia to pitch inertia will probably be not significantly more than 1.0 for integrated design

sequences: first, the high temperature of the structure means lower allowable mechanical properties, and hence an increase in shell thickness (and weight) will be required; second, the insulation material is carried on the inside of the pressure vessel, and this means making the load carrying structure larger; also extra weight will be involved in providing thermal isolation for the equipment package as this must be supported from the hot structure. Further weight penalties are introduced by the shape of the structure, as this must be less efficient than the sphere of the baseline design. The end result is a design that is somewhat heavier than the proposed solution, and therefore unless size becomes a dominant selection criteria, there is little justification for changing to this concept.

Thor/Delta Baselines

Large Probe Deceleration Module Structure (Figure 5.3-8)

The main structural member for the aeroshell is the frustum with its integral stiffening rings. At first sight the integrally machined concept may appear to be an uneconomical approach, but a study demonstrated that competitive costwise with other concepts; in addition, it reduces the amount of joints to be made (always desirable with beryllium) and allows the skin thickness to be varied along the shell to conform more closely to the theoretical requirements. A machined dome is rivetted to the frustum to complete the nose. Two rings are fitted to the shell; a two-piece ring, forming a closed triangular section, is used to stiffen the outer edge of the

FOLDOUT FRAME

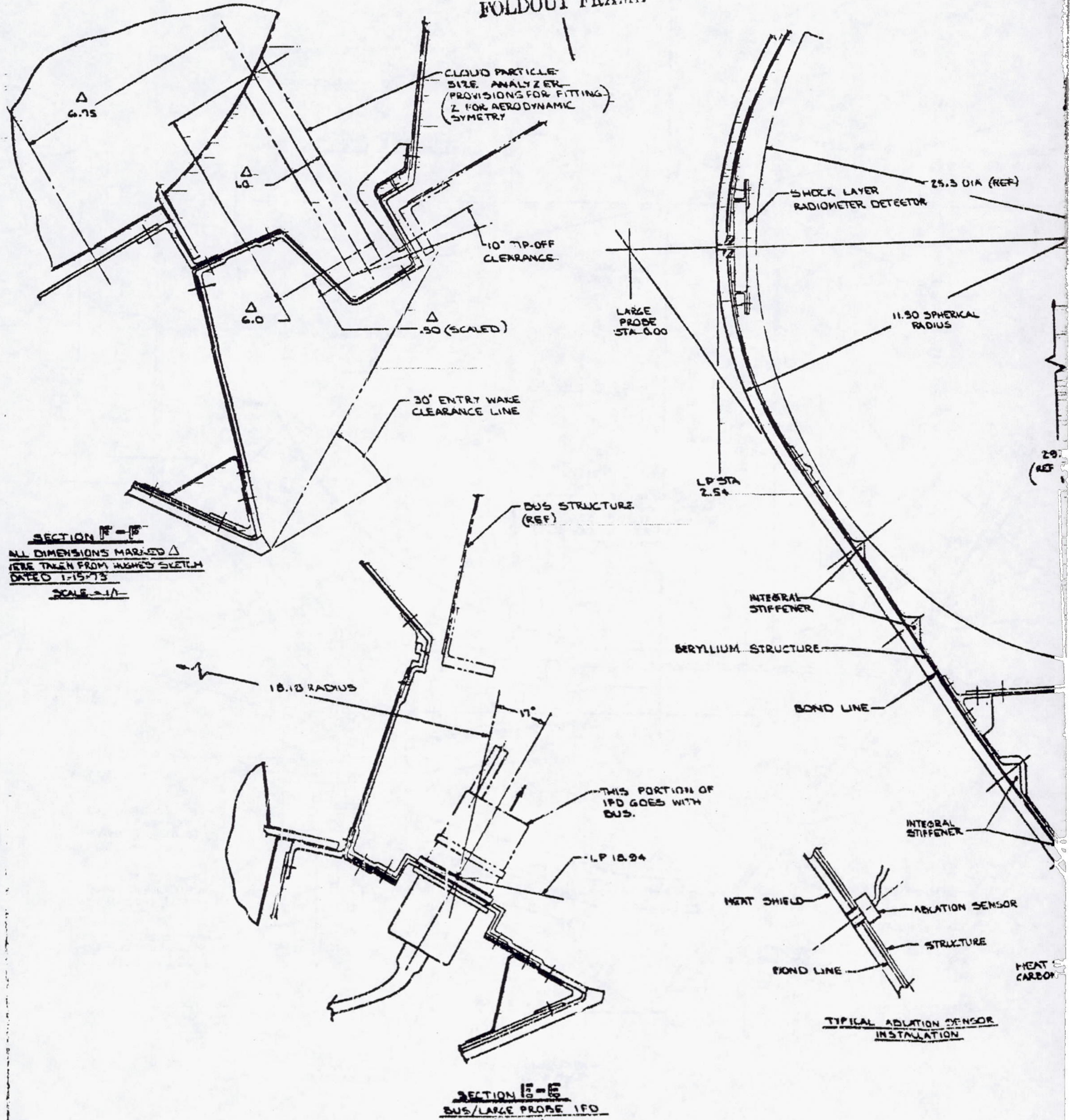

FIGURE 5.3-8. LARGE PROBE INTERFACE DEFINITION

FOLDOUT FRAME 5

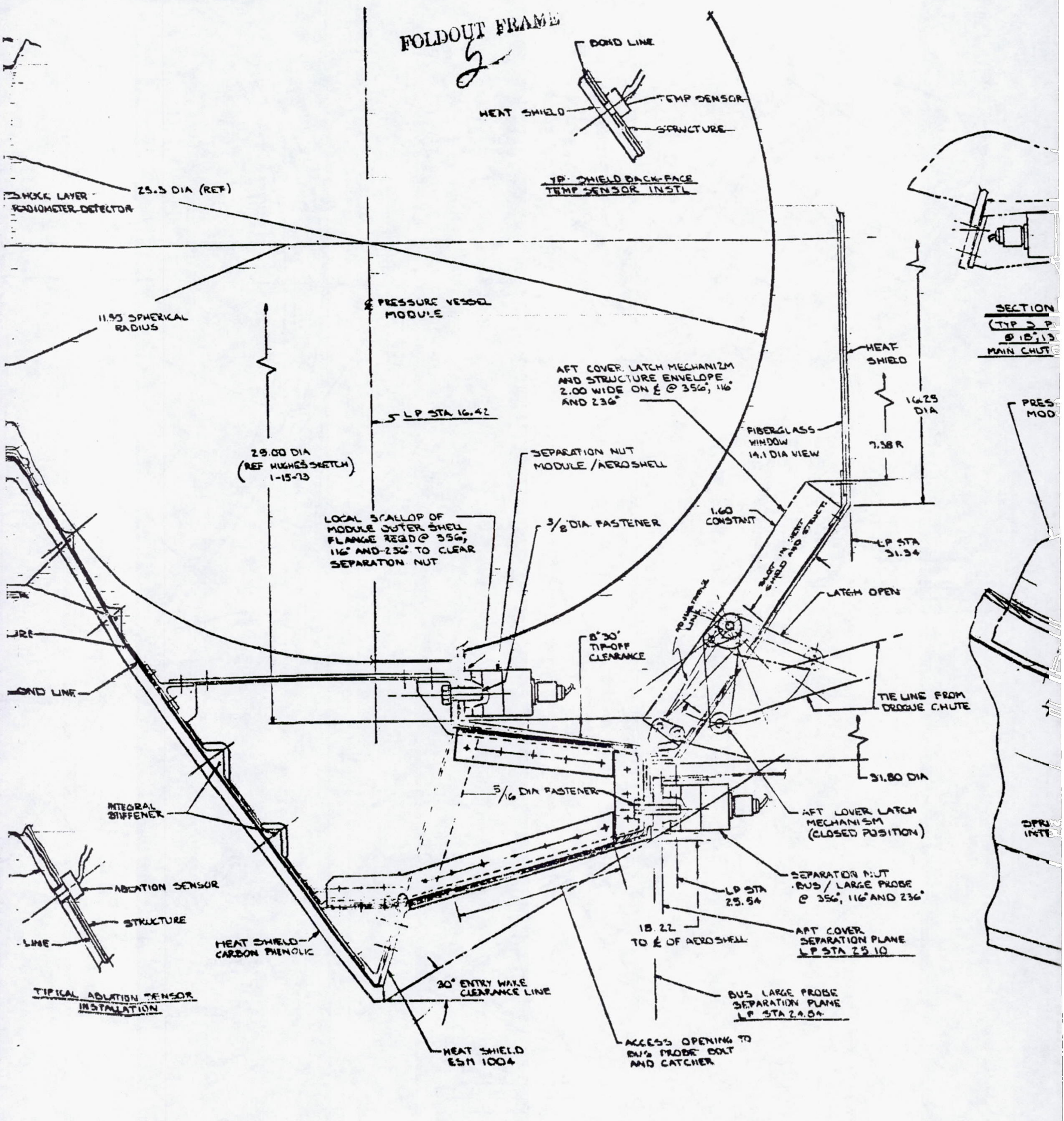

REPRODUCIBILITY OF THE ORIGINAL PAGE IS POOR.

FOLDOUT FRAME 2

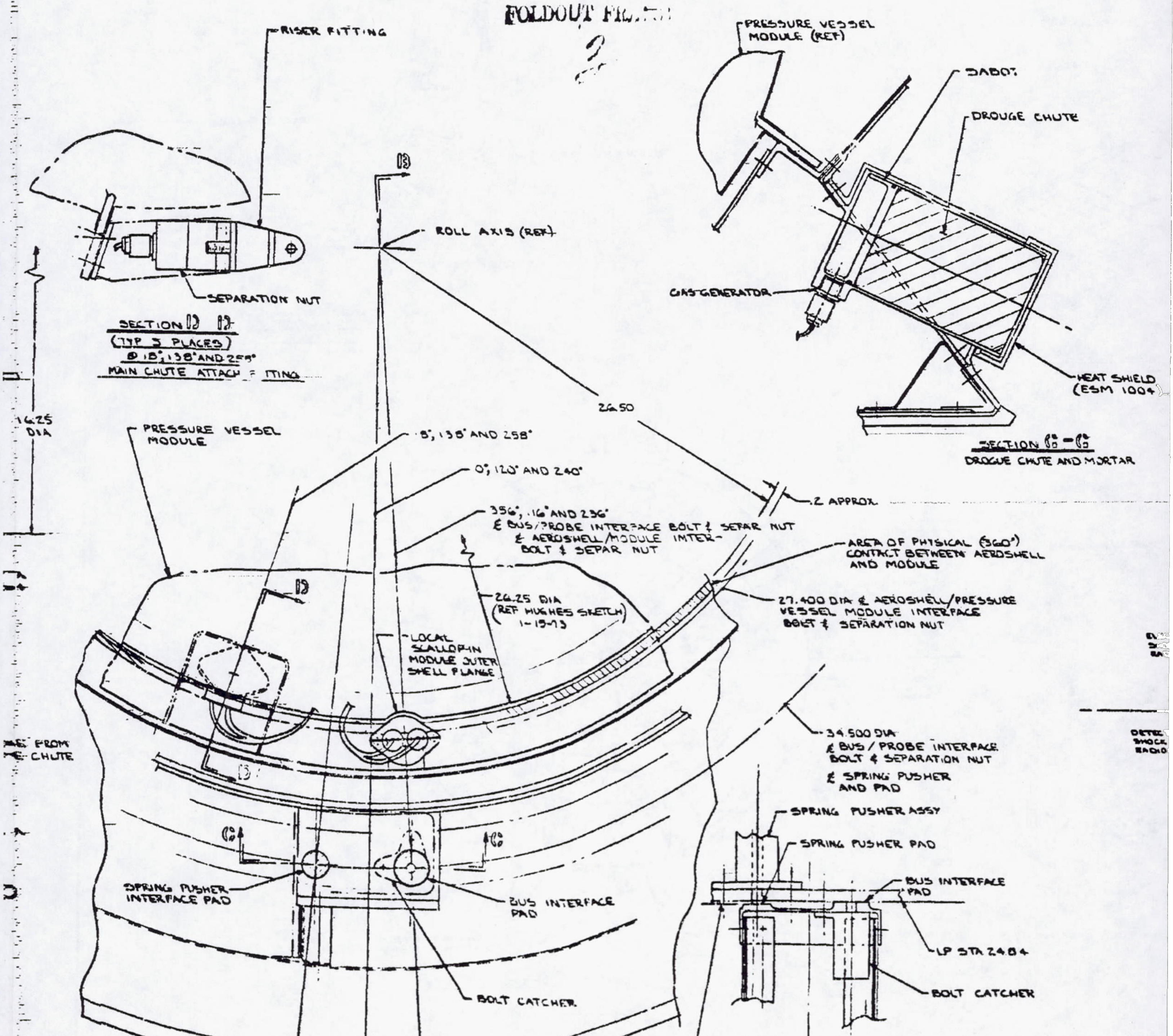

SECTION B - B
(TYP 3 PLACES)
@ 15°, 138° AND 255°
MAIN CHUTE ATTACH FITTING

SECTION C - C
DROGUE CHUTE AND MORTAR

SECTION C - C
(TYP 3 PLACES)
SCALE = 1/1

DETAIL A (TYP 3 PLACES)
FULL SIZE
AFT COVER OMITTED

FOLDOUT FRAME

30163-505(U)

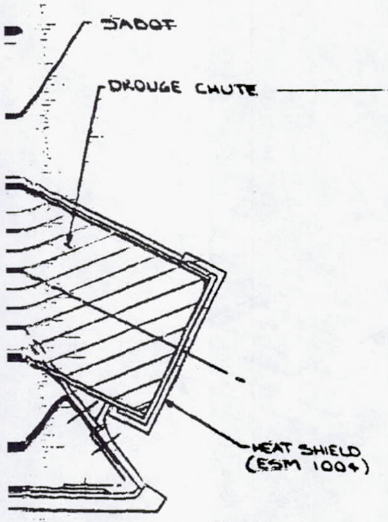

SECTION G-G
DROGUE CHUTE AND MORTAR

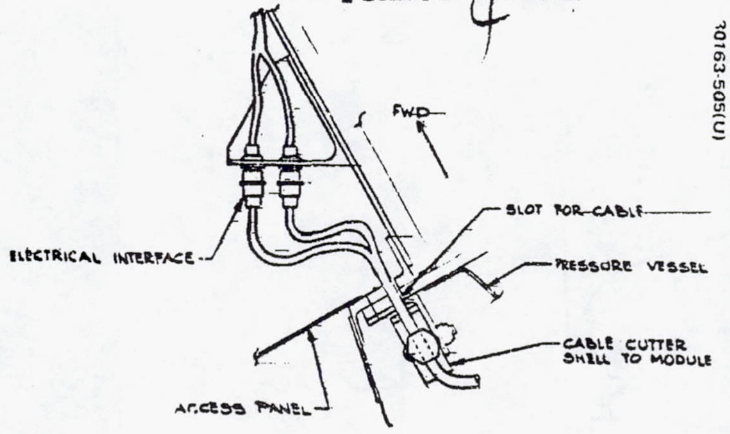

SECTION H-H
AEROSHELL/MODULE IFD
SCALE 2/1

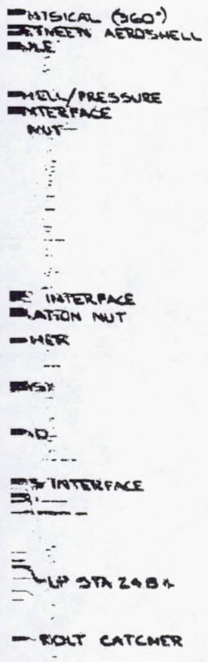

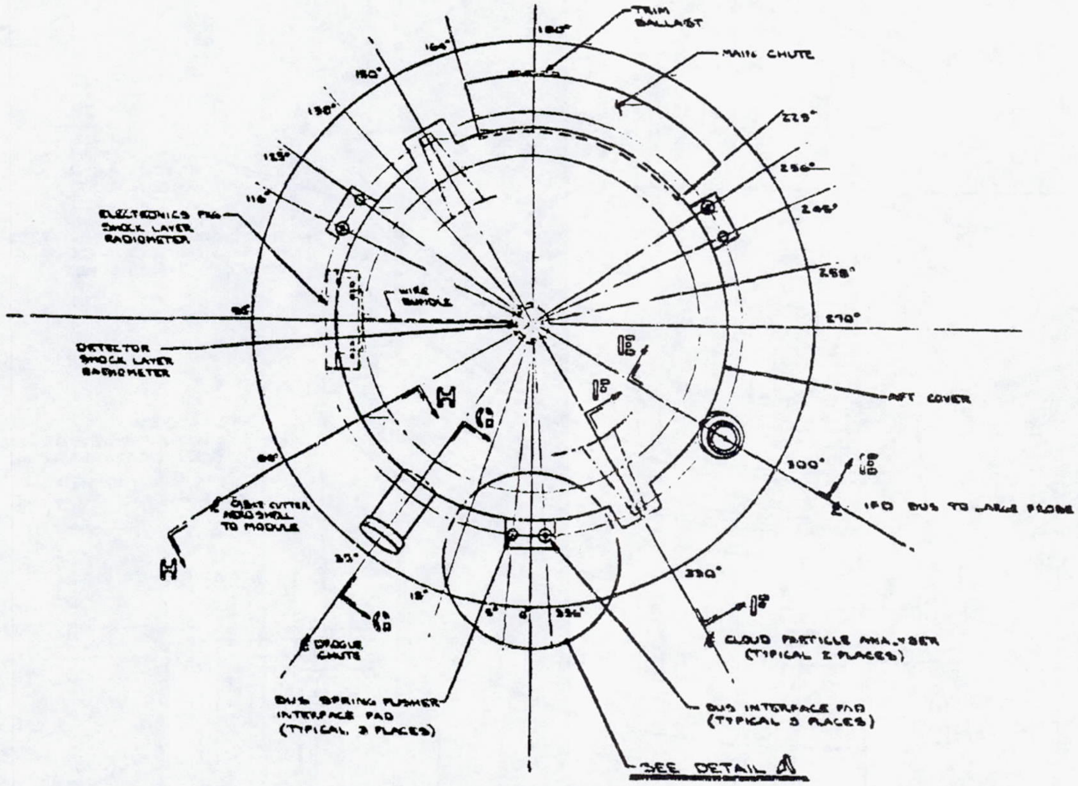

VIEW LOOKING FWD
AT AFT END OF
LARGE PROBE
SCALE: 1/4

REPRODUCIBILITY OF THE ORIGINAL PAGE IS POOR.

shell, and a tee shaped ring is used for attaching the payload support structure. This latter structure is a cylindrical "can" with a "zee" section ring at its aft end for mounting the pressure vessel. The pressure vessel is attached by three bolts which react the booster acceleration loads. The main design load for this area is the entry deceleration; this is reacted by compression between the pressure vessel flange and the payload support ring, the latter being machined to give a narrow support area as close as possible to the pressure vessel to reduce bending stresses in both members to a minimum. The aft face of the aeroshell is covered by a thin sheet member which is fitted with a series of removable panels for access to the experiments, instrumentation and electrical harnessing and for fitting the parachute. Strengthening members are fitted for mounting the pilot chute mortar.

For attaching the probe to the bus, three fabricated longeron assemblies are fitted. These fittings extend from the booster interface (where one pad is provided for the attachment bolt and its catcher and another for the separation spring push rod) to the aeroshell. The area between the longerons is filled in with a thin sheet metal aft structure. A light ring around the aft end of the structure provides the attachment features for the aft cover; the aft cover, which is retained by mechanically operated latches, is a dished metal structure, with a fiberglass insert to act as the antenna window. In general, attempts to substitute other materials for beryllium for certain components in the hope that a mixed construction would be more cost effective proved fruitless, as using light alloys introduced a thermal stress problem, and titanium, although compatible with beryllium, increased the weight significantly and may be incompatible with the Venusian atmsophere. The aft cover could be one area where aluminum would be acceptable structurally and the weight increase would be approximately 3 lb.

Two of the science experiments have a direct impact on the deceleration module design. The cloud particle analyzer experiment requires a pylon-type structure to mount a mirror. This protrusion from the pressure vessel requires a cut out in the aft structure to provide clearance, and a fairing added to provide a cover; a local extension on the aft cover forms a lid for the aft end of the fairing. The shock layer radiometer sensor is fitted to the nose of the aeroshell. In addition to the structural ring required for the attachment bolts, this installation requires a quartz window and a local thickening of the heat shield. The electronics for this instrument are mounted on the aeroshell, positioned as close to the sensor as the pressure vessel will allow, the angular position being chosen so that the weight of the unit will contribute towards the mass balancing of the probe.

The instrumentation of the aeroshell is confined to two heat shield backface temperature sensors and two ablation sensors of the multiwire resistive type. The electrical wiring consits of a harness routed around the aeroshell with branches going to the IFD, the pressure vessel electrical interface, the shock layer radiometer, and the instrumentation. The wires are supported at frequent intervals along the structures, and adequate access is proposed for the installation of the harness and components, and for the mating of the connectors.

Points for attaching ballast are provided around the aft ring of the aeroshell. This will enable the lateral position of the c.g. to be controlled, but will give only limited control of the products of inertia; if the principal axis requires greater positional accuracy, a further ballast plane will be provided at the forward end of the payload support structure.

Small Probe Deceleration Module Structure (Figure 5.3-9)

In general, the small probe closely follows the structural concepts used on the large probe, but the complexity is greatly reduced because of the small size and the lack of parachute and pressure vessel separation subsystems. The smallness of the aeroshell allows a monocoque to be used without the stiffening rings that characterize the structure of the large probe; this results in a simpler structure without a significant weight increase. No aft structure is required other than the thin diaphragm that closes off the back of the aeroshell. This skin is reinforced locally to mount the IFD and electrical interface, the despin rockets and the deployable temperature sensor. The outer ring of the aeroshell, in addition to its stiffening function, incorporates the V ring for the attachment of the probe to the bus. Roll control/stabilization fins are fitted to mounting slots provided by Hughes on the pressure vessel; they are machined from beryllium plate stock, so that their heat capacity may be used for thermal protection to avoid the use of a separate shield.

There are two experiments that directly affect the probe design. There is a temperature sensor that is mounted near the outer periphery of the aeroshell; it is protected by a fairing through entry, and is then deployed by a pyrotechnic device. The aeroshell structure provides the attachment features for the unit, and an electrical interface to facilitate installation. The pressure vessel houses a pressure transducer which requires a connection to the deceleration module stagnation point; this is effected through a probe at the front end of the vessel that will "blind" mate with a flexibility mounted fitting on the aeroshell. The degree of movement that the joint allows is sufficient to allow for both tolerance buildup and in-flight distortions that arise from the loading and temperature changes.

The electrical harness and the trim ballast will be installed in a similar manner to that used on the large probe. An electrical interface is provided between the pressure vessel and the deceleration module for the temperature sensor and the despin subsystem firing circuits.

Atlas/Centaur Trades

The structural trade studies were extended to cover the Atlas/Centaur probes. The scope of the work was considerably reduced from the Thor/Delta trades, as the emphasis on cost eliminated the need to consider beryllium. Honeycomb was not considered at this time as the original trades indicated that it would be heavier than a shell; if the new sizes and design criteria reversed this, any small weight saving would not be worth the additional complexity. Hence, the trades centered on monocoque structures, and for the large probe an aluminum shell was selected with various combinations of stiffening rings. The results, summarized in Table 5.3-6, show that pure monocoque is approximately 4.5 kg (10 lb) heavier than a stiffened monocoque.

FOLDOUT FRAME

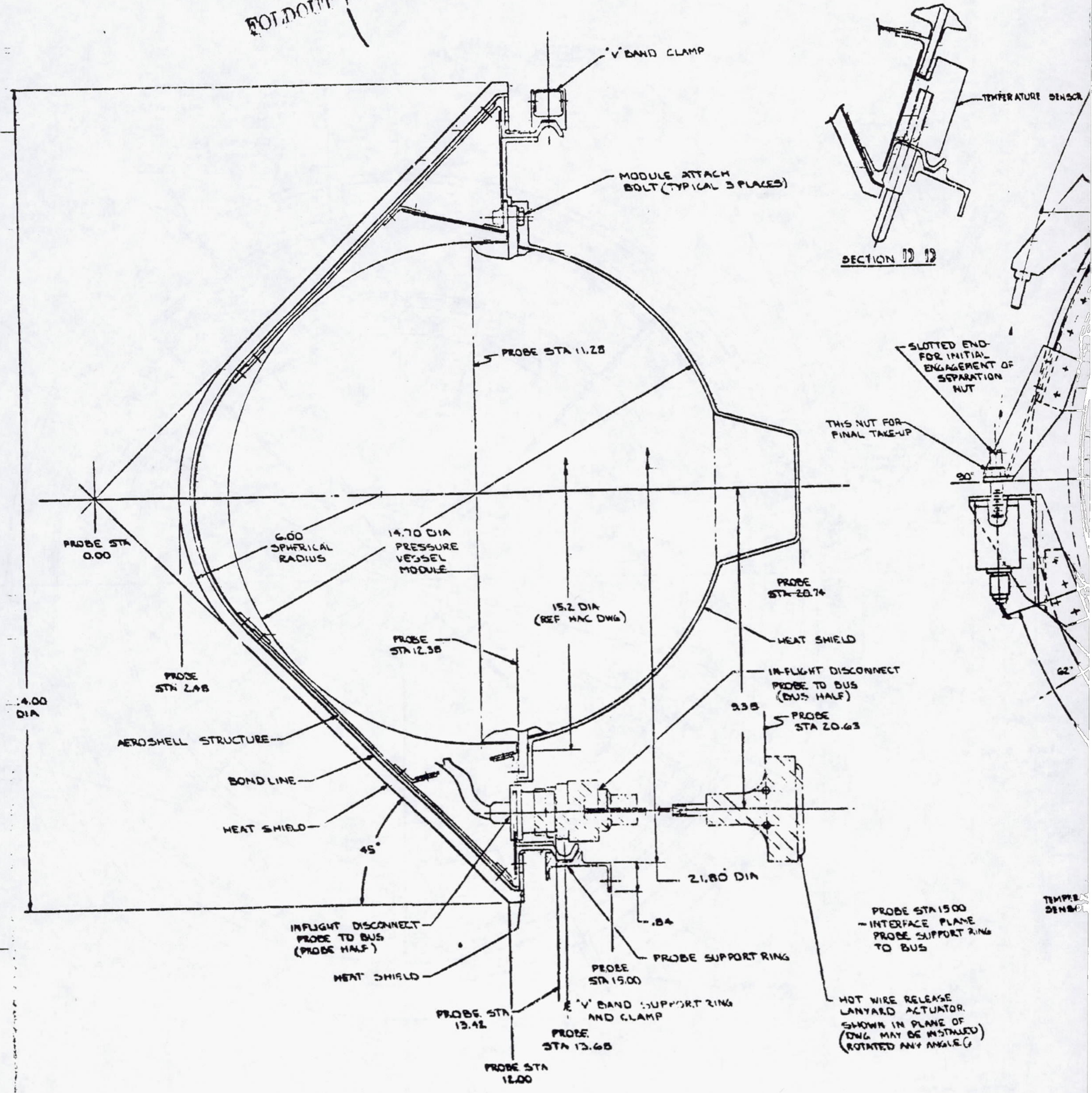

FIGURE 5.3-9. SMALL PROBE INTERFACE DEFINITION

FOLDOUT FRAME

2

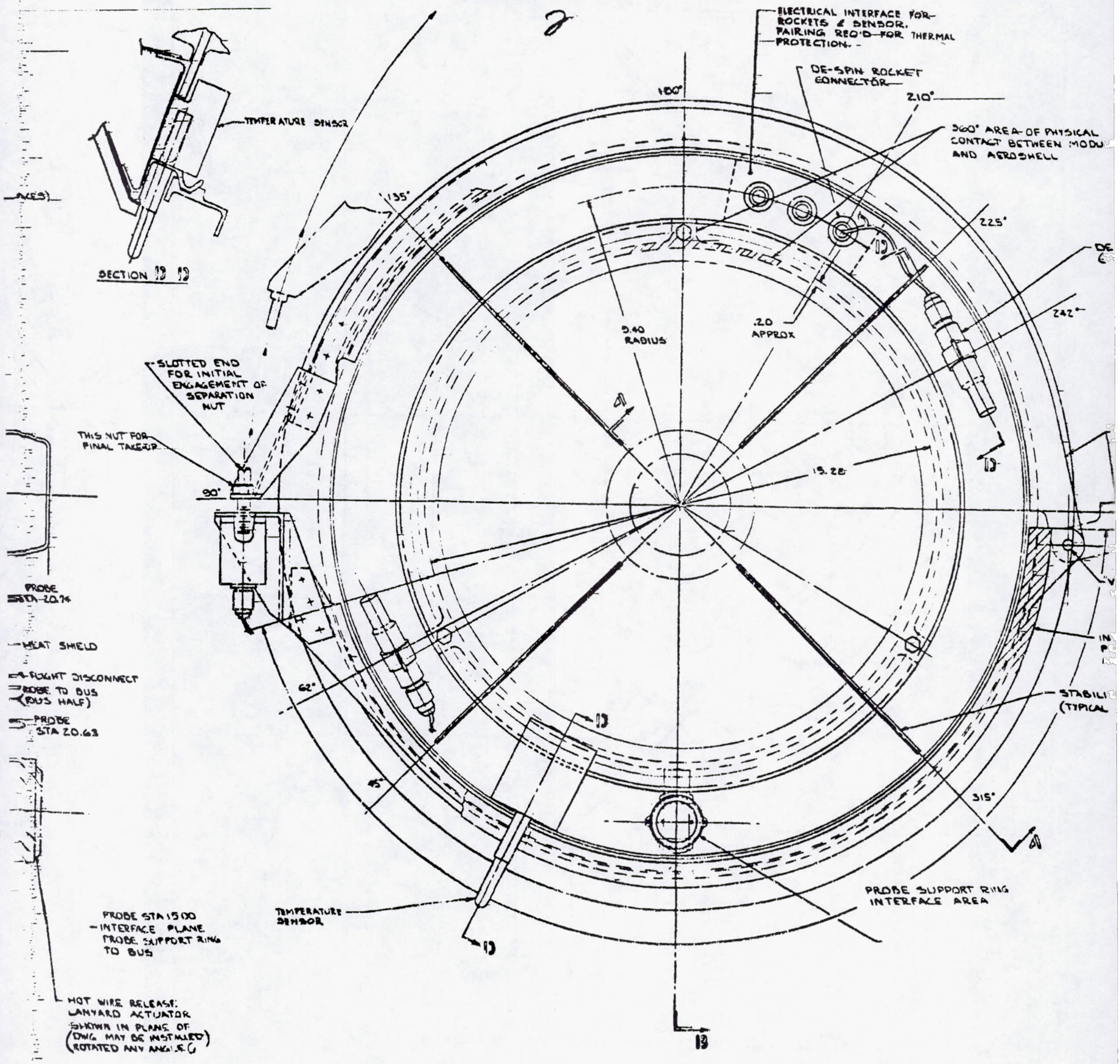

ORIGINAL PAGE IS POOR

FOLDOUT FRAME 3

30163-506(U)

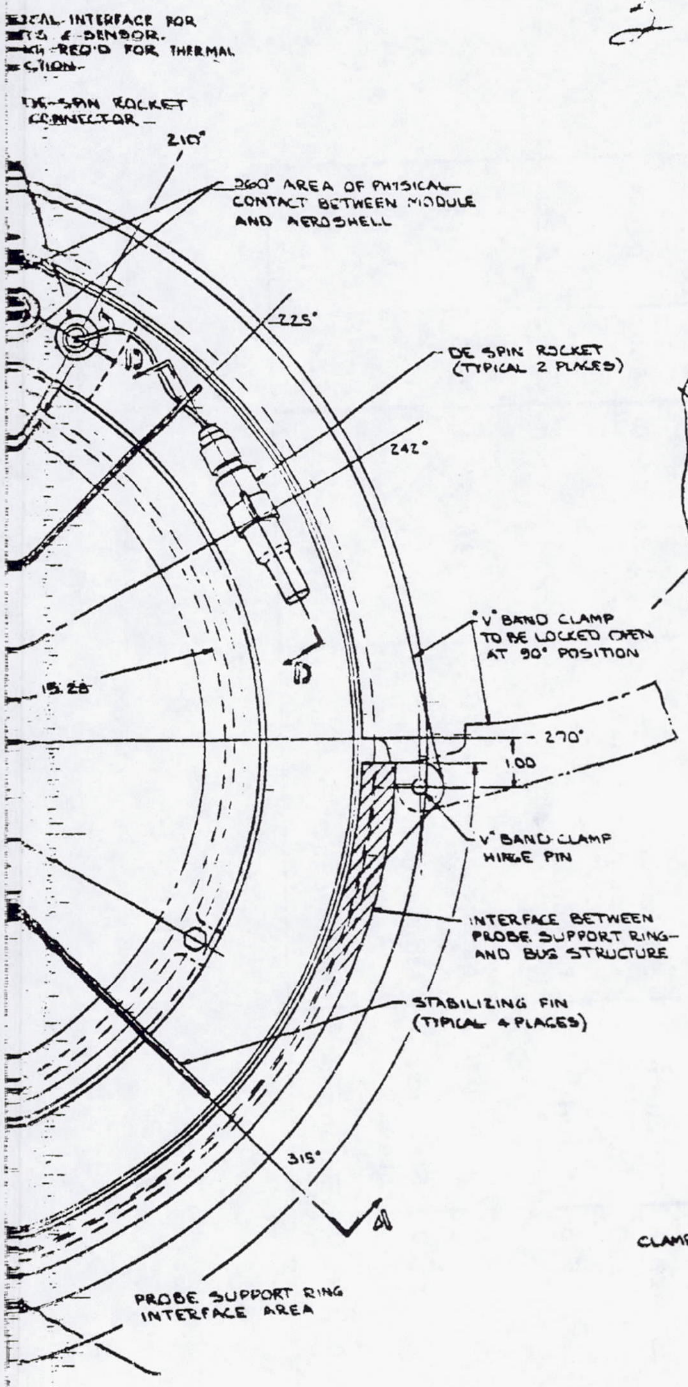

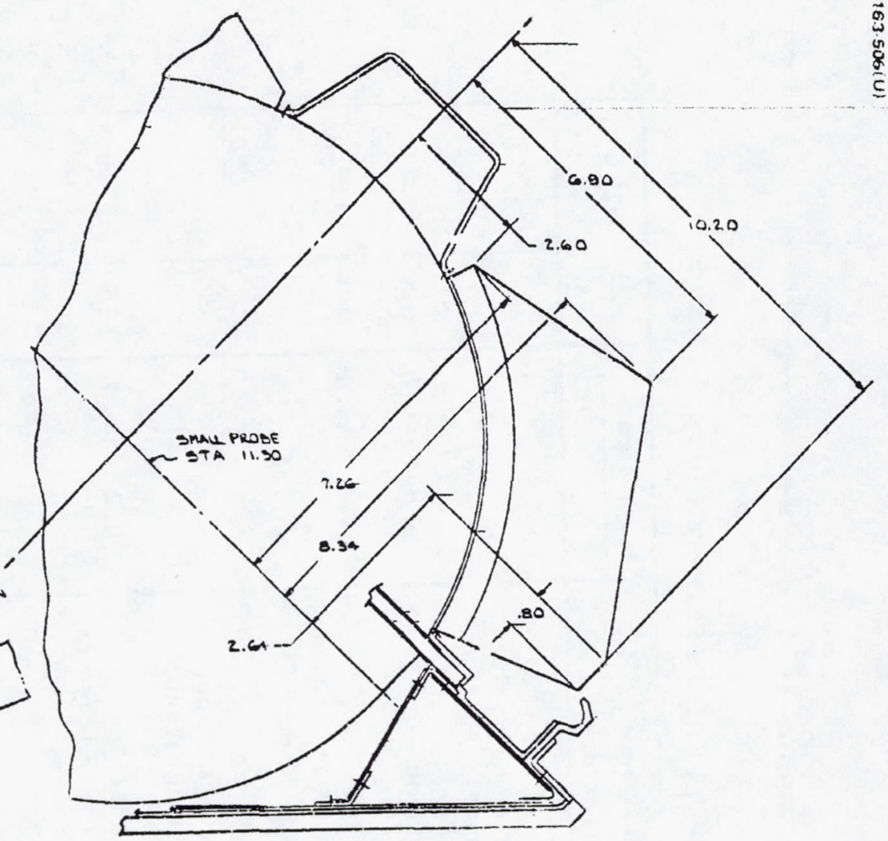

SECTION A - A
SHOWING FIN CONFIGURATION
(TYPICAL 4 PLACES)

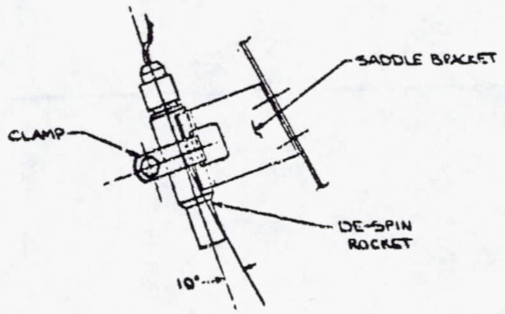

VIEW D - D
TYP 2 PLACES

REPRODUCIBILITY OF THE ORIGINAL PAGE IS POOR.

TABLE 5.3-6. STRUCTURAL DESIGN STUDY

Probe	Diameter		Material	Structure	Weight		g	Design Factor
	m	in.			kg	lb.		
Large	1.232	48.5	Aluminum	Stiffened: Two rings, frustum Two rings, skirt	24.1	53.1	500	1.25
Large	1.232	48.5	Aluminum	Monocoque	26.8	59.0	500	1.25
Large	1.232	48.5	Aluminum	Stiffened: Three rings, frustum Three rings, skirt	22.4	49.4	500	1.25
Large	1.346	53.0	Aluminum	Stiffened: Four rings, frustum Three rings, skirt	27.1	59.7	575	1.50
Large	1.395	55.0	Aluminum	Stiffened: Four rings, frustum Three rings, skirt	30.2	66.4	575	1.50
Small	0.725	28.6	Titanium	Stiffened: One ring, frustum	7.26	16.0	560	1.25
Small	0.725	28.6	Stainless steel	Monocoque	9.58	21.1	560	1.25
Small	0.725	28.6	Titanium	Monocoque	7.26	16.0	560	1.25
Small	0.660	26.0	Stainless steel	Monocoque	8.53	18.8	595	1.50
Small	0.660	26.0	Titanium	Monocoque	6.44	14.2	595	1.50

Manufacturing studies indicate that similar fabrication processes would be used for either concept (i.e., both would be machined from a roll ring forging), therefore, the ring stiffened structure was selected, as the weight saving was considered to be cost effective. As with the Thor/Delta structures, additional weight saving could be effected by increasing the number of stiffening rings; the number of rings was limited to four in the skirt area because a greater number would not be practical for rivetting the webs to the shell; four rings were also selected for the frustum area as being the best compromise between weight and complexity. For the small probes, structures in titanium and stainless steel were considered. Monocoque structure was selected because stiffening rings gave no apparent weight advantage. Stainless steel, although weighting approximately 30 percent more than the equivalent structure in titanium, was chosen to avoid the autoignition problems associated with the latter material. The fins are beryllium because they are small simple structures, and the material is an effective heat sink. The increase in weight incurred by changing these components to stainless steel would have a deleterious effect on the probe center of gravity.

Both probes remain similar in general layout to those described in the previous section. Detail differences include: 1) the deletion of the shock wave radiometer experiment from the large probe, and 2) the IFD of the small probe has been changed from the 45 pin connector to the 65 pin lot wire actuated IFD for commonality with the large probe.

Atlas/Centaur Baselines

Large Probe Deceleration Module Structure (Figure 5.3-10)

The general structural layout for the Atlas/Centaur baseline remains similar to that described for the Thor/Delta baseline, and is shown in Figure 5.3-10. It is a ring stiffened, monocoque, aluminum shell with a nose radius one-half the baseline diameter of 1.395 m (55 in.), and a conical frustum of 45 deg half angle. One detail change from the Thor/Delta baseline is the deletion of the shock wave radiometer experiment.

Small Probe Deceleration Module Structure (Figure 5.3-11)

Here also the general structural layout shown in Figure 5.3-11 is similar to that of the Thor/Delta baseline. It is a plain monocoque (no stiffening rings), stainless steel shell with a nose radius one-half the base diameter of 0.673 m (26.5 in.). The cone half angle of 45 deg is the same as the Thor/Delta.

One detail difference is a change from the 45 pin IFD connector to a 65 pin hot wire actuated IFD, in order to provide commonality with the large probe.

FOLDOUT FRAME

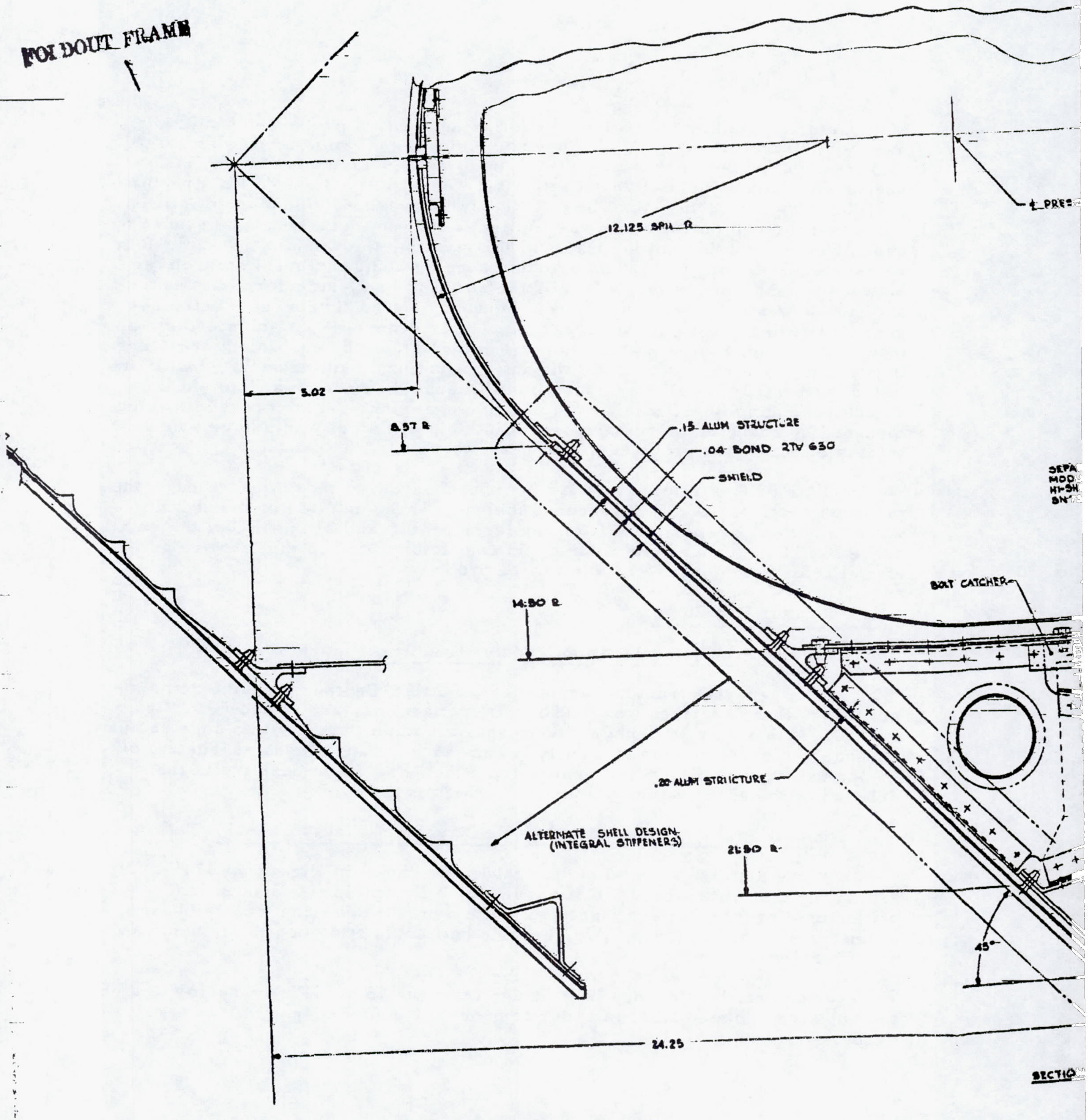

FIGURE 5.3-10. LARGE PROBE INBOARD PROFILE

FOLDOUT FRAME 2

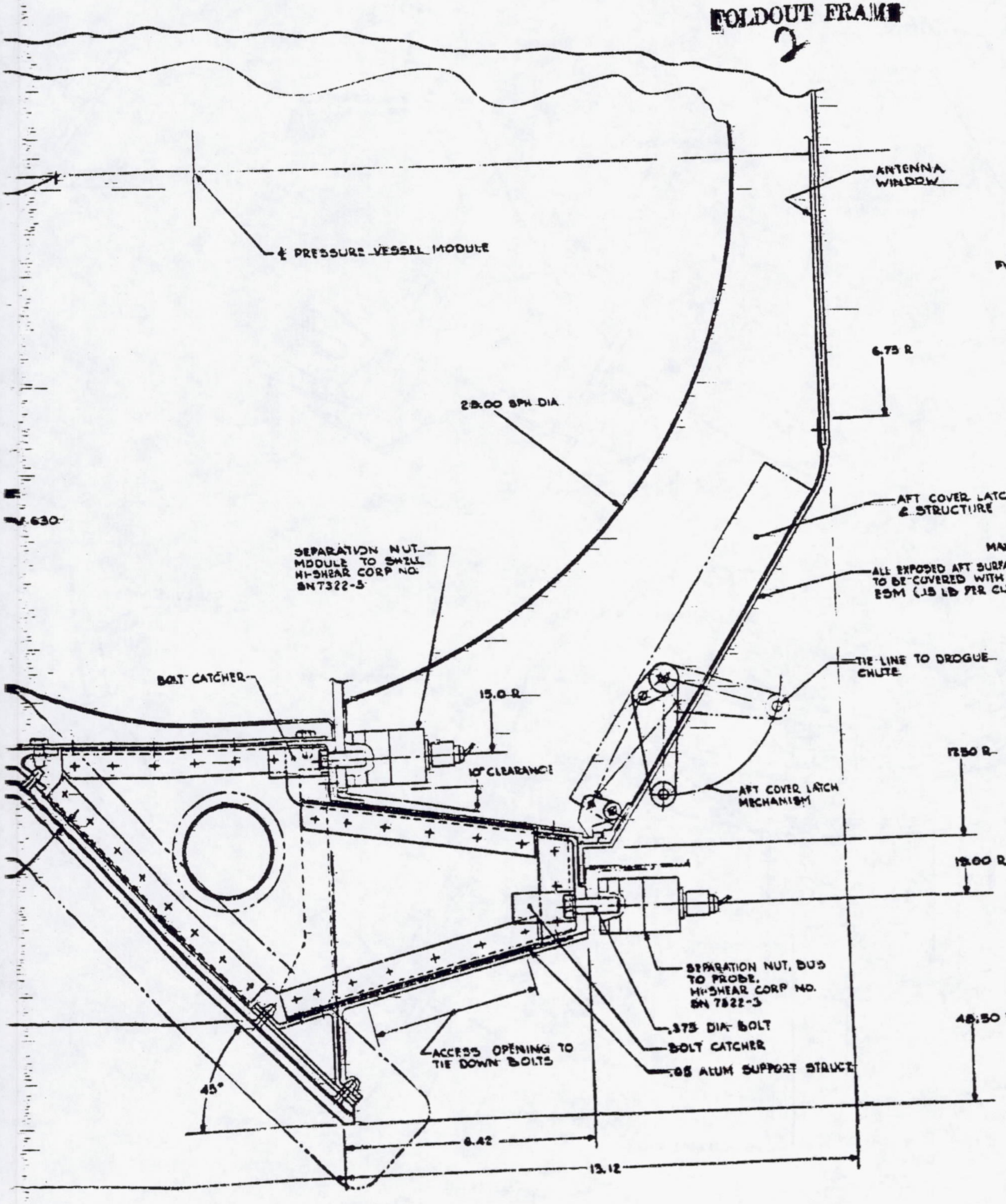

SECTION H-H

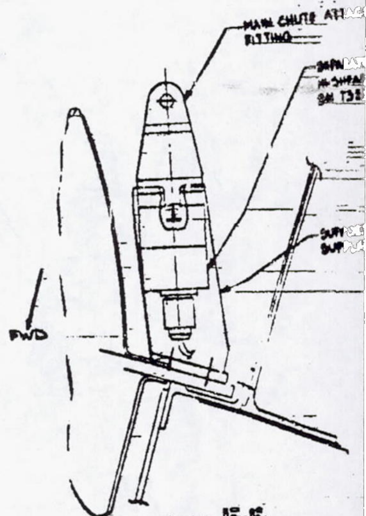

SECTION F-F

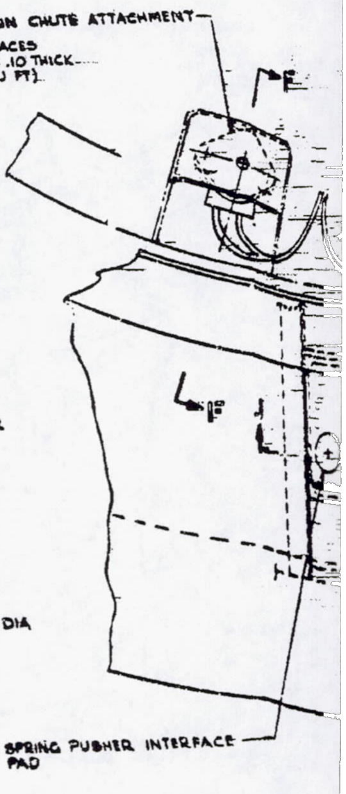

REPRODUCIBILITY OF THE ORIGINAL PAGE IS POOR.

FOLDOUT FRAME 3

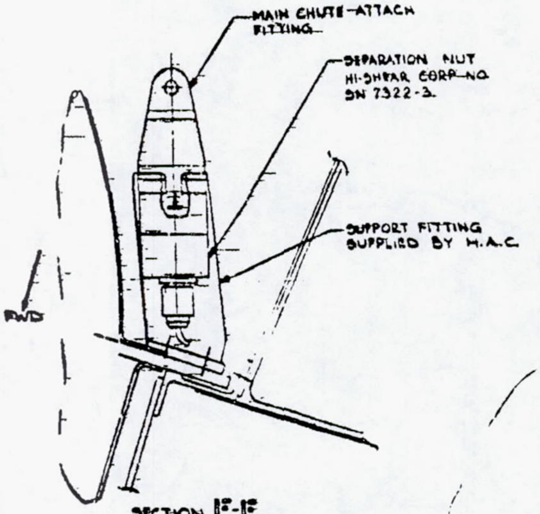

SECTION F-F

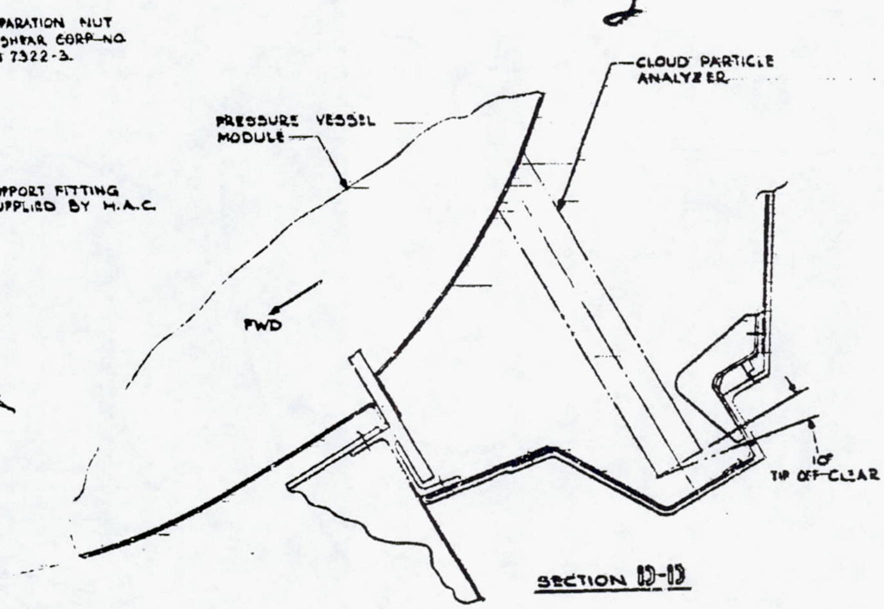

SECTION B-B

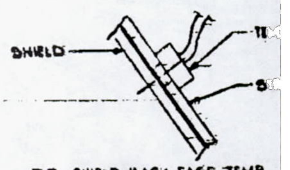

TYP SHIELD BACK-FACE TEMP SENSOR INST'L

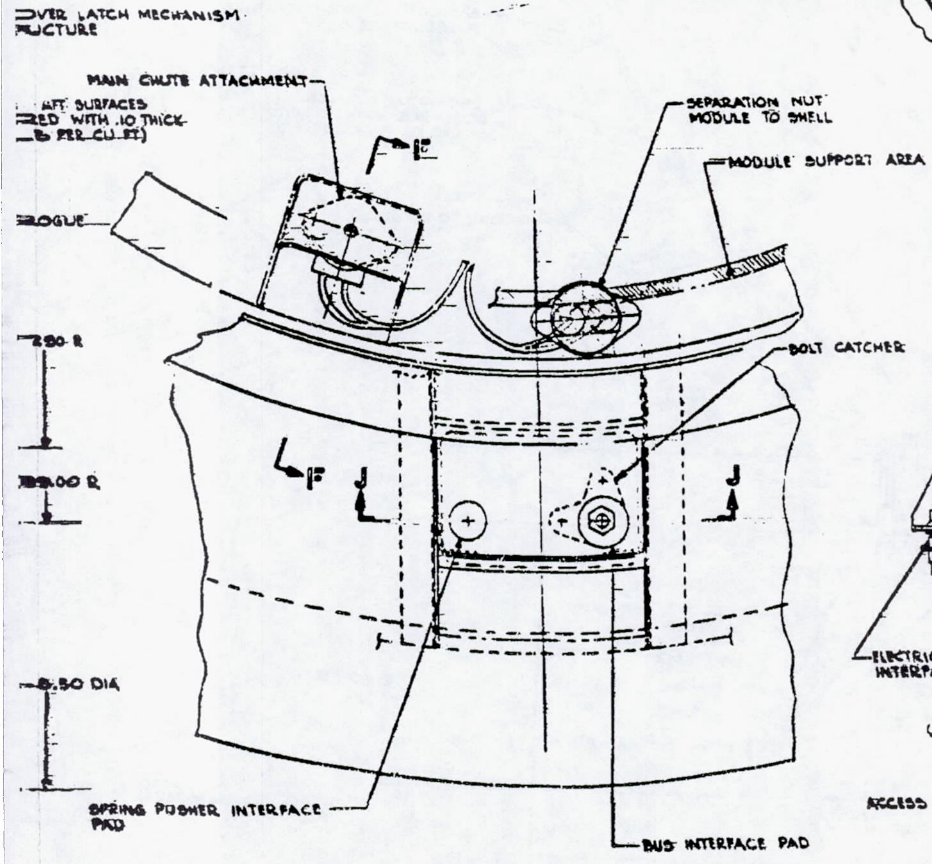

DETAIL A
3 PLACES
AFT COVER OMITTED

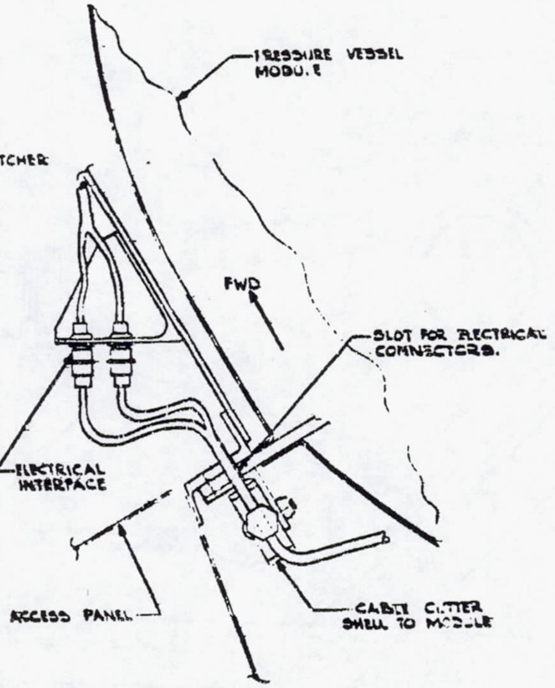

SECTION B-B

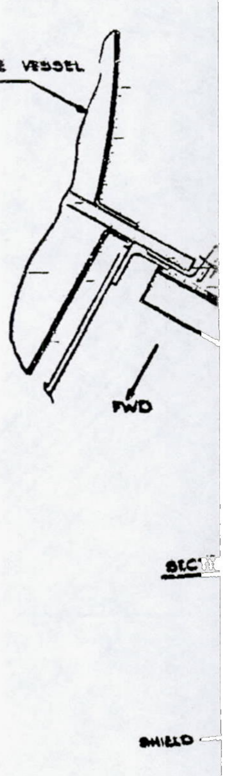

REPRODUCIBILITY OF THE ORIGINAL PAGE IS POOR.

FOLDOUT FRAME 4

TEMP SENSOR

STRUCTURE

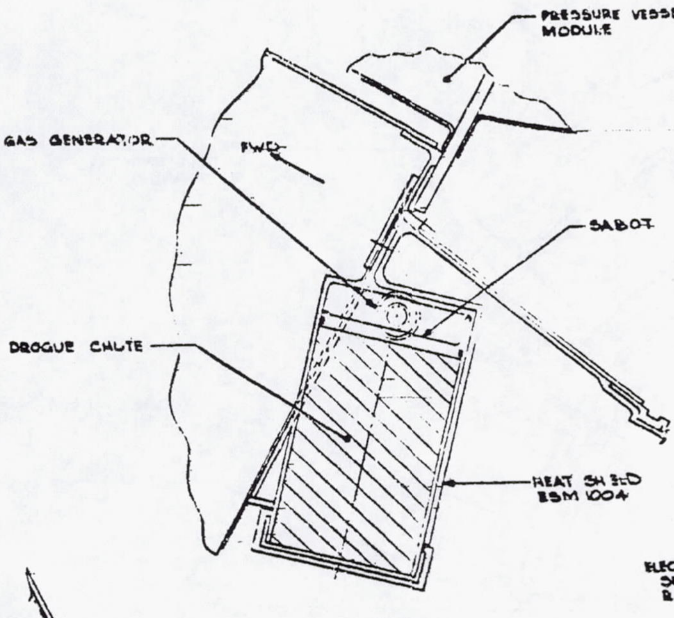

SECTION C-C

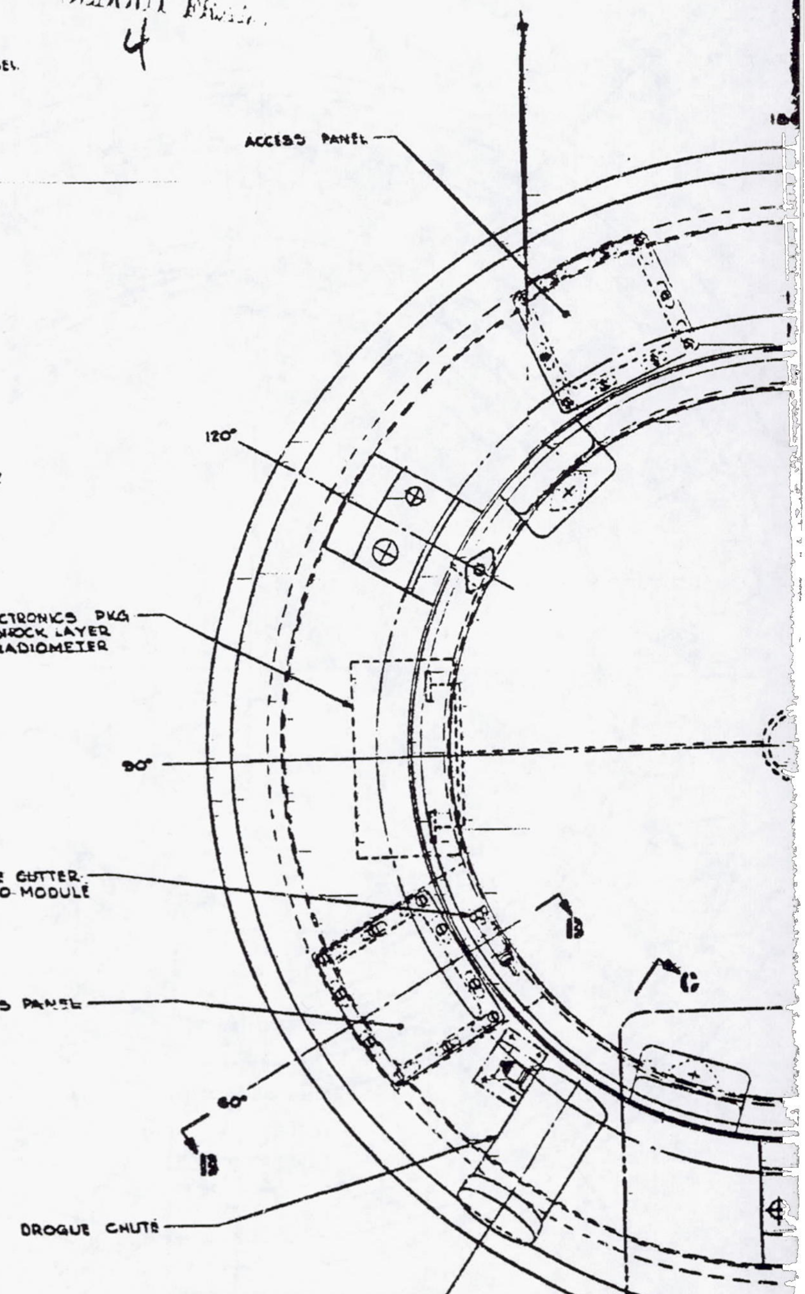

35°

C

SEE DETAIL A

VIEW

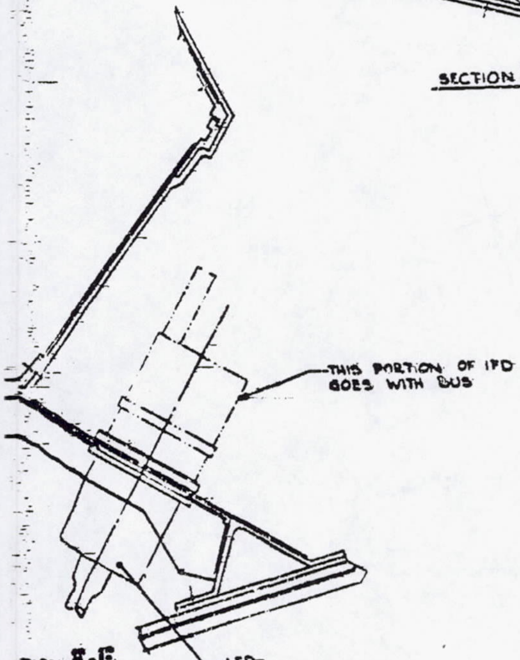

TION E-E

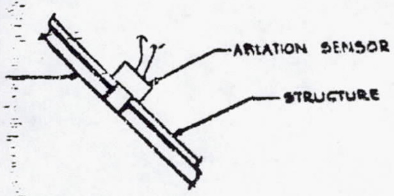

TIP ABLATION SENSOR INST'L

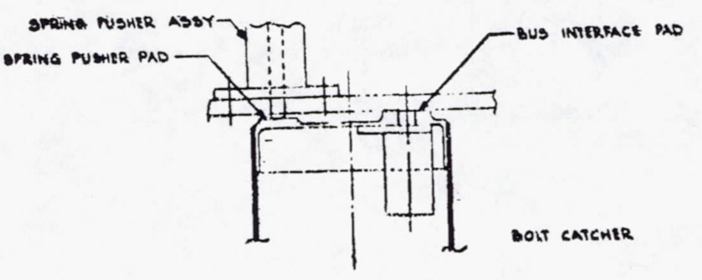

SECTION J-J
TYP 3 PLACES

30163-507(U)

FOLDOUT FRAME 5

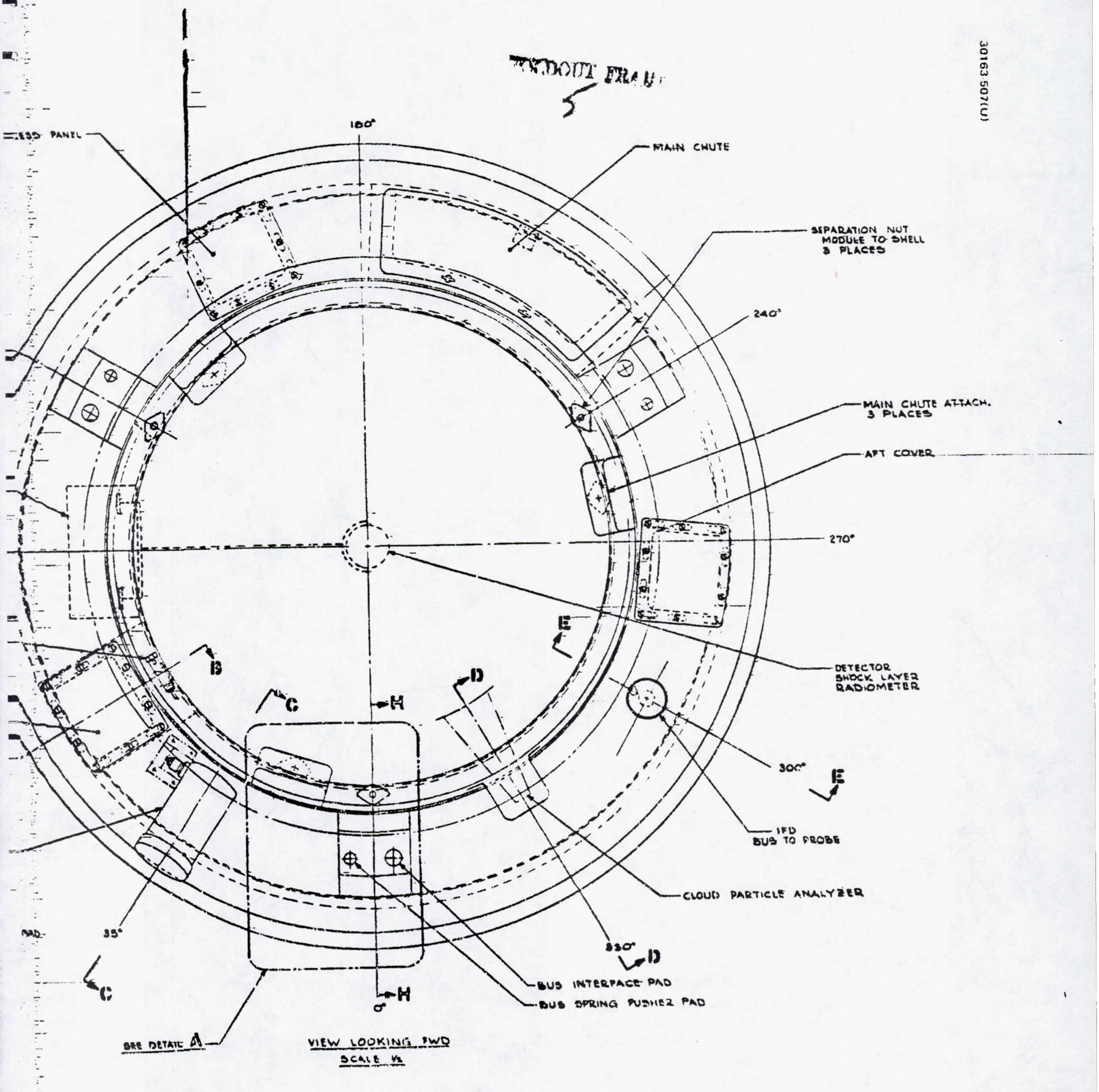

VIEW LOOKING FWD
SCALE 1/2

REPRODUCIBILITY OF THE ORIGINAL PAGE IS POOR.

FOLDOUT FRAME

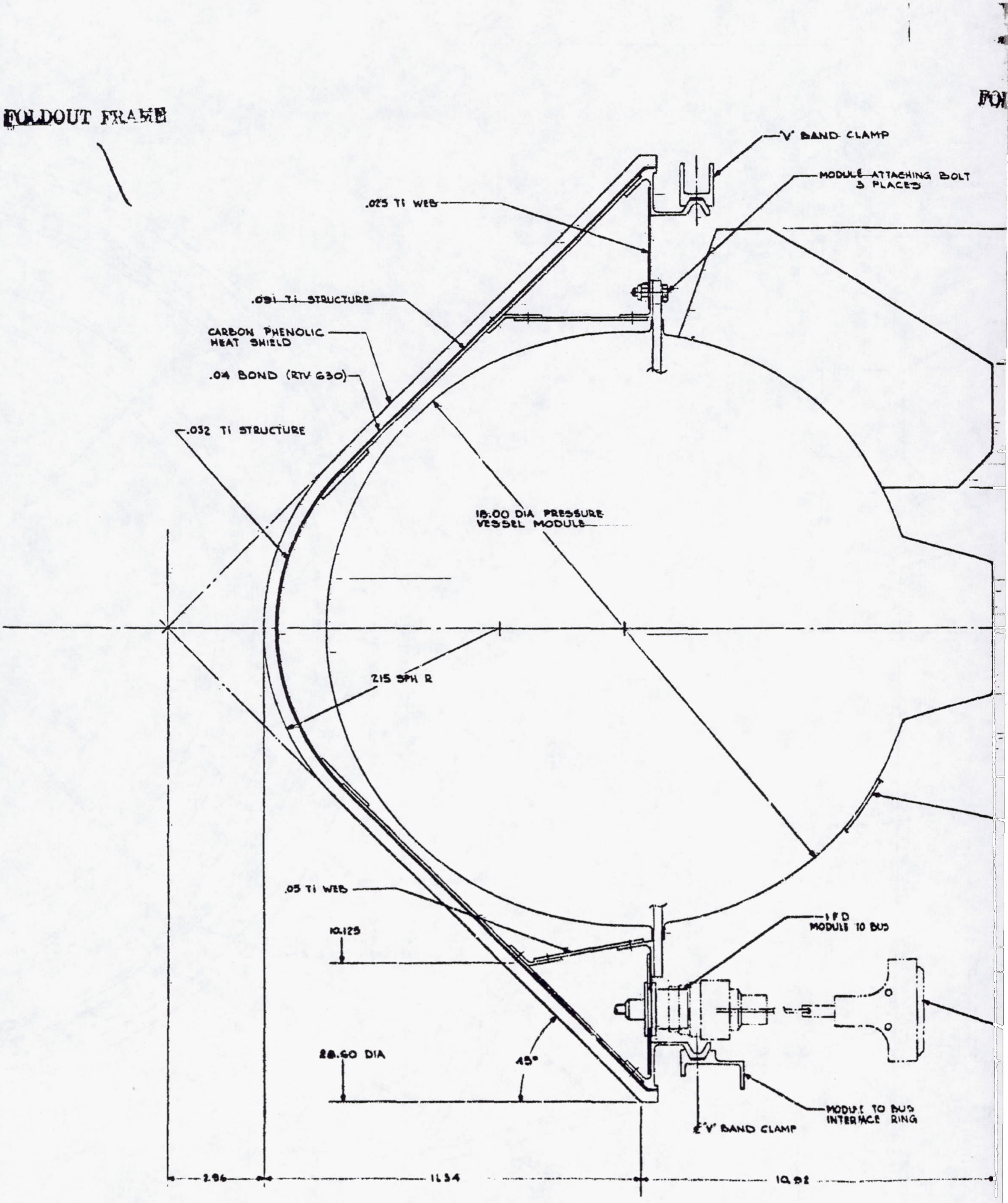

FIGURE 5.3-11. SMALL PROBE INBOARD PROFILE

FOLDOUT FRAME 2

FOLDOUT FRA 3

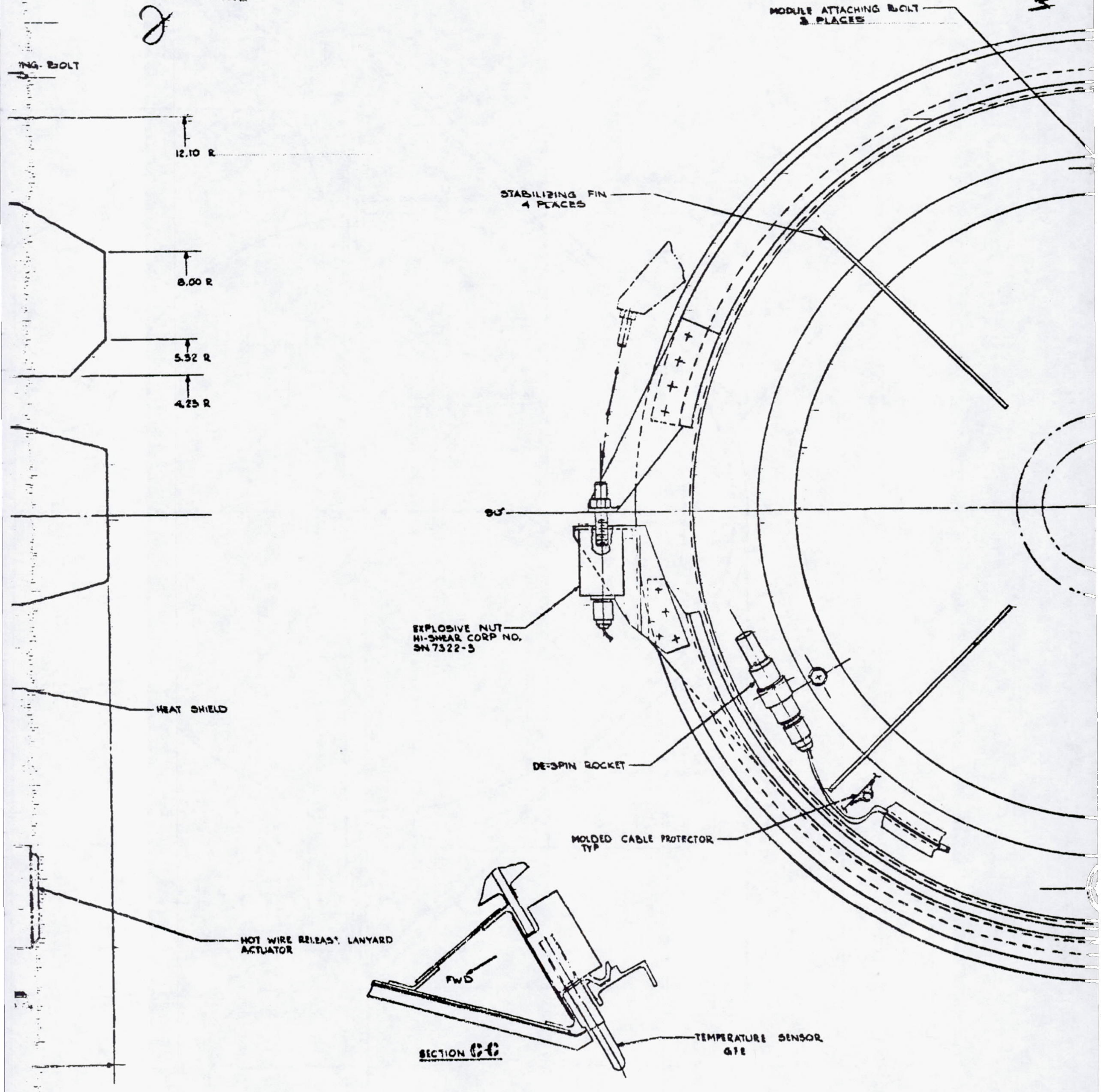

FOLDOUT FRAME

3

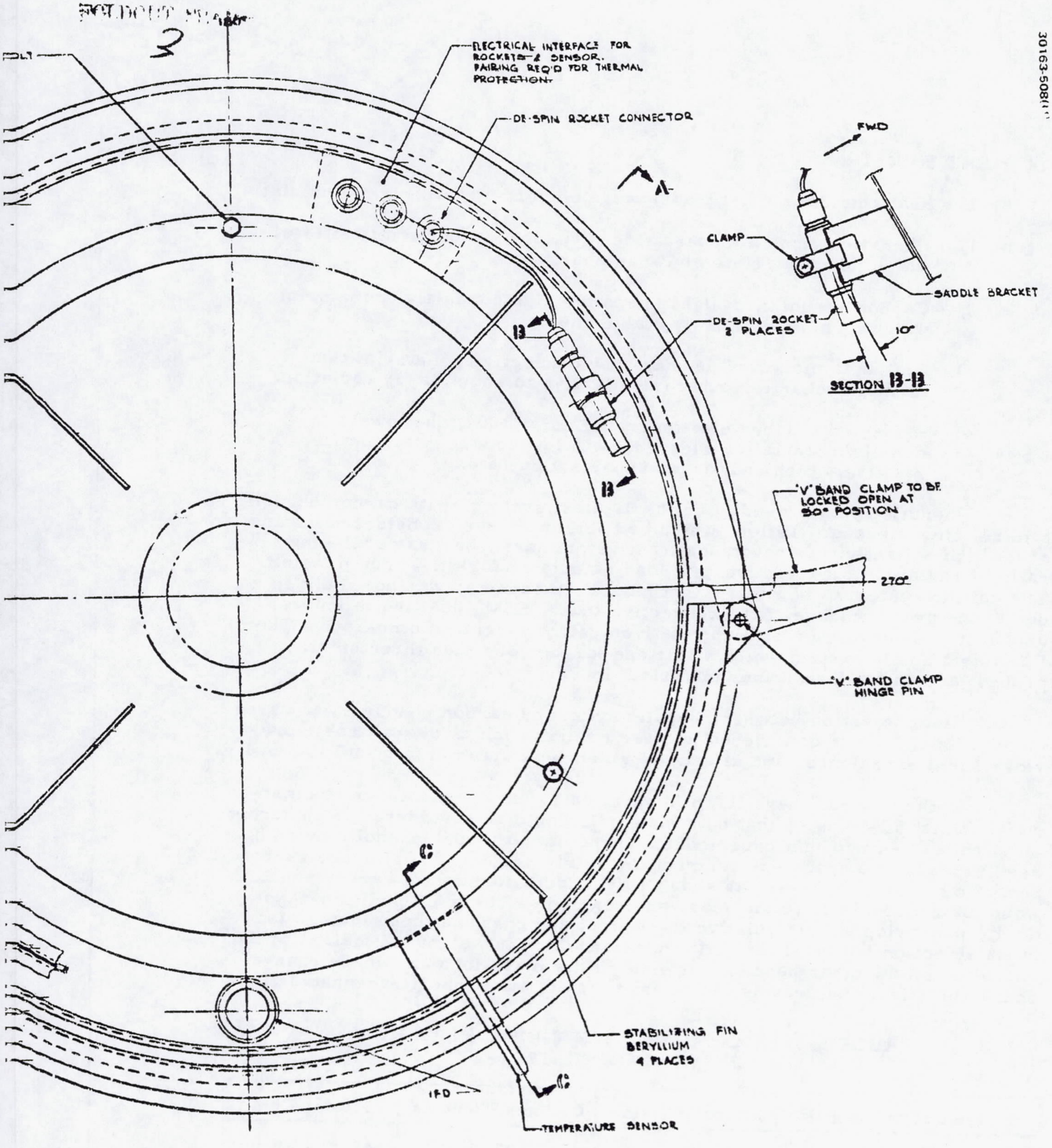

VIEW LOOKING FWD

30163-508(1)

Page intentionally left blank

5.4 HEAT SHIELD

The heat shield material trades were performed for four materials:

1) Phenolic nylon, a moderate density, low conductivity material, which forms a relatively weak char layer.

2) Carbon phenolic, a higher density, high conductivity material which forms a relatively stable char.

3) Teflon, a moderate density, low conductivity material that forms no char layer but is reflective to shock layer radiation.

4) A foamed silicone elastomer, GE ESM 1004, the lowest density material considered, with low conductivity, but a relatively high char layer vaporization rate.

Phenolic nylon proved to be the lightest system, with carbon phenolic a fairly close second. Teflon, which had originally been considered because of its high reflectivity, proved unattractive primarily because of the low ratio of radiative to convective heat load calculated for the Venus mission. The gain in system weight that might have been expected was not realized due to the predominance of the convective load. ESM 1004 like teflon was unacceptable because of its high relative system weight. Comparative Thor/Delta heat shield system weights (for one large probe plus three small probes) are shown for all four materials in Table 5.4-1.

Final selection between phenolic nylon and carbon phenolic was based on additional factors considered in these studies such as overall cost, previous flight experience, and effects on science as summarized in Table 5.4-2.

Both materials have flown in earth entry environments approximately equal to that of Venus so that both materials could be considered to be acceptable from an entry flight experience standpoint. Although phenolic nylon has been exposed to a space environment for fairly prolonged flights and carbon phenolic has not, analysis has shown that no deterioration of carbon phenolic would be expected due to the space environment. The main points in favor of phenolic nylon are its relative low weight and cost and these factors led to its selection for the Thor/Delta mission which is weight critical. Carbon phenolic, on the other hand, is superior in its mass loss and shape change characteristics, thus easing the science task of atmospheric reconstruction.

TABLE 5.4-1. COMPARATIVE THOR/DELTA HEAT SHIELD SYSTEM WEIGHTS, kg

Substructure Material	Phenolic Nylon	Carbon Phenolic	Teflon	ESM
Al	22	27.6	48.4	89.0
Be	20.5	24.1	45.5	87.0

TABLE 5.4-2. HEAT SHIELD SELECTION FACTORS

Factor	Phenolic Nylon	Carbon Phenolic	Choice
$m/C_D A$ accuracy, percent	2	0.5	CP
System weight — 1976, kg*	22.6**	27.4***	PN
System weight — 1978/80, kg	+8 percent	+1 percent	PN (?)
Cost	Nominal	Nominal + 0.3 m	PN
Potential application to outer planet mission	Not competitive	Applicable to some missions	CP (?)
Flight experience			
Flux levels	Comparable to Venus mission	Comparable to Venus mission	No obvious choice
Vacuum exposure	to 30 days	20 min	CP
Entry performance uncertainties	—	—	CP

*System weights are for total of 1 large and 3 small heat shields — Thor/Delta.

**Includes 1.25 safety margin on nominal thickness requirement.

***Includes 1.20 safety margin on nominal thickness requirement.

Another major point in favor of carbon phenolic (CP) is its relative insensitivity to uncertainties in the calculated heat load. Phenolic nylon with its high mass loss rate is much more sensitive to any changes in heat load, thus CP would be less susceptible to unknowns.

With the final selection of the Atlas/Centaur launch vehicle, the weight advantage of phenolic nylon (PN) over CP because of secondary importance. Therefore, considering the already stated advantages, CP was selected as the heat shield material for the Atlas/Centaur design.

Following the trades that lead to a selection of CP as the preferred heat shield material for the Atlas/Centaur application, studies were conducted to determine the performance of this material. These studies established the entry heating loads, the heat shields thermal responses and led to the selection of the heat shield thicknesses. An orbital cold soak analysis and entry thermal stress analysis provided further confidence in the application of carbon phenolic to this mission. Supporting discussions of bonding materials and carbon phenolic heat shield fabrication techniques are included to provide a further technical base for the evaluation of carbon phenolic heat shields.

Requirements

The heat shield material selection and sizing was based upon the following system parameters:

THOR/DELTA

Entry velocity	11.1 km/sec
Entry angle	35 to 60 deg large probe 20 to 90 deg small probe
Atmosphere	September 1972 Venusian atmosphere Model No. I, NASA SP8011

ATLAS/CENTAUR

Entry velocity	11.6 km/sec
Entry angle	25 to 60 deg large probe 20 to 90 deg small probe
Atmosphere	September 1972 Venusian atmosphere Model No. I, NASA SP8011

In order to achieve a relatively low cost design consistent with the program objectives, the candidate materials were limited to flight proven concepts. Other factors that were considered were weight, ease of manufacturing, repairability, susceptibility to changes in design conditions, and the resultant mass loss in the supersonic portion of the flight. Mass loss became a critical parameter by affecting the accuracy with which atmospheric reconstruction could be accomplished.

Trade Studies

Hypersonic Entry Heating -- Thor/Delta

Convective and radiative heat transfer rate histories have been calculated for the large and small probes for both forebody and afterbody vehicle locations using the methods described in Reference 1. Calculations were performed at the shallow end of the flight path angle entry corridor, since experience has shown that generally the heat shield is sized by the trajectory that maximizes the time integrated heat transfer and has the longest heating duration.

Convective and radiative heat transfer rate histories to the probe stagnation point and to the location on the skirt where the turbulent heat transfer is the maximum are illustrated in Figures 5.4-1 through 5.4-4 for the large and small probes. Transition from a laminar to turbulent boundary layer is assumed to occur between a Reynolds number, based on local boundary layer edge properties and wetted length of 100,000 and 200,000.

The variation of entry heat load with path angle has been estimated using approximate techniques. The baseline analysis at the shallow path angle limit of the entry corridor has been used as the reference point. It can be seen, Figure 5.4-5, that the total heat load decreases with increasing path angle.

Heat transfer in the separated flow base region is illustrated in Figure 5.4-6 for the large probe, which is also typical of the small probe.

Phenolic Nylon Ablation Modeling

The laminar and turbulent hypersonic ablation of PN in air has been extensively investigated both analytically and experimentally. Much of the analysis and testing has been done at local pressures less than 1 atm and very low aerodynamic shear levels. At these conditions in air, Wakefield et al, have demonstrated that the consumption of the available oxygen at the char surface by the pyrolysis gases must be accounted for in order to accurately compute the char surface oxidation rates. G. E. flight experience on both Discoverer and Biosatellite vehicles is consistent with the results of Wakefield. In the mild satellite entry environment where the local aerodynamic shear is less than 48 N/m^2 (1 lb/ft^2) and the local pressure is less than 10^5 N/m^2 (1 atm), there is negligible char surface oxidation for time integrated heating loads as high as 2.3×10^8 J/m^2 (20,000 BTU/ft^2).

As the local pressure increases above about 10^5 N/m^2 and the aerodynamic shear above about 48 N/m^2, the char layer begins to fail and erode due to local stresses. This effect is demonstrated by the data of Hiester and Clark for local pressures above one atmosphere. A summary of the G. E. phenolic nylon flight test data in air from high performance reentry vehicles where the aerodynamic shear ranged up to 4.8×10^3 N/m^2 (100 lb/ft^2) and the local pressure up to 4×10^6 N/m^2 (40 atm) is presented in Figure 5.4-7, and demonstrates that the char mass loss, in the high pressure/shear environment is more than one would predict using the graphite oxidation theory. The total data scatter at the higher enthalpies is about 25 percent. The effective heat of albation, Q^*, is defined as the hot wall convective heat transfer rate divided by the char mass loss rate.

Additional low pressure plasma arc ground test data are shown in Figure 5.4-7 for various combinations of convective-radiative heat flux and various test gases. It is seen that generally the effective heat of ablation is much higher for these low pressure plasma arc tests than for the high pressure-shear flight environments.

The correlation of Figure 5.4-7 includes only the convective heat flux. As hot gas radiation is superimposed upon the convective flux and reaches a value of about three times the convective heating, the total mass loss consists only of the sublimation mass loss due to radiation. This occurs because nearly all of the convective heat flux is blocked (Figure 5.4-8).

As a check of the validity of Figure 5.4-8, some of the GE PN flight data were superimposed upon it at the appropriate value of predicted hot gas radiation. Note that the measured mass loss rate is about two times that predicted by the theory. Hence, it is concluded that the increase in char mass loss rate, due primarily to the aerodynamic shear effects, masks any effect due to the hot gas radiation.

In this design trade study, the empirical correlation suggested by Kettock, Figure 5.4-7, that includes the mechanical removal of the char due to the aerodynamic shear effect has been employed. Since the char layer is removed by shear forces as it is produced and since both the convective and radiative heat transfer contribute to char production, the radiative and convective heat transfer rates were combined to calculate the char mass-loss rates in this study. The validity of this approach for use in CO_2 and combined convective-radiative heating was demonstrated in the ablation screening test program.

Carbon Phenolic Ablation Modeling

Carbon phenolic heat shield material is flying on the present generation high performance earth re-entry vehicles. This material has several advantages, including high char erosion resistance and extreme shape stability after fabrication.

As CP is heated in air, the phenolic resin decomposes, leaving a dense carbonaceous residue that undergoes oxidation at the char surface for temperatures above 1000°K. The oxidation rates at the char surface are controlled by the available oxygen diffusing through the boundary layer. In this diffusion limited region, the char oxidation rates are computed in air by:

Laminar flow $$\dot{m}_D = \frac{\dot{q}_c}{5.88\,(h_r - h_w)}$$

Turbulent flow $$\dot{m}_D = \frac{1}{6.8}\,\frac{\dot{q}_c}{(hr - hw)}$$

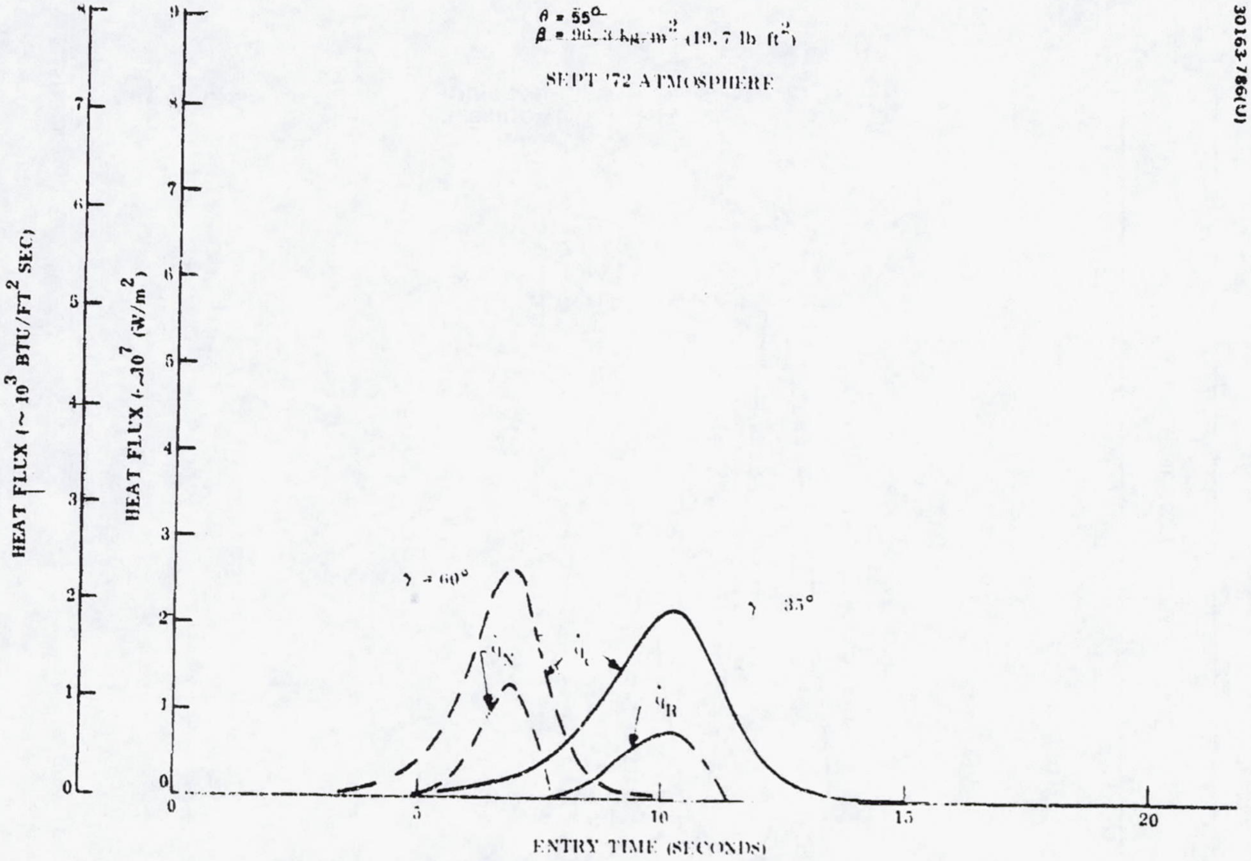

FIGURE 5.4-1. LARGE PROBE STAGNATION HEAT FLUX HISTORIES

30163-786(U)

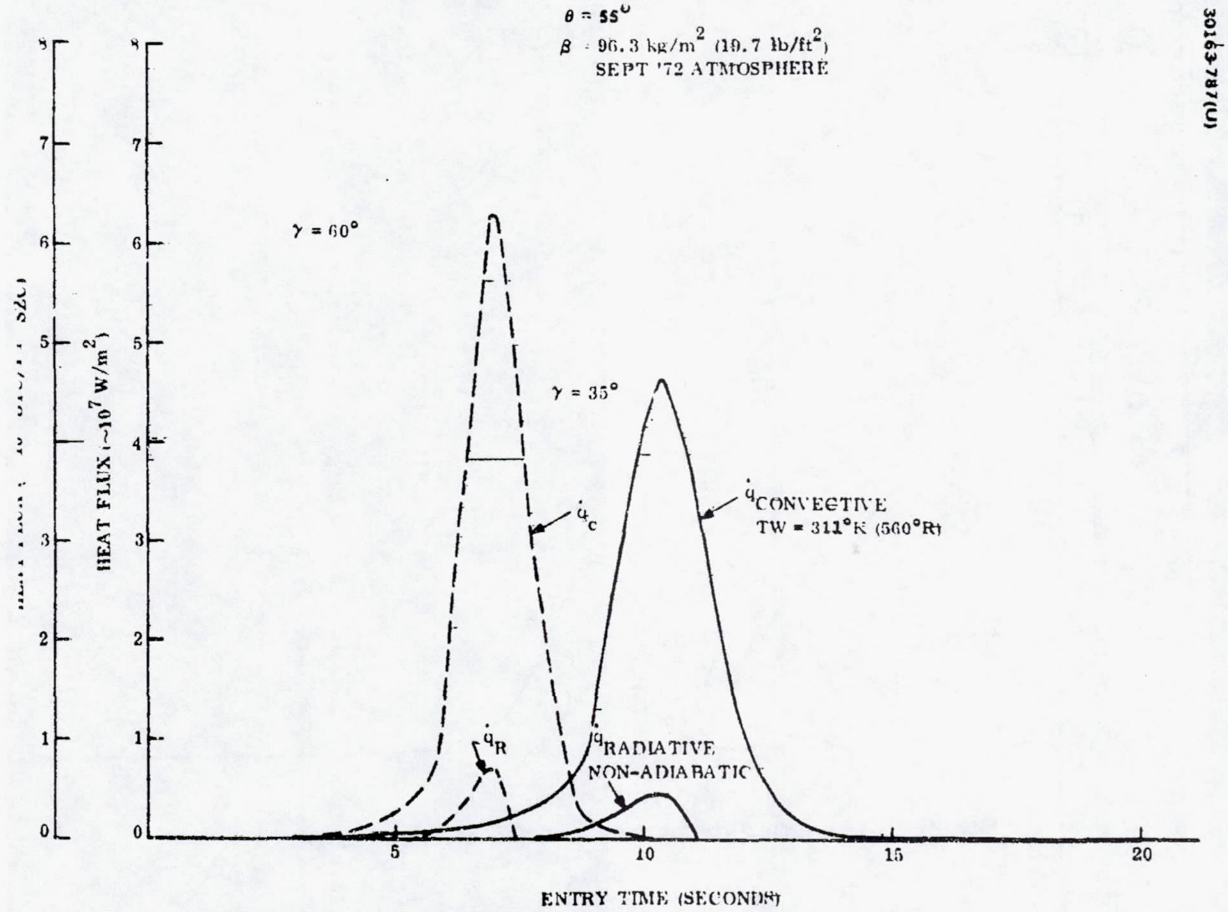

FIGURE 5.4-2 LARGE PROBE SKIRT MAXIMUM HEAT FLUX HISTORIES

30163-787(U)

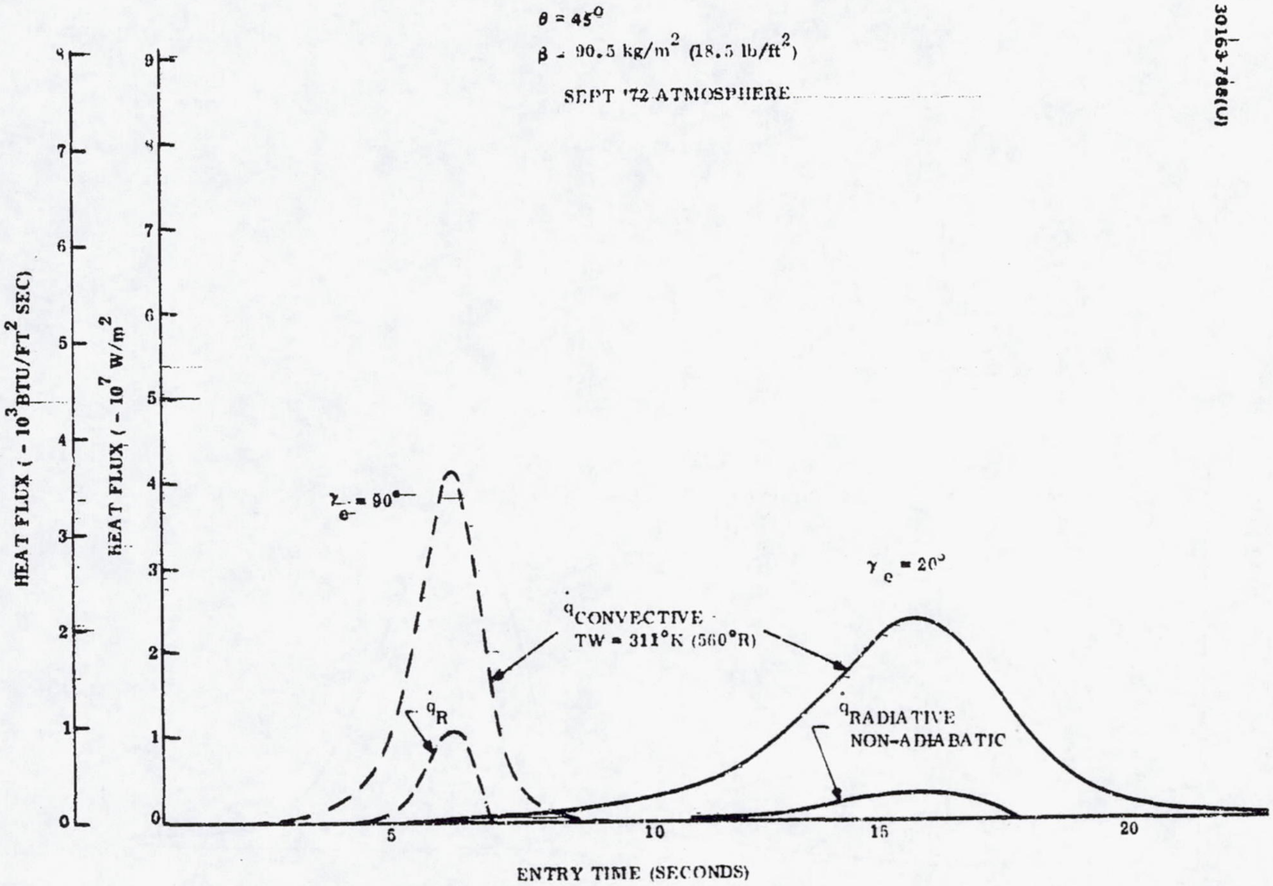

FIGURE 5.4-3 SMALL PROBE STAGNATION HEAT FLUX HISTORIES

30163-788(U)

30163-789(U)

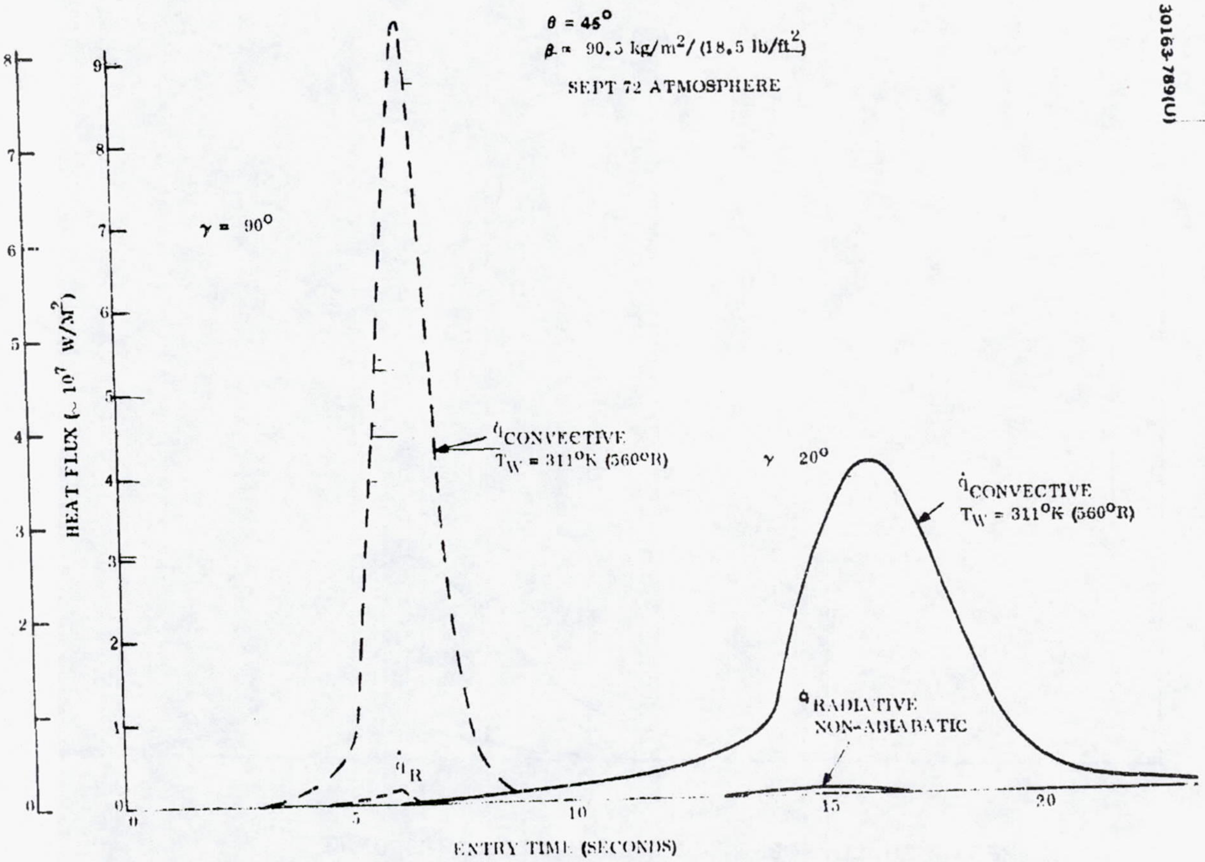

FIGURE 5 4-4. SMALL PROBE SKIRT MAXIMUM HEAT FLUX HISTORIES

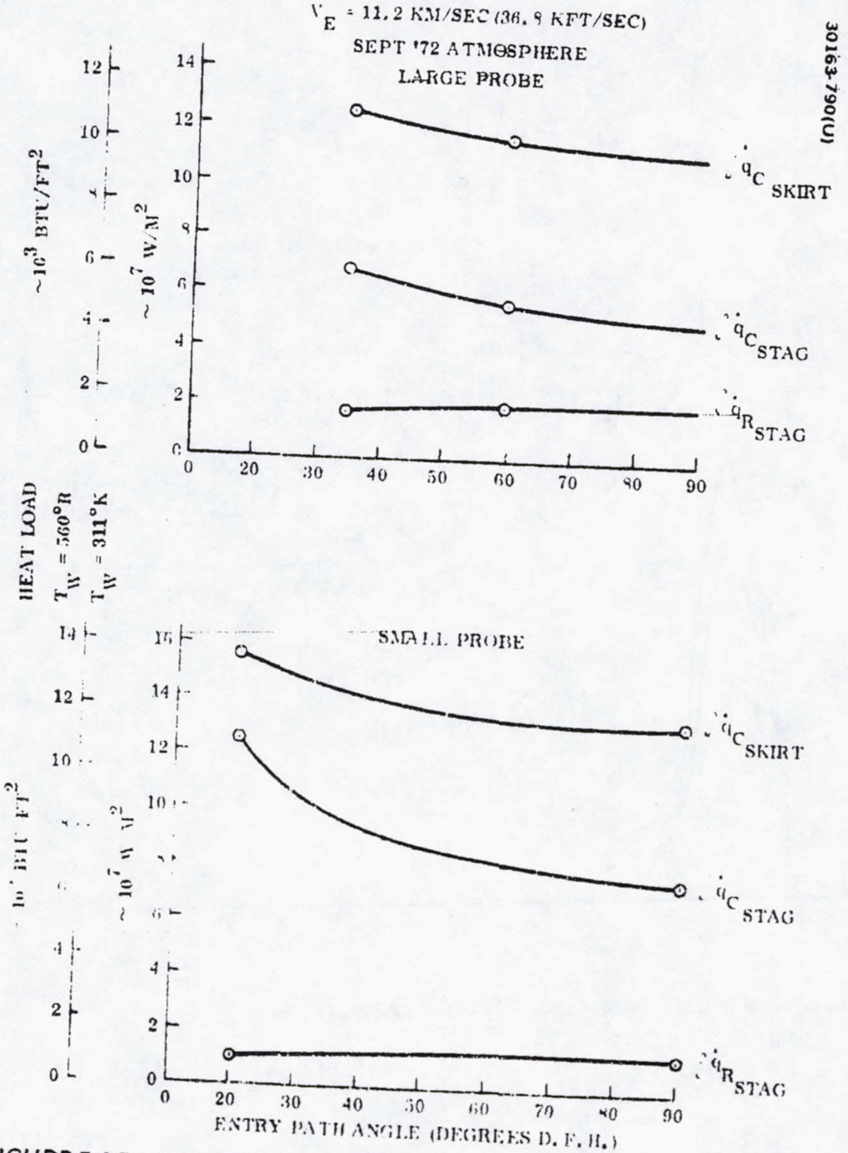

FIGURE 5.4-5. VARIATION OF ENTRY HEAT LOAD WITH PATH ANGLE

REPRODUCIBILITY OF THE ORIGINAL PAGE IS POOR

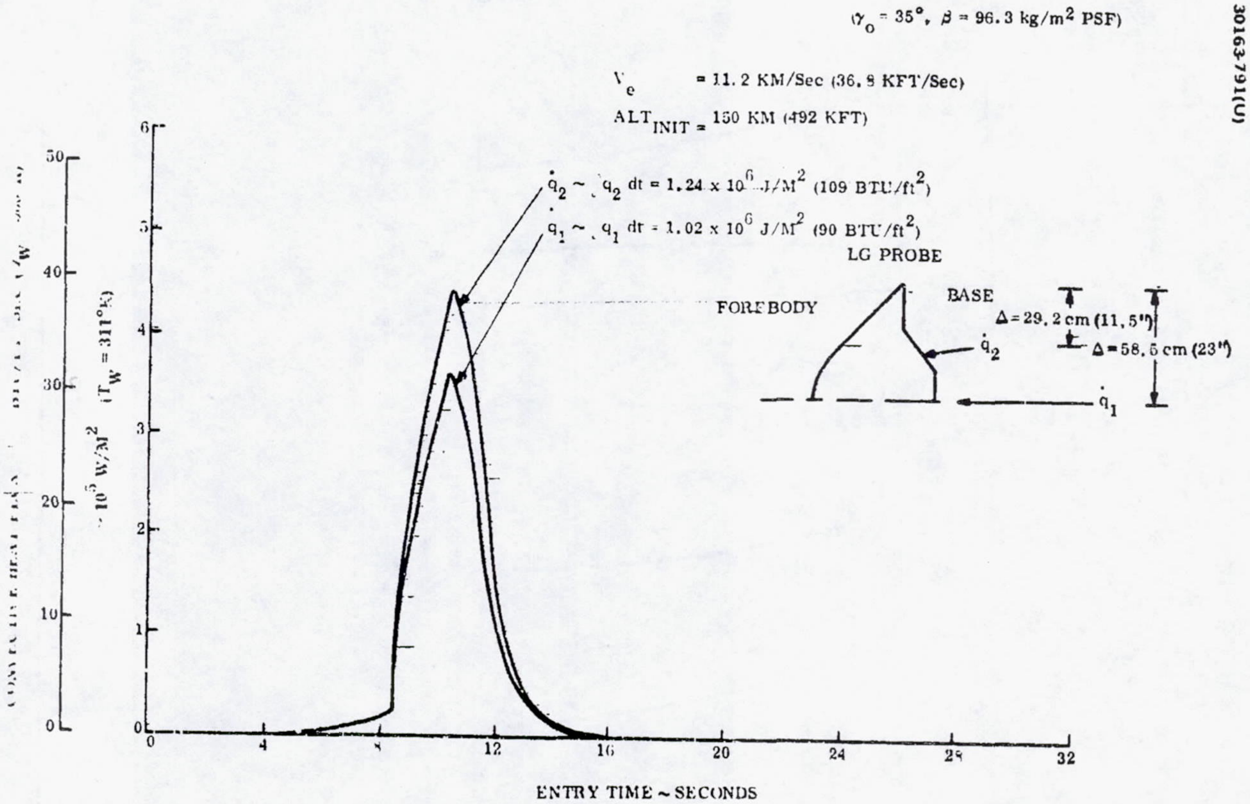

30163-791(U)

FIGURE 5.4-6. LARGE PROBE BASE CONVECTIVE HEAT FLUX HISTORIES

REPRODUCIBILITY OF THE ORIGINAL PAGE IS POOR.

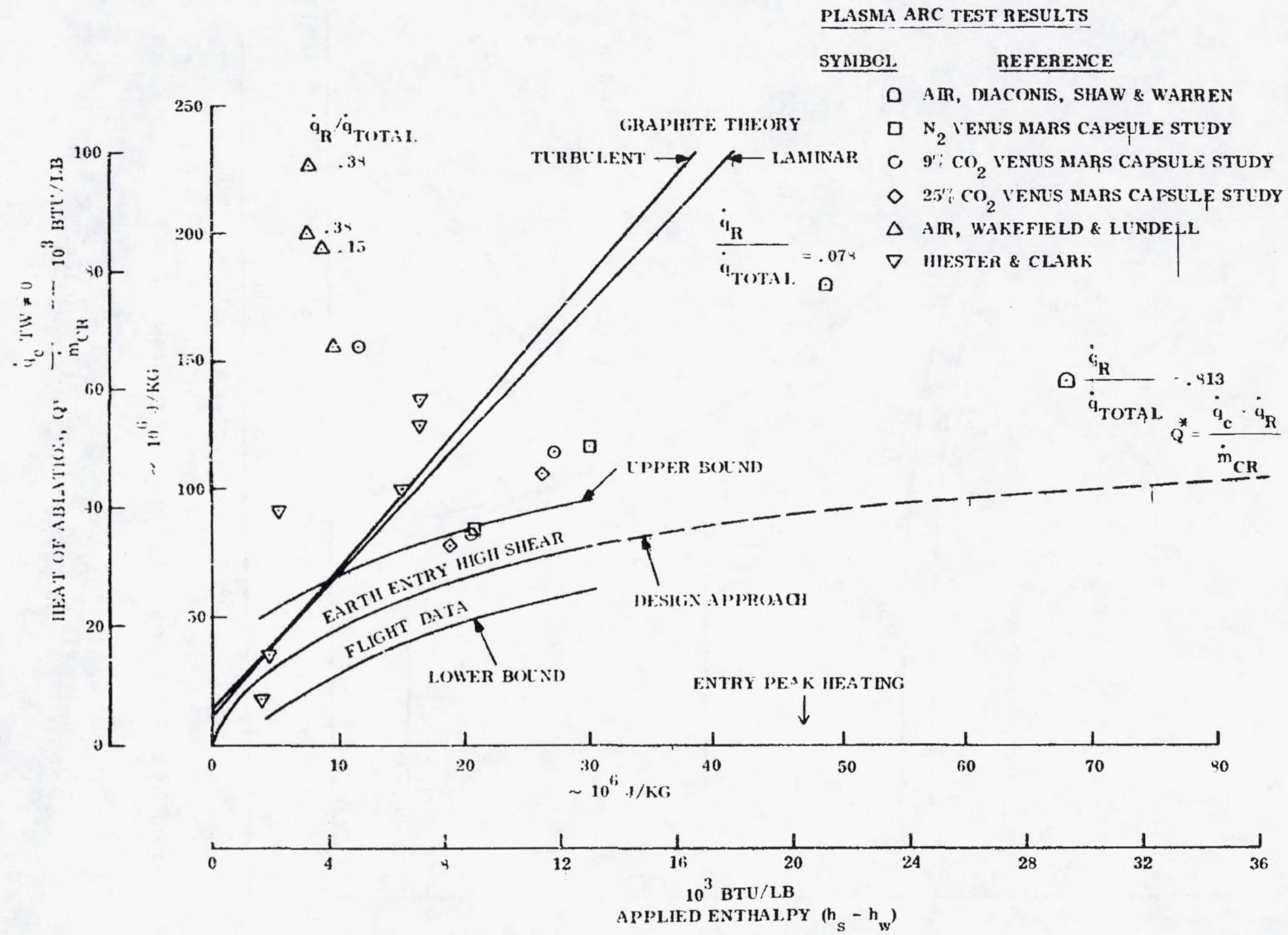

FIGURE 5.4-7. PHENOLIC NYLON HEAT OF ABLATION

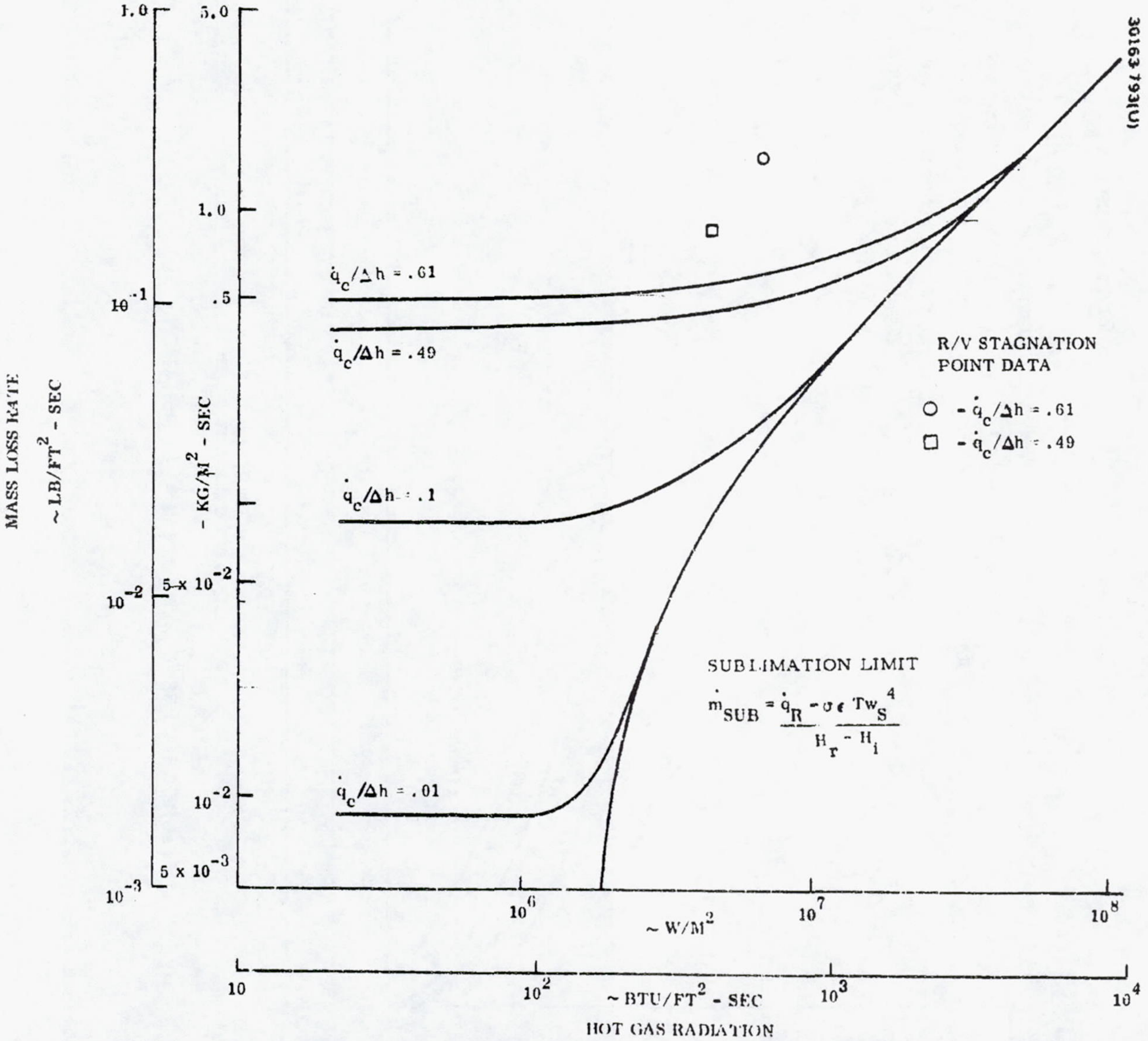

FIGURE 5.4-8. REENTRY VEHICLE STAGNATION POINT DATA

REPRODUCIBILITY OF THE ORIGINAL PAGE IS POOR.

As the heating is increased and the surface temperature approaches 2800 °K, sublimation of the carbonaceous char commences. This sublimation region has been extensively investigated, both analytically and experimentally. It has been demonstrated that all of these approaches predict char erosion rates that fall within the scatter of available flight test data for pressures less than about 2.4×10^5 N/m^2 (24 atm) and there is no clear-cut preferred analytical approach. The design technique employed is that developed at GE for earth entry by Fogaroli and Brant.

The convective heating in the absence of char recession, $\dot{q}_o$, is altered for carbon recession by the combined effects of blowing and chemical reactions of the carbon in air. This alteration is expressed by

$$\frac{\dot{q}conv}{q_o} = \frac{C_h}{C_{ho}} \left\{ \frac{Hr - hw - B\,(hw - hs)}{Hr - h_{w_o}} \right\}$$

where

$$B = \frac{\dot{m}_s}{\rho_e u_e C_h}$$

The carbon mass loss rate, $\dot{m}_s$, and accompanying wall gas enthalpy are determined through use of the sublimation mass loss formulations of Fogaroli and Brant.

For the purpose of generating carbon phenolic char erosion rates for the heat shield design trade study, the results of the Fogaroli-Brant analyses were also employed. The radiative and convective heating was treated separately in the design calculations. Verification of this approach was obtained during the ablation screening program.

Heat Shield Safety Factor Analysis

A number of uncertainties exist in the predicted magnitude of the hypersonic heating environment and the thermal protection system performance. Before determining final thermal system weights, it is necessary that the magnitude of these uncertainties for the various materials be determined, and a required thermal safety margin assigned for each material. The uncertainties in the hypersonic heating environment parameters considered here include laminar, turbulent, and radiative heat transfer and time of transition from laminar to turbulent flow. The magnitude of the uncertainties in the heating environment are the same for all thermal protection materials considered in the trade study, although the sensitivity of the various materials to the heating environment uncertainties is different. The uncertainties in thermal protection system performance considered here include thermal response and surface recession (oxidation, sublimation, melting, or mechanical erosion).

Common practice is to assume that a normal distribution of these uncertainties exists and to translate the 3 σ deviations of each uncertainty separately determined into an equivalent 3 σ deviation in heat shield thickness requirement. A summary of results is presented in Table 5.4-3.

TABLE 5.4-3. AEROTHERMODYNAMIC SAFETY FACTORS
SMALL PROBE – SKIRT

Parameter	Uncertainty in Parameters, percent	Effect on Shield Unit Weight, percent			
		PN	CP	ESM	TEF
Turbulent convective heat transfer	±15	11	2	14	12
Time integrated turbulent heat transfer due to transition uncertainty	+4	3	0.4	4	4
Radiative heat transfer	+60	0.9	0.1	1.5	0
Ablation process modeling					
PN	±20	20			
CP	±15		4		
ESM	±108			108	
TEF	±30				30
Total uncertainty in shield unit weight		23	5	109	33
Thermodynamic safety factors recommended for design		1.25	1.20	2.09	1.33

Shield thickness requirement = [Nominal shield thickness reqmt. to hold 590°K max structure temperature at M_∞ = 0.8] x [Safety Factor]

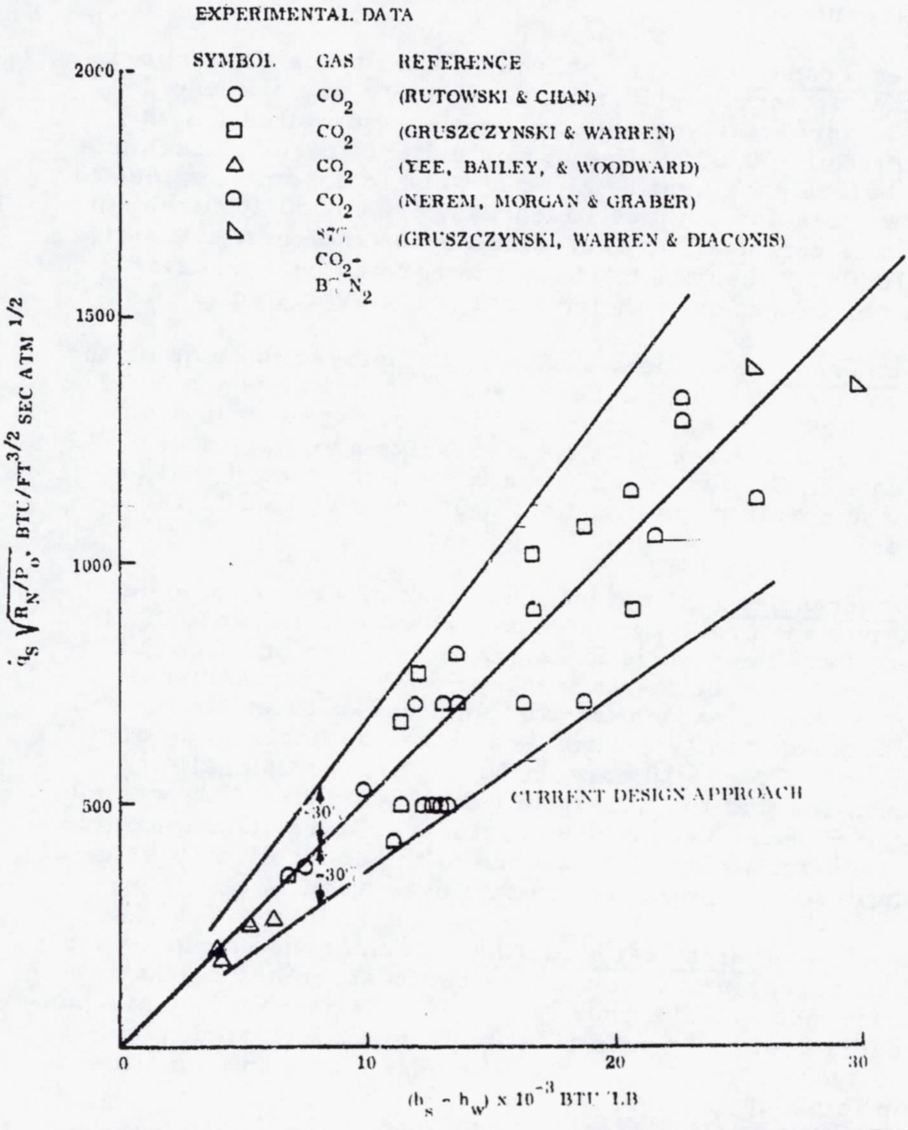

30163-794(U)

FIGURE 5.4-9. COMPARISON OF AVAILABLE STAGNATION POINT CONVECTIVE HEATING DATA WITH CURRENT DESIGN APPROACH

Stagnation Point Convective Heat Transfer. The methodology employed to compute stagnation point convective heat transfer in CO_2 has been described in Reference 1. A comparison is shown in Figure 5.4-9, between the currently employed computational technique and a collection of experimental results. It is seen that the data scatters about the predicted levels by about ±30 percent.

Boundary Layer Transition. The boundary layer transition criteria employed in the thermal protection materials trade study was a Reynolds number based on local boundary layer edge properties and wetted length from the stagnation point of 150,000. Use of this criteria results in transition to turbulent flow before peak heating. If one were to assume that due to the high mass addition rates and surface roughness, transition to turbulent heat transfer levels were computed as exceeding the laminar heat transfer (this occurs at $Re \cong 10,000$), then the total time integrated heat transfer will increase by about 4 percent over the nominal cases evaluated.

Turbulent Heat Transfer. The methodology employed to compute the local turbulent heat transfer in CO_2 has been described in Reference 1. The scatter of Earth entry flight test data on a blunt 51.5 deg cone is shown in Figure 5.4-10 to be about ±15 percent. Comprehensive summaries of turbulent heat transfer data in CO_2 are not currently available, so it will be assumed that the total uncertainty on turbulent heat transfer in CO_2 is equivalent to that in air.

Radiative Heat Transfer. The methodology employed to compute radiative heat transfer to the probe has been described in Reference 1. No summary comparisons have been made to compare the Page and Woodward (Reference 2) predictions to experimental data. However, comparisons have been made on previous occasions for combinations of other theory and test data. Jaworski and Nagler (Reference 3), selected an uncertainty of 40 percent for 90 percent CO_2 and 10 percent N_2. Wolf and Spiegal (Reference 4) demonstrated that the uncertainty for 100 percent CO_2 was 60 percent. Since for the Pioneer Venus entry corridor, the relative magnitude of the radiative heat transfer is small compared to the convective, a value of ±60 percent uncertainty will be employed for this evaluation.

Ablation Process Mathematical Modeling. Techniques employed for calculating the surface recession of the various candidate materials have been described in Reference 1. The char layer of PN is removed by mechanical erosion and is calculated by an empirical technique illustrated in Figure 5.4-7. It is seen from Figure 5.4-7 that the uncertainty in phenolic nylon heat of ablation is about ±20 percent.

Carbon phenolic char is removed by oxidation until the surface temperature reaches about 2800°K, at which time sublimation commences. GE flight test experience has demonstrated that carbon phenolic char recession rates can be predicted to within ±15 percent.

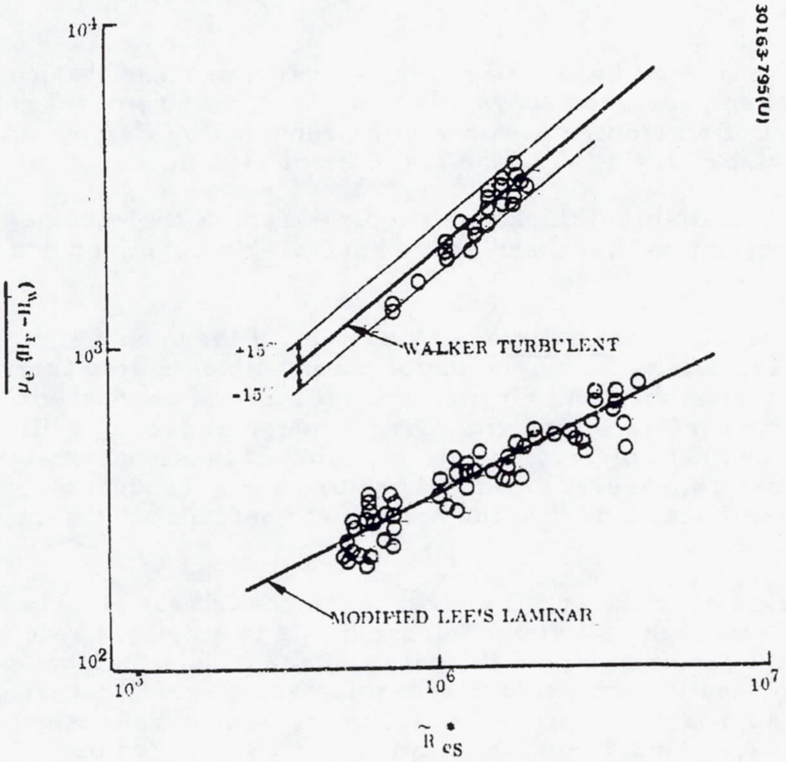

30163-795(U)

$$\text{LAMINAR:}\quad \tilde{R}^*_{c_s} = \frac{\left[\rho_e \, U_e \, R_b \, S \left(\frac{\rho^*}{\rho_e}\frac{\mu^*}{\mu_e}\right)\right]^2}{\int_0^S \rho^* \, \mu^* \, U_e R_b^2 \, dS}$$

$$\text{TURBULENT:}\quad \tilde{R}^*_{c_s} = \frac{\rho_e \, U_e \, S}{\mu_e}\left(\frac{\mu^*}{\mu_e}\right)^{0.2}\left(\frac{\rho^*}{\rho_e}\right)^{0.8}$$

FIGURE 5.4-10. BLUNT 51.5 DEG CONE PEAK LAMINAR AND TURBULENT FLIGHT DATA

Teflon is removed by a sublimation process for surface temperatures above 1000°K. The Teflon sublimation rates are computed by use of the semiempirical correlation illustrated in Figure 5.4-11. Note that the total data scatter for the laminar flow regime is about $^{+50}_{-20}$ percent and for the turbulent flow regime about ±10 percent. An alternative approach to computing laminar flow sublimation rates is available from the test data correlation of Heister and Clark (Reference 5) which shows a ±3σ deviation of ±30 percent.

ESM char is removed by a melting/vaporization process that commences for surface temperatures above 1930°K. ESM char removal rates are computed by use of an empirical correlation reported by Heister and Clark and indicate a ±3σ deviation of the test data of ±108 percent.

The effect on heat shield thickness requirements of the various surface recession uncertainties discussed above have been determined and are illustrated in Table 5-4-2.

Thermal Response Uncertainties. A number of thermophysical properties and parameters effect the magnitude of the predicted shield thermal response. These include char and virgin material thermal conductivity, specific heat, density surface emissivity, virgin material decomposition kinetics constants, and heat of decomposition. Most of these parameters have been independently measured in the laboratory and subsequently employed in a mathematical model of the heat shield performance such as described in Reference 1.

Current design practice at GE for carbon phenolic heat shields performing in a short term high heat flux environment is to employ a safety factor on the nominal required shield thickness of 1.2. This includes provisions for uncertainties in both surface recession and thermal response predictions. This approach has proven satisfactory in numerous flight tests. Hence, for the Pioneer Venus Thor/Delta mission, a safety factor of 1.2 was employed on the nominal carbon phenolic thickness requirements. This factor was increased to 1.5 in the Atlas/Centaur mission design in order to minimize the amount of developmental testing necessary.

As the entry path angle is increased above the value used for design, the resultant safety margin increases, due to the decreasing heat load. Hence, for nominal flight performance, the safety factors employed exist only at the shallow end of the entry corridor, and are greater for steeper path angles.

Total Uncertainty in Shield Thickness Requirement. The separate error sources previously identified, evaluated and tabulated in Table 5.4-3 are rss to determine the total uncertainty in shield thickness requirement. These values are tabulated at the bottom of the table for the small probe skirt area. Similar calculations were performed for the small probe stagnation point area and the large probe. However, the total uncertainty was

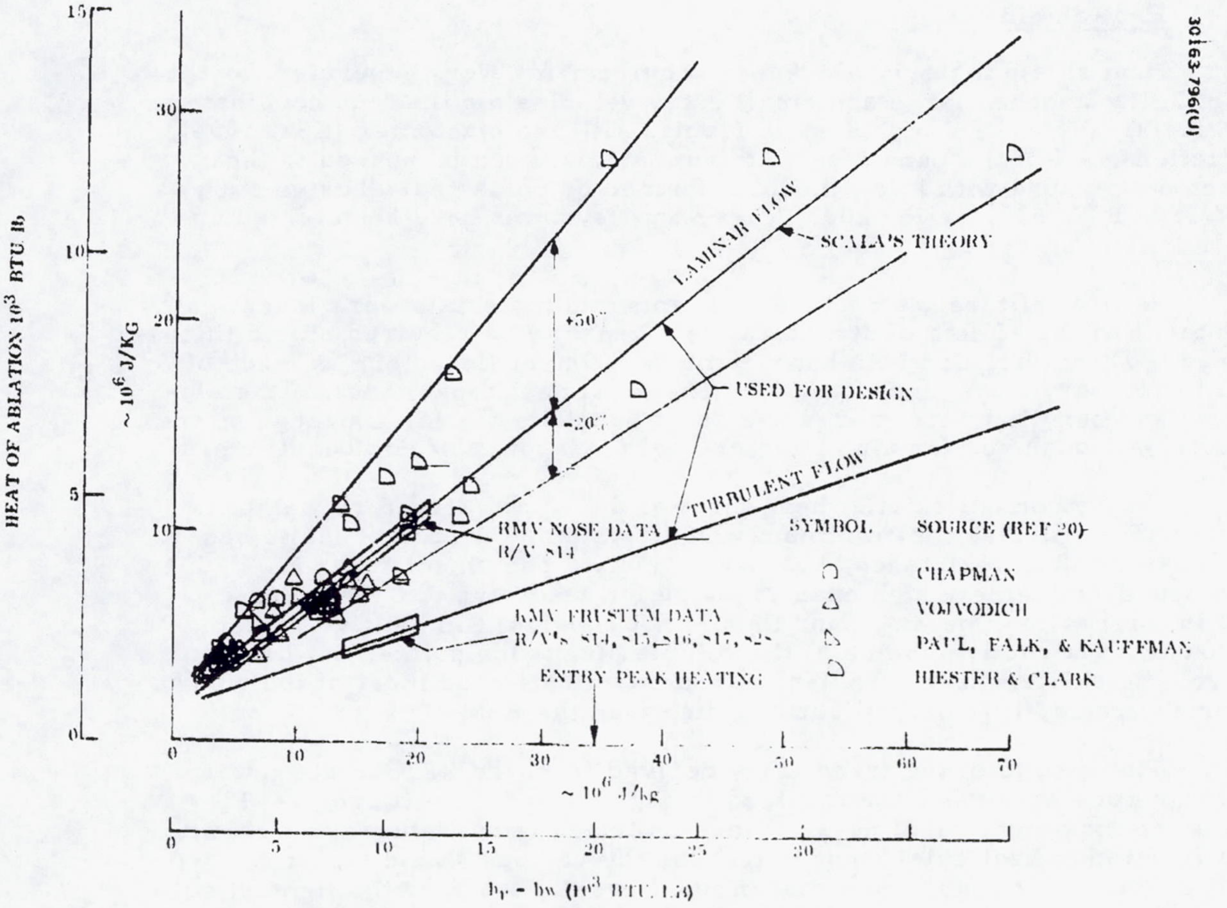

FIGURE 5.4-11. TEFLON HEATS OF ABLATION IN AIR

slightly greater in all cases for the small probe skirt area than for any of the other cases evaluated, so to simplify design procedures the small probe skirts uncertainties will be employed as safety factors on both large and small probes.

Heat Shield Weight

Heat shield material thickness requirements were generated for the Thor/Delta launched large and small entry vehicles for the four candidate materials: PN, CP, a high density foamed silicone elastomer (ESM 1004), and teflon. All of the candidate ablative materials can be bonded to the selected structure with a low modulus foamed or unfoamed adhesive such as RTV-560, RTV 630, or PD 200. These bond systems have been tested up to 612°K.

Several different structural concepts and materials were investigated to determine the effects of structural heat capacity on required shield thicknesses. These included both honeycomb and ring stiffened shells made of aluminum, beryllium, and titanium. The local heat capacitance of the aluminum and beryllium structures are about equal for the large probe, so the results, although run for aluminum are equally applicable for beryllium.

On the conical skirt, where most of the shield/structure weight is located, PN provides the minimum weight system. Carbon phenolic has high char erosion resistance, but is relatively a poor insulator. ESM 1004 experiences extremely high char vaporization rates, up to 0.76 cm/sec (0.3 in/sec) at peak heating, and thus is not a weight competitive system. Teflon is an attractive choice at the vehicle stagnation points, but back on the vehicle skirts where turbulent flow predominates and most of the weight is concentrated, it is only slightly lighter than the ESM 1004.

The results of the trade study derived from the REKAP computer program runs have been summarized in Figures 5.4-12 through 5.4-15 where the maximum bondline-structure interface temperatures are shown as a function of heat shield unit weight for the various shield materials. A review of these results shows that in most cases PN offers the lightest solution. At the stagnation point, where the flow is laminar, teflon is a very efficient material and compares favorably with the PN results. However, at the skirt location, where turbulent flow is dominant, teflon is less efficient and hence much heavier than the PN. If the radiative heat transfer were higher, teflon would become more competitive due to its high reflectivity. It is demonstrated in these figures that ESM is nearly always the heaviest solution, due to its very high char surface vaporization rates. The CP experiences very little surface recession, but requires a considerable amount of material for structural insulation. The insulation requirement varies significantly as the structural heat capacity is varied. This effect can be observed in Figures 5.4-16 and 5.4-17 showing crossplots of the trade study results. It is clear from Figure 5.4-17 that in the range of baseline structures being considered, the PN offers the lightest shield-structure combination.

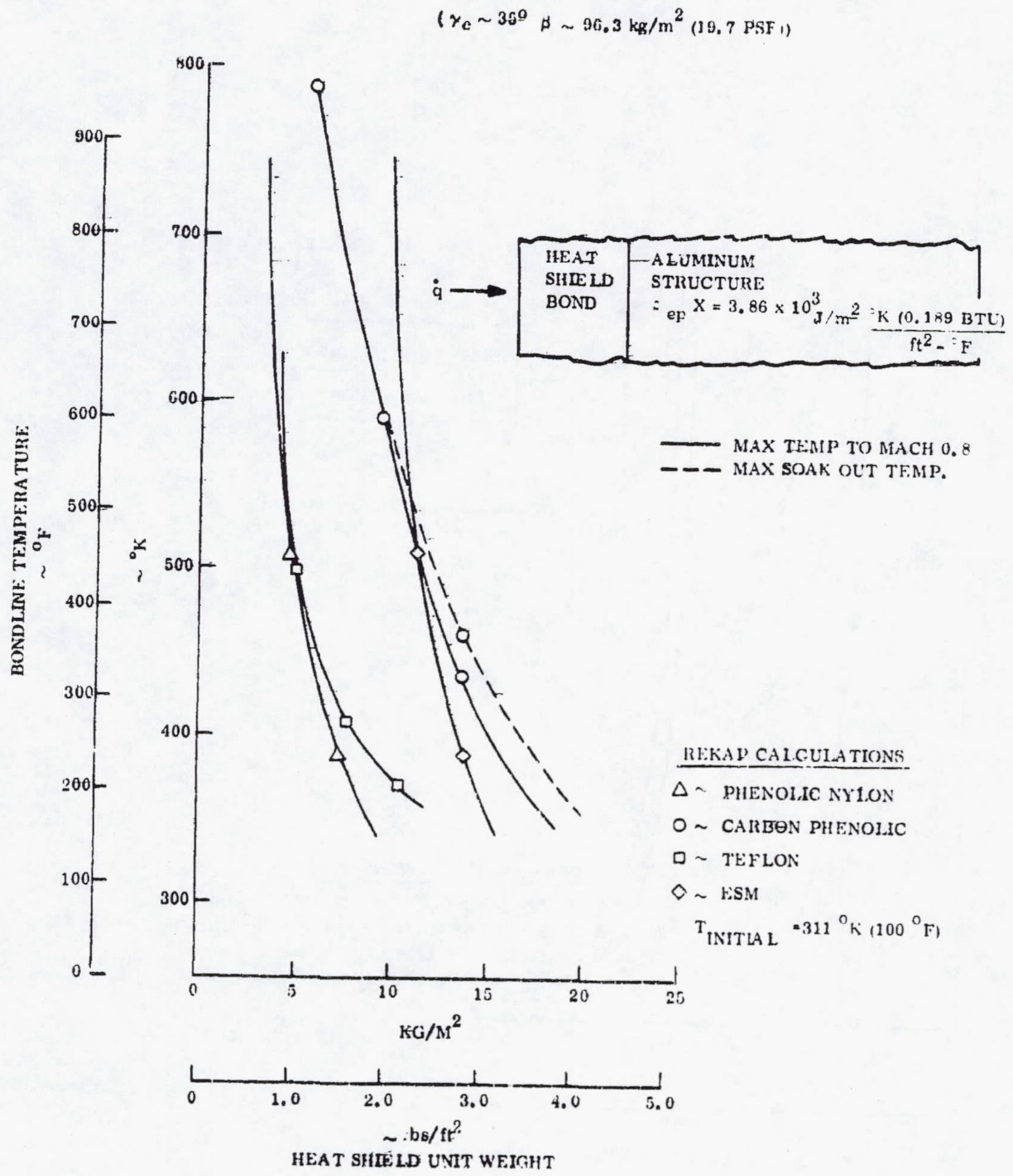

FIGURE 5.4-12. LARGE PROBE HEAT SHIELD MATERIAL COMPARISON STAGNATION POINT – MAXIMUM (TO MACH 0.8) BONDLINE/STRUCTURE TEMPERATURE VERSUS SHIELD WEIGHT

30163-797(U)

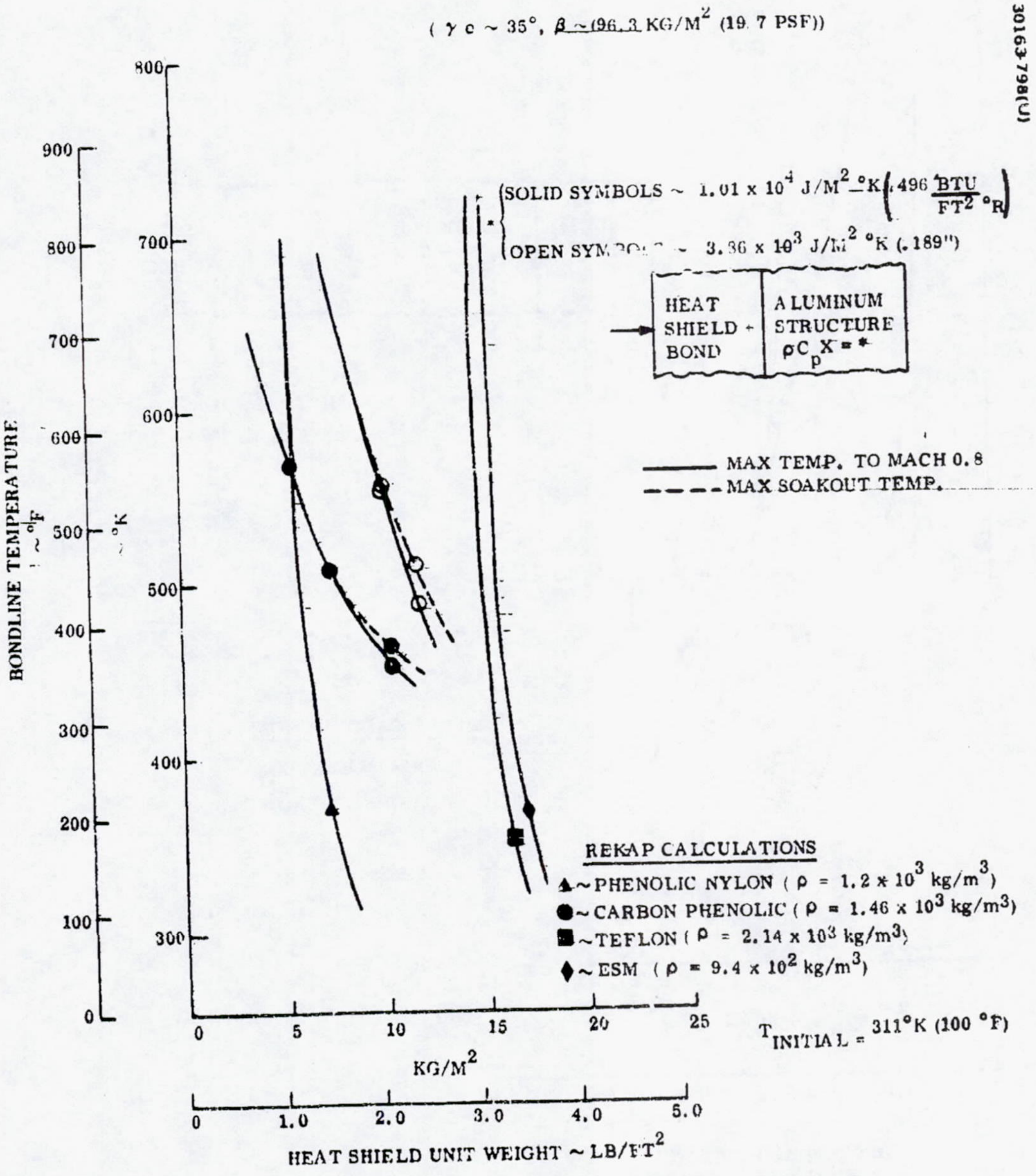

FIGURE 5.4-13. LARGE PROBE HEAT SHIELD MATERIAL COMPARISON SKIRT – MAXIMUM (TO MACH 0.8) BONDLINE/STRUCTURE TEMPERATURE VERSUS SHIELD WEIGHT

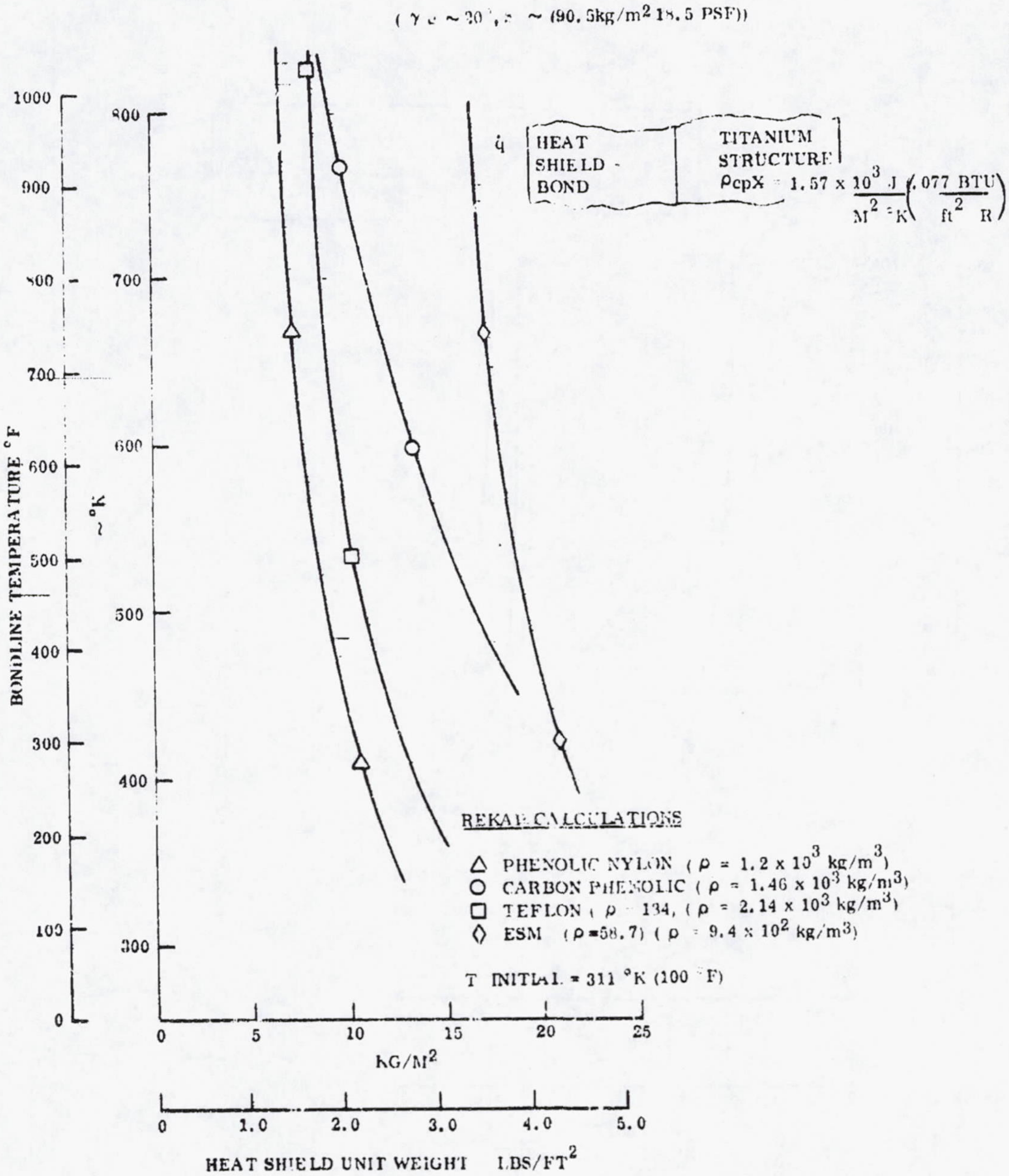

30163-799(U)

FIGURE 5.4-14. SMALL PROBE HEAT SHIELD MATERIAL COMPARISON STAGNATION POINT – MAXIMUM (TO SOAKOUT) BONDLINE/STRUCTURE TEMPERATURE VERSUS SHIELD WEIGHT

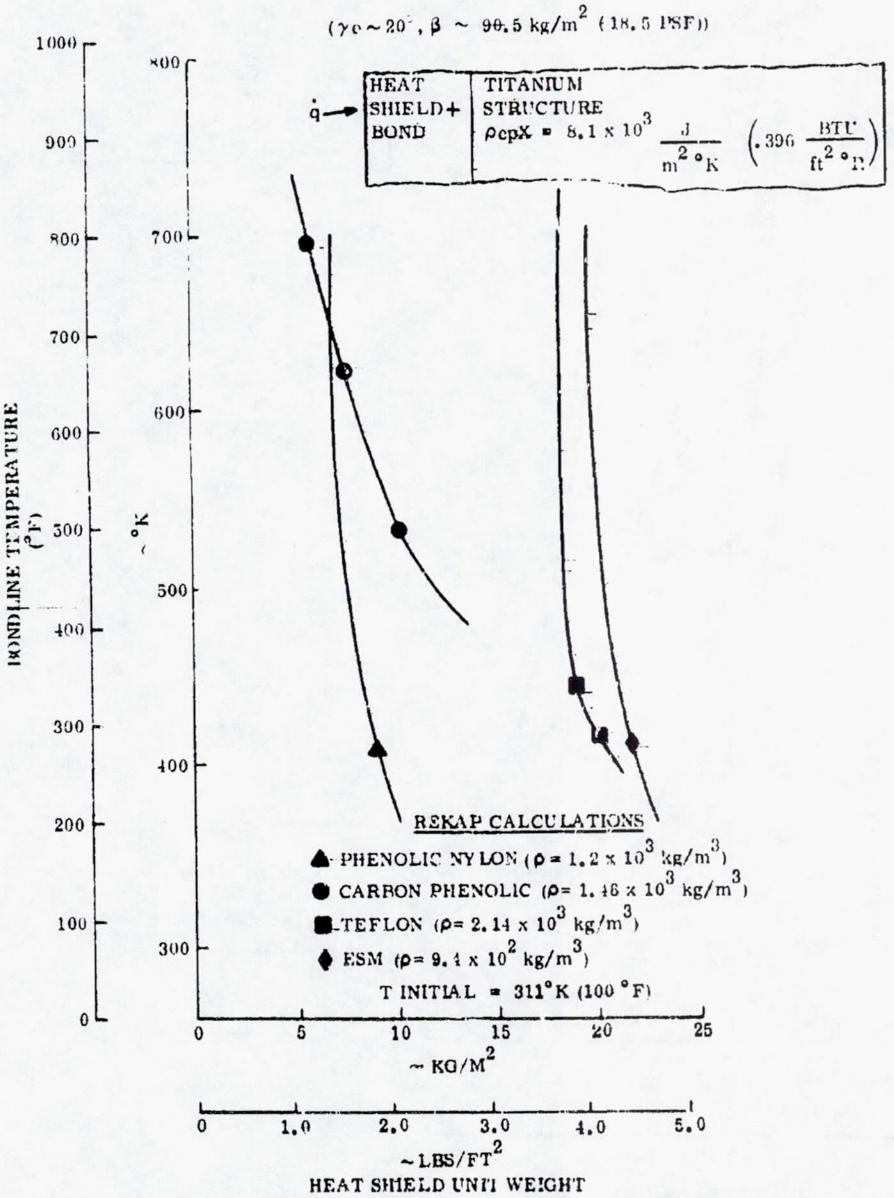

FIGURE 5.4-15. SMALL PROBE HEAT SHIELD MATERIAL COMPARISON SKIRT – MAXIMUM (TO SOAKOUT) BONDLINE/STRUCTURE TEMPERATURE VERSUS SHIELD WEIGHT

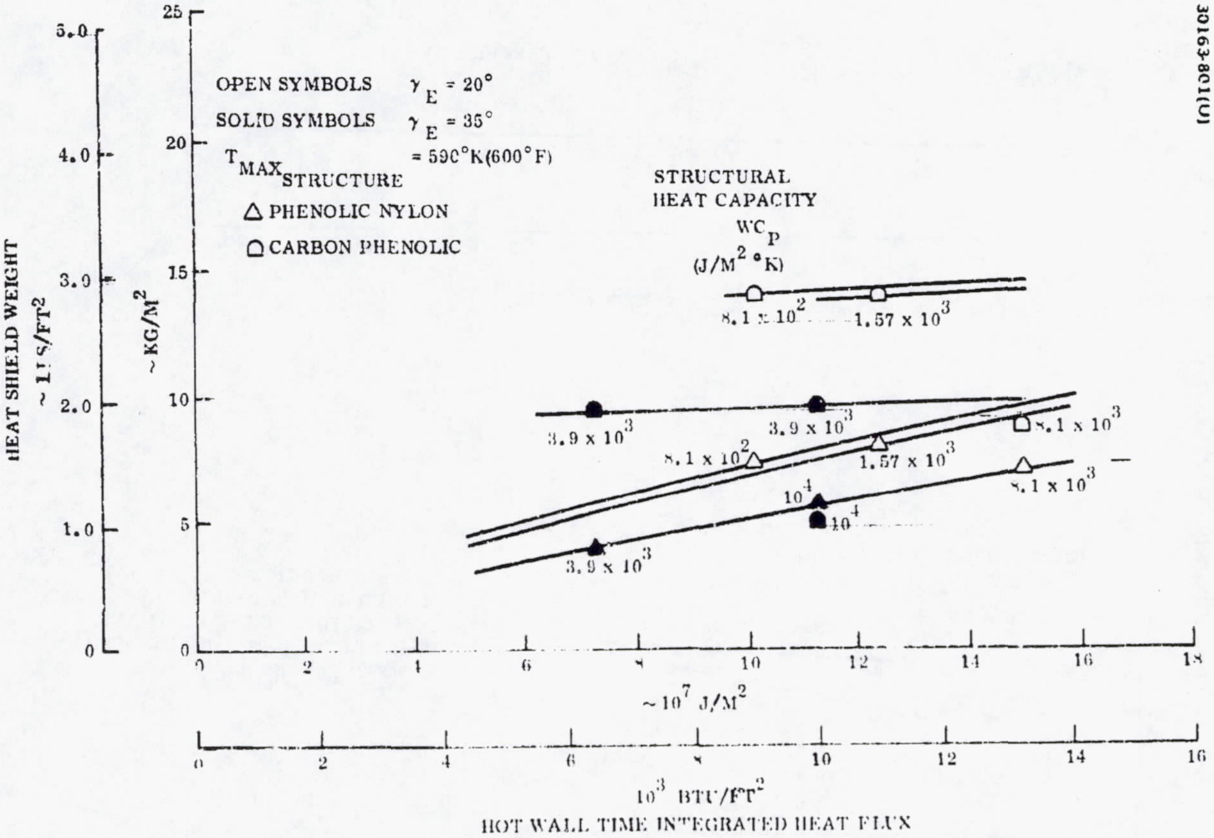

FIGURE 5.4-16. COMPARISON OF PHENOLIC NYLON AND CARBON PHENOLIC HEAT SHIELD WEIGHTS

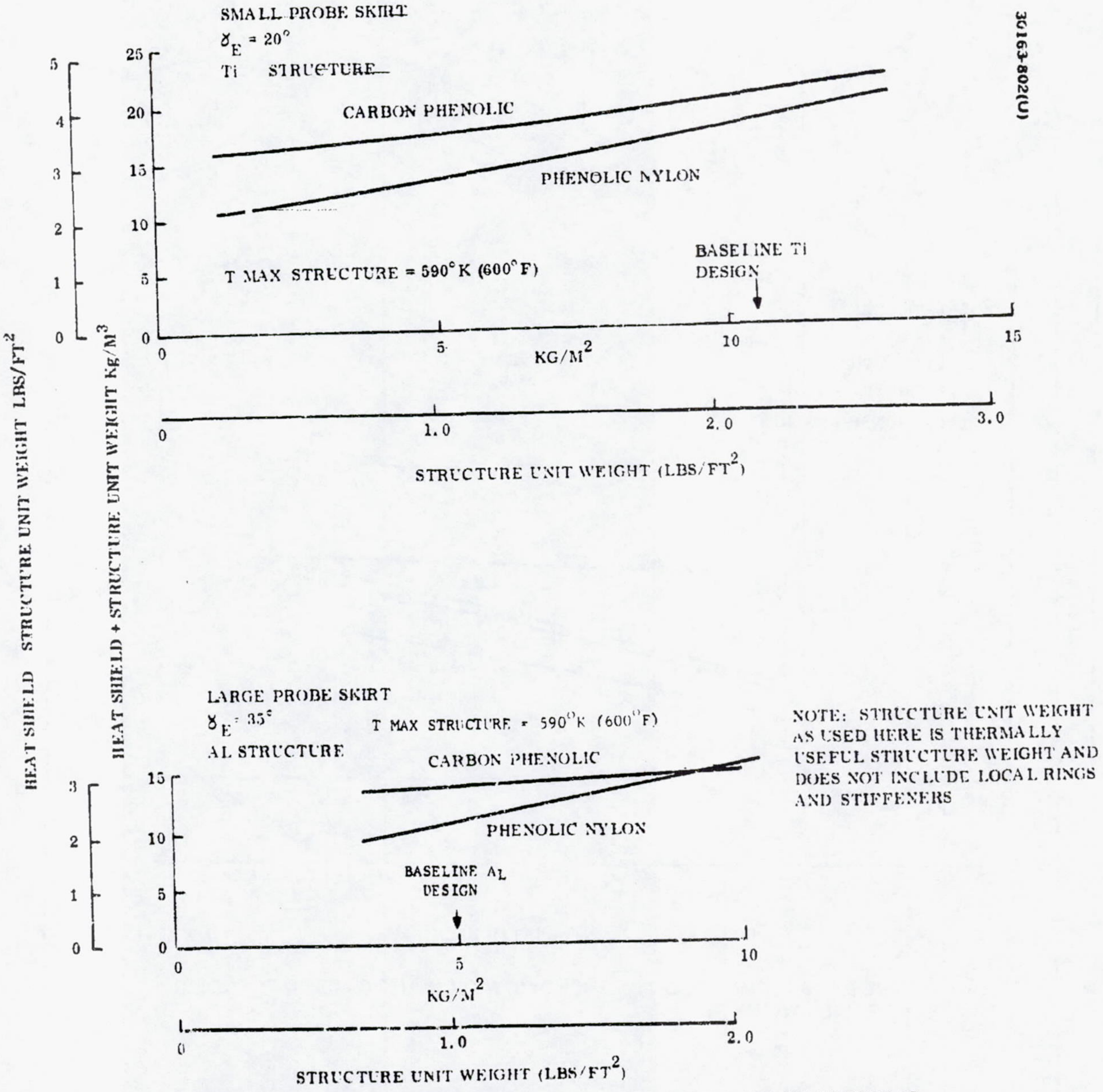

NOTE: STRUCTURE UNIT WEIGHT AS USED HERE IS THERMALLY USEFUL STRUCTURE WEIGHT AND DOES NOT INCLUDE LOCAL RINGS AND STIFFENERS

FIGURE 5.4-17. COMPARISON OF PHENOLIC NYLON AND CARBON PHENOLIC SHIELD AND STRUCTURE

3C163-802(U)

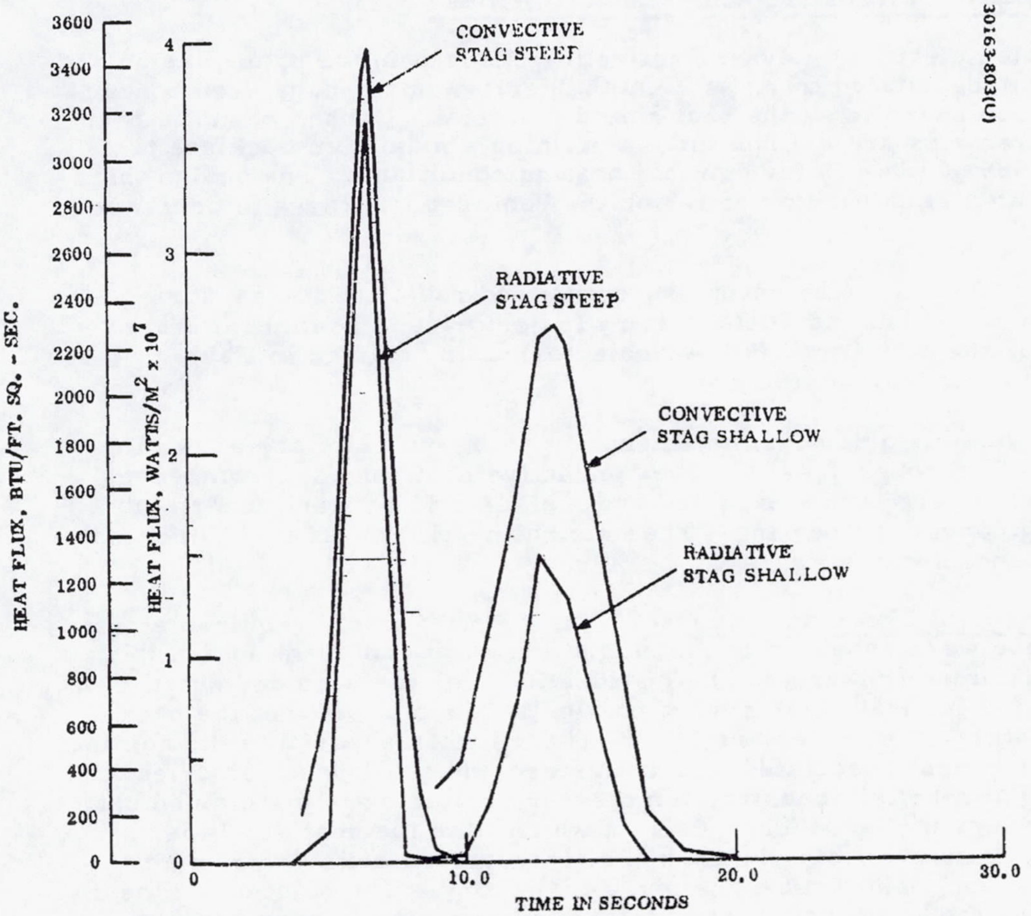

FIGURE 5.4-18. CONVECTIVE AND RADIATIVE HEAT FLUX HISTORIES FOR LARGE PROBE STAGNATION POINT

30163-803(U)

These heat shield trade results are nominal expected values and do not reflect any thermal safety margin.

Considering the safety margins shown in Table 5.4-3, the resultant thermal protection system weights required to prevent the substructure from exceeding 600°K are shown in Table 5.4-4.

Thermal Analyses for Atlas/Centaur Probes

Updated thermal analyses, reflecting changes in the probe design and trajectories necessitated by Atlas/Centaur performance, have been conducted with carbon phenolic as the heat shield material. Carbon phenolic heat shield requirements are defined for maintaining a maximum backface temperature of 589°K (600°F) for nominal heating conditions. The design thicknesses contain a safety factor of 1.5 on the required thickness to decrease mission risk.

Entry Heating. The entry convective and radiative fluxes were evaluated for the steep and shallow entry trajectories. The initial entry conditions for the steep and shallow trajectories are defined in Table 5.4-5 for a reference altitude of 150 KM.

Heat-flux histories for the stagnation point and skirt are shown in Figures 5.4-18 through 5.4-21. The convective heat fluxes shown represent the most severe levels expected and include a 15 percent uncertainty in predicting convective heating. The nominal heating rates are 15 percent below those shown in the figures.

Heat Shield Thermal Response. The CP heat shield requirements for each probe were assessed at the stagnation point and at the end of the skirt, the maximum integrated heating locations for the nose and skirt, respectively. The heat shields were nominally sized to prevent the backface temperature from exceeding 589°K (600°F) when exposed to the nominal heating environment associated with both steep and shallow trajectories. For the large probe this backface temperature criterion is maintained until parachute deployment at Mach = 0.7, at which time the heat shield is ejected; for the small probe the backface temperature criterion is maintained throughout soakout after the entry trajectory. The nominal CP heat shield unit weight as a function of backface temperature is shown in Figure 5.4-22.

TABLE 5.4-4. THOR/DELTA HEAT SHIELD SYSTEM COMPARATIVE WEIGHTS, kg (includes one large plus three small probe heat shields)

Substructure	PN	CP	Teflon	ESM
Al	22	27.6	48.4	89.0
Be	20.5	24.1	45.5	87.0

TABLE 5.4-5. INITIAL ENTRY CONDITIONS
(150 km Entry Altitude)

Probe	Trajectory	Ballistic Coefficient		Path Angle, deg	Velocity		Time to Mach 0.7, second
		lbs/ft^2	kg/m^2		ft/sec	m/sec	
Large	Shallow	31.2	152	25	38,060	11,600	39
Large	Steep	31.2	152	60	38,060	11,600	19
Small	Shallow	25.5	125	20	38,060	11,600	--
Small	Steep	25.5	125	90	38,060	11,600	--

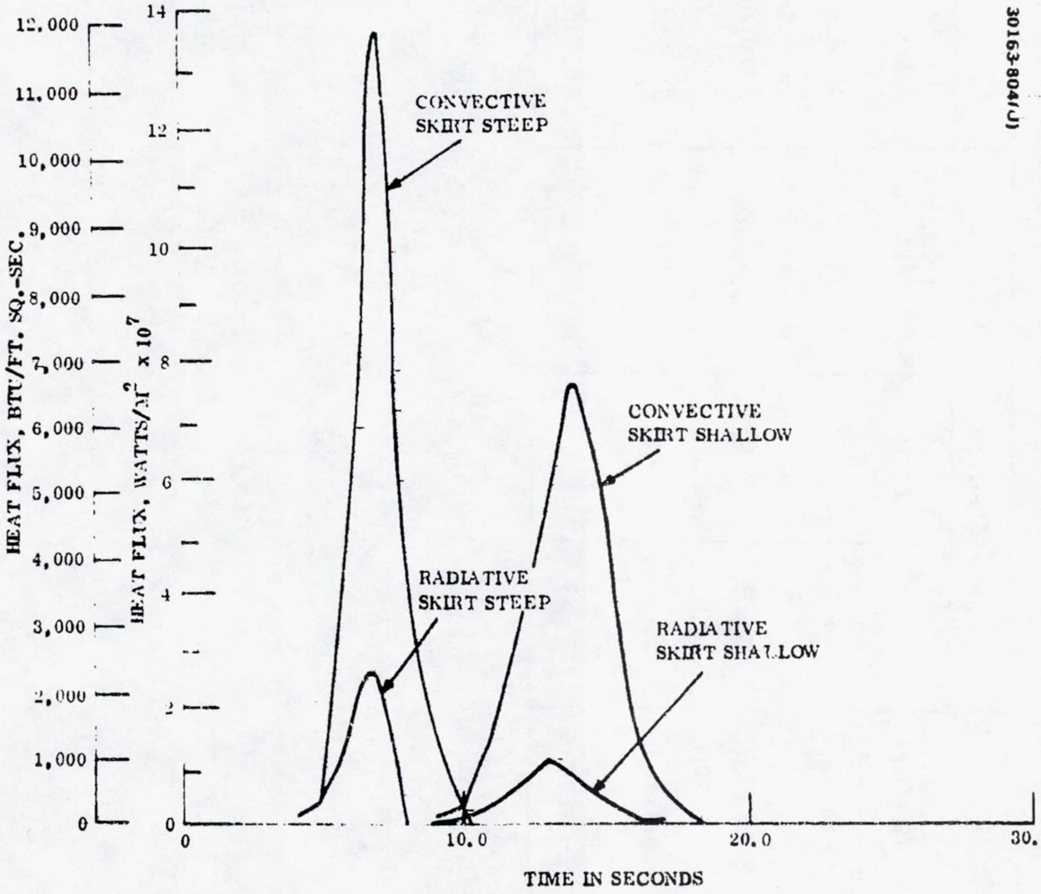

FIGURE 5.4-19. CONVECTIVE AND RADIATIVE HEAT FLUX HISTORIES FOR LARGE PROBE SKIRT

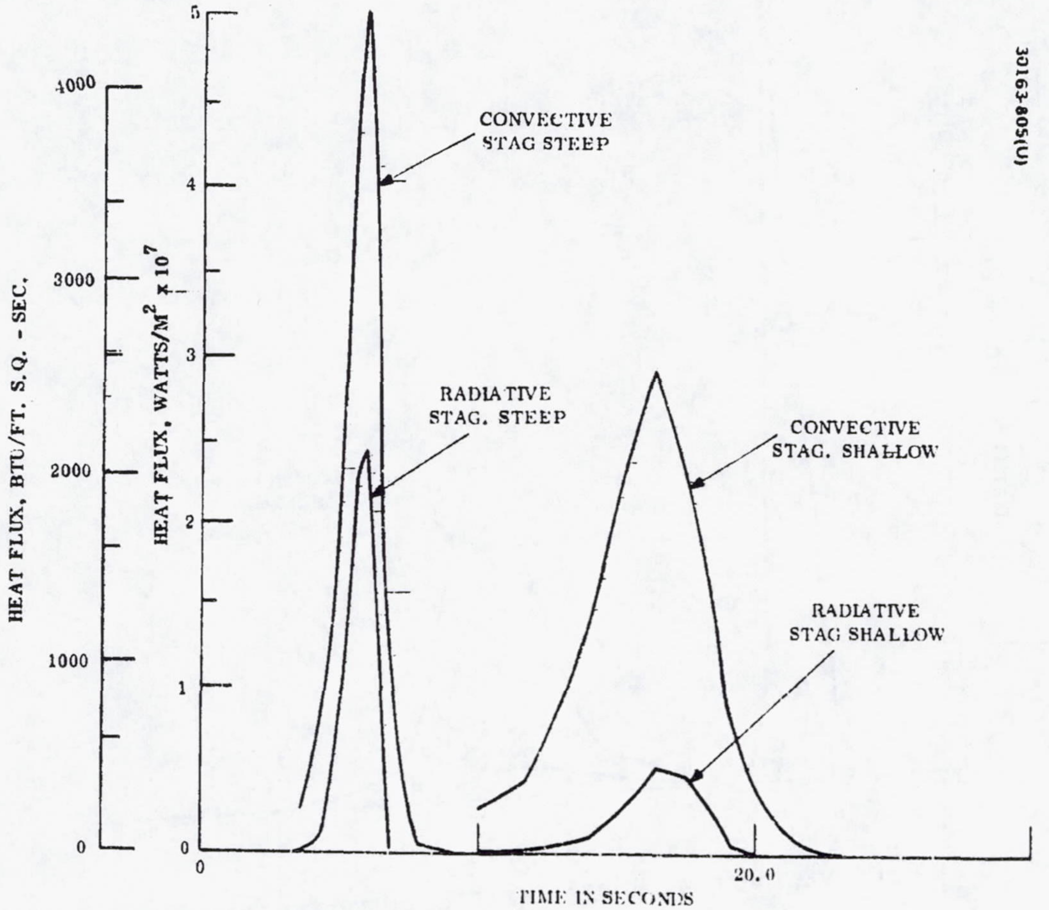

FIGURE 5.4-20. CONVECTIVE AND RADIATIVE HEAT FLUX HISTORIES FOR SMALL PROBE STAGNATION POINT

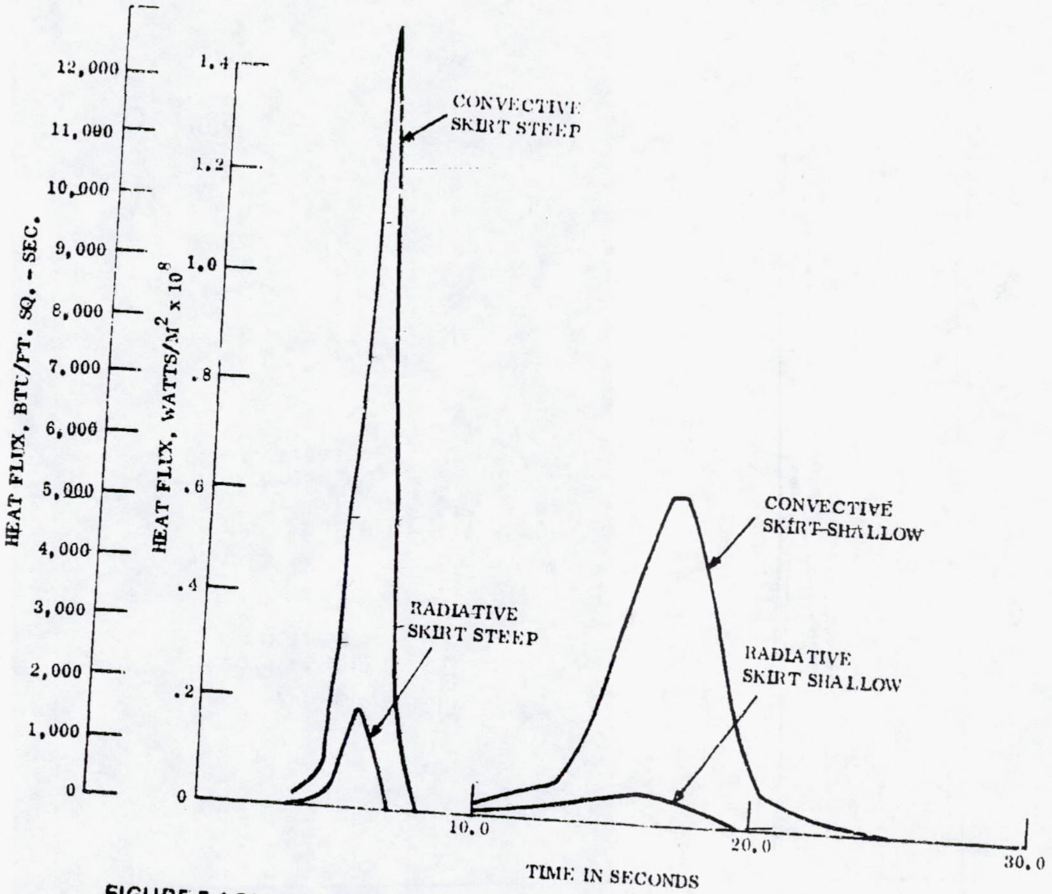

FIGURE 5.4-21. CONVECTIVE AND RADIATIVE HEAT FLUX HISTORIES FOR SMALL PROBE SKIRT

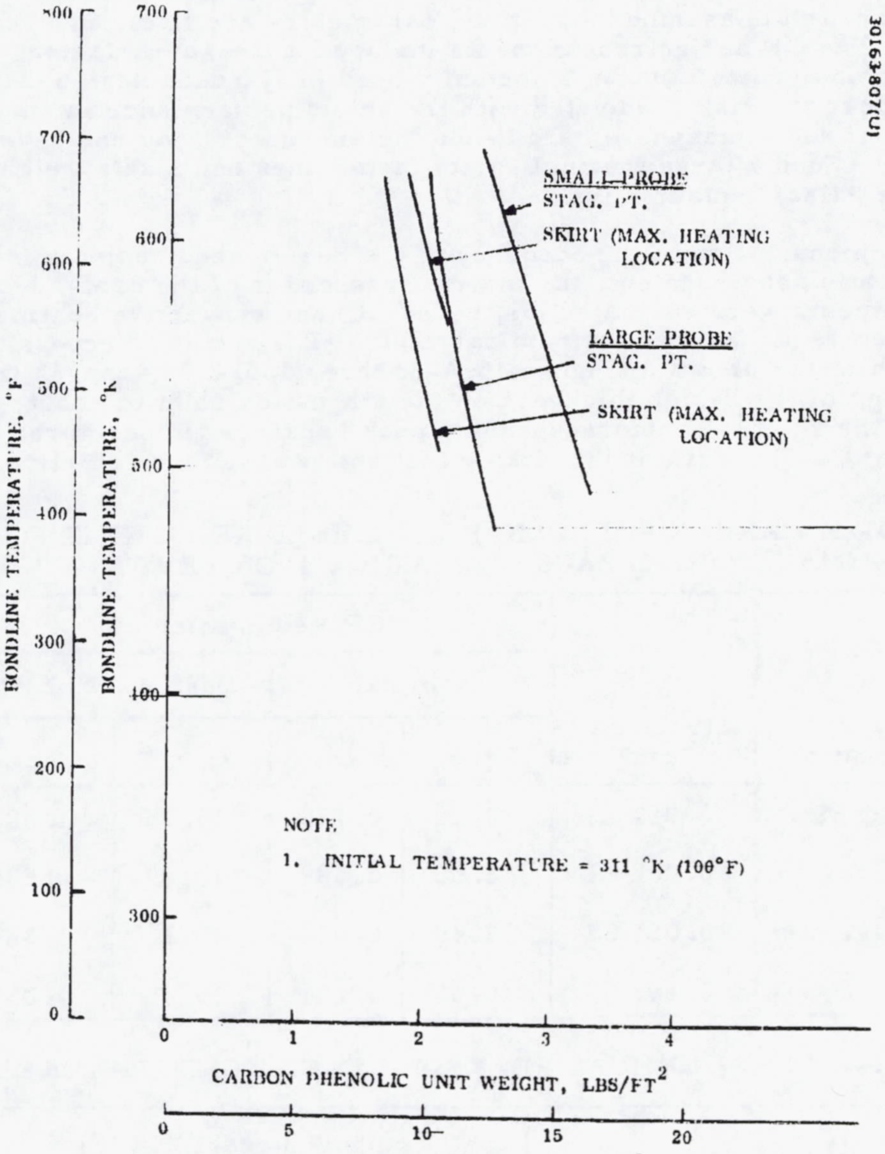

FIGURE 5.4-22. MAXIMUM BONDLINE TEMPERATURE VERSUS CARBON PHENOLIC HEAT SHIELD UNIT WEIGHT

The CP requirements for maintaining the backface at 589°K or below together with the assumed structural parameters are listed in Table 5.4-6. The CP design requirements included a 1.5 safety factor, which, while being greater than 1.2 normally used in standard design practice, reduces the risk associated with the shield performance in an incompletely defined atmosphere, and hence the amount of required developmental testing. Such a large thermal safety factor does not pose a weight problem in the Atlas/Centaur mission.

As a demonstration of the adequacy of the design requirements in the off-nominal heating environment, the thermal responses of the design heat shield requirements were evaluated for the worst case convective heating, which is defined as 1.15 times the nominal value. The resulting recession histories of which are shown in Figures 5.4-23 through 5.4-26, ranges from about 14 percent of the design thickness on the stagnation point to about 40 percent on the skirt. The corresponding peak backface temperatures are listed in Table 5.4-7. While it is unlikely that both worst case radiative

TABLE 5.4-6. CARBON PHENOLIC HEAT SHIELD REQUIREMENTS FOR MAINTAINING BACKFACE AT 589°K OR BELOW

Probe	Location	Structure, cm	CP Requirements			
			Nominal		Design (SF=1.5)	
			kg/m^2	cm	kg/m^2	cm
Large	Stag. pt.	0.060 Al	10.50	0.725	15.75	1.087
Large	Skirt	0.267 Al	8.55	0.589	12.80	0.884
Small	Stag. pt.	0.051 SS	13.40	0.924	20.10	1.387
Small	Skirt	0.191 SS	10.03	0.691	15.05	1.039

TABLE 5.4-7. OFF-NOMINAL PEAK BACKFACE TEMPERATURES

Probe	Trajectory	Temperatures, °K (°F)	
		Stag. Pt.	Skirt
Large	Shallow	456 (362)	486 (415)
Large	Steep	346 (162)	471 (390)
Small	Shallow	389 (240)	394 (249)
Small	Steep	317 (111)	345 (161)

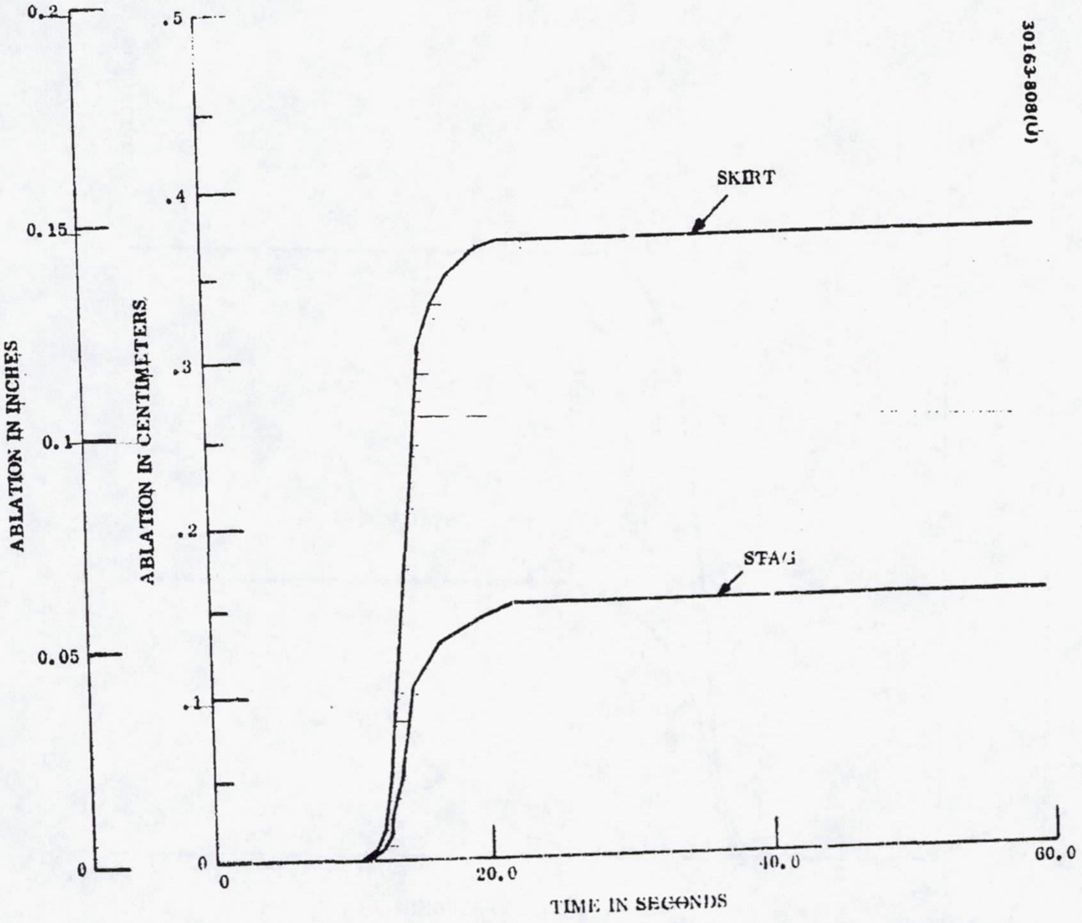

30163-808(U)

FIGURE 5.4-23. ABLATION HISTORIES FOR LARGE PROBE, SHALLOW ENTRY

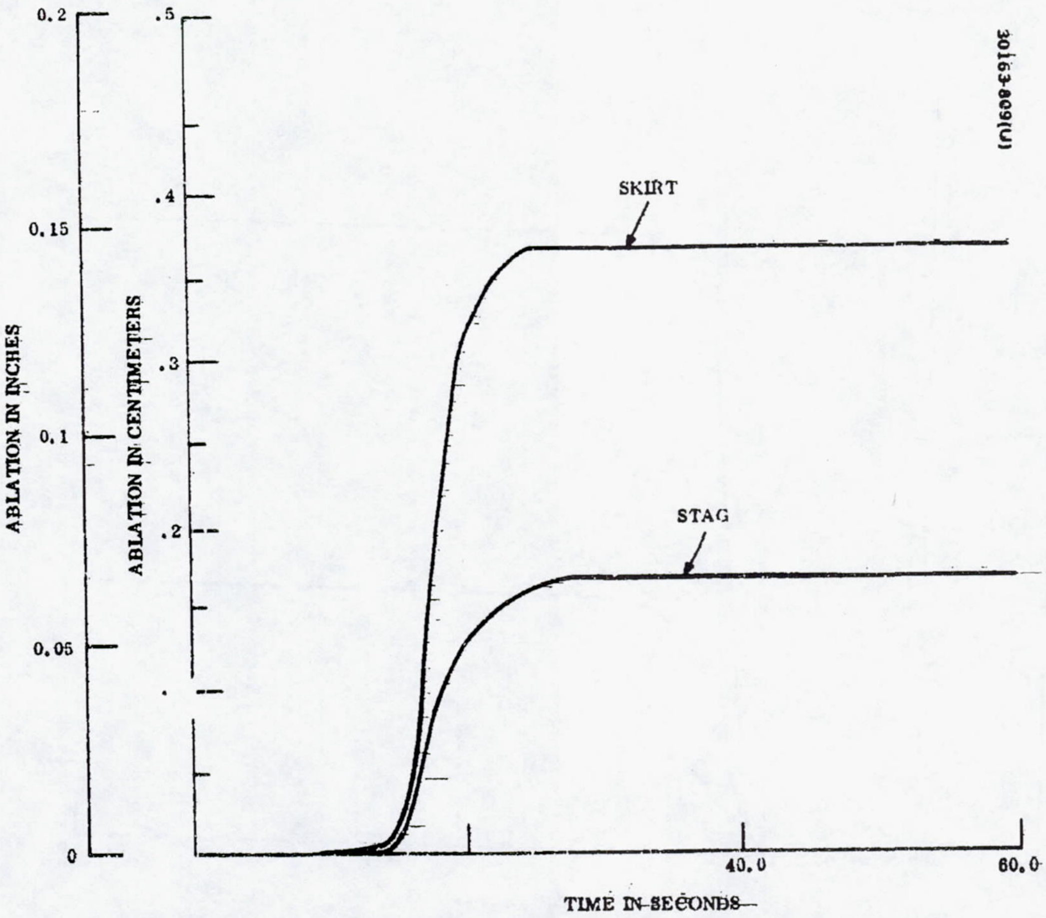

FIGURE 5.4-24. ABLATION HISTORIES FOR SMALL PROBE, SHALLOW ENTRY

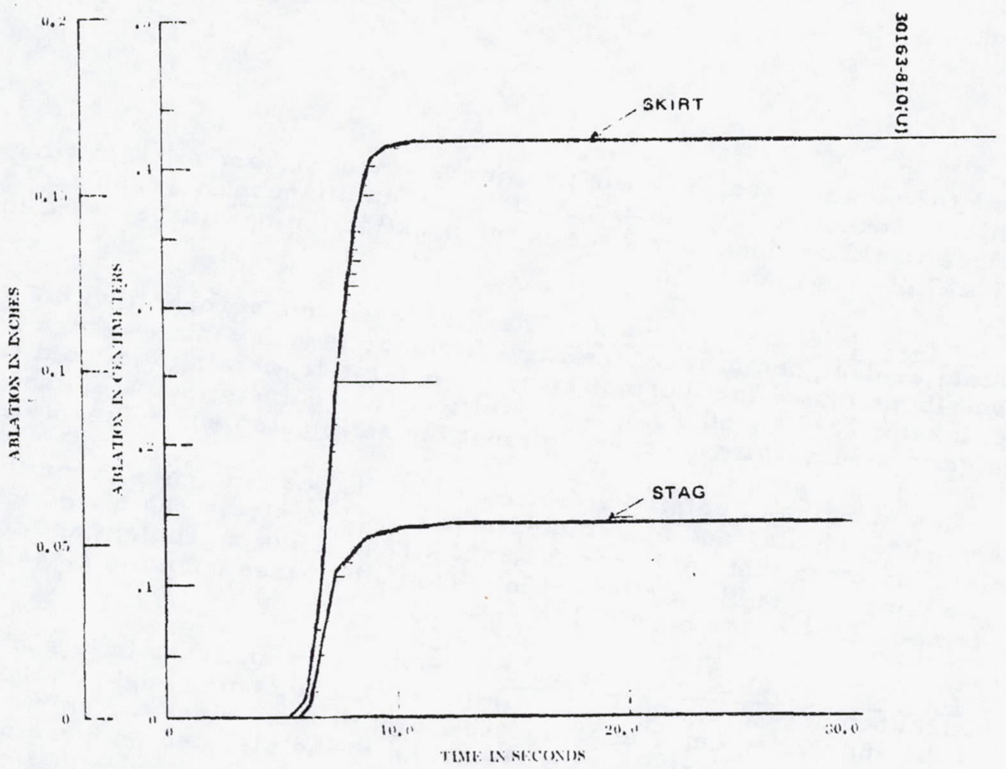

FIGURE 5.4-25. ABLATION HISTORIES FOR LARGE PROBE, STEEP ENTRY

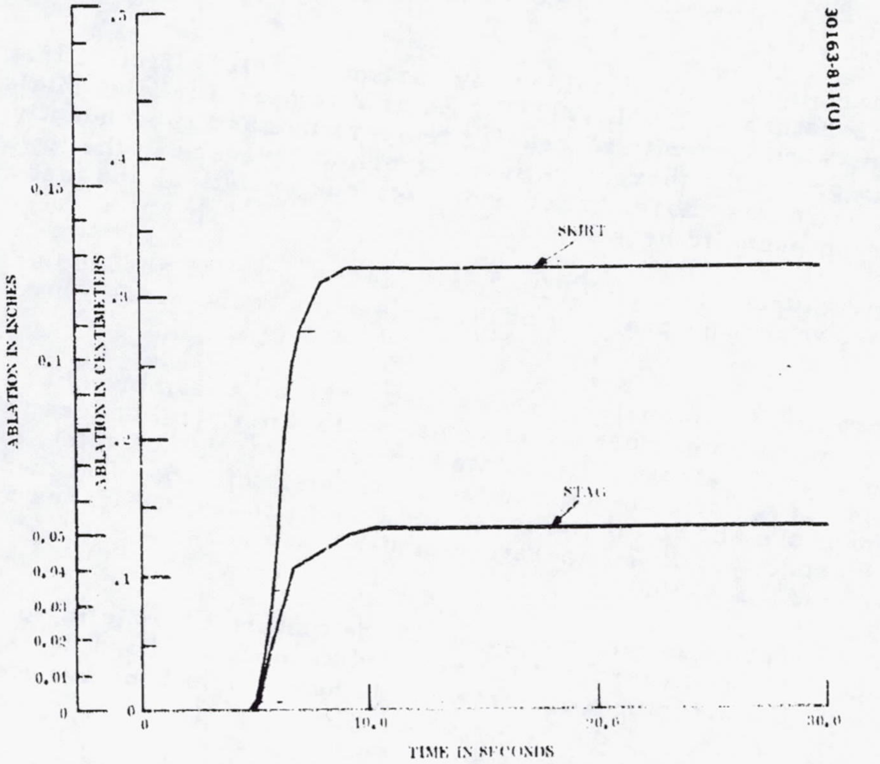

FIGURE 5.4-26. ABLATION HISTORIES FOR SMALL PROBE, STEEP ENTRY

(1.6 time the nominal radiative flux) and worst case convective (1.15 times the nominal convective flux) heating will occur simultaneously, such an occurrance would produce increases in the backfire temperatures listed in Table 5.4-7 of less than 17°C.

Orbital Cold Soak Analysis. The Pioneer Venus aeroshell with CP heat shield as designed to meet the Atlas/Centaur launch vehicle design criteria was investigated for thermal stresses arising from minimum cold soak temperature of 228°K (-50°F). The results of the analysis indicates that the design is structurally adequate to meet the anticipated environments.

High margins of safety exist because of the good match between the aeroshell, heat shield, and bond materials. The low strain calculated for the shield indicates that cold soak thermal stress is not a problem and that the lower temperature limit of the shield should be based upon the glassification temperature of the bond 211°K (-80°F).

Entry Thermal Stress Analysis. Preliminary analyses have shown that critical temperature profiles occur for the 25 deg entry angle on the large probe and 20 deg entry angle on the small probe. Since the skirt region on the probes offers the most restraint to the elevated temperature shield, this region is the most critical from a thermal stress view point. Therefore, the detail analysis was confined to those two profiles and the skirt regions.

The analysis does not consider any carbon phenolic effective that exceeds a temperature of 755°K (900°F). At this temperature the shield material begins shrinking with increasing temperature and subsequently forms fissures or cracks thereby relieving thermal stresses in the lower layers. This point was chosen based upon previous analytical and test results of carbon phenolic heat shields.

The structural adequacy of the heat shield system is assured as long as it can be shown that no cracking of the CP occurs at the bond to heat shield interface.

The results of the analysis shows that, typically, compression stresses exist in the outermost effective heat shield material at less than the allowable ultimate stress. Calculated minimum margin of safety of +10 percent is based upon an ultimate factor of safety of 1.5. The thermal stress histories are shown for the large and small probes in Figures 5.4-27 and 5.4-28, respectively. Temperature profiles are shown in Figures 5.4-29 and 5.4-30.

Since no tension cracks can occur in the material that is in compression and since the tension strained material adjacent to the bond has a high margin of safety the structural integrity of the heat shield bond system is assured.

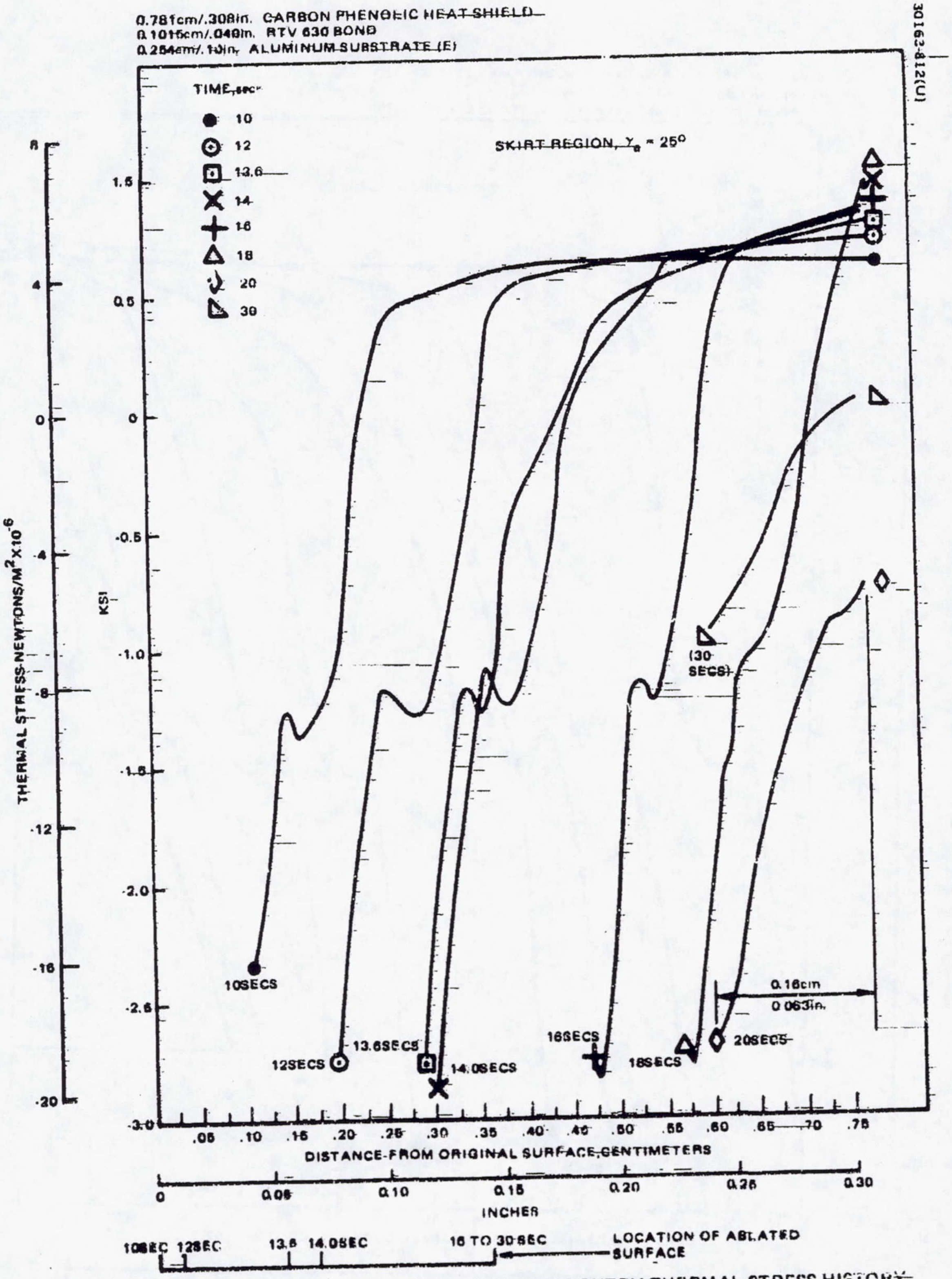

FIGURE 5.4-27. LARGE PROBE THROUGH THICKNESS ENTRY THERMAL STRESS HISTORY

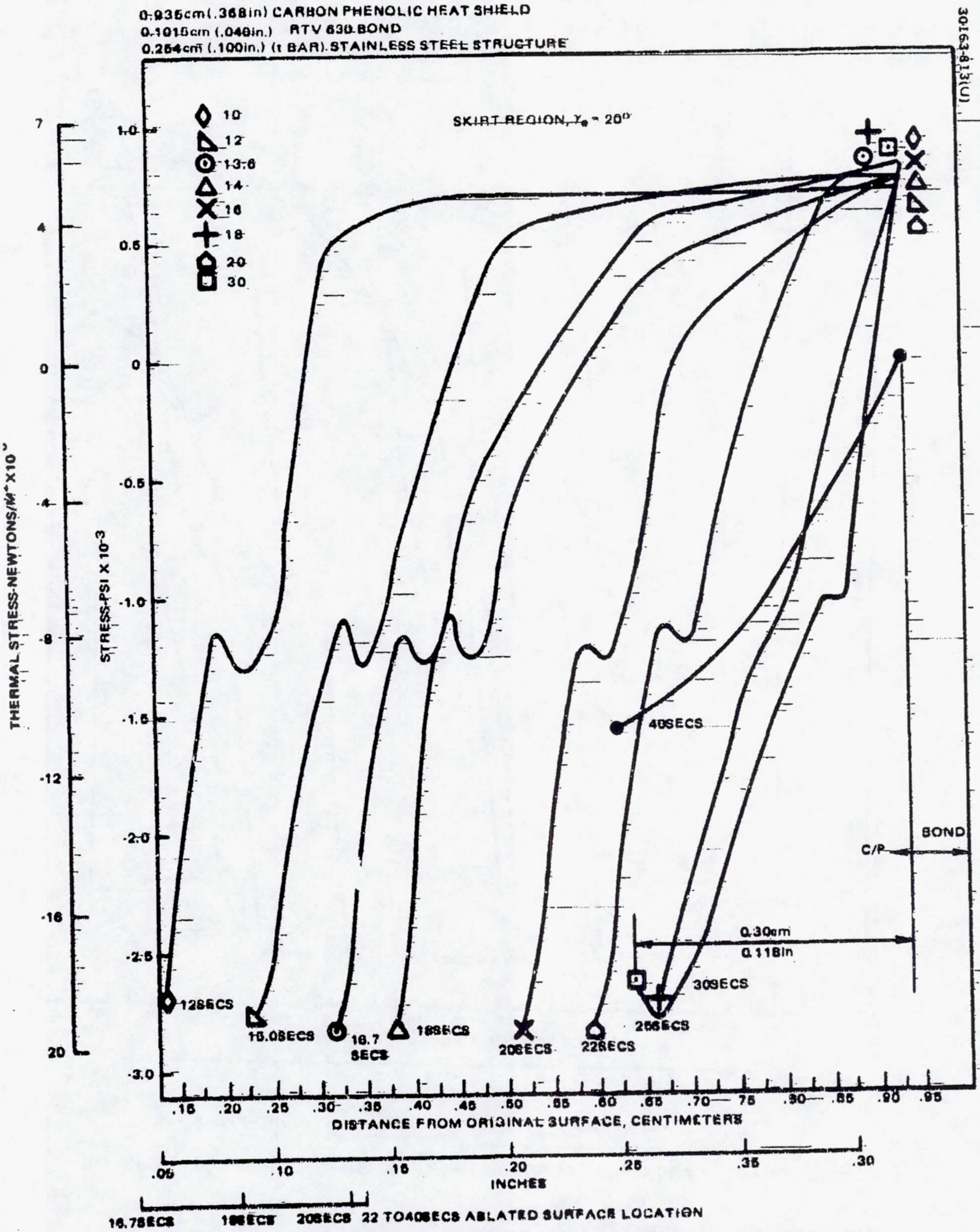

FIGURE 5.4-28. SMALL PROBE THROUGH THICKNESS THERMAL STRESS HISTORY

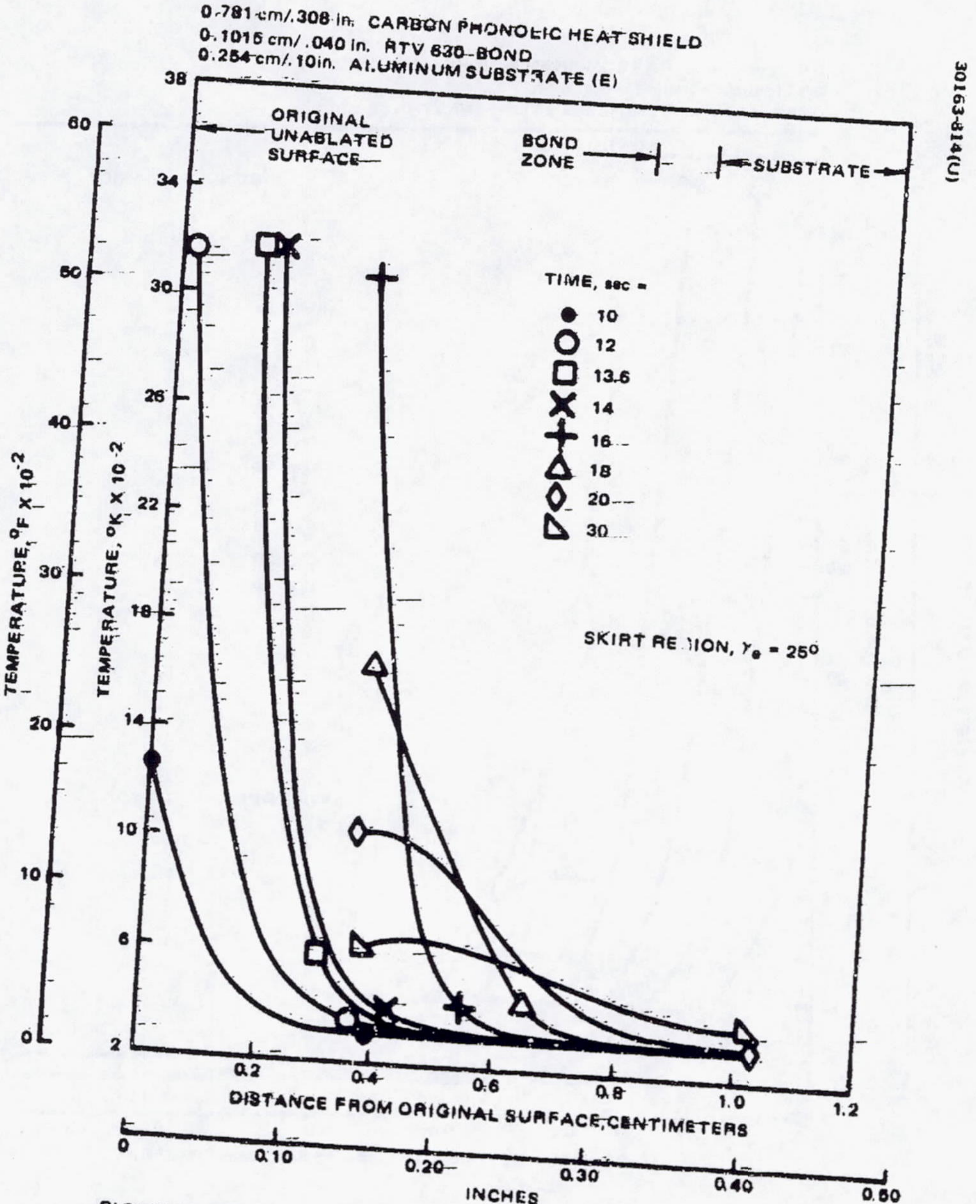

FIGURE 5.4-29. LARGE PROBE THROUGH THICKNESS ENTRY TEMPERATURES

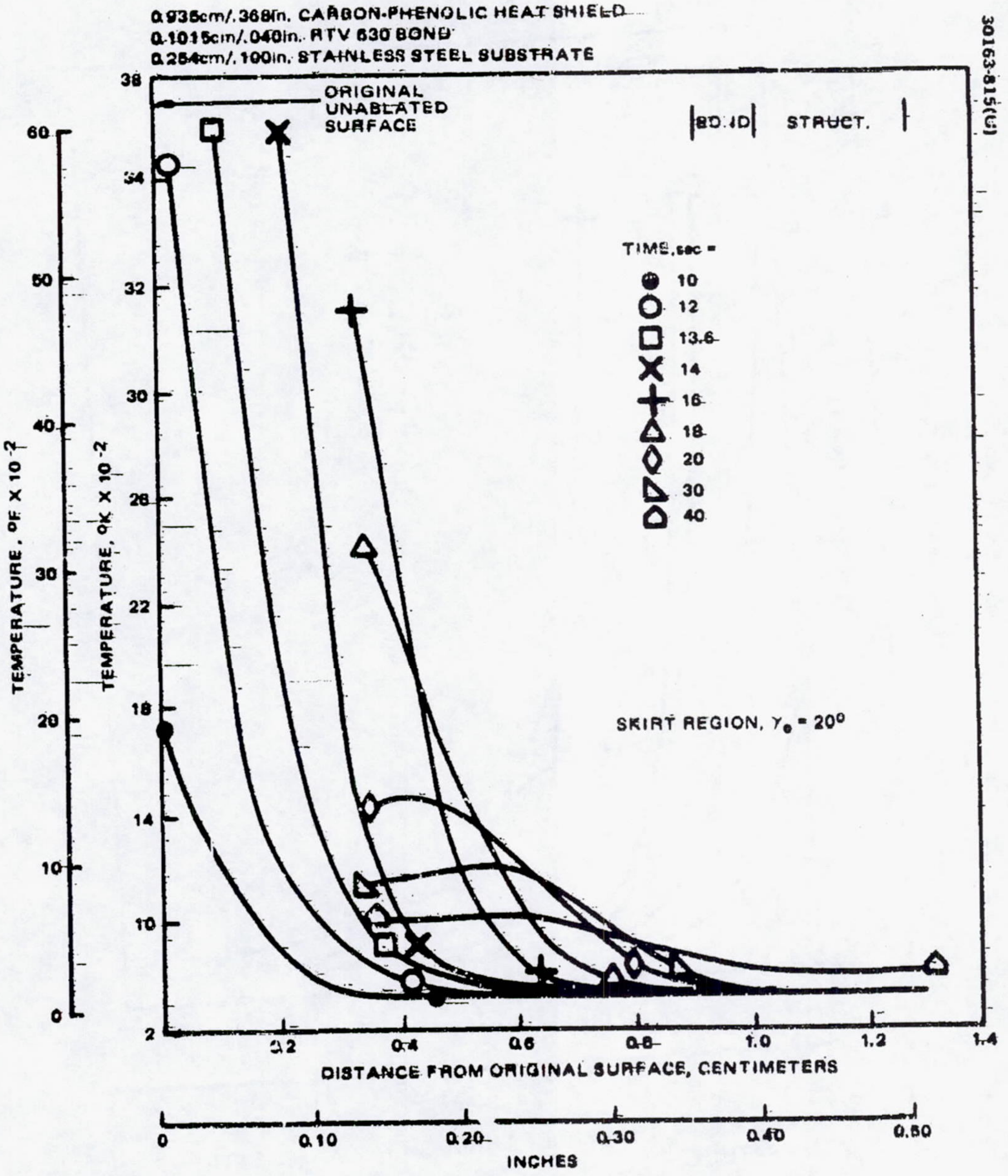

FIGURE 5.4-30. SMALL PROBE THROUGH THICKNESS ENTRY TEMPERATURES

TABLE 5.4-8. PLASMA ARC SCREENING TEST MATRIX

Facility	Test Gas	Flow Condition	Convective Heat Transfer		Radiative Heat Transfer		Local Pressure		Number of Models			
			w/m^2	Btu/ft^2-sec	w/m^2	Btu/ft^2-sec	N/m^2	atm	PN	CP	TEF	ESM
G.E. hyperthermal arc	Air	Laminar splash	5.1×10^7	4,500	0	0	$3\text{-}4 \times 10^5$	3 to 4	1	1	1	1
	CO_2	Laminar splash	5.0×10^7	4,400	0	0	$3\text{-}4 \times 10^5$	3 to 4	1	1	1	1
	CO_2	Laminar splash	1.6×10^7	1,400	0	0	$3\text{-}4 \times 10^5$	3 to 4	1	1	1	1
	Air	Turbulent wedge	2.4×10^7	2,100	0	0	$1\text{-}2 \times 10^5$	1 to 2	1	1	1	1
	CO_2	Turbulent wedge	2.5×10^7	2,200	0	0	$1\text{-}2 \times 10^5$	1 to 2	1	1	1	1
NASA Ames AEHS	Air	Laminar splash	1.1×10^7	1,000	0	0	10^5	1	2	2	2	2
	Air	Laminar splash	1.1×10^7	1,000	1.7×10^7	1,500	10^5	1	2	2	2	1
	Air	Laminar splash	1.8×10^7	1,600	0	0	10^5	1	1	1	1	0
	Air	Laminar splash	1.8×10^7	1,600	1.1×10^7 to 2.3×10^7	1,000 to 2,000	10^5	1	4	4	4	3
								Total	14	14	14	11

Ablation Test Program

Each of the four candidate heat shield materials was tested in plasma arc ablation facilities at GE-RESD and NASA Ames. The environmental and heating parameters of the test program are summarized in the test matrix shown in Table 5.4-8. Comparison of flight and ground test conditions are shown in Figures 5.4-31 through 5.4-33. The data obtained from each test are listed in Tables 5.4-9 through 5.4-12.

Analysis of Results

The PN design recession correlation (Reference 2) relates heat of ablation to the applied enthalpy and is shown in Figure 5.4-34. This correlation represents the best fit of data from ground test and earth entry flights with environmental parameters spanning the following ranges:

Heat flux	5.7×10^5 to 3.4×10^7 w/m^2 (50 to 3000 Btu/ft^2-sec)
Enthalpy	3.5×10^6 to 3.1×10^7 J/kg (1500 to 13550 Btu/lb)
Pressure	0.0 to 20 atm
Shear	48 to 3300 N/m^2 (1 to 70 lbs/ft^2)

In the recent tests, each of the PN models, regardless of gas environment or heat transfer mode, exhibited greater heat of ablation values and lower recession than would be predicted by the design correlation, and thereby indicated that the heat shield requirements defined in the system trades study are more than adequate. Pressure effects are included as lumped parameters in the design correlation and the levels associated with the correlation apparently are greater than those experienced in the current test series. The pressure effect causes char scrubbing and results in accelerated recession and is demonstrated by the tendency of the G.E. models (3 to 4 atm) to approach the correlation more closely than do the Ames models (1 atm). Some reduction in the calculated heat of ablation of the Ames models would be expected if blockage of hot gas radiation by ablation vapors were included in the calculation. With complete blockage, the heat of ablation values would be reduced by 40 to 60 percent of the values indicated.

While the test recession performances appear much better than those predicted by the design correlation, they are consistent with other recession correlations that include pressure effect as shown in Figure 5.4-35. These curves were developed analytically for PN in air where the shear levels were low and the char was not mechanically removed (scrubbed). The correlation shown in Figure 5.4-36 is based on ground test data, and exhibits a strong pressure dependence that is followed quite closely by most of the data. The scatter of the Ames data might be reduced if hot gas radiation blockage were assessed and incorporated. While no significant CO_2 effect was discerned in the current test series, the potential for increased heat shield requirements

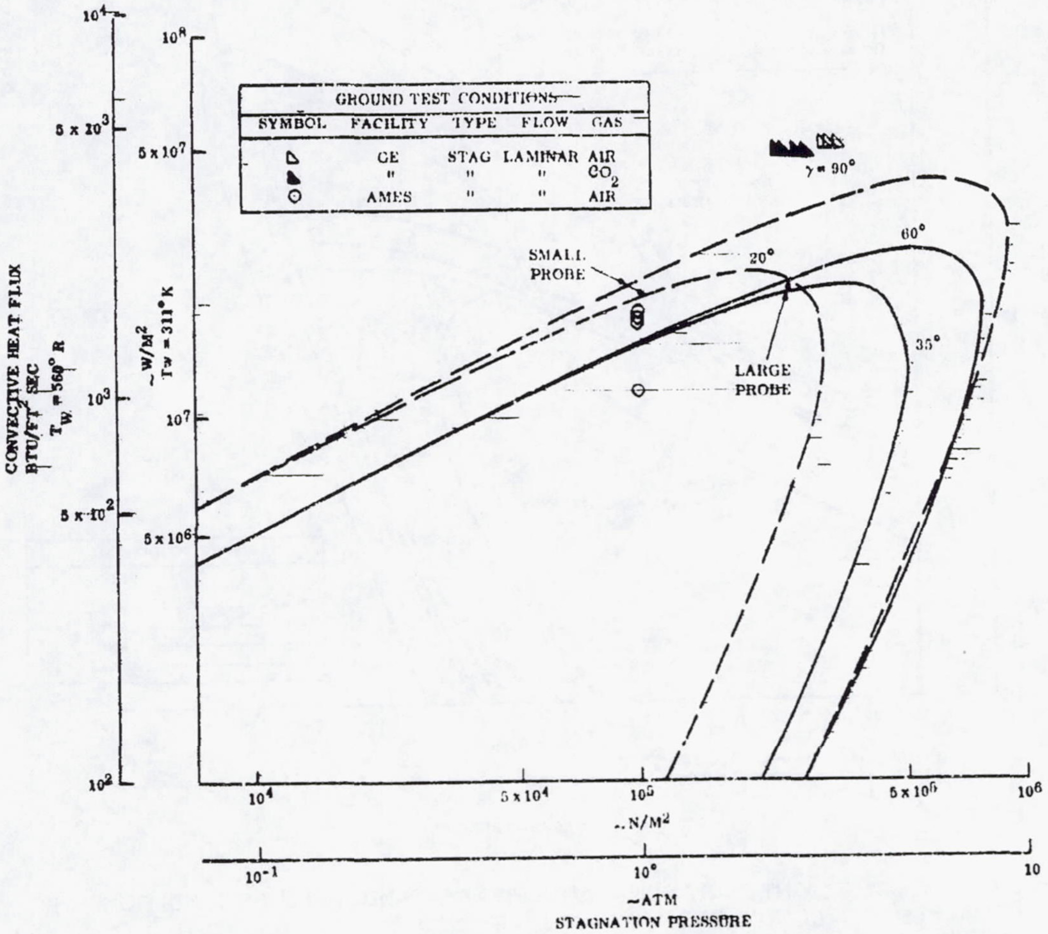

FIGURE 5.4-31. FLIGHT SKIRT CONVECTIVE HEATING AND PRESSURE CONDITIONS COMPARED WITH CONDITIONS IN FLIGHT TESTS

30163-816(U)

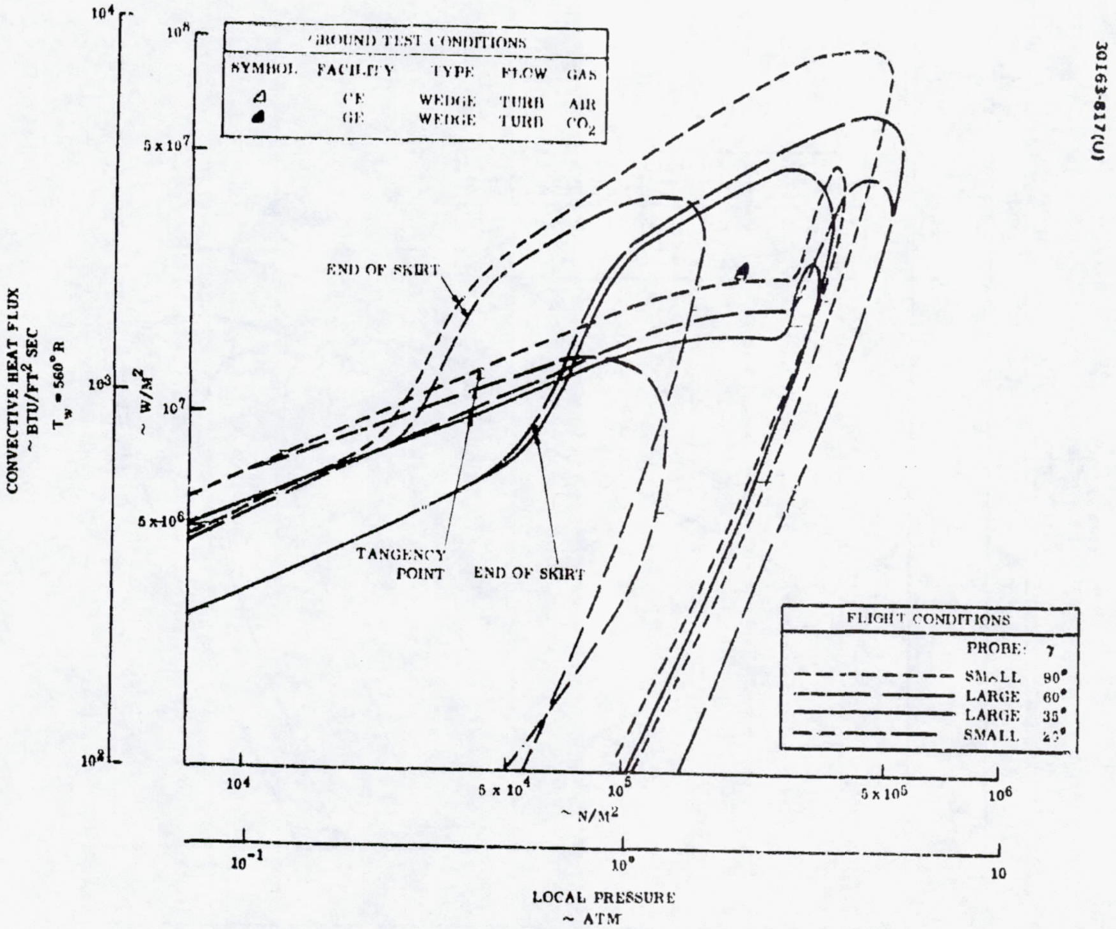

FIGURE 5.4-32. FLIGHT SKIRT CONVECTIVE HEATING AND PRESSURE CONDITIONS COMPARED WITH CONDITIONS IN GROUND TESTS

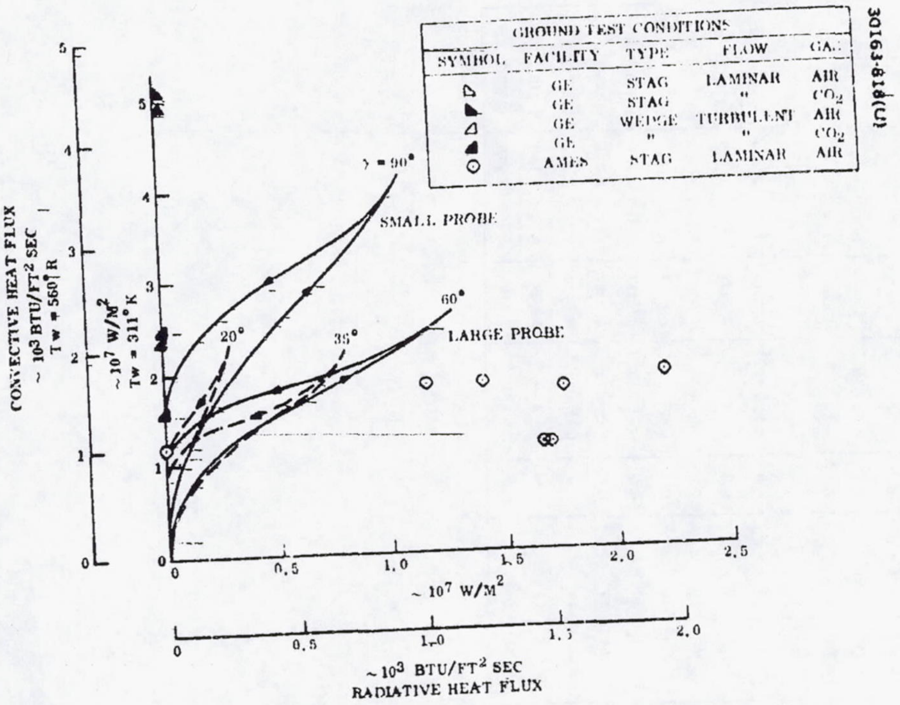

FIGURE 5.4-33. FLIGHT AND GROUND TEST CONVECTIVE AND RADIATIVE HEATING CONDITIONS

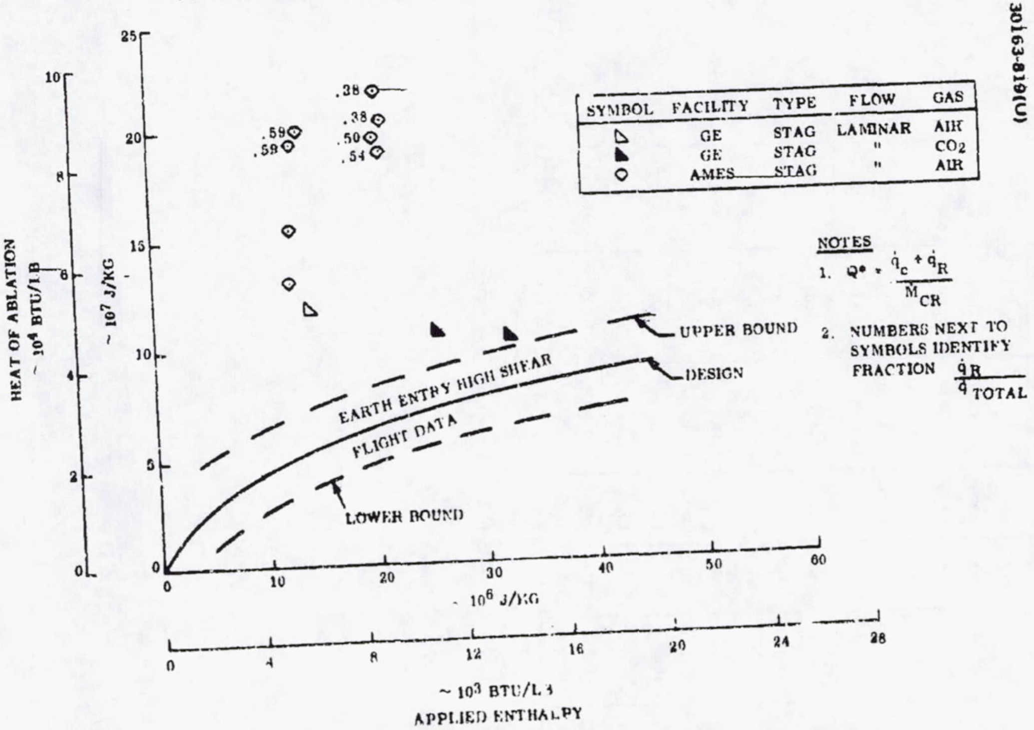

FIGURE 5.4-34. PHENOLIC NYLON HEAT OF ABLATION DESIGN CORRELATION

TABLE 5.4-9. PHENOLIC NYLON TEST DATA

Facility	Test No.	Type	Flow	$\dot{q}_{cw}$		$\dot{q}_R$		H		P		$\dot{S}$		Test Time	T_s		Gas
				w/m^2	Btu/ft^2-sec	w/m^2	Btu/ft^2-sec	J/kg	Btu/lb	N/m^2	ATM	m/sec	in/sec	sec.	°K	°R	
GE	5-73C	Stag.	Lam.	5.15×10^7	4,560	0	0	1.79×10^7	7,700	3.91×10^5	3.86	1.45×10^{-3}	0.0571	2.4	--	--	Air
GE	12-73C	Stag.	Lam.	5.0×10^7	4,400	0	0	2.9×10^7	12,500	3.74×10^5	3.69	1.55×10^{-3}	0.0608	2.5	--	--	CO_2
GE	17-73C	Stag.	Lam.	1.57×10^7	1,386	0	0	3.62×10^7	15,600	3.26×10^5	3.22	5.02×10^{-4}	0.01974	3.9	--	--	CO_2
GE	5-73W	Wedge	Turb.	2.33×10^7	2,050	0	0	1.79×10^7	7,700	2×10^5	2	3.81×10^{-5}	0.0015	9.6	--	--	Air
GE	12-73W	Wedge	Turb.	2.46×10^7	2,170	0	0	2.9×10^7	12,500	2×10^5	2	--	Char Growth	4.0	--	--	CO_2
Ames	15-1	Stag.	Lam.	1.18×10^7	1,040	0	0	1.67×10^7	7,180	10^5	1.0	2.54×10^{-4}	0.010	3.78	2,840	5,110	Air
Ames	16-2	Stag.	Lam.	1.18×10^7	1,040	0	0	1.65×10^7	7,096	10^5	1.0	3.0×10^{-4}	0.0118	5.95	2,980	5,350	Air
Ames	17-3	Stag.	Lam.	1.17×10^7	1,028	1.67×10^7	1470	1.76×10^7	7,569	10^5	1.0	4.67×10^{-4}	0.0184	3.97	--	--	Air
Ames	18-4	Stag.	Lam.	1.18×10^7	1,040	1.7×10^7	1500	1.65×10^7	7,095	10^5	1.0	4.87×10^{-4}	0.0192	6.55	3,216	5,790	Air
Ames	19-5	Stag.	Lam.	1.79×10^7	1,580	1.76×10^7	1524	2.44×10^7	10,493	10^5	1.0	6.03×10^{-4}	0.0237	2.95	3,216	5,790	Air
Ames	20-6	Stag.	Lam.	1.92×10^7	1,690	2.2×10^7	1945	2.50×10^7	10,751	10^5	1.0	7.29×10^{-4}	0.0287	3.94	3,216	5,790	Air
Ames	21-7	Stag.	Lam.	1.85×10^7	1,630	1.15×10^7	1018	2.47×10^7	10,622	10^5	1.0	4.62×10^{-4}	0.0182	3.90	3,240	5,830	Air
Ames	22-8	Stag.	Lam.	1.86×10^7	1,635	1.41×10^7	1240	2.385×10^7	10,279	10^3	1.0	2.3×10^{-4}	0.009	4.00	3,000	5,410	Air
Ames	21-9	Stag.	Lam.	1.85×10^7	1,630	1.15×10^7	1018	2.47×10^7	10,622	10^5	1.0	4.9×10^{-4}	0.0193	4.15	3,216	5,790	Air

Notes

$\dot{m}_{C_R} = \rho_c \dot{S} = (18.75\ lb/ft^3)\ \dot{S}/12$

$$Q^* = \frac{\dot{q}_{cw} + \dot{q}_R}{\dot{m}_{C_R}}$$

REPRODUCIBILITY OF THE ORIGINAL PAGE IS POOR.

TABLE 5.4-10. TEFLON TEST DATA

Facility	Test No.	Type	Flow	$\dot{q}_{cw}$		$\dot{q}_R$		H		P		$\dot{S}$		Test Time, sec	T_e	Gas
				w/m^2	Btu/ft^2-sec	w/m^2	Btu/ft^2-sec	J/kg	Btu/lb	N/m^2	ATM	m/sec	In/sec			
GE	7-73C	Stag.	Lam.	5.17×10^7	4.560	0	0	1.76×10^7	7,600	4.15×10^5	4.09	2.76×10^{-3}	0.1082	2.2	---	Air
GE	15-73C	Stag.	Lam.	5.0×10^7	4.400	0	0	2.46×10^7	12,300	3.08×10^5	3.04	2.45×10^{-3}	0.0965	2.0	---	CO_2
GE	17-73C	Stag.	Lam.	1.565×10^7	1,380	0	0	3.62×10^7	15,600	3.26×10^5	3.22	8.76×10^{-4}	0.0345	1.65	---	CO_2
GE	7-73W	Wedge	Turb	2.33×10^7	2,050	0	0	1.76×10^7	7,600	2×10^5	2	7.75×10^{-4}	0.0305	4.0	---	Air
GE	14-73W	Wedge	Turb	2.45×10^7	2,170	0	0	3.08×10^7	13,300	2×10^5	2	8.4×10^{-4}	0.033	4.0	---	CO_2
Ames	15-1	Stag.	Lam.	1.18×10^7	1,040	0	0	1.67×10^7	7,180	10^5	1.0	1.02×10^{-3}	0.0403	3.92	---	Air
Ames	16-2	Stag.	Lam.	1.18×10^7	1,040	0	0	1.65×10^7	7,096	10^5	1.0	9.9×10^{-4}	0.039	3.10	---	Air
Ames	17-3	Stag.	Lam.	1.17×10^7	1,028	1.67×10^7	1,470	1.76×10^7	7,569	10^5	1.0	1.04×10^{-3}	0.0409	3.96	---	Air
Ames	18-4	Stag.	Lam.	1.18×10^7	1,040	1.7×10^7	1,500	1.65×10^7	7,096	10^5	1.0	8.56×10^{-4}	0.0337	3.80	---	Air
Ames	19-5	Stag.	Lam.	1.79×10^7	1,580	1.76×10^7	1,549	2.44×10^7	10.493	10^5	1.0	1.17×10^{-3}	0.0459	3.07	---	Air
Ames	20-6	Stag.	Lam.	1.92×10^7	1,690	2.2×10^7	1,945	2.50×10^7	10,751	10^5	1.0	1.04×10^{-3}/ 2.24×10^{-3}	0.0409/ 0.088	4.20	---	Air
Ames	21-7	Stag.	Lam.	1.85×10^7	1,630	1.15×10^7	1,018	2.47×10^7	10,622	10^5	1.0	1.16×10^{-3}	0.0456	3.09	---	Air
Ames	22-8	Stag.	Lam.	1.86×10^7	1,635	1.41×10^7	1,240	2.385×10^7	10,279	10^5	1.0	1.13×10^{-3}	0.0443	3.00	---	Air
Ames	22-9	Stag.	Lam.	1.86×10^7	1,635	0	0	2.385×10^7	10,279	10^5	1.0	6.0×10^{-4}	0.0236	3.00	---	Air

Note

$\dot{m} = \rho_v \dot{S} = 134 \dot{S}/12$

$Q^* = \dot{q}_c/\dot{m}$

REPRODUCIBILITY OF THE ORIGINAL PAGE IS POOR.

TABLE 5-4-11. CARBON PHENOLIC TEST DATA

Facility	Test No.	Type	Flow	$\dot{q}_{cw}$ w/m^2	$\dot{q}_{cw}$ Btu/ft^2-sec	$\dot{q}_R$ w/m^2	$\dot{q}_R$ Btu/ft^2-sec	H J/kg	H Btu/lb	P N/m^2	P ATM	$\dot{S}$ m/sec	$\dot{S}$ In/sec	Test Time, sec	T_s °K	T_s °R	Gas
GE	6-73C	Stag.	Lam.	5.17×10^7	4,560	0	0	1.93×10^7	8,300	4.11×10^5	4.05	1.13×10^{-3}	0.0445	6.2	---	---	Air
GE	13-73C	Stag.	Lam.	5.0×10^7	4,400	0	0	2.76×10^7	11,900	3.62×10^5	3.57	2.17×10^{-3}	0.0855	4.0	---	---	CO_2
GE	21-73C	Stag.	Lam.	1.565×10^7	1,380	0	0	3.82×10^7	16,500	3.23×10^5	3.19	4.54×10^{-4}	0.01785	3.5	---	---	CO_2
GE	6-73W	Wedge	Turb.	2.33×10^7	2,050	0	0	1.93×10^7	8,300	2×10^5	2	---	Char Growth	3.9	---	---	Air
GE	13-73W	Wedge	Turb.	2.46×10^7	2,170	0	0	2.76×10^7	11,900	2×10^5	2	---	Char Growth	4.0	---	---	CO_2
Ames	15-1	Stag.	Lam.	1.18×10^7	1,040	0	0	1.67×10^7	7,180	10^5	1.0	1.22×10^{-4}	0.0048	9.86	3,216	5,790	Air
Ames	16-2	Stag.	Lam.	1.18×10^7	1,040	0	0	1.65×10^7	7,096	10^5	1.0	1.57×10^{-4}	0.0062	14.40	3,220	5,800	Air
Ames	18-3	Stag.	Lam.	1.18×10^7	1,040	1.7×10^7	1500	1.65×10^7	7,096	10^5	1.0	4.4×10^{-4}	0.0173	10.50	3,395	6,110	Air
Ames	18-4	Stag.	Lam.	1.18×10^7	1,040	1.7×10^7	1500	1.65×10^7	7,096	10^5	1.0	4.96×10^{-4}/ 4.42×10^{-4}	0.0195/ 0.0174	14.92	3,380	6,090	Air
Ames	19-5	Stag.	Lam.	1.79×10^7	1,580	1.76×10^7	1549	2.44×10^7	10,493	10^5	1.0	6.38×10^{-4}/ 9.4×10^{-4}	0.0251/ 0.037	4.92	3,395	6,110	Air
Ames	20-6	Stag.	Lam.	1.92×10^7	1,690	2.2×10^7	1945	2.50×10^7	10,751	10^5	1.0	5.0×10^{-4}	0.0197	4.92	3,395	6,110	Air
Ames	21-7	Stag.	Lam.	1.85×10^7	1,630	1.15×10^7	1018	2.47×10^7	10,622	10^5	1.0	1.96×10^{-4}	0.0077	4.92	3,345	6,020	Air
Ames	22-8	Stag.	Lam.	1.86×10^7	1,635	1.41×10^7	1240	2.385×10^7	10,279	10^5	1.0	3.91×10^{-4}/ 5.64×10^{-4}	0.0154/ 0.0222	5.00	3,240	5,830	Air
Ames	29-9	Stag.	Lam.	1.92×10^7	1,690	0	0	2.50×10^7	10,751	10^5	1.0	3.56×10^{-4}/ 8.39×10^{-4}	0.014/ 0.033	5.13	2,900	5,220	Air

REPRODUCIBILITY OF THE ORIGINAL PAGE IS POOR.

TABLE 5.4-12. ESM 1004 TEST DATA

Facility	Test No.	Type	Flow	$\dot{q}_{cw}$		$\dot{q}_R$		H		P		$\dot{S}$		Test Time, sec	T_s		Gas
				w/m²	Btu/ft²-sec	w/m²	Btu/ft²-sec	J/kg	Btu/lb	N/m²	ATM	m/sec	In/sec		K	R	
GE	8-73C	Stag.	Lam.	5.17×10^7	4,560	0	0	1.88×10^7	8,100	4.21×10^5	4.15	5.03×10^{-3}	0.198	1.5	---	---	Air
GE	14-73C	Stag.	Lam.	5.0×10^7	4,400	0	0	3.08×10^7	13,300	3.38×10^5	3.33	6.43×10^{-3}	0.253	0.75	---	---	CO_2
GE	18-73C	Stag.	Lam.	1.565×10^7	1,380	0	0	3.73×10^7	16,100	3.46×10^5	3.41	1.68×10^{-3}	0.066	0.90	---	---	CO_2
GE	8-73W	Wedge	Turb.	2.33×10^7	2,050	0	0	1.88×10^7	8,100	2×10^5	2.	6.96×10^{-4}	0.0274	2.85	---	---	Air
GE	15-73W	Wedge	Turb.	2.46×10^7	2,170	0	0	2.46×10^7	12,300	2×10^5	2	1.3×10^{-3}	0.051	2.0	---	---	CO_2
Ames	15-1	Stag.	Lam.	1.18×10^7	1,040	---	---	1.67×10^7	7,180	10^5	1.0	9.65×10^{-4}	0.038	2.92	--	--	Air
Ames	16-2	Stag.	Lam.	1.18×10^7	1,040	---	---	1.65×10^7	7,096	10^5	1.0	1.02×10^{-3}	0.040	3.92	--	--	Air
Ames	18-3	Stag.	Lam.	1.18×10^7	1,040	1.7×10^7	1500	1.65×10^7	7,096	10^5	1.0	1.72×10^{-3}	0.0676	3.0	2920	5,250	Air
Ames	21-4	Stag.	Lam.	1.85×10^7	1,630	---	---	2.47×10^7	10,622	10^5	1.0	1.86×10^{-3}	0.0731	2.86	2745	4,940	Air
Ames	22-5	Stag.	Lam.	1.86×10^7	1,635	---	---	2.38×10^7	10,279	10^5	1.0	1.82×10^{-3}	0.0717	3.00	3050	5,490	Air
Ames	22-6	Stag.	Lam.	1.86×10^7	1,635	---	---	2.38×10^7	10,279	10^5	1.0	1.16×10^{-3}	0.0456	3.00	---	---	Air

Note

$$\dot{m} = \rho_v \dot{S} = 35 (\dot{S} \cdot 12)$$

$$Q^* = \frac{q_c - q_R}{\dot{m}}$$

REPRODUCIBILITY OF THE ORIGINAL PAGE IS POOR.

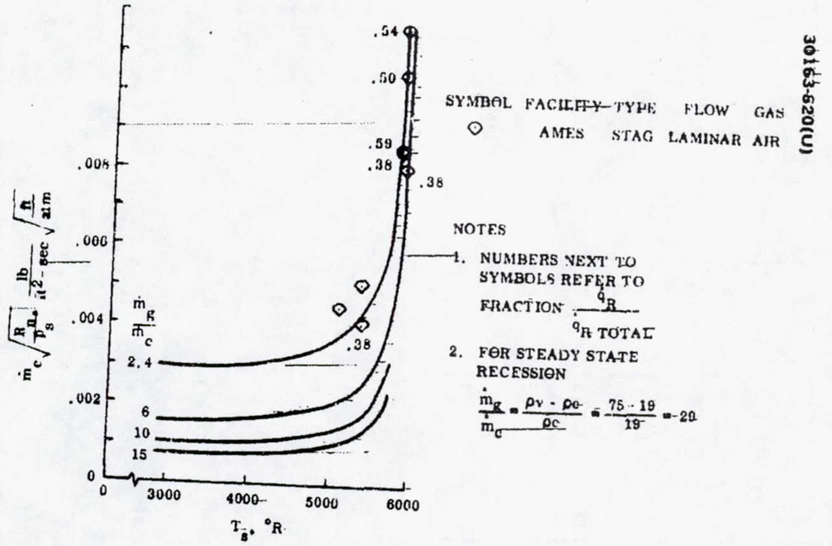

FIGURE 5.4-35. NASA MASS LOSS CORRELATION FOR PHENOLIC NYLON

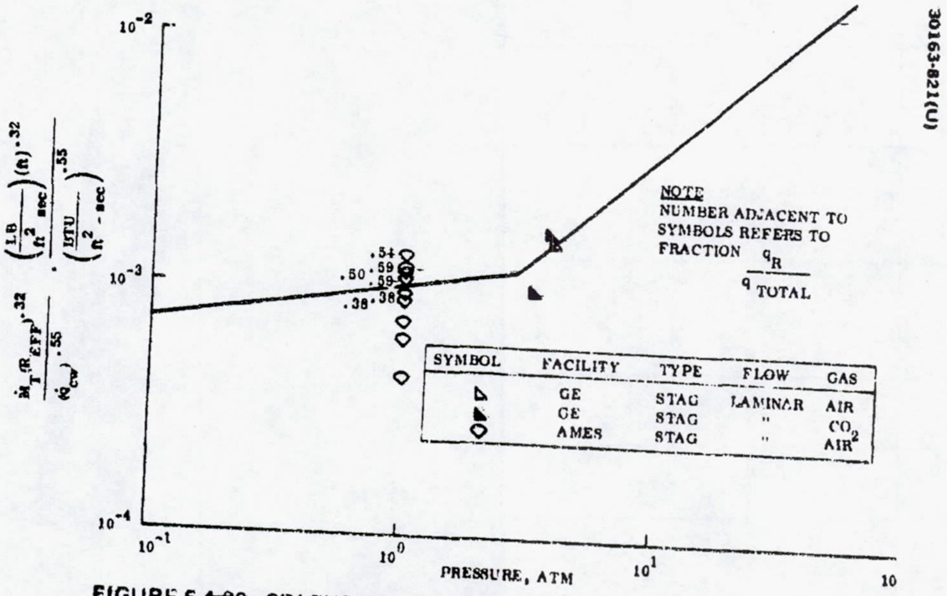

FIGURE 5.4-36. SRI PHENOLIC NYLON MASS LOSS CORRELATION

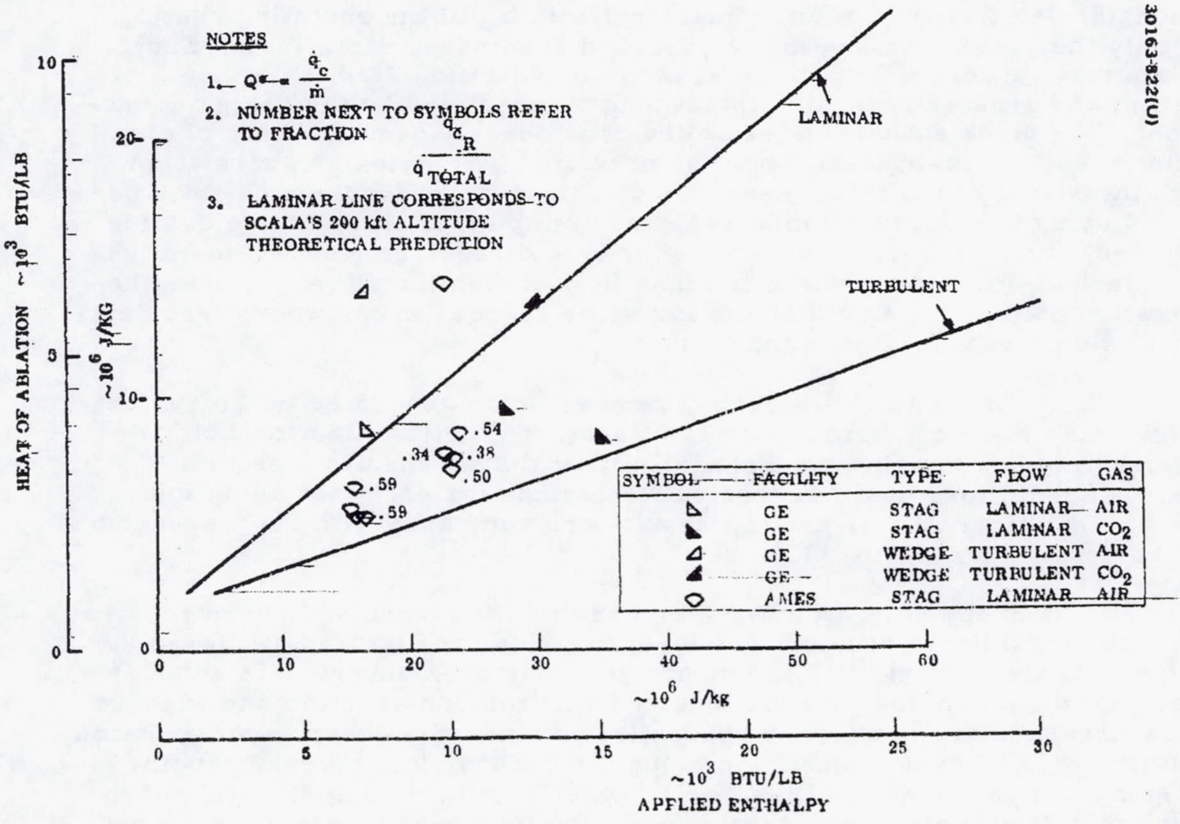

FIGURE 5.4-37. TEFLON HEAT OF ABLATION DESIGN CORRELATION

in a CO_2 environment should not be ignored, particularly if the flight conditions indicate that chemically induced recession will prevail. Analysis of the effect of boundary layer chemical reactions for heat shield materials in various gaseous environments can be performed with the Ablating Boundary Layer Equilibrium (ABLE) Computer Program.

The teflon recession design correlation was developed from flight data, and relates heat of ablation to applied enthalpy shown in Figure 5.4-37. The heat of ablation values for this test series were computed by considering that the Teflon surface reflects all of the radiative heating and only the convective heating is absorbed and causes mass loss. Except for one test, all of the laminar stagnation models exhibited lower heats of ablation and greater recession than would be predicted by the design correlation. The turbulent models exhibited considerably greater heats of ablation and less recession than would be predicted by the design correlation. Since the sizing of the teflon heat shield in the system trades study was performed using this correlation and the assumption that all radiative heating is reflected, it would appear that the teflon shield requirements would be less than adequate in regions where laminar flow predominated (e.g., near the stagnation point), and would be conservative in those areas where turbulent flow was dominant (e.g., on the skirt).

The CP heat shield thickness requirements generated in the system trades study were computed using the Reaction Kinetics Ablation Computer Program, which contains the Fogaroli-Brant thermochemical erosion option. Predictions of CP recession were made for each test using the REKAP analytical model, and the results are compared with the measured test values in Figure 5.4-38.

Some of the stagnation models made by the inverted chevron construction method exhibited drastically uneven ablation profiles and displayed evidence of "dixie cupping." This phenomenon has been observed in some other test models made with the inverted chevron construction and exposed to low pressure arc heating. Apparently, the inverted chevron construction permits rapid in-depth conduction along the carbon cloth layers, causing softening and gasification of the resin, which results in deterioration of the interlaminate structural integrity. When the internal gas pressure exceeds the sum of the external pressure and interlaminate strength, the "dixie cup" is mechanically ejected. Inverted chevron construction has been used satisfactorily in nose tips exposed to high heating and pressure levels, but would not be proposed for a CP Pioneer Venus heat shield. Unfortunately, the small size of the stagnation models restricted the fabrication method to inverted chevron construction.

The turbulent wedge models, representative of the tape wrapped construction used in the skirt regions of an entry vehicle, exhibited no abnormal behavior during testing. As indicated in Figure 5.4-38, the performance of the CP in air and in carbon dioxide was better than predicted by the REKAP model. The char depths for the wedge models measured 1.5 mm (0.06 in).

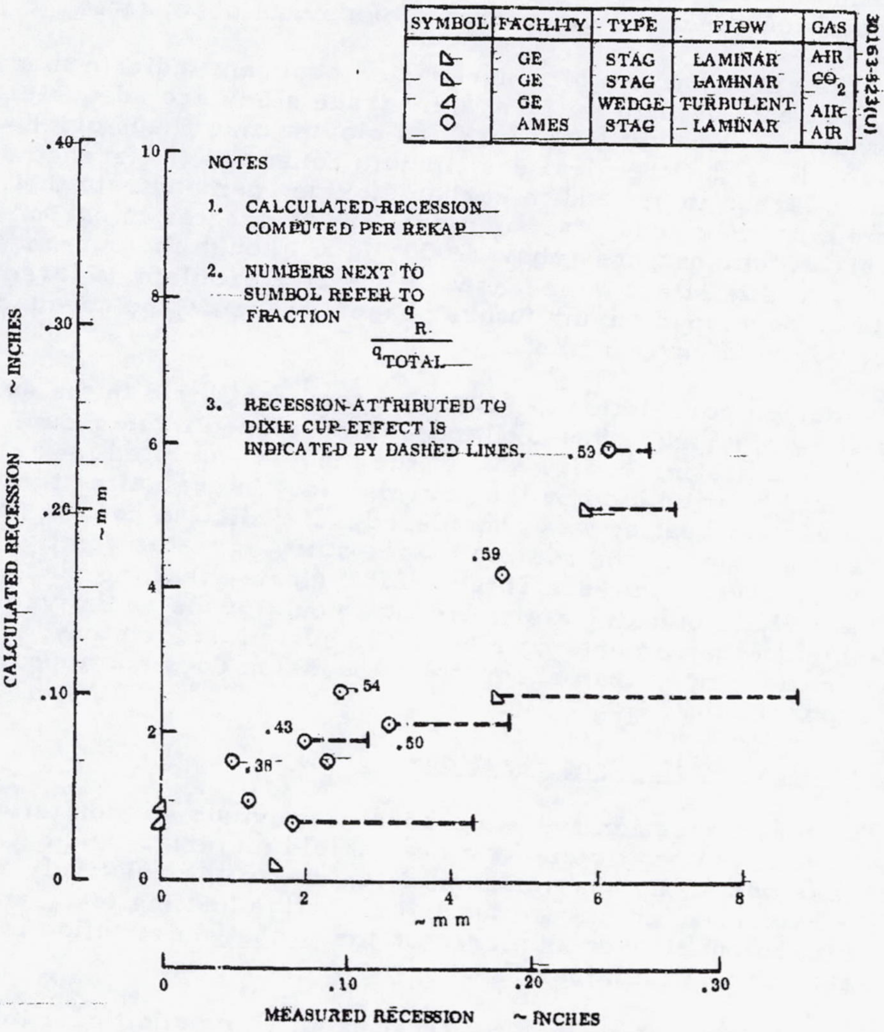

FIGURE 5.4-38.- COMPARISON OF MEASURED AND CALCULATED RECESSION FOR CARBON PHENOLIC

No visual differences were observed between the model tested in air and that tested in carbon dioxide.

If the test data for the models exhibiting the "dixie cup" effect are ignored, the recession predictions for the remainder of the models compare reasonably well with the measured values. Both convective and radiative heating effects appear to be adequately accounted for by the REKAP solution. No recession sensitivity to carbon dioxide was observed.

Overall, the results from this current test program indicate that the heat shield requirements defined in the system trade study are adequate. It should be remembered, however, the work of Golovina and Khaustovich (Reference 7) as well as the chemical equilibrium constants (Reference 8) for the reaction of carbon in air and in carbon dioxide, demonstrate that, at least under some circumstances, carbon mass loss is greater in carbon dioxide than in air at temperatures above 2000°K. Although the current test data do not show that this effect is necessarily a major problem, a larger data bank should be developed during future phases to ensure the adequacy of CP in a carbon dioxide environment.

The ESM design correlation used to size the heat shield in the system trades study is shown in Figure 5.4-39, and was developed from ground test results for convective heating in air. All of the models exhibited lower recession than would be predicted by the correlation. In evaluating the abscissa only convective heating was considered. If radiative heating had been included, as was done in the system trades study, greater positive safety margin would have resulted. This result indicates that the mass addition from the ESM is blocking a significant amount of the radiative heating. The heat shield requirements defined in the system trade study, therefore, appear to be more than adequate. Recession does not appear to be affected by exposure to CO_2.

Reflective Heat Shield Considerations

In the thermal protection system trades in previous section teflon was considered as the primary reflective heat shield material candidate. In general, teflon was one of the heavier candidates due to the relatively small magnitude of the radiative, compared to the convective heating load, and the large amount of turbulent flow encountered on the probe where teflon is not as efficient an ablator as in laminar flow.

The purpose of this study was to: 1) present some additional information on the teflon versus other ablator weight trades, 2) provide some general guidance on increases required in probe nose radius and ballistic coefficient to increase the radiative to convective heating fraction, and 3) identify two alternate approaches to flight testing a reflective heat shield material.

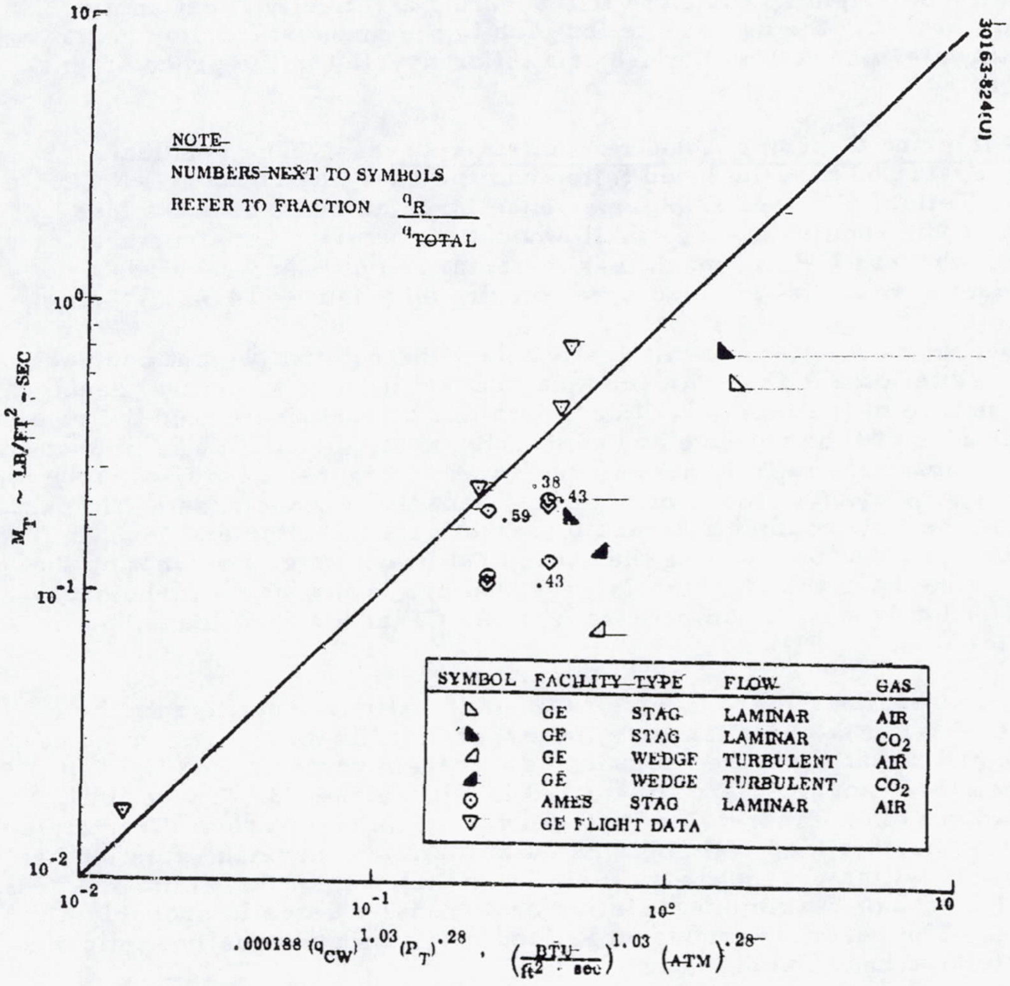

FIGURE 5.4-39. SRI MASS LOSS CORRELATION FOR ESM 1004 DESIGN CORRELATION

In summary it is demonstrated that 1) the weight penalty associated with a teflon heat shield is dependent not only on the magnitude of the convective heating load but also on the structural heat capacitance Figure 5.4-40 2) the radiative to convective heating fraction can be increased if the probe nose radius and ballistic coefficient can be increased (Figure 5.4-41), and 3) the minimum weight approach to flight testing a reflective heat shield material is probably the use of a teflon plug in the probe stagnation region and an alternate approach is the use of a teflon overlay in the probe stagnation region.

Teflon and Charring Ablative Materials Trades. The candidate materials evaluated have included teflon and the charring ablators PN, CP, and ESM. Teflon, PN, and ESM experience large amounts of mass loss during entry and require a very small amount of material for structural insulation, whereas CP has much less material removal and requires a large amount of material for structural insulation (Figure 5.4-42).

Several parameters dramatically affect the relative weight comparisons between teflon and the charring ablators and include structural heat capacity, nature of the local flow (i.e., laminar or turbulent), and the relative magnitudes of the radiative and convective heating loads. The impact of the structural heat capacitance is illustrated in Figure 5.4-40, where it is seen that utilization of the structure heat capacity has the greatest impact on reducing the CP requirements and lesser effects on teflon and PN. It can also be seen that by ignoring the structural heat capacity and noting that the small probe heat shield weight is governed primarily by the turbulent skirt, the teflon is weight competitive with the CP at low heat loads, but is still heavier than the PN.

By increasing the probe nose radius and ballistic coefficient, the peak value of radiative heat transfer increases significantly. The combination of R_N and β that generate radiative heat transfer rates at the limit of NASA Ames test capability are illustrated in Figure 5.4-43. These limits are superimposed on Figure 5.4-41 to show the maximum value of radiative to convective heating load ratio obtainable to maintain the peak radiative heat transfer rates within current test capability. Violation of this limit by a factor of 1.5 to 2 on maximum radiative heat transfer rates is probably acceptable. The resultant trends on R_N and β effects are equally applicable to any reflective heat shield material.

Configurations for Increasing Radiative to Convective Heating Fraction. Several other configurations offer the potential for increasing the probe nose radius. These include an Apollo shape, a sphere, or a Discoveror configuration. The hypersonic drag coefficients or these configurations are 1.5, 1.05, and 0.7 respectively, compared to a value of 1.05 for the baseline configuration. Hence, Discoveror represents possibly the only configuration with a large ballistic coefficient, assuming to the first order that weight and base diameter remains constant between the configurations. Both the Apollo shape and sphere exhibit tendencies toward decreasing hypersonic stability

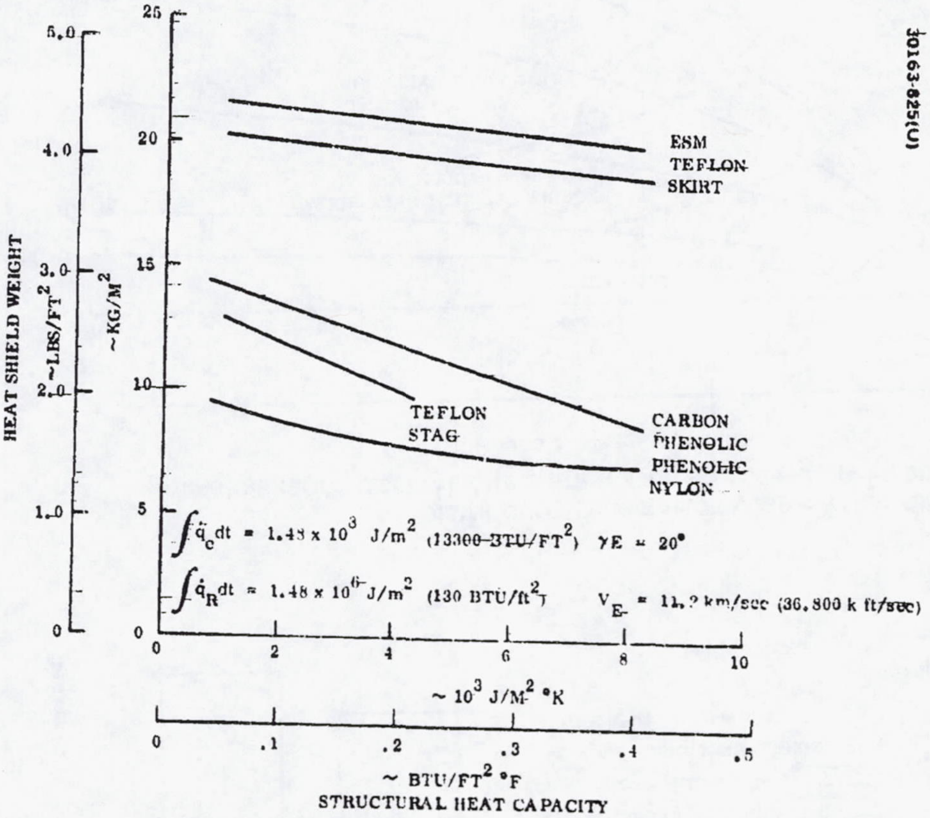

FIGURE 5.4-40. EFFECT OF STRUCTURAL HEAT CAPACITY ON HEAT SHIELD WEIGHT REQUIREMENTS

30163-825(U)

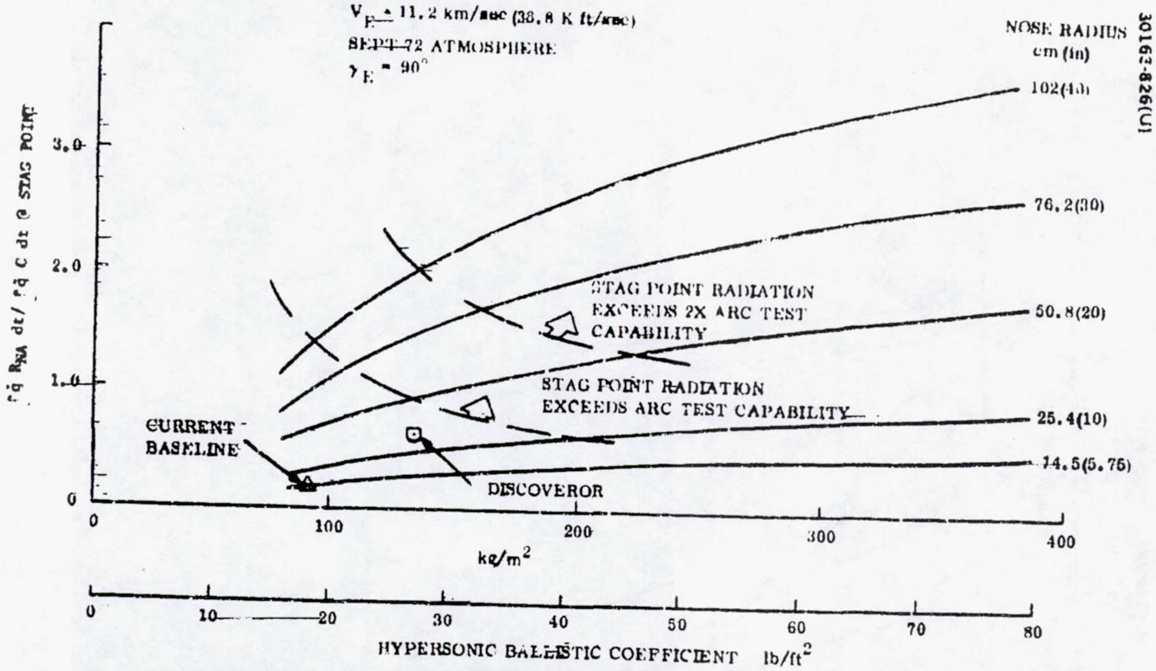

FIGURE 5.4-41. EFFECT OF NOSE RADIUS AND BALLISTIC COEFFICIENT ON RADIATIVE – CONVECTIVE HEAT LOAD RATIO

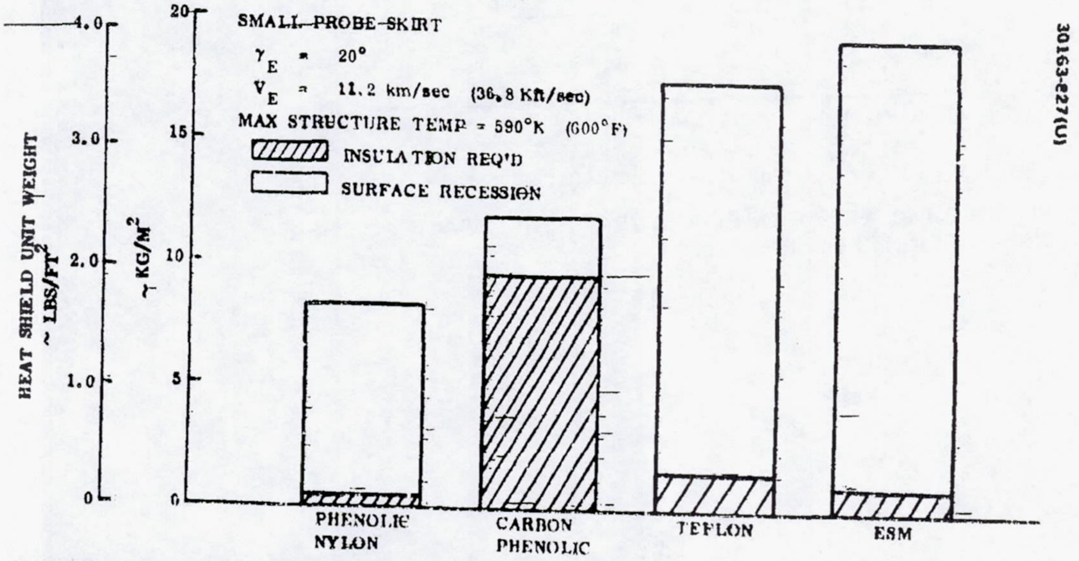

FIGURE 4.5-42. COMPARISON OF SURFACE RECESSION AND INSULATION REQUIREMENTS FOR VARIOUS CANDIDATE MATERIALS

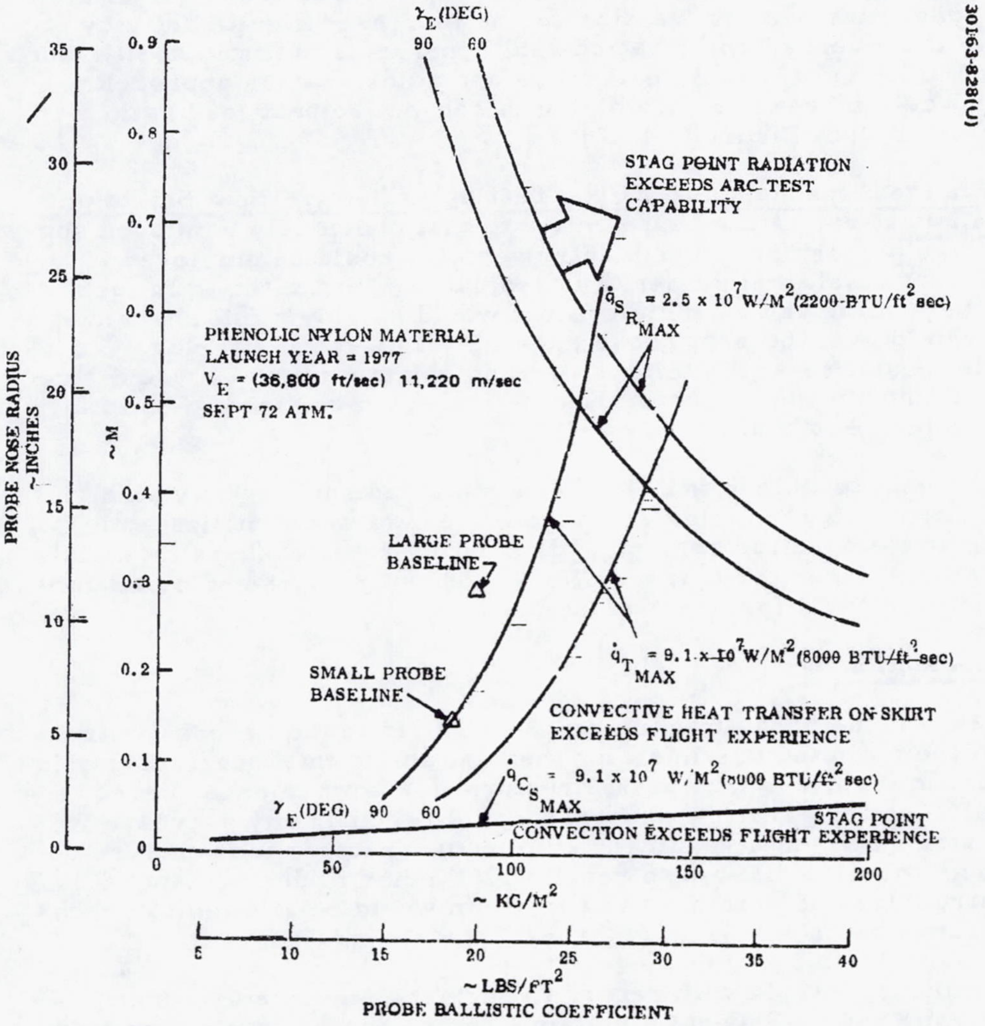

FIGURE 5.4-43. CONFIGURATION CONSTRAINTS TO MAINTAIN FLIGHT ENVIRONMENT WITHIN PREVIOUS FLIGHT EXPERIENCE AND CURRENT RADIATIVE TEST CAPABILITY

when combined with the science payload. The Discoveror configuration represents a stable, well characterized aerodynamic shape, with a large data band of aerodynamic coefficients available. The current baseline design, a sphere cone with 45 deg half cone angle, represents a state of the art vehicle that will meet the overall mission objectives, but will provide a flight test on a reflective heat shield of limited meaning, since it develops such a low ratio of radiative to convective heating (Figure 5.4-41). The radiative to convective heating fraction can be increased significantly by employing the Discoveror configuration with hypersonic ballistic coefficient in the 120 to 150 kg/m^2 (25 to 30 psf) range and a nose radius approaching 30 cm. This would increase the radiative to convective heat load ratio from 0.17 to about 0.6 (Figure 5.4-41).

Alternative Approaches to Flight Testing Reflective Heat Shield on Baseline Configuration. A concept similar to that previously employed successfully on high performance earth entry vehicles could be employed to minimize the heat shield weight penalty associated with the teflon in turbulent flow on the vehicle skirt. This concept would employ a full charring ablator heat shield over the probe nose covered with a teflon overlay. Thermocouples installed at the teflon/charring ablator interface would give a clear indication of teflon removal. The teflon would be sized to be totally removed just after peak heating.

An alternate technique that has been employed successfully on high performance earth entry vehicles as antenna windows would utilize a plug of teflon in the probe stagnation region. The ablation rates of these materials are considerably different so that the effects of having a forward or aft facing step would have to be further evaluated.

Bond Selection

Selection of the bond attaching the heat shield to the aeroshell structure is one of the main factors in sizing the heat shield thickness. Early in the study it became obvious that peak structural loads were encountered before the backface temperature response would result in any decrease in the material strength. As a result the aluminum structure temperature on the large probe would be allowed to reach 600°K prior to deployment of the chute while structures of titanium and beryllium would be allowed to reach much higher temperatures.

The limiting criteria with regard to backface temperature then appeared to be the bond. Several high temperature bond materials were considered as potential candidates namely RTV 560, RTV 630, or primed RTV 560, which is designated PD 200. The latter is presently available in two density levels – 520 kg/m^3 (32 lbs/ft^3), designated PD 200-32 and 260 kg/m^3 (16 lbs/ft^3), designated PD 200-16.

RTV 560 although exhibiting some desirable characteristics was eliminated because of the need for venting and supplying a controlled relative humidity during the curing process. It was felt that the shimming required to provide venting for such a large diameter shield would result in an unnecessarily cumbersome manufacturing process.

The requirements of the bond are different, depending on whether one considers PN or CP as the heat shield material. In the case of PN, the bond requirement is based upon orbital cold soak capability. PD 200-32 was found to be the optimum bond material for PN, since it provided the greatest cold soak capability, and although its strength characteristics are lower at elevated temperatures than RTV 630 no high strength characteristics were required during this period when considering PN.

However, CP although not subject to a cold soak problem during orbit will undergo considerable thermal stress during the cool down period after entry. As a result RTV 630 was selected as the bond material with carbon phenolic because of its high strength at elevated temperature capability.

Analysis of Phenolic Nylon Cold Soak

A postcured PN heat shield bonded to the aeroshell structure with a room temperature curing adhesive system was analyzed to determine the mechanical performance of the composite under minimum cold soak temperature exposure. The postcured PN exhibits the stable mechanical properties necessary to survive the anticipated Pioneer Venus flight environment. The postcured PN has negligible shrink under both vacuum and elevated temperature exposure up to the postcure temperature. This means that residual stresses or strains due to fabrication or aging can be safely ignored when the heat shield is bonded to a structure using a room temperature curing bond system. Therefore, room temperature becomes the zero stress/strain reference point for the thermal stress analysis. The results of the analysis indicate that the large probe postcured PN heat shield bonded with RTV-560 to the aluminum aeroshell will survive to 164°K (-164°F) using a 0.10 cm (0.040 in.) bond thickness cured at room temperature. The minimum predicted temperature on the shield is 225°K (-50°F).

The small probe baseline configuration which is a postcured PN heat shield bonded with RTV-560 to a titanium aeroshell will survive 200°K (-100°F) with a 0.150 cm (0.060 in) bond thickness cured at room temperature. Increasing the RTV-560 bond thickness to 0.25 cm (0.100 in) (an additional 0.5 kg [(1.05 lb)] total weight increase) would permit the phenolic nylon heat shield and titanium aeroshell small probe to survive to a temperature of 172°K (-150°F).

The use of PD 200 foam pad bonded to both the heat shield and the aeroshell was also investigated. The results of this study indicate that using a PD 200 pad at 505 kg/m^3 (32 lb/ft^3) with two 0.0125 cm (0.005 in.) RTV-560 bond interfaces would result in a 7 percent weight increase over 0.1 cm (0.04 in.) RTV-560 bond system since the minimum PD 200 pad thickness is approximately 0.25 cm (0.090 in.). However, a weight saving can be achieved by using PD 200 pad on the beryllium aeroshell configuration of the large probe for minimum design temperatures lower than 200°K (-100°F).

On the small probe with a beryllium aeroshell, no weight saving is indicated by going to a PD 200 pad; however, weight savings of 0.25 kg (0.5 lb) and 0.75 kg (1.5 lb) are obtained over the RTV-560 bond system at 200°K (-100°F) and 172°K (-150°F) minimum design temperatures, respectively, with a titanium aeroshell on the small probe.

RTV-560 is the structurally optimum bond system for both of the Pioneer Venus probes for temperatures to 172°K (-150°F) because of its superior tensile and shear strength. However, PD 200 at 520 kg/m^3 (32 lb/ft^3) density is structurally adequate for utilization on both probes in order to facilitate assembly of the phenolic nylon to the aeroshell.

Effects of Space Environment Upon Carbon Phenolic Heat Shields

The space environment, as far as material behavior is concerned, may be considered to be a combination of high vacuum (1.3 x 10^{-3} N/m^2 or 10^{-5} torr), moderately elevated temperature (up to 100°C) and intense ultraviolet radiation, plus some ionic bombardment.

The combined effects of heating to moderate temperatures and high vacuum on cross-linked polymeric materials result usually in removal of low molecular weight constituents such as water and unreacted resinous components. Since, in a well cured composite system such as a PC laminate, these entities comprise only a small fraction of the total system, weight losses from exposure to the heated vacuum environment may be expected to be small. Mechanical properties of the laminate may be expected to change very slowly under these conditions, with the ultimate result being a gradual increase in flexural strength and modulus. Tensile strength characteristics would be changed very little, if at all, since the orientation and properties of the reinforcement predominate in the determination of tensile strength.

A number of surveys have been published in which the effect of the space environment on materials was evaluated. Jaffe, et al (Reference 9 and 10) surveyed the behavior of plastics in vacuum at high temperatures, and concluded that most polymers are as stable in the vacuum in space at temperatures as high as they can withstand in air. A further observation noted that loss of engineering properties will not occur unless significant weight losses take place. Flom, of General Electric Co., pointed out the effect of vacuum and heat on properties of materials containing low molecular weight plasticizers and additives. Such materials would be drastically affected. Ringwood (Reference 11) discussed the effect of the volatilization process and mentions that some plastics are improved when impurities are outgassed. This would be true especially of condensation polymers such as phenolics.

To conclude, therefore, phenolic carbon laminates would be expected to survive exposure to vacuum at 100°C for long periods of time with little change in engineering properties, particularly if the laminate is well cured. Indeed, the effect of this environment may be less damaging than comparable exposure in air, since oxidative deterioration would not be a factor.

Ultraviolet radiation under vacuum conditions tends to cause depolymerization of simple polymers by photon entrapment. A highly cross-linked resin such as a phenolic does not decompose readily under these conditions, but opacifies, limiting the damage from ultraviolet exposure to the surface.

Ionic bombardment of phenolic resins results in electron capture due to the resonant structure of the phenol molecule and its ability to accommodate extra charged species. Phenolic resins are quite stable under these conditions.

Carbon fiber is relatively unaffected by either ultraviolet or ion bombardment.

Tape Wrapped Carbon Phenolic Heat Shields

Since the introduction of the concept of ablative heat protection of reentry vehicles, emphasis has been placed on the development of polymers and composites that combine such properties as high char yield upon exposure to heat, relatively low thermal conductivity, and fabricability. When combined with refractory fibers to give a composite structure, the polymeric matrix must provide mechanical support as well as the low molecular weight gases generated during the ablative processes.

Phenolic resins have been used extensively as resinous binders in applications where good thermal stability and mechanical properties are desired. The Mil. R9299II phenolic resins currently employed to make PC heat shields are base catalyzed, single stage, and heat reactive compositions. Typically, they contain 1.05 to 1.10 mols of formaldehyde to each mol of phenol. The reaction is catalyzed by the addition of an ammonia type chemical, and the mixture is heated until the desired amount of reaction has taken place; at which point, the resin is placed in solution for application to the carbon fabric.

It should be noted that pure, cured phenolic resin has a char yield of approximately 65 percent as determined by thermogravimetric analysis. In order to provide a higher char yield, and additional sites for nucleation, carbon powder to the extent of 5 to 8 percent is added to the resin solution.

Carbon fabric is the reinforcement most widely used in the manufacture of heat shields for high performance reentry vehicles. The material is made from a precursor fabric of regenerated cellulose (also known as xanthate rayon or viscose rayon) that is pyrolyzed in a neutral atmosphere to produce a fabric having the following properties:

Carbon assay weight, percent	94 to 98
Specific gravity at 25°C	1.8 to 1.9
Weight	0.24 to 0.30 kg/m^2 to 7.0 to 9.0 oz/yd^2
Fiber diameter	8.9 to 11 μ (0.00035 to 0.00045 in.)
Thread count	
Warp	2.0 to 2.4 picks/mm (50 to 60 picks/in.)
Fill	1.8 to 2.2 picks/mm (45 to 55 picks/in.)
Filaments per Yarn — nominal	720
Weave	Eight harness satin

Depending on the pyrolysis temperature, the carbon content can be varied within limits of 85 to 98 percent to give fibrous materials having lower or higher thermal conductivity characteristics. The fabric used in heat shields was selected as a compromise between thermal conductivity and carbon content to provide a material having adequate mechanical properties and insulation capabilities.

Prepreg material is prepared by coating and impregnating the carbon fabric with the filled phenolic resin solution, then removing enough solvent under controlled conditions to yield a readily processable material. Typical prepreg contains 60 to 65 percent carbon fabric by weight, while the rest is resin and volatile material.

Fabrication Techniques. In view of the stringent requirements imposed upon heat shield materials, caused by the high temperature, high shear force environment to which they are subjected, it is necessary to control the orientation of the reinforcement in such a way that part of the fiber or fabric is locked into the subsurface of the shield, while the outer portion is ablating. Several fabrication techniques have been used to prepare ablative composites, the most common being molded chopped squares (or fibers), rosette pattern layup, and tape wrapping.

Molded chopped squares (or fibers). In this process, prepregged fabric is chopped into squares approximately one inch on a side. Alternatively, chopped impregnated roving can be used. A heat shield or other shape is then prepared by placing preforms of the molding compound in a matched metal mold and forming to final shape by means of heat and pressure. The composite thus made has mechanical properties that are governed to a certain degree by the ability of the molding process to confer a preferred orientation on the reinforcement. Surface recession characteristics are unpredictable because of the randomness of the orientation of the carbon fibers.

Rosette pattern layup. This process utilizes a layup technique to produce a low angle spiral wrap composite. The layup can be made on either a male or a female form; but the usual practice, in order to avoid wrinkles, is to use a female form. Relatively large sheets of prepreg are cut into the form of trapezoids (assuming that a frustum is to be made) and laid up on the interior of the mold so that each sheet forms a continuous path from the outer surface of the form to the mold. The following diagram shows an end view of the ply orientation of the material as molded:

This is a simplified view showing the ply path. In actual practice, the plies are placed closer together.

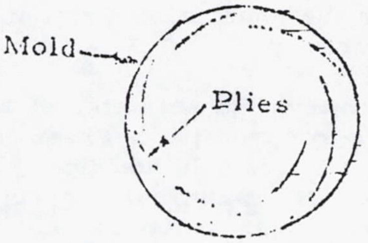

Curing is accomplished by vacuum bag autoclave techniques. The part thus formed has excellent thermophysical and mechanical properties, approaching those of a flat laminate. This layup pattern was originally selected for use in a high performance reentry vehicle, but the first test flights showed that the edges of the plies exposed to the airstream upon reentry acted like tiny fins, imparting an unacceptable rapid spin to the vehicle. Accordingly, the final selection of the CP heat shield material was made based on the factors previously discussed – resulting in a tape wrapped shield.

Tape wrapping carbon phenolic shields. When this technique is used, the uncured CP prepreg tape is wrapped at an angle around a mandrel such that the inner edge of the tape forms the inner surface of the thermal shield while the outer edge of the tape forms the ablating surface. The most common angle of wrap for reentry vehicle thermal shields is a 20 deg (to the ablating surface) wrap shingled aft. The angle of wrap can be varied from parallel-to-the-axis of rotation to almost 90 deg to the axis of rotation dependent on the reinforcement weave and the wall thickness requirement.

Once the carbon fabric has been impregnated and "B" staged to the proper flow and volatile content, it is processed into tape in the following manner.

Rationale for Tape Orientation and Lap Control. Since bias oriented-CP tape can be applied to a mandrel at a wide variety of angular orientations, the selection of the 20 deg to the surface as the proper orientation deserved some review. It was mentioned in the preceding paragraphs that the tape wrapping process can produce almost any desired orientation from 0 to 90 deg to the mandrel surface. From a mechanical property point of view, maximum axial tensile properties and elongation to failure are achieved at a low angle wrap. Thermal conductivity appears to be little affected by orientations between 0 and 20 deg. At higher angles, an increase in thermal conductivity can be expected.

Ablation characteristics deteriorate at low orientation angles. A 0 deg angle laminate tends to lose plies by peeling, and angles up to about 15 deg expose a large edge area to the heat flux, causing excessive resin degradation. Ply angles between 15 and 25 deg were found to have an optimum balance between ablation and conductivity characteristics, and 20-deg was chosen for the production wrap angle because of prior experience on the Mark 12 program.

In summary, the selection of a 20 deg bias tape wrapped heat shield was based on a compromise between mechanical, ablative, and thermophysical requirements. In addition, there is an existence a large data bank of experimental and analytical characteristics on the material which can be applied to Pioneer Venus programs.

Details of the Tape Wrapping Process. A tape wrapping machine, such as the Edwards "Wrap-Master", is not unlike a highly specialized lathe. It is designed to rotate a heavy mandrel while simultaneously moving an application head under relatively large lateral loads.

Mandrel design. The mandrel on which the tape wrapped form takes shape, while simple in appearance, must be designed so that the forces imposed upon it by the tape application head to not distort the surface or move the assembly out of alignment. The mandrel is usually a casting that is machined to shape and equipped with a sturdy shaft, as shown in Figure 5.4-44. Since the tape application head will press upon the surface of the mandrel at an angle of 65 deg, the horizontal component of force will be large, and the mandrel must be designed with adequate backup material, as shown. In this design, the 20 deg ramp is an integral part of the mandrel. In order to assure easy removal of the cured heat shield, the mandrel is either coated with teflon or a silicone mold release prior to the wrapping operation.

Tape application head. The bias tape is applied to the mandrel by means of a specialized roller application head that simultaneously advances along the axis of the mandrel as each layer is laid down, applies pressure to consolidate the tape, heats the tape just prior to contact with the previously applied layer, and cools it just after laydown, thus freezing the tape into position.

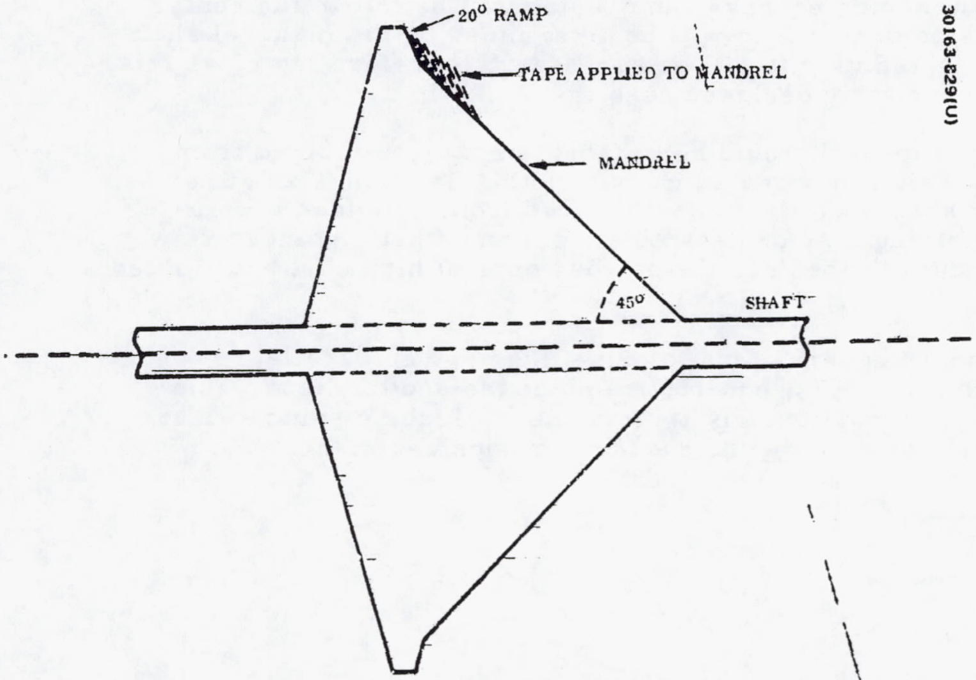

FIGURE 5.4-44. SCHEMATIC DIAGRAM OF TAPE WRAPPING MANDREL WITH BUILT-IN 20 DEG RAMP

This series of operations is shown schematically in Figure 5.4-45. By proper control of all these parameters, it is possible to tape wrap a form to 90 to 95 percent of final cured density.

Nose tip and heat-shield design. Figure 5.4-46 is a cross sectional diagram of a proposed design for the assembly of the molded nose cap and tape wrapped skirt to the structural shell. In this design the structural shell is made in two parts – the nose cap and the skirt. The ablative parts are bonded to the structural components with a hard (RTV 630) bond, and the assembly is made as shown in the figure.

Nose Tip Fabrication. Since the heat-shield skirt will be fabricated by means of a tape-wrapping process, an opening will be left in the center of the shield. The size of this hole will be determined by the mandrel shaft diameter and the nose radius. It will be necessary, therefore, to close this opening with an appropriately designed nose tip.

The simplest approach would be to fabricate a piece molded from chopped squares of resin impregnated carbon cloth. The nose can either be molded precisely to shape, or it can be machined from a molded billet. While a precision molding may be desirable from an esthetic point of view, it offers two disadvantages (besides the obvious ones of high cost and limited versatility):

1) The chopped squares tend to orient themselves parallel to the mold face. Consequently, a piece molded to shape would have a disproportionately large number of fabric squares that are poorly oriented with regard to erosion resistance.

Orientation tendency in molded-to-shape piece

Orientation tendency in piece machined from molded billet

2) Prepreg variability would become a critical factor in a precision molding operation.

Heat-Shield Baseline – Thor/Delta

Large Probe

The basic shape is a sphere-cone with a spherical nose radius of 29.2 cm and a half cone angle of 55 deg continuing to the base diameter of 116.8 cm. The heat shield is formed of PN, which is bonded to the

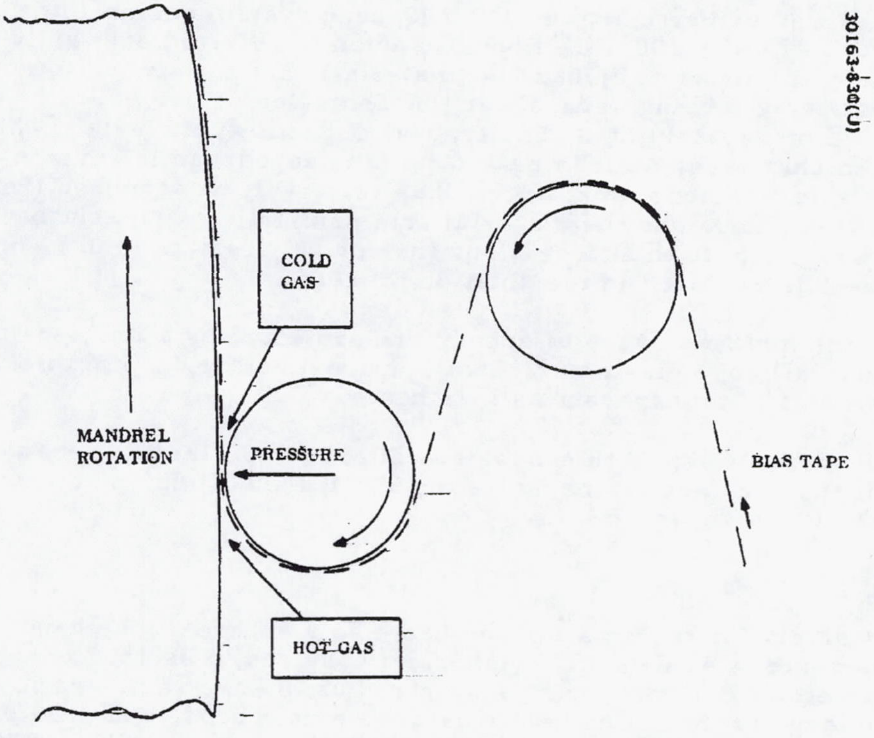

FIGURE 5.4-45. BIAS TAPE APPLICATION TO MANDREL SCHEMATIC

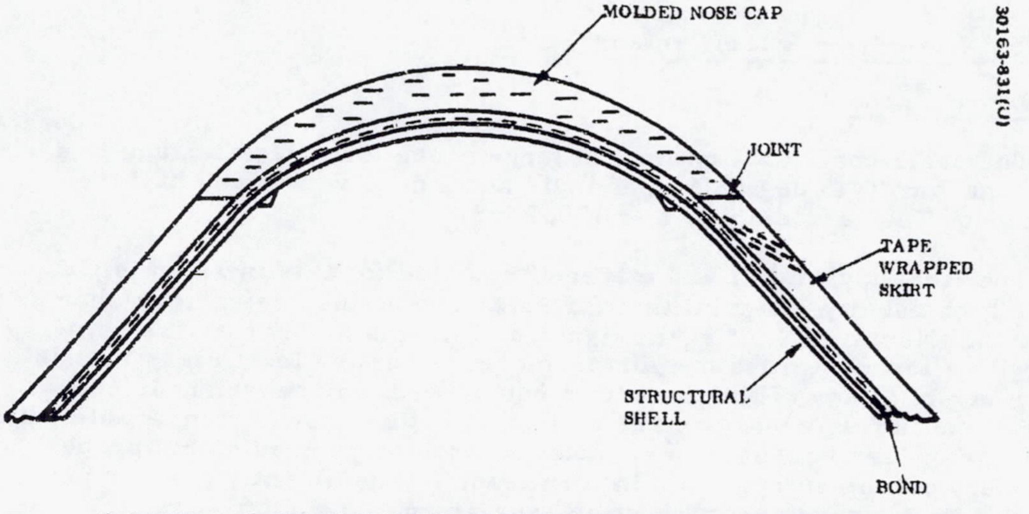

FIGURE 5.4-46. CROSS SECTION OF NOSE CAP AND SKIRT ASSEMBLY

beryllium aeroshell structure using an PD-200 bond system designed to permit cold soak to -73°C (-100°F). Phenolic nylon is selected primarily because it requires the lowest weight of all materials that satisfy the low cost criterion; low weight being critical for the Thor/Delta mission. Phenolic nylon is a moderately high density, low conductivity material, which decomposes into a char layer as it is heated. In the aerodynamic environment expected in this mission, most of the char layer will be scrubbed from the vehicle as it is formed, and the material acts primarily as an ablative heat shield. Average shield thickness along the conical frustum is 0.7 cm, of which 90 percent is removed in the ablation process.

All external surfaces of the afterbody are protected by a low density, chemically-foamed silicone elastomer (ESM), approximately 0.3 cm thick. The material remains rf transparent as it is heated.

The forebody heat shield thickness and afterbody protection are designed to limit the backface temperature to <589°K (600°F) during entry. The total heat shield weight is 12.0 kg.

Small Probe

The heat shield for the small probe has also a sphere-cone shape, but the half cone angle is 45 deg. The spherical nose radius is 15.2 cm and the base diameter 61.0 cm, giving a nose radius to base-radius ratio of 0.5, as with the large probe. The heat shield material, bond, and substructure are the same as for the large probe, i.e., PN for the forebody, ESM for the afterbody, and an PD-200 bond system.

The heat shield is designed to limit the backface temperatures to < 589°K (600°F) during the entry. The total heat shield weight is 4.6 kg.

Heat Shield Baseline — Atlas/Centaur

Large Probe

The basic configuration for the large probe for Atlas/Centaur is a sphere-cone with a 45 deg half cone angle and a nose radius one half the base radius. The base diameter is 139.7 cm.

The forebody heat shield material selected for this mission is CP. This is a high density material that forms a very stable, refractory char as it is heated. Next to PN, it is the lightest of the materials that are compatible with a low cost mission; furthermore, it has the least mass loss (by a large margin) of any of the materials considered. Since weight is not the primary issue in the Atlas/Centaur mission, and its cost is comparable with PN, CP was chosen because it permitted a much more predictable probe mass history during entry. This in turn leads to significantly greater accuracy in the atmosphere reconstruction experiment.

The heat shield thickness averages 0.28 cm along the conical frustum tapering to 1.09 cm at the nose. This thickness includes a 50 percent margin, chosen in order to provide a very safe design, thereby reducing the requirement for developmental testing and hence the program cost. The heat shield is bonded to an aluminum aeroshell structure using a bond similar to that described in the Thor/Delta design, RTV 630. The large probe afterbody is protected by a 0.3 cm thick layer of elastomer (ESM).

The forebody heat shield thickness and afterbody protection are designed to limit the backface temperatures to <589°K (600°F) during entry. The total heat shield weight is 35.5 kg.

Small Probe

The small probe heat shield has a sphere-cone shape geometrically similar to that of the large probe; its nose radius is one-half the base radius and the half cone angle is 45 deg. The nose radius is 16.7 cm and base diameter 67.3 cm.

The heat shield forebody material is CP, the same as for the large probe, but with slightly different thickness. The thickness varies from 1.04 cm at the skirt to 1.39 cm at the nose stagnation point. Afterbody material (ESM) and bonding method and material are the same as for the large probe. However, the substructure to which the shield is bonded is of stainless steel rather than aluminum.

The heat shield is designed to limit the backface temperature to <589°K (600°F) during entry. The total heat shield weight is 10 kg.

References

1. D. Florence, A. Hecht, and E. Vogel, "Hypersonic Entry Heat Transfer and Thermal Protection System Trades," GE PIR 9151-ARSTA-191, 15 December 1972.
2. W. A. Page, and H. T. Woodward, "Radiative and Convective Heating During Venus Entry," AIAA J., Vol. 10, pp. 1379-1381, October 1972.
3. W. Jaworski, and R. G. Nagler, "A Parametric Analysis of Venus Entry Heat Shield Requirements," JPL Tech Report 32-1468, 15 April 1970.
4. F. Wolf and J. M. Spiegal, "Status of Basic Shock Layer Radiation Information for Inner-Planet Atmospheric Entry," JSR, Vol. 4, No. 9, September 1967.

5. N. Hiester and C. Clark, "Comparative Evaluation of Ablating Materials in Arc Plasma Jets," Report No. 18, Final Report, Contract NAS-49(15), 13 March 1968.

6. T. W. Shaw, D. Garner, and D. Florence, "The Effect of Uncertainties in Thermophysical Properties on the Ablative and Insulative Efficiency of Char Forming Materials in Intense Convective and Radiative Heat Transfer Environments," AIAA Paper 65-639, presented, AIAA Thermophysics Specialist Conference, Monterey, California, September 1965.

7. E. Golovina and G. Khaustovich, "The Interaction of Carbon Dioxide and Oxygen at Temperatures Up to 3000°K," Eighth Symposium (International) on Combustion, California Institute of Technology, Pasadena, Calif., August/September 1960.

8. O. Hougen, K. Watson, and R. Ragatz, Chemical Process Principles, Part 2, 2nd Edition, John Wiley and Sons, Inc., New York, 1959.

9. L. D. Jaffe and J. B. Rittenhouse, "How Materials Behave in Science," Materials in Design Engineering, Vol. 56, No. 3, September 1962.

10. L. D. Jaffe, "Effects of Space Environment Upon Plastics and Elastomers," Chemical Engineering Progress Symposium Series, Vol. 59, No. 40, 1963.

11. A. F. Ringwood, "Behavior of Plastics in Space Environments," Modern Plastics, Vol. 4, No. 5, January 1964.

5.5 PARACHUTE

The pressure vessel module is extracted from the aeroshell and slowed during the initial phases of its descent by the parachute subsystem. Two baseline systems have been defined, one for the Thor/Delta mission, and the other for Atlas/Centaur. They differ in dimensions and in their operational altitude range, but both systems have the same concept and sequence: A mortar-deployed pilot chute is ejected at about Mach 0.8. The pilot chute removes the aeroshell aft cover and deploys the main parachute. After a time delay for system stabilization, the bolts attaching pressure vessel to aeroshell are released and separation is effected. The parachute remains attached to the pressure vessel module until a predetermined lower altitude is reached, at which it is jettisoned. This sequence is illustrated in Figure 5.5-1.

The pilot is a conical ribbon parachute, and the main is a disc-gap-band (DGB) configuration in both the Thor/Delta and Atlas/Centaur designs. For Thor/Delta, the pilot diameter is the same, while the main parachute is 4.6 m (15 ft) in diameter. In the Thor/Delta mission, the subsystem is initiated at about 69 km, and chute jettison occurs at 55 km, while for the Atlas/Centaur mission, the subsystem is initiated at about 67 km, and chute jettison occurs at 40 km.

Requirements

The parachute system must be designed to meet two basic mission objectives in addition to the pressure vessel separation function; namely, to provide terminal velocity prior to entry into the cloud layer, and to provide a suitably configured descending vehicle to meet scientific data collecting objectives during terminal descent. Parachute system design requirements to meet these objectives are as follows:

1) State-of-the-art parachute hardware and techniques are used

2) The system is designed for maximum simplicity, using the minimum number of staging and separation events to accomplish the retardation function

3) The parachutes are designed for the subsonic deployment environment established by nominal entry conditions of:

Thor/Delta	Atlas/Centaur
γ_E = 41 deg (down from horizontal)	31 deg (dfh)
V_E = 11,156 m/sec (36,605 ft/sec)	11.6 km (37,030 ft/sec)

4) Trajectory computations and loads are based on the Venus "September 1972" atmospheric profile.

5) The system is fully deployed at a minimum altitude of 66 km above the planet surface.

6) The main parachute canopy is selected for maximum steady state stability during final descent through data collecting regime.

7) The main parachute is capable of descending with the payload to within 40 km of the planet surface.

Trades/Studies

The studies leading to the selection of the baseline parachute subsystem were performed mainly for the Thor/Delta mission. These include parachute diameter and mortar selection criteria, separation events, deployment sensitivity to systems parameters, and coupled parachute probe motion similation.

Pilot Parachute Sizing

Sizing criteria for the pilot parachute requires that sufficient drag be provided to remove the aft cover, extract the main parachute pack, and strip the deployment bag from the main chute canopy. Also, the drag area must be minimized to limit both the size of the pilot parachute mortar and the reaction loads induced into the vehicle at the time the pilot chute is ejected. These requirements are satisfied by a minimum size, $D_o = 0.84$ m (2.75 ft), conical ribbon chute. The mortar length required for its pack volume of 460.3 cc satisfied the minimum space (14.6 cm length) envelope available for mounting.

Decelerator devices operating in the vehicle wake will experience degraded performance depending on the trailing distance and the size of the decelerator relative to the vehicle. This effect becomes more pronounced with small diameter decelerators. For instance, for the recommended system, the initial force generated by the pilot at deployment is 276 N (62 lb), while the free stream loading would be approximately (97 lb) 431 N, if wake effects were not considered. Wake effects are included in the time history of the pilot parachute aft cover separating from the aeroshell pressure vessel shown in Figure 5.5-2. It should be noted that the aft cover weight in this analysis includes the weight of the main parachute and bag. In the actual design, a short line one vehicle base diameter long would be connected to the cover such that the main parachute would not be extracted until the cover had traveled that distance. This analysis further assumes that the cover is free to move at pilot parachute deployment (i.e., no restraining forces or friction exist to retard separation). The 0.84 m baseline pilot parachute is seen to provide positive separation in an acceptable time within the above constraints.

Main Parachute Sizing

The main parachute has two functions: pressure vessel separation and velocity retardation in the upper atmosphere. Data rate/rf power/battery trades for the Thor/Delta mission indicated that a main chute diameter (D_o)

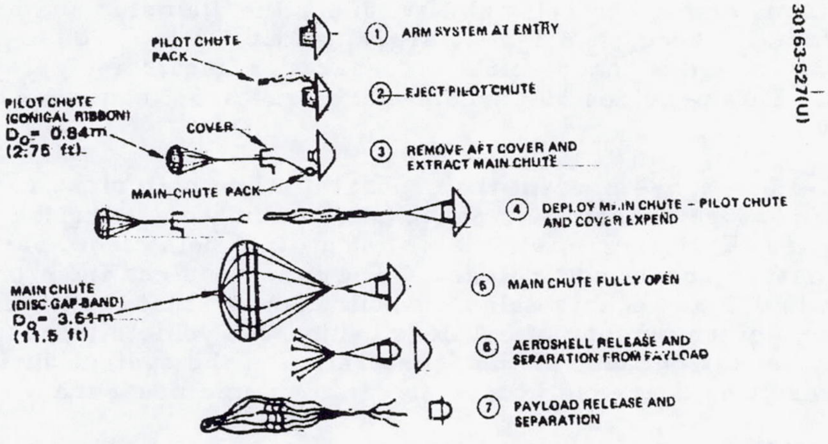

FIGURE 5.5-1. PARACHUTE SEQUENCE

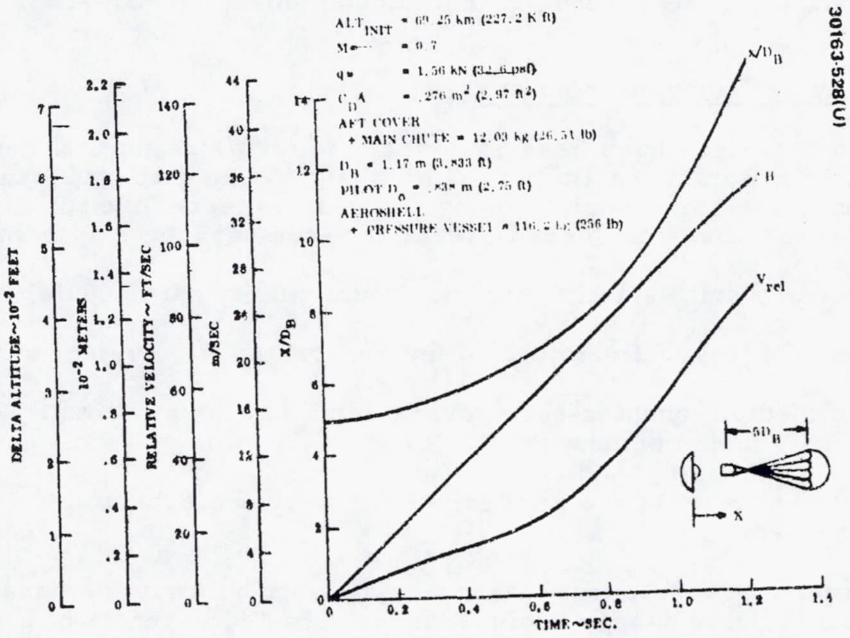

FIGURE 5.5-2. PILOT – AFT COVER SEPARATION HISTORIES

of approximately 3 m would provide the optimum descent velocity for a minimum weight system. A separation analysis on the other hand indicated that the minimum diameter for neutral stability, i.e., the diameter at which the net separation force is zero, is slightly larger, about 3.1 m. Consequently, the diameter choice is taken solely on separation requirements, and is 3.51 m (11.5 ft). This provides 50 percent more drag area than needed for neutral stability.

Figures 5.5-3 and 5.5-4 present the separation time histories of the aeroshell from the pressure vessel main parachute combination using the baseline 3.5 km chute. Each figure is for a different time delay from parachute release to pressure vessel bolt release. The time required from chute release to full open is 0.2 sec of this delay. It will be noted that the time required to separate a given number of calibers behind the vehicle increases as the time delay increases because of the deceleration of the system during this delay and the resulting decrease in free stream dynamic pressure.

The time at which the forebody should be separated must be traded off against the inherent vehicle motion at separation. In other words, the fastest separation would occur using no time delay; however, it is desirable that the vehicle motion be steady so as to prevent bumping between the pressure vessel and the forebody. This latter requirement would dictate a short time delay ≈2.0 sec after main parachute deployment as will be discussed later.

Main Parachute Canopy Candidates

Three canopy designs have been considered in terms of general performance and weight to select a main parachute design: The disc-gap-band, ring slot, and ribbon designs. Each of these designs possesses the following performance characteristics considered essential to the parachute system.

1) Good steady state stability for maximum quality data acquisition

2) Medium C_d (approximately 0.5) for reasonably low system weight

3) Low to medium opening shock characteristics for minimum structural design penalty

4) Operational state of the art designs for easy and economical procurement

Since the main parachute is a major weight contributor in the parachute system, the three candidate canopy designs were evaluated in terms of a weight tradeoff. Calculated weights for the three candidate canopies at design deployment loadings of $q = 1200\ N/m^2$ ($25\ lb/ft^2$), $q = 2400\ N/m^2$ ($50\ lb/ft^2$), and $4788\ N/m^2$ ($100\ lb/ft^2$) are shown in Table 5.5-1. It should be noted in the table that the 3.51 m (11.5 ft) D_o disc-gap-band parachute is capable of higher loads than the nominal deployment q_∞ of $1530\ N/m^2$ (32 psf) without an increase in parachute weight. This performance capability, therefore, permits increased safety margins for off-nominal deployment conditions without an associated weight penalty.

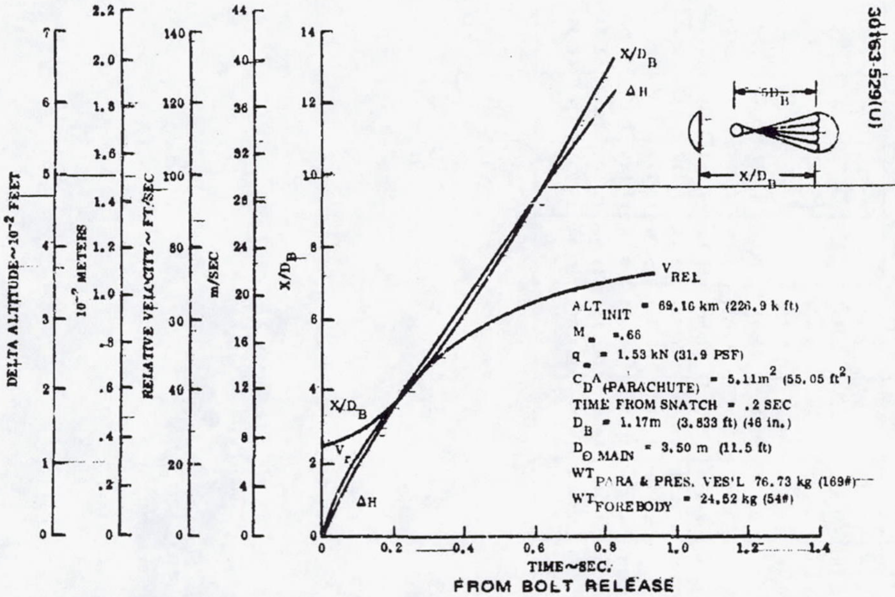

FIGURE 5.5-3. SEPARATION HISTORIES – MAIN PARACHUTE AND PRESSURE VESSEL, FOREBODY – TIME FROM SNATCH = 0.2 SEC

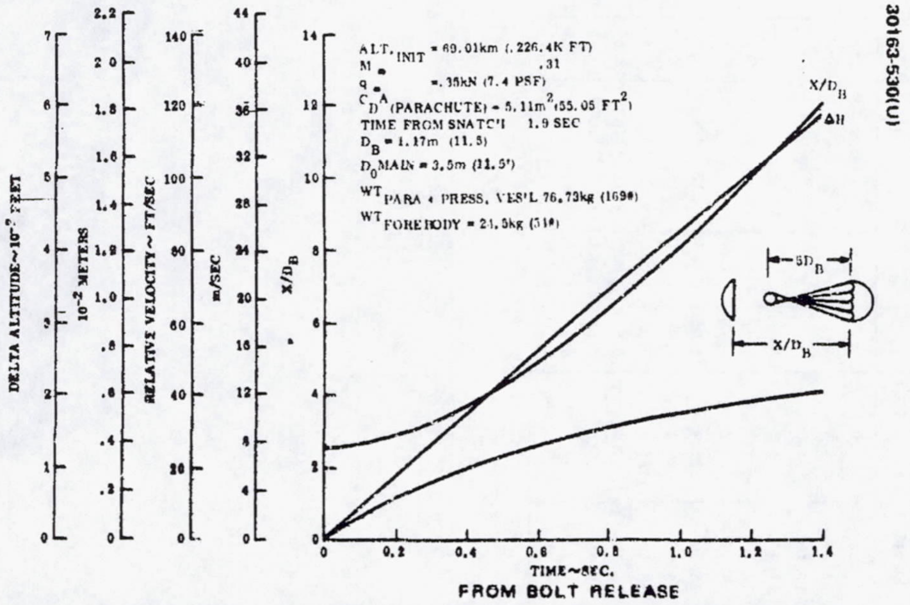

FIGURE 5.5-4. SEPARATION HISTORIES – MAIN PARACHUTE AND PRESSURE VESSEL, FOREBODY -- TIME FROM SNATCH = 1.9 SEC

ORIGINAL PAGE IS POOR.

TABLE 5.5-1, MAIN PARACHUTE WEIGHT

Deployment q N/m^2 (lb/ft^2)		Canopy Type															
		Disk-Gap-Band						Conical Ribbon (25 deg)						Ring Slot			
		1197	(25)	2394	(50)	4788	(100)	1197	(25)	2394	(50)	4788	(100)	1197	(25)	2394	(50)	4788	(100)
Diameter(D_0) cm	Diameter(D_0) in	kg	lb	kg	lb	kg	lb	kg	lb	kg	lb	kg	lb	kg	lb	kg	lb	kg	lb
7.62	3.0	–	–	–	–	–	–	0.14	0.314	0.15	0.314	0.19	0.409	–	–	–	–	–	–
8.89	3.5	–	–	–	–	–	–	0.17	0.379	0.19	0.422	0.24	0.537	–	–	–	–	–	–
10.16	4.0	–	–	–	–	–	–	0.20	0.448	0.23	0.497	0.28	0.616	–	–	–	–	–	–
11.43	4.5	–	–	–	–	–	–	0.25	0.545	0.28	0.615	0.34	0.756	–	–	–	–	–	–
12.70	5.0	0.47	1.028	0.47	1.028	0.47	1.028	0.29	0.642	0.34	0.757	0.41	0.916	0.67	1.471	0.67	1.471	0.67	1.526
25.40	10.0	1.14	2.505	1.14	2.505	1.14	2.505	0.99	2.186	1.42	3.133	2.49	5.480	1.06	2.336	1.23	2.707	1.58	3.490
38.10	15.0	2.02	4.463	2.02	4.463	2.39	5.273	2.25	4.958	3.37	7.430	5.75	12.669	1.88	4.150	2.45	5.399	4.16	9.170
50.80	20.0	3.04	6.694	3.20	7.048	4.70	10.366	4.79	10.560	8.09	17.839	13.40	29.532	3.27	7.212	4.68	10.313	8.16	17.997
58.42	25.0	4.22	9.311	5.08	11.199	7.80	17.202	8.29	18.278	13.71	30.215	29.96	66.059	5.78	12.732	9.49	20.912	14.42	31.782
76.20	30.0	5.81	12.809	8.11	17.887	12.59	27.752	11.79	26.001	19.18	42.274	42.78	94.314	8.11	17.884	14.75	32.516	23.44	51.667
88.90	35.0	7.81	17.208	11.37	25.074	20.15	44.433	21.82	48.106	31.83	70.165	64.48	142.155	11.63	25.629	23.84	52.553	40.69	89.772
101.60	40.0	10.23	22.547	15.49	34.139	33.55	73.966	28.77	63.436	47.44	104.584	119.32	263.059	16.94	37.357	31.00	68.336	54.67	120.537

REPRODUCIBILITY OF THE ORIGINAL PAGE IS POOR.

Parachute Materials

Both nylon and dacron appear to be suitable materials for parachute and fabric component construction since they are available in a wide variety of material weaves and strength retention at higher temperature is satisfactory. Of these two materials, nylon is recommended since it is considered the standard material by the parachute industry and physical properties are suitable for long term space environment where high loads at high temperature are not a major consideration. In addition, nylon has the advantage of having a large number of parachute vendors who will fabricate with it, while those using dacron are limited to only one or two.

The tensile strength of nylon fabric is approximately the same in air and vacuum at temperatures up to 148°C (300°F)*, whereas, this holds true with dacron for up to approximately 205°C (400°F). Dacron would be the more suitable material if thermal soak temperature were to reach the higher level. Also, dacron has the ability to retain strength properties through temperature cycling and for that reason has been considered more suitable for interplanetary missions where temperature cycling processes such as sterilization is a requirement.

Using nylon as the material, main parachute survival can be expected to approximately 30 km altitude where the temperature is 525°K (251°C). At this point, each of the 12 main parachute shroud lines rated at 2460 N (550 lb) strength would be loaded to approximately 126 N (28 lb), or about 5 percent of its strength under standard conditions.

For survival to lower altitudes, other material selections must be made commensurate with strength loss properties. Such a requirement would result in the use of nonstandard materials which may induce prohibitive hardware and development costs.

Ejection Mortar

Several ejection candidates are available to initiate the recovery system including a pyrotechnic-deployed aft cover and an ejection mortar, both of which have a considerable backlog of experience. Although several hundred successful flights have been made with a GE vehicle using ejection pistons, there have been two flight failures which were traced to this portion of the recovery subsystem. For this reason, as well as for the added reliability, an ejection mortar was selected for the Pioneer Venus recovery subsystem.

The ejection mortar will consist of an aluminum cylinder with internal disc sabot and a pyrotechnic ejection charge. The pilot parachute canopy with suspension lines will be packed within a cylindrical configured deployment bag at a minimum pack density of 640 kg/m^3 (40 lb/ft^3).

---

* W.D. Freeston, Jr., and D.S. Johnstone, "Mechanical Properties of High Temperature Fibrous Structural Materials," AFML-TR-67-267.

Mortar sizing is primarily a function of the material mass to be stowed or ejected and the ejection velocity. A curve showing these relationships is presented in Figure 5.5-5. A significant mortar weight saving of approximately 1.3 kg (2.9 lb) is apparent with the recommended system using a 0.84 m (2.75 ft) D_o pilot chute as compared to a system which ejects the main parachute directly.

Also of concern in establishing a system concept is the peak reaction load that can be expected at the time of ejection. These data are shown in Figure 5.5-6, where the maximum reaction load is plotted versus the ejected weight for various ejection velocities from 12.2 to 30.5 m/sec (40 to 100 ft/sec). For the recommended system with an ejection velocity of 23.9 m/sec (78.5 ft/sec), Figure 5.5-6 indicates that a peak reaction load of approximately 2020 N (450 lb) can be expected from ejection of the 0.84 m (2.75 ft) D_o pilot parachute.

Mortar Induced Tip-Off Rates. An analysis of the pilot parachute deployment was developed which derives tip-off rates induced by mortar position error. Tolerance assumptions, which were in most cases conservative, are listed below:

Probe c.g.	±0.0890 cm (0.035 in) radial
Mortar location	±0.076 cm (0.03 in) along each axis
Angular alignment of mortar	0.5 deg in-plane and out of plane
Impulse direction	0.5 deg in plane and out of plane

Other parameters assumed were:

Pilot chute weight	0.91 kg (2 lb)
Pilot chute velocity	24.4 m/sec (80 ft/sec)
Mortar location (center of bracket)	0.505 m (20 in) from probe centerline 0.102 m (4 in) from c.g.
Probe inertia	
Axis of symmetry	14000 kg-m^2 (9.427 sl-ft^2)
Transverse axis	9100 kg-m^2 (6.11 sl-ft^2)
Probe spin rate	15 rpm

The analysis was based on small angle approximations and the axes were treated as being uncoupled with no gyroscopic moments. Aerodynamic restoring moments and parachute stabilization after deployment have not been included.

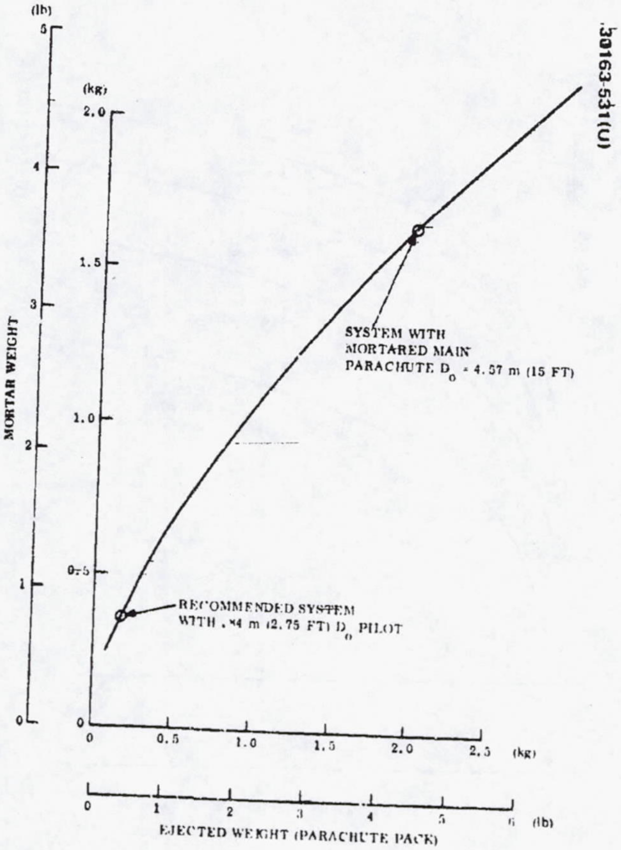

FIGURE 5.5-5. MORTAR WEIGHT VERSUS EJECTED WEIGHT – EJECTION VELOCITY = 80 FT/SEC

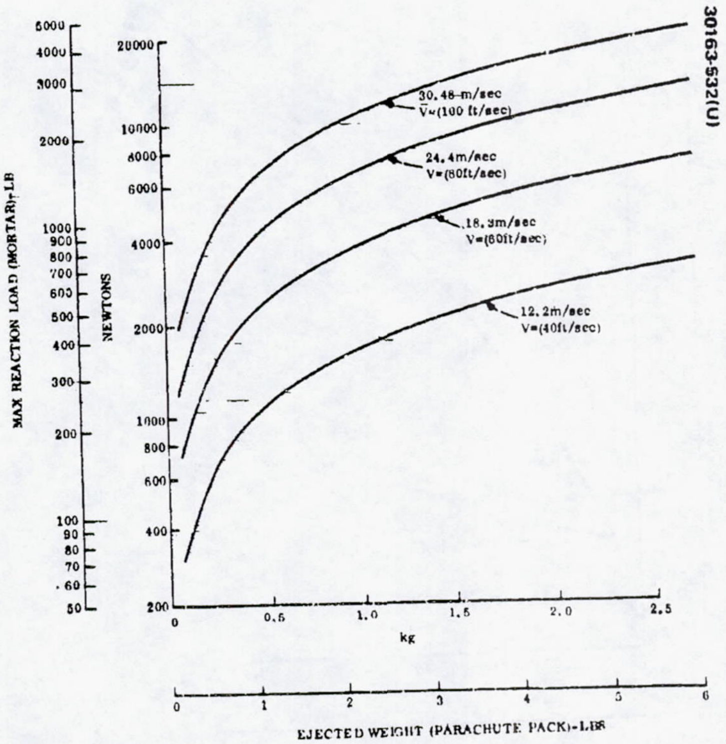

FIGURE 5.5-6. MAXIMUM REACTION LOAD (MORTAR) VERSUS EJECTED WEIGHT OF PARACHUTE PACK

Results of this analysis using various bracket angle errors are presented in terms of tip-off in Table 5.5-2. Other tolerances presented above have been combined in a worst case manner. It is expected that bracket misalignment can be held below 5 deg, so that tip-off rates are seen to be bounded by 3.3 deg/sec. Main chute deployment will occur less than 1.5 sec after mortar initiation, at which time the induced probe angle of attack will therefore be less than 5 deg.

Subsystem Tradeoffs

In addition to the previous design studies, a parallel effort was conducted to evaluate performance of various subsystem concepts and to observe the effects of varying deployment conditions and parachute sizes using the Retardation System Selection Program (RESSEP)*

The trades discussed in this section were developed for conditions compatible with the Thor/Delta mission, but are in general applicable to either mission.

TABLE 5.5-2. MORTAR-INDUCED TIP-OFF RATES

Bracket Misalignment, Deg	Tip-Off Rate, Deg/Sec
1.0	1.1
3.0	2.2
5.0	3.3
7.0	4.4
9.0	5.5
11.0	6.6
13.0	7.7
15.0	8.8

---

*Hoyt, T., "Retardation System Selection Program," GE-TIS 71SD263, 11/71.

All data were computed using the following parameters:

1) Nominal Entry Trajectory Conditions of:

γ_E = 41-deg (down from horizontal)

h_E = 150 km (492,120 ft)

V_E = 11,156 m/sec (36,605 ft/sec)

2) Atmosphere: NASA SP8011 (1972)

Vehicle: Configuration - 55 deg sphere cone

Mortared Main Parachute — Variable Mach Number Deployment. Computer program results of mortaring the main parachute at five different Mach numbers (0.7, 0.9, 1.1, 1.3, 1.5) without use of a pilot or drogue indicated several problems. In particular, the higher Mach number environments required a reefed stage so as not to exceed the 17800 N (4,000 lb) opening load.

The main disadvantages in using such a system for Pioneer Venus are the volume restrictions in mounting the large ejection mortar for the 3.51 m (11.5 ft) D_o main chute, and the more critical alignment required as a result of relatively high ejection loads at the time of main chute ejection.

Mortared Decelerator — Variable Decelerator D_o. The effects of using a decelerator parachute (drogue) in the system were examined. The decelerator provides drag to the vehicle prior to extraction and deployment of the main parachute.

For the three cases examined, variable decelerator diameters of 0.61 m (2.0 ft), 1.22 m (4.0 ft), and 1.83 m (6.0 ft) were considered; all were deployed at Mach 1.5. The case for nominal deployment at M = 0.7 was not included because it offers no advantages and has the disadvantage of increased complexity. Advantages would exist at higher deployment loadings where comparisons could be made between a reefed main deployment chute and a drogue. At these conditions, a drogue could decrease the main parachute deployment environment to the extent that lighter materials could be used.

The main disadvantages in using a mortared decelerator parachute as compared to a mortared pilot are:

1) Increased system complexity requiring a timed drag interval, with associated hardware to release the drogue and deploy the main chute

2) Greater altitude loss from a given deployment point before equilibrium velocity is reached on the main chute.

In the three cases examined, altitude losses from the point of initial system deployment to terminal velocity on the main parachute amounted to approximately 0.9 km (3,000 ft).

Main Chute Variable Do – With Pilot. Sensitivity of recovery system performance to main parachute diameter has been evaluated by the RESSEP computer program around the baseline diameter of 3.51 m (11 ft). Cases examined using main chute diameters of D_o = 2.89 m (9.5 ft) and 4.42 m (13.5 ft) with pilot are shown in Table 5.5-3. In all cases, initial system deployment occurred at Mach 0.8.

It is noted that, as the main parachute diameter decreases from 4.11 m (13.5 ft) to 2.90 m (9.5 ft), the maximum load decreases significantly (≈50 percent). Total subsystem weight on the other hand is quite insensitive to D_o. All systems provide terminal velocity well above 66 km.

Parachute Deployment Environment Sensitivity

Sensitivity of parachute deployment environment (altitude, Mach number, and dynamic pressure) to various error sources occurring during entry has been identified. Once again, the analysis was based on parameters compatible with the Thor/Delta mission, but the results are, in general, applicable to the Atlas/Centaur mission.

Error sources considered were:

1) Timer
2) G-switch
3) Entry path angle
4) Ballistic coefficient
5) Scale-height
6) Density

Three path angles were analyzed (35, 41, and 60 deg) for four values of time delay from main chute release (0, 2, 5, and 10 sec). The 41 deg entry angle condition was analyzed at deployment Mach numbers of 0.7 and 0.9. The 35 and 60 deg entry conditions were analyzed for a deployment Mach number of 0.7 only.

Conclusions reached as a result of this analysis are:

1) For all cases, Mach number errors are less than $\Delta M = 0.005$, dynamic pressure errors less than $\Delta q = 19\ N/m^2$ ($0.4\ lb/ft^2$), and altitude errors less than $\Delta h = 0.13$ km, all for 1 percent errors in each of the sources. That is, the critical chute deployment parameters are very insensitive to these error sources.

TABLE 5.5-3. RESSEP ANALYSIS OF LARGE PROBE PARACHUTE SYSTEMS

			Baseline			
Input						
D_o main, m (ft)	4.11	(13.5)	3.51	(11.5)	2.90	(9.5)
D_o pilot, m (ft)	0.84	(2.75)	0.84	(2.75)	0.84	(2.75)
Total weight, kg (lb)	139.4	(307)	139.4	(307)	139.4	(307)
Shield weight, kg (lb)	53.1	(117)	53.1	(117)	53.1	(117)
Output						
Deploy pilot						
Altitude, km (kft)	69.8	(228.7)	69.8	(228.7)	69.8	(228.7)
Q, N/m^2 (lb/ft^2)	1963	(41)	1963	(41)	1963	(41)
M	0.802		0.802		0.802	
γ, deg down from horizontal	54.8		54.8		54.8	
Deploy main						
Altitude, km (kft)	69.6	(228.3)	69.6	(228.3)	69.6	(228.3)
Q, N/m^2 (lb/ft^2)	1915	(40)	1915	(40)	1915	(40)
M	0.78		0.78		0.78	
Loads						
Pilot snatch, N (lb)	1103	(248)	1100	(247)	1100	(247)
Pilot open, N (lb)	761	(171)	761	(171)	761	(171)
Main snatch, N (lb)	4893	(1100)	5306	(1193)	5840	(1313)
Main open, N (lb)	10533	(2368)	7895	(1775)	5524	(1242)
Shield Drop						
Altitude, km (kft)	69.5	(228)	69.5	(228)	69.5	(228)
Velocity, m/sec (ft/sec)	174.3	(572)	174.7	(573)	175.3	(575)
Terminal (1.1 g)						
Altitude, km (kft)	68.8	(225.8)	68.8	(225.4)	68.5	(225.0)
Velocity, m/sec (ft/sec)	40.2	(132)	46.0	(151)	53.0	(174)
V ejection, m/sec (ft/sec)	21.7	(71.3)	21.7	(71.3)	21.7	(71.3)
Total weight, kg (lb)	3.21	(7.08)	3.01	(6.62)	2.79	(6.15)
Pack volume, km^3 (ft^3)	0.0027	(0.097)	0.0024	(0.085)	0.0021	(0.074)
Descent time (to 55 km), sec	348		306		267	

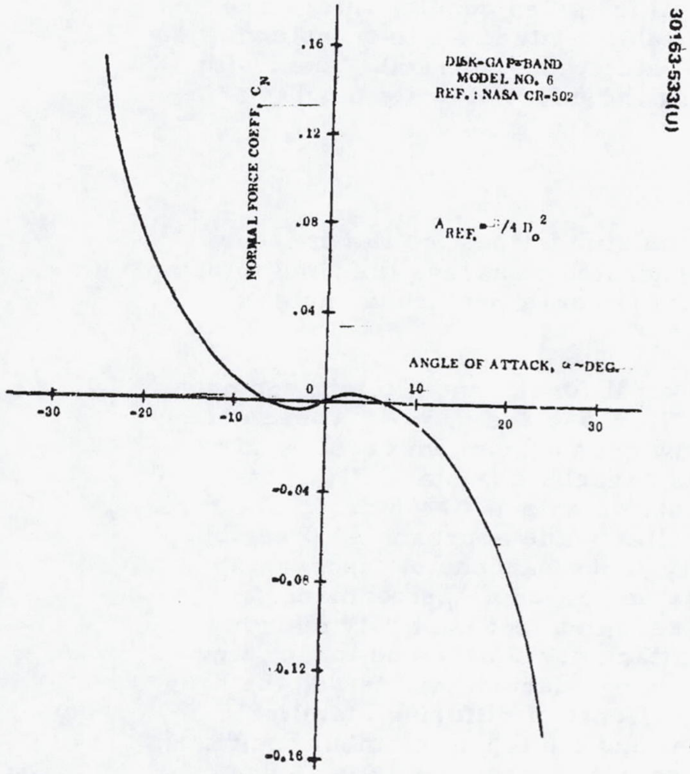

FIGURE 5.5-7. DGB PARACHUTE NORMAL FORCE COEFFICIENT VARIATION WITH ANGLE OF ATTACK – LOW SUBSONIC SPEEDS

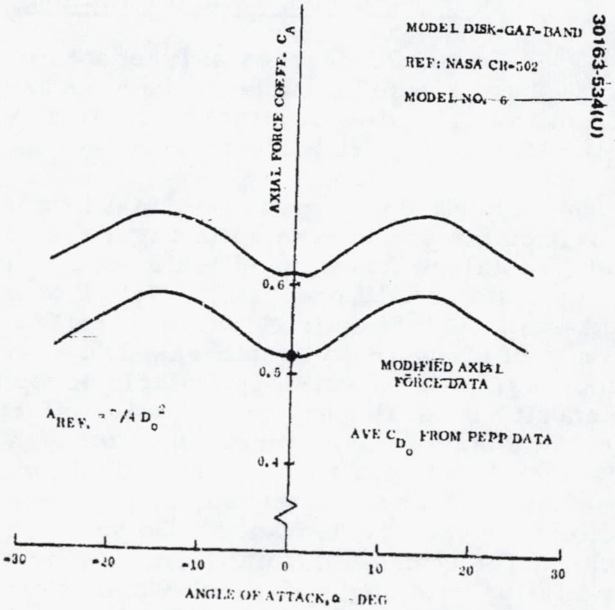

FIGURE 5.5-8. DGB PARACHUTE AXIAL FORCE VARIATION WITH ANGLE OF ATTACK

2) Density errors produce altitude errors, but do not produce Mach number or dynamic pressure errors. This is true, since a constant factor density error simply shifts all trajectory parameters up or down some given altitude increment.

3) Scale height errors were obtained by linearly stretching or shrinking the altitude scale at which given density values are defined. The point about which this altitude scale transformation was applied was 75 km. This value was arbitrarily taken with the intention of not compounding the effect of scale height variation with density variation.

Main Parachute Dynamic Motion

Coupled 3 degrees of freedom motion simulations for the pressure vessel parachute combination have been generated to assess the time to damp from initial angles of attack at deployment or from a perturbed angle of attack resulting from a wind gust.

Pertinent curves of normal force, axial force, and pitching moment coefficients are presented in Figures 5.5-7, 5.5-8 and 5.5-9. These data were obtained from model tests but do show good agreement to full scale drop tests (PEEP program). Note that the parachute is statically unstable at small angles of attack with neutrally stable points at $\alpha = \pm 6$ deg. The trim angle of 6 deg could be decreased to a smaller value approaching 0 deg by increasing the effective geometric porosity of the parachute. Increasing porosity generally has two negative effects on parachute performance: 1) the slope of the moment curve through zero moment (stability margin) is decreased resulting in larger angle of attack oscillation and longer time to damp out when perturbed, and 2) the opening characteristics and the drag effectiveness are degraded. To bound the effects of differing stability characteristics, a normal force coefficient and a pitching moment coefficient variation with angle of attack were assumed which were zero for $-6 \text{ deg} < \alpha < +6$ deg (i.e., simulating a higher porosity design), and were otherwise the same as the aerodynamic characteristics presented in Figures 5.5-7 and 5.5-9. Motion computations were made using both sets of aerodynamic characteristics. Aerodynamic characteristics used for the pressure vessel were simple linear functions of angle of attack for near-zero Mach numbers.

Selection of the spring and damping constants for modeling the shroud line response was made following a preliminary effort to determine motion sensitivity to them. Within the range of parameters studied, computed angle of attack motion was virtually independent of the spring and damping constants used; a nominal set of values was therefore chosen for the shroud line characteristics and used in the subsequent analyses. The spring constant used was 4360 N/m (300 lb/ft) and the damping constant used was 1090 N-sec/m (75 lb sec/ft)

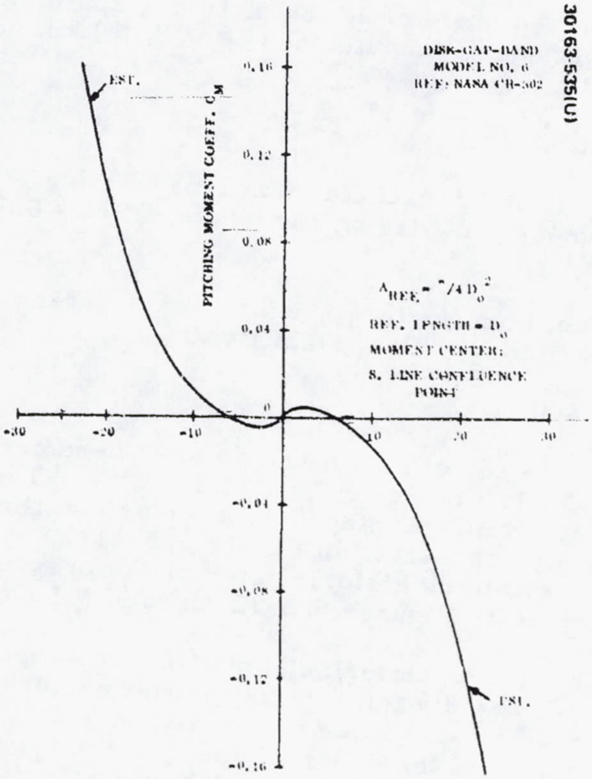

FIGURE 5.5-9. DGB PARACHUTE PITCHING MOMENT COEFFICIENT VARIATION WITH ANGLE OF ATTACK – LOW SUBSONIC SPEEDS

Motion computations were performed using a Planar 3-degree of freedom (one rotational), two-body parachute program.

Analysis. The following discussion of parachute-pressure vessel motion is based on motion computations for the following cases:

1a: nominal initial conditions ($\alpha = 0$ for parachute, 2 deg for pressure vessel) at M = 0.7, 69 km, nominal model stability

1b: as above, "flat" stability

2a: maximum expected angle of attack of 10 deg applied to pressure vessel and parachute, at M = 0.7, 69 km nominal model stability

2b: as above, "flat" stability

3: Pressure vessel and parachute misaligned 10 deg, $\alpha = 10$ deg on pressure vessel, 20 deg on parachute, at M = 0.7, 69 km, nominal stability.

4a: effect of sudden impulse (e.g., wind shear) in terminal fall at 69 km, $\alpha = 30$ deg, "flat" stability

4b: as above, at 44 km.

Angle of attack histories for cases 1a and 1b are presented for pressure vessel and parachute in Figures 5.5-10 and 5.5-11. The flight path angle history for the parachute and planet-relative orientation of the pressure vessel for case 1a are presented in Figure 5.5-11. For cases 2a, 2b, 3, 4a, and 4b, angle of attack histories only of the pressure vessel and the parachute are presented in Figures 5.5-12 through 5.5-16.

An assessment of the motion histories shows that the angle of attack is well behaved and converges rapidly following an initial perturbation. An estimate of time to half-damping, analogous to the characterization for a second-order, linear system, is of the order of 0.5 to 2 sec for motion reflecting nominal model stability, and 2 to 5 sec for motion reflecting "flat" stability. Both vehicles tend to align with each other about a non-zero trim point determined primarily by the parachute aerodynamic characteristics (i.e., static aerodynamic forces and moments acting on the pressure vessel are nearly negligible compared to those acting on the parachute). This characteristic of the motion is exhibited in all the angle of attack histories.

In the static equilibrium condition, the system orients itself along the planet gravity vector regardless of the shape of the pitching moment curve — as shown in Figure 5.5-17 — but with equilibrium path angles determined by the trim characteristics. Nominal model aerodynamics yields a path angle off the vertical equal to the trim angle of attack, 6 deg, since the

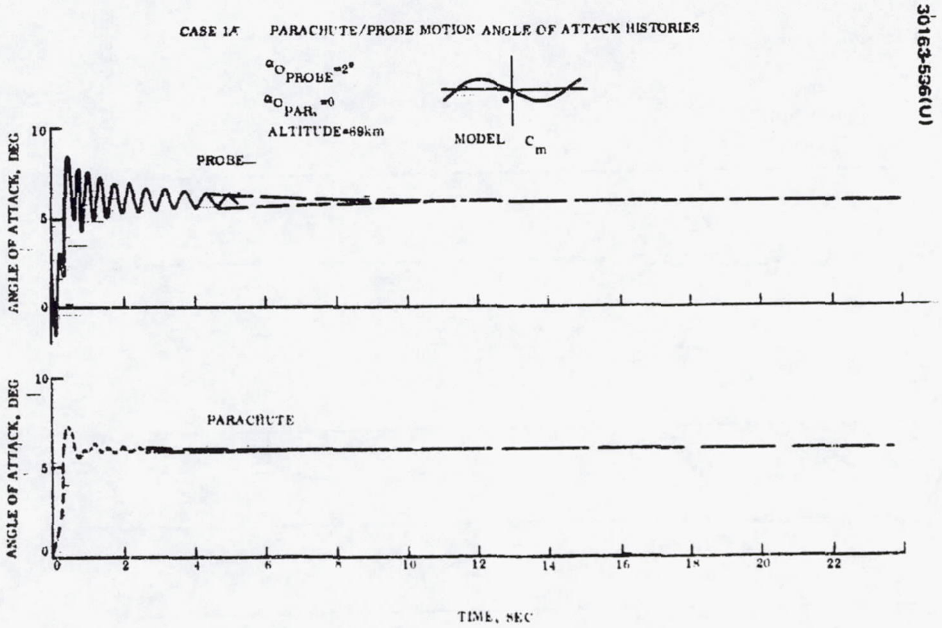

30163-536(U)

FIGURE 5.5-10. PARACHUTE/PROBE MOTION ANGLE OF ATTACK HISTORIES — CASE 1A

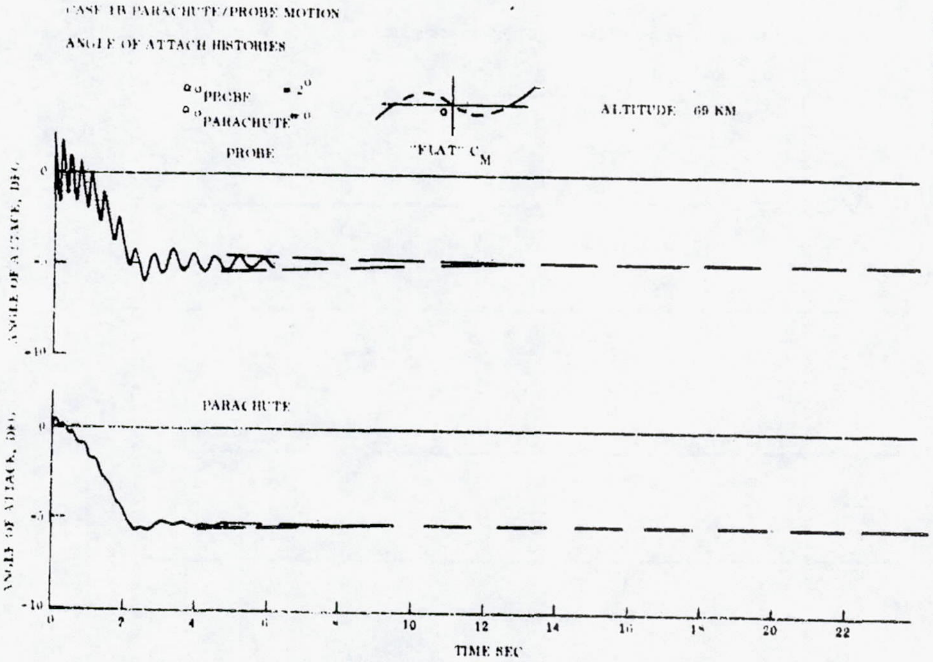

30163-537(U)

FIGURE 5.5-11. PARACHUTE/PROBE MOTION ANGLE OF ATTACK HISTORIES – CASE 1B

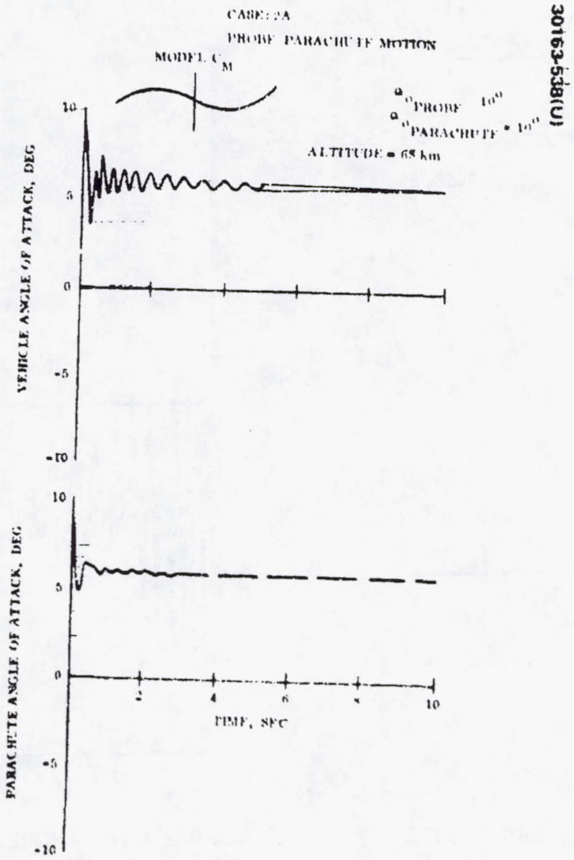

FIGURE 5.5-12. PROBE/PARACHUTE MOTION - CASE-2A -

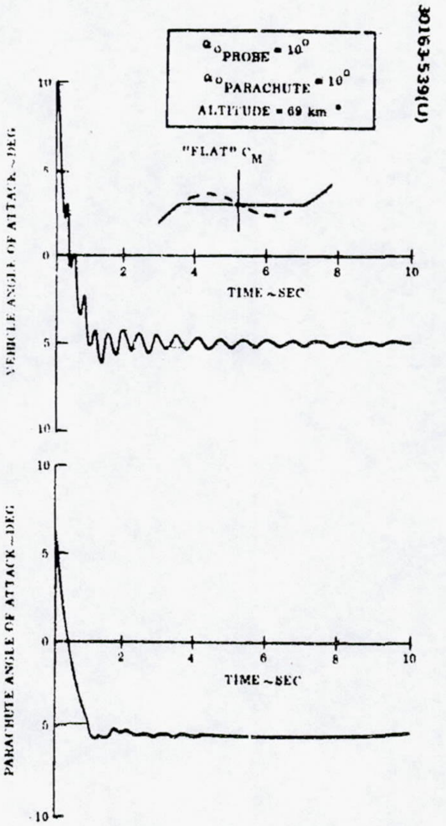

FIGURE 5.5-13. PROBE/PARACHUTE MOTION – CASE 2B

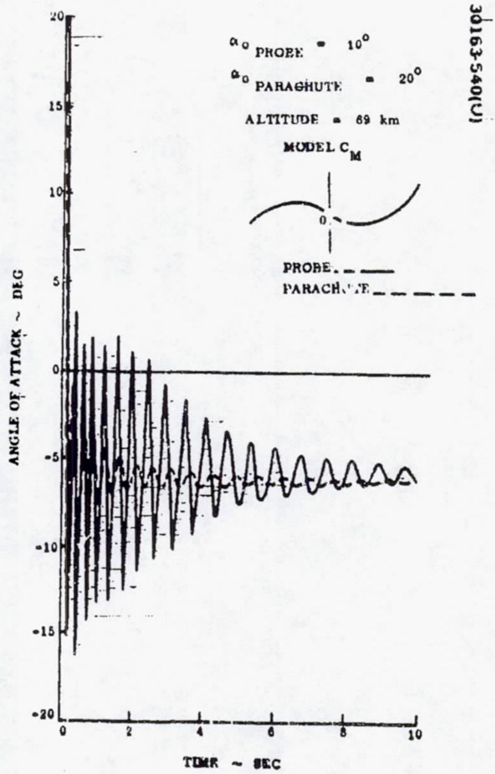

FIGURE 5.5-14. PROBE/PARACHUTE MOTION – CASE 3

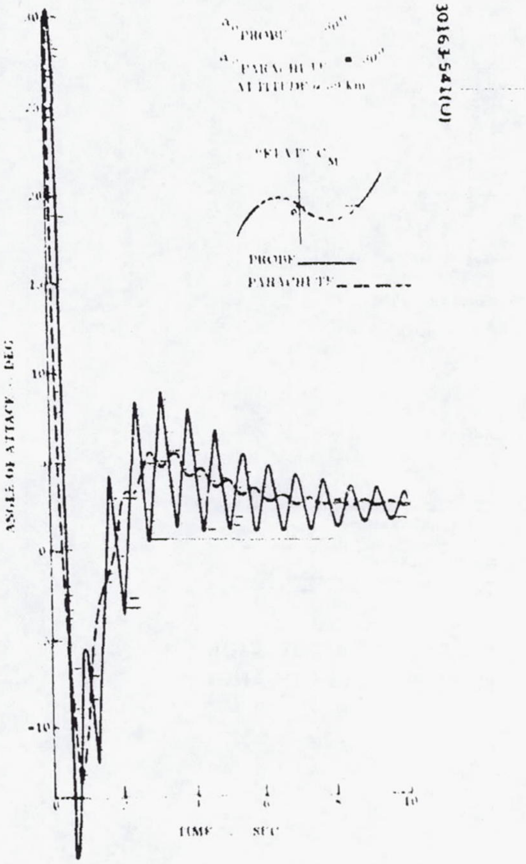

FIGURE 5.5-15. PROBE/PARACHUTE MOTION – CASE 4A

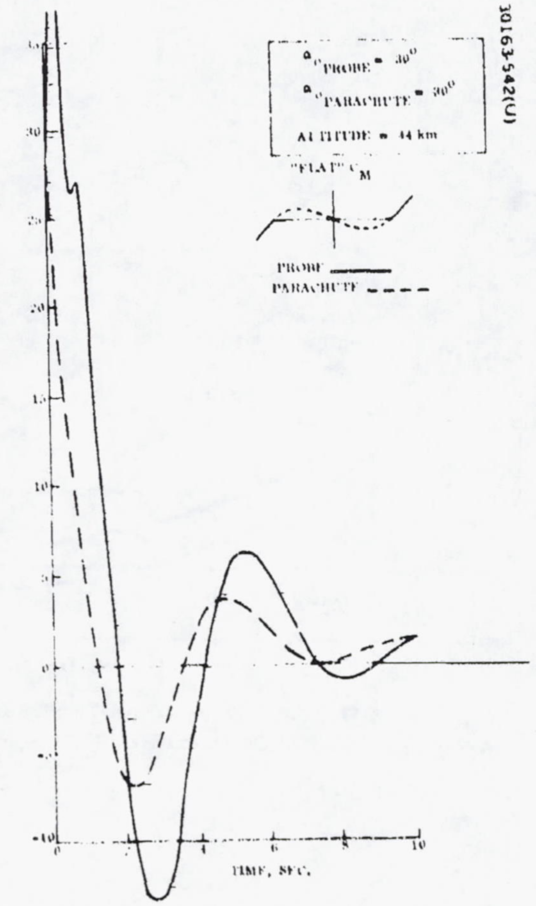

FIGURE 5.5-16. PROBE/PARACHUTE MOTION – CASE 4B

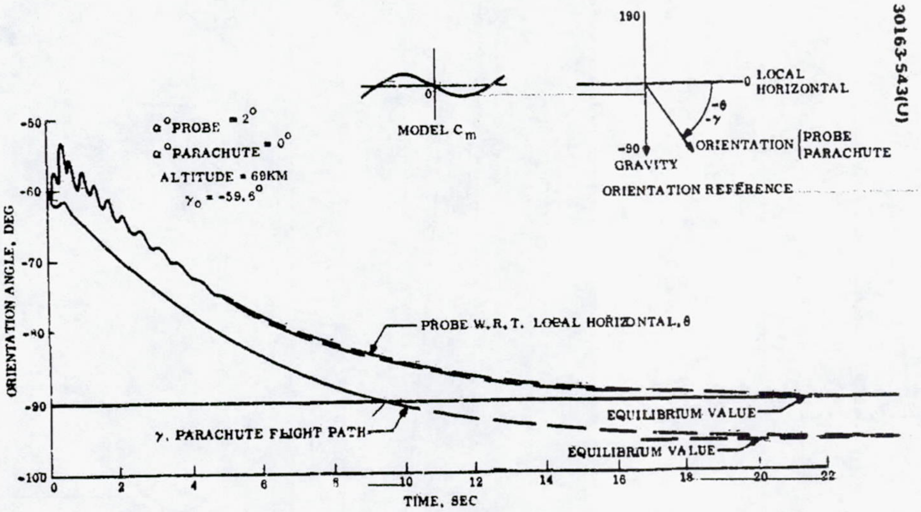

FIGURE 5.5-17. CASE 1A PARACHUTE/PROBE MOTION – PROBE ORIENTATION WITH RESPECT TO LOCAL HORIZONTAL AND PARACHUTE FLIGHT PATH ANGLE

normal force coefficient C_N is also zero at that point. Thus, the system will drift 6-deg off the vertical in terminal, equilibrium fall. For the "flat" stability characteristics, the equilibrium path angle is vertical and the equilibrium angle of attack is zero. Since the parachute has neutral stability and zero C_N for -6 deg $< \alpha < +6$ deg, its dynamic stability will cause angle of attack to approach zero and path angle to approach vertical.

Thor/Delta Baseline Description

The parachute subsystem for the Thor/Delta mission consists of the following:

1) One 3.51 m (11.5 ft) D_o disc-gap-band nylon main parachute
2) One 0.84 m (2.75 ft) D_o conical ribbon nylon pilot parachute
3) One pilot chute ejection mortar with ejection charge

On electrical command, the mortar ejects the pilot parachute to the side and aft of the probe vehicle at an angle of 83.5 deg from the vehicle roll axis.

The pilot parachute serves to remove the vehicle aft cover and to extend the main parachute pack for fully open deployment of the canopy. Release devices are provided on the vehicle to accomplish aft cover release.

After a time delay of approximately 2 sec for system stabilization, the bolts attaching the pressure vessel module to the aeroshell are released and the module is separated from the aeroshell. Pressure vessel/aeroshell release is timed from mortar initiation.

During the final equilibrium descent phase of the mission and at approximately 55 km altitude, the main parachute is released from the pressure vessel at the three bridle attachment points and the vehicle is allowed to free fall to the planet surface. General recovery system events are shown in Figure 5.5-1.

Atlas/Centaur Baseline Description

The parachute system for the Atlas/Centaur mission consists of a 0.84 m (2.75 ft) diameter conical ribbon nylon pilot deployed by an ejection mortar and a 4.57 m (15 ft) D_o disc-gap-band main parachute. Parachute diameter selection was based, as in the Thor/Delta mission, on the requirement for a positive separation margin, except that here parachute area is four times that needed for incremental separation.

A summary of the deployment environments and other critical events is included in Table 5.5-4. Altitude of main parachute deployment (M = 0.7) has decreased slightly from the Thor/Delta mission due to the increase in ballistic coefficient. Coupling this increase with the larger parachute diameter results in opening loads of 15,356 N (3,452 lb) compared to 7,900 N (1,775 lb) for the Thor/Delta design. Terminal velocity of the parachute pressure vessel has decreased from 46 m/sec (151 ft/sec) to 34.3 m/sec (112.4 ft/sec).

With the change in vehicle mass properties and parachute diameter, it was necessary to re-evaluate the pressure vessel-forebody separation. Figure 5.5-18 shows the resultant separation histories assuming a 2 sec time delay to permit any initial angle of attack oscillations to damp. Time to separate one diameter is 0.5 sec. This is comparable to the time required for the Thor/Delta design and, based on previous separation studies, will be adequate to prevent recontact.

General recovery system events remain compatible with Figure 5.5-1.

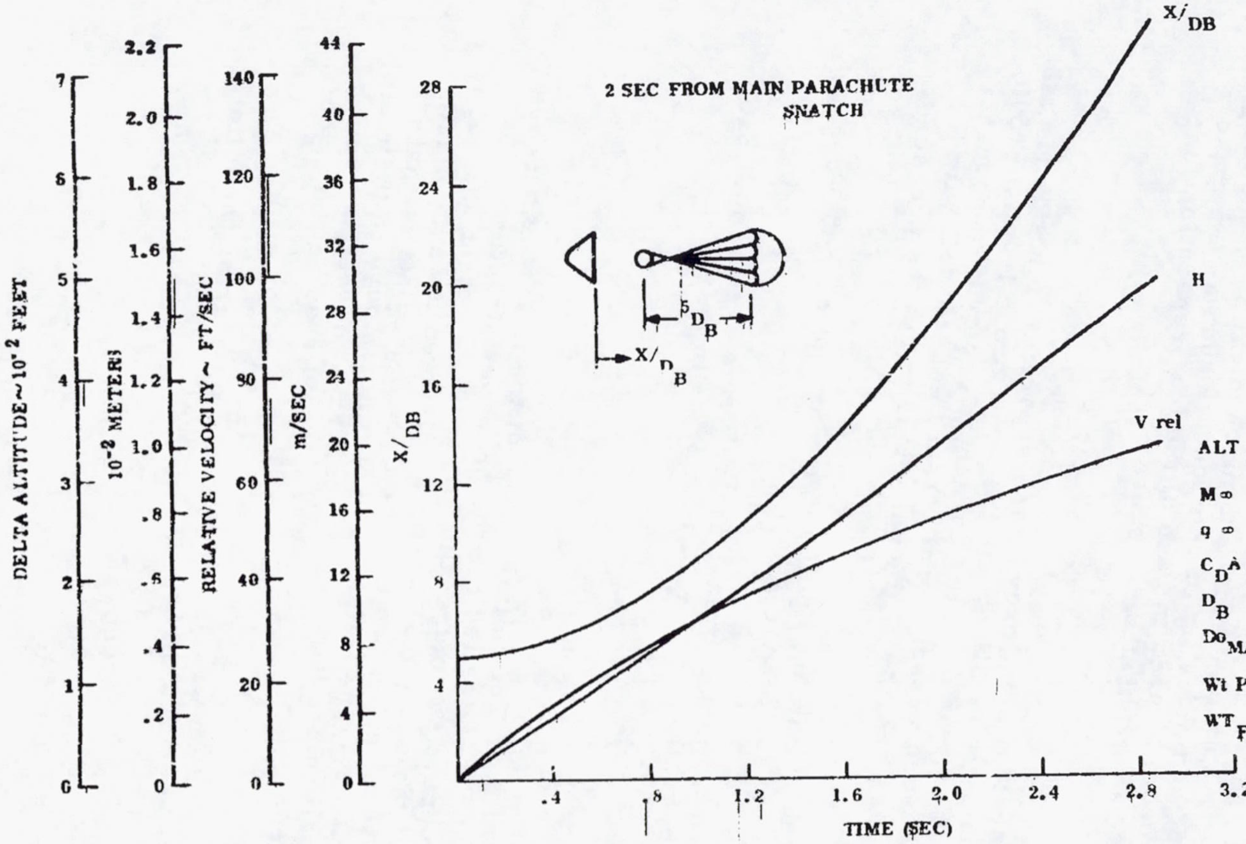

$ALT_{INIT} = 68.04$ km (223.2 K ft)

$M_\infty = 0.26$

$q_\infty = 294\ NT/m^2$ (6.14 psf)

$C_D A_{par} = 8.70\ m^2$ (93.66 ft^2)

$D_B = 1.397$ m (4.583 ft)

$Do_{MAIN} = 4.572$ m (15 ft)

Wt PAR - P. VESS = 129.8 kg 286 lbs

$WT_{FOREBODY} = 71.6$ kg 157.6 lbs

FIGURE 5.5-18. SEPARATION HISTORIES - MAIN PARACHUTE AND PRESSURE VESSEL FROM FOREBODY

5.6 SEPARATION AND DESPIN

Summary

The separation subsystem has been designed to insure that: 1) all separation events will occur without imparting excessive tipoff rates to the bus, probes, or pressure vessel, and 2) adequate clearance exists at all required points in the design to eliminate the possibility of collision or hangup.

All separation devices, both electrical and mechanical have been flight qualified. Where applicable, commonality of components such as the explosive nuts (where the same model is used in each of the four separation functions) and the IFD's has been incorporated to reduce cost.

Requirements

The separation subsystem must provide the separation function for all probes from the spinning bus. In addition, for the large probe it must provide for: 1) the release of the aft cover during the parachute deployment sequence, 2) the separation of the pressure vessel module from the aeroshell with the parachute deployed, and 3) the release of the parachute to put the pressure vessel module into free-fall.

At probe separation, maximum tipoff rates must not exceed 3-deg/sec for the large probe and 2 deg/sec for the small.

The despin subsystem must decrease the roll rate of the small probe from its value at probe separation to 15 ± 10 rpm prior to entry.

Tests and Trade Studies

Large Probe

Bus/Probe Separation. The initial design of the interface between the probe and the bus (Figure 5.6-1) called for the probe aft structure to be carried within the bus support structure; this presented a potential clearance problem, hence, most of the analytical work was directed towards maximizing the clearance. The present design has the interface moved aft so that the above problem is eliminated. The following separation study, in the main, still holds good, but small improvements in tipoff rate and weight could be made by reducing the separation velocity, which would require the use of smaller springs.

Separation perturbation was determined by considering the following error sources and their expected three sigma values:

1) Spring preload ± 5 percent

2) Spring rate ± 7 percent

3) Geometric centroid alignment ± 0.15 cm (0.060 in.)

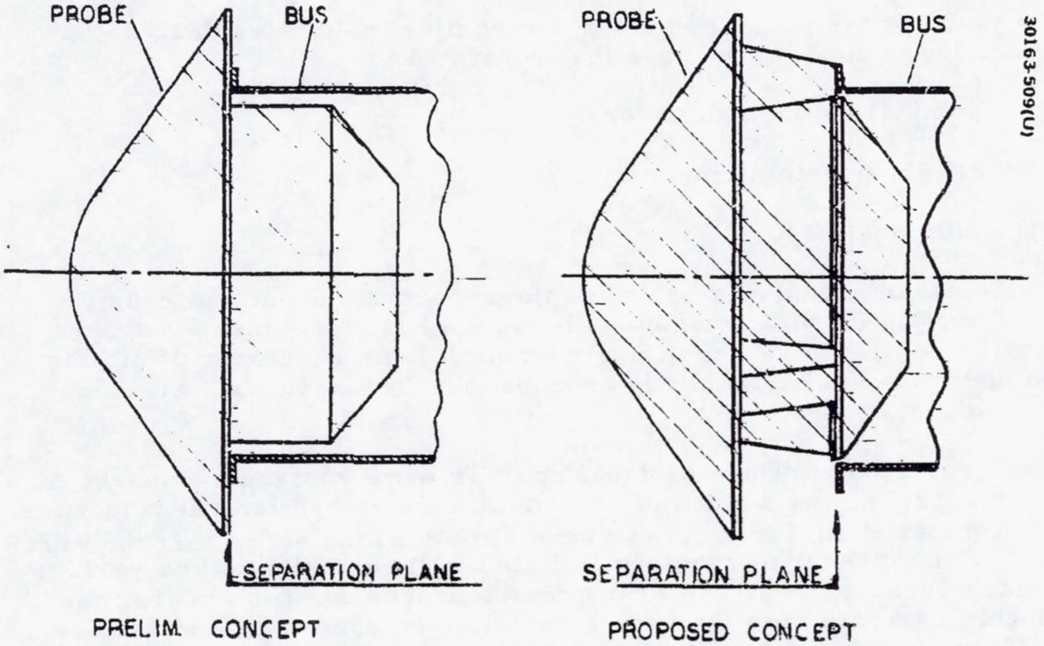

FIGURE 5.6-1. PROBE/BUS SEPARATION

REPRODUCIBILITY OF THE ORIGINAL PAGE IS POOR.

4) Bus c.g. location ± 0.3 cm (120 in.)

5) Probe c.g. location ± 0.15 cm (0.060 in.)

6) Radial location of spring attachment ± 0.09 cm (0.036 in.) (each spring independent)

7) Angular location of spring attachment ± 1 deg (each spring independent)

8) Initial body orientation of probe ± 1 deg (each axis)

9) Effect of initial body tumble rates - nominal precession of 2 deg/sec

For each of the various springs and nominal velocities desired, a series of computer runs were made that consisted of:

1) Nominal values, no errors

2) All errors simultaneously active

3) Individual errors

The clearance analysis begins at the separation event and ends when the vertical section of the after cover clears the bus. A computer program was generated consisting of equations determining the envelopes of motion of the two bodies, each having 3 deg of freedom. The envelopes are added to form a "clearance required".

The errors due to the individual sources were root-sum-squared as an indication of three sigma values of body tumble rates and lateral velocities. These are compared on Table 5.6-1 to the simultaneous set to test for error correlation. The clearance required is listed in three columns for various ΔV's for each error source. The required clearance for rss errors, the most probable case, and for all errors run simultaneously, the worst case, are noted at the bottom of the columns. Initial precession, probe body angular orientation and preload force are the major contributors to clearance.

The clearance required for simultaneous errors is plotted versus ΔV in Figure 5.6-2. A minimum occurs at ΔV = 76 cm/sec (2.5 ft/sec). For small ΔV's the time for separation is high which causes the curve to rise as ΔV approaches zero. For large ΔV's, the tipoff causes the rise. The half-cone angles corresponding to this case (simultaneous errors) are plotted versus ΔV in Figure 5.6-3; tumble rate is shown in Figure 5.6-4.

Aft Cover Separation. The aft cover is attached to the aeroshell by means of three mechanical, over center latches. Lanyards attached to the pilot chute bridle operate the latches upon chute deployment. This passive separation method was chosen over active designs using explosive nuts, cable cutters, or pin pullers because it does not require an electrical firing command and the

TABLE 5.6-1. SEPARATION ERROR SENSITIVITIES

Error Source	Clearance Required, cm (in.)		
	V = cm/sec (ft/sec)		
	30 (1)	61 (2)	91 (2)
Force ±(1.35) 6 N	0.51 (0.20)	0.66 (0.26)	0.84 (0.33)
Spring rate ±(22 lb/ft) 320 N/m	0.20 (0.08)	0.30 (0.12)	0.38 (0.15)
Central location ±(0.060 in.) 0.15 cm	0.38 (0.15)	0.51 (0.20)	0.66 (0.26)
Bus c.g. location ±(0.120 in.) 0.3 cm	0.38 (0.15)	0.30 (0.12)	0.28 (0.11)
Probe c.g. location ±(0.060 in.) 0.15 cm	0.25 (0.10)	0.23 (0.09)	0.25 (0.10)
Spring radius location ±(0.036 in.) 0.09 cm	0.20 (0.08)	0.25 (0.10)	0.36 (0.14)
Probe body orientation ±1 deg	0.68 (0.27)	0.86 (0.34)	1.12 (0.44)
Spring angle location ±1 deg	0	0	0
Initial precession rate at 2 deg/sec	3.33 (1.31)	2.26 (0.89)	1.93 (0.76)
RSS errors	3.51 (1.38)	2.62 (1.03)	2.52 (0.99)
All errors run simultaneously	4.62 (1.82)	4.06 (1.60)	4.11 (1.62)

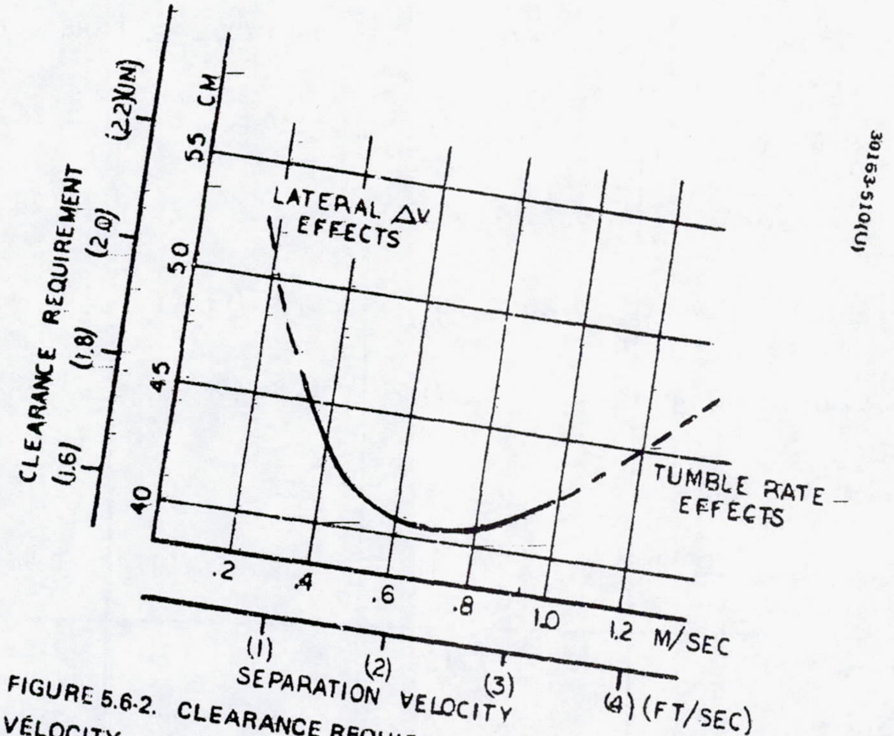

FIGURE 5.6-2. CLEARANCE REQUIREMENT VERSUS SEPARATION VELOCITY

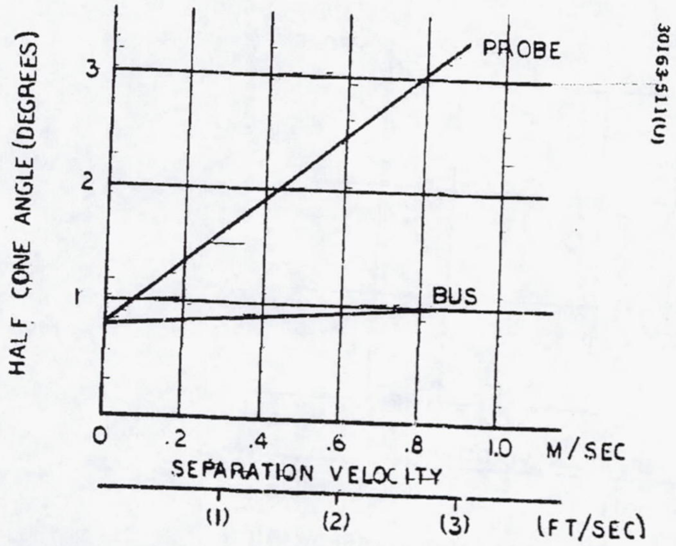

FIGURE 5.6-3. HALF CONE ANGLE VERSUS SEPARATION VELOCITY

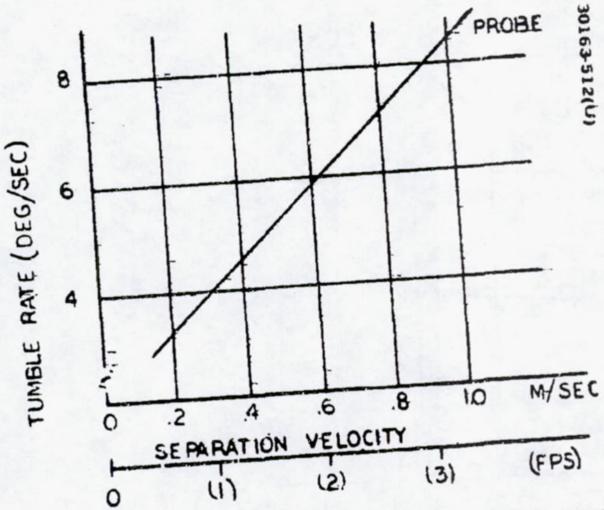

FIGURE 5.6-4. TUMBLE RATE VERSUS SEPARATION VELOCITY

actual flight hardware can be tested on the ground. One factor that must be considered is the effect of back pressure acting on the cover. With the resultant pilot chute forces shown in subsection 5.5, the ΔP must not be greater than 689 N/m^2 (0.1 psi). A preliminary venting analysis of the aeroshell shows that the ΔP is less than 207 N/m^2 (0.03 psi) at the time of chute deployment.

Aeroshell/Pressure Vessel Module Separation. The aeroshell will be separated shortly after chute deployment in order to expose experiments in the pressure vessel. The time window for separation begins at chute deployment and ends when the separation force due to differential drag between the aeroshell and the pressure vessel on thechute equals 178 N (40 lb), which corresponds to a 4 sec delay after main chute deployment. It is desirable to have some time delay in order for the chute opening transients to damp out; conversely, the sooner separation occurs, the greater the separation force and the faster separation occurs. Subsection 5.5 presents the resultant damping characteristics, separation velocities, forces, etc., as a function of the time delay between main chute deployment and aeroshell separation. The results show that any transient vehicle motion should be largely damped within 2 sec after main chute deployment. In addition, the separation force and velocity will be adequate 2 sec after main chute deployment. Therefore, as a compromise, the separation time delay was selected at 2 sec.

The cable cutter cuts the harness between the aeroshell and the pressure vessel at mortar fire +0.5 sec. The three explosive nuts attaching the pressure vessel to the aeroshell are actuated at mortar +3.26 sec (2 sec after the main chute is fully opened).

Analysis of the aeroshell separation investigated collision possibility due to nonsimultaneous explosive nut release. The analyses assumed that the aeroshell-pressure vessel interface structure is rigid, so that no relative motion exists until the last nut releases. It was also assumed that no relative accelerations existed except the relative drag forces. Based on the initial separation force, the time to travel a relative separation distance of 16.5 cm (6.5 in.) is 0.062 sec, at a delay time of 2 sec. The relative tipoff rate is 10.2 deg/sec resulting from the impulse of the last nut to fire. This rate causes a 0.63 deg relative rotation of the aeroshell, which is small compared to the 8.5 deg clearance angle. If the aeroshell and pressure vessel were spinning at 60 rpm prior to separation and the aeroshell had a 3 cm (0.12 in.) c.g. offset, it would acquire a relative lateral ΔV of 1.8 cm/sec (0.06 ft/sec), which is small compared to 39 cm/sec (1.27 ft/sec) which can be tolerated. It should be kept in mind that the parachute would damp any forces imparted to the pressure vessel during separation, before large motion can result. Therefore, it can be stated that aeroshell separation from the pressure vessel can be accomplished satisfactorily.

Parachute Release. Three methods of attaching the parachute to the pressure vessel were considered; one, two, or three point tiedown systems. The main factor in the selection of three points was the increase in the aerodynamic stability for this arrangement with the parachute deployed; the single point concept was not considered practical because of the location of the antenna in the area required for the attachment fitting.

The effect of nonsimultaneous release of the explosive nut was investigated. It was assumed that the pressure vessel has its own weight acting, trying to rotate it about the last attachment fitting, until the nut fires. The impulse from the nut provides a restoring moment, so that for a 0.004 sec Δt, the net tipoff rate imparted to the pressure vessel is 1 deg/sec. When Δt is very small, the maximum rate is 5.5 deg/sec. The magnitude rates should not cause any instability to the pressure vessel during its terminal descent phase.

Small Probe

Separation Subsystem. Theoretically, the proposed separation concept (Figure 5.6-5) provides clean, instantaneous release of the probe, with nominally zero tipoff and zero Δt, except for the tangential velocity due to bus spin. Furthermore, the opening velocity of the arm is sufficient to provide adequate clearance and insure a collision free escape of the probe. Realistically, however, the probe is not released instantaneously; but there is a finite time period for the structures (bus, arm, probe) to reach a zero load condition. It was assumed therefore that an average force of 445 N (100 lb) acts radially on the probe for 2 ms. This force imparts a radial ΔV of 2.9 cm/sec (0.096 ft/sec) to the probe, and because of the distance between the c.g. and the plane of the arm, the force also imparts a tipoff of approximately 4 deg/sec, which results in a precession half cone angle 0.5 deg.

The clearance study shows that an opening angular velocity of 400 deg/sec must be imparted to the arm, assuming a bus spin of 60 rpm. The expected impulse from the separation nut is approximately 0.9 N-sec (0.2 lb-sec), which is sufficient to impart such a velocity. The arm must rotate or open in the same direction as the bus. Both the arm and the bus structure must be offset away from the probe at the trailing edge, which corresponds to the attachment point.

The bus structural interface with the probe is essentially a semicircle, except at the trailing edge where it must be cut away from the periphery of the probe. Adequate clearance is attained with a 2.5 cm (1 in.) cutback, as shown in Figure 5.6-5. Changes in probe diameter do not alter the need for offsetting the structure at the trailing edge. Changes in bus spin rate do not affect clearance of the structure with the probe.

The principal assumption in the study of the arm clearance is that the arm is a rigid body, so that the impulse from the explosive nut causes rotation of the arm, with no elastic deformation, at constant angular velocity. A study of various arm cross sections led to the selection of a closed, tubular section as the baseline design. Using aluminum, the arm has a total weight of approximately 0.27 kg (0.06 lb) including fittings.

A computer program was prepared which calculates the distance from an "imputed" point of interest on the arm to the probe's center, and compares it to the probe's radius. The arm has an initial angular velocity due to the bus spin rate. The primary collision point on the arm is the attachment point. The other principal point of interest is where the arm first contacts the ring, also

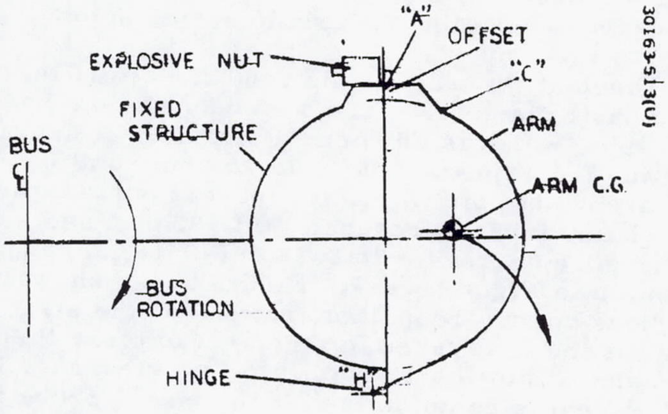

FIGURE 5.6-5. SMALL PROBE SEPARATION

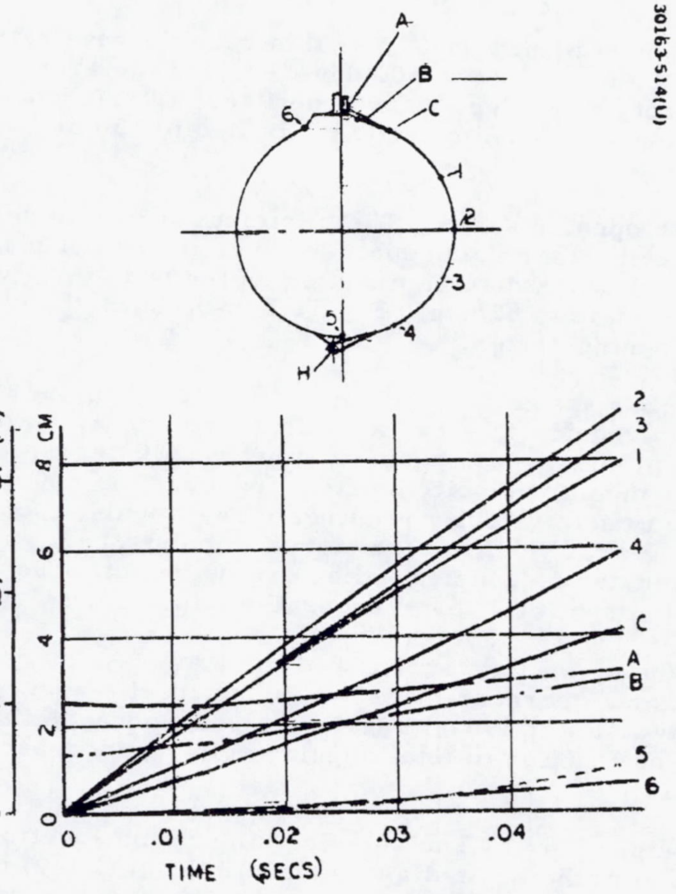

FIGURE 5.6-6. SMALL PROBE CLEARANCE STUDY

referred to as the contact or tangency point. In our subsequent discussions, these points are denoted points A and C, respectively (Figure 5.6-6). Actually, the analyses have shown that if point A clears, then all points on the arm clear the probe. Several conditions were examined and summarized below:

1) Baseline case. Hinge at the leading edge and 2.5 cm (1 in.) inboard from the basic diameter. The arm opens in the same direction as bus spin, which is 60 rpm. Point A must be offset 2.5 cm (1 in.) away from the probe. With an arm rotation of 400 deg/sec, the clearance of point A always increases from the nominal 2.5 cm (1 in.) initial clearance. At 300 deg/sec arm rotation, the clearance decreases to 0.38 cm (0.16 in.) and then increases, as shown in Figure 5.6-7. Figure 5.6-6 shows the clearance of various points around the arm and on the structure. Figure 5.6-8 shows the time taken for the arm to clear the V ring. Note that point C has attained a 1.2 cm (0.5 in.) clearance in about 16 ms. The arm is completely clear from the probe in 150 ms, at which time the arm has rotated 92 deg relative to the bus. Figure 5.6-7 shows the effect of initial angular velocity on clearance, justifying the selection of 400 deg/sec.

2) Hinge located on trailing edge. For this case the arm's angular velocity must be increased to 500 deg/sec, and the arm must be permitted to rotate 180 deg. At 400 deg/sec, interference results. Likewise, if the arm opening angle is limited to 150 deg, collision would result.

3) Minimum band opening angle. The minimum angle which the arm can open and still clear the probe was investigated because of other equipment which may be mounted on the bus, in between the probes. This angle is 60 deg. Figure 5.6-9 shows the clearance for various opening angles.

4) Sensitivity to bus spin rate. The only effect of changing the bus spin rate is to require a higher arm angular velocity. For a spin rate of 90 rpm, the angular velocity must be 530 deg/sec, and for 120 rpm, the angular velocity must be increased to 800 deg/sec. The increase in arm velocity requires more impulse from the separation device. The need for higher impulse can be satisfied by using a thruster bolt instead of an explosive nut. Such devices are commonly used for V-band separation, (see Figure 5.6-10).

5) Effect of changing mass properties of the arm. An increase in arm weight, or a decrease in its rotational inertia about the hinge permits a reduction in initial angular velocity because the centrifugal force contribution to total angular velocity increases, (see Figure 5.6-11).

6) Location of hinge point. The selected hinge point location is 2.5 cm (1 in.) inboard of the basic diameter and 2.5 cm (1 in.) below the tangent line. Moving the point to 2.5 cm (1 in.) outboard of the

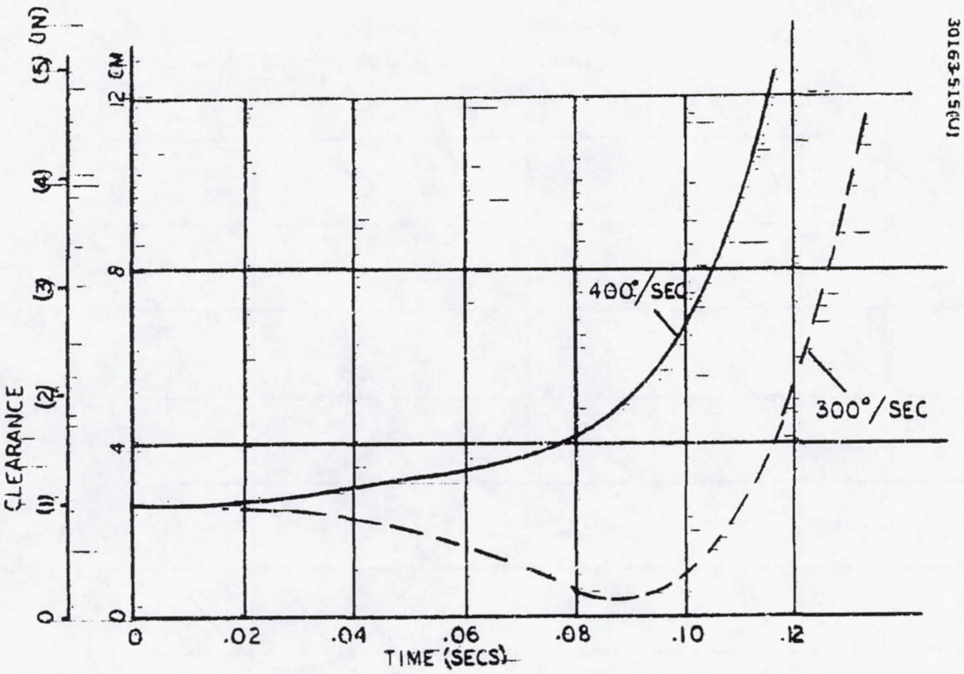

FIGURE 5.6-7. SMALL PROBE SEPARATION CLEARANCE OF POINT A WITH ARM VELOCITY

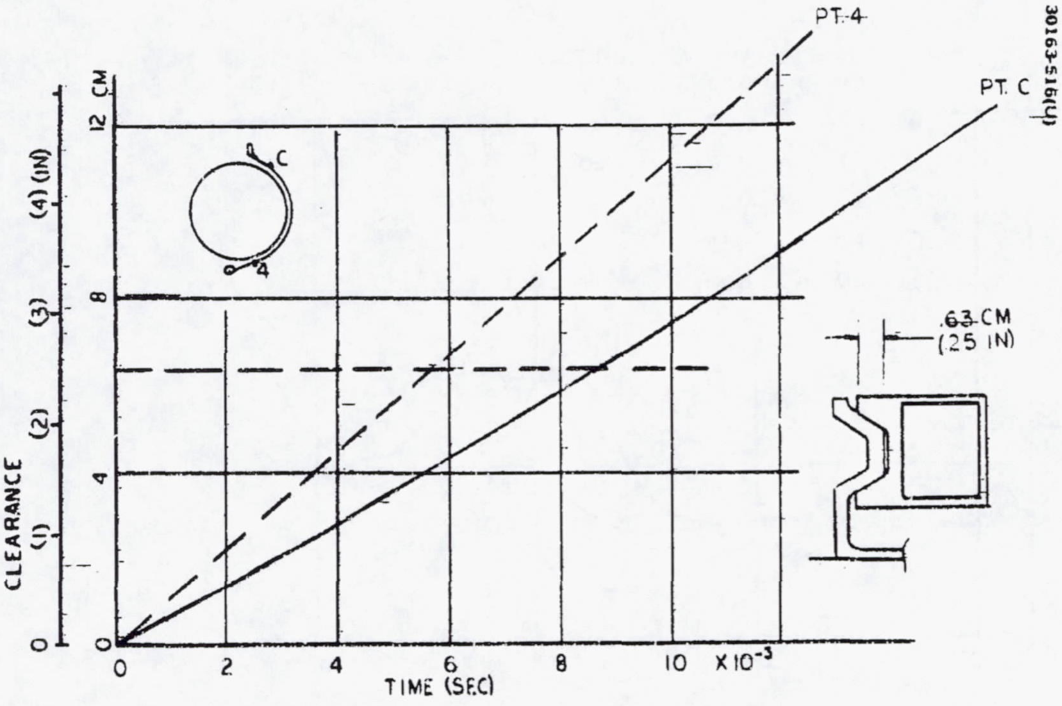

FIGURE 5.6-8. TIME FOR ARM TO CLEAR V RING

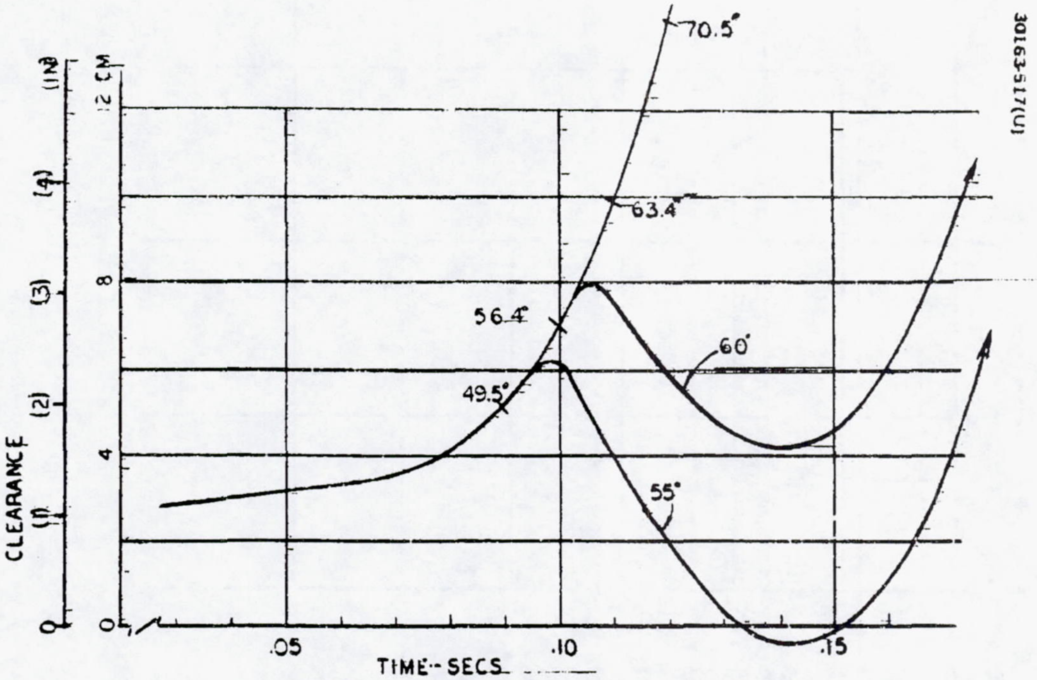

FIGURE 5.6-9. VARIATION OF CLEARANCE WITH ARM ROTATION – ARM ROTATION 400 DEG/SEC

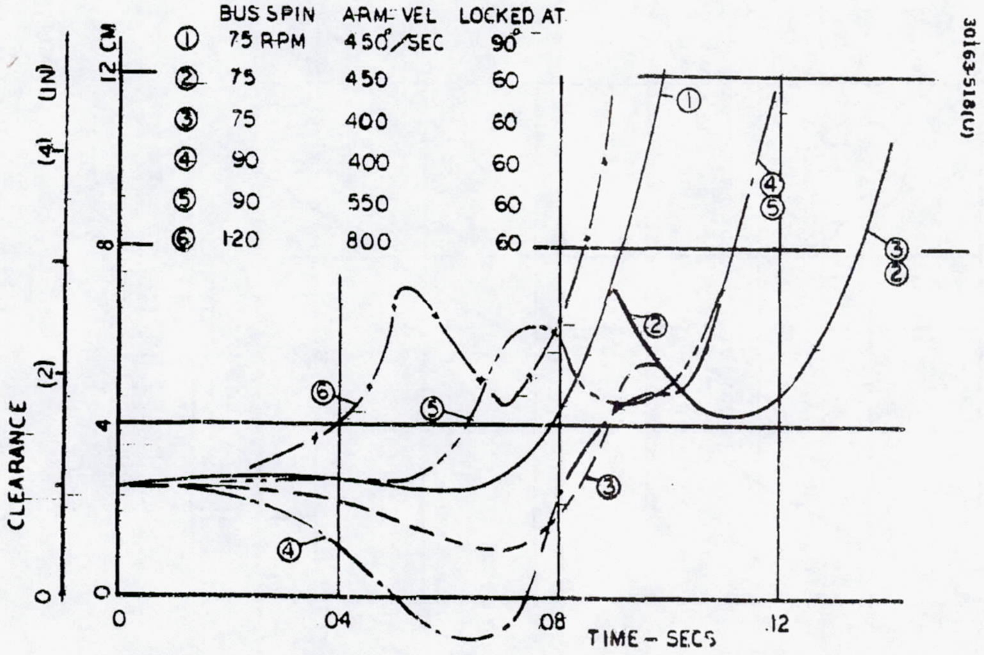

FIGURE 5.6-10. EFFECT OF BUS SPIN RATE ON ARM CLEARANCE

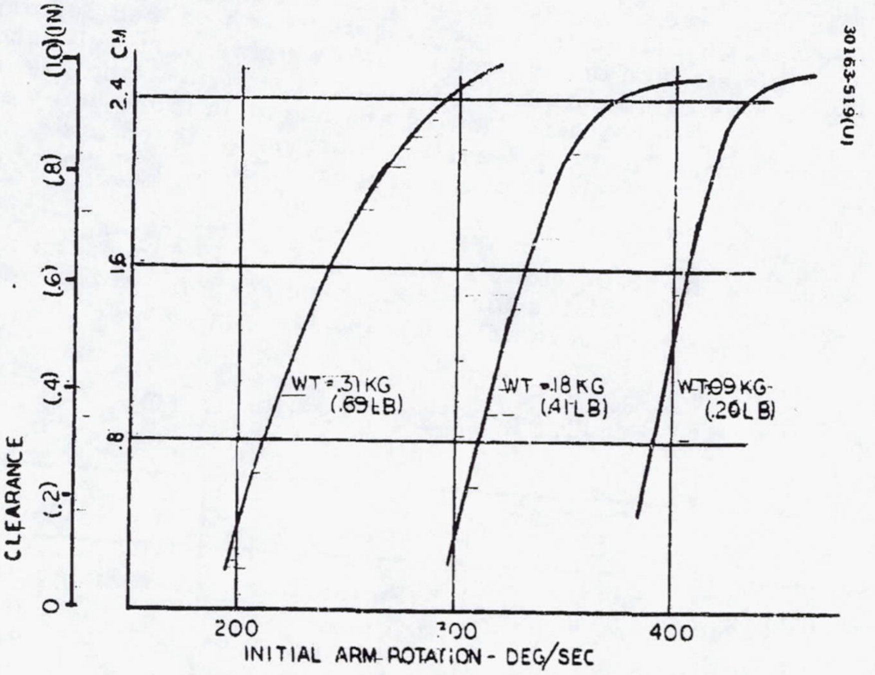

FIGURE 5.6-11. EFFECT OF BAND WEIGHT ON CLEARANCE

diameter improves the clearance of point C somewhat, but not sufficient to warrant a change at this time. It also requires that the structure extend beyond the diameter, although this does not appear to pose any clearance problems (see Figure 5.6-12).

The condition of a fully opened arm colliding with the probe from the next station was investigated and no problem exists. The maximum opened radius to the tip of the arm is about 1.42 m (56 in.). The probe, ejected at 60 rpm, travels 1.67 m (66 in.) along the tangential vector during the 1/3 revolution that it takes the arm to catch up to the next station, therefore collision cannot occur. This condition is insensitive to bus spin rate.

Despin Subsystem. Two methods for despinning the small probe were considered. The first was a "yo-yo" system, which consisted of two weights mounted 180 deg apart. Cables from the weights were wrapped 360 deg around a track on the aft face of the probe. The weights were released from their stored position by cable cutters. The second system is the use of two small rocket motors. The baseline motors are based on those being developed for the MK500 program. The despin system must be designed to decrease the roll rate from an initial 120 rpm at probe separation to 15 ± 10 rpm prior to entry.

The results of the trade study are shown in Table 5.6-2; the two concepts are very close as candidates for a despin subsystem, with the rockets being chosen mainly for ease of installation and testing, and weight.

TABLE 5.6-2. ROCKET VERSUS YO-YO

Criteria	Rocket	Yo-Yo
Performance	Satisfactory	Satisfactory
Weight, kg (lb)	0.18 (0.4)	0.36 (0.8)
Plume impingement	Some	None
Debris	Exhaust	Weights
Contamination	Minimal	None
Packaging/installation	Good	Medium
Safety	Class B	Class C
Firing discrete	Same	Same
Design/development costs	Higher	Lower
Ease of testing	Good	Difficult

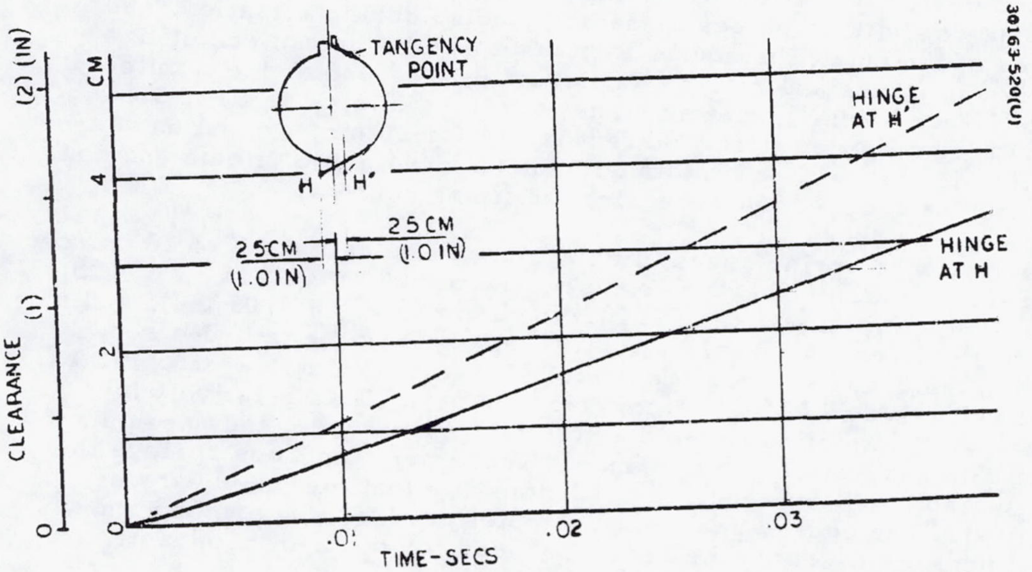

FIGURE 5.6-12. EFFECT OF HINGE POSITION ON TANGENCY POINT CLEARANCE

Thor/Delta Description

Large Probe

Bus/Probe Separation (Figure 5.6-13). The separation velocity requirement for the large probe was established at 76 cm/sec (2.5 ft/sec) ±10 percent to minimize collision probability with the bus. It is also desirable to accomplish the separation in a reasonably fast time, 50 ms, to reduce time dependent errors such as lateral motion due to bus coning at separation.

The design consists of three explosive nuts, with redundant cartridges. A 0.95 cm diameter (3/8 in.) bolt was selected; the bolt hole diameter is large enough to permit ejection of the bolt by the explosive nut. The nut configuration selected is that of the Hi Shear Corp. SN 7300 series. It is completely captive, with no pieces or debris ejected during actuation, and can be torqued at the nut. The squibs to be used are redundant and utilize stable pyrotechnic mixes and reliable construction as found on the Apollo initiator of MK12 or Viking initiators. They are 1 A, 5 min, no fire, 3.5 A all fire. The recommended firing current is 5 A for 20 ms, which guarantees actuation within 10 ms, with a simultaneity of ± 2 ms. Action items and non-simultaneity can be reduced by increasing the firing current.

Three matched spring assemblies are used to obtain a ΔV of 76 cm/sec ± 10 percent (2.5 ft/sec). They are compressed to 669 ± 13 N (150 ± 3.0 lb), have a controlled working stroke of 2.13 ± 0.08 cm (0.837 ± 0.03 in.), and a spring rate of 153 N/cm (87.2 lb/in.). The separation time is 0.044 sec, which is within the 0.050 sec requirement. The spring material is chrome-silicon steel, stressed to 52,000 N/cm^2 (75,000 psi). This relatively low working stress will minimize creep due to long time storage, thus assuring more predictable separation performance. There are numerous springs that can be designed to meet the required conditions, so that the size described above is typical. The energy pack unit, complete with spring preload and travel adjustment, is based on the assembly used for the LAR program.

Electrical separation is accomplished via a 61 pin hot wire IFD identical to the ones used on GE-RESD space vehicles. The IFD has 61, #22 gage contacts of the crimp removable type, in conformance with NAS-1600. The connector meets NAS-1599 electrical requirements, has 360 deg RFI shell continuity, potted wire entry seals, hard oxodized aluminum shells and antibind rolloff shells. It is a G&H Technology, Type 704 E. The two redundant hot wire actuators allow separation of the IFD upon receipt of the firing command. They withstand 0.5 A, 5 min current without actuating, and will actuate at 6 A within 20 ms. Similar hot wire elements have been flow on GE-RESD's MK 12 program, on the Apollo flights, and are planned for use on the Viking Mars Lander. The IFD is actuated about 2 sec prior to mechanical separation to permit the impulsive separation forces to dampen out. The plug has a retracting/restraining spring to prevent it from striking the probe. The time to complete IFD separation is less than 50 ms.

Aft Cover Separation (Figure 5.6-14). The aft cover is attached to the aeroshell aft structure by means of three mechanical latches which are

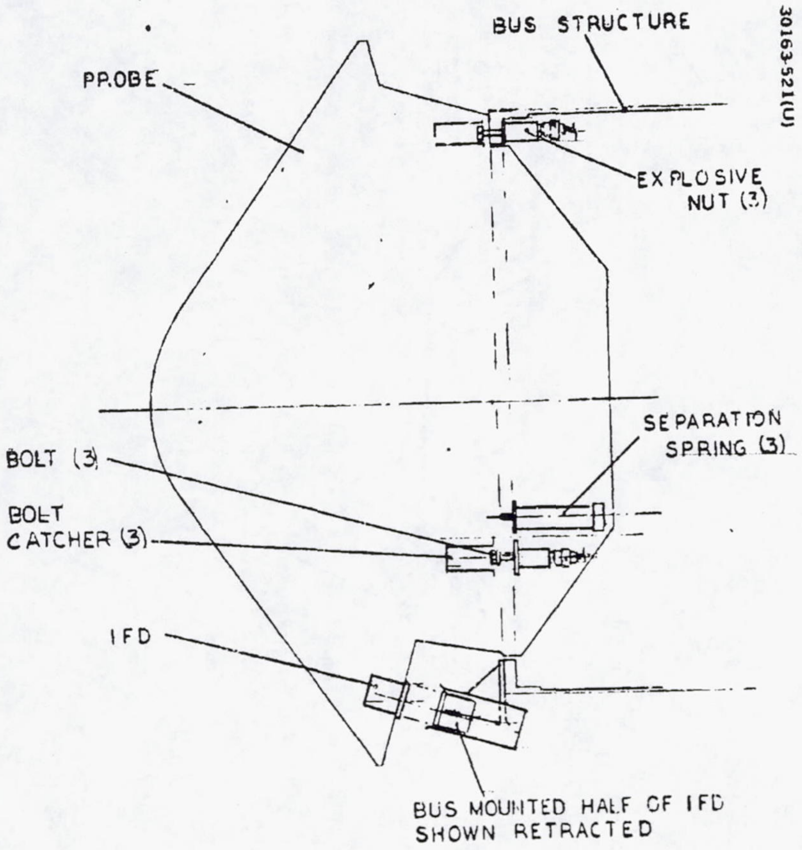

FIGURE 5.6-13. LARGE PROBE/BUS SEPARATION SUBSYSTEM

REPRODUCIBILITY OF THE ORIGINAL PAGE IS POOR.

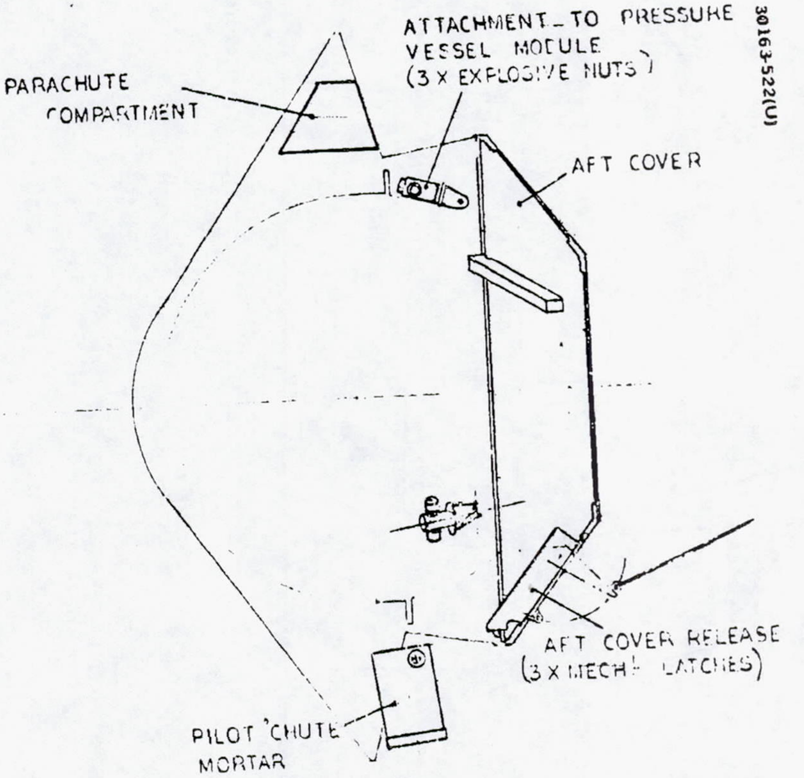

FIGURE 5.6-14. LARGE PROBE PARACHUTE DEPLOYMENT SUBSYSTEM

REPRODUCIBILITY OF THE ORIGINAL PAGE IS POOR.

released by the deployed pilot chute. The latches incorporate a high mechanical advantage to amplify the loads available from the parachute. An over-center mechanism with a preload spring is used to ensure that the latches are not prematurely operated by vibration of flight acceleration loads. The catch traps the aft structure between the latch and the aft cover lip to ensure that it will not be released by deformation of the structure. The mechanism is adjustable from the outside of the aft cover to take up any slop between the aft cover and aft structure. The operating lever, attached to the parachute liner, also acts as a flap valve to vent the interior at release, thus preventing differential pressure from holding the aft cover in place.

Aeroshell/Pressure Vessel Module Separation (Figure 5.6-15). The aeroshell/pressure vessel function is provided by three explosive nuts mounted on the flange of the pressure vessel. The bolts, mounted on the aeroshell with bolt catchers, are inaccessible, and therefore torquing nuts are used. This method of attachment has only to react the acceleration loads; the deceleration loads (the structural design case) are reacted by compression between the flange and the aeroshell mounting ring. A separate shear attachment is provided; this feature also positions the pressure vessel to insure that the attachment bolts are always free to move axially on release of the nuts.

The nuts and their redundant cartridges remain with the pressure vessel, so that their firing current comes directly from the pressure vessel. The aft structure is an inverted cone; this allows clearance from the pressure vessel at separation while maximizing the space available for the parachute on the aeroshell skirt.

The electrical separation is accomplished by a cable cutter mounted on the pressure vessel. The harness to be severed is a pigtail from the pressure vessel, and is fitted with a connector which mates with an electrical interface accessible through the aeroshell skirt.

Parachute Release (Figure 5.6-14). The main parachute is attached to the pressure vessel at three points using explosive nuts with redundant pressure cartridges, as used on the probe and on the aeroshell. The nuts are retained with the pressure vessel, so that their firing current comes directly from the pressure vessel. There is no IFD required in this separation.

The behavior of the parachute upon release of the load is to virtually come to a stop. The suspension lines contract to their zero load length, and in doing so pull the attachment fitting up and away from the pressure vessel. The impulse imparted by the explosive nut to the bolt, bolt catcher, and fitting aid in ejecting the parachute attachment fitting away from the pressure vessel.

Small Probe

Separation Subsystem (Figure 5.6-16). The baseline design consists of a rigid, semicircular arm, with a "V" cross section, which encircles the probe

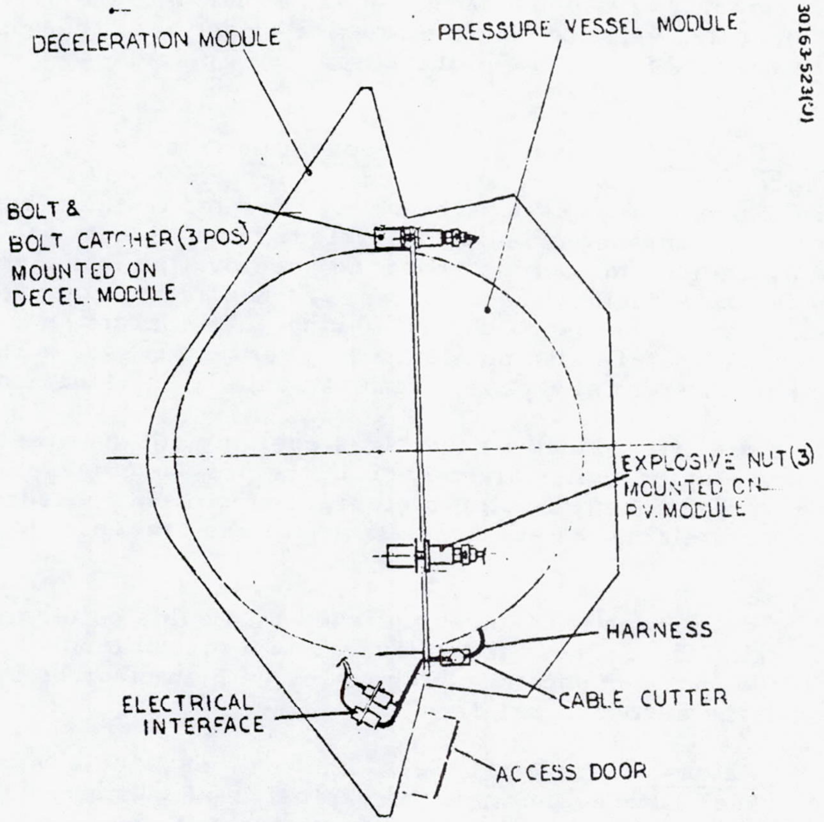

FIGURE 5.6-15. LARGE PROBE PRESSURE MODULE/ DECELERATION MODULE SEPARATION

REPRODUCIBILITY OF THE ORIGINAL PAGE IS POOR.

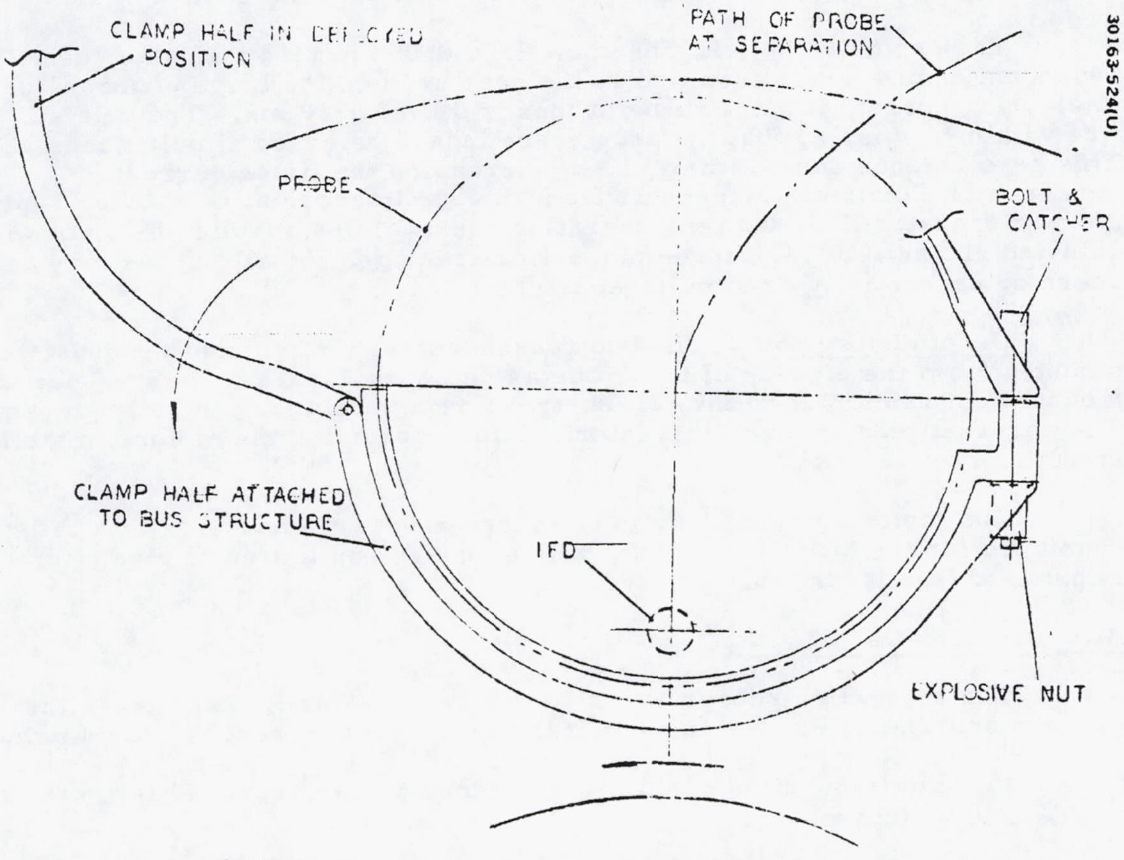

FIGURE 5.6-16. SMALL PROBE SEPARATION SUBSYSTEM

REPRODUCIBILITY OF THE ORIGINAL PAGE IS POOR.

at a V-shaped ring just aft of the aeroshell base diameter and preloads it against the bus structure. During the earlier studies the probe was held at the base diameter of the aeroshell proper. However, increases in base diameter forced the relocation of the arm within the base diameter, due to constraints on space envelope. The arm is hinged at one end and clamped at the other by an explosive nut mounted on the bus. The impulse resulting from the actuation of the explosive nut propels the bolt, and this impulse is transmitted to the arm, causing it to rotate at a constant angular velocity of approximately 400 deg/sec. The arm is hinged at the leading edge, that is, in such a manner that it rotates in the same direction as the rotation of the bus.

The explosive nut, Hi Shear SN 7300 0.95 cm (3/8 in.) size, uses redundant squibs and is identical to the ones used on the large probe. The total firing current for the three probes is 30 A for 20 ms. The nuts all fire within ± 2 ms, so that the probes are indeed released simultaneously. This performance can be improved by increasing the firing current, if necessary. Electrical disconnect from the bus is accomplished by a 45-pin, lanyard operated IFD, with the operating energy being supplied by a hot wire actuated pin-puller. The three pin-pullers required for all probes may be operated sequentially or simultaneously.

Despin Subsystem. The two rocket motors of the despin subsystem are mounted from the aft ring of the probe as shown in Figure 5.6-17. They are mounted perpendicular to the roll control fins to minimize plume impingement. The aeroshell has an electrical interface for connecting the motors to the firing circuit.

The motor selected (shown in Figure 5.6-18) is based on that being developed for the MK500 program, with a charge configured to give a total impulse of (1.5 lb-sec) 6.67 N-sec.

Atlas/Centaur Description

The separation subsystem is basically the same for both the Atlas/Centaur and Thor/Delta variants, but the following differences should be noted:

1) The separation springs are resized to the increased large probe weight

2) The despin rocket charge is resized for the increased small probe roll inertia

3) The small probe IFD is changed to that used on the large probe for commonality

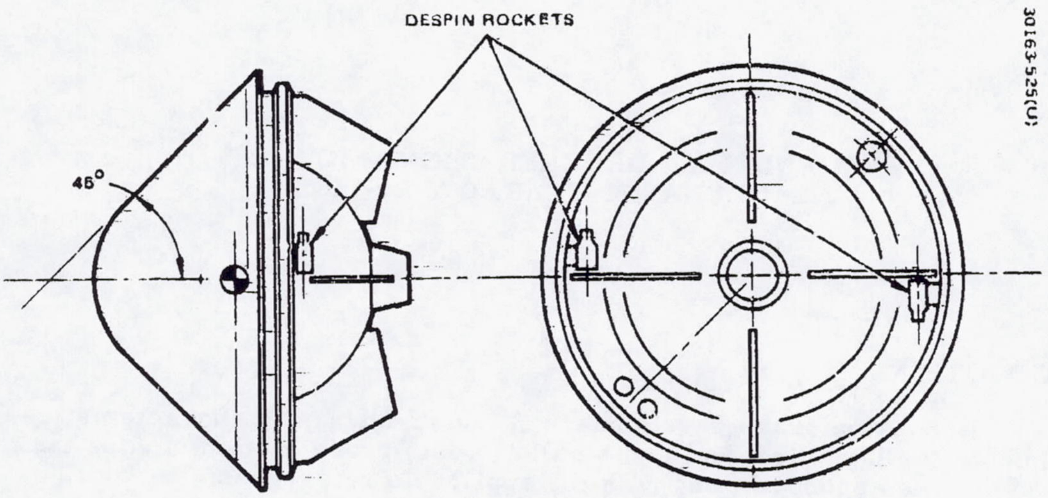

FIGURE 5.6-17. SMALL PROBE CONFIGURATION

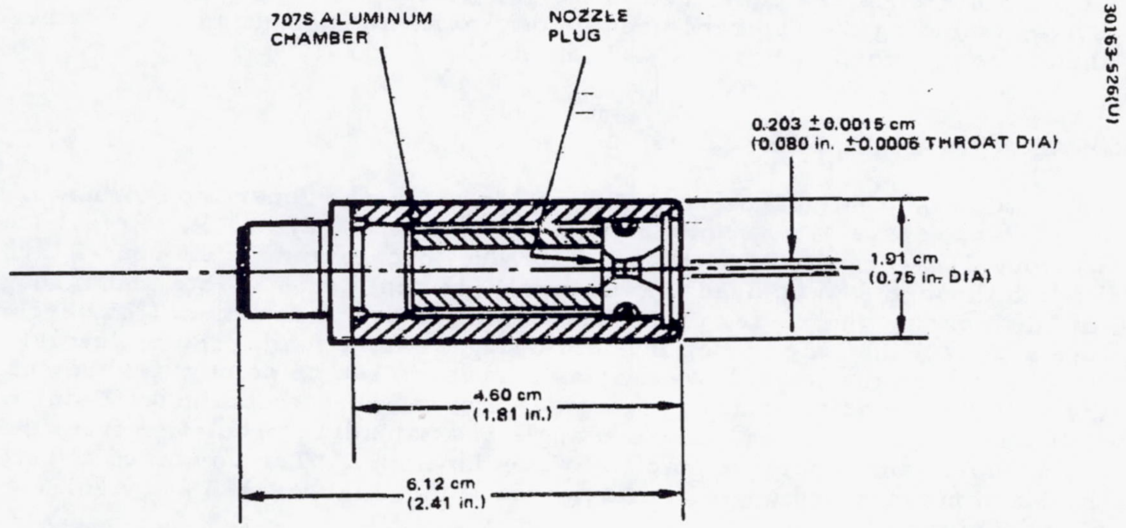

IMPULSE = 6.67 N/sec (1.5 lb-sec)

PRESSURE = 6.895 X 10^6 N/m^2 ABS (1000 psia AT - 75°F)

BURNTIME = 0.250 sec

MOTOR WEIGHT = 0.0498 kg (0.11 lb)

FIGURE 5.6-18. PROBE MOTOR

APPENDIX A. DECELERATION MODULE AERODYNAMIC CHARACTERISTICS

INTRODUCTION

A discussion of the development of the aerodynamic characteristics used in both the large (55 deg) and small (45 deg) probe motion studies is provided in this appendix along with the applicable references.

CONFIGURATIONS

Reference sketches used in the generation of the aerodynamic characteristics, including the reference center of gravity and definition of the afterbody shape are provided in Figures A-1 and A-2.

DRAG AND AXIAL FORCE

Ground test data were compiled for use in the generation of the drag coefficient versus Mach number curves (Figures A-3 and A-4). References 1 through 12 were used for the large (55 deg) probe, and References 1 through 3 and 5 through 8 were used for the small (45 deg) probe. Note that through the Mach range the 45 deg probe has a smaller drag coefficient (25 percent less at M=20) than the 55 deg probe. Using Newtonian and free molecular flow runs, and the Reynolds variation curves, based on point mass trajectories, the altitude variation of drag versus angle of attack was obtained. Using these altitude variation curves, the zero angle of attack drag prediction from the atmospheric entry point to Mach 20 were developed. The combined effect of the Mach number and angle of attack variations (Figures A-5 and A-6) were also developed.

NORMAL FORCE

Ground test data were compiled to help generate the normal force versus Mach number curves (Figures A-7 and A-8). References 1 through 6, 8, 11 and PAET data were used for the 55 deg probe, and References 1 through 3, 5 and plus Aerodynamic data from previous Mars and Venus entry studies were used for the 45 deg probe. Not only does the 45 deg probe have a greater normal force dependence on angle of attack at a given Mach number than the 55 deg probe, but its sensitivity to Mach

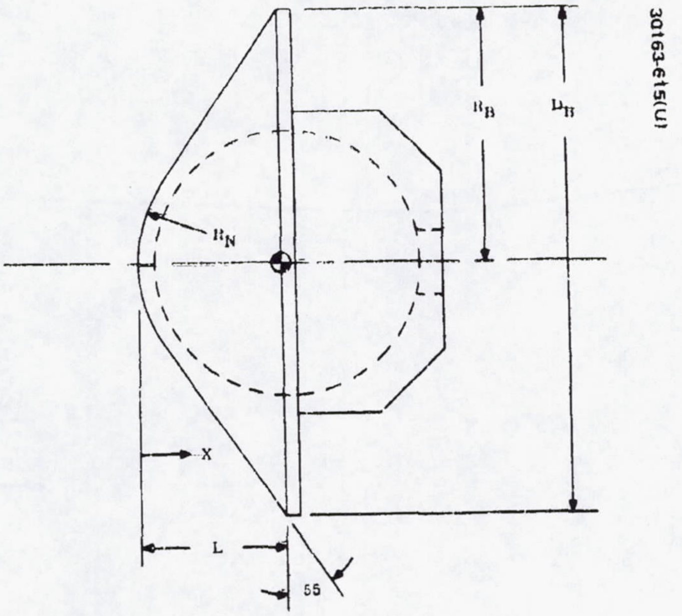

REF X_{CG} AT FIRST MAXIMUM DIAMETER

FIGURE A-1. LARGE PROBE CONFIGURATION

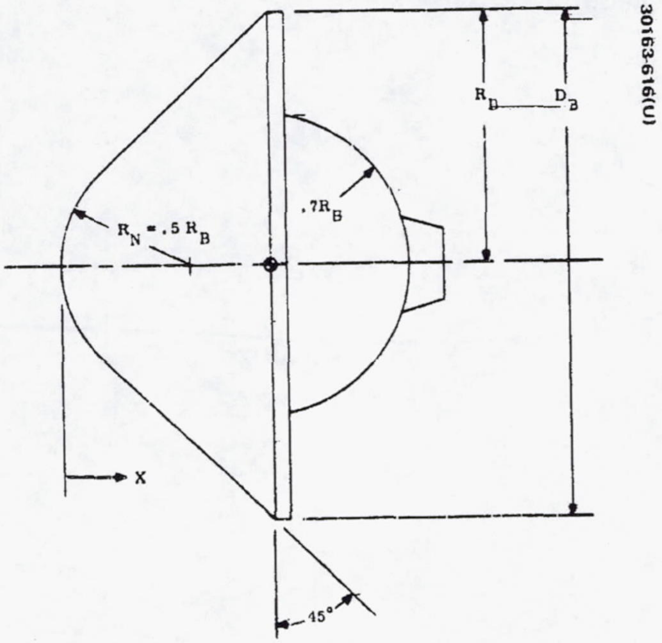

REFERENCE X_{cg} AT FIRST MAXIMUM DIAMETER

$$\left[\frac{X_{cg}}{D_B} = .386\right]$$

FIGURE A-2. SMALL PROBE CONFIGURATION

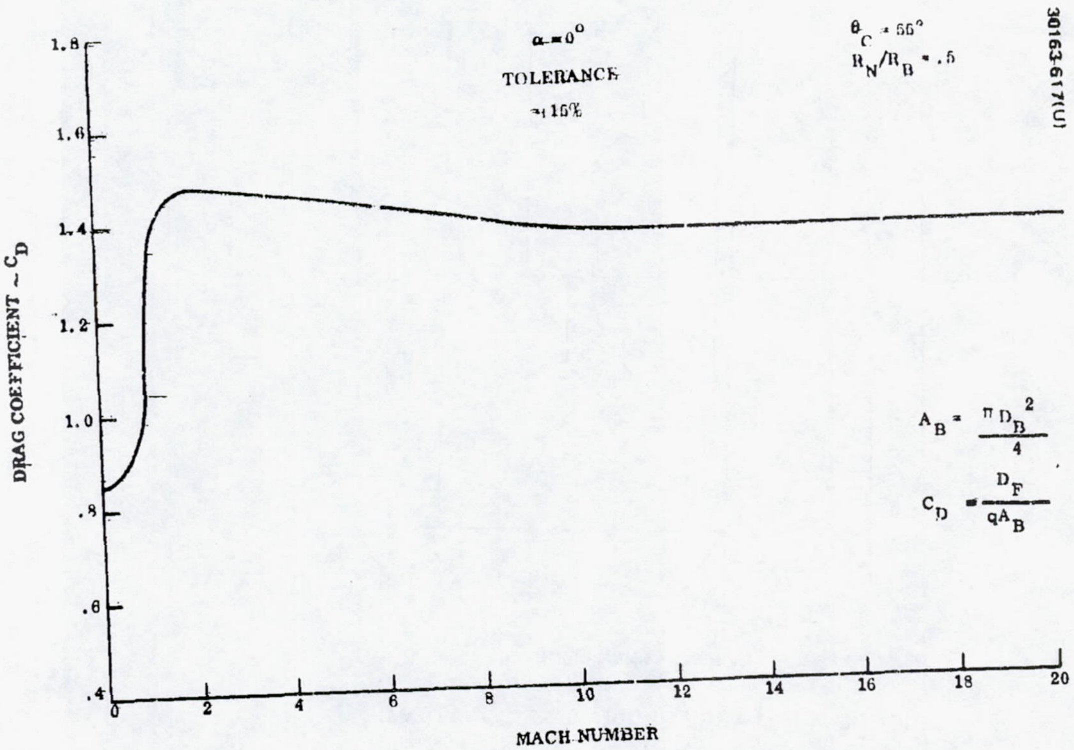

FIGURE A-3. LARGE PROBE DRAG VARIATION WITH MACH NUMBER

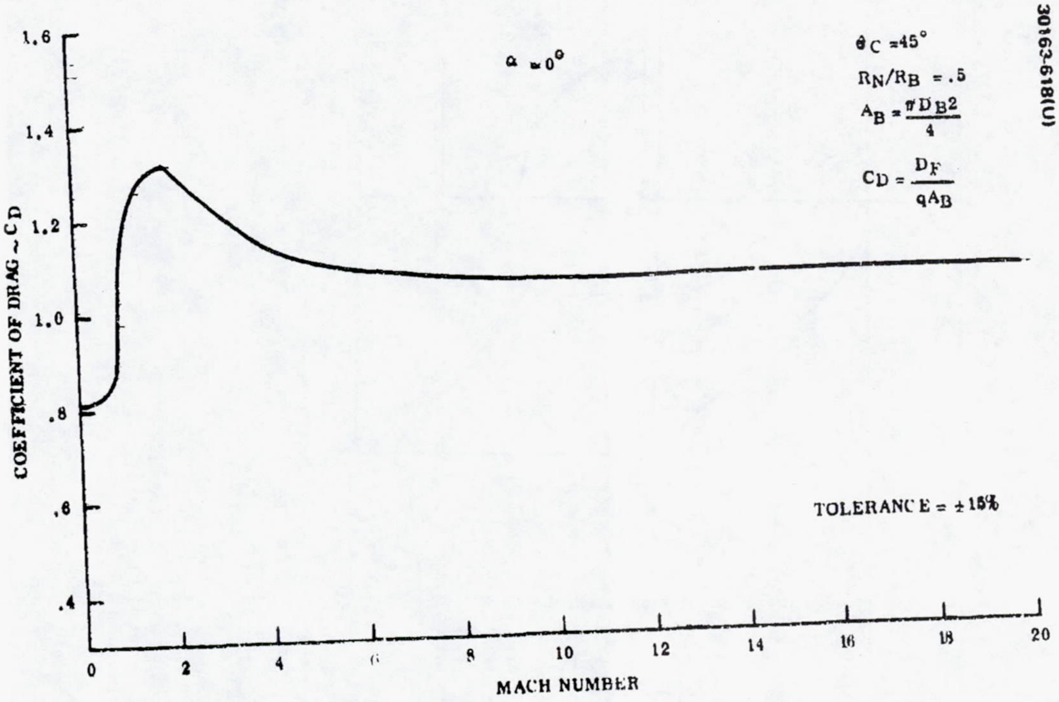

FIGURE A-4. SMALL PROBE DRAG VARIATION WITH MACH NUMBER

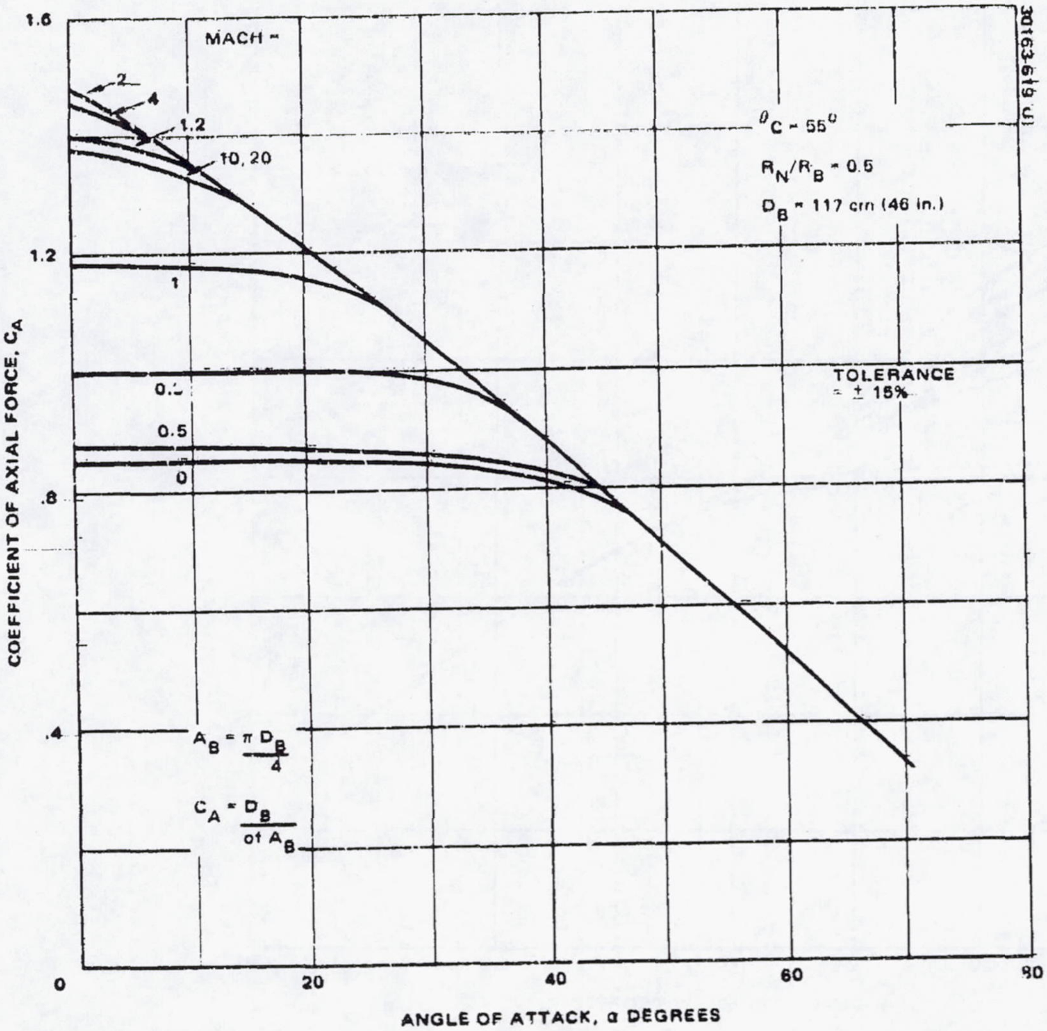

FIGURE A-5. LARGE PROBE AXIAL FORCE VARIATION WITH ANGLE OF ATTACK AND MACH NUMBER

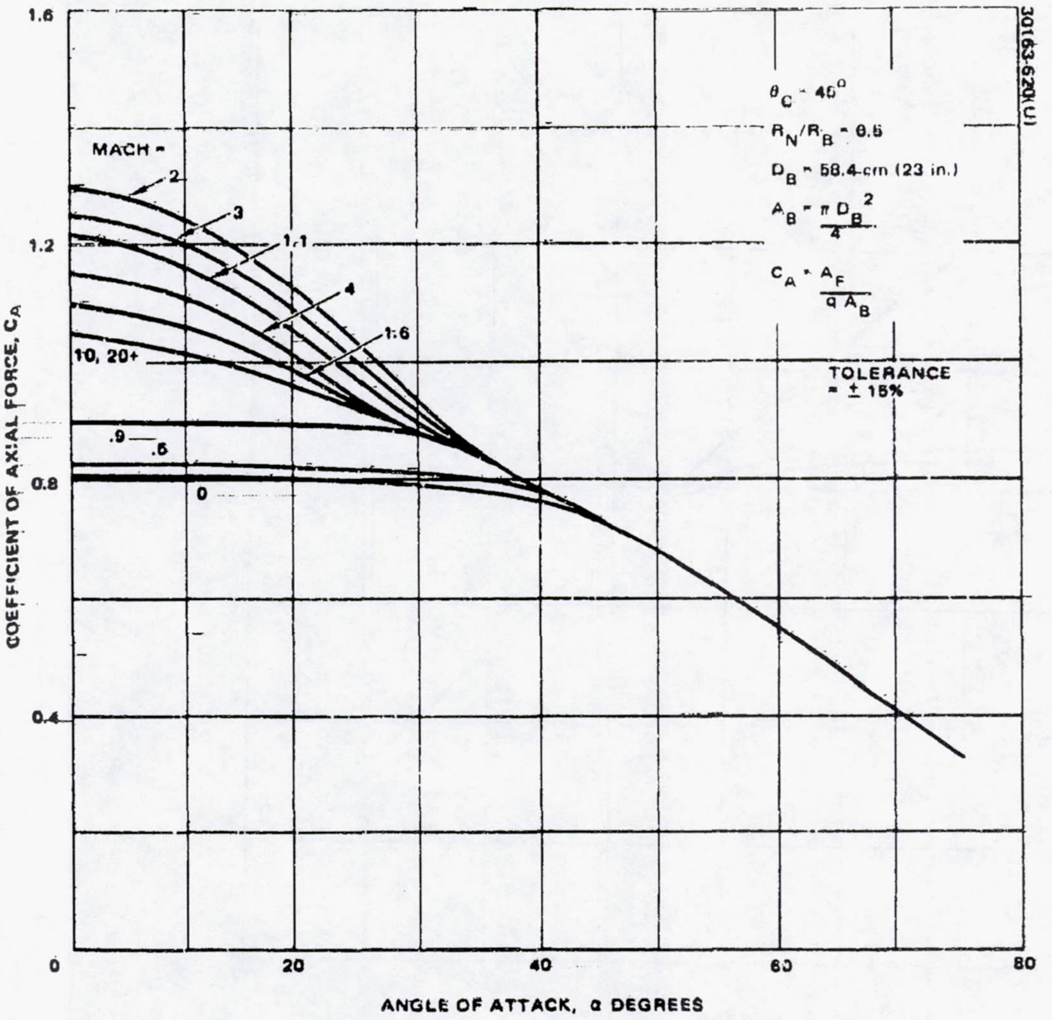

FIGURE A-6. SMALL PROBE AXIAL FORCE VARIATION WITH ANGLE OF ATTACK AND MACH NUMBER

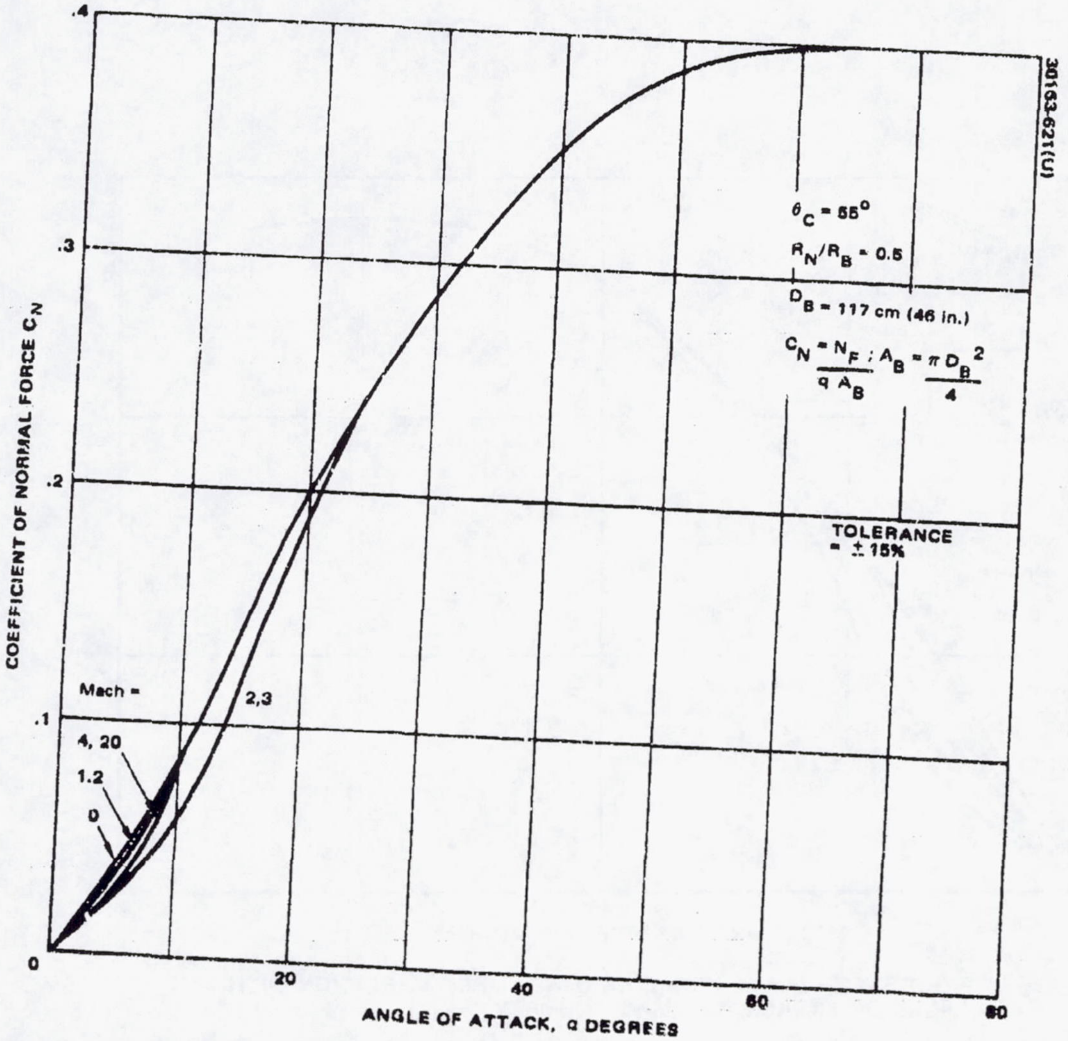

FIGURE A-7. LARGE PROBE NORMAL FORCE VARIATION WITH ANGLE OF ATTACK AND MACH NUMBER

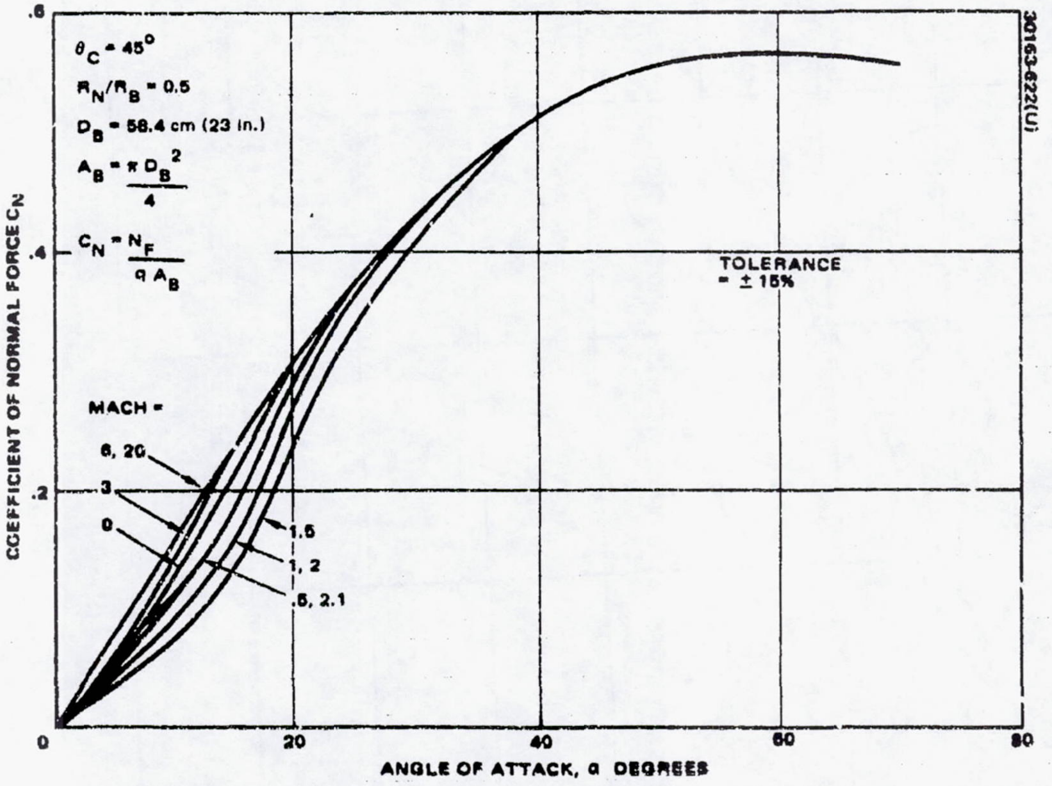

FIGURE A-8. SMALL PROBE NORMAL FORCE VARIATION WITH ANGLE OF ATTACK AND MACH NUMBER

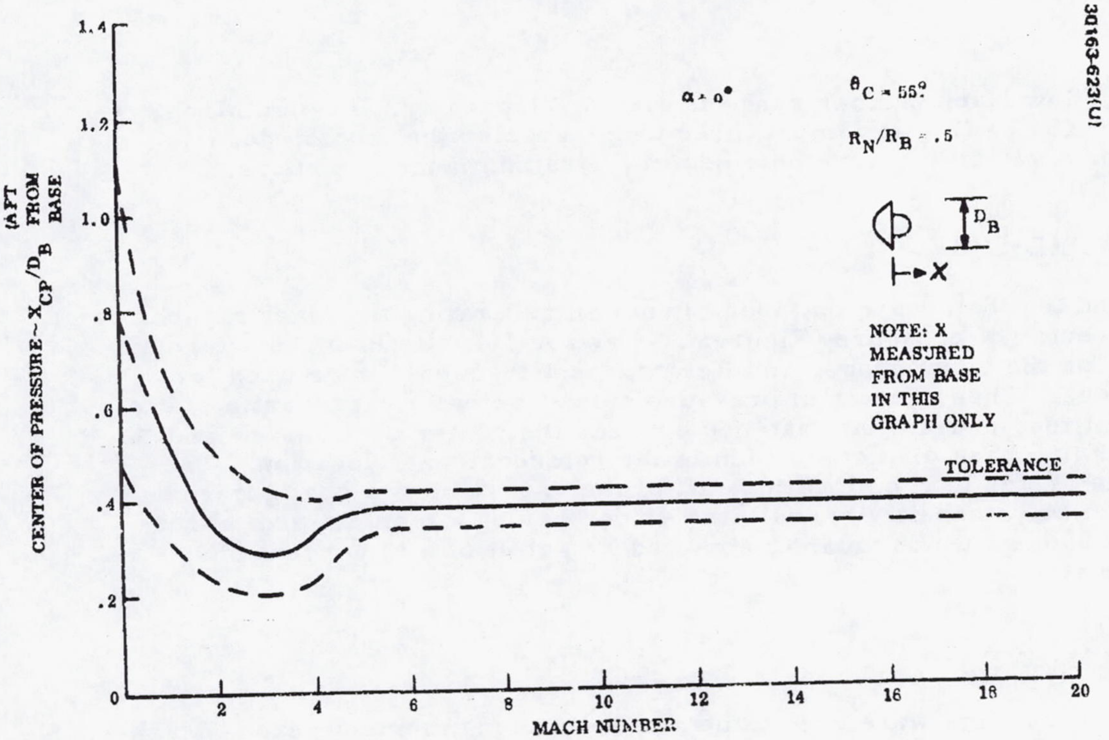

FIGURE A-9. LARGE PROBE CENTER OF PRESSURE VARIATION WITH MACH NUMBER

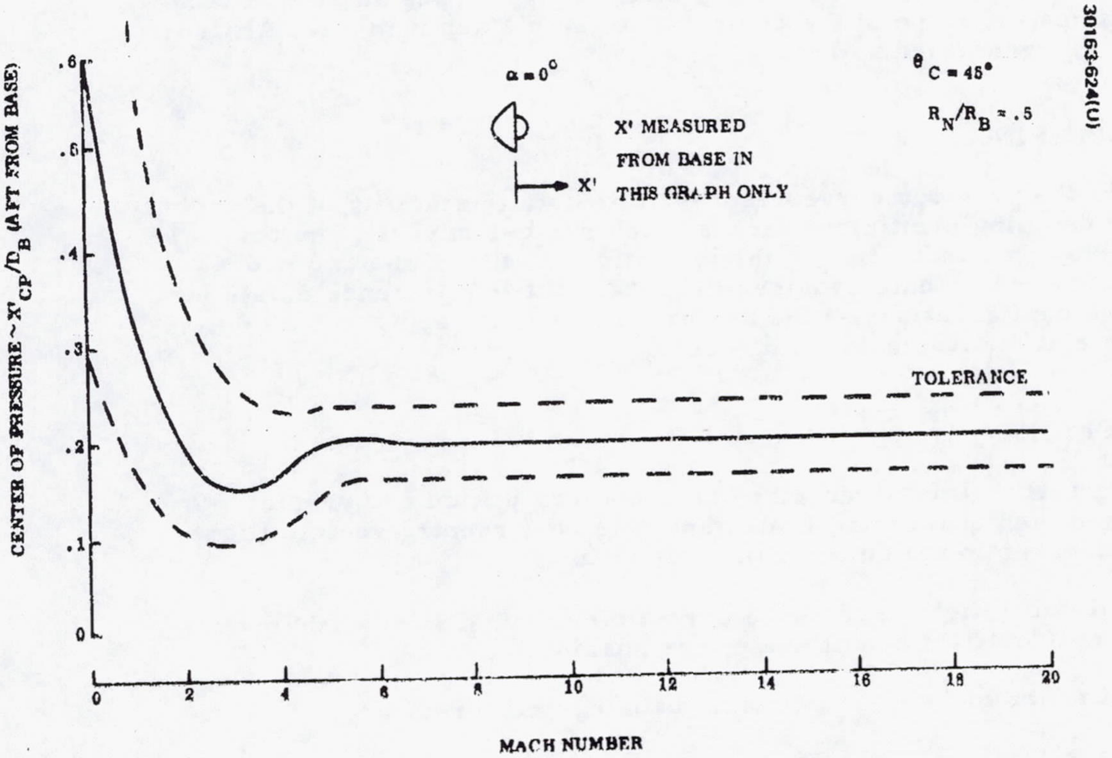

FIGURE A-10. SMALL PROBE CENTER OF PRESSURE VARIATION WITH MACH NUMBER

number in the low Mach number range is also much greater. At high Mach numbers, the 45 deg $C_{N\alpha}$ is almost three times greater than the 55 deg value. Altitude variations were obtained in the same manner as above.

CENTER OF PRESSURE

Ground test data were obtained for use in generating the Mach number variation of center of pressure (Figures A-9 and A-10). References 1 through 4 were used for the large probe, and References 1 through 3 were used for the small probe. These center of pressure curves actually represent a static margin in that they present the distance between the center of pressure and the first maximum base diameter which is the reference c. g. location. The positive values refer to c. p. locations aft of the c. g. The two configurations are similar in Mach sensitivity, with the 45 deg having a moment arm about half that of a 55 deg, which means a forward X_{cp} shift of ≈ 20 percent of the base diameter.

PITCHING MOMENT

Ground test data were used to obtain the pitching moment versus Mach number curves (Figures A-11 and A-12). References 2, 4, 12, and PAET data were used for the 55 deg probe, and References 2 and 5 were used for the 45 deg probe. By comparison, the 45 deg probe has the same Mach sensitivity as the 55 deg, with the former having a steeper C_m versus angle of attack slope (1.5 times the slope of the 55 deg) at a given Mach number. Altitude variations were generated as before.

DYNAMIC DAMPING

While the previous curves represent the static stability of the probes, the dynamic damping coefficient versus Mach number curves (Figures A-13 and A-14) give some indication of the dynamic stability of the two probes. Reference 2 and PAET data provided the data. Little difference exists between the two configurations at the higher Mach numbers, but the 55 deg is more unstable at transonic Mach numbers.

ROLL COEFFICIENT

Historically, this parameter has been very difficult to predict accurately and then quantitatively demonstrate on a reentry vehicle flight. The approach taken in the current analysis is to:

1) Review flight experience on vehicles having similar materials and/or flight conditions where possible.

2) Understand the mechanisms causing roll torques

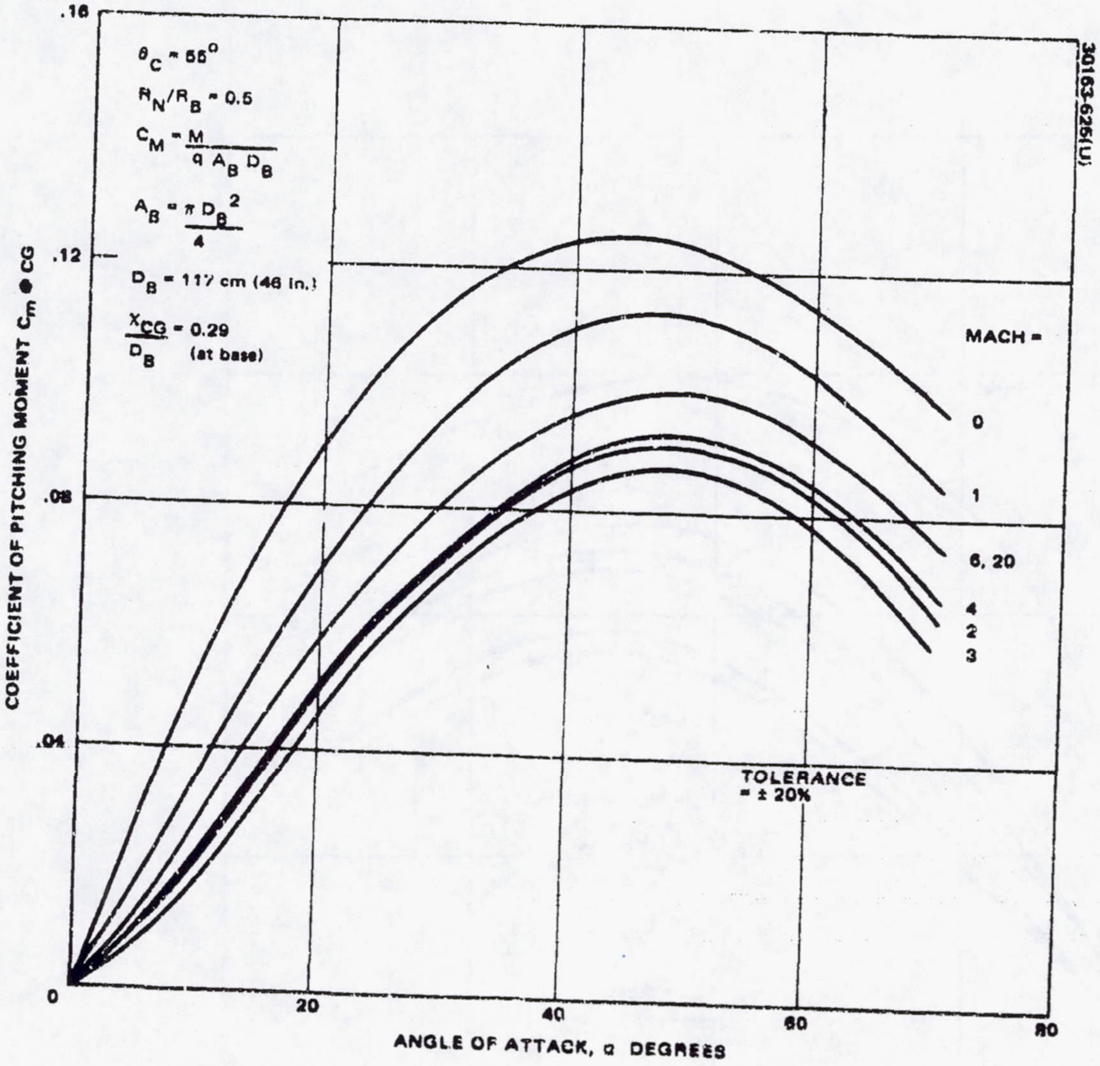

FIGURE A-11. LARGE PROBE PITCHING MOMENT VARIATION WITH ANGLE OF ATTACK AND MACH NUMBER

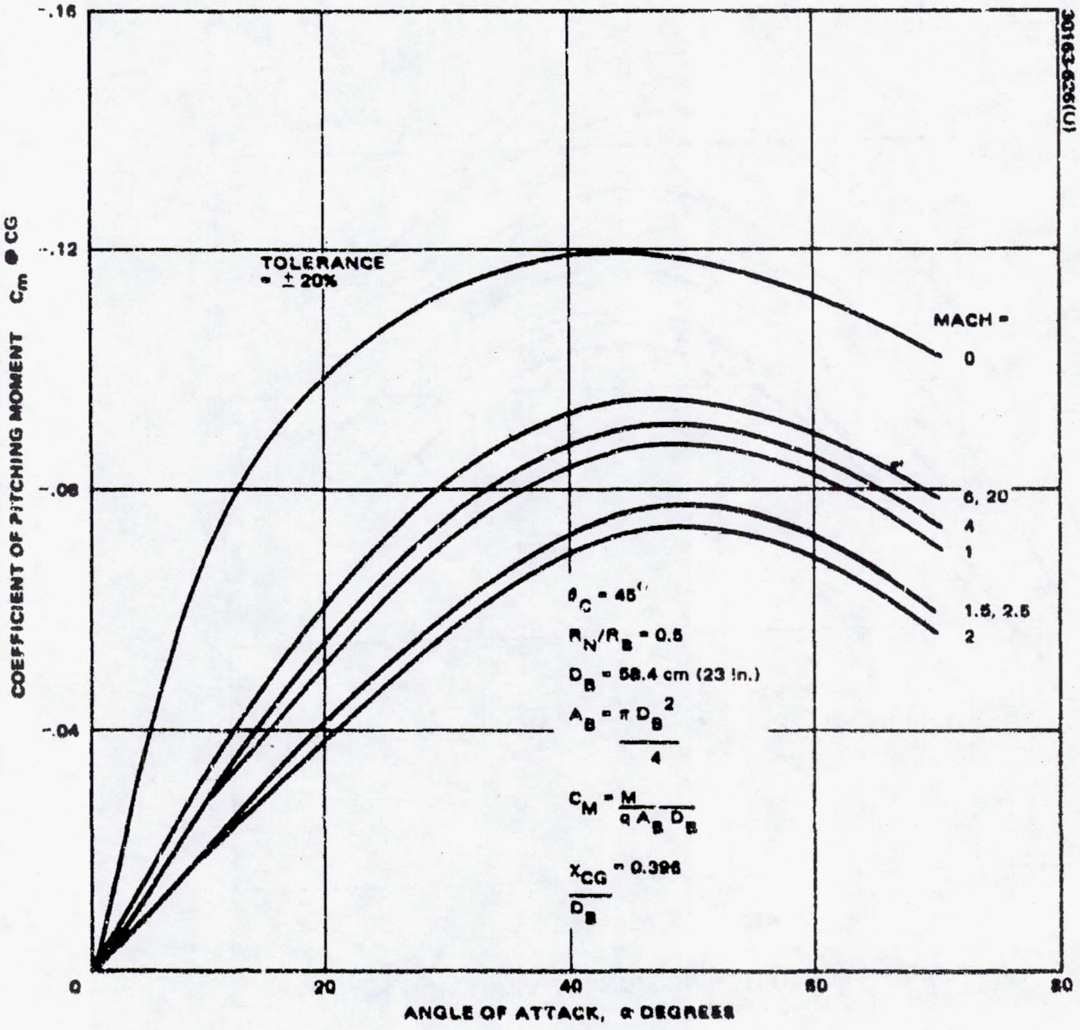

FIGURE A-12. SMALL PROBE PITCHING MOMENT VARIATION WITH ANGLE OF ATTACK AND MACH NUMBER

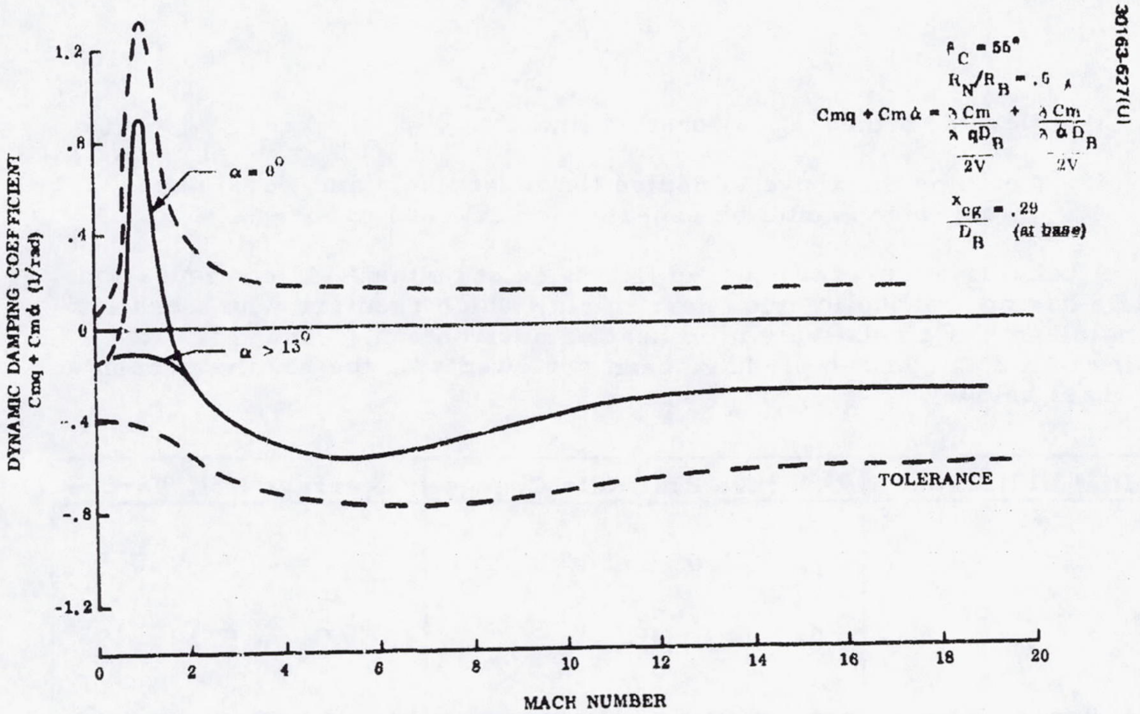

FIGURE A-13. LARGE PROBE DYNAMIC DAMPING VARIATION WITH MACH NUMBER

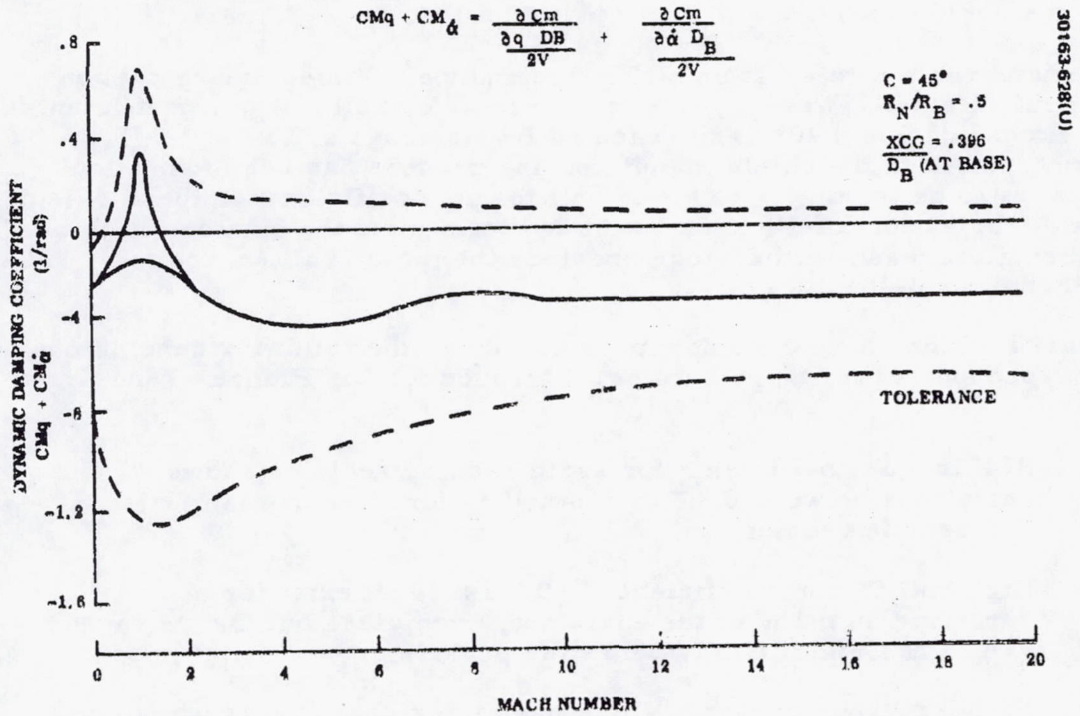

FIGURE A-14. SMALL PROBE DYNAMIC DAMPING VARIATION WITH MACH NUMBER

3) Develop a theoretical best estimate

4) Combine the above to derive the most likely and worst case value, which could be expected for a Venus probe.

A backlog of several hundred flights exist on the A-45 configuration, a vehicle having a phenolic nylon heat shield, which reenters with a shallow path angle and has a relatively mild heating environment. The roll rate histories of a 25 flight sample have been reviewed with the results presented in the chart below.

Initial Roll Rate	Average Roll Rate Change	Average Roll Torque
10 to 20 rpm	$\Delta p = -1.0$ rpm $1\sigma \Delta p = 5.2$ rpm	$C_{1_o} = -0.04 \times 10^{-4}$ $1\sigma C_{1_o} = 0.19 \times 10^{-4}$

The mechanism causing these roll torques, namely a rough thick char layer representative of long term laminar heating, will not be present on the Venus entry probes.

Considerable data exist on high performance vehicles having carbon phenolic heat shields. These shields tend to produce roll torques coefficients typically exceeding 0.5×10^{-4} and reaching levels above 1.0×10^{-4}. (A mechanism related to the shield manufacturing process has been identified which appears to be the major cause of roll torque coefficient for these shields. Heat shield fabrication for Pioneer Venus will eliminate the bias due to this manufacturing process and therefore preclude the major roll source for Carbon Phenolic shields.)

Based on the above considerations and data, the following conclusions have been reached regarding potential roll torques for the Pioneer Venus probes:

1) Roll torque coefficients for earth reentry vehicles shows variations between 0.04 to 1.6×10^{-4} for various materials and vehicle geometries.

2) High roll torque coefficients ($\geq 0.75 \times 10^{-4}$) exist for short durations on many of the earth entry vehicles, but the average values are significantly below the peaks.

3) Pioneer Venus probes will not have thick char layers which are characteristic of A-45 phenolic nylon heat shields.

4) Crosshatching will occur, although the degree of asymmetry is unknown. Assuming a 10 percent asymmetry, a maximum torque coefficient level of 0. 16 x 10^{-4} is estimated, based on scaling the levels for slender earth entry vehicles.

5) Average roll torque coefficient levels for Pioneer Venus are expected to peak at a maximum value of 0. 5 x 10^{-4}, and the nominal value should be ≈0. 2 x 10^{-4}.

REFERENCES:

1. J. Nichols and E. Nierengarten, "Aerodynamic Characteristics of Blunt Bodies, " JPL TR-32-677, 1964.
2. W.R. Lawrence, "Free Flight Range Tests of Two Blunt Bodies of Revolution at Mach Numbers from 0. 8 to 16, " AEDC TR 68-169, 1968.
3. R. V. Owens, "Aerodynamic Characteristics of Spherically Blunted Cones at Mach Numbers from 0. 5 to 5, " NASA TND-3088, 1965.
4. W. Walker and R. Weaver, "Static Aerodynamic Characteristics of Blunted Cones in the Mach Number Range from 2. 2 to 9. 5, " NASA TR-32-1213, 1967.
5. J. Campbell, "Supersonic Aerodynamic Characteristics and Shock Standoff Distances for Large-Angle Cones with and without Cylindrical Afterbodies, " NASA TND-5334, 1969.
6. C. Harris, "Transonic Aerodynamic Investigation of Tension Shell and Blunted 100° Conical Shapes for Unmanned Entry Vehicles, " NASA TND-3700, 1966.
7. J. Campbell, "Longitudinal Aerodynamic Characteristics of Several High-Drag Bodies at Mach Numbers from 1. 50 to 4. 63, " NASA TND-3915, 1967.
8. J. Campbell and D. Howell, "Supersonic Aerodynamics of Large Angle Cones, " NASA TND-4719, 1968.
9. J. Campbell and D. Howell, "Supersonic Lifting Capabilities of Large Angle Cones, " NASA TND-5499, 1969.
10. H. G. Heinrich, S. R. Hess, and G. Stumbris, "Drag Coefficients of several Bodies of Revolution at Transonic and Supersonic Velocity, " ASD TDR 63-66, 1964.

11. R. Bendura, "Low Subsonic Static and Dynamic Stability Characteristics to Two Blunt 120° Cone Configurations," NASA TND-3853.

12. R. Sammonds, "Dynamics of High-Drag Probe Shapes at Transonic Speeds," NASA TND-6489, 1971.

APPENDIX B. SMALL PROBE LANGLEY SPIN TUNNEL TESTS

INITIAL LANGLEY TESTS

Facility

The Langley Research Center spin tunnel is an atmospheric wind tunnel with a vertically rising airstream which produces a maximum velocity of about 27. 4 m/sec (ft/sec). The models are tested in free vertical descent and the aerodynamic stability characteristics are observed both visually and photographically. Model drag is determined at conditions when the model is essentially suspended with no vertical velocity and essentially no oscillations.

Launches were made with the models undisturbed at zero angle of attack, at large angles of attack (45 deg or greater), and at various spin rates (≈0. 5 to 2 rps.)

Test Models

The primary series of test models consisted of four forebodies which are interchangeable with three different afterbodies. Three of the forebodies consist of 45, 51. 5, and 55 deg half angle sphere cones with a nose radius-to-base radius ratio of 0. 5. The fourth is a hemisphere. Two of the afterbodies are hemispheres having afterbody diameter to forebody diameter ratios of 0. 9 to 0. 7. The third is a 55 deg conical afterbody with a 0. ? diameter ratio.

The effects of stabilization fins were investigated on four of the configurations, namely, the 45 and 55 deg forebodies with the 0. 7 and 0. 9 hemispherical afterbodies.

Sketches showing the various configurations tested are included as Figures B-1 and B-2. The maximum diameter of the models is 34. 3cm (13. 5 in).

For tests of several configurations, a ring (≈1. 27 cm (0. 5 in) wide) of No. 60 sandpaper was installed near the maximum diameter on the 45 and 55 deg forebodies.

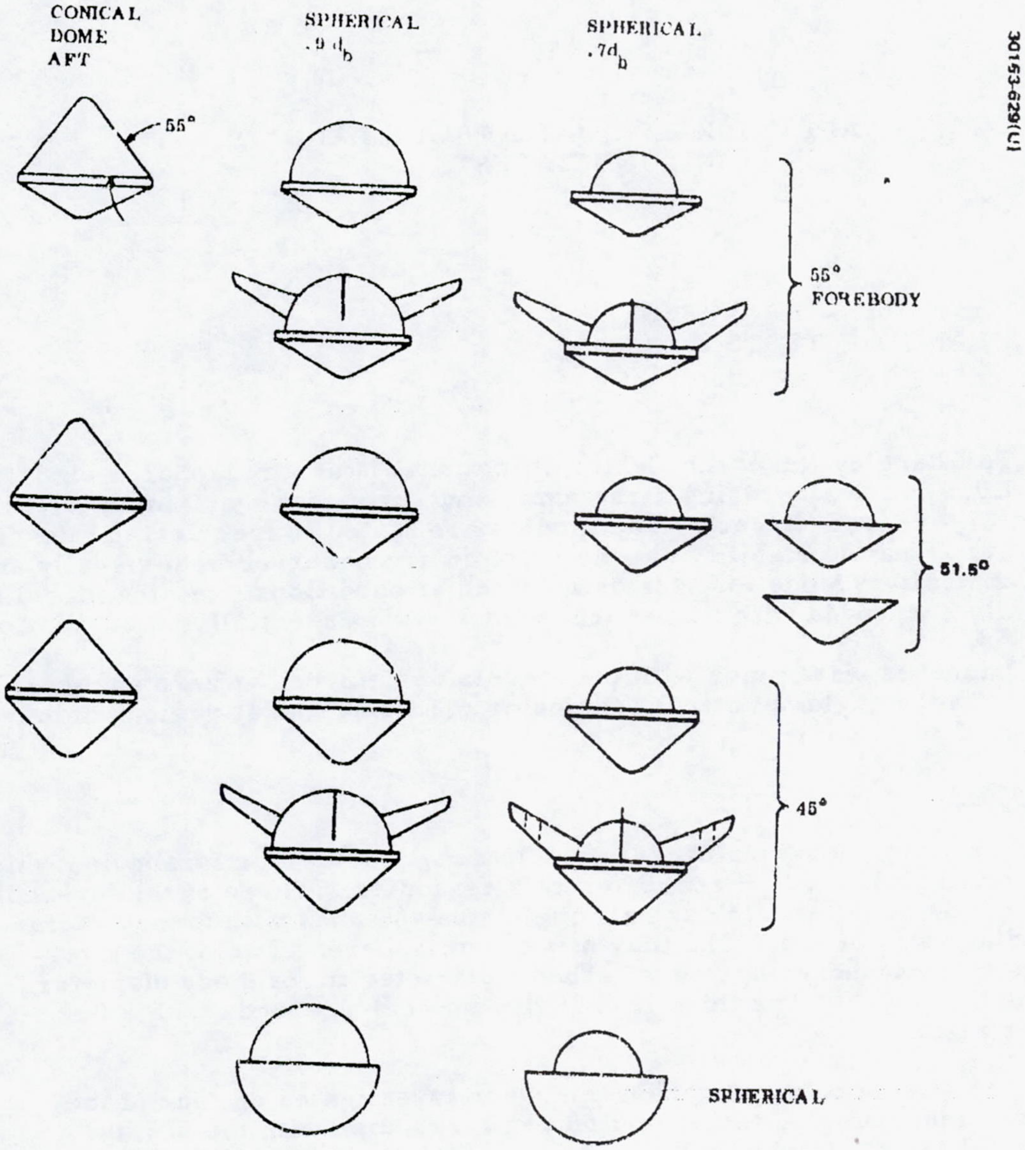

FIGURE B-1. CONFIGURATIONS TESTED

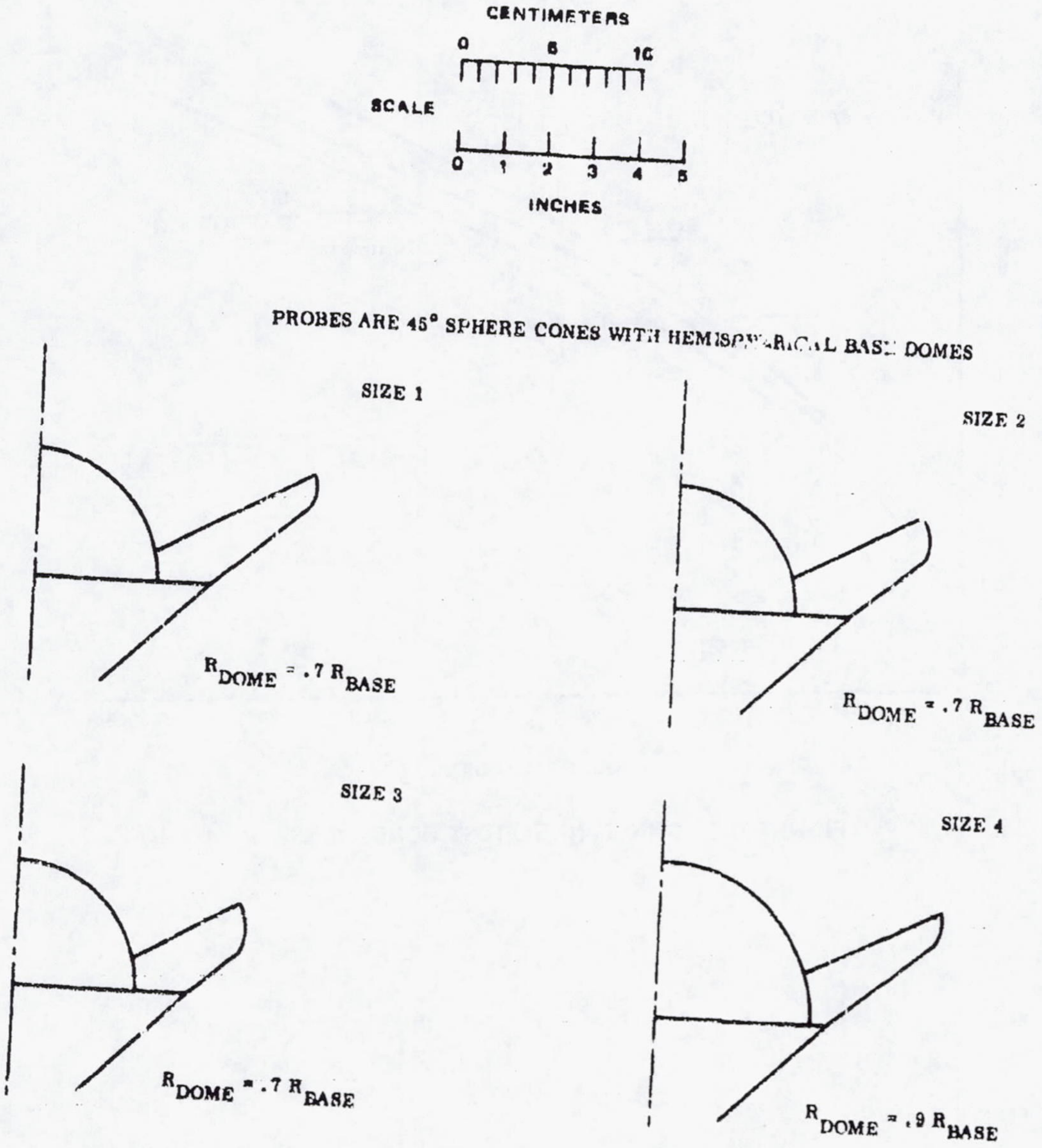

PROBES ARE 45° SPHERE CONES WITH HEMISPHERICAL BASE DOMES

FIGURE B-2. FIN CONFIGURATIONS

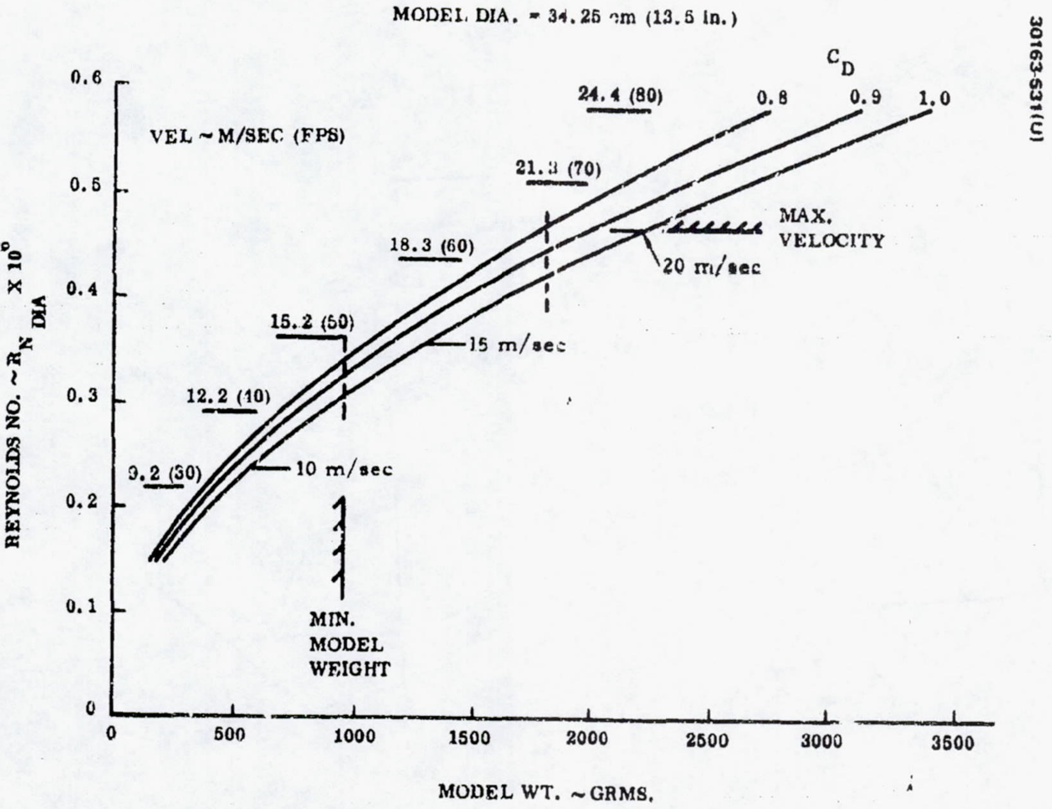

FIGURE B-3. SPIN TUNNEL TEST CONDITIONS

Tests

Sensitivity to small probe parameter variations was achieved by varying the c. g. location, weight (change in Reynolds number), adding different fin configurations, and adding a ring to the configuration. Reynolds number variation for various model weights and velocities are shown in Figure B-3.

FINAL LANGLEY TESTS

During the initial tests discussed in the previous section conducted at the NASA-Langley Free Flight Subsonic Wind Tunnel, predicted spin induced dynamic instabilities were observed. At that time large fins were attached to the models and were noted to be extremely effective in damping the initial roll rate and hence preventing the instability. Additional tests were completed with the object of evaluating the effect of various fin designs on the roll damping moment, C_{l_p}. Both solid and fabric drogue devices were tested at various axial locations behind the model with, and without, high initial spin rates. In addition tests were conducted using tufts and smoke to evaluate the state of the boundary layer.

Models

A sketch of the 45 deg sphere-cone with the 0. 7 afterbody is shown in Figure B-4. It should be noted that a simulated attachment ring and an antenna cover have been added to the basic vehicle since the earlier tests. Figure B-5 shows the various fin geometries which were examined. Fin sizes 1, 2, and 3 were designed to prevent flow attachment due to hypersonic wake closure, including a 10 deg angle of attack. Fins 4 and 5 would have attached flow at high Mach numbers, while Fin 6 would protrude into the free stream.

Figure B-4 includes a sketch of one of the two simulated temperature probes which were fabricated out of aluminum and placed, as shown, on the model.

Figure B-6 shows the solid foam drogue device which was used in several of the tests as a means of stabilization. Two additional parachute models were obtained from NASA-Langley personnel and tested. The first was a solid flat circular parachute having a 25. 4 cm (10 in) D_o and a drag coefficient of 0. 65; the second was of unknown vintage but resembled a high geometric porosity ring sail parachute with a diameter D_o of 30. 5 cm (12 in).

1) Placing a simulated temperature probe perpendicular to the vehicle centerline into the free stream at the base of the model did not appear to influence the resulting motion.

2) Using a solid drogue device with a single point attachment to the vehicle made the resulting model motion less stable. When the model was spun, a gyroscopic effect resulted. Using a three point attachment to the model resulted in a total angle of attack of ≈0 deg even when a high roll rate was introduced.

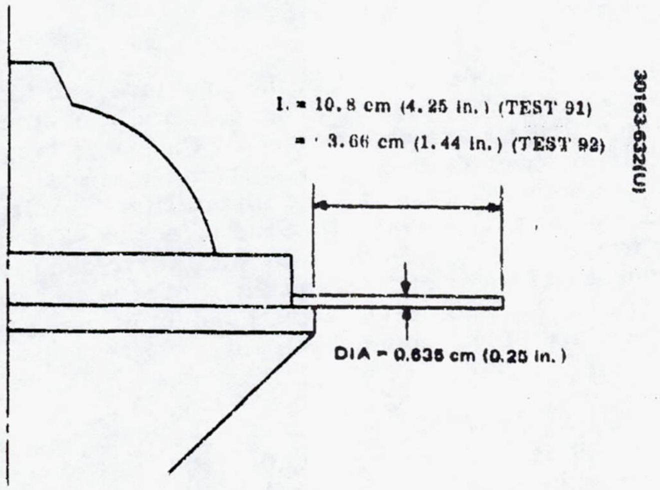

FIGURE B-4. SIMULATED TEMPERATURE PROBES

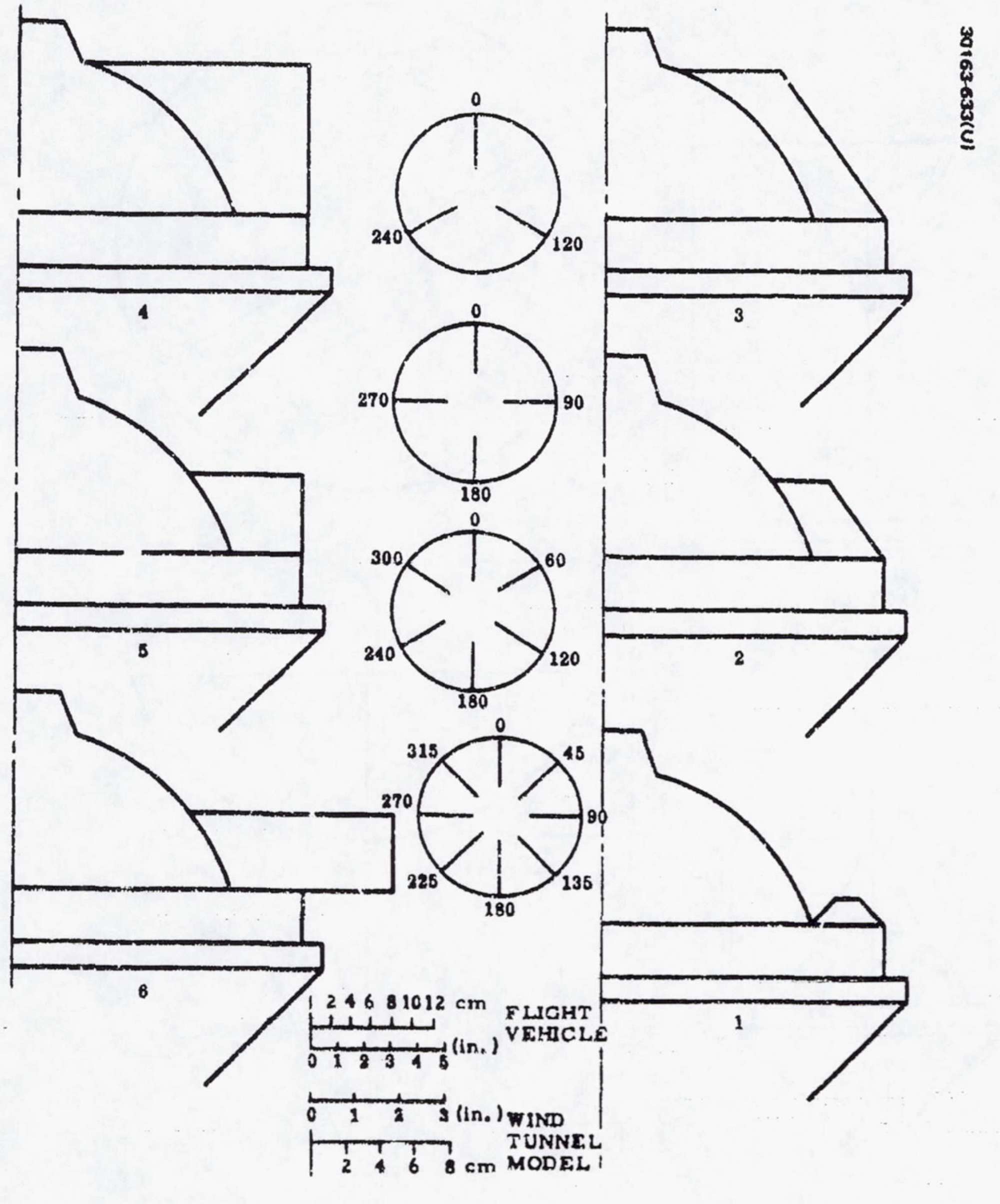

FIGURE B-5. FIXED FIN MODELS

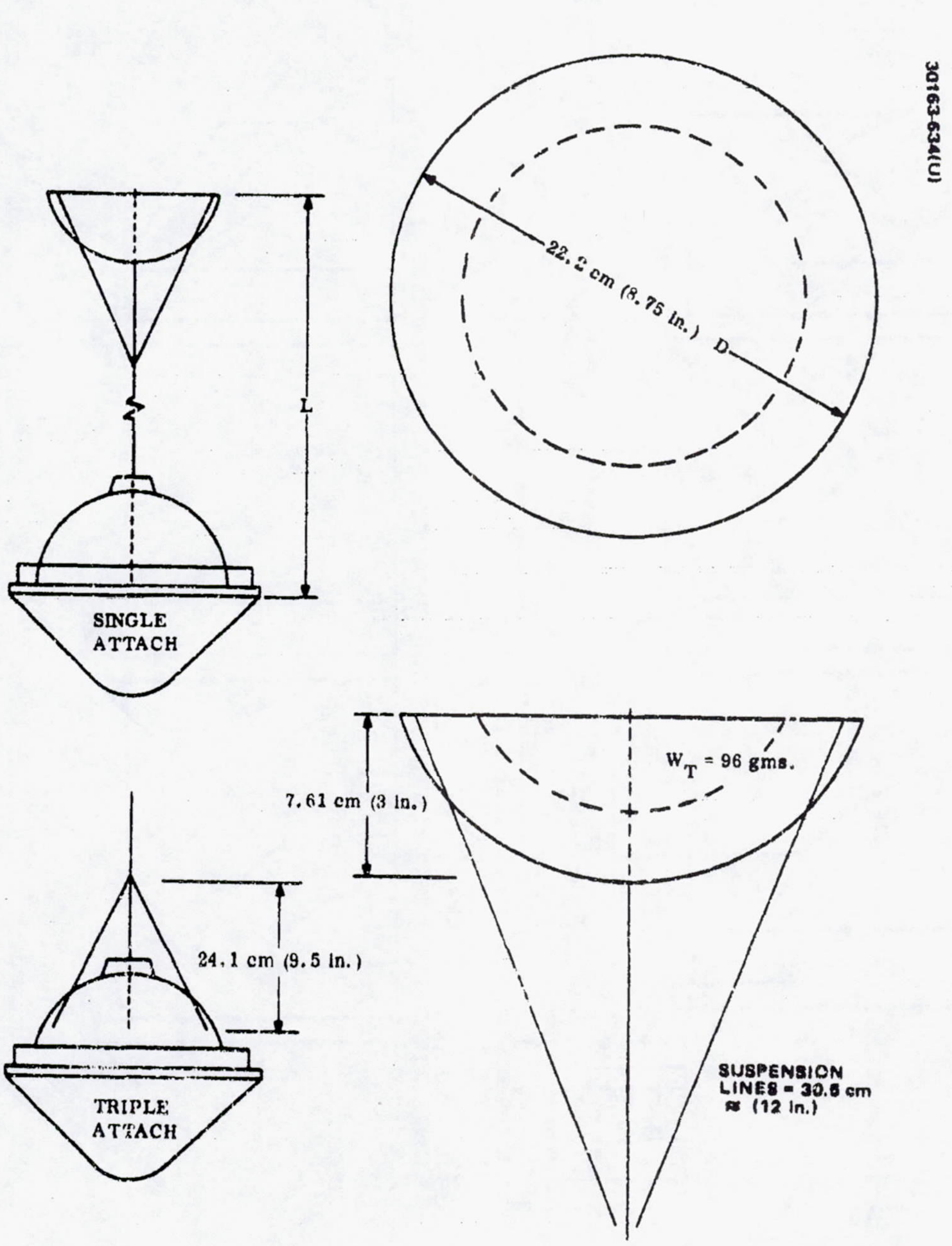

FIGURE B-6. SOLID FOAM DROGUE

3) Varying riser line lengths and, hence, relative position of the solid drogue behind the model from 230 to 620 percent of model base diameter did not appear to have a significant effect on resulting motion.

4) Fabric parachutes attached to the vehicle using a single point made the vehicle motion less stable than one of high geometric porosity.

5) The parachute with high geometric porosity attached to the model at three points 120 deg apart resulted in small total angle of attack osciallations (<5 deg) and was effective in damping roll rate.

6) No discernable change in the motion of tufts located on the forebody and at the maximum diameter to identify the state of the boundary layer was observed when increasing the tunnel velocity from ≈20 ft/sec up to ≈60 ft/sec.

7) Smoke visualization showed very dramatically the location of the reverse flow region in the wake of the model.

APPENDIX C. SMALL PROBE TEST ANALYSIS TECHNIQUES

INTRODUCTION

The sole intent of the subsonic stability tests is to observe stability and angle of attack behavior, and translate the results to the full scale small probe. The basic model used is that of Reference 1, wherein extensions and modifications have been made as required, the most important being to modify the model of Reference 1 to apply to the case of a vehicle in a condition (approximately) of "terminal fall".

Valuable data were obtained on the dynamic and spin behavior of a matrix of candidate probe configurations. Typical plots of data from the spin tunnel tests are presented in Figures C-1 and C-2. This information has been used in the overall design analysis of the small probe.

Specifically, for the spherically blunted configurations it was found that:

1) All had adequate static stability

2) Dynamic stability was highly dependent upon longitudinal c.g. position and spin rate

3) Probe engineering considerations regarding the c.g. range possible have shown c.g. position trades very favorably with reducing cone angle

4) With realistic c.g. ranges:

    a) The 55 deg configuration was either dynamically unstable at zero spin rate, or at best, stable for spin rates of about 30 rpm or less (model $X_{cg} = 6.35$ mm [0.25 in.] forward of maximum diameter). The corresponding spin rate for full scale is approximately 25 rpm.

    b) The 45 deg configuration was dynamically stable for all c.g. values tested at zero spin rate. Spin rates in the range 50 to 80 rpm (scaled values ≈ 40 to 65 rpm) produced neutral stability over the c.g. range tested (model c.g. from 1.52 cm to 3.04 cm [0.6 to 1.2 in.] ahead of maximum diameter.

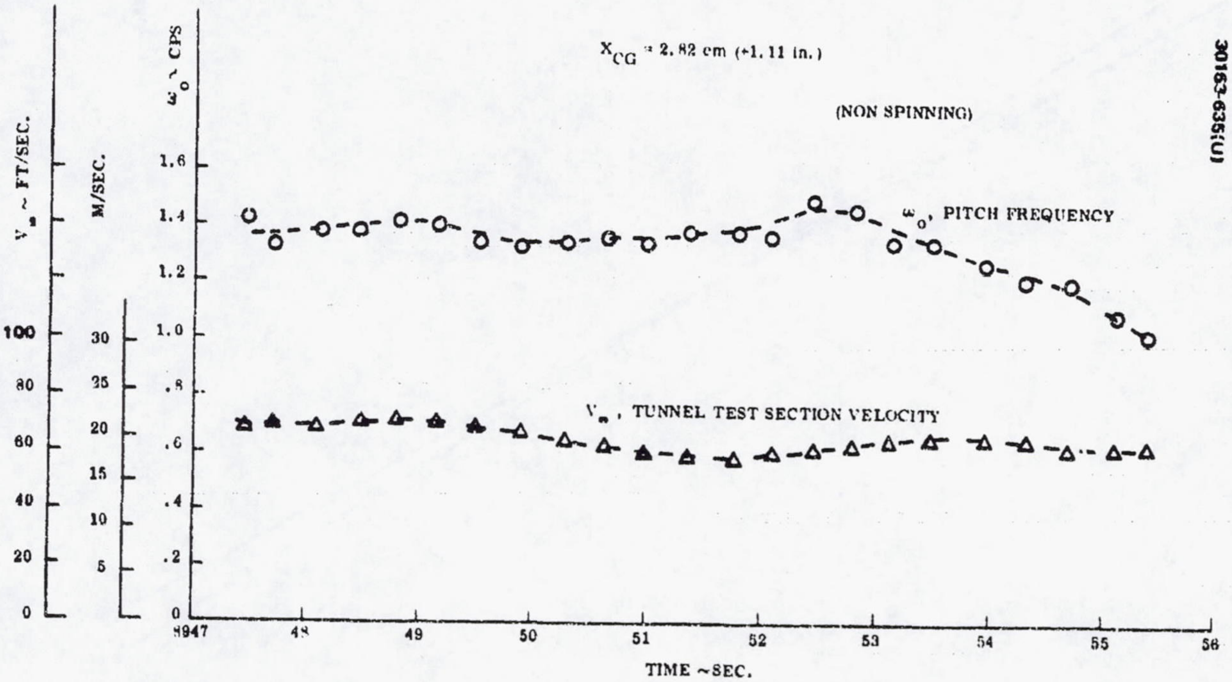

FIGURE C-1. TEST 61 MOTION DATA - STABILITY

30163-635(U)

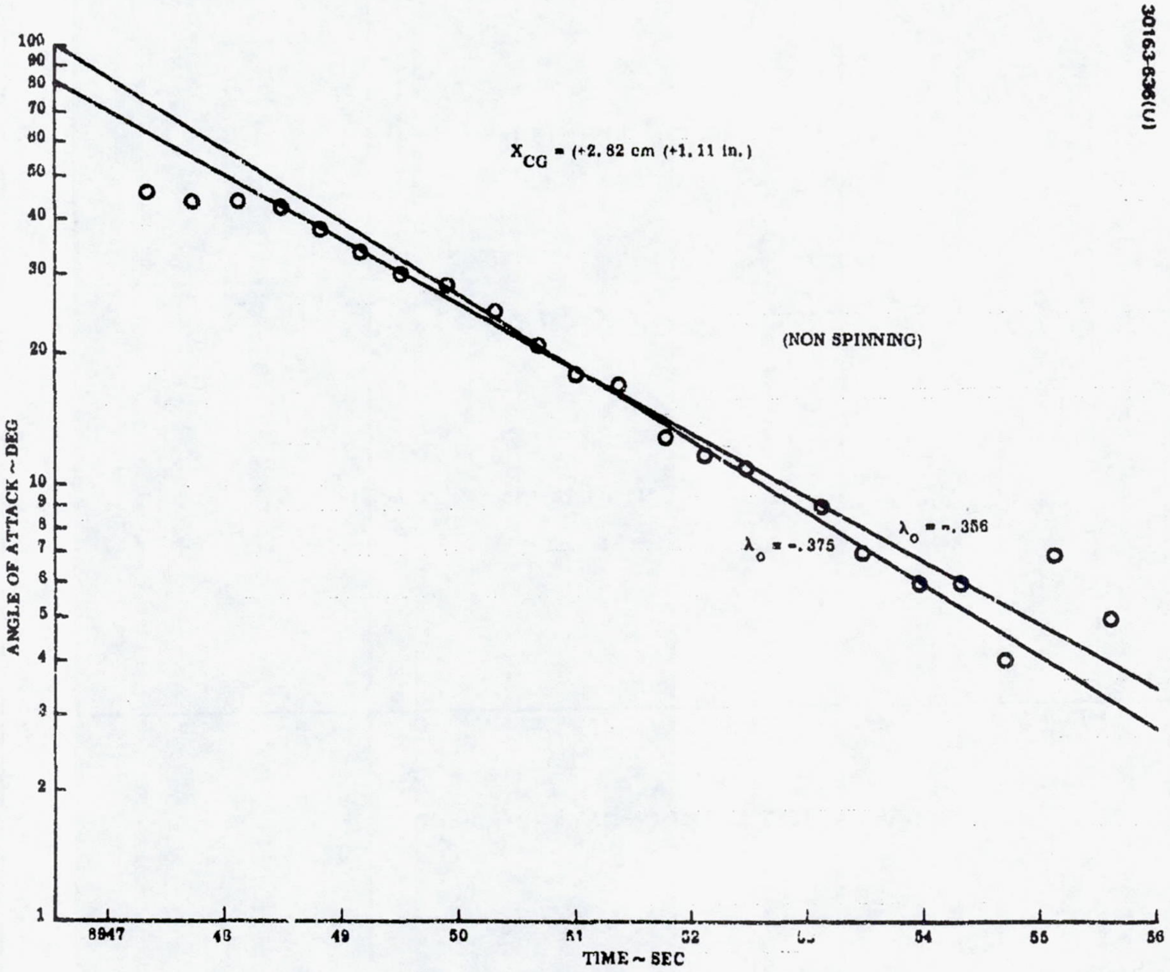

FIGURE C-2. TEST 61 MOTION DATA - ANGLE OF ATTACK

MOTION ANALYSIS

Stability observations of spin tunnel model tests can be extrapolated to conclusions about full scale stability if:

1) The models are inertially scaled versions of the full scale probe, (e.g., be built from the same materials with all dimensions linearly scaled).

2) Full scale spin rates are scaled from the model spin rate as the inverse square root of the length ratio, i.e., when

$$P_{F.S.} = P_{model}\sqrt{\frac{\text{model diameter}}{\text{F.S. diameter}}}$$

3) The model and full scale probe lift force derivative (C_{L_α}) and pitch damping derivative (C_{m_q}) are the same. The coefficients will be the same if:

   a) The model and full scale probe bodies are the same shape

   b) Mach number and Reynolds number are in the same range as will be expected in the Venus atmosphere

If all these conditions are met, then the aerodynamic coefficients need not be determined at all. Observation of dynamic stability in a test would immediately imply full scale dynamic stability at a full scale spin rate given by the spin rate scaling equation. For nonspinning models there would, of course, be a direct correspondence, not requiring any scaling calculations.

Finally, static stability would be common between model and full scale probe provided simply that the two bodies were of identical outer shape, had geometric scaled c.g. locations, and that the static pitching moment slope (C_{m_α}) were unaffected by CO_2.

MOTION MODEL SUMMARY

General observations based on the analysis of the spin tunnel film data are summarized below:

1) Virtually all of the configurations tested had ample static stability (as predicted).

2) The 55 deg cone forebody models all featured markedly worse dynamic stability than the 45 deg cone forebody models.

3) Longitudinal c.g. position had a profound effect on dynamic stability for all configurations with conical forebodies, regardless of afterbody shape, and regardless of whether fins were used.

4) Large fins (projecting into the airstream) had a large effect on dynamic stability, but a small effect on static stability (in both cases an improvement).

5) Large fins, as expected, had a very large effect on roll-damping characteristics.

6) The effect of spin rate tended to damp the high-frequency mode and undamp the low-frequency mode (as predicted). The magnitude of the effect, however, was somewhat larger than predicted. For the 55 deg configuration with forward-most c.g. location, spin rates less than 40 rpm were required to maintain dynamic stability. In the worst c.g. positions, however, the model tumbled even at zero spin rate. Large fins corrected the instability for the intermediate c.g. position -1.27 cm (-0.5 in.) but not for the aft-most c.g. -2.95 cm (-1.16 in.). For the 45 deg configuration, dynamic instability or larger than acceptable limit cycle motion occurred for spin rates in the general range between approximately 50 to 80 rpm, depending upon longitudinal c.g. location. This scales to a spin rate range of approximately 40 to 65 rpm, full scale, assuming inertial similarity.

It is important to note that longitudinal c.g. range tested in each of the blunted conical forebody configurations corresponded to a (scaled) range which was truly representative of the actual c.g. values realizable in the associated full scale configurations.

Thus the preference for the 45 deg forebody over the 51.5 or the 55 deg forebodies reflects primarily the fact that it is possible to achieve more forward c.g. positions the shallower the cone angle. The shallower cone angle is also more dynamically stable because changes in aerodynamic lift curve slope, C_{L_α}, with cone angle tend to improve stability.

DATA EXTRACTION FROM FILMS

Velocity and time are recorded digitally on film. Pitch and body frequency is determined from the oscillation period. Angle of attack amplitude is estimated visually, using the background printed reference stripes on the inside of the test section and the model geometric features as references.

For non-zero spin rates, the above information, except ω_0, is recorded, and in addition, the following:

f = body frequency (invariably the low-frequency, and occasionally, in addition, the high-frequency)

p = spin rate

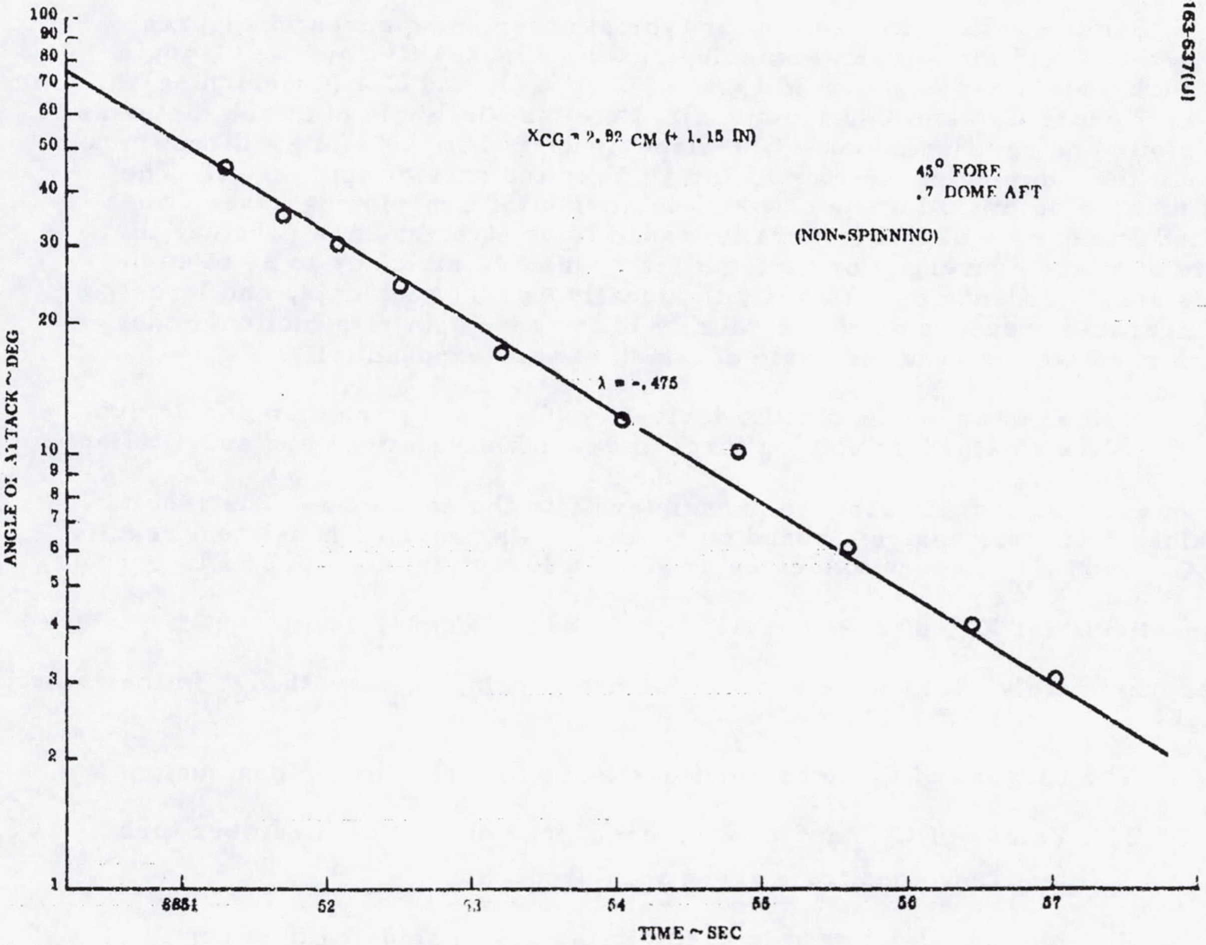

FIGURE C-3. TEST 57 MOTION DATA

30163-637(U)

Spin rate is determined by timing roll periods using the reference stripes on the model, and "eyeball" accounting for biases due to vehicle lateral translation with respect to the camera.

Sample results are shown for typical nonspinning cases in Figures C-1 and C-5 and for a typical spinning case in Figures C-7 and C-9. Angle of attack histories are shown in Figures C-2, C-3, and C-4 (nonspinning) and in Figures C-6 and C-8 (spinning). Note that the angle of attack histories are plotted on semilog paper. The slope measured is therefore a direct measure of the damping parameter λ_o (or $\lambda_o \pm \Delta\lambda$ in the case of spin tests). The fact that the estimated angle of attack histories for nonspinning cases, when plotted on semilog paper, generally tended to be straight lines (whether the angle of attack converged or diverged) for angles of attack up to 30 to 40 deg lends some credence to the ability to visually extract such data, and lends considerable credence as to the validity of the zero spin rate motion model which predicts the dynamic angle of attack to vary exponentially.

Values of aerodynamic lift derivative (C_{L_α}) and pitch damping derivative C_{m_q} are obtained by solving force and moment equations and substituting known and spin tunnel observed parameters into the equations. The results obtained from this analysis based on several tests provided consistent results for C_{L_α} and C_{m_q}, mean values being -0.17 ± 20 percent and -0.22 ± 15 percent, respectively for X_{cg} of 2.92 cm (1.15 in.) and 2.83 cm (1.11 in.). C_{m_q} values of approximately -0.13 were derived for nonspinning cases with X_{cg} in the same range.

The success of these calculations leads to the following conclusions:

1) Values of C_{L_α} and C_{m_q} at conditions of low Mach number turbulent flow conditions agree with predictions.

2) Motion model used to predict stability in spinning cases is in error.

The most likely sources of error in the spinning motion equations are as follows:

1) Existence of low subsonic magnus effects

2) Insufficient validity in representing the static pitching moment coefficient derivative (C_{m_α}) as a constant (e.g., nonlinear effects at large amplitude motion, hysteresis effects, etc.)

3) Insufficient validity in representing the pitch-damping derivative (C_{m_q}) independent of motion amplitude and motion character (e.g., planar versus circular).

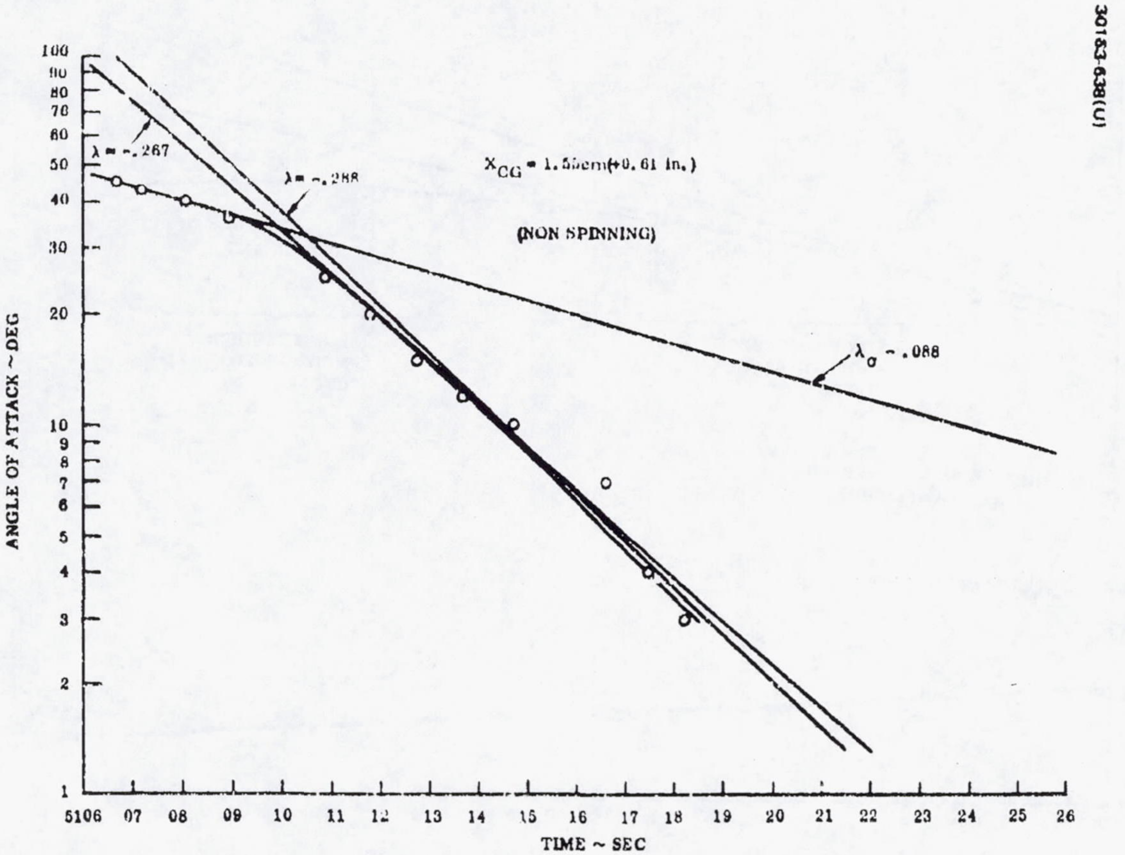

FIGURE C-4. TEST 20 MOTION DATA - ANGLE OF ATTACK (NON SPINNING)

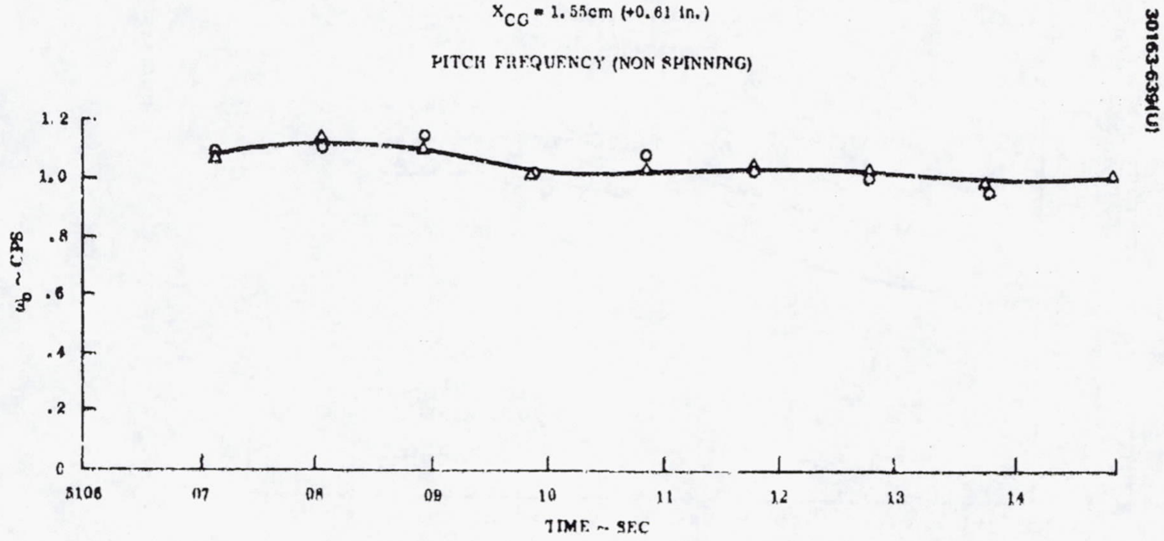

FIGURE C-5. TEST 20 MOTION DATA - PITCH FREQUENCY (NON SPINNING)

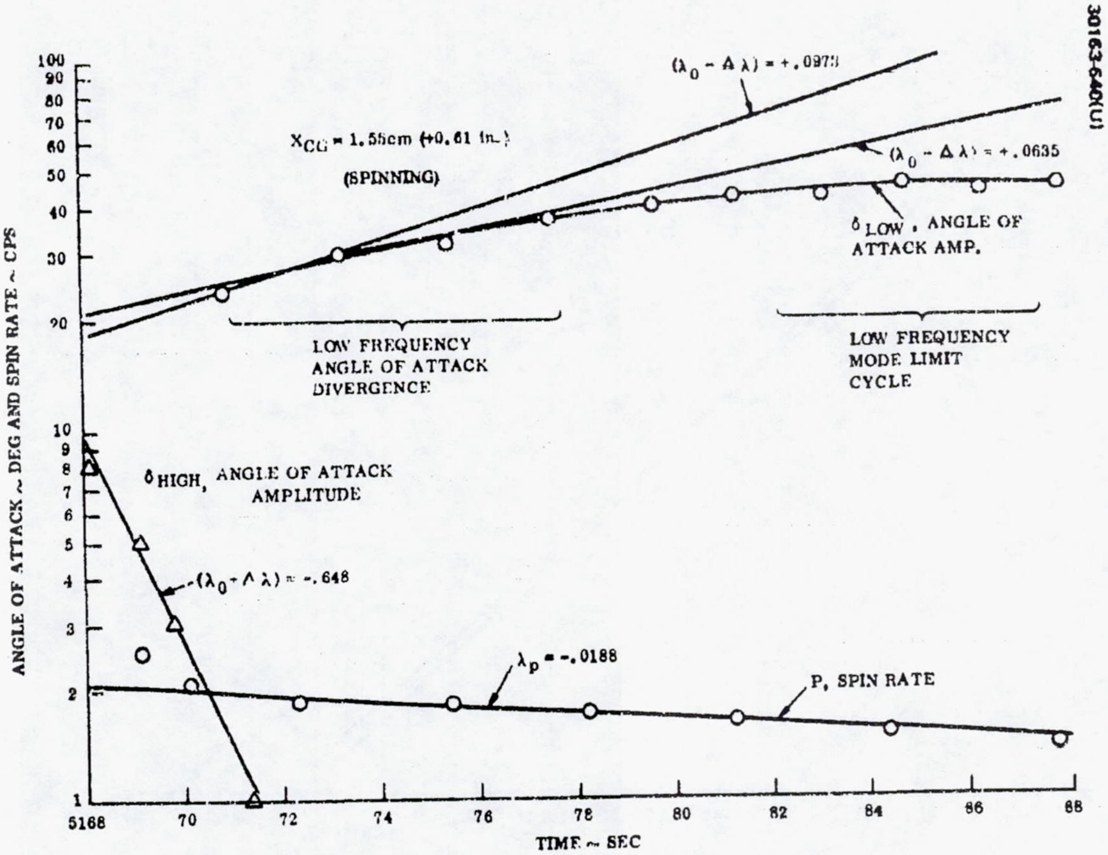

FIGURE C-6. TEST 20 MOTION DATA - ANGLE OF ATTACK AND SPIN RATES

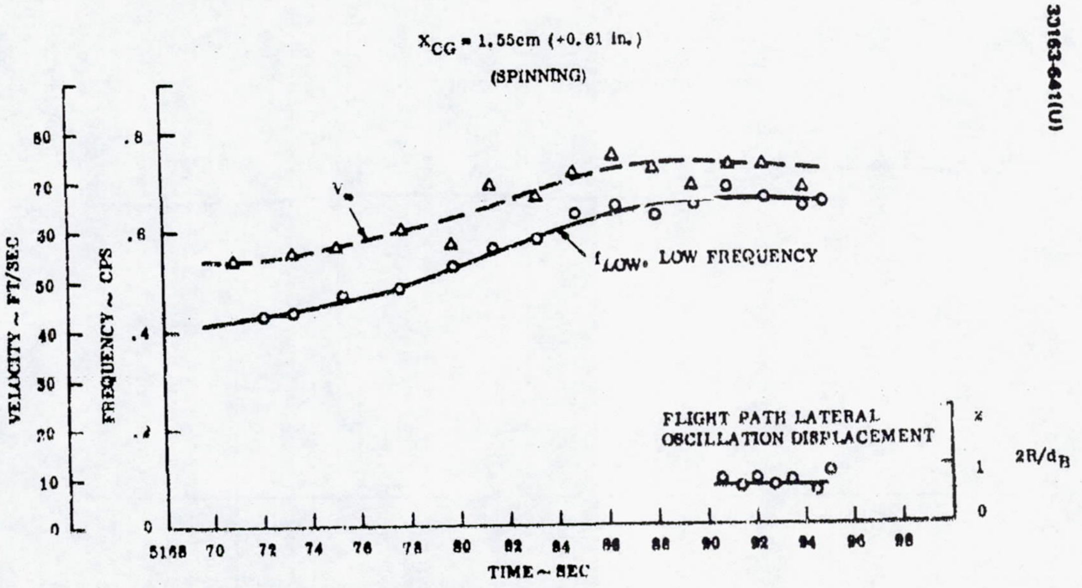

FIGURE C-7. TEST 20 MOTION DATA - STABILITY

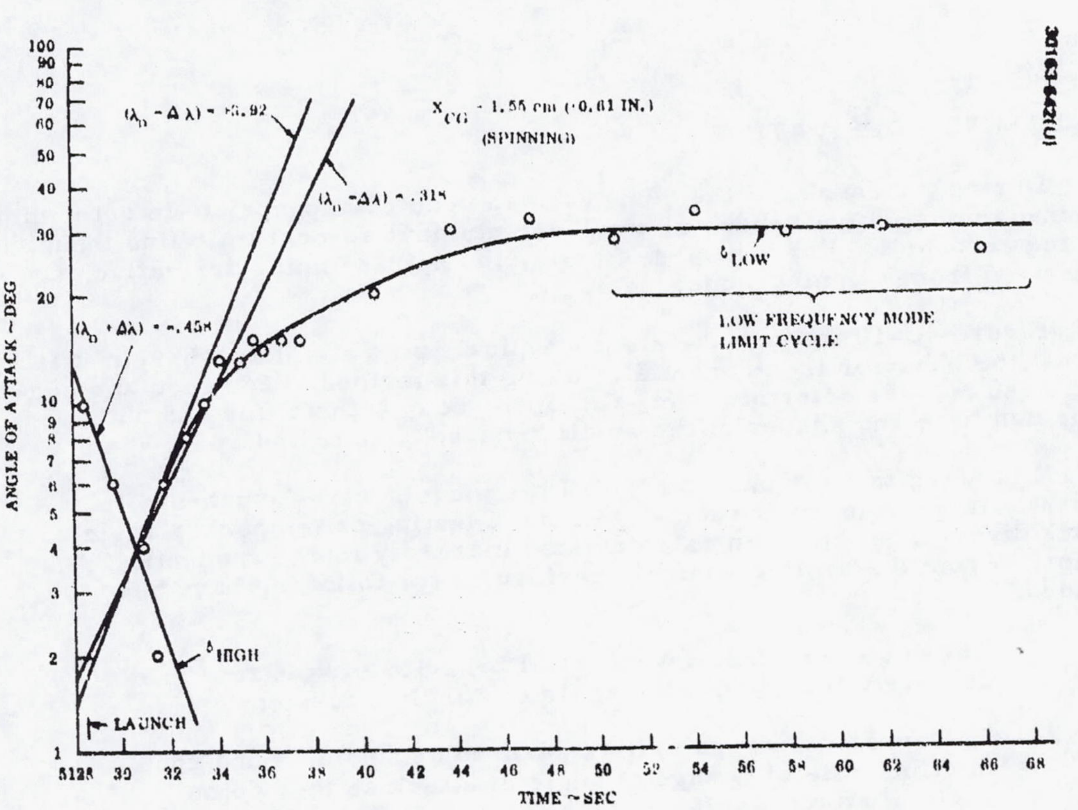

FIGURE C-8. TEST 20 MOTION DATA - ANGLE OF ATTACK

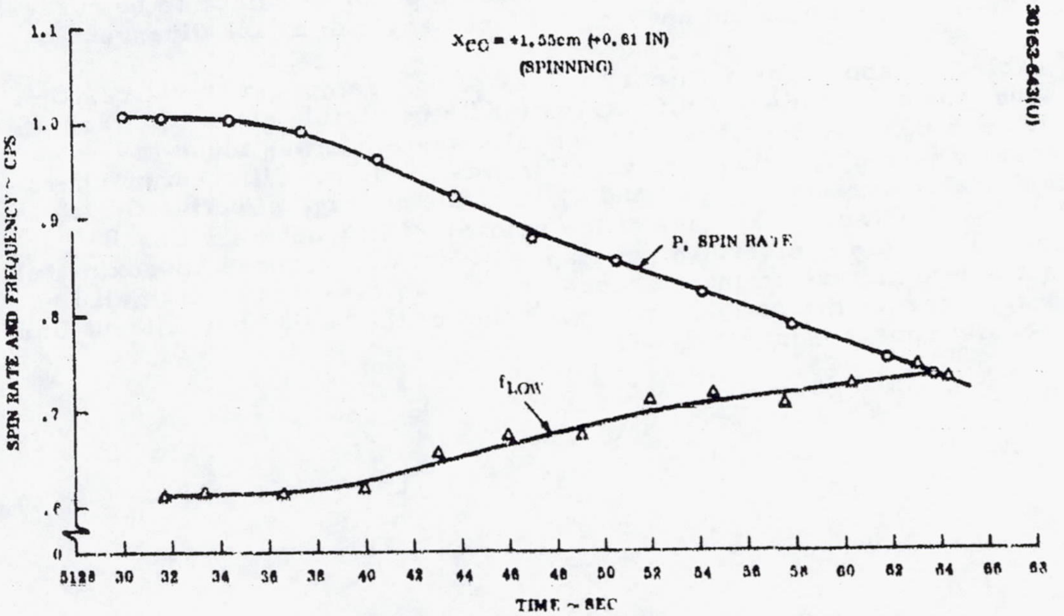

FIGURE C-9. TEST 20 MOTION DATA - SPIN RATE AND FREQUENCY

SPIN-DAMPING DERIVATIVE

During the course of the design it was deemed appropriate to determine the spin-damping effectiveness of small longitudinal aerodynamic fins mounted aft of the aeroshell. For a series of tests, the spin-damping derivative, C_{l_p} was derived from spinning model tests.

Figures C-10 through C-12 show typical spin rate plots wherein it is seen that the behavior is exponential. Using this method, very good and consistent results were determined for C_{l_p} of the body without fins and with various numbers and shapes of the small "shaded" fins tested.

It is noted that for cases in which the models were launched with sufficiently large spin rates such as to induce lasting or temporary angle of attack divergence, the spin rate deviated markedly from exponential behavior. From the limited analysis performed the following have been concluded:

1) The deviations from exponential behavior of spin rate are definitely linked with the angle of attack excursions.

2) The observed irregularities seem to depend as much upon the time rate of change of angle of attack as they do on angle of attack itself.

While this behavior is presently not understood, it may be regarded primarily as an academic curiosity rather than a problem, since to be successful, the full scale probe should not feature large angle of attack divergences.

Table C-1 shows the summary values of roll damping derivative, C_{l_p}. In all cases, the data were taken from tests with negligible angle of attack amplitude, and represent averages of repeated tests. It was found in comparing cases where a common configuration was used, but different numbers of symmetrically-arranged fins (3 and 4), that the average effective C_{l_p}/fin was relatively constant regardless of the number of fins until six fins were used. With this number, the average C_{l_p}/fin was reduced approximately 20 percent due to mutual fin interference. In general these small fins significantly improve the roll damping over that of the basic body without fins. This is readily apparent in Table C-1.

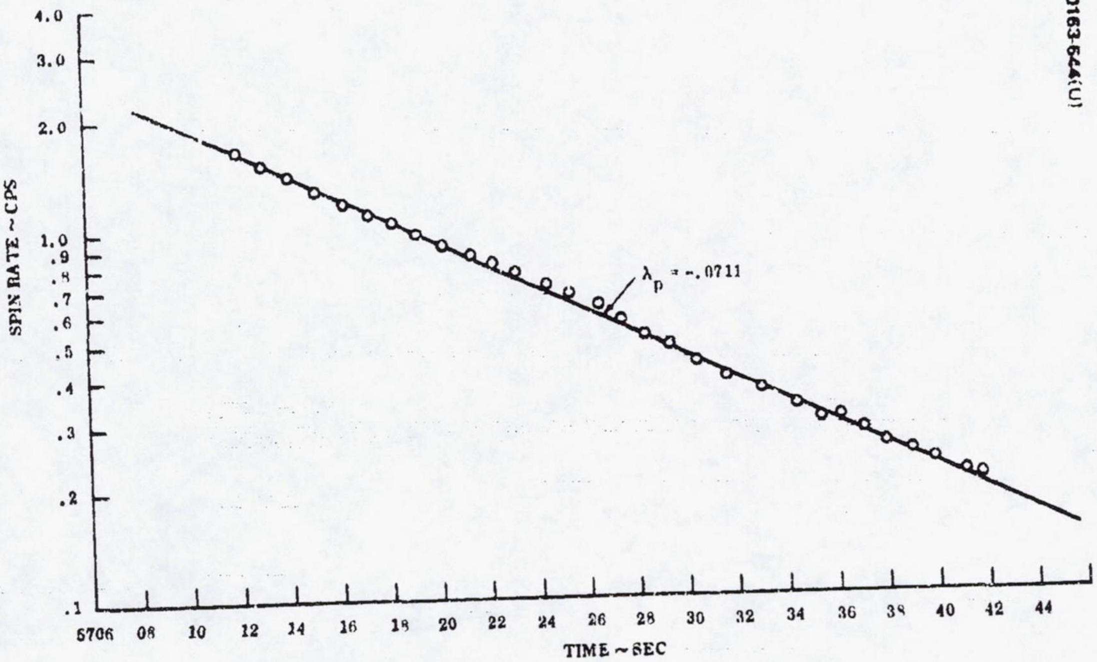

30163-644(U)

FIGURE C-10. SPIN RATE HISTORIES - FIN CONFIGURATION 5 (SIX FINS)

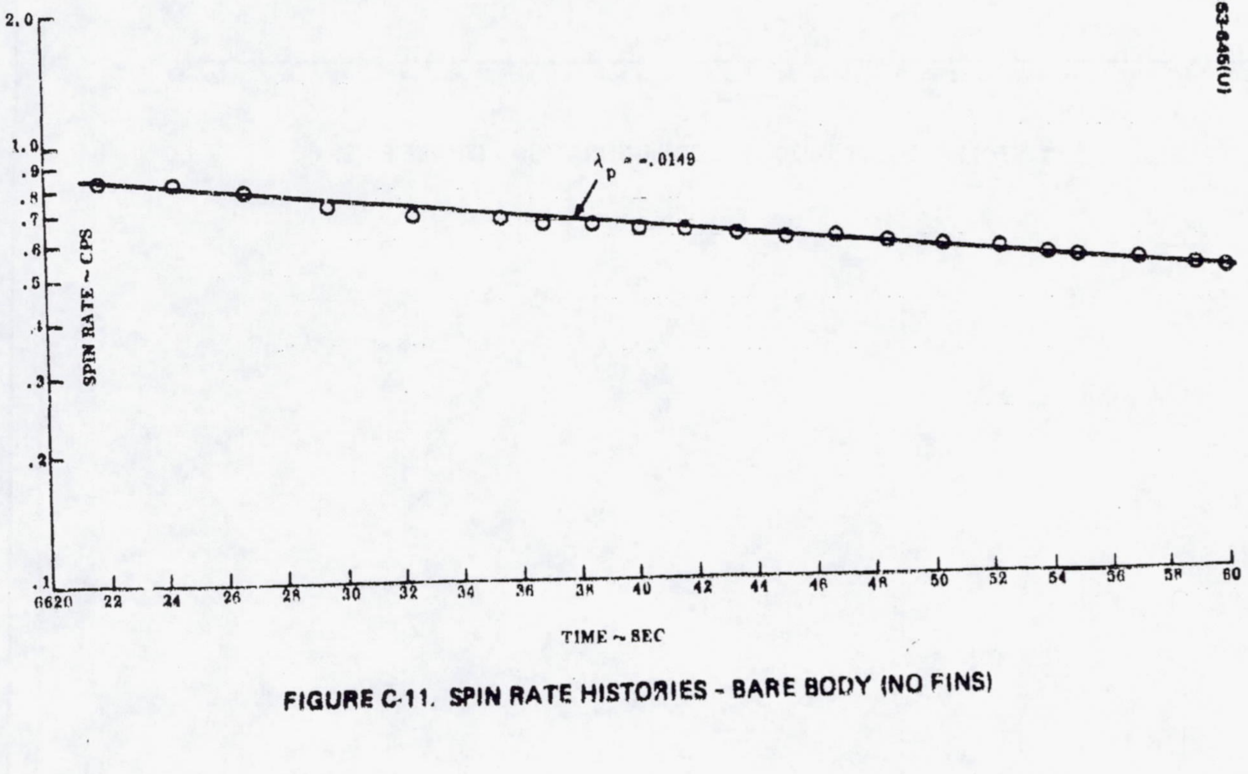

30163-646(U)

FIGURE C-11. SPIN RATE HISTORIES - BARE BODY (NO FINS)

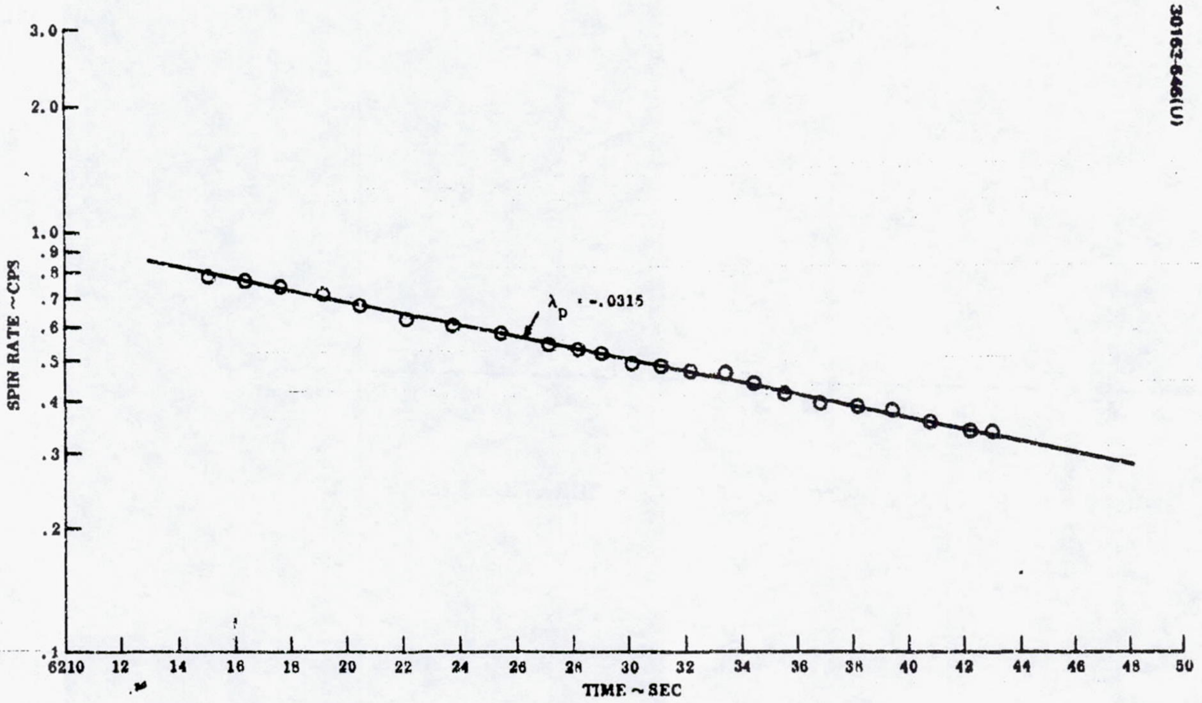

FIGURE C-12. SPIN RATE HISTORIES - FIN CONFIGURATION 2 (THREE FINS)

30163-646(U)

TABLE C-1. SUMMARY ROLL DAMPING, C_{l_p}, RESULTS

Fin Configuration	Number of Fins	C_{l_p} Fin	Total C_{l_p} (Body and Fins)
6 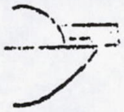	2	-0.102	
	3	-0.016	
	4	-0.012	-0.0520
	6	-0.0119	-0.0752
4 	3	-0.0059	
	4	-0.0080	-0.0356
	6	-0.0063	-0.0414
5 	3	-0.0034	
	4	-0.0032	-0.0168
	6	-0.0025	-0.0190
3 	3	-0.0032	
	4	-0.0032	-0.0166
	6	-0.0024	-0.0184
2 	3	-0.00194	
	4	-0.00178	-0.0109
	6	-0.00134	-0.0127
No fins (bare body)			-0.00375
Barn door 	4	-0.085	-0.34

REFERENCES

1. R. L. Nelson, "The Motions of Rolling Symmetrical Missiles Referred to a Body-Axis System," NACA Tech. Note 3737, November, 1956.

APPENDIX D. SMALL PROBE AMES WATER TUNNEL TESTS

INTRODUCTION

A series of drop tests were conducted at the NASA-Ames Water Tank Facility to evaluate the qualitative stability behavior of a small probe model. The ~~tests~~ were planned to provide initial configuration screening prior to tests at the NASA Langley Subsonic Spin Tunnel, although due to scheduling constraints the tests were run almost concurrently. Since the wind tunnel tests were considered more representative of flight conditions encountered in Venusian terminal flight environment the data reduction and subsequent analysis was concentrated on that data.

MODELS

A sketch of the water tank models is shown in Figure D-1. They consist of 45, 55, 65 deg, and spherical forebodies with 0.7, 0.9, full dome, and 45 deg conical afterbodies. Duplicate pieces were made using stainless steel and magnesium to permit variations in c.g. position and in terminal velocity with the same external geometry. Provisions for a "heavy metal" slug was also made to permit small variations in c.g. location. Model base diameters were 2 in. with nose radii equal to 1 in.. For comparison purposes between the various configurations, the c.g. location was placed at, or as close as possible, to the base plane of the forebody.

TEST RESULTS

General trends observed include that: 1) going from a large to a small dome results in a destabilizing influence and a higher angle of attack amplitude, 2) increasing cone angle from 45 to 65 deg results in decreased stability. It should be noted, however, that this trend may be partially due to the aft c.g. travel encountered due to physical mass property limitations on the models tested. That is, the c.g. plane is slightly ahead of the base plane for the 45 deg, slightly, aft of the base plane for the 55 deg, and further aft for the 65 deg, 3) in general, heavier weight models were more stable than lighter weight models. Reference 1 would

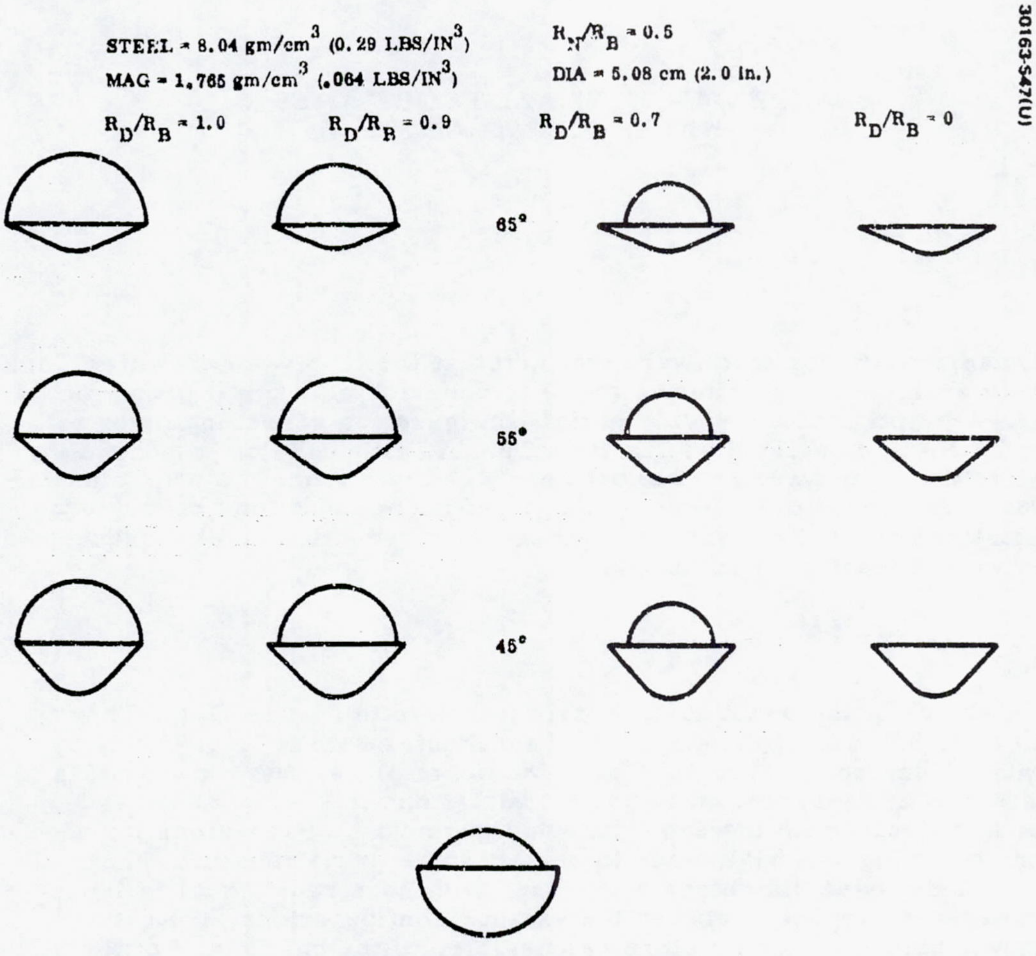

FIGURE D-1. TEST MATRIX

indicate this effect is due to a Reynolds Number variation from a laminar to a turbulent flow regime. Additional unpublished data obtained by Reference 1 indicates transition occurs between 3.7×10 and 7.7×10 for blunt conical bodies in this flow environment; 4) aft center of gravity travel will result in decreased stability. With far aft locations the models were stable at 180 deg angle of attack even though they were launched initially at 0 deg angle of attack.

Coefficients result from initial position measurements and computer matching of resultant trajectories. Attempts to obtain velocity and hence drag coefficients by straight measurements introduced large uncertainties in the coefficients (± 50 percent) and for that reason are not included here.

General trends observed in the water drop tests agree with those obtained in the wind tunnel tests; namely, smaller cone angles show better stability than larger angles for the range of allowable c.g. positions; forward movement in c.g. results in better stability. The sensitivity to afterbody size however was not observed in the wind tunnel tests. No apparent motion changes occurred between the 0.7 and 0.9 afterbody. This effect may be dependent on the Reynolds Number which was an order of magnitude higher for the wind tunnel than that of the water tank.

REFERENCES

1. J. J. Hurt, "Contract NAS 2-7250 Reynolds Number Effect in Water Drop Tests." NASA Ames letter to Hughes Aircraft/GE (from T. Canning) 7 December 1972.

APPENDIX E. AUXILIARY STABILIZATION – SMALL PROBE

INTRODUCTION

Prior to the Atlas/Centaur booster decision, several options were considered to enhance subsonic terminal stability of the small probe. As shown in Appendix C, high roll rates resulted in large angle of attack build-up in terminal flight; hence fins were added to the baseline small probe to provide roll damping. Two additional auxiliary stabilization devices were considered for the small probe, namely a rigid drogue device and a drogue parachute. Either of these would be deployed at high subsonic Mach Numbers (≈0.9) and remain attached in the vehicle wake to impact. A summary of the analysis performed on each of the options will be discussed. In addition, wind tunnel test results, using both rigid and fabric drogue devices, will be reviewed.

GENERAL GUIDELINES

Several general guidelines were applied to the stabilization devices under consideration: 1) the drag area of the vehicle plus the drag device should be approximately the same as the current baseline design so as not to alter the descent time and increase power requirements (battery weight), 2) the device should be deployed at high subsonic Mach numbers where potential instabilities would initiate angle of attack diversions, 3) the device should survive to the Venusian surface and therefore withstand a ≈810°K (1000°F) temperature environment, and 4) the design must not degrade antenna performance either during the initial entry or after deployment.

EFFECT ON PROBE DESIGN

Using these guidelines, the changes permitted on the small probe vehicle design were assessed. If a stabilization device is attached to enhance subsonic stability, the required probe static margin may be reduced and the fixed fins may be eliminated. Decreased static margin may be used to advantage by reducing the base diameter, thus reducing the bus installational problems and decreasing the basic probe weight. Reducing the diameter from 61 cm (24 in.) to 50.9 cm (22 in.) saves 1.125 kg (2.5 lb) in heat shield and structure, and eliminating the fins provides another 0.272 kg (0.6 lb), making a total of 1.41 kg (3.1 lb) that can be applied to the weight of the new stabilization device subsystem. It should be noted that the reduced static margin

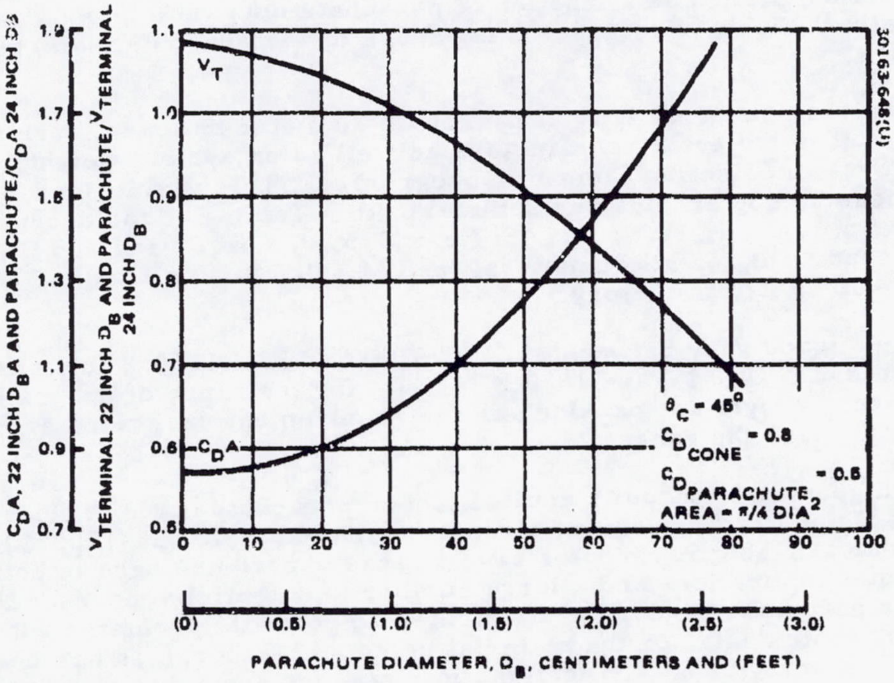

FIGURE E-1. EFFECT OF PARACHUTE ON SMALL PROBE DRAG AREA AND TERMINAL VELOCITY will not degrade supersonic performance since the c.g. will still be at, or ahead of, the base plane and the most forward center of pressure (at any Mach number) will be aft 15 percent of D_B.

DROGUE PARACHUTE

A drogue parachute has been designed to meet the stabilization device guidelines. Figure E-1 shows the drag area and terminal velocity for a 50.9 cm (22 in.) D_B probe plus parachute divided by the corresponding 61 cm (24 in.) D_B values plotted as a function of parachute plus vehicle equal to the current baseline. From the figures this occurs for a parachute diameter of 30.5 cm (1 ft).

To evaluate the sensitivity of parachute diameter on loads, terminal velocity, and other trajectory parameters as well as on system weight, the Retardation System Selection Computer program RESSEP was utilized. Results of these computer runs are summarized in Table E-1 for drogue diameters of 15.3, 24.4, 30.5, and 45.7 cm (0.5, 0.8, 1.0, and 1.5 ft). Deployment conditions for all diameters were M = 0.9 at an altitude of 67 km based on $\gamma_e = 90°$ entry trajectory.

Opening loads vary between 31 N (6.9 lb) and 236 N (63.8 lb), snatch loads between 852 N (190 lb) and 1980 N (441 lb) for the range of drogue diameters examined. Weight and packing volume requirement variations are relatively small over the range.

A high geometric porosity conical ribbon parachute made of fiberglass which is capable of 10 to 15 percent strength retention at 922°K (1200°F) was selected. Conical ribbon parachutes have a large experience base in both pilot and drogue applications and a large number of potential vendors. Inquiries with a parachute vendor have indicated no potential problems with either the parachute design or the material selected. Fiberglass has been used extensively in high heat applications in riser line and vehicle harness shrouds, but not in complete parachute fabrication.

A mortar system is proposed for deployment, and the space available (bounded by the payload internally and the probe expansion cone externally) allows for a mortar case 5.71 cm diameter by 15.25 cm long (2.25 in. diameter by 6 in. long) (firing aft) or 10.19 cm diameter by 50.8 cm long (4 in. diameter by 2 in. long) (firing radially). This allows 296 cm^3 (18 in^3) packing volume for the parachute and lines. The aft firing mortar is selected as being the most practical shape for packaging the parachute, although the direction of ejection will produce a greater disturbance on probe motion (Figure E-2). Total transient angle of attack excursion will be below 15 deg, however. The total subsystem weight is 1.815 kg (4.0 lb); hence, allowing for the 1.41 kg (3.1 lb) savings on the aeroshell, the total probe penalty is 0.408 kg (0.9 lb). A summary weight statement of the parachute subsystem is provided in Table E-2.

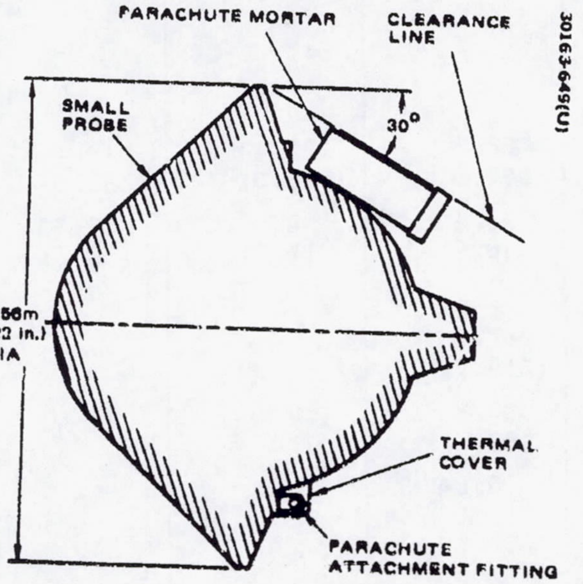

FIGURE E-2. PARACHUTE CONCEPT

TABLE E-1. RESSEP ANALYSIS OF SMALL PROBE PARACHUTE SYSTEMS

INPUT				
D_o drogue, m (ft)	0.15 (0.5)	0.24 (0.8)	0.30 (1.0)	0.46 (1.5)
OUTPUT				
Deployment				
Altitude, m (kft)	67.0 (219.8)			
Q, kg/m^2 (lb/ft^2)	443.0 (90.66)			
Mach	0.9			
γ, deg (down from horizontal)	89.1			
Loads				
Snatch, kg (lb)	86.3 (190.0)	107.1 (236.0)	119.4 (263.0)	200.2 (441.0)
Open, kg (lb)	3.1 (6.9)	8.0 (17.7)	12.53 (27.6)	29.0 (63.8)
Full open				
Altitude, m (kft)	67.0 (219.7)			
Q, kg/m^2 (lb/ft^2)	400.7 (82.0)			
Mach	0.84			
γ, deg (down from horizontal)	89.92			
Terminal				
Altitude, m (kft)	63.5 (208.3)	63.7 (209.0)	63.8 (209.4)	64.3 (210.9)
Velocity, m/sec (ft/sec)	94.7 (310.7)	93.0 (305.0)	91.4 (300.0)	86.9 (28.5)
V eject, m/sec (ft/sec)	21.7 (71.3)			23.9 (78.5)
Time on mortar, (sec)	0.03	0.03	0.04	0.04
F_{avg} on mortar, N (lb)	24.9 (5.6)	33.4 (7.5)	38.3 (8.6)	49.5 (11.12)
Weight R/S, kg (lb)	1.03 (2.27)	1.09 (2.40)	1.12) (2.47)	1.21 (2.67)
Pack volume, m^3 (ft^3)	0.00012 (0.0043)	0.00019 (0.0067)	0.0024 (0.0084)	0.00035 (0.0123)

TABLE E-2. PARACHUTE CONCEPT WEIGHT STATEMENT

Item	Weight, g	Weight, lb
Parachute	136.0	0.3
Swivel	90.8	0.2
Bridle	181.6	0.4
Riser line	136.0	0.3
Mortar	227.0	0.5
Charge	90.8	0.2
Structure	136.0	0.3
Harness	90.8	0.2
Ballast	272.0	0.6
P/V electronics	454.0	1.0
Subsystem weight	1.816	4.0
Aeroshell reduction	1.407	3.1
Probe increase	408.6	0.9

RIGID DROGUE

The stabilization device for this concept was a rigid drogue which would be carried as part of the aft cover until it is deployed. It could be used in either an inverted mode or upright as shown below.

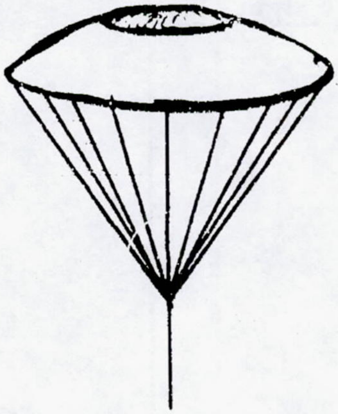

Deployment of the rigid drogue required that it be ejected through the reverse dynamic pressure region extending behind the vehicle approximately two base diameters. Using the Aerothermodynamic Lab's Cover Ejection Computer Program (COVER), the required ejection velocity was found to be 12.7 m/sec (41.7 ft/sec) (see Figure E-3). A safety factor of 50 percent is commonly used to compensate for inaccuracies in prediction, mechanical design performance, and atmospheric modeling as well as to provide growth into more severe deployment environments due to weight or trajectory changes. For preliminary design therefore, it was recommended that a 18.3 m/sec (60 ft/sec) ejection velocity be used.

From a vehicle design standpoint, the two main problems were the choice of material for the drogue and the method of deployment to penetrate the wake. Material selected must be radio transparent since deployed it would be positioned over the antenna, and it must survive a temperature of approximately 494.3°C (1000°F); the most promising candidate was ADL 10, a quartz fiber/silicone composite. Two methods of deployment were considered. Figure E-4 shows the drogue attached by a ring which contains a linear explosive charge. The ring must be of rigid (heavy) construction to contain the explosion and the high shock load imparted to the probe. The selected deployment concept is shown in Figure E-5. Here the drogue was mounted to a metallic aft cover, the subassembly being ejected by three pyrotechnic thrusters. GE has extensive flight experience using similar ejection devices in recovery systems on a number of major programs. The drogue was then mechanically unlatched from the rest of the aft cover. A large percentage of the extra weight for this design was due to the structure required to react the load from the thrusters. Total subsystem weight was 2.220 kg (4.9 lb) (see Table E-3) and, allowing for the 1.41 kg (3.1 lb) aeroshell savings, the total probe penalty is 0.818 kg (1.8 lb).

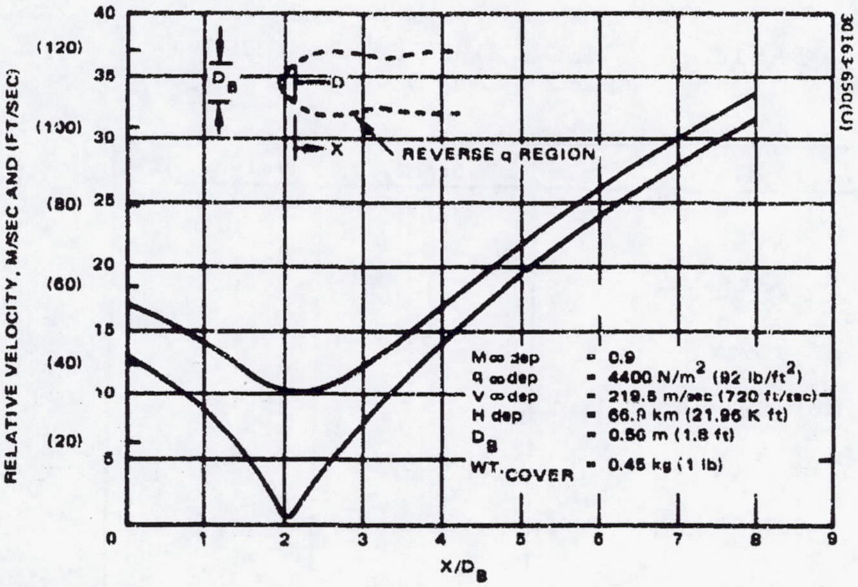

FIGURE E-3. SMALL PROBE AFT COVER SEPARATION HISTORY

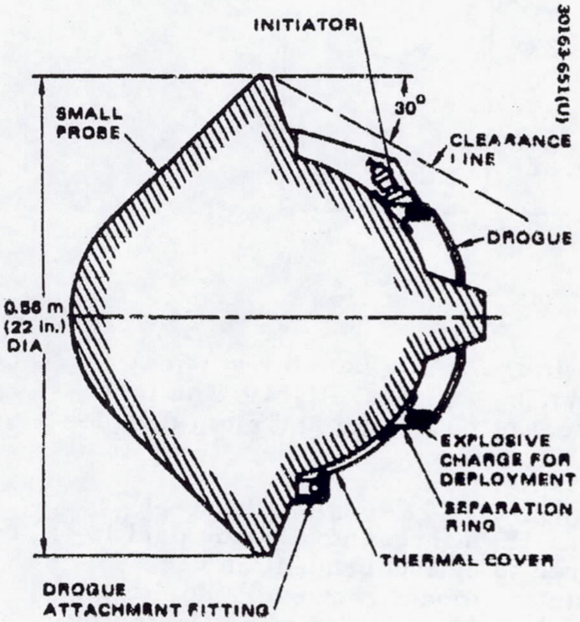

FIGURE E-4. DROGUE CONCEPT A

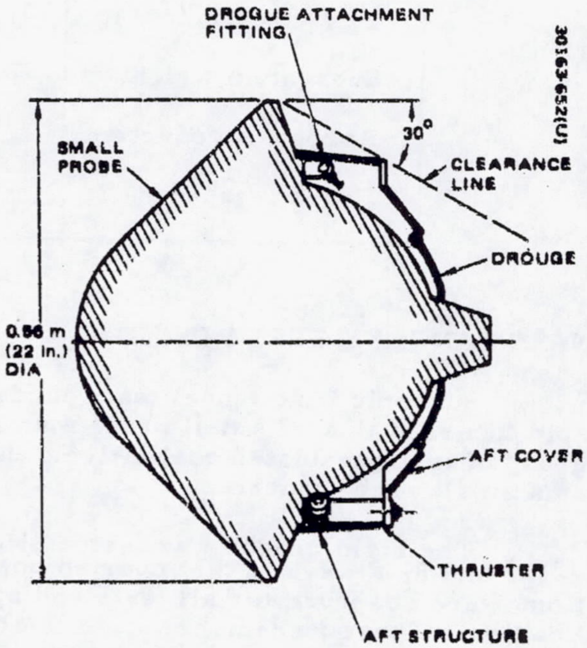

FIGURE E-5. DROGUE CONCEPT B

TABLE E-3. RIGID DROGUE CONCEPT WEIGHT STATEMENT

Item	Weight, g	Weight, lb
Drogue	136.0	0.3
Aft structure	317.8	0.7
Aft cover	272.0	0.6
Release mechanism	45.4	0.1
Thruster (3)	408.6	0.9
Bridle	181.6	0.4
Swivel	90.8	0.2
Riser line	136.0	0.3
Harness	181.6	0.4
P/V electronics	454.0	1.0
Subsystem weight	2.224	4.9
Aeroshell reduction	1.497	3.1
Probe increase	0.82	1.8

NASA LANGLEY TEST RESULTS

Subsonic wind tunnel tests conducted in the NASA Langley vertical spin tunnel evaluated small probe stability during terminal flight. The last group of tests evaluated qualitatively the effect of both rigid and cloth drogues on a small probe model.

The rigid drogue was tested at varying X/D BASE values between 2-1/2 and 8, always in the inverted position. High frequency drogue oscillations were observed for all tests and appeared to be independent of wake location. These were not carried totally into the model, however, due to the damping available from the riser line. Model angle of attack was affected by the drogue up to a maximum excursion of ±5 deg. Average rigid drogue drag coefficient from these tests was 0.52 with a ±10 percent estimated tolerance.

A solid flat circular parachute having a D_O = 25.4 cm (10 in.) was tested at an X/D_B of 5. Having very little geometric porosity, the parachute attempted to trim at approximately ±20 deg angle of attack. These high angle oscillations produced vehicle angles of attack in the 10 to 15 deg range. Parachute motions were shown not to be wake dependent in a subsequent test in which the same motions were observed with lead weight suspended from the parachute. Average drag coefficient on the solid flat circular parachute was 0.42, also having a ±10 percent tolerance.

A high geometric porosity drogue was then tested at the same relative location as that discussed above to evaluate the effect on parachute stability. Some high frequency oscillations were observed although the amplitude was significantly reduced compared to that of the solid flat circular parachute.

All of the above tests were conducted using a single-point vehicle attachment. A marked improvement in vehicle motion occurred when a three-point attachment was introduced. Not only were vehicle induced angles of attack reduced, but in addition the high spin rate large angle of attack motion was damped much faster.

CONCLUSIONS

Of the two auxiliary stabilization devices examined, the parachute appears most attractive, due largely to the cleaner deployment afforded by a mortar compared to three pyro thrusters and the greater experience base existing on a parachute compared to a rigid device.

Although total development costs have been estimated at $500K for either design, it is thought that guaranteeing simultaneity on the pistons would increase costs. Weight comparisons show a 0.408 kg (0.9 lb) advantage for the parachute.

It should be noted that current vehicle motion predictions for the Atlas/Centaur small probes indicate no need for auxiliary stabilization. Furthermore, if such a device were added, overall system reliability would be degraded due to increased complexity. Thus, with the decision to go to an Atlas/Centaur booster with its increased flexibility for larger base diameters and hence c.g. location, the need for auxiliary stabilization devices has been eliminated.